N°d'ordre NNT : 2022LYSEI040

THESE de DOCTORAT DE L'UNIVERSITE DE LYON
opérée au sein de
INSA Lyon

Ecole Doctorale N° 162
Mécanique, Energétique, Génie civil, Acoustique (MEGA)

Spécialité/ discipline de doctorat :

Mécanique

Soutenue publiquement le 10/05/2022, par :
Nathalie Casas

Insights on the behavior of fault gouges during seismic sliding: a numerical investigation from granular rheology to friction laws

---

Devant le jury composé de :

NICOT, François	Directeur de Recherche	Univ. Savoie Mont Blanc	Président du jury
MARONE, Chris	Professor	La Sapienza – Italy	Rapporteur
RADJAÏ, Farhang	Directeur de Recherche	CNRS – Montpellier	Rapporteur
VIOLAY, Marie	Assistant Professor	EPFL – Switzerland	Examinatrice
MORGAN, Julia K.	Professor	Rice University – US	Examinatrice
BAYART, Elsa	Chargée de Recherche	CNRS – ENS Lyon	Examinatrice
NICOT, François	Directeur de Recherche	Univ. Savoie Mont Blanc	Examinateur
DAOUADJI, Ali	Professeur	INSA Lyon	Directeur de thèse
MOLLON, Guilhem	Maitre de conférences	INSA Lyon	Co-directeur de thèse
BLAISONNEAU, Arnold	Docteur	BRGM – Paris	Invité

Administrative document

Département FEDORA – INSA Lyon - Ecoles Doctorales

SIGLE	ECOLE DOCTORALE	NOM ET COORDONNEES DU RESPONSABLE
CHIMIE	**CHIMIE DE LYON** **https://www.edchimie-lyon.fr** Sec. : Renée EL MELHEM Bât. Blaise PASCAL, 3e étage secretariat@edchimie-lyon.fr	**M. Stéphane DANIELE** C2P2-CPE LYON-UMR 5265 Bâtiment F308, BP 2077 43 Boulevard du 11 novembre 1918 69616 Villeurbanne **directeur@edchimie-lyon.fr**
E.E.A.	**ÉLECTRONIQUE, ÉLECTROTECHNIQUE, AUTOMATIQUE** **https://edeea.universite-lyon.fr** Sec. : Stéphanie CAUVIN Bâtiment Direction INSA Lyon Tél : 04.72.43.71.70 secretariat.edeea@insa-lyon.fr	**M. Philippe DELACHARTRE** INSA LYON Laboratoire CREATIS Bâtiment Blaise Pascal, 7 avenue Jean Capelle 69621 Villeurbanne CEDEX Tél : 04.72.43.88.63 **philippe.delachartre@insa-lyon.fr**
E2M2	**ÉVOLUTION, ÉCOSYSTÈME, MICROBIOLOGIE, MODÉLISATION** **http://e2m2.universite-lyon.fr** Sec. : Sylvie ROBERJOT Bât. Atrium, UCB Lyon 1 Tél : 04.72.44.83.62 secretariat.e2m2@univ-lyon1.fr	**M. Philippe NORMAND** Université Claude Bernard Lyon 1 UMR 5557 Lab. d'Ecologie Microbienne Bâtiment Mendel 43, boulevard du 11 Novembre 1918 69 622 Villeurbanne CEDEX **philippe.normand@univ-lyon1.fr**
EDISS	**INTERDISCIPLINAIRE SCIENCES-SANTÉ** **http://ediss.universite-lyon.fr** Sec. : Sylvie ROBERJOT Bât. Atrium, UCB Lyon 1 Tél : 04.72.44.83.62 secretariat.ediss@univ-lyon1.fr	**Mme Sylvie RICARD-BLUM** Institut de Chimie et Biochimie Moléculaires et Supramoléculaires (ICBMS) - UMR 5246 CNRS - Université Lyon 1 Bâtiment Raulin - 2ème étage Nord 43 Boulevard du 11 novembre 1918 69622 Villeurbanne Cedex Tél : +33(0)4 72 44 82 32 **sylvie.ricard-blum@univ-lyon1.fr**
INFOMATHS	**INFORMATIQUE ET MATHÉMATIQUES** **http://edinfomaths.universite-lyon.fr** Sec. : Renée EL MELHEM Bât. Blaise PASCAL, 3e étage Tél : 04.72.43.80.46 infomaths@univ-lyon1.fr	**M. Hamamache KHEDDOUCI** Université Claude Bernard Lyon 1 Bât. Nautibus 43, Boulevard du 11 novembre 1918 69 622 Villeurbanne Cedex France Tél : 04.72.44.83.69 **hamamache.kheddouci@univ-lyon1.fr**
Matériaux	**MATÉRIAUX DE LYON** **http://ed34.universite-lyon.fr** Sec. : Yann DE ORDENANA Tél : 04.72.18.62.44 yann.de-ordenana@ec-lyon.fr	**M. Stéphane BENAYOUN** Ecole Centrale de Lyon Laboratoire LTDS 36 avenue Guy de Collongue 69134 Ecully CEDEX Tél : 04.72.18.64.37 **stephane.benayoun@ec-lyon.fr**
MEGA	**MÉCANIQUE, ÉNERGÉTIQUE, GÉNIE CIVIL, ACOUSTIQUE** **http://edmega.universite-lyon.fr** Sec. : Stéphanie CAUVIN Tél : 04.72.43.71.70 Bâtiment Direction INSA Lyon mega@insa-lyon.fr	**M. Jocelyn BONJOUR** INSA Lyon Laboratoire CETHIL Bâtiment Sadi-Carnot 9, rue de la Physique 69621 Villeurbanne CEDEX **jocelyn.bonjour@insa-lyon.fr**
ScSo	**ScSo*** **https://edsciencessociales.universite-lyon.fr** Sec. : Mélina FAVETON INSA : J.Y. TOUSSAINT Tél : 04.78.69.77.79 melina.faveton@univ-lyon2.fr	**M. Christian MONTES** Université Lumière Lyon 2 86 Rue Pasteur 69365 Lyon CEDEX 07 **christian.montes@univ-lyon2.fr**

*ScSo : Histoire, Géographie, Aménagement, Urbanisme, Archéologie, Science politique, Sociologie, Anthropologie

Abstract

The fault gouge, generated by the wear of previous slips, plays a key role in the slip stability and weakening mechanisms of a fault. For a sheared gouge, physicochemical transformations such as rock dissolution or high-temperature fusion can occur. The latter can give rise to infill materials that lodge within the pores of the gouge and strongly impact the mechanical and rheological behavior of the fault. Through this thesis work, three 2D models of sheared gouges were proposed using the Discrete Element Method for a thorough understanding of : (i) how infill materials (matrix or cement) participate in the weakening of the fault during a slip reactivation, (ii) the rheological behavior observed through the formation of shear bands and its link with the physical and mechanical characteristics of the gouges, (iii) the contribution of each of these properties in the breakdown energy and friction laws observed. A first model highlights three types of cemented materials with different rheological behaviors and shearing resistance, depending on the initial surface percentage of cementation. This study also leads to a redrawing of the breakdown energy dissipated by the fault considering the three mechanisms involved in gouge shearing: fault dilation, Coulomb friction, and the cemented bond failure. Then, a material only consisting of the "matrix" element is modeled to highlight the relationship between the intrinsic properties of the matrix and its rheological behavior. The importance of the percentage of matrix present within the gouge is evaluated in a third model. Finally, we detail an energetic method to link the evolution of each deformation band (Riedel bands) with the behavior of the entire gouge. The friction laws resulting from these models can be used in larger-scale dynamic models to study fault seismic and aseismic behavior.

Résumé

La gouge de faille, créée par l'usure des précédents glissements, joue un rôle prépondérant dans la stabilité des glissements et les mécanismes d'affaiblissement d'une faille. A cela peuvent s'ajouter des transformations physico-chimiques telles que la dissolution ou encore la fusion à haute température. Ces dernières peuvent donner naissance à des matériaux de remplissage se logeant dans les pores de la gouge et impactant le comportement mécanique et rhéologique de la faille. Au cours de ce travail de thèse, des modèles 2D (Méthode des Eléments Discrets) de gouges cisaillées ont été proposés pour mieux comprendre : (i) comment les matériaux de remplissage (matrice, ciment) participent à l'affaiblissement de la faille lors d'une réactivation de glissement, (ii) le comportement rhéologique observé à travers la formation de bandes de cisaillement et son lien avec les caractéristiques physiques et mécaniques des gouges, (iii) la contribution de chacune de ces propriétés dans l'énergie de rupture et les lois de frottement observées. Un premier modèle met en avant trois types de matériaux cimentés montrant des comportements rhéologiques et de résistance aux glissements différents en fonction du pourcentage de cimentation. Cette étude donne lieu à un nouveau découpage de l'énergie de fracture considérant trois mécanismes : la dilatance de la faille, les frottements de Coulomb et la rupture des liaisons cimentées. Ensuite, un matériau uniquement constitué de l'élément « matrice » est modélisé pour mettre en évidence la relation entre les propriétés intrinsèques de la matrice et son comportement rhéologique. L'importance du pourcentage de matrice présent dans la gouge est évaluée dans un 3ème modèle. Nous détaillons finalement une méthode énergétique permettant de relier l'évolution de chaque bande de déformation avec le comportement de la gouge entière. Les lois de frottement issues de ces modèles pourront être utilisées dans des modèles dynamiques à plus grande échelle.

Remerciements

Cette histoire commence alors que je suis embauchée en tant qu'ingénieure dans une entreprise et que je me rends compte que finalement, je retournerais bien faire de la recherche… Et surtout de la recherche en cohérence avec mes valeurs : pouvoir utiliser la mécanique pour comprendre la Terre ! Je me suis souvenue qu'un de mes anciens professeurs avait fait un super cours sur les matériaux granulaires…Je l'ai donc contacté pour savoir si par hasard, il avait de la place pour une thèse. Merci Guilhem (mon co-directeur) pour m'avoir accueilli à bras ouvert dès mon premier mail de recherche de Thèse, pour m'avoir aidé et préparé à obtenir une bourse doctorale à l'INSA de Lyon. Un grand merci Ali (mon directeur) pour m'avoir fait confiance dès le début sur un sujet nouveau pour moi (et un peu pour vous deux aussi ?) et pour toutes les discussions intéressantes que l'on a eu pendant la Thèse et ton aide au cours de mon parcours de doctorante. Le sujet a beaucoup évolué depuis le début où nous avions des grands projets sur des modèles complexes, et surtout un lien avec la sociologie sur la perception de la géothermie profonde par les habitants ! Merci Jean-Yves Toussaint pour ta patience et toutes ces discussions sociologiques sur le rôle du chercheur et le lien avec les objets que l'on a eu au début de ma thèse. Merci aussi Yann Voisin pour ces très enrichissants échanges entre anthropologie et sciences dures. Mais je voulais remercier Guilhem encore une fois, pour son aide inépuisable, sa patience, sa disponibilité (presque) sans limite, les relectures de papiers… et toutes les discussions que l'on a eu au bureau, en conférence, autour d'un verre. J'ai vraiment eu l'impression de faire partie d'une équipe et je te remercie pour ça !

I wanted to thank again all the defense committee members for agreeing to be part of my thesis jury and for granting me the title of Doctor. A first thanks to Ali Daouadji and Guilhem Mollon obviously, without whom I would not have made it this far…A special thanks to the two rapporteurs Farhang Radjai and Chris Marone who allowed me to defend my Thesis, with very positive reports on my manuscript and research. Thank you Françoit Nicot for being the president of the jury and for your touching speech after the jury's deliberation. Thank you Julia Morgan, Elsa Bayart, and Marie Violay, for your implication, interest, and kind remarks on my research work. We can also note that we were almost at equal parity if I count myself, which is rarely the case, especially in Mechanics...Thanks to all of you for all the positive comments you made about my work and presentation and for the very interesting questions that were asked after the presentation. I hope to meet you again at conferences or further projects, and that we will have the opportunity to discuss other interesting topics.

Après à peine un mois de Thèse, je suis allée en conférence à Lausanne au SEG 2018, où j'ai pu, entre autres, faire la connaissance d'une des équipes du BRGM avec qui je suis restée en contact tout au long de ma thèse. Merci à Arnold, Julie et Théophile pour les nombreux échanges et présentation à Paris ou en visio, j'espère que l'on pourra poursuivre cela dans les années qui viennent.

Bien sur la réussite de cette thèse est aussi due à toutes les belles personnes qui composaient mes deux laboratoires de recherche le LaMCoS et GEOMAS. Merci à la team doctorants

LaMCoS, pour la bonne humeur, la bonne ambiance de travail, les sorties extérieures, diner, jeux, laser Game et j'en passe ! Merci Lucas mon collègue de bureau depuis le 1er jour et jusqu'à la fin, pour les discussions scientifiques, mais aussi politiques, sociologiques, les sorties concerts, les bars …pour avoir été là pour les meilleurs moments et aussi pour écouter mes plaintes tous les jours, désolée si je t'ai empêché de travailler quelques fois… Merci Anaïs, pour tous les petits moments, à discuter ensembles, les concerts, ma compagne de gossip forever. Merci Marjolaine, pour ton écoute et ta bienveillance, et d'être toujours là pour nous. Merci Olivier, fidèle compagnon de MELODY, toujours serviable, toujours de bonne humeur, et toujours prêt pour la pause de 16h ! Merci Alejandro, Bilel, Lucas, Julien, Fan, Georges, et Maxence pour ces quelques années (ou mois) passés dans le même bureau ! C'était fun, c'était studieux, c'était incroyable, vous allez me manquer…Merci Adriana, pour ces quelques années, les repas avec les italiens, les discussions et d'être toujours une bonne amie. Merci Pierrick, l'ancien, pour tous les moments partagés au bureau comme en dehors… Toujours à fond, toujours là pour discuter et encore aujourd'hui. Merci aussi à Valentin, Emmanuel, Samy, Benoit, Ruibin, Sarra, Martial, Guillaume, Alessandro, Charlotte, Kevin, Tudor, Alyzée, pour toutes les belles discussions scientifiques et moments partagés. Merci aussi à toute l'équipe des doctorants GEOMAS, Joao, José, Thomas, Adnan, Rosy, Nicole, Janet, Nour, pour votre bel accueil et les repas partagés, même si l'on se voyait moins souvent. Spécial remerciement pour Joao, pour les discussions « scientifiques » de qualité…ils sont sympas les brésiliens quand même :) Merci aussi à tous les permanents/personnels des Labos pour les supers moments, climats, scientifiques, personnels, musicaux : Aurélien S., Nathalie B., Amandine P., Laetitia M., Sylvie D., Nicolas F., David P., Arnaud S., Claire S., Manu M., Stéphane G., Eric C., Marion F., Jacques M. et Lionel M.

J'ai eu aussi la chance de faire un ATER à l'ENS Lyon pour finir la fin de ma thèse…Je savais que ça allait être dur, mais c'était EPUISANT, de jongler entre la fin de la rédaction et les cours… bien sur je ne regrette pas du tout, j'ai beaucoup aimé l'ambiance de ce beau laboratoire dans lequel j'ai été très bien accueillie. Merci Frédéric C. et Marianne M. pour m'avoir poussé à candidater. Merci Chloé M. pour ta confiance, j'ai beaucoup aimé partager ces cours de mécanique avec toi. Merci Valentin et Alexandra mes collègues d'informatique, quelle équipe ! Big thanks pour Delphine pour ta gentillesse et ton aide quand je suis arrivée. Et merci à tous les doctorants et assimilés, pour les moments passés et à venir : Samuel, Jean, Chloé, PJ, Valentin, Valentine, Danaé, Alexandra, Asma, Laetitia, Robin, Marwane, Line, Mathilde, Marianne, Enguerrand, Salomé et Delphine.

Merci à tous mes amis lyonnais, grenoblois, parisiens, bordelais, allemand, anglais, les campagnards, pour avoir été là ces dernières années, et pour avoir été un petit bol d'air au milieu des difficultés de la fin de thèse. Merci Morgane, toi qui es là depuis si longtemps et qui est toujours aussi incroyable d'année en année. Un spécial remerciement à mes amis de l'INSA, les zik'et, 10 ans déjà, toujours là et en plus en musique. Merci à tous mes amis de la Chorue, pour votre belle prestation pour mon pot de thèse, et pour tous les moments partagés ces dernières années, qu'est-ce que c'est bien de chanter avec vous.

Merci aussi à ma famille, de m'avoir soutenue, encouragée et accompagnée durant ces presque 4 années, et sans qui je ne serai pas là : Alain, Brigitte, Emile, Thibaud et Pauline. Et à mes grands-parents, partis trop tôt et qui n'ont pas pu voir l'aboutissement de mon parcours…

Et pour finir, merci au plus beau, mais surtout à celui qui m'a supporté au quotidien pendant toute ma thèse, saute d'humeur, fatigue, manque de confiance en moi, stress et j'en passe… Merci beaucoup Noé, d'être la personne que tu es, de m'avoir fait confiance et de continuer à me suivre dans mes aventures de recherche, qui sait où ça va nous mener… ?

Le 24/05/2022

Nathalie Casas

Résumé étendu

Introduction générale

Cette thèse académique a pour objectif d'apporter une contribution à des questions posées dans le cadre des grands enjeux sociétaux actuels. Alors que les modèles urbains sont de plus en plus repensés pour répondre à la croissance démographique et à la transition énergétique, il est important de disposer d'une production d'énergie durable et fiable ayant un faible impact sur l'environnement et l'Homme. La géothermie profonde (EGS) permet une continuité temporelle de la production par rapport à d'autres sources d'énergie renouvelables intermittentes. Elle pourrait contribuer à répondre à la demande d'énergie actuelle, mais semble faire l'objet de controverses en raison de la sismicité induite observée dans certains projets (Grigoli et al., 2017). Lors des séismes naturels, le glissement par frottement libère l'énergie accumulée dans le milieu environnant d'une faille. En fonction des conditions de pression et de température dues à la profondeur de la faille, les processus de rupture peuvent se dérouler : de manière lente et continue, réduisant la probabilité qu'une instabilité sismique se produise ou de manière rapide et brutale pouvant générer un fort glissement sismique. Les séismes induits sont régis par les mêmes lois physiques, mais sont en partie générés par les technologies et infrastructures de géo-ingénierie qui peuvent modifier le champ de contraintes environnant d'une faille. Que l'on soit dans le cas d'un séisme naturel ou induit, une gouge de faille est identifiée comme le matériau d'usure issu des précédents glissements. Elle contribue à la stabilité du glissement et joue un rôle prépondérant dans la libération d'énergie lors du relâchement des contraintes accumulées dans la faille. Au sein d'une gouge de faille mature, la cimentation minérale provenant de la dissolution de la roche, de la fusion, ou des particules de matrice issues de la fragmentation de glissements antérieurs, peuvent remplir les espaces poreux restants entre les particules et modifier l'état global de cohésion du matériau. Ces phénomènes donnent naissance à un nouveau matériau granulaire plus résistant combinant son histoire, l'état de la densité initiale, et le matériau de remplissage présent au sein de la gouge de faille.

L'objectif principal de cette thèse est d'étudier le comportement des matériaux de remplissage (ciment et matrice) présents dans les failles à des profondeurs proches de celles observées dans les systèmes de géothermie profonde. Les gouges de faille sont ensuite modélisées grâce à un modèle numérique permettant d'étudier le comportement granulaire de la gouge et de ses matériaux de remplissage (Chapitre 2). Un premier modèle numérique permet d'étudier le rôle que joue la cimentation dans l'affaiblissement des gouges de failles matures, en regardant notamment si les matériaux cimentés favorisent ou non les glissements dans les failles (Chapitre 3). Grâce à ces résultats, il a ensuite été possible de décomposer l'énergie de rupture libérée pendant le glissement et proposer une loi de frottement pour décrire le comportement de ces matériaux cimentés (Chapitre 5, Partie B). Un deuxième modèle numérique permet cette fois de focaliser sur le rôle que jouent les particules de matrices dans le comportement d'affaiblissement des gouges de failles matures et plus particulièrement sur l'importance des différentes caractéristiques physiques et géométriques de la matrice dans le comportement de glissement observé (Chapitre 4, Partie A). Il est également étudié dans quelle mesure la

proportion de matrice ou de grain angulaire influe sur le comportement d'affaiblissement de la faille (Chapitre 4, Partie B). Il s'agit ensuite de pouvoir relier directement le comportement de chaque bande de cisaillement observée dans les gouges de faille au comportement global de la gouge (Chapitre 5, Partie C). Une comparaison des différents résultats obtenus dans les différents modèles numériques avec le modèle classique de slip weakening linéaire est ensuite réalisée (Chapitre 5, Partie A). Le travail de Thèse a été limité à des cas de frottement sec, c'est-à-dire sans considérer de fluide.

Ce travail de thèse résumé dans ce qui suit est schématisé par la Figure 1 suivante :

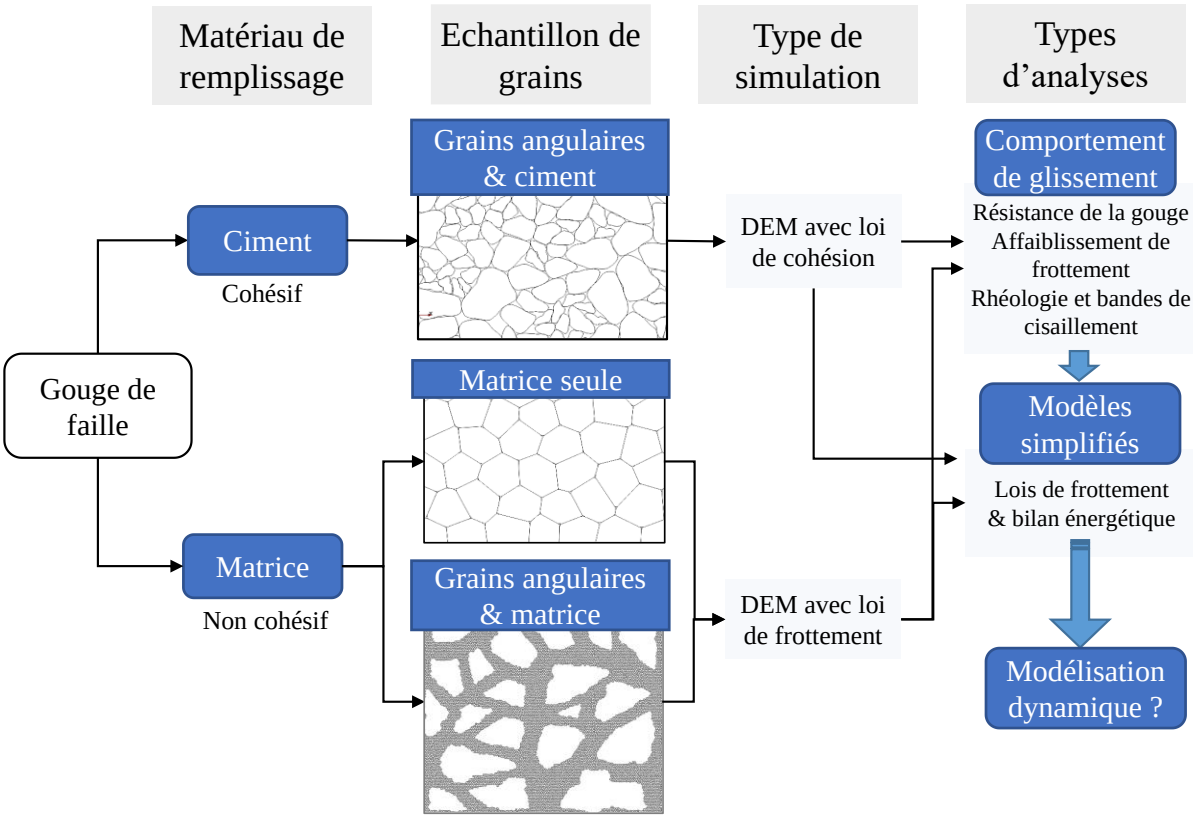

Figure 1. Schéma principal de la thèse. La colonne « Matériau de remplissage » décrit les deux matériaux de remplissage étudiés « ciment » et « matrice ». La colonne « Echantillon de grains » décrit les trois échantillons générés pour la thèse et ensuite insérés dans le modèle numérique. La colonne « Type de simulation » présente les 2 types de lois de contact utilisées et la colonne « type d'analyses » ce qui a été étudié pour chaque combinaison d'échantillon + simulation.

Chapitre 1 : Etat de l'Art et Stratégie de recherche

Dans les deux premières parties, ce chapitre donne un aperçu des concepts fondamentaux et des avancées récentes dans la compréhension des tremblements de terre et de la mécanique des failles. La troisième partie se concentre sur la gouge de faille, cœur de la thèse, ainsi que sur ses propriétés mécaniques et rhéologiques. Elle décrit aussi les matériaux de remplissage (matrice ou ciment) présents dans la gouge et leur influence sur le comportement de la faille. Enfin elle introduit également la stratégie de recherche adoptée pour la thèse et les possibilités de modélisation numérique existantes. Pourquoi la gouge de faille est-elle si importante ? Elle est d'abord considérée comme un matériau d'usure issu des différents glissements entre les

parois de la faille. La gouge est aussi importante car elle fait le lien entre la tribologie et la mécanique des faille grâce à la théorie du troisième corps et des modèles d'usure : même sans la présence de fluide, la gouge joue un rôle de lubrification dans le contact, Figure 2. Dans le cadre de cette thèse, il a été décidé de rester dans le régime de lubrification limite, qui est le contact solide-solide classique (pas de lubrifiant liquide, contact sec). La gouge de faille est définie comme des particules d'usure, similaire au processus de production du 3ème corps. Un autre objectif est de reproduire des grains réalistes dans la gouge avec des formes angulaires et à facettes telles qu'on les trouve dans le cœur de la faille [(Olgaard & Brace, 1983), (Lin, 1999)].

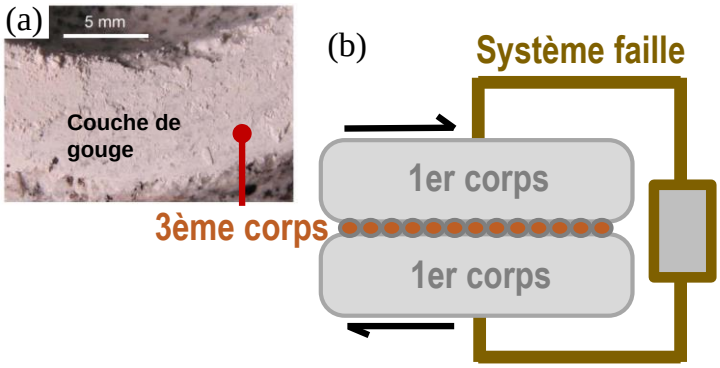

Figure 2. Schéma de représentation de la théorie du troisième corps et lubrification par poudre. (a) Surface de glissement avec gouge adhérente et couche de gouge, provenant du granite Sierra White en cisaillement rotatif. Image tirée de (Reches & Lockner, 2010), (b) Schéma de la théorie du troisième corps appliquée au système de la faille.

Les mécanismes de déformation des gouges de faille sont des éléments clé dans la compréhension du comportement des failles. Les zones de déformation sont des structures complexes qui présentent des cinématiques et géométries variables en fonction du mécanisme de déformation adopté et des caractéristiques de la roche. Pour un système de failles suffisamment mature (couche de gouge suffisamment épaisse), la localisation du cisaillement a été observée selon des angles spécifiques, et appelée « bandes de cisaillement de Riedel », ou bandes de déformation cataclastiques, (Tchalenko, 1970). Elles reflètent un champ de contraintes hétérogènes se développant en réponse à la déformation [(Marone & Scholz, 1989), (Morgan & Boettcher, 1999), (Kaminskaite et al., 2019)]. La présence de ces bandes de Riedel a été identifiée comme pouvant être responsable d'un affaiblissement mécanique [(Gu & Wong, 1994), (Beeler et al., 1996)] et comme étant un indicateur d'un changement de stabilité dans le glissement (Byerlee et al., 1978). Il est donc essentiel d'étudier le moment de leur formation au cours du glissement et leur orientation. Le lien entre l'orientation des bandes de Riedel et les schémas de glissement n'est pas encore totalement compris. Une partie de la thèse sera donc consacrée à l'étude de la temporalité des bandes de Riedel en fonction des caractéristiques des gouges. Le mécanisme de glissement étudié a lieu dans une faille mature, c'est-à-dire après de nombreux glissements successifs au cours des temps géologiques précédents. Cette faille a pu avoir été cimentée, ou remplie de particules de matrice, au cours du temps sans glissement (par exemple, dans une période inter-sismique). On peut donc affirmer que l'on étudie la réactivation d'une zone de faille remplie de gouge, sans étudier le processus de fragmentation qui est notre point de départ. Deux types de gouges sont considérées, contenant des matériaux de remplissage (matrice ou ciment) qui peuvent se former dans la zone de faille. La « cimentation minérale »,

désigne un matériau cristallin provenant de la dissolution ou de la précipitation de la roche (Walderhaug, 1994), de la fusion partielle (pseudotachylite, matériau non cristallin), [(Di Toro et al., 2009), (Fondriest et al., 2020)] ou d'autres processus dérivés de glissements antérieurs, c'est un matériau à nature cohésive. En revanche, le terme « Matrice » désigne ici les très fines particules sans cohésion, produites par une comminution locale ou par l'introduction d'autres sédiments [(Lee & Kim, 2005), (Woodcock & Mort, 2008)]. Les particules de matrice sont en partie similaires à un matériau granulaire à haute dimension fractale et présentent les mêmes conséquences mécaniques (zone granulaire plus dense avec réduction de la porosité).

Afin d'observer le comportement de ces matériaux de remplissage au sein d'une gouge cisaillée, un modèle numérique est utilisé avec la méthode des éléments discrets (DEM) en 2D. Le premier objectif est de modéliser une seule portion de faille composée d'une gouge granulaire, suffisamment grande pour observer les déformations de cisaillement. L'intérêt est également de pouvoir modéliser les phénomènes se produisant à l'échelle du grain, en représentant le ciment et la matrice remplissant les pores autour des particules de gouge. La modélisation numérique permet d'accéder facilement aux deux échelles sans avoir à construire un système d'observation complexe. La méthode des éléments discrets (DEM) est également utilisée pour comprendre la physique granulaire de la gouge de faille en étudiant les interactions entre les grains et leur influence sur les mécanismes de glissement. L'intérêt est également de partir d'une configuration granulaire initiale identique et de pouvoir facilement faire varier la quantité de matrice et de ciment présente dans les échantillons de gouge pour tester une large gamme de comportements différents. L'utilisation d'un modèle numérique permet également de quantifier et de suivre l'évolution des liens cohésifs créés entre les grains au cours du temps, car de telles données sont difficiles à voir ou à suivre lors d'une expérience en laboratoire ou *in situ*.

Chapitre 2 : Modèle numérique et méthodes

La Méthode des Eléments Discrets (DEM) est utilisée en mécanique des failles pour comprendre les propriétés de frottement et de contact du cœur de la faille [(Morgan & Boettcher, 1999), (Da Cruz et al., 2005), (Cho et al., 2008), (Dorostkar et al., 2017a), (Mollon et al., 2021b)]. Elle permet de décrire l'écoulement d'un matériau granulaire où chaque particule a ses propres déplacements et interactions avec les autres particules. Le code utilisé pour les simulations de cette Thèse, MELODY 2D (Multibody ELement-free Open code for DYnamic simulation), est un code C++ permettant de simuler une grande variété de milieux granulaires en 2 dimensions [(Mollon, 2016), (Mollon, 2018a)]. Un des intérêts de ce code est sa capacité de prise en compte des formes de grains angulaires grâce à un algorithme de contact en 3 étapes qui peut traiter une large variété de complexités de forme et d'anisotropie.

Dans le cadre du travail de Thèse, des corps rigides sont utilisés pour les grains de la gouge de faille et les parois rocheuses. Ces corps sont caractérisés par leur masse et leur inertie de rotation avec 3 degrés de liberté (deux en déplacements et un en rotation pour la modélisation 2D). Le contour des particules est alors une succession de nœuds et de segments de contact permettant l'application de lois de contact spécifiques. Les travaux de Thèse étant axés plus particulièrement sur l'étude des matériaux de remplissage, l'objectif est de pouvoir modéliser des particules matricielles ou cimentées. Deux lois de contact sont alors considérées : (a) une loi de contact de type Damped-Mohr-Coulomb (utilisée dans le chapitre 4 pour les particules

de la matrice), qui est une loi de DEM classique avec un frottement inter-particulaire uniquement entre les particules en contact, et (b) une loi de contact de type Bonded Mohr-Coulomb avec un frottement inter particulaire et une cohésion. Cette loi de contact est similaire au modèle de particules liées (utilisé au chapitre 3 pour les particules cimentées).

Le package Matlab « Packing2D » permet de créer des milieux granulaires avec des formes de particules angulaires et à facettes, qui restent complexes à générer directement à partir du code DEM. Le logiciel est basé sur une méthode Fourier-Voronoï qui génère un ensemble de grains avec une distribution de taille définie par l'utilisateur. Il est aussi possible de contrôler les descripteurs morphologiques des grains tels que l'élongation, la circularité et la rondeur. Ce contrôle est effectué en choisissant un spectre de Fourier qui quantifie les fréquences et les amplitudes des aspérités de la surface des grains. Une transformation de Fourier inverse permet alors de passer du spectre représentant le contour d'une particule à la vraie forme de la particule. De plus amples informations sont disponibles dans (Mollon & Zhao, 2012). Trois différents échantillons granulaires sont conçus pour la thèse grâce à ce code, Figure 3: (a) un échantillon de gouge avec des grains angulaires seuls, (b) un échantillon de gouge avec des grains de matrices seuls et (c) un échantillon de gouge composé de grains angulaires et de grains de matrices.

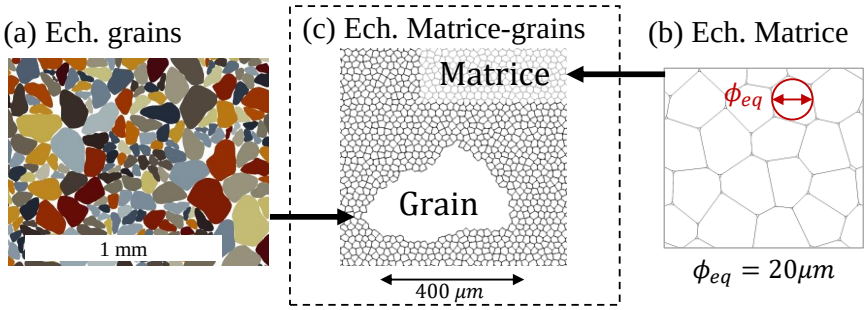

Figure 3. (a) Zoom sur un échantillon granulaire généré avec Packing2D, avec des formes angulaires et à facettes. (b) Zoom sur un échantillon de matrice généré avec Cvoro_2D, avec des formes hexagonales modifiées (c) Zoom sur l'échantillon fusionné entre les cellules matricielles et les particules angulaires. Pour ce dernier type d'échantillon, les cellules matricielles ont un diamètre équivalent $\phi_{eq} = 20\ \mu m$ et une perturbation $P_{0.i} = 0.5$.

Après avoir été soumis à une compaction uni-axiale pour avoir un échantillon de gouge stabilisé, ces trois échantillons sont ensuite insérés dans le modèle de faille DEM créé sous MELODY2D (Figure 4). Tous les modèles utilisés dans la Thèse présentent la même structure et les mêmes paramètres externes : la paroi inférieure est fixe, tandis qu'une contrainte normale σ_N (direction y) et une vitesse de cisaillement V (direction x) sont appliquées sur la paroi rocheuse supérieure. La gravité est ignorée dans le modèle, en supposant que la faille peut être orientée dans une large gamme de directions, et que les forces de gravité sont négligeables par rapport à celles liées aux contraintes normales et déviatoriques appliquées sur la faille. Des conditions aux limites périodiques sont présentes sur les côtés droit et gauche de l'échantillon pour maintenir la continuité du mouvement lors de grands glissements. Le mouvement de la paroi rocheuse supérieure dans la direction y reste libre pour tenir compte de la dilatation ou de la compaction de l'échantillon.

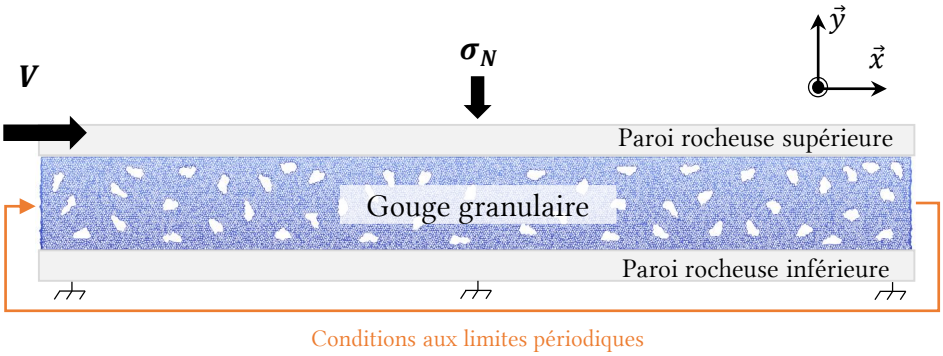

Figure 4. Schéma du modèle DEM d'une gouge de faille granulaire cisaillée. Un modèle de contact sec est considéré ici. La gouge de faille et les parois rocheuses sont considérées comme rigides avec une raideur numérique constante et utilisée pour limiter l'interpénétration entre les grains. Dans cette étude, une densité de 2600 kg/m^3 est utilisée pour les particules, ce qui conduit à un pas de temps approprié pour ces simulations de 10^{-9} s. Un solveur explicite est utilisé.

En raison de la complexité des paramètres intervenant dans le comportement des gouges de faille il a été décidé de fixer certains paramètres physiques. Suite aux études préliminaires réalisées, la contrainte normale appliquée sur la faille a été fixée à 40 MPa correspondant à une profondeur d'environ 1.5 km (début de la zone sismogénique naturelle et profondeur intéressante pour la géothermie profonde). Afin d'avoir des résultats observables dans un temps de calcul raisonnable tout en évitant de perturber les effets inertiels, une vitesse de cisaillement de 1 m/s a été choisie pour le reste de la Thèse. Il a aussi été confirmé que la forme des grains a une influence significative sur le coefficient de frottement et le comportement en cisaillement de la gouge, justifiant l'utilisation de grains angulaires à facettes plutôt que de grains circulaires.

Chapitre 3 : Comportement au glissement d'une gouge cimentée cisaillée

Au sein d'une gouge de faille mature, la cimentation minérale provenant de la dissolution de la roche, de la fusion, ou d'autres processus dérivés de glissements précédents, peut remplir les espaces interstitiels restants entre les particules et modifier l'état global de cohésion (Philit et al., 2018). Un modèle de gouge de faille granulaire 2D a été implémenté avec la Méthode des Eléments Discrets (DEM) afin d'établir un lien entre les propriétés de la gouge (cimentation et porosité initiale) et son comportement rhéologique sous cisaillement. L'originalité de ce chapitre réside aussi dans la forme angulaire des particules simulées.

Grâce à une étude préliminaire sur l'influence du frottement inter-particulaire pendant les étapes de compaction et de cisaillement, deux états de porosités initiales ont été retenus : un échantillon de gouge « moyennement dense » avec une porosité initiale de 16 % et un échantillon de gouge « dense » avec une porosité initiale de 11 %. Ces deux échantillons sont ensuite insérés dans le modèle 2D de cisaillement direct et une loi de cohésion est appliquée entre les particules pour venir simuler une cimentation entre les grains (de 0 à 95 % de cimentation). Chaque échantillon est ensuite cisaillé à une vitesse de 1 m/s et sous une contrainte normale de 40 MPa. Pour caractériser les gouges cimentées synthétiques (au sens de Coulomb-Mohr), des simulations biaxiales indépendantes ont aussi été effectuées avec des échantillons de gouge présentant les mêmes caractéristiques que celles utilisées pour les gouges de faille cisaillées. Les gouges simulées présentent des valeurs cohérentes d'angle de frottement interne (entre 30° et 45°) et de cohésion (entre 0 et 70 MPa).

Les différentes simulations ont permis de mettre en évidence un pic de résistance au frottement très élevé et rapide pour les matériaux denses et fortement cimentés, et un pic plutôt lisse, retardé et d'amplitude modérée pour les matériaux moyennement denses et moyennement cimentés. Le caractère fragile des matériaux est renforcé par la présence de cimentation, en particulier dans le cas des matériaux denses. Il évolue de manière similaire à la présence de cohésion interne (Coulomb-Mohr) au sein de la gouge et conduit à trois schémas de rupture différents, Figure 5.

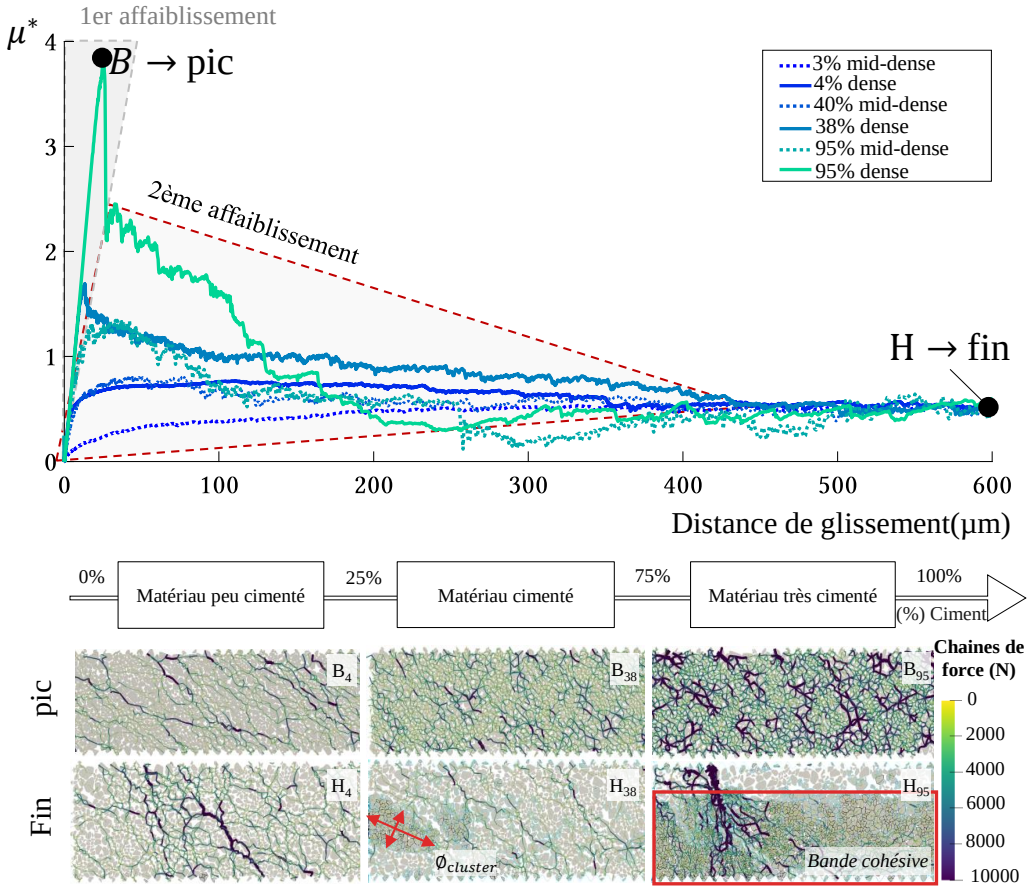

Figure 5. Courbes de frottement macroscopique en fonction de la distance de glissement et images des chaînes de force pour des échantillons denses au pic de frottement [B] et à la fin de la simulation [H] pour 3 cas de cimentation (4%, 40% et 95%). Les chaînes de force sont définies en fonction du niveau de contrainte présent dans le système (ici la contrainte normale appliquée) et l'épaisseur est évaluée entre 0 et 1 entre la force minimale et maximale (0 à 10^4 N). Vue d'un quart de la gouge granulaire.

Le matériau fortement cimenté avec une faible porosité initiale présente une formation claire de bandes de Riedel évoluant comme dans la théorie. Les valeurs élevées de cohésion et d'angle de frottement interne rendent ce matériau très proche des propriétés des roches intactes. En revanche, le matériau le plus faible est obtenu avec l'état de porosité le plus élevé et pour une absence de cimentation : aucun mode de rupture n'est observé et un écoulement de Couette granulaire est mis en évidence.

Les bandes de cisaillement observées nécessitent un taux de dilatation critique de la gouge pour se former. Cette dilatance critique est différente selon la cimentation initialement présente dans la gouge et la porosité initial de l'échantillon : la dilatance critique semble être plus faible pour

les échantillons plus denses et augmente avec la cimentation, alors que les échantillons moyennement denses présentent le comportement inverse.

Les courbes de frottement présentent un double affaiblissement pour les échantillons denses avec suffisamment de cimentation, Figure 5, dû à trois mécanismes différents (frottement, dilatance, rupture des liaisons cimentées). La longueur du pic, distance critique de glissement, diminue principalement avec l'augmentation du pourcentage de cimentation. Les valeurs de frottement au pic, issues du critère de rupture de Coulomb (Byerlee & Savage, 1992) ou du critère de plasticité de Coulomb (Marone et al., 1992), ne prédisent pas très bien les valeurs obtenues pour les gouges de failles cimentées. Ces variations peuvent notamment être dues aux hypothèses de départ différentes utilisées dans chacun des cas.

Les résultats confirment que la porosité initiale et la cimentation influencent le comportement de la gouge. Elles jouent un rôle dans la structure interne et la géométrie de la gouge et modifient ainsi le comportement rhéologique de la faille. Dans la gamme de nos expériences numériques (contrainte normale de 40 MPa et taux de glissement de 1m/s), l'augmentation de la cimentation dans la gouge conduit à une augmentation de la résistance effective alors qu'une augmentation de la porosité initiale tend à une réduction de la résistance.

Chapitre 4 : Rhéologie et affaiblissement du cisaillement d'une gouge de faille avec des particules de matrices

Au sein d'une gouge de faille mature, il est aussi possible d'observer un autre matériau de remplissage, cette fois non cohésif, appelé « matrice ». Il se réfère à des particules très fines produites par fragmentation des roches dû aux précédents glissements dans la faille ou à l'introduction de sédiments dans la gouge de la faille (Woodcock & Mort, 2008). Deux autres modèles de gouge de faille granulaire 2D ont été implémentés en DEM afin d'étudier l'influence des caractéristiques des particules de la matrice sur le comportement rhéologique de la faille, l'évolution des bandes de Riedel et l'influence du pourcentage de matrice/grain dans l'échantillon de gouge.

La **Partie A** présente des échantillons de gouge contenant uniquement des particules de matrice hexagonales dans le but de caractériser ce matériau. Ce milieu granulaire très dense révèle la formation de bandes de Riedel lors du cisaillement. Cette première partie permet de comprendre les schémas de localisation de ces bandes et leur évolution lorsque différentes caractéristiques physiques et géométriques des particules de matrice sont modifiées. La variation des propriétés géométriques (forme, taille et distribution des grains) ou physiques (raideur et frottement inter-particulaire) de la matrice peuvent représenter différentes lithologies rocheuses, avec une grande variété de comportements rhéologiques. Il est apparu que toutes ces variations lithologiques pouvaient être résumées en seulement trois paramètres ayant une influence sur le comportement de glissement et les bandes de Riedel au sein du modèle: (a) le module de cisaillement global de la gouge (modification de la raideur inter-particulaire ou la taille des particules), (b) le rapport entre l'épaisseur de la gouge et la taille des grains (c'est-à-dire le nombre de particules dans l'épaisseur de la gouge), et (c) le frottement inter-particulaire. Une gouge de faille avec un faible coefficient de frottement inter-particulaire, un faible nombre de grains dans l'épaisseur de la gouge ou encore un module de cisaillement élevé présentera, dans les trois cas, une diminution de l'angle d'orientation des bandes de Riedel par rapport à la

direction de cisaillement. Cette réduction d'angle est en partie dû à la présence d'une structure de Riedel avec un grand nombre de bandes de Riedels conjuguées (*R'*) limitant la formation de bande *R* et retardant l'arrivée d'un état stabilisé. Comme l'angle d'orientation des bandes de Riedels peut être considéré comme un indicateur de stabilité pour la gouge de faille granulaire (Moore & Byerlee, 1992), la modification d'un de ces paramètres (a), (b) ou (c) est susceptible de faire passer le comportement de la gouge de faille d'un glissement soudain et sismique à un glissement modéré et lent, ou inversement. Cependant, les conséquences sur la résistance au cisaillement de la gouge, la longueur de nucléation et l'énergie de rupture ne sont pas similaires dans tous les cas et conduisent à différents types de comportement de glissement. Les effets combinés de ces trois paramètres principaux conduisent à différents matériaux de gouge plus ou moins susceptibles de générer des glissements stables ou instables.

La **Partie B** présente quelques résultats sur des mélanges composites entre des grains anguleux entourés de cellules hexagonales représentant la matrice. Elle met en évidence les similitudes et les différences avec le modèle précédent avec uniquement des particules de matrice (Partie A) et avec de la cimentation (Chapitre 3).

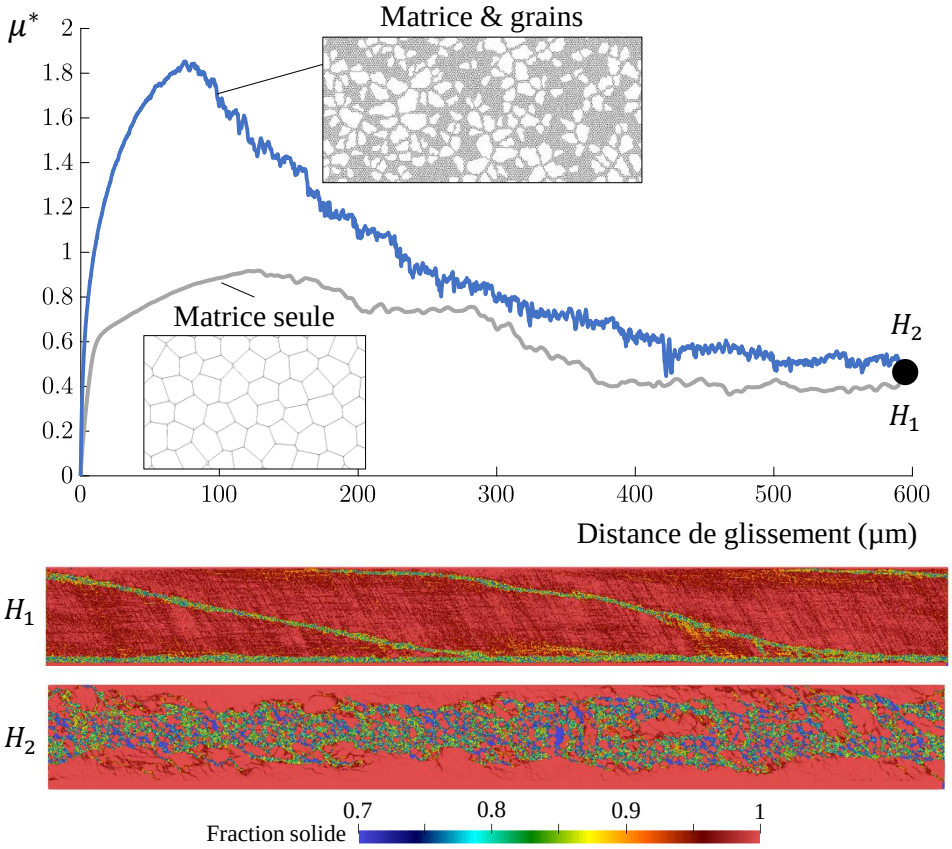

Figure 6. Frottement effectif μ^* en fonction de la distance de glissement (μm) pour deux échantillons granulaires : l'échantillon de gouge standard avec uniquement des particules de matrice et la gouge avec des particules de matrice et une distribution fractale de particules angulaires. H représente une distance de glissement total de la faille de 600 μm. Deux visualisations de l'intérieur de la gouge sont observées grâce à la fraction solide dans l'échantillon H_1 (matrice seule) et H_2 (matrice + grains).

Les essais de cisaillement direct menés sur les mélanges composites montrent clairement que les pourcentages de particules de matrice et de grains angulaires ont une énorme influence sur la mécanique et la rhéologie de la gouge de faille. La présence d'une porosité initiale affecte

également la forme et l'épaisseur des bandes de cisaillement dans les échantillons. L'insertion de particules angulaires dans une gouge initialement composée de cellules matricielles ou, l'ajout de cellules de matrice dans un échantillon granulaire renforce la gouge (pic de frottement plus important), et donne des comportements d'affaiblissement différents selon le type de distribution des particules dans l'échantillon, Figure 6. Dans tous les cas, le radoucissement du frottement par glissement sera plus soudain pour un matériau mixte (matrice + grains) que pour un matériau composé seulement d'un seul type de matériau. Cette variation dans la pente de radoucissement implique également la possibilité de faire évoluer le comportement de la faille vers un glissement sismique. Lorsque que le nombre de particules angulaires est assez élevé, une distribution non homogène des particules dans l'échantillon augmente encore la résistance au cisaillement et l'énergie nécessaire pour affaiblir la faille est beaucoup plus élevée : les bandes de Riedel ne peuvent pas rejoindre les parois rocheuses conduisant à une déformation de toute l'épaisseur de la gouge, Figure 6, H_2. La temporalité de formation des bandes de Riedel dépend elle aussi du pourcentage du matériau matrice dans l'échantillon.

D'autres résultats sont nécessaires pour analyser les différents comportements observés tels qu'une modification de la déformabilité intrinsèque du matériau de la matrice, pour représenter la teneur en argile par exemple.

Chapitre 5 : Du bilan énergétique aux modèles simplifiés, vers les simulations dynamiques

Ce dernier chapitre est à la fois une synthèse des chapitres précédents et une ouverture à donner à la thèse. A partir des résultats des chapitres 3 et 4, et en se focalisant sur les lois de frottement et le bilan énergétique, l'objectif est de définir des lois de frottement caractéristiques de chaque type de matériau de remplissage pouvant être injectées dans un modèle de faille dynamique à grande échelle.

La **Partie A** permet d'étudier plus en profondeur les résultats obtenus dans les chapitres précédents (ciment et matrice), en les interprétant selon un modèle très simplifié tel que le modèle linéaire de radoucisseent par glissement (linear slip weakening). Grâce à cette représentation, il est possible d'extraire la pente de radoucissement associée aux modèles, ce qui donne une information sur la stabilité du système. L'énergie de rupture et la longueur critique de nucléation associées à chaque modèle sont calculées pour être mises en relation avec l'intensité des événements sismiques qui pourraient se produire. Après avoir décrit la méthode utilisée pour récupérer et calculer les différents paramètres, les résultats obtenus pour les différents modèles sont comparés et discutés, en mettant l'accent sur la longueur de nucléation critique associée aux simulations et sur l'influence de chacun des matériaux testés, Figure 7 (a). Les matériaux de remplissage ont un rôle majeur dans la longueur critique de nucléation et l'énergie de rupture libérée. La cimentation à l'intérieur de la gouge semble être le paramètre le plus influent testé. Un matériau cimenté initialement dense aura tendance à avoir une distance de glissement très courte avant que les instabilités ne se produisent (petit L_c) ainsi qu'une énergie de rupture élevée (grand E_G). Même s'ils ont lieu dans une gamme spécifique d'expériences (pression et vitesse de glissement imposées et constantes), les résultats soulèvent la question de la forme de la pente d'affaiblissement du glissement. Il apparaît que seuls les échantillons cimentés moyennement denses et certains échantillons de matrice peuvent être

facilement modélisés avec la forme linéaire classique. Les échantillons cimentés denses présentent une forme bilinéaire décroissante qui peut être comparée à un modèle proposé par (Abercrombie & Rice, 2005). La fracture réelle est bien connue pour être beaucoup plus complexe, mais les modèles complexes sont difficiles à mettre en œuvre. Un équilibre doit être trouvé entre un modèle trop simple et un modèle trop complexe. Pour cette raison, d'autres lois de frottement et d'énergie reliant la rhéologie locale et la mécanique de la gouge sont proposées dans les deux parties suivantes.

La **Partie B** reprend les résultats du Chapitre 3 sur les modèles cimentés. Afin d'isoler les principaux mécanismes agissant sur le processus de fracture, un découpage du frottement macroscopique total généré lors du cisaillement d'un échantillon de gouge granulaire est proposé. Sur la base du contenu physique du modèle numérique utilisé, trois facteurs sont identifiés comme jouant un rôle dans le frottement effectif total et le bilan énergétique, Figure 7 (b) : la **dilatance** de la gouge, ou déformation dans la direction y perpendiculaire au glissement, les **dommages** provenant de la rupture des liens cohésifs dus à la cimentation et le **frottement** généré par les interactions de contact glissant. Cette représentation permet la construction d'un modèle de frottement macroscopique simplifié qui a pour objectif final d'être injecté dans des modèles de rupture dynamique à une échelle supérieure. L'énergie de rupture et le comportement de glissement de la gouge de faille semblent être contrôlés par l'intensité et la temporalité de ces trois mécanismes. L'énergie de rupture est principalement composée de l'énergie liée à la dilatance de l'échantillon, qui a toujours un rôle prépondérant dans les mécanismes de rupture et de propagation des fissures. Selon la porosité initiale de l'échantillon ou le pourcentage de cimentation, l'influence de la dilatation n'est cependant pas similaire et n'induit pas le même comportement mécanique. En effet, le matériau le plus susceptible de générer des instabilités de glissement semble être un matériau dense et cimenté (entre 25 % et 75 % de cimentation) : les agglomérats de particules cohésives générés dans la gouge rendent la faille plutôt hétérogène et augmentent la rugosité dans la faille, ce qui augmente l'énergie de dilatation de manière plus significative et implique une réponse de vitesse de glissement beaucoup plus élevée. Le premier affaiblissement observé est un mélange des trois mécanismes (dilatance, frottements et rupture des liaisons cimentées), et présente une augmentation de l'énergie de frottement avec l'augmentation de la cimentation dû à la réduction du nombre de particules en contact. Les résultats montrent un second affaiblissement, principalement dû à la diminution de l'énergie de dilatance. Les modèles simplifiés proposés sont assez convaincants quant à la forme finale des courbes obtenues et pourraient être adaptés à d'autres contraintes et vitesses imposées. Cependant, la caractérisation des modèles cimentés moyennement denses pourrait être améliorée, car l'énergie totale de rupture ne s'accorde pas très bien avec les données observées.

La **Partie C** est construite sur les résultats du Chapitre 4 Partie A, et présente une analyse spatio-temporelle de l'activation des bandes de Riedel et de leur implication dans le comportement global des gouges de faille. Tout d'abord, il est possible d'observer des variations à la fois globales et locales de l'ouverture et du glissement au sein des bandes de Riedel. L'angle d'orientation de ces bandes peut être différent selon que la zone observée se trouve au centre de la gouge ou près des parois rocheuses. Ensuite, l'évolution temporelle des bandes de Riedel

avec la distance de glissement peut être observée en se focalisant sur la variation globale d'ouverture de chaque bande. Les bandes primaires et les bandes secondaires apparaissent ensembles, mais les bandes primaires croissent plus rapidement, laissant place aux bandes secondaires seulement au moment du pic de frottement. Lorsque les bandes secondaires deviennent « actives », elles désactivent alors les bandes primaires. Les bandes *Y* évoluent progressivement jusqu'à l'état d'équilibre où elles deviennent les seules bandes « actives » dans la gouge, c'est-à-dire le lieu principal des déformations et glissements. Cette représentation des bandes de Riedel est vraiment prometteuse pour réaliser des microanalyses de l'intérieur de chacune des bandes *R* et *Y*. Enfin, le lien entre le comportement mécanique à l'intérieur de chaque bande à la cinématique globale de la gouge a été étudié. Une vue d'ensemble de la méthode est proposée avec une description énergétique et des relations appropriées entre chaque bande et la gouge, Figure 7 (c). La contribution énergétique de chaque bande est en accord avec leur localisation dans le temps et l'espace mais donne une autre façon d'observer les mécanismes de Riedel et de conclure sur leur rôle et leur activité. Bien que certaines simplifications et recherches soient encore nécessaires pour obtenir un meilleur modèle énergétique, ce petit modèle simplifié est très prometteur pour étudier le bilan énergétique et le rôle de chaque bande de Riedel dans le mécanisme d'affaiblissement en fonction des caractéristiques de chaque matériau de remplissage.

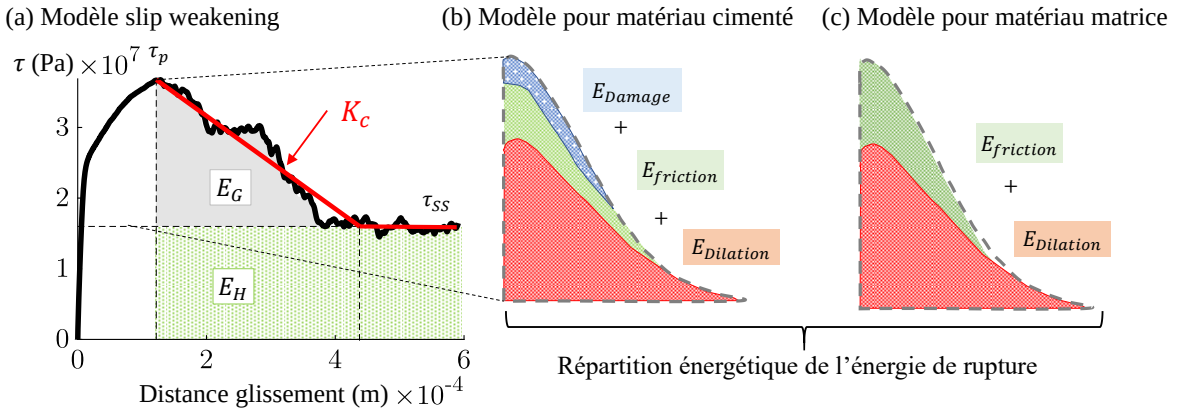

Figure 7. (a) Illustration de la contrainte de cisaillement τ (Pa) en fonction de la distance de glissement (m) pour un échantillon de gouge standard. La pente d'affaiblissement $K_c = (\tau_{SS} - \tau_p)/D_c$ est calculé pour avoir la même énergie en J/m^2 pour le triangle généré par la ligne de pente que pour l'énergie de rupture E_G (en gris). Avec τ_p la contrainte de cisaillement maximale (Pa), τ_{ss} la contrainte de cisaillement steady-state (Pa) et D_c la distance critique de glissement (m). (b) Modèle proposé pour les gouges cimentées avec la décomposition de l'énergie de rupture E_G. E_G regroupe une énergie de dilatation $E_{Dilation}$, une énergie E_{Damage} provenant de la rupture de la cimentation (énergie de création de surface) et E_f une partie de l'énergie de frottement de Coulomb E_H. (c) Modèle proposé pour les gouges avec matrices avec la décomposition de l'énergie de rupture E_G : E_G regroupe une énergie de dilatation $E_{Dilation}$ et une énergie du aux frottements E_f.

Conclusions et perspectives

Le gouge de faille, provenant de l'usure des glissements précédents, agit sur la stabilité du frottement et joue un rôle clé dans la libération soudaine d'énergie. Une grande partie des mécanismes de glissement est influencée, voire contrôlée, par les caractéristiques de la gouge de faille et son environnement. Au cours de ce travail de thèse, une modélisation par éléments discrets en 2D a été réalisée pour mieux comprendre (i) comment le matériau de remplissage

(matrice ou ciment) participe au renforcement ou à l'affaiblissement de la faille, (ii) les comportements rhéologiques observés mettant en évidence la formation de bandes de cisaillement, et le lien avec les caractéristiques de la gouge, (iii) la contribution de chacun de ces mécanismes dans l'énergie de rupture et les lois de frottement observées. Trois types principaux d'échantillons de gouge ont été générés pour simuler une gouge de faille mature avec un matériau de remplissage, puis insérés entre deux parois rocheuses pour réaliser des expériences numériques de cisaillement direct à l'aide du logiciel MELODY2D. Un modèle de contact sec a été considéré pour étudier les mécanismes sans fluide (à vitesse de cisaillement et contrainte normale constantes). Les simulations numériques réalisées et les analyses associées ont permis de répondre aux questions soulevées dans l'introduction générale et mettent en évidence que les deux matériaux de remplissage étudiés (matrice et ciment) ont un rôle prépondérant dans l'affaiblissement des gouges de failles matures. Ils jouent un rôle dans la résistance de la gouge au cisaillement (fragilité, raideur, cohésion) et dans l'écoulement granulaire et les déformations de la gouge (agglomérats de particules, bandes de Riedel). Dans un second temps, le frottement macroscopique a été décomposé en plusieurs mécanismes principaux dans le but d'obtenir un modèle de frottement simplifié qui pourra ensuite être injecté dans un modèle dynamique à plus grande échelle.

Suite au travail effectué, plusieurs perspectives sont proposées à cette thèse. La recherche effectuée s'est concentrée sur un ensemble d'expériences numériques sous une contrainte normale, une vitesse de glissement et une épaisseur initiale constantes. Il pourrait être intéressant d'étendre la campagne numérique à une gamme plus large de contraintes normales, de vitesses et d'épaisseurs de gouge, afin d'améliorer les lois de frottement empiriques basées sur les propriétés micromécaniques de la gouge. L'analyse détaillée de l'évolution des bandes de Riedel pendant le glissement n'a été réalisée que pour un seul échantillon de gouge, il est envisagé de réaliser la même étude sur les autres simulations avec des cinématiques différentes. Les résultats permettront d'observer comment chaque caractéristique de la gouge va influencer l'ouverture et l'activité des différentes bandes de Riedel. Ils permettront également d'enrichir le modèle énergétique proposé en fonction des caractéristiques de la gouge. Maintenant que des modèles énergétiques ont été proposés pour les différentes gouges de failles étudiées, il serait intéressant de les insérer dans des modèles dynamiques à plus grande échelle pour étudier le comportement sismique ou asismique de ces différents matériaux de gouge. Ces modèles seraient très instructifs pour compléter les informations apprises sur les matériaux de remplissage (ciment et matrice) à l'échelle millimétrique et surtout pour tester les lois de frottement à des échelles plus grandes : cette partie fera l'objet d'une prochaine étude. D'autres perspectives sont aussi envisageables telles que : l'étude de gouges de faille cimentées hétérogènes, la modélisation de grains déformables avec la soft DEM pour représenter des matériaux faibles tel que l'argile, l'évolution de l'usure des parois de faille avec un modèle type CZM ou encore le contrôle de la température dans la gouge.

Contents

General introduction

Motivations

During natural earthquakes, frictional sliding releases the stresses accumulated in the pre-stressed surrounding medium of a fault. Depending on the pressure and temperature conditions due to the depth of the fault, rupture processes can take place: slowly and continuously, reducing the probability that a seismic instability occurs or in a fast and brutal manner which can generate strong seismic sliding. There also exist induced earthquakes, governed by the same physical laws, but partly generated by geoengineering technologies and infrastructures that can modify the surrounding stress field of a fault.

While urban models are increasingly rethought to respond to population growth and energy transition, it is important to have sustainable and reliable energy production with low impact on the environment and human beings. Enhanced Geothermal Systems (EGS) lie in the temporal continuity of the production compared to other renewable energy sources such as solar or wind power, which depend on climatic conditions. They could help meet energy demand but appear to be a controversial issue due to the induced seismicity observed in some projects (Grigoli et al., 2017). In order to promote the economic viability of geothermal extraction, EGS are generally located on deep rock reservoirs corresponding to depths of 3 to 5 km [(Gentier, 2013), (S.-M. M. Lu, 2018)]. At this depth, fault networks are already present and subjected to high stresses reducing the permeability of host rocks. Hydraulic stimulation is often used to re-open existing fault systems and improve fluid transport capacity. Although techniques are available to reduce the increase in pore pressure generated by the introduction of fluid, the effective stress is still reduced within the fault, which may induce fault rupture and re-activate slips in the existing fracture network. The slips generated can either be aseismic (slow slip (Cornet, 2016)) or seismic with “induced micro-seismicity” (Talebi & Cornet, 1987). Even if the magnitude is generally smaller than for natural earthquakes ($M_w < \sim 3$), tremors can be felt at the Earth's surface (Bourouis & Bernard, 2007). These tremors remain perceptible most of the time and lead to negative reactions from the inhabitants who stand out against this energy (Majer et al., 2007). Recently, the relation between scientists working EGS, and citizens living near the EGS project of Strasbourg in France was questioned and reported in an interesting Master Thesis, directly associated with the present Thesis, as a socio-political understanding of the research on EGS and induced-seismicity, (Voisin, 2020).

The fault gouge, identified as the wear material of previous slips, contributes to friction stability (Marone & Scholz, 1988) and plays an important role in the sudden energy release during seismic sliding (Sammis et al., 1987). The number and amplitudes of successive slips occurring within the gouge reduce the size of particles towards a fractal distribution, which also reduces pore spaces [(Sammis & Biegel, 1989), (Blenkinsop, 1991), (Muto et al., 2015)]. Within a mature fault gouge, mineral cementation coming from rock dissolution, melting, or matrix particles from previous slips fragmentation, can fill remaining pore spaces between particles and change the global state of cohesion (Philit et al., 2018). These phenomena give birth to a new, stronger granular material combining its history, the state of initial density (i.e. porosity

within the sample), and infill material present within the granular fault gouge (Schellart, 2000). Through this Thesis work, properties of infill materials, which could have been formed on the fluid's paths, are investigated as well as their influences on seismic sliding. This work is based on previous research done on deep geothermal energy systems considering slip reactivation in fault zones where fluid may have flowed and on research on fault gouge mechanics. The role played by the fluid itself will not be considered. The results can be either used within the deep geothermal community, as a post or pre-installation state of deep geothermal power plants or within the seismic fault community since they obey to the same basic principles without fluid. My thesis work was carried out in the LaMCoS Laboratory (Contact and Structural Mechanics Laboratory), team TMI (Tribology and Interface Mechanics) and at GEOMAS Laboratory (Civil Engineering Laboratory) at INSA Lyon. We also exchanged a lot with the BRGM through Arnold Blaisonneau, Julie Maury and Théophile Guillon.

Objectives and outlines

The main objective of this thesis is to study the behavior of infill materials in faults at depths close to those observed in deep geothermal energy systems. However, we have restrained our work to dry friction. We have chosen to focus specifically on numerical granular physics to study the behavior of fault gouges within the fault core. For that purpose, we will address and answer the following questions all along the report:

- What role plays cementation in the weakening of mature fault gouges? Do cemented materials promote slips in faults? How can the energy balance of a cemented gouge be decomposed and what mechanism remains most influential?
- What role plays the matrix particles in the weakening behavior of mature fault gouges? How important are the different physical and geometric characteristics of matrix particles in the slip behavior? To which extent is there an influence on the proportion of matrix/grain and their distribution in the fault gouge samples?

Based on the main questions mentioned, a few more questions need to be addressed:

- How can the characteristics of the fault gouge material be related to its rheological properties? Which type of Riedel patterns are observed and with which orientation?
- What friction law better represents the behavior of a cemented granular fault? And what frictional models can be used in modeling dynamic slips?
- How the behavior of each shear band observed in a fault gouge can be related to the overall behavior of the gouge?

This report thesis is structured into five Chapters reported in the following and schematized by Figure 8:

- Chapter 1 gives an overview of the basics of earthquake, fault mechanics as well as the study of friction in faults and empirical models used. It also focuses on the properties of the fault gouge whose mechanical and rheological characteristics are key elements in the understanding of the sliding mechanisms of a seismic fault. This chapter also presents the research strategy adopted for the work.
- Chapter 2 describes the numerical models and methods. It starts by presenting the main concepts of DEM, the code used as well as all parameters and contact laws necessary

for the model. It ends with a global description of the 2D direct shear fault models used and the main assumptions and choices we made for these models.

- Chapter 3 focuses on the modeling of a sheared granular fault with cementation. A link is established between the micro-mechanical and structural properties of a cemented gouge layer, and its rheological behavior under shearing. The last section offers a discussion on new insights and relations between cementation within the gouge, shear localization, and the relevance of Coulomb-Mohr theory for fault models.
- Chapter 4 focuses on the modeling of a sheared granular fault with matrix particles. The first part focuses on a homogeneous model representing a simple "matrix" material alone allowing to study the evolution of shear localization (Ridel bands) as a function of the parameters of this matrix gouge. The second part represents a "grains/matrix" model that highlights the importance of the matrix percentage within the fault gouge, especially from a rheological point of view.
- Chapter 5 represents a second objective of this research, which is to link micro-mechanical models at the grain scale (what we model) and dynamic models at the fault scale (what we want to participate in). Thanks to the numerical models carried out, the extracted friction laws, and the energy balance of the studied fault gouge patch, we generate simplified friction and energetic models which can then be injected into larger-scale dynamic models.

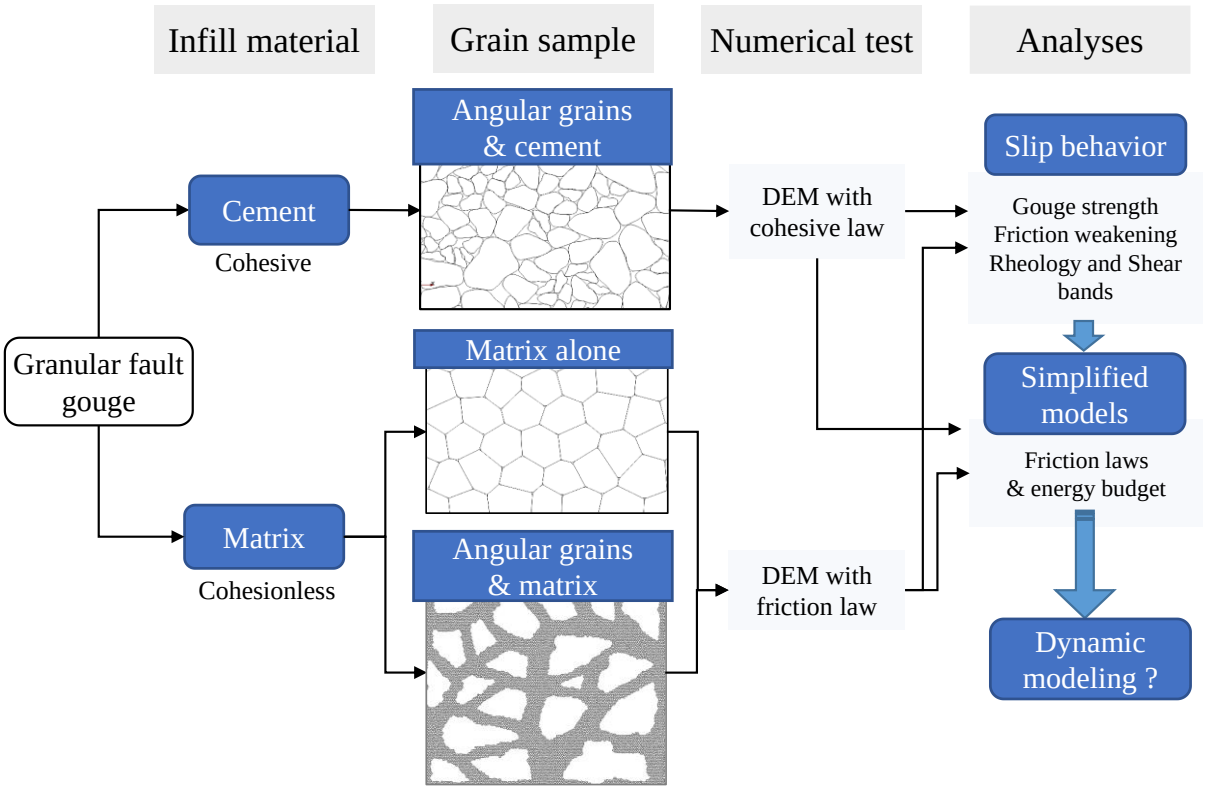

Figure 8. Main schema of the Thesis.

Chapter 1. State of the Art and Research strategy

1.1. Foreword

In the first two parts, this chapter gives an overview of the basics of earthquake and fault mechanics as well as the study of friction in faults and empirical models used. These concepts are quite well known, so the advised reader can start reading directly from part 1.3 which focuses on fault gouge properties whose mechanical and rheological characteristics are key elements in the understanding of the sliding mechanisms of a seismic fault. This third part focuses in particular on the research strategy adopted for the thesis.

1.2. Earthquakes, faults and rocks

1.2.1. What is an earthquake?

When the energy accumulated in the fault reaches the critical stress allowed by the material, the fault suddenly slips and releases the energy resulting in the main seismic shock. The stress excess is then reduced via energy liberation enabling to accommodate the large-scale motion of the earth's plates. The stress drop only concerns shear stress and was estimated to be about ~1-10Mpa in natural faults for large earthquakes (as opposed to larger values in the lab), (Kanamori & Brodsky, 2004). This stress drop mechanism is then repeated during geological time as a succession between shear stress accumulation (interseismic period) and shear stress drop (coseismic period), forming the basis of the seismic cycle (Byerlee & Brace, 1968).

Plates tectonics

An earthquake can also be presented as a plate motion, or sudden displacement of the crust inducing the propagation of elastic waves (Kanamori & Brodsky, 2004). The understanding of plate tectonics and its relation to earthquakes only appear in the 1960s with the "plate tectonic revolution". It was found that the distribution of seismicity was mostly located along tectonic plates boundaries while important earthquakes use to be observed along subduction zones (i.e. the frontier between two converging plates) as presented in Figure 9. Nowadays, geodesy technics let us measure the size and shape of the earth's surface, using Global Positioning Systems or Satellite Interferometry. All of these methods give access to patterns of crustal movements (cm/year for example) and strain accumulation within plates and make appear larger movements at the plate boundaries than in plate interiors (Uyeda, 1978).

The size of earthquakes can be measured posterior to an event thanks to their magnitude M_w obtained from the seismic moment M_0 (Wyss, 1970), itself determined from seismic data (wave amplitude and normal modes), geodetic data (GPS, InSAR), or geological data (surface break of the fault), (Kanamori & Brodsky, 2004).

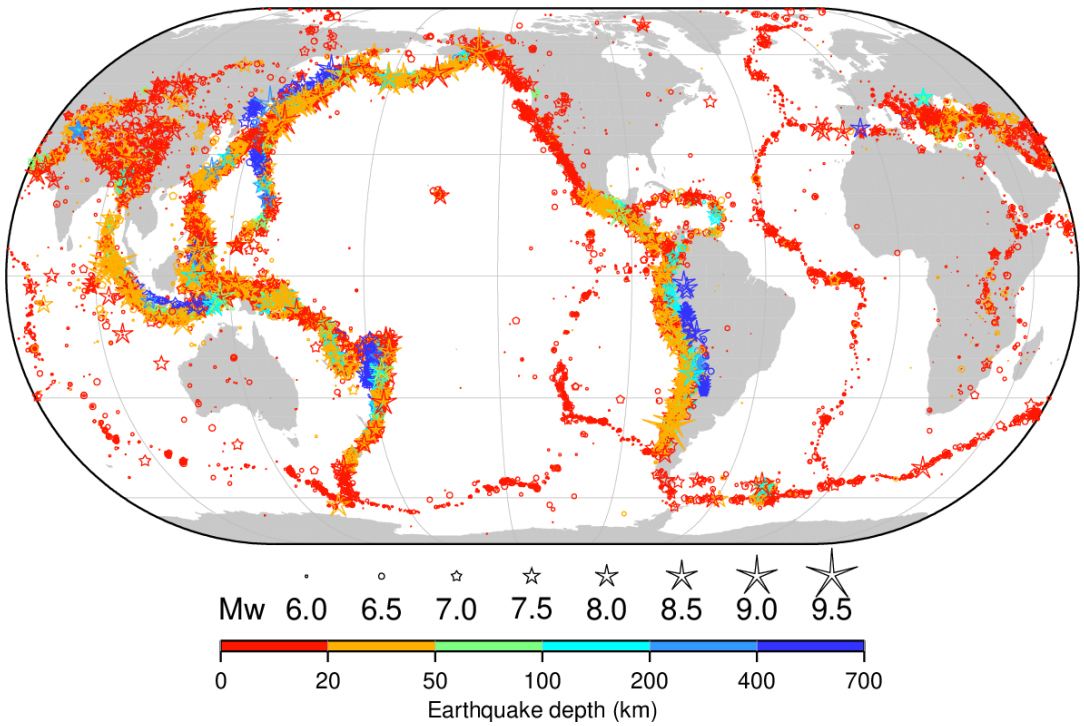

Figure 9. World seismicity map: ISC-GEM catalog of about 42,000 earthquakes (version 8.0). The earthquake selection is based on magnitude Mw 5.5 and above, between 1904 and 2017. The earthquakes recorded take place at the boundaries between rigid plates of the Earth's surface. Symbols from (Agnew, 2014) and image from ISC-GEM (Di Giacomo et al., 2018).

Induced earthquakes?

In addition to the previous definitions of earthquakes, it is also interesting to mention induced seismicity. When the released strain energy is predominantly from natural origin but was provoked by a human action we talk about triggered seismicity and when most of the energy is anthropogenic the word "induced" is used. Nowadays, Humans with their technologies and infrastructures for geo-applications can modify the surrounding stress field of a fault or add new variables into the global system. These stress changes can be due for example to a decrease (hydrocarbon extraction…) or increase (Enhance Geothermal Systems, hydraulic fracturing…) of fluid pressure in the subsurface and can be a source of seismicity. (Grigoli et al., 2017) present the industrial activities responsible for induced seismicity (Figure 10 (b)) and their physical mechanisms. We number lots of cases of induced seismicity all over the world, Figure 10 (c), gathered by HIQuake (Human-Induced earthquake) database (Wilson et al., 2017).

Slow or fast earthquakes?

As the seismic cycle is complex, a wide range of earthquakes exists from slow to fast slip events [(J. R. Leeman et al., 2016), (Stefanou, 2020)], seismic or aseismic motion [(Bourouis & Bernard, 2007), (Chen & Lapusta, 2009), (Cornet, 2016), (McGarr & Barbour, 2018), (Chen & Lapusta, 2019)], or large to small events. A distinction must be made between fast and slow earthquakes:

- Fast earthquakes mostly present seismic and unstable slips, with a large number of seismic waves radiating during a few instants (seconds to minutes). High rupture fronts

velocities are recovered around 3 km.s^{-1} and are superior to 3.5 km.s^{-1} for supershear earthquakes (Passelègue et al., 2013).

– Slow earthquakes (i.e. Slow Slip Events (SSE)), more recently discovered thanks to better GPS technics, have lower involved rupture fronts velocities (Bürgmann, 2018) and present less or negligible radiated energy. Their time duration also varies from a few days to years. The formation of slow slips can be due to several factors or phenomena within a wide range of depth and temperature but the presence of both high-pressure fluids and heterogeneous fault-zone structure/composition/assemblage seems to be needed. Changes in fluid pressure, for example, or in the coefficient of friction can switch sliding regimes from seismic to aseismic (Bürgmann, 2018).

(a)

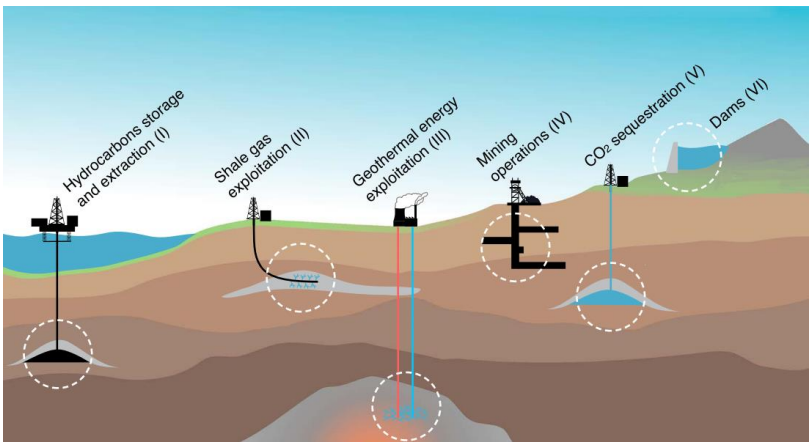

(b)

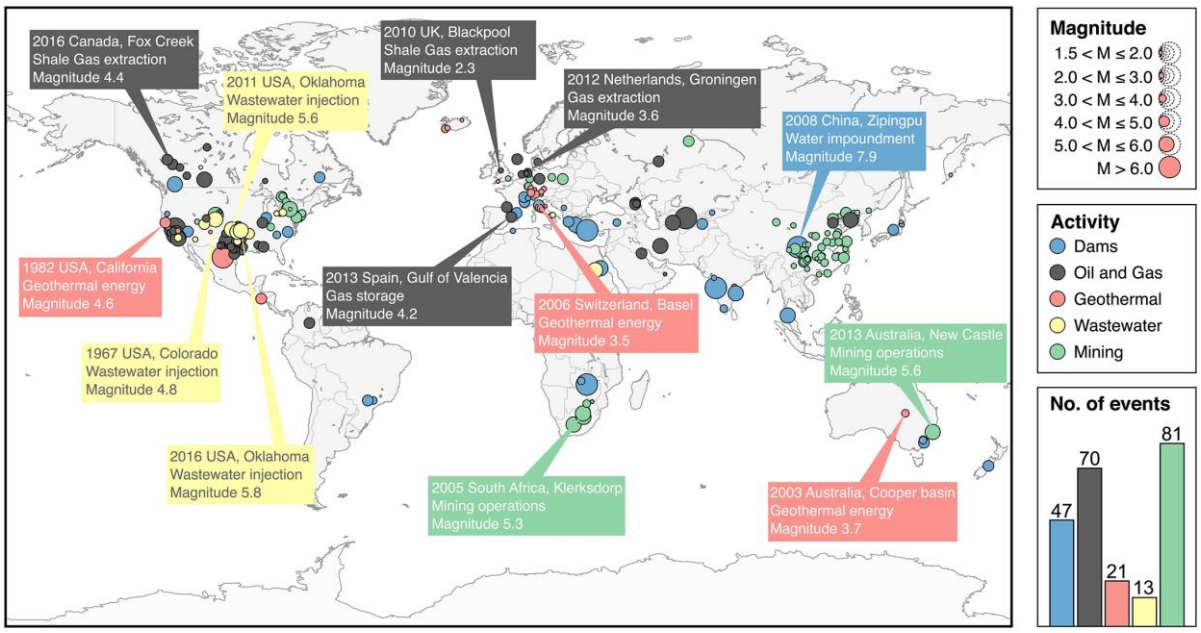

Figure 10. (a) Induced seismicity: the different types of industrial activities. Image from (Grigoli et al., 2017) (b) Location of the induced earthquakes within the Earth with their associated magnitude, (source: Davies et al. [2013]), updated until August 2016, (each type of industrial activity is represented by a particular color). The picture presents declustered seismic sequences with only the maximum magnitude of the sequence (if ML >1.5). Image from (Grigoli et al., 2017).

There is still a debate on scaling laws, on whether slow and fast earthquakes are controlled or not by similar dynamic properties (Michel et al., 2019). The understanding of the different

behaviors between fast earthquakes and SSE is relevant for fault mechanics, as it can indicate how and why a slip may be initiated or not at a critical frictional stress (Scholz, 2019). For more details on seismicity (seismic and aseismic motions), and the size of events, the reader may refer to [(Bürgmann, 2018), (McGarr & Barbour, 2018), (Scholz, 2019), (Stefanou, 2020)].

Both natural or induced earthquakes need a fundamental understanding of fault and rock mechanics. Mechanisms of failure in intact rocks or slips in pre-existing fault networks need to be well understood to reduce earthquake hazards and develop safer geo-energy activities. In the Thesis, we will apply the seismic cycle at a smaller scale of fault rupture, and focus on the role of fault zone internal structure within the schizosphere part of the Earth. In the next sections, we will present the fault zone structure observed, and the basics of the fault and rock mechanics needed to study fault slip behavior.

1.2.2. Fault zone

When talking about earthquakes, it is also essential to define what a fault is. One may first think of the well-known natural faults, such as the San Andreas Fault (F. Chester et al., 1993), but the variety of geological variables (lithology, displacement, depth, pre-existing fabric…) present within the Earth leads to a wide range of different types of faults and internal fault zone structures that also depend on the depth of formation, tectonic environment, protolith, and hydrothermal context.

Brittle-plastic transition: faults and deformation

The lithosphere is the only place where earthquakes can happen as generally, no earthquake happens within the asthenosphere or beyond. Stresses applied to the lithosphere induce deformation of crustal rocks that transform and store elastic energy. Depending on the tectonic context and stress state, it exists three main types of faults: (i) normal faults, corresponding to an extension of plates, quite rare on the continental crust (New Madrid fault zone), (ii) Reverse fault, or thrust faults which are derived from a compressional tectonic context (Main Himalayan Trusts) and (iii) the strike-slip fault or transform faults, derived from lateral sliding along a vertical plane (North Anatolian fault). Figure 11 schematizes the evolution of rocks' behavior in the lithosphere as a function of temperature and pressure. As in rock mechanics, any type of deformation will first admit a reversible elastic deformation (linear stress-strain dependence) then once the yield stress (elastic limit) of the material is passed three main regimes are observed:

- The first 10 km from the surface, or the upper layer of the lithosphere (i.e. schizosphere), generally deform in a brittle manner. Of course, it depends on the temperature and pressure conditions. Irreversible deformations such as rupture or localizations are observed after reaching the yield stress point: **microfractures** (Scholz, 2019), which first form and gather to create a macroscopic fault, **gouge particles** (Scholz, 1987), as a consequence of rock fragmentation, or even **asperity ploughing** (Scholz & Engelder, 1976) can be observed during shearing. This brittle mechanism also implies an increase of the rock volume (i.e. dilatancy).
- The bottom part of the lithosphere (i.e. plastosphere) is considered as a ductile zone. It belongs to the so-called "plastic" regime where the rock can deform irreversibly within a

deformation band (shear zones) or in a more distributed way. Then, we tend either towards stabilization of the stress characteristic in a stable flow or towards hardening by deformation. This regime is thermodynamically promoted at high pressures and temperatures. The high ductility in the plastosphere also leads to a decrease in rock strength (Brace & Kohlstedt, 1980).

– Between these two regimes, a semi-brittle regime exists as a mixture between brittle and crystal plastic processes. This is the so-called "Brittle-plastic" transition (Byerlee & Brace, 1968), promoted by pressure and temperature increase.

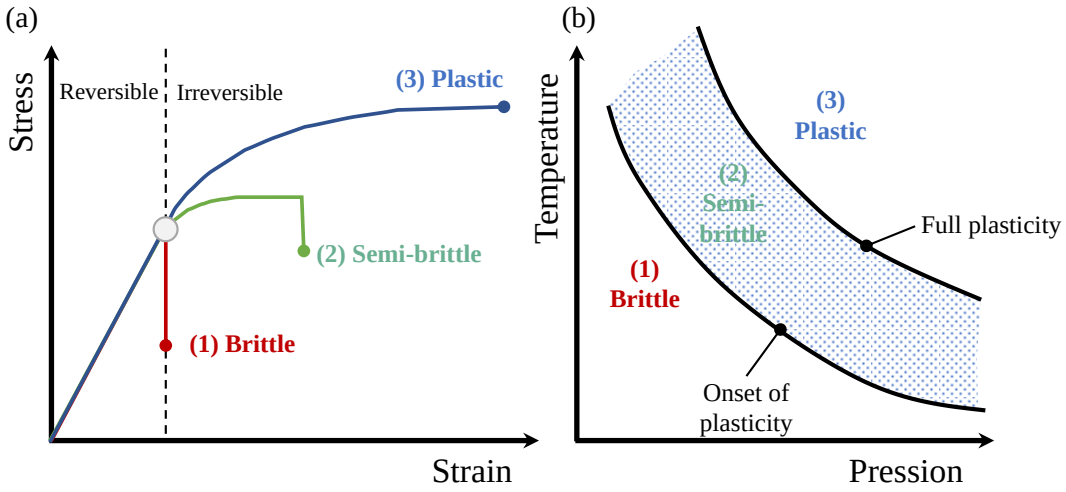

Figure 11. (a) Stress-strain representation of brittle-plastic behaviors, curves exhibit (1) elastic deformation followed by rupture, (2) elastic deformation followed by plastic deformation and then by rupture or (3) elastic deformation followed by plastic deformation with viscous flow or hardening. (b) Evolution of the behavior of rocks in the lithosphere as a function of temperatures and pressures. The brittle-plastic transition mostly depends on temperature (increase in ductility with temperature), pressure (ductility increases with applied stresses), and velocity rate (rapid tests show more brittle behavior and slow tests show more ductile behavior). It should also be noted that the water content influences the strength and deformability of rocks. Image modified from (Jérôme Aubry, 2019)

Internal structure from brittle zone

Even if many models propose a planar representation of two fault surfaces in contact, the reality is obviously more complex. The internal structure of fault zones subjected to external loads and strain rate is progressively damaged by the earthquake cycle and shearing. The investigations [(F. Chester et al., 1993), (Rice & Cocco, 2002), (Billi et al., 2003), (Wibberley et al., 2008), (Faulkner et al., 2010), (Scholz, 2019)] on this internal structure and data collected on faults that have already been sheared several times, propose a large scale fault zone model displayed in Figure 12. For the sake of simplicity, the model described here in detail is a one-core fault zone structure, but multiple cores models have also been discussed (Faulkner et al., 2003). The fault can be divided into different, more or less damaged zones, Figure 12 (a) & (c):

1) The core zone, or fault core, is the contact interface of the fault where slip is localized on one or several principal slip surfaces. It is composed of pulverized rock material described as a layer of granular material. The fault core can be separated into two parts: the first one is the Principal Slip Surface (Rice, 2006), generally, fault gouge (Woodcock & Mort, 2008), which is the central zone with a thickness inferior to 1 - 5 mm (Rice &

Cocco, 2002). It has lost the original cohesion of the load-bearing rocks. This gouge is surrounded by zones of breccia with coarser particles on both sides or one side of the fault gouge (brecciation process), Figure 12 (b). Frictional heating can also melt the interface, resulting in a fault core mostly composed of pseudotachylyte [(Sibson, 1977), (Di Toro et al., 2009)]. The fault core contributes to friction stability (Marone & Scholz, 1988) and plays an important role in the sudden energy release at the onset of seismic sliding (Sammis et al., 1987), (cf section 1.4.1).

2) The highly fractured damage zone, of 1-100m thickness (depending on the history of previous slips), envelops the core zone. This damage zone is deformed by seismic waves release. It can be composed of foliated and non-foliated cataclasites (granular material) and is generally assumed to be highly permeable regarding the amount of porosity [(Faulkner et al., 2010), (Rice & Cocco, 2002)].
3) Finally, the quasi-undamaged host rocks are submitted to the external load. They are protected by the inner fault zones which take all the deformation and release energy. The host rock type, stress and strain rate, deformation mechanisms, or fault architecture also influence the permeability of the fault which is a key parameter for fluid pressure distribution and volume characterization (for Geo-engineering applications for example).

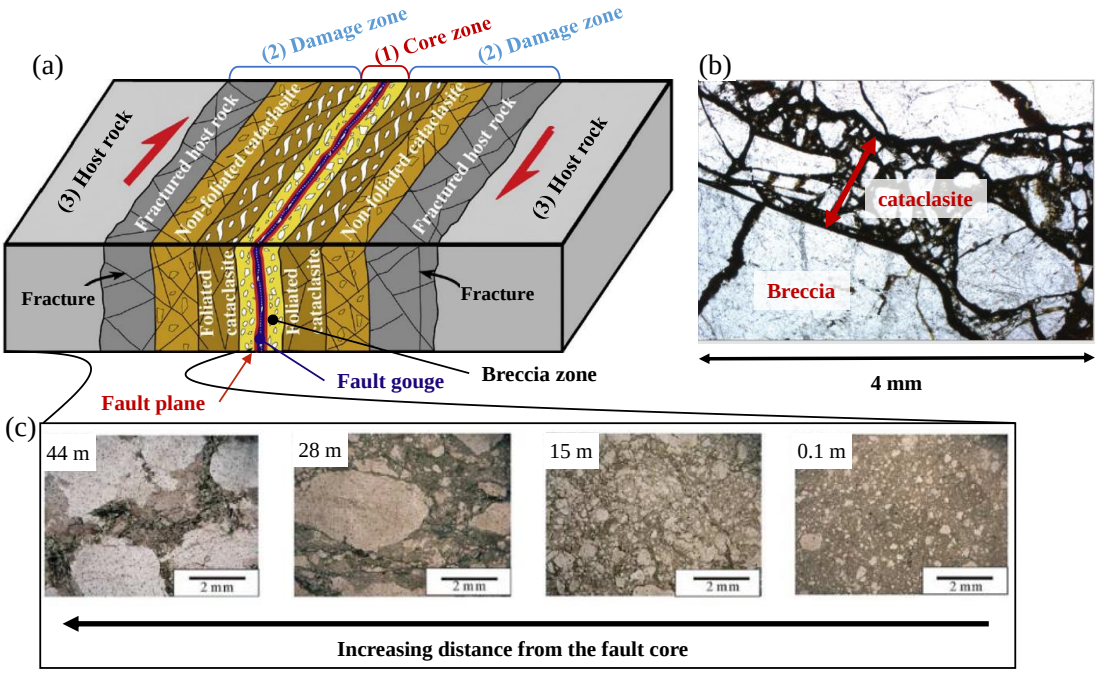

Figure 12. Typical fault zone structures. (a) Schema of fault zone for strike-slip faulting. The core zone consists of fault gouge and fault breccia. The damage zone consists of foliated and non-foliated cataclasite and fractured host rocks. The red arrows show the shear stress acting on the host rock. Image modified from (Lin & Yamashita, 2013). (b) A narrow zone of fault breccia and cataclasite in a quartzitic parent rock. Buzios, Rio de Janeiro States SE Brazil. Width of view 4 mm. PPL. From (Trouw et al., 2009). (c) Photomicrographs in plane-polarized light from the internal structure of the Keumwang fault zone, images from (Lee & Kim, 2005)

The large-scale model presented here describes highly slipped fault zones named as **mature faults** by (Rice & Cocco, 2002), and we will use this definition in the rest of the Thesis. It is important to specify that most of the variables influencing fault zone are scale-dependent and that the sum of all these scale-dependent variables leads to a very complex

mechanism. Fault zone needs to be both studied at small and large scales if we want to understand the entire mechanism. The seismic or aseismic character of a fault greatly depends on this fault zone anatomy [(Scholz, 2002), (Wibberley et al., 2008)] but is also controlled by fault frictional properties, which are essential to determine the way the fault behaves between stable or unstable slips (cf. section 1.3). Now that we have defined what an earthquake and a fault are, it becomes interesting to detail rock mechanics mechanisms to understand the internal phenomena occurring just before a rupture.

1.2.3. Notions in rock and fracture mechanics

Griffiths' theory

For any real loaded material, imperfections can exist within the microstructure (i.e. fracture, asperities, crack…) creating local stress concentrations within the material that can give birth to seismic nucleation (Wibberley et al., 2008). The notion of fracture mechanics was introduced by (Griffith, 1924), in order to explain the phenomenon of fracture and propagation. From this definition, three different failure modes can be observed [(Lawn, 1993), (Scholz, 2002)]: Mode I is called 'tensile mode' (i.e. opening mode), mode II is the 'longitudinal mode' (i.e. in-plane shearing), and mode III is the transverse shear (i.e. antiplane shear), Figure 13. However, Griffiths' equations can only predict the initiations of local crack, and the equations related to each mode present a nonphysical behavior: infinite stresses at the crack tip. To face this problem, the general concept of fracture energy E_G was introduced by (Irwin, 1957) as the energy to fracture the entire material (as opposed to *G*, energy for a single crack creation), (cf. section 1.3.3). More details on the associated equations, stresses, and energies can be found in (Scholz, 2019). The energy released by crack propagation in rock generally increases with the length of the fault, until a state of equilibrium is reached (i.e. for critical stress). This maximum strength, or resistance to cracking, depends on the grain size and stress singularities appearing at the edges of the crack.

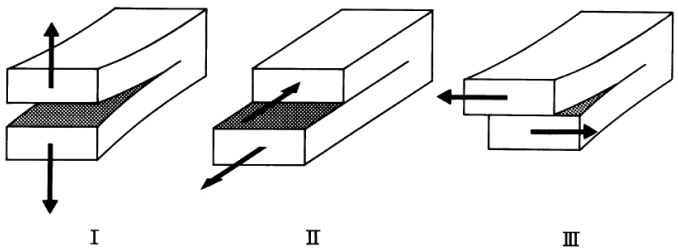

Figure 13. Sketch of the three main crack propagation modes: Mode I, opening or tensile mode (the tensile, or the crack displacement is normal to the crack), Mode II in-plane shearing (crack displacement in the shearing plane and normal to the crack edge), Mode III, antiplane shear (crack displacement in the shearing plane and parallel to the crack edge). Image from (Scholz, 2002).

Principal stresses and failure criteria

Friction and fracture patterns show different characteristics (Lockner & Beeler, 2002) and need criteria to quantify the critical stress and strength needed for the different mechanisms involved. The stress field observed on both the upper crust or a piece of rock submitted to an external load is defined by its principal stresses σ_1 and σ_3 (in 2D). These stresses come from the eigenvectors of the stress tensor and represent the normal stresses applied on two properly

oriented orthogonal facets. Figure 14 (a) presents a relevant type of rock rupture observed for brittle rocks, with oblique sliding with respect to the maximum compression direction (2D). By convention in rock mechanics, positive stress values are compressional and it is assumed that σ_1 and σ_3 are positive in the Earth. The equilibrium condition of a small element subjected to stresses in 2D gives the following equations, with τ the shear stress and σ_N the normal stress on the fault plane, and β the angle between the shearing plane and the major principal stress σ_1:

$$\tau = \frac{(\sigma_1 - \sigma_3)}{2}\sin(2\beta) \tag{1.1}$$

$$\sigma_N = \frac{(\sigma_1 + \sigma_3)}{2} - \frac{(\sigma_1 - \sigma_3)}{2}\cos(2\beta) \tag{1.2}$$

Failure criteria were first designed for the strength of "intact rock", as opposed to other granular material found in the crust or fault as a granular gouge. Considering intact rock first, the rock strength is generally considered to follow the Coulomb-Mohr failure criterion [(Handin, 1969), (Jaeger, 1971)], which states that the maximum tangential stress τ_{max} that the material can withstand is the sum of a constant term "C" (generally called "cohesion") and an additional term $tan\varphi$ (generally called "coefficient of internal friction") multiplied by the normal stress:

$$\tau_{max} = C + \sigma_N \tan(\varphi) \tag{1.3}$$

$$\mu_f = \tan(\varphi) \tag{1.4}$$

φ being the internal friction angle of the material, or angle between the failure surface (i.e. envelope) and the horizontal axis when drawn in a Mohr plane. Figure 14 (b) shows the stresses represented in a Mohr plane. It is possible to construct what we call the failure envelope, or envelope of points defining failure for specific range or shear and normal stresses. Considering a cohesionless material, the C value is null and the failure envelope passes through the zero-stress value. For more details on failure criteria, the reader can refer to [(Lockner & Beeler, 2002), (Jaeger et al., 2007)].

The cohesion value C can be easily determined with Biaxial or Triaxial experiments for a specific temperature, pressure range, and loading rate [(Sammis et al., 1986), (Marone & Scholz, 1989), (Marone, 1998), (Noël et al., 2019)]. During these tests, the specimen is subjected to both an axial compressive stress (force exerted on the top of the specimen) and a radial confining pressure (exerted by a fluid on the walls of the specimen), Figure 14 (a). Several tests may be carried out on the same sample, to consider the history of stresses. Hubbert-type shear box can also be used to determine the extrapolated cohesion and friction coefficient (Abdelmalak et al., 2016). If pore fluid pressure P_f is present within the fault, the same Mohr-circle representation is possible but considering effective pressure instead of normal stress ($\sigma_{eff} = \sigma_N - P_f$).

From Mohr-Circles representation, it is possible to relate β to the internal friction angle φ. Major and minor principal planes can be observed during shearing and each point of the circle represents a fault orientation. The combination of the previous equation and trigonometrical relations enables to link the fault plane orientation angle to the coefficient of internal friction:

$$2\beta = \frac{\pi}{2} - \varphi \tag{1.5}$$

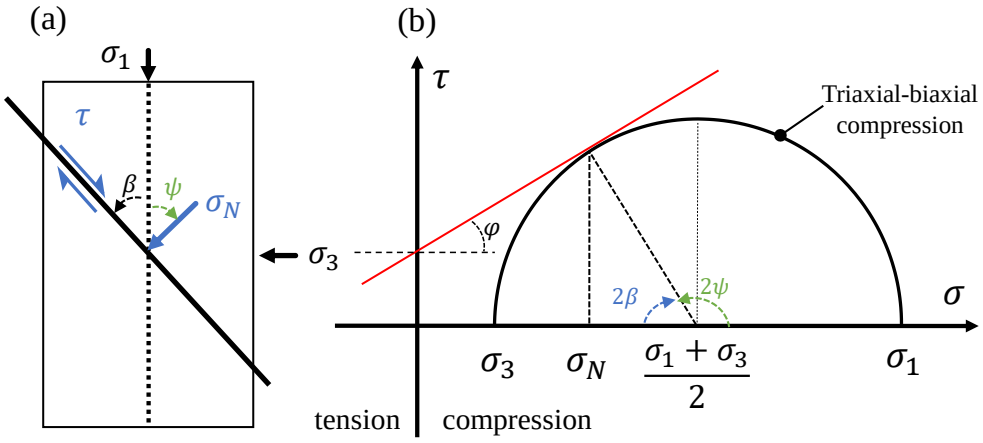

Figure 14. (a) Schema of stresses applied on a representative volume (biaxial (2D) compression test), with major stress σ_1, minor stress σ_3 applied on the rock sample and resulting tangential and normal stresses τ and σ_N applied on the fault plane. β is the angle between the principal stress and the fault plane and ψ the angle between the principal stress and the normal stress (b) Mohr-circle with stress representation and angle relations, shear stress τ as a function of the principal stresses applied on the volume.

All these definitions allow us to describe the large-scale behavior of a fault and its formation (rupture tip), i.e. the state of limit stress that a fault can support as well as the type of rupture (brittle, semi-brittle, plastic) observed. However, fault mechanics is also played out on a smaller scale, and by considering the properties of the contact between the two rock walls of a fault. The way the walls slide against each other primarily depends on the frictional properties of the materials. We explore in more detail the frictional and energetical contact theories in the next subsection.

1.3. Rock friction and empirical models

From a physical point of view, friction is described as a resisting force opposed to the relative displacement between two contacting surfaces. Friction is the focal point of tribology (the Science of contacts), but it appears to be present wherever a contact is observed between two different bodies. Rock and fault mechanics are not exceptions, and also assign a great importance to this parameter that acts at different scales (Jaeger et al., 2007). This section presents some methodological elements to study and model faults sliding using tribological concepts.

1.3.1. Theoretical concepts

Leonardo Da Vinci brought the first bases of friction and resistance to motion in the 15th century. Two centuries later in France, Amonton studied the characteristics of two contacting bodies and proposes that (i) the friction force is independent of the size of the contact surface and the second that (ii) the friction force is proportional to the normal load acting on the surface. Dividing the two forces by the nominal contact area gives a relation between the shear stress τ and the normal stress σ_N, known as the 2nd Amonton's law:

$$\tau = \mu \ \sigma_N \tag{1.6}$$

It is important to specify that this link existed before the Coulomb-Mohr criterion and does not consider a possible cohesion of the material. Combining equations 1.3 (Coulomb-Mohr) and 1.6 (Amonton's law), we are able to extract what we can call **the effective friction μ^*** different from the coefficient of friction μ_f used for Coulomb-Mohr (cf. eq. 1.4):

$$\mu^* = \frac{\tau}{\sigma_N} = \frac{C}{\sigma_N} + \mu_f \tag{1.7}$$

Amonton's friction and the effective friction are similar in the case of zero cohesion within the intact rock. ***This effective friction will be used all along the Thesis*.**

As friction coefficient μ_f is weakly dependent on normal stress (Lockner & Beeler, 2002), effective friction μ^* mostly depends on the presence of a third body (i.e. material filling the contact interface, as a granular fault gouge (section 1.2.2), and surface geometry (roughness of rocks in contact, asperities…). Later, (Byerlee, 1978) proposed that for intact rocks, the maximum shear strength before failure was independent of rock mineralogy. These observations were gathered in the well-known Byerlee's rules presenting a bilinear strength dependence on normal stress as the relation below:

$$\tau = \begin{cases} 0.85.\sigma_N & \sigma_N < 200\ MPa \\ 50 + 0.6.\sigma_N & 200 < \sigma_N < 1700\ MPa \end{cases} \tag{1.8}$$

From these rules, Figure 15 presents Byerlee's friction (grey part) in a graph of shear stress as a function of normal stress, with effective friction ranging from $0.6 \leq \mu^* \leq 0.85$. However, Byerlee's law is just Coulomb failure, and only gives information about brittle deformation, failure, and critical strength of intact rocks (Marone, 1995). Even though these rules are widely used to predict rock strength and effective friction for many materials, certain layered minerals and phyllosilicates [(Niemeijer & Spiers, 2005), (Collettini et al., 2009), (Collettini et al., 2019)], gouge material layers (Marone, 1995), or fluid-filled faults [(Schmocker et al., 2003), (Collettini et al., 2009)], present weaker behaviors that don't fit with these rules (Imber et al., 2008). Some effective friction coefficients obtained for weaker rocks are also displayed in Figure 15 (Collettini et al., 2019). **For granular materials, powders, and fault gouge, special attention needs to be paid to frictional properties, which are more complex than for classical intact rock (section 1.4).**

These new definitions of the contact allow us to characterize the stability of the fault according to empirical friction models that we will present in the following section. Friction is a key parameter to follow the weakening of a fault, and its dual dependency on time and velocity gave birth to friction laws.

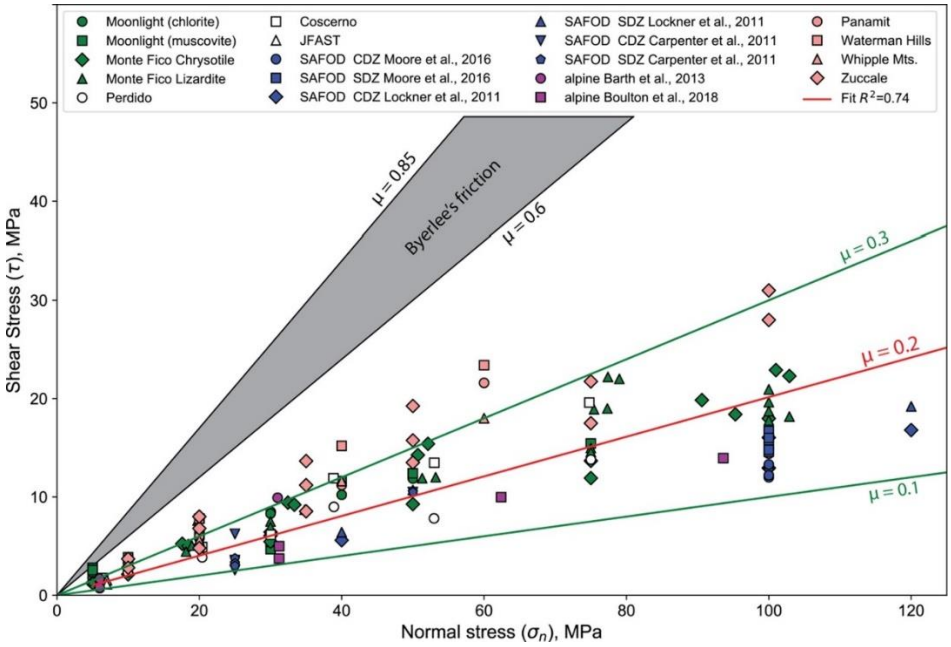

Figure 15. Effective friction properties of different rocks, gouge, fabric, and phyllosilicate-rich faults materials. (a) Shear stress as a function of normal stress, first linear part of Byerlee's rules. Image from (Collettini et al., 2019).

1.3.2. Stick-slip and friction scaling laws

Stick-slip and stability

The seismic cycle, previously presented in subsection 1.2.1 with stress drop, is the analogy of the "stick-slip" demonstrated by (Byerlee & Brace, 1968) during experimental tests on a cylindrical sample of rock. When a slip is initiated within the fault, it can either be slow and stable or sudden with an associated stress drop enhancing dynamic instabilities. These instabilities are followed by a period without movement during which the stresses are restored (stick), and then again by instabilities (slip).

From an engineering point of view, this phenomenon is often presented as an analogy of a mass-spring sliding system [(Scholz, 2002), (Marone, 1998)], Figure 16 (a). The spring represents the stiffness of the material surrounding the fault and the bloc system is submitted to both external load (normal force N) and constant velocity (V) applied on the free spring extremity. These stick-slip experiments are highly reproduced in laboratories or numerical experiments, as analogs to natural earthquakes [(Byerlee & Brace, 1968), (Byerlee et al., 1978), (Aharonov & Sparks, 2004), (J. Leeman et al., 2015), (Dorostkar, 2018), (Passelègue et al., 2019)]. These notions are very important for the following since they will allow characterizing the stable or unstable character of the observed fault slips.

As presented in Figure 16 (b), slip instabilities may occur if the stiffness of the fault K (i.e. stiffness of the loading system for experimental setup) appears to be lower than K_c. In this case, the slope of the force-slip curve passes through a possible friction peak ($K_c > K$). Conversely, sliding can occur in a stable manner if $K > K_c$ (Figure 16 (b), blue line).

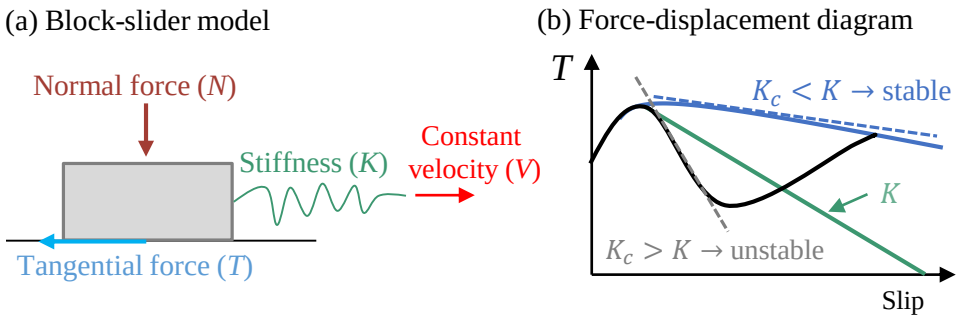

Figure 16. (a) a block-slider model submitted to normal and tangential forces with a stiffness K and a constant velocity V. In the first phase, the spring stores energy, and the tangential resisting force is strong enough to maintain a static contact of the system: this is the stick phase (or interseismic period). Even if the shear strength is increasing, there is no displacement of the mass block. In a second phase, the external force applied to the spring becomes higher than the resisting force, triggering sliding. The block mass is suddenly put into motion and slides until part of the stored energy is released: this is the slip phase (b) Schematic diagram which illustrates the limit of stability as a force-displacement.

Friction scaling laws

Since stick-slip is defined as the analogy of a seismic cycle, it becomes interesting to establish frictional laws to define and model precisely the contact between two fault walls sliding against each other. Frictional forces evolution can be modeled by constitutive laws grouped into two main classes: the slip-dependent laws (considering that friction only depends on fault slip and basic geometry) and the rate-and-state dependent laws (friction is a function of slip velocities and state variables), (Rice & Cocco, 2002).

Slip-dependent laws, slip weakening – First observations of the weakening effect were made by [(Dieterich, 1972), (Scholz et al., 1972)]. The slip weakening is related to fracture mechanics and slipping zone and is mainly based on surface geometry and contact properties. It is thus influenced by both the roughness of the fault surface and the thickness of the gouge (Marone & Kilgore, 1993). Figure 17 shows two schematic views of slip-weakening, (a) is the theoretical "linear-weakening", which is the most simplified view of a weakening from the peak of friction to residual friction, and (b) is the same slip weakening but with a more realistic aspect of a non-linear weakening, (Ohnaka, 2013). The shape of the slip weakening curve can differ as a function of fault characteristics and other representations are employed [(Kanamori & Heaton, 2000), (Abercrombie & Rice, 2005)].

In the case of a classic stick-slip phenomenon, (Rabinowicz, 1951) demonstrated the existence of a critical sliding distance D_c, at the end of which the friction has dropped from μ_p^*, the peak of static friction to μ_d^*, the residual friction. This well-known critical slip distance D_c is the slip distance corresponding to a drastic decrease in frictional strength, and is considered to be the distance necessary for the renewal of the contact surfaces (Dieterich, 1979). We can thus define the slope of friction drop as follows:

$$K_c = \frac{|\mu_d^* - \mu_p^*|\sigma_N}{D_c} \tag{1.9}$$

The critical sliding distance is very large for natural earthquakes (cm to meter), and from 10^{-5} to 10^{-3} for lab experiments at low slip velocity (Marone & Kilgore, 1993). As first proposed by

(Rice & Cocco, 2002), these classical slip weakening models may be incomplete and weakening mechanisms do not depend on interface properties only [(Barras et al., 2019), (Barras et al., 2020)]. It is interesting to note that the magnitude of the stress drop with the stick-slip phenomenon also varies with the loading rate, fault geometry, elastic properties, etc.

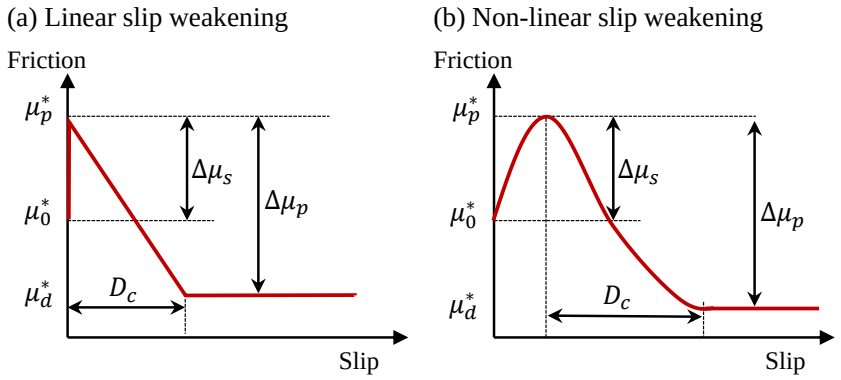

Figure 17. (a) Linear slip weakening, (b) Non-Linear slip weakening, with μ_0^* the initial static friction value, μ_p^* the peak of static friction (after healing), μ_d^* the dynamic or residual friction. $\Delta\mu_s$ is the static friction difference, $\Delta\mu_p$ the friction drop from the peak value to its residual value, or breakdown friction.

Rate and state friction laws – Other authors have tried to create a more general model to represent these mechanisms, not only based on "static" and "dynamic" friction. In order to describe the seismic movements of rocks, (Dieterich, 1979) introduced the "Slip rate and state variable constitutive laws for rock friction" (RSF laws). These are empirical laws based on laboratory and numerical observations, showing that the frictional force is logarithmically dependent (i) on the time that surfaces are in contact and (ii) on slip velocity (Sliding friction decreases with increasing velocity rate, also known as "velocity weakening") [(Dieterich, 1979), (Rice & Ruina, 1983), (Marone, 1998)]. The first Rate and State friction laws have been called "aging law" (Dieterich, 1979) and depend on two empirical constants a and b. There are also different versions of the RSF law, such as the slip law of (Ruina, 1983), or the PRZ law of (Perrin et al., 1995) involving a different static friction drop as a function of time. From these laws, it is also possible to determine the frictional stability of the fault, and whether the fault motion is seismic or aseismic. These laws have the advantage to reproduce both laboratory experiments for low sliding velocities (i.e. from 0.001 to 10 m/s), [(Marone, 1998), (Lockner & Beeler, 2002), (Scholz, 2019), (Im et al., 2019)], and observations of frictional sliding [(Chen & Lapusta, 2009), (Chen & Lapusta, 2019)]. However, RSF laws remain complicated to understand and to interpret, and they are also not representative of some fault behavior for earthquake nucleation (for high stresses, fluid pressures, and high temperatures) [(Stesky et al., 1974), (Passelègue et al., 2019)] or earthquake propagation (high slip rate) [(Brodsky & Kanamori, 2001), (Mizoguchi et al., 2007), (Sone & Shimamoto, 2009)]. We will not enter more in detail in the RSF laws because, as we elaborate later, our numerical models do not include any rate- or state-dependence. The reader may refer to [(Dieterich, 1979), (Rice & Ruina, 1983), (Marone, 1998)].

In this thesis, we restrict our focus on the most immediate (fracture-related) slip weakening phenomena and dedicate consideration to simpler friction laws. We then still need to look

into the energy budget of the sliding fault to complete the knowledge of the mechanical fault behavior from an energetical point of view.

1.3.3. Energy budget and dynamic weakening

Throughout an earthquake, energy is dissipated during fault sliding by the means of different mechanisms. Figure 18 schematizes the total energy budget ΔW ($J.m^{-2}$) of this rupture propagation based on classical slip weakening models [(Kanamori & Heaton, 2000),(Rice & Cocco, 2002), (Abercrombie & Rice, 2005), (J. Aubry et al., 2018)]. ΔW is the total deformation energy dissipated in the process and is the sum of a fracture energy E_G, a radiated energy E_R (propagating by the mean of elastic waves) and a frictional energy E_H (dissipated within the slip zone by frictional heating):

$$\Delta W = E_H + E_r + E_G \tag{1.10}$$

Although E_H represents an important part of the total energy budget, it does not strongly influence rupture processes that mainly depend on E_G (Fulton & Rathbun, 2011). The radiated part E_r is only a few percent of the total work and can be measured with the stress drop value and total displacement *Ds* of the fault, Figure 18. This radiated energy released during an earthquake is linked with the magnitude of the earthquake thanks to the seismic moment M_0 (depending itself on the fault displacement, its Young modulus and its surface pf sliding).

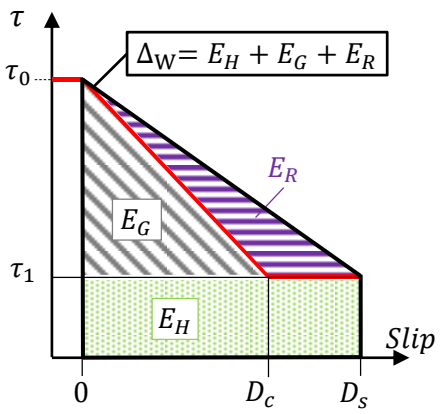

Figure 18. (a) A theoretical model of energy budget with ΔWas the sum of a fracture energy E_G, a radiated energy E_R (propagating by the mean of elastic waves) and a frictional energy E_H (dissipated within the slip zone). τ_0 is the initial static shear stress, τ_1 the dynamic shear stress, D_c is the slip weakening distance and D_s the end of slip displacement. This energy budget model is based on linear slip weakening theory. This is a simplification of the total balance of energy which also depends on the size of earthquakes and additional thermal weakening (Kanamori & Heaton, 2000).

Even though many studies focus on the understanding and distribution of these different energies, they remain complex in their relationship with the different sliding mechanisms. Literature reports a large range of phenomena occurring during faulting, after the end of the first slip weakening phase, and mainly observed under high pressure and velocity and within a very thin slipping zone [(Rice & Cocco, 2002), (Di Toro et al., 2011)]. These "dynamic weakening" mechanisms, to differentiate with the so-called "slip weakening", need a certain amount of sliding before occurring [(Kanamori & Heaton, 2000), (Scholz, 2002), (Rice, 2006), (Acosta et al., 2018)], and are generally caused by thermal effects. The temperature rise can lead to several dynamic weakening mechanisms enhanced with water presence such as: (i)

Rock melting, large slip and high slip velocities, [(Rice & Cocco, 2002), (Otsuki et al., 2003), (Niemeijer et al., 2011), (Di Toro et al., 2011), (Violay et al., 2014), (Aharonov & Scholz, 2018), (Fondriest et al., 2020), (Mollon et al., 2021b)] ; (ii) **Flash Heating**, asperity contact [(Rice & Cocco, 2002), (Rice, 2006), (Acosta et al., 2018), (Cornelio, Passelègue, et al., 2019)]; or (iii) **Thermal pressurization**, fluid within porosities [(Rice & Cocco, 2002), (Wibberley & Shimamoto, 2003), (Otsuki et al., 2003) (Rice, 2006), (Violay et al., 2013), (Acosta et al., 2018), (Lambert & Lapusta, 2020), (Badt et al., 2020)].

(J. Chester et al., 2005) found that fracture energy E_G is small compared to other energies (~1% for fault gouge according to (Fulton & Rathbun, 2011)). However small, this energy is needed to weaken a fault during an earthquake and to allow fracture propagation. Linking friction model and crack model (Kanamori & Brodsky, 2004), the fracture energy E_G corresponds to the work needed to drop the shear strength τ_0 to the residual strength τ_1 for a slip weakening distance *Dc:*

$$\mathrm{E_G} = \int_0^{D_c} (\tau\,(U) - \tau_1\,)\,d_U \tag{1.11}$$

Recent researches on the fracture process also try to understand how and to which extent the frictional rupture can be viewed as an ordinary fracture process [(Barras et al., 2019), (Barras et al., 2020)] offering some insight into open questions relating to energy budget. However, even though some crucial information can be found in the following papers [(Kanamori & Heaton, 2000), (Abercrombie & Rice, 2005), (J. Chester et al., 2005), (Rivera & Kanamori, 2005), (Fialko, 2007), (J. Aubry et al., 2018), (Okubo et al., 2019b), (Barras et al., 2019), (Barras et al., 2020)], earthquake energy budget still needs further research in the relationship they have with each internal mechanism happening during slipping.

In this Thesis, we restrict our focus on the most immediate (fracture-related) slip weakening phenomena and disregard all thermal effects, which are supposed to happen only after a certain amount of slip. A fault zone remains a very complex system in which many parameters interact at different scales. We would now like to add another degree of complexity by considering the properties of a granular fault gouge that can be found in the main slipping zone defined in (1.2.2). We propose for this purpose a look into granular material science and tribology to detail current knowledge on this material and its interaction with fault slip mechanisms. Section 1.4 will detail the granular fault gouge importance, its rheology, and the link with our research strategy.

1.4. The role of granular fault gouge

(Lockner & Beeler, 2002) reported that a wide range of parameters can affect the strength of both faults and rocks including a variation on mineralogy, porosity, cementation, packing geometry of gouge, surface roughness and wavelength, angularity and size of gouge particles, temperature, pore-fluid pressure, and composition, deformation rate, deformation and stress history, fabric, foliation, or other anisotropic properties, etc. Figure 19 is a simplified version of the fault core previously presented in section 1.2.2, schematizing the main parameters acting on fault slip mechanisms and contact stability, gathered as (a) external constraints (pressure,

slip velocity, temperature…), (b) Rock properties and lithology (roughness, stiffness, hardness…), (c) fluid, (d) Granular material properties (Particle Size Distribution, shape of particles, thickness…) and (e) infill material within the gouge.

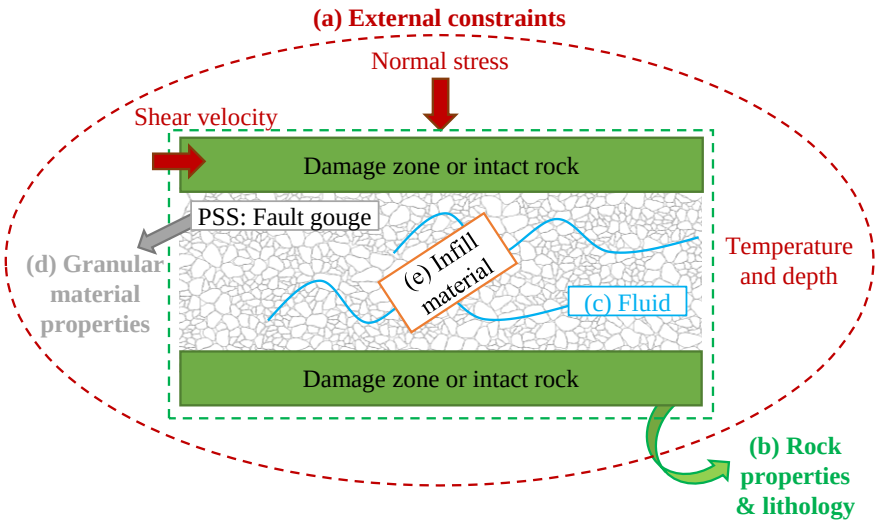

Figure 19. A simplified version of the fault zone structure previously presented in section 1.2.2, highlighting the granular fault gouge. The main influent factors are: (a) external constraints (pressure, slip velocity, temperature…), (b) Rock properties and lithology (roughness, stiffness, hardness…), (c) fluid, (d) Granular material properties (Particle Size Distribution, the shape of particles, thickness…) and (e) infill material within the gouge.

Gouge characteristics are believed to influence, if not control, a large part of slip mechanisms. Such gouge parameters have been studied in the literature from Lab or in-situ points of view [(Byerlee & Brace, 1968), (Sammis et al., 1987), (Biegel et al., 1989), (Marone & Scholz, 1989), (Mair & Marone, 1999), (Anthony & Marone, 2005)], and also numerically by the mean of Discrete Element Modelling (DEM) [(Morgan & Boettcher, 1999), (Morgan, 1999), (Guo & Morgan, 2004), (Da Cruz et al., 2005), (Cho et al., 2008), (Zhao et al., 2012), (Gao et al., 2018)]. As for intact rock, fault gouge stability mainly depends on normal and deviatoric stresses applied to the fault. High stress will tend towards a fractured regime with unstable deformations while low stress will be more likely to result in an unfractured regime (stable deformation), [(Byerlee et al., 1978), (Mair & Marone, 1999)]. Elements (a), (b), and (c) are widely studied in the literature and known as major elements acting in the fault behavior. Although they still need further research they will not be the main subject of this manuscript. The reader may access some interesting information on these topics in the following papers: external constraints [(Byerlee & Brace, 1968), (Stesky et al., 1974), (Mair & Marone, 1999), (Guo & Morgan, 2004), (Niemeijer et al., 2011), (Violay et al., 2012), (Geng et al., 2018), (Bedford & Faulkner, 2021), *etc.*], rock properties and lithology [(Marone, 1998), (Anthony & Marone, 2005), (Fournier & Morgan, 2012), (Insua-Arevalo et al., 2021), and fluid [(Violay et al., 2013), (Violay et al., 2014), (Scuderi et al., 2014), (Scuderi & Collettini, 2016), (Bayart et al., 2016), (Dorostkar et al., 2017a), (Acosta et al., 2018), (Cornelio, Spagnuolo, et al., 2019).

In this chapter and the rest of the Thesis, we will focus on the fault gouge material, its mechanical and rheological properties as well as the potential infill material present within the gouge and their influence on fault behavior. Section 1.4.1 describes the main fault gouge characteristics from a mechanical and granular point of view. Subsection a. answers

why the gouge is so important and makes the link between tribology and fault mechanics by the mean of the Third Body Theory and wear models. It also details the importance of a lubricant presence within the contact, even without fluid. Subsection b. explains how the gouge deforms, showing the different kinds of deformation observed within a granular fault gouge in direct shearing and the main shearing bands formed all along the gouge life (Riedel bands, Y bands…). Then section 1.4.2 restrains the Thesis to the study of infill material within the fault core (i.e. cement and matrix material). It proposes a description of these materials and presents some work already done in the research field. Finally, section 1.4.3 presents a small review on numerical modeling and fault gouge modelization and concludes on the modeling choices kept for the rest of the Thesis.

1.4.1. Research Strategy #1: focus on fault gouges mechanics and rheology

a. Gouge as a geological third body

Wear and grain fragmentation

As previously discussed in section 1.2.2, the fault core mainly contains fragmented rock particles coming from host rocks shearing. These granular particles can also be defined as wear material from damage or erosion of surfaces in contact (Scholz, 1987). As shown in Figure 20 (a), wear rate first presents a period of rapid wear due to surface asperities, followed by a lower stable wear rate, corresponding to the established gouge layer (Scholz, 2019). The wear rate mainly depends on lithology (ex: sandstone wears much faster than granite) and on the applied normal stress, showing a behavior close to that of Archard's law (Archard, 1953). As wear continues, the initially rough surfaces in contact become, at some point, totally separated by gouge particles, meaning that the thickness of the gouge zone increases linearly with total slip for brittle faults (Scholz, 1987). The experimental wear rate was also found to be smaller than the one of natural fault due to surface roughness in contact.

A particle size reduction is observed from the comminution process [(Sammis et al., 1987), (F. Chester et al., 1993), (Sibson, 2003)] also called grain breakage [(Daouadji et al., 2001), (Daouadji & Hicher, 2010)] in granular mechanics. The number and amplitudes of successive slips reduce the size of particles towards a fractal distribution (depending on the type of mineral), which also reduces pore spaces [(Sammis & Biegel, 1989), (Olgaard & Brace, 1983), (Blenkinsop, 1991), (An & Sammis, 1994), (Billi & Storti, 2004), (Billi, 2005), (Muto et al., 2015)]. The evolution of this fractal dimension also relies upon the amount of shearing (time scale) and the distance from the fault core (geometric scale), as in Figure 20 (b). Mineral grains morphologies can be very diverse, but granular gouges generated by comminution are expected to exhibit rather rough and angular shapes [(Olgaard & Brace, 1983), (Sammis et al., 1987), (An & Sammis, 1994), (Lin, 1999)], Figure 20 (c). A collection of these angular shapes can be observed in Appendix 1.A.

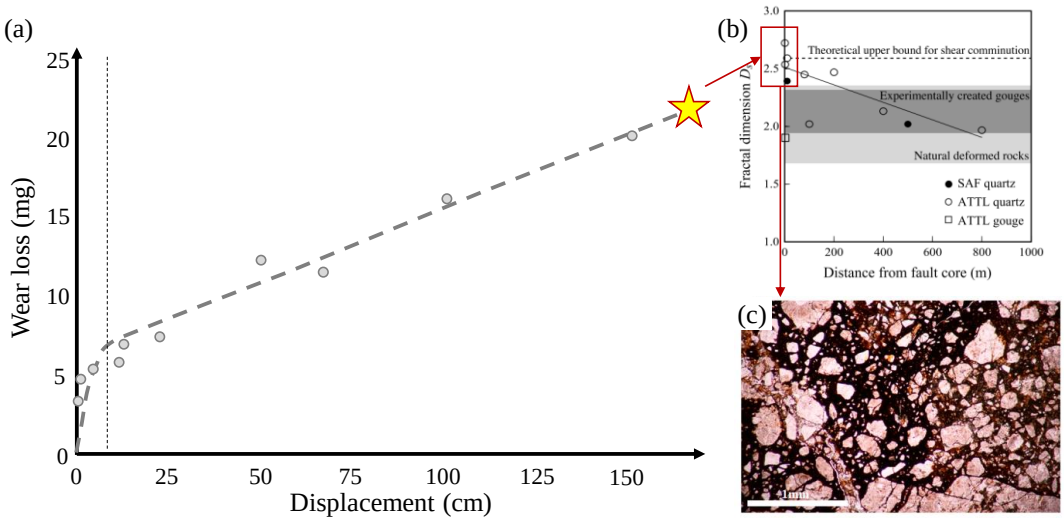

Figure 20. (a) A complete wear curve for Westerly granite, for an applied normal stress of 3 MPa. The first part is the running-in wear, which can evolve to steady-state wear at a constant rate. Image from (Scholz, 2019). (b) Fractal dimension of the ATTL and San Andreas Fault quartz grains as a function of the distance from the fault core. (c) Pulverized rock of the Arima-Takatsuki Tectonic Line (ATTL) fault gouge, photomicrograph, Both images are from (Muto et al., 2015).

Granular gouge as a lubricant

From an engineering point of view, any type of lubrication between two solids in contact, may it be fluid or solid, is supposed to decrease friction at the interface. The lubricant may have a different role on the mechanical contact depending on the quantity and thickness between the two contacting bodies (Hardy, 1920) and is seen as a good ingredient in tribological applications by decreasing friction and reducing energetic loss. The role of fault gouge is similar at the fault scale, the presence of gouge induces an important weakening in comparison with fault friction without or with negligible wear formation, explaining the difference found with Byerlee's rule in section 1.3.1 for gouge material. This mechanism was compared to "powder lubrication" by (Reches & Lockner, 2010) who also proposed a model for fault weakening as velocity rate increases. The accumulation of wear material also tends to stabilize slip relatively to shear between bare rock surfaces [(Scholz, 1987), (Biegel et al., 1989), (Marone et al., 1990), (Marone, 1998), (Morgan & Boettcher, 1999), (Reches & Lockner, 2010)].

To illustrate the evolution of the different contact mechanisms, with or without lubricant (i.e. fluid or powder), Stribeck proposed in the early 1900s a model of friction coefficient evolution as a function of a hydrodynamic number proportional to (viscosity*velocity)/load. The Stribeck curve was initially proposed for tribological application but was recently used and compared to fluid-lubricated faults [(Spikes, 1997), (Kanamori & Brodsky, 2001), (Cornelio, Spagnuolo, et al., 2019), (Cornelio & Violay, 2020)]. In the 1980s, the concept of "Third Body" was pointed out by (Godet, 1984), inspired by lubrication theories, to characterize the material or medium at the contact interface between two solids, Figure 21 (c). This third body can be a "liquid" lubricant (as fluid already present within the fault or artificially injected (as with EGS)), but in the case of "Dry" contact, this 3rd body is still present and is composed of wear particles, Figure 21 (a) and (b). In this mechanism, the granular layer has several interesting functions as (i)

supporting the load applied on the contact, (ii) participating to velocity accommodation, and (iii) separating surfaces in contact to avoid direct interaction (Godet, 1984).

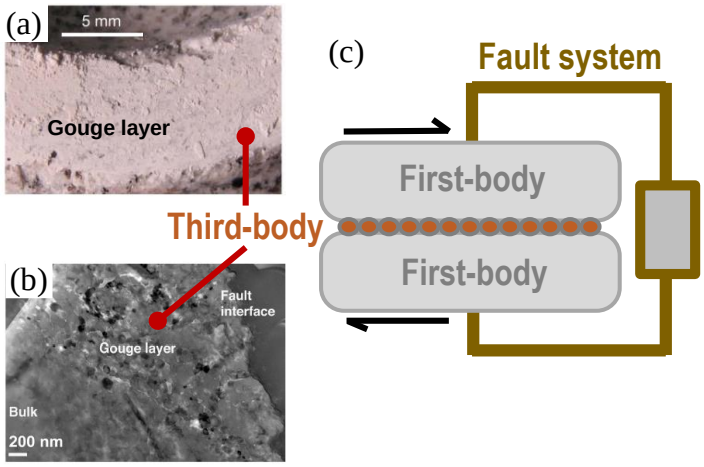

Figure 21. Third body theory representation schema and powder lubrication. (a) Sliding surface with adhered gouge and gouge layer, from Sierra White granite in rotary shear. Image from (Reches & Lockner, 2010), (b) TEM observations on post-mortem fault sections at 180 MPa, triaxial experiment. Image from (Jérôme Aubry, 2019). (c) schema of the third-body theory applied to the fault system. More information on the third body concept are available in [(Iordanoff et al., 2005), (Fillot et al., 2007)].

[(Mair et al., 2002), (Nouguier-lehon et al., 2003), (Anthony & Marone, 2005)] have shown that angular and faceted particle shapes (instead of circular grains) led to higher friction coefficients and different mechanical behaviors. These results also need to be related to the roughness of the bare rock which increases the shear ratio observed for any shape of particles. As particle shape influences frictional properties, it also controls stick-slip dynamics: spherical particles mostly show a production of stick-slip motion, whereas angular particles promote stable sliding (Mair et al., 2002). The influence of the grain shape on friction increases with the decrease in the normal stress (Guo & Morgan, 2004).

Within this Thesis, we decided to stay in the boundary lubrication regime, which is the classical solid-solid contact (no liquid lubricant, dry contact). We define the fault gouge as wear particles, as the process of 3rd body production, and friction as the rheology of this 3rd body (similar to fluid viscosity). Another objective is to reproduce realistic granular shapes of gouge with angular and faceted shapes as found in fault core (Appendix 1.A). The evolution of gouge properties with slip and its influence on slip mechanism and rheology are described within the next subsection b.

b. Deformation mechanisms and rheology of fault gouges

The understanding of fault gouge deformation mechanisms is a key element in the construction of fault models. Deformation zones are complex structures, they have variable aspects (geometry and kinematics), depending on the mechanism of deformation adopted and rock characteristics, section 1.2.3. A word about dilatancy? (Marone et al., 1990) indicate that granular gouges can show a rather "velocity-strengthening" behavior induced by a significant dilation of fault gouges (dilation implying a variation in the porosity state of the granular gouge sample). It is clear that shear between bare rock surfaces does not involve dilation as great as observed in the case where a granular gouge is present [(Marone et al., 1990), (Kilgore et al.,

1993), (Beeler et al., 1996)] and that denser granular samples show larger dilating behavior than a loose sample. However, shear localization can also form within fault gouge to accommodate the inelastic shear strain. They appear as a common phenomenon in granular mechanics, widely studied both experimentally and theoretically [(Dunn et al., 1973), (Vardoulakis & Graf, 1985), (Antonellini et al., 1994), (Antonellini & Pollard, 1995), (Haines et al., 2013)].

Riedel shear bands

For a sufficiently mature fault system (sufficient gouge layer), shear localization was observed at specific angles and called Riedel Shear bands (or cataclastic deformation bands) (Tchalenko, 1970). They reflect a heterogeneous stress field developing in response to deformation [(Marone & Scholz, 1989), (Morgan & Boettcher, 1999), (Lockner & Beeler, 2002), (Kaminskaite et al., 2019)]. Figure 22 schematizes the main deformation bands forming within the shearing gouge. Secondary **Riedel bands** in the R orientation (sense of shear zone) are commonly observed to be predominant, but in some cases, **antithetic shears** (i.e. conjugate shears) can form in the R' orientation, rotating with granular flow [(Davis et al., 2000), (Y. Katz et al., 2004), (Misra et al., 2009)]. **Y surfaces** are parallel to the direction of shearing and can also form within the **boundary shear bands B**, also parallel to the shearing direction but located at the boundaries [(Gu & Wong, 1994), (Blanpied et al., 1995)]. In some granular materials, such as Clay-rich fault gouge (Rutter et al., 1986), **a primary foliation P** can be observed normal to σ_1 (angle 135° from the direction of shearing in the simple shear and progressively rotating until 180°). E**xtension fractures** T, normal to the least principal stress direction can form for low and medium-grade metamorphic terranes or high fluid pressure. Even though Riedel shears were first used to describe brittle deformation, a foliation can also be observed within ductile deformation in the R orientation (Scholz, 2019). The shear zone at a small scale is only one part of a more complex structure at a higher scale called "shear zone structure" or "Riedel shear structure" (Y. Katz et al., 2004)**.**

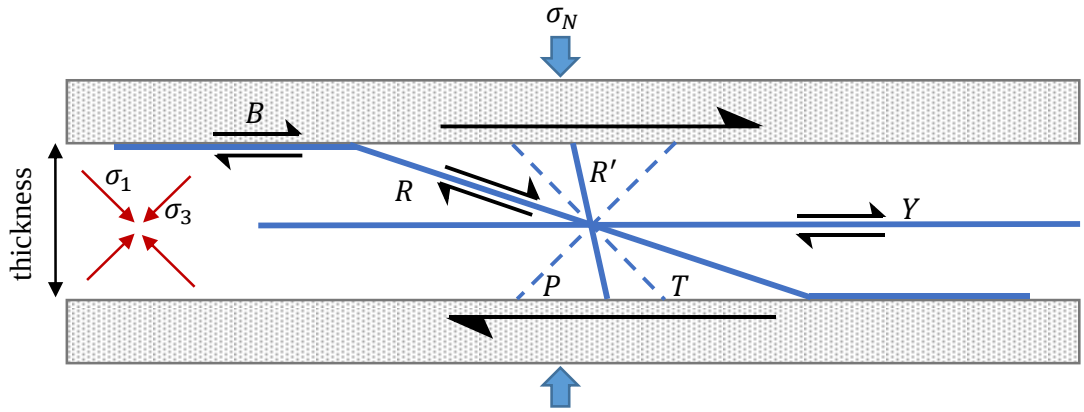

Figure 22. Schematic diagram of a sheared gouge zone, showing the geometrical relationships of the main structural elements and the orientations of the principal stresses with the shear zone.

The presence of Riedel bands (R) has been identified as being responsible for a mechanical weakening [(Gu & Wong, 1994), (Beeler et al., 1996)] and to be an indicator of a change in stability in frictional sliding (Byerlee et al., 1978). It is therefore essential to study the timing of their formation during the sliding and their orientation.

The temporality of Riedel bands and their consequences

The onset of Riedel bands is mainly associated with a significant dilatancy rate and a reduction in the comminution rate of the granular layer [(Marone, 1998), (Borja et al., 2013)]. The interplay between porosity [(Dunn et al., 1973), (Antonellini et al., 1994)] and particle size distribution [(Marone & Scholz, 1989), (Antonellini & Pollard, 1995)], confining pressure (Byerlee et al., 1978), clay or weak mineral content [(Haines et al., 2013), (Kenigsberg et al., 2019)] and amount of strain may develop these Riedel bands at different stages and with different characteristics [(Antonellini et al., 1994), (Philit, 2017)]. Figure 23 schematizes the main stages of Riedel shears formation gathered from different studies [(Tchalenko, 1970), (Byerlee et al., 1978), (Marone & Scholz, 1989), (Gu & Wong, 1994), (Beeler et al., 1996), (Marone, 1998), (Hadizadeh et al., 2015), (Kenigsberg et al., 2019), (Scholz, 2019), (Bedford & Faulkner, 2021)]:

- **Step 1 – elastic phase**. Due to external loading, the granular layer is compacted and reorganized (particle movement or grains fragmentation) during the elastic phase. The global stiffness increases and the porosity is reduced, controlling the mechanical et elastic responses (Kenigsberg et al., 2019). The stress ratio (i.e. effective friction) increases progressively until it reaches the maximal shear strength where Riedel bands formation is observed.

- **Step 2 – weakening**. The R-bands are still prominent, but Y-bands begin to form. They are sufficiently developed to take part in the control of gouge behavior and mechanical properties. Interparticle bridges (or force chains networks) are formed to support the shear loads applied to the assembly. They can sometimes correspond to T-bands. These chains are often inclined at 45 ° from the direction of shearing and evolve throughout the shear (Morgan & Boettcher, 1999). Conjugate Riedels R' are not observed within the images, Figure 23 (b), but if they form it must be at this step with strain-hardening behaviors (Davis et al., 2000). A decrease in shear resistance from yield is observed (i.e. the weakening mechanism).

- **Step 3: end of weakening**. The main Riedel bands R are less prominent but B & Y bands are still developing and increasing again the weakening of fault gouge. R-bands progressively connect with the boundary bands.

- **Step 4: steady-state**. This is a residual stage, where shear resistance has reached a stable steady-state friction with one or several parallel principal Y-shears lying in the slip direction. The Y-shears can be developed at the center of the gouge (Marone, 1998) or within the Boundary shear zone (Bedford & Faulkner, 2021). A stable frictional strength is reached at the point at which well-developed Y shears become prominent (Marone, 1998).

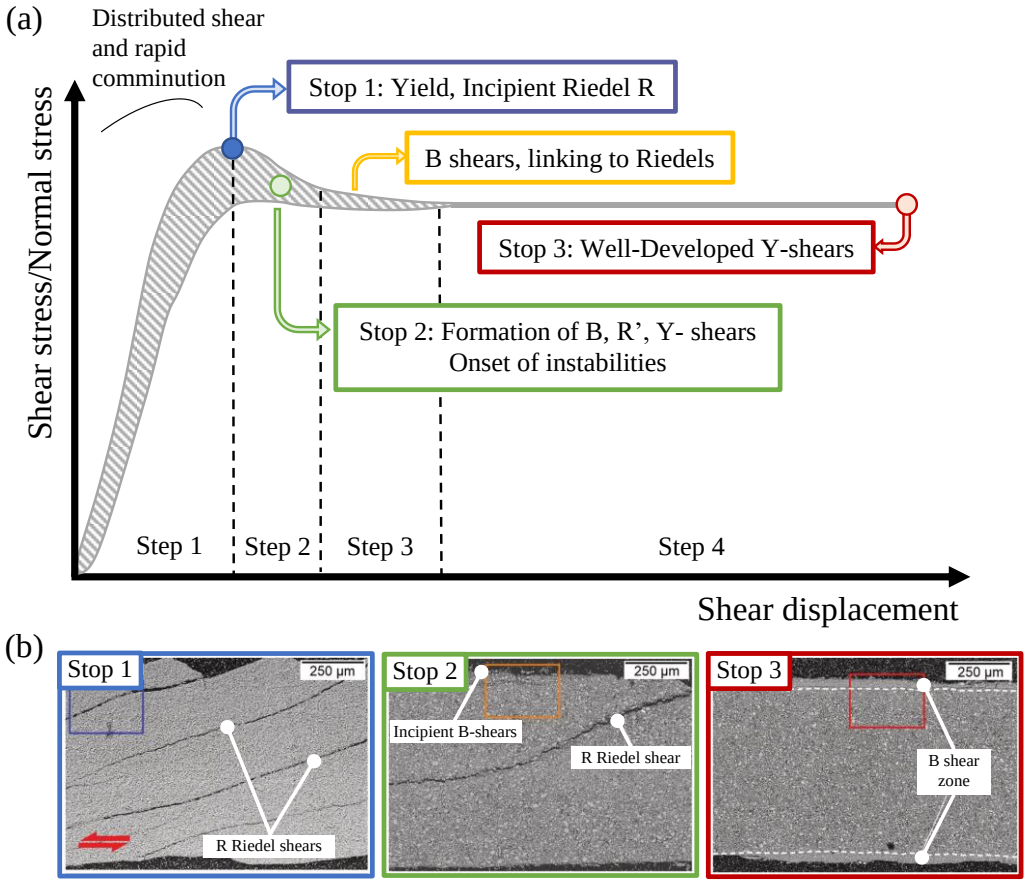

Figure 23. (a) Riedel band formation within the granular fault gouge illustrated with stress ratio as a function of shear displacement. Image modified from (Marone, 1998). (b) Backscatter electron (BSE) images of 15 µm quartz gouge layers sheared $\sigma_n = 80$ MPa. Stops 1–3 correspond to the different displacements where shearing is stopped, Stop 1: just after the yield (slip=1.5 mm), R Riedel shears within the layer. Stop 2: at the onset of stick-slip instabilities (slip=3.2 mm), R Riedel shears and incipient B-shears are observed. Stop 3: end of the experiment after multiple stick-slip events (slip=6 mm), B-shears are observed at the top and bottom of the layer, with discrete Y-shear planes within the B-shear-zone. Images from (Bedford & Faulkner, 2021).

The transition from stick-slip to stable sliding corresponds to the formation of boundary and Y-shear bands (Gu & Wong, 1994). Even though Riedel shear bands are a necessary condition for stick-slip instabilities to occur in gouges, they are not sufficient, as they were also observed for some stable slidings (Moore et al., 1988). It has been speculated that the R' bands may inhibit gouge movement by preventing the connection between the R and Y bands (Moore et al., 1988), but the link between the orientation of the Riedel bands and the slip modes is not yet fully understood. As suggested by [(Moore et al., 1988), (Gu & Wong, 1994)], it also exists a critical angle α_i between the bands and the direction of shearing that indicates whether or not instabilities can occur, higher angles tending to destabilize the gouge. According to Coulomb-Mohr criteria and geometry, α_i could be equal to $\varphi/2$ for simple shear (with φ being the internal friction angle). However, this relation has to be used with care, as other factors can be involved in the α_i angle (Moore et al., 1988). Recently, it was confirmed that Riedel bands can differ from the center of the granular fault gouge to the rock boundaries. They appear to develop at lower angles to rock-gouge boundaries toward unstable slip (Hirata et al., 2017), and mostly depend on normal stress and strain velocity in major and minor stress orientation axes.

The link between the orientation of Riedel bands and slip patterns is not yet fully understood. One part of the thesis will be devoted to studying the temporality of Riedel bands as a function of gouge characteristics. For this, we will focus on two types of gouges containing infill material, described in the next section.

1.4.2. Research strategy #2: study of infill materials

Once considering a mature enough fault zone that has already been sheared, infill material can be observed within void spaces around granular particles. They bring additional heterogeneities to the fault gouge modifying the stress field (Scholz, 2019) and petrophysical properties (Philit, 2017). Even though these materials are well described from a geological point of view, it is more difficult to find associated lab experiments or simulations. In this section, we gather the main characteristics of two types of infill material, matrix particles, and cement, and wonder what is their influence on fault zone behavior and stability. This distinction was made thanks to a bibliography of different gouges and infill materials available in Appendix 1.A.

Cement or matrix?

Within a mature fault gouge, the distinction between cement and matrix between breccia clasts is not easy to make and partly depends on brecciation processes in fault zones [(Wise et al., 1985), (Sibson, 1986), (Riedmüller et al., 2001)]. Many rock classifications have been proposed from structural geology and based on the parameters fabric, texture, clast size, and matrix percentage but they all depend on the scale of observation and resolution of the individual component with the naked eye, giving sometimes really different classifications [(Sibson, 1977), (Riedmüller et al., 2001), (Woodcock & Mort, 2008)]. Figure 24 proposes a classification for cohesive and incohesive fault core and associated infill material from (Riedmüller et al., 2001) combined with explanations from (Woodcock & Mort, 2008).

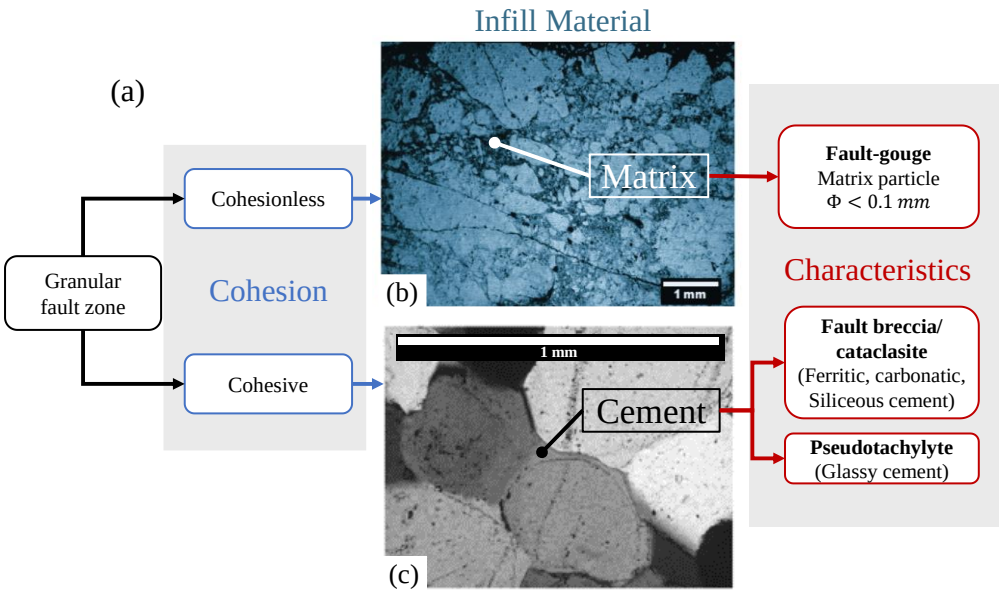

Figure 24. (a) Image created from (Riedmüller et al., 2001), rock classification from (Sibson, 1977) and (Woodcock & Mort, 2008) and internship from Heiarii Pons. The limit size between 'small clasts' and 'matrix' is settled at 0.1mm, which is the resolution of an individual component with naked eye (Wise et al., 1985). (b) Blocks embedded in a matrix, random distribution of blocks varying in size and orientation, microscale (thin section), image from (Riedmüller et al., 2001). (c) Micrographs of thin sections showing sandstone with abundant quartz cement and some reduced primary pores plane (polarised light with crossed polarization filters, length of photomicrographs is 0.96 mm). Image from (Molenaar et al., 2007).

Mineral cementation, generally evolving with burial, refers to a crystalline material coming from rock dissolution or precipitation (Walderhaug, 1994), partial melting (pseudotachylite, non-crystalline material), [(Di Toro et al., 2009), (Fondriest et al., 2020)], or other processes derived from previous slips. It fills remaining pore spaces between particles, reducing permeability and changing the global state of cohesion of the gouge material [(Woodcock & Mort, 2008), (Philit et al., 2018)]. The behavior of this cement depends on the material composition [(Caine et al., 2010), (Philit, 2017), (Kaminskaite et al., 2019)], on the volume, and on the contact interface between cement and particles. By contrast, the term M**atrix** refers here to very fine cohesionless particles whether produced by local comminution or by the introduction of other sediments [(Lee & Kim, 2005), (Woodcock & Mort, 2008)]. The scale of observation and classifications allow us to distinguish a weak gouge matrix from fragments or clasts with a limiting size between 'small clasts' and 'matrix' settled at 0.1mm (resolution of an individual component with naked eye (Wise et al., 1984)). Matrix particles are from parts similar to a granular material with high fractal dimension and will present the same mechanical consequences (denser granular zone with porosity reduction). The lithology of matrix or clasts particles also influences the frictional behavior. For example, an increase in the percentage of clay matrix drastically reduces the effective friction toward 0.1-0.2 (Wojatschke et al., 2016).

Impact of cementation on rheology and contact stability

For cohesive materials such as cemented rocks, two types of situations are observed: the low-cohesive (or non-cohesive) materials, where external stress is preponderant on interparticle cohesion, and ultra-cohesive materials where cohesion controls particles interactions (that will tend to a brittle behavior). Macroscopic cohesion can either be expressed as a tensile, or a shearing resistance (Topin, 2009). From a particle point of view, cohesion can be similar to an adhesion force or a slip-rolling resistance between particles (Estrada et al., 2008). The cohesion in the sense of Coulomb-Mohr is easy to measure (cf. section 1.2.3) and it was widely studied for intact rocks [(Handin, 1969), (Schellart, 2000), (Abdelmalak et al., 2016), (Roy & Luding, 2017)]. Not surprisingly, cohesive rocks are also those with the highest friction compared to low cohesion rocks [(Schellart, 2000), (Abdelmalak et al., 2016)]. Indeed, (Lade & Overton, 1989) showed that, for low confining pressures, the increase of cementation and the associated tensile strength lead to an enhancement of friction coefficient (as well as shear and bulk elastic moduli): both porosity and permeability of shears bands are also reduced [(M. Wangen, 1999), (Ogilvie & Glover, 2001), (Fisher & Knipe, 2001), (Molenaar et al., 2007), (Al-Hinai et al., 2008)]. The process of cementation gives birth to a new, stronger granular material combining its history, the state of initial density (i.e. porosity within the sample), and cementation (Schellart, 2000). During granular fault shearing at low confining pressure, cement first increases the brittleness at failure and prevents grain rearrangement by increasing cohesion between particles (Johansen et al., 2005). For low cementation, the progressive breakage of cement bridges between particles enhances local kinematic freedom and allows grains reorganization. This loss of cement contribution reduces the stability of the system with a global softening and dilatant behavior letting appear shear plane failures previously described [(Rad & Clough, 1982), (Das et al., 2014), (Lade & Overton, 1989), (Menendez et al., 1996)]. For

high cementation, breakage of cement is very sudden, enabling fracture instead of shear failure [(Schellart, 2000), (Schmocker et al., 2003), (Kettermann & Urai, 2015)].

From a geological point of view, fault gouge is seen as an incohesive material, so it would have been reasonable to call granular fault with cement "cemented cataclastic fault". However, for the sake of simplicity, we will name as "fault gouge" all the granular materials tested, may they be cohesive or not. It appeared that many field observations exist on these infill materials, but they count only a few representations in tribological studies dedicated to the understanding of fault sliding mechanisms. This Thesis aims to add a new key of understanding on these materials at the fault scale through granular mechanics and tribology research.

1.4.3. Research strategy #3: Modeling fault gouges

Why numerical modeling?

- The first objective is to model a single fault patch with granular fault gouge inside, large enough to observe shear deformations. We also want to model phenomena occurring at the grain scale, by representing cement and matrix filling pores around gouge particles. Numerical modeling allows easy access to both scales without building a complex observation system. The Discrete Element Method can be useful to understand granular physics of fault gouge by studying grains interactions and their influence on slip mechanisms.
- The interest is also to start with identical initial granular configuration and to be able to easily vary the amount of matrix and cement present in our samples to test a wide range of different material behaviors. We also want to quantify and follow the evolution of the cohesive bonds created between the grains over time, since such data is impossible to see or to follow during a lab or in-situ experiment.

a. Discrete Element Modelling (DEM)

Discrete Element Modeling (Cundall & Strack, 1979) is a powerful tool to model micrometric to centimeter scales and observe the grain-scale deformation. A granular material (i.e. fault gouge) can be explicitly represented as a collection of rigid bodies, allowing to study very local fault behavior (grains movements) and highlighting the links between the mechano-physical properties of the fault and its rheological behavior. In order to be representative of the local behavior, a high number of particles needs to be modeled, and the movement and dynamic of each particle are computed. Moreover, is it possible to test and vary a huge number of physical and numerical parameters as well as different contact laws.

DEM has been already used in fault mechanics to understand frictional and contact properties of a fault core [(Morgan & Boettcher, 1999), (Morgan, 1999), (Guo & Morgan, 2004), (Aharonov & Sparks, 2004), (Da Cruz et al., 2005), (Cho et al., 2008), (Zhao et al., 2012), (Zhao, 2013), (Ferdowsi et al., 2014), (Dorostkar et al., 2017a), (Dorostkar et al., 2017b), (Gao et al., 2018), (Ferdowsi & Rubin, 2020), (Mollon et al., 2021b)], and also in some interesting

granular mechanics researches not directly applicated to fault mechanics [(Jensen et al., 1999), (Aharonov & Sparks, 1999), (K Maeda, 2006), (Kenichi Maeda et al., 2010), (Mollon et al., 2012), (Zhou et al., 2017), (Y. Lu et al., 2017), (Mollon, 2018b)]. More recently, the DEM has been enhanced by additional coupling or plug-in: the "extended DEM" considers thermodynamics in order to study the high-temperature rise and melting within the granular fault zone, using a mixture between compliant and rigid bodies, Figure 25 [(Mollon et al., 2021a) & (Mollon et al., 2021b)], the Computational Fluid Dynamic-DEM (CFD-DEM) is designed to observe fluid interaction within particles [(Goren et al., 2011), (Kloss et al., 2012), (Dorostkar et al., 2017a), (Dorostkar et al., 2017b), (Dorostkar, 2018), (Tomac & Gutierrez, 2020)] and FEM-DEM coupling enables to link granular fault to a continuous damage zone [(Munjiza et al., 2004), (Dratt & Katterfeld, 2017)]. Grain fragmentation has also been modeled with DEM using different methods [(Zhao, 2013), (D. Wang et al., 2021)].

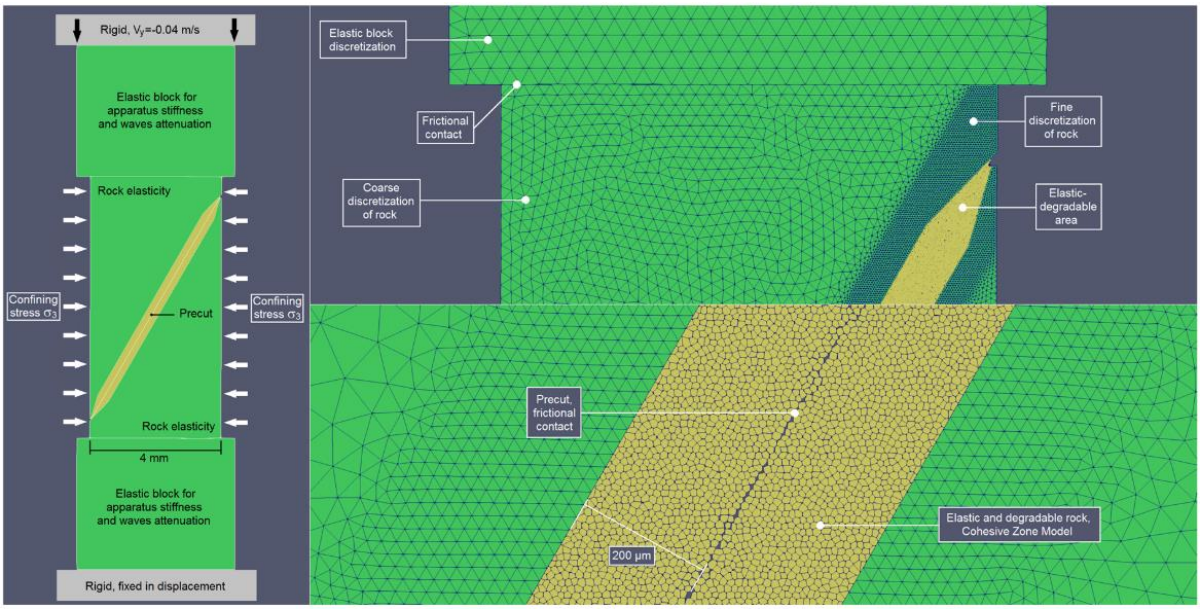

Figure 25. Setup model for the reproduction of laboratory earthquakes with a discrete-continuum model, software MELODY, image from (Mollon et al., 2021a).

Nowadays, the wide variety of modeling technics enables to study both 2D and 3D problems. 3D modeling is a considerable technical advance in numerical modeling as it provides access to new information in a third direction and more realistic interactions between particles [(Ferdowsi et al., 2014), (Dorostkar et al., 2017a), (C. Wang et al., 2019), (Ferdowsi & Rubin, 2020)]. However, the current 3D numerical experiments are not entirely satisfactory as they mostly propose a very thin bandwidth of granular layer: the behavior of tens of particles is not representative of the entire granular fault thickness (Dorostkar et al., 2017a). Besides, the calculation cost of 3D DEM is much higher than that of 2D modeling, leading to other restrictions in the length of the model, the number of particles, shapes of particles, interaction laws, etc. Another interesting aspect of computational modeling is the possibility to choose particle shapes. However, due to simplicity, convenience, and calculation costs in terms of contact detection and repulsive forces computation, most DEM studies use circular (2D) or spherical (3D) shapes of particles. This shape simplification: (i) is not very representative of fragmented particles found within mature granular fault (1.4.1), (ii) does not provide accurate predictions of granular behavior due to the different contact interaction [(Nouguier-lehon et

al., 2003), (Mair et al., 2002), (Mollon et al., 2020)] and is unable to yield interlocking forces, (iii) needs some research and additional numerical parameters to change contact properties and balance the oversimplification.

Figure 26 displays the steady-state effective friction as a function of the topological dimension and shapes of particles based on results from [(Mair et al., 2002), (Frye & Marone, 2003)], and personal results with the software MELODY. Lower effective friction is observed for 2D experiments which do not account for out-of-plane contacts and circular particles compared to angular particles. According to the results, friction also varies systematically between numerical and experimental studies. These changes can be explained by different initial and laboratory conditions.

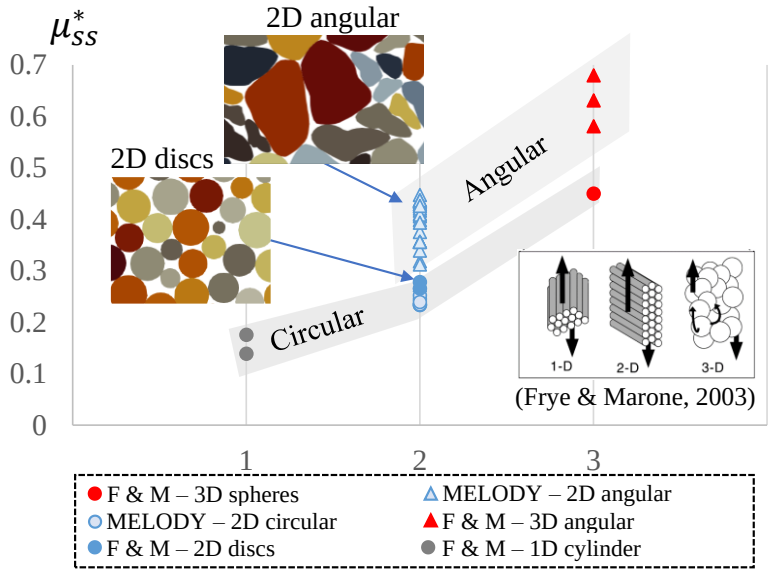

Figure 26. Steady-state effective friction μ_{SS}^* as a function of the topological dimensions of the model from 1D to 3D for angular or circular grains, (Frye & Marone, 2003) and personal results with the software MELODY.

b. Cement and matrix modeling

Cemented materials can be represented as cohesive granular materials, both playing on the type of contact law used (friction, cohesion), properties of the contact network (force distributions), and the rheology (dilatancy and effective friction), (Rognon et al., 2008). The Finite Element Method (FEM) is not very suitable for cemented granular material, due to the very fine mesh needed to accurately represent the rupture of cemented elements. The Lattice Element Method (LEM), in between the DEM and the FEM, has been widely used within the framework of the statistical analysis of fracture or for cracking of concrete and ceramics [(Topin et al., 2007), (Topin, 2009)]. This approach considers a medium reduced as a set of nodes belonging to a grid. However, in the present study, once the cemented links are broken, the granular fault core may recover a granular behavior, which won't be possible with the LEM. That is why Discrete Element Modelling (DEM) also seems to be a good way to complete knowledge on cemented materials and their influence on slip mechanisms. The increase of global cohesion (in the sense of Coulomb-Mohr) generated by the increase of cementation (cf. section 1.4.2) tends to a brittle rock behavior that can be easily schematized with DEM by cohesive and breakable bonds between particles changing the contact kinematics. Bonded Particle Models (BPM) are often

used to approximate the fragmentation process of rock (parallel bond rock model), [(Potyondy & Cundall, 2004), (Cho et al., 2007), (Kazerani & Zhao, 2010), (Potyondy, 2012),] or to represent cementation in granular mechanics (contact bond model), [(Estrada et al., 2010), (Jiang et al., 2013), (Das et al., 2014), (McBeck et al., 2019)]. This BPM method mostly uses circular particles in 2D (or spherical in 3D) connected at a point of contact and representing a compact and dense rock, Figure 27 (a). The objective is to be able to study the influence of the micro properties of grains, such as density, shape, distribution, and even grain stacking. The reader can access more information on the different DEM and BPM in the review made by (Lisjak & Grasselli, 2014). A really recent study from (Harmon et al., 2021) presents a new method to model cemented particles with what they call the Level Set Discrete Element Method for Bonded Particles (LS-DEM-BPM enabling to connect granular material with arbitrary particle shape existing in both 2D and 3D). They used their method to first model a granular fault gouge with rate-and-states friction laws and their results seem to be very promising for 3D modeling with real particle shapes.

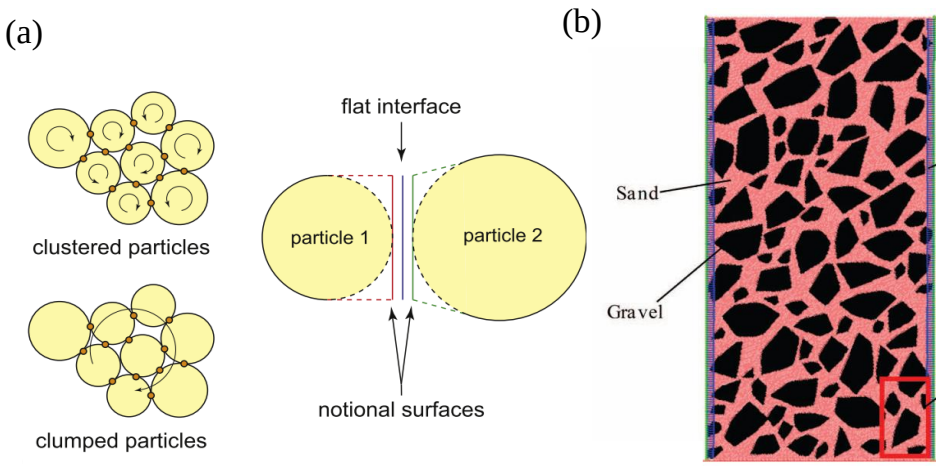

Figure 27. Different types of BPM (a) Clustered particles vs. clumped particles, image redrawn from (Cho et al., 2007), and flat-joint contact model showing the effective interface geometry (from (Potyondy, 2012)] redrawn). Image from (Lisjak & Grasselli, 2014) (b) Example of a mixture between clasts (i.e. gravel) and matrix (i.e. sand), image from (Y. Lu et al., 2017).

The modeling of matrix particles only requires the classical DEM modeling without cementation (only frictional contacts), with a very dense packing of fine particles. (Y. Lu et al., 2017) modeled Irregularly Shaped Gravel Grains surrounded by sand particles, using circular particles to represent the sand (which is a kind of matrix in this context). Circular particles however tend to an initial void ratio of about 30%, which is very important within the granular media, Figure 27 (b). To have a denser "matrix" representation, a Voronoï Tesselation [(Mollon & Zhao, 2012)] can be the basis of 'matrix' elements, providing a granular material with almost no initial porosity. In summary, the study of a modification in percentage of matrix particles within the granular fault core is similar, in some aspects, to a change in Particle Size Distribution, as done in [(Morgan, 1999), (Morgan & Boettcher, 1999)].

In this Thesis, a 2D numerical modeling of a granular fault gouge is proposed with DEM to study the impact of cement or matrix particles on slip mechanisms. As this new material is somehow complex, we decided to restrain the study to a pure dry contact mechanism but chose to use angular shapes of particles.

1.5. Concluding remarks

This chapter provided fundamental concepts and reviewed recent advances in understanding earthquakes, fault mechanics, and the role of granular fault gouge. The main objective of this Thesis work is to study the rheology and mechanics of a geological third body, more commonly called “granular fault gouge” in fault mechanics, with a focus on infill materials. The slip mechanism we are studying takes place in a mature fault (i.e. after many successive slips in previous geological times) that may have been cemented, or filled with matrix particles, over time without slip (e.g. in an interseismic period). We can therefore say that we are studying the reactivation of a gouge-filled fault zone, without studying the fragmentation process which is our starting point. Most fault core numerical models do not consider the infill material within the fault gouge. Moreover, the studies considering these materials with mature fault are not with DEM, or they use circular particles. The present Thesis proposes to combine 2D explicit DEM modeling with fault mechanics, and to investigate the onset of seismic sliding and slip mechanisms in presence of infill materials. 2D modeling still has a lot to bring to granular fault behavior, to which we add the originality of using realistic angular and faceted particle shapes for gouge particles.

Chapter 2. Numerical model description and methods

2.1. Foreword

In the previous chapter, we described the fault core as a granular medium. Even though certain continuous methods are used to model granular fault gouge, they commonly face difficulties sticking the reality due to the continuity assumption. As an alternative to the classical Finite Element Method, the Discrete Element Method (DEM) describes the flow of a granular material where each particle has its own behaviors and interactions. In this chapter, schematized in Figure 28, section 2.2 presents the DEM techniques used within the research and details the general contact model, governing equations, and solver. Section 2.3 proposes a method to model the angular shape of particles and displays the different types of granular media chosen to model infill materials. Finally, section 2.4 introduces the numerical framework, models, and choices made for granular gouge modeling. This last section also discusses the criteria and methods employed to calibrate and control the simulations.

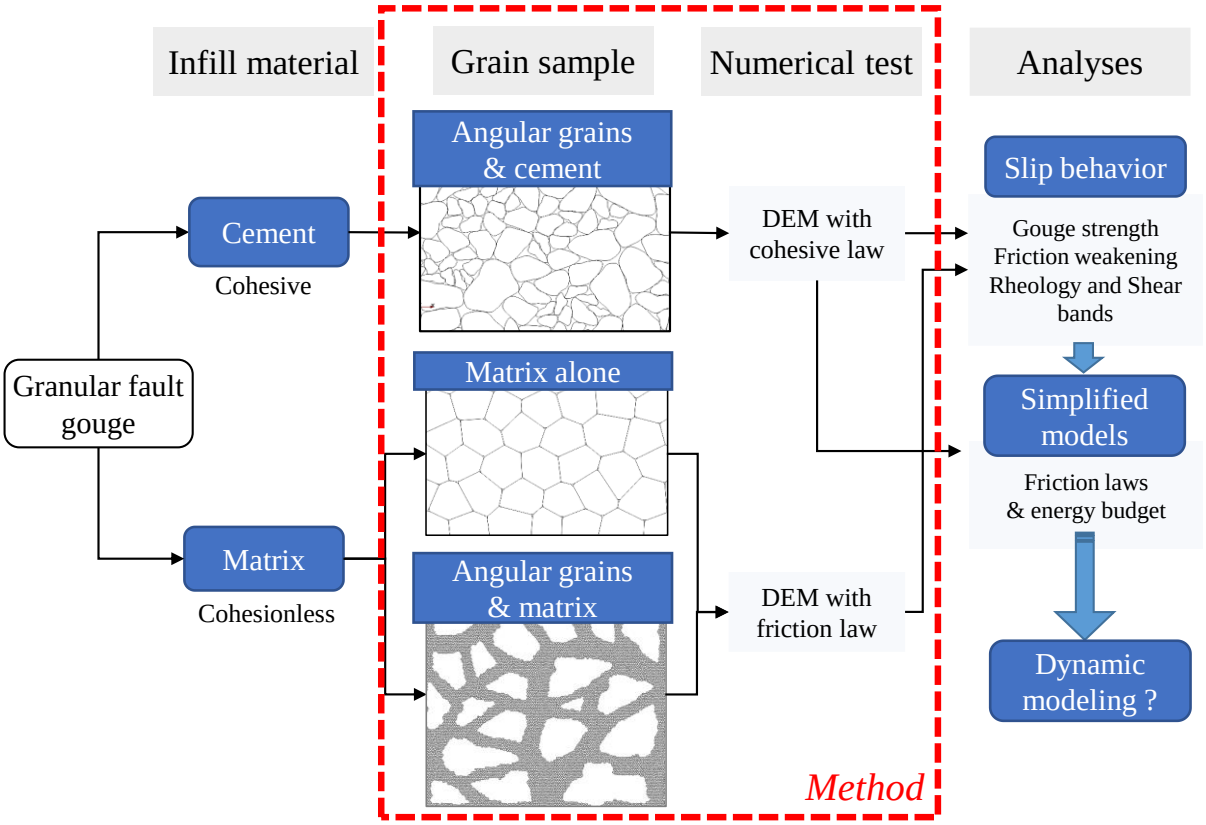

Figure 28. Main schema of Chapter 2.

2.2. Discrete Element Modelling (DEM)

The code used for the simulations, MELODY 2D (Multibody ELement-free Open code for DYnamic simulation), is a C++ code allowing to simulate a broad variety of granular media [(Mollon, 2016), (Mollon, 2018a)] in 2D. This software is a multibody code, as it can represent

in the same numerical framework first and third bodies with their deformation and dynamic (Chapter 1) keeping the discontinuity of the 3rd body. This subsection describes the DEM algorithms with the software MELODY.

2.2.1. General contact algorithm

DEM was first proposed by (Cundall & Strack, 1979). In their approach, each particle has its own movement and trajectory, driven by Newton's laws of motion:

$$\sum \overrightarrow{F_A} = m_A \left[\frac{d^2\overrightarrow{x_A}}{dt^2}\right] \tag{2.1}$$

For a particle A, m_A is the mass of the grain, $\overrightarrow{x_A}$ is its position vector, and $\overrightarrow{F_A}$ is the resultant of forces acting on this particle. The movement is controlled by user-defined and physics-based contact interactions and constitutive laws inside the sample.

In contrast with conventional codes (circular particles, clump logic, convex polygonal particles…), MELODY can deal with arbitrary 2D shapes, and different behavior of particles, from rigid circular to highly compliant angular grains.

Figure 29 presents the two types of bodies that can be modeled with MELODY. The main difference is that rigid bodies are represented by nodes and segments, whereas compliant bodies are discretized in field nodes (this latter case is outside of the strict DEM framework, and uses a Multibody Meshfree Approach, [(Mollon, 2016), (Mollon, 2018a) and (Mollon, 2018b)].

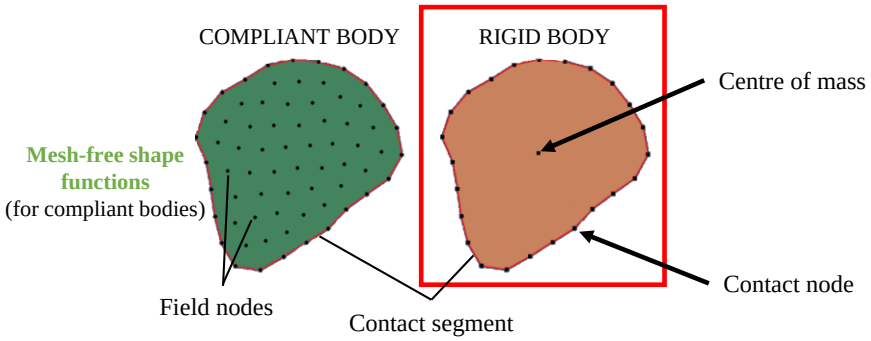

Figure 29. Difference between the Compliant and rigid particle, image modified from (Mollon, 2018a).

> For our research, we do not try to model highly compliant material such as clay or talc, and no high deformation is observed at the grain scale. Since the use of compliant bodies also highly increases the calculation cost, we decided to stick with rigid bodies for the granular fault core particles and rock walls.

Contact detection

Rigid bodies are characterized by their mass (located in the center of mass) and rotational inertia with 3 degrees of freedom (two in displacements and one in rotation for 2D modeling). The contour of particles is then a succession of contact nodes and segments allowing the application of specific contact laws. In order to have both accurate results, and reduce calculation costs, a

compromise has to be found for node discretization. As an example, it was found that 32 nodes is an acceptable value to discretize each particle contour (Mollon et al., 2020), but it can be less or more according to the situation. The contact forces calculated (with a penalization method) are then transferred to the center of mass to solve the equations of motion.

Since the contour of each grain is discretized by a piecewise linear frontier with nodes and segments, each contact considered in the code concerns a given node from a grain A and a given segment from a grain B. From this node and this segment, it can be computed at any moment a normal gap δ_n (obtained by projecting the node on the segment) and a tangential gap δ_t (integrated in time based on the history of the relative motions of the node and the segment in the tangential direction), Figure 30. δ_n can be either negative (i.e. there is a small interpenetration between the grains, contact) or positive (i.e. there is a separation distance between the grains, no contact). The contact detection is bi-directional, meaning that each grain can adopt the roles of grains A and B at the same time. Edge-edge contacts hence do not need any special treatment in this framework, since they are automatically accounted for through their extremity nodes. To control overlapping, a contact stiffness is introduced in the normal and tangential directions (k_n and k_t) as well as numerical damping (γ_n and γ_t) in both directions. The normal and tangential gaps are extracted from particles geometry and kinematics.

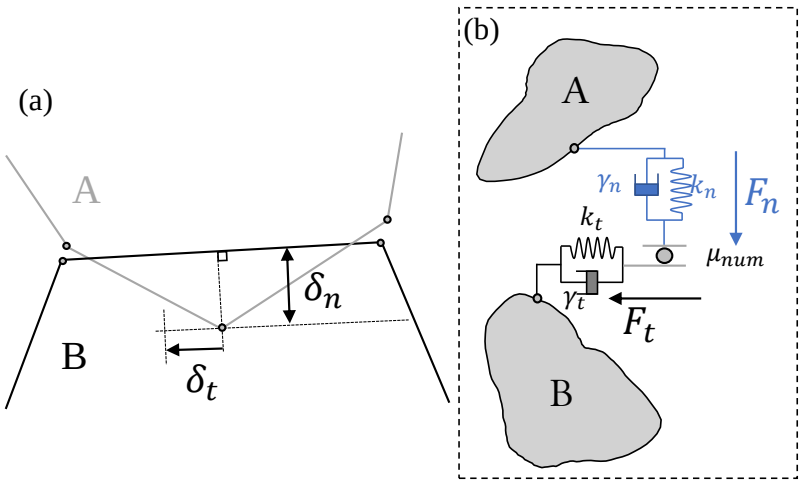

Figure 30. (a) Sketch of a typical contact between two grains A and B with corresponding normal and tangential gaps δ_n and δ_t used to control interpenetrations between particles. (b) Schema of the different parameters acting on a typical frictional contact, k_n and k_t are respectively the normal stiffness and the tangential stiffness and γ_n and γ_t normal and tangential damping fixed within the model.

One of the interests of this code is its ability to represent realistic angular grain shapes, where most of the simulations reported in the literature use circular (2D)/spherical (3D) grains. The contact algorithm can handle particles with complex shapes and with anisotropic orientation. To do so, it is divided into three main steps, (Mollon, 2018a):

i. **A broad proximity detection** (Figure 31 (i)) – The objective of this first detection is to select pairs of close particles, considering as close any pair overlapping both when a projection is made on the x- and y-axis. This detection is based on a sweep-and-prune algorithm (Cohen et al., 1995).

ii. **A close proximity detection** (Figure 31 (ii)) – This step defines potential contact between a node from particle A and a segment from particle B (considering a pair of close particles A and B). This detection is purely geometrical and considers that each segment and node have their own detection zone. Users can define the time period of this step, as it is not necessarily at each time step.

iii. **A regular detection** every time step (Figure 31 (iii)) – This last contact detection is called at each time step and only considers the actual contacting particles (i.e. some close proximity detections remain useless). To avoid a double detection (sharp particles) or loss of detection, a contact zone (i.e. contact box in the picture) is defined for each segment of particle A, considering only nodes of particle B inside this zone. For all the selected nodes (B_j) which have been detected to be in a proximity detection with the particle A (step i), classical mechanical and kinematics values are computed such as normal and tangential vectors, the projection of nodes B_j in the segment A, and the normal and tangential gaps (δ_n and δ_t) used for the different contact laws.

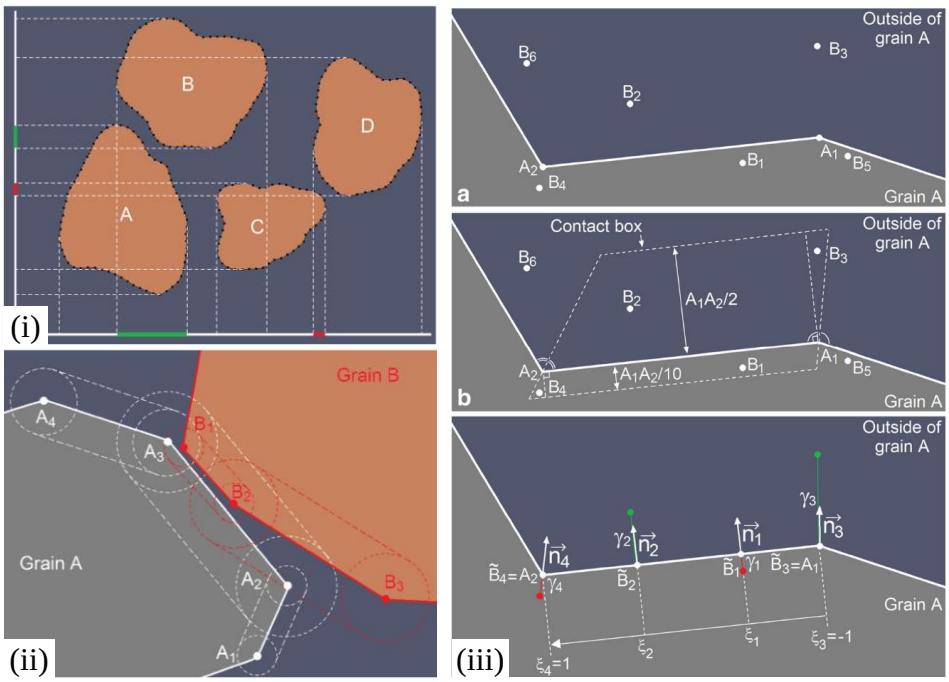

Figure 31. Three main steps of the contact detection algorithm are (i) Broad proximity detection, (ii) Close proximity detection, and (iii) regular detection at each time step. Images from (Mollon, 2018a).

2.2.2. Contact laws

As our research focuses on the study of infill materials within a granular fault gouge, the objective is to be able to model matrix or cemented particles. We consider within this Thesis two contact laws: (a) a **Damped-Mohr-Coulomb** contact law (used in chapter 4 for matrix particles), which is a classical DEM law with interparticle friction only between contacting particles, and (b) a **Bonded Mohr-Coulomb with** interparticle friction and cohesion. This contact law is similar to the Bonded Particle Model (used in chapter 3 for cemented particles).

The Damped-Mohr-Coulomb contact law (DMC)

In chapter 4, we will consider a fault zone that has already been sheared in previous slip episodes, and which is fragmented enough to observe matrix particles filling pores around big clasts. A classical friction law can be used to model a displacement between non-cohesive particles. This DMC law considers the typical geometrical and numerical parameters described in Figure 30 with interparticle friction only between particles in contact. Normal and tangential contact forces can be related with the following expression:

$$\left|\sigma_t\right| \leq \mu_{num}\,\sigma_n \tag{2.2}$$

With σ_t and σ_n the tangential and normal stresses between two particles in contact, μ_{num} the interparticle friction. μ_{num} limits the tangential force for two particles sliding over each over.

σ_n and σ_t can then be computed thanks to the physical and numerical parameters of the contact:

$$if\ (\delta_n > 0) \rightarrow \sigma_n = \sigma_t = 0 \tag{2.3}$$

$$if\ (\delta_n < 0) \rightarrow \begin{cases} \sigma_n = -k_n\,\delta_n - 2\gamma_n \dfrac{d\delta_n}{dt}\sqrt{\dfrac{m_a k_n}{L_{p-c}}} \\ \sigma_t = min\left(\left|k_t\,\delta_t + 2\gamma_t \dfrac{d\delta_t}{dt}\sqrt{\dfrac{m_a k_t}{L_{p-c}}}\right|, \mu_{num}\sigma_n\right) \end{cases} \tag{2.4}$$

$$\delta_t = \pm\frac{\mu_{num}\sigma_n}{k_t} \tag{2.5}$$

L_{p-c} is the numerical contact length between two particles in contact.

The Bonded-Mohr-Coulomb contact law

In Chapter 3, we will consider a fault zone that has already been sheared in previous slip episodes, and which became aged (mature) enough to observe mineral cementation between particles. By aged we mean with no slip for a long-time, enabling cementation or precipitation processes. As the cement present a rather "cohesive" behavior [(Riedmüller et al., 2001), (Wibberley et al., 2008)], this cementation can be explicitly simulated in DEM by considering breakable cohesive bonds between particles (Chapter 1).

The "Bonded Mohr-Coulomb" law, adapted to complex grain shapes, is therefore applied. This contact law is similar to the classical law previously presented, except that a numerical cohesion is initially added as a pressure link between particles. This contact law is close to the Bonded-Particle-Model (BPM) from (Potyondy & Cundall, 2004) and presents two main statuses (intact or broken) described below:

1. After compaction and before shearing, all contacts for which $\delta_n < (\delta_{detec} = C_{num}/k_n)$, where k_n is the contact stiffness previously described and C_{num} is the numerical cohesion, receive the status "intact", Figure 32 (a).

- If the contact is "intact", the following contact stresses are computed based on a purely elastic contact law:

$$\sigma_n = k_n \delta_n \tag{2.6}$$

$$\sigma_t = k_t \delta_t \tag{2.7}$$

- If σ_n, or $abs(\sigma_t)$, exceeds the prescribed value of cohesion C_{num}, the status of the contact is updated to "broken", Figure 32 (b).

2. If the contact is "broken", Figure 32 (b), either because it is a former intact bond or because it is newly created by grains motions at any time in the simulation, the following contact stresses are computed based on a purely frictional contact law:

$$if\ (\delta_n > 0) \rightarrow \sigma_n = \sigma_t = 0 \tag{2.8}$$

$$if\ (\delta_n < 0) \rightarrow \begin{cases} \sigma_n = k_n \delta_n \\ \sigma_t = min(k_t \delta_t,\ \mu_{num} \sigma_n) \end{cases} \tag{2.9}$$

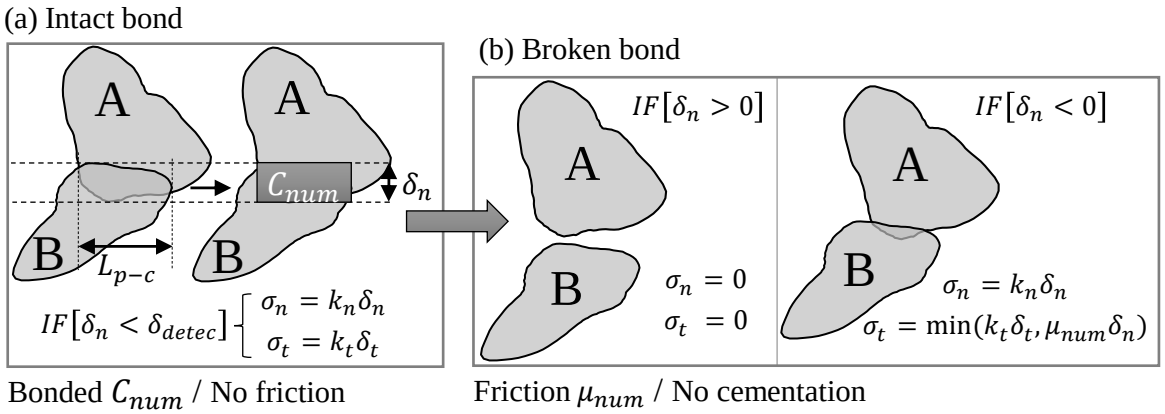

Figure 32. (a) Intact bond. Initialization of the contact law. A cohesive law links all grains in contact. The bond corresponds to a constant pressure to maintain particles in contact (Pa). (b) Broken bond. When the force applied to the particles becomes higher than the cohesive strength, the bond is broken. The contact becomes cohesionless and follows a classical Coulomb-Mohr law with interparticle friction only. Broken contacts cannot be cohesive again and this induces an augmentation of broken bonds during the shearing. Normal interpenetration is exaggerated in the figure for the sake of clarity.

From these stresses, the associated contact forces (in the normal and tangential direction, as well as the associated torque) are computed on each grain, by considering that contact stresses act on a contact length L_{p-c} (equal to the sum of half-lengths of the segments around contact nodes in grain A):

$$F_n = L_{p-c}\ \sigma_n \tag{2.10}$$

$$F_t = L_{p-c}\ \sigma_t \tag{2.11}$$

These laws are completed by a classical viscous dashpot to dissipate kinetic energy by contact damping and to stabilize the simulation (γ_n & γ_t), Figure 30.

The numerical cohesion C_{num} considered in the code cannot be directly related to real cementation in rocks and does not bear much physical meaning by itself. A good way to associate a quantitative description to this numerical parameter is to define an associated level of cementation. It will be defined in Chapter 3.

2.2.3. Solver and numerical parameters

The DEM methods are divided into two main categories based on the type of contact between bodies, the deformability representation of particles, the contact detection of particles, and the resolution of the equations of motion (Lisjak & Grasselli, 2014): (i) Distinct Element Method (DEM) with explicit time-domain integration scheme for equations of motions (for both rigid and deformable bodies) [(Cundall & Strack, 1979) & codes from Itasca Consulting group]; (ii) the implicit DEM, or Discontinuous Deformation Analysis (DDA) method, which has almost disappeared, and (iii) the NSCD "Non-Smooth Contact Dynamics" (Jean, 1999). Very heavy in computing time, simulations are nevertheless limited in terms of number of particles or simulation time and it can be very advantageous to carry out parallelization of calculations. MELODY uses an explicit solver to integrate in time the deformation and motion of each particle (Mollon, 2018a).

Code resolution scheme

At the beginning of the simulation, it is possible to choose about using a constant time step or an adaptative time step Δt (meaning that the value of the time step is automatically calculated from previous errors). In order to quantify the difference between adaptive time step and constant time step, studies have been carried out with mass scaling of particles (Appendix 2. A). It appears that the evolution of the effective friction (peak and steady-state) is quite different depending on whether we used an adaptive time step for the calculations or a constant time step. Indeed, the adaptive time step of the software MELODY has been coded for compliant particles, having no or very little numerical stiffness. If a high numerical stiffness is used within the contact, it will disturb the adaptive computation of the time step. It is, therefore, preferable to use a constant time step in these simulations with rigid bodies. The value of the time step used is provided in each corresponding chapter. The main algorithm is parallelized for each time step following the scheme provided in (Mollon, 2018a).

Choice of numerical parameters

In order to have meaningful particular contacts for particles considered as rigid, it is important to limit the interpenetration between two particles. This interpenetration is limited to a certain percentage (e.g. 1% or 0.1%) of the size of the smallest particle. In addition, the interparticle

stiffness was also calibrated to have a consistent value of equivalent Young modulus regarding the other parameters used within each model (detailed value in each corresponding chapter). The damping value is constant and chosen equal to 0.2. According to the parameters chosen within the model and the equations of motion, it is then possible to compute the magnitude of the time step Δt necessary for the simulation (and that has to correspond to Verlet schema):

$$\Delta t = e \sqrt{\frac{m_{min}}{k_n \, L_{p-c}}} \tag{2.12}$$

Where e is a chosen parameter around 1/50, m_{min} the mass of the smallest particles, k_n the interparticle stiffness and L_{p-c} the contact length. In most cases, although it is important to have a high enough stiffness to limit interpenetration, a too high stiffness is disadvantageous for the time step. In this assumption k_n is considered as a numerical parameter and if it increases too much it can lead to high numerical costs. In our simulation k_n is both a numerical and a physical parameter as it represents the characteristic deformability of the materials considered. In this case, there is no real cost-accuracy compromise but rather a physical calibration.

Granular fault zone and rock walls are considered piecewise-rigid with a constant numerical stiffness used to limit interpenetration between grains while mimicking the local deformation of the grains in the contact vicinity (value detailed in every model in chapters 3 and 4). An explicit solver is used (Symplectic Euler scheme), to integrate in time the motion of each body.

2.3. Generation of a numerical gouge layer

In this thesis, we have chosen to represent angular-shaped gouge particles. For this purpose, we have presented in the previous section, the DEM code MELODY which allows managing the contacts between complex shapes of particles. This section presents a method to generate angular-shaped gouge samples.

How to create non-spherical particles?

Some authors highlighted the limitations of the software Particle Flow Code with circular particles (PFC^{2D} from ITASCA Consulting Group 1995) and suggest the use of a cluster of particles rather than single particles allowing for a more realistic grain shape than disks (Cho et al., 2007). Other researchers tried to represent a more realistic shape of particles, but they were mainly based on geometric simplifications and disc combinations (cf. Clump or Cluster Particle Model), [(Guo & Morgan, 2004), (Cho et al., 2007), (Ferellec & McDowell, 2008), (Kenichi Maeda et al., 2010), (Härtl & Ooi, 2011), (Zhou et al., 2017)]. For these geometric shapes, contact parameters need to be adjusted to mimic a more realistic shape with pre-calibrated parameters such as inter-granular friction, stiffness, or viscosity. Only a few of them represent angular particle shapes [(Nouguier-lehon et al., 2003), (Kawamoto et al., 2018), (Mollon et al., 2021b)].

A relevant approach to generate realistic shapes of particles based on Fourier Descriptors has been developed in both 2D (Mollon & Zhao, 2012) and 3D (Mollon & Zhao, 2014). The authors identify statistical properties for unique particle shape characteristics gathered in a Fourier spectrum (projected contours of grains, Figure 33 (a)), with which they perform an inverse Fourier transform in order to obtain the real angular shapes, Figure 33 (b). The 2D DEM code called MELODY2D (Section 2.2) can deal with the contact interaction of these complex shapes in 2D, but the associated 3D-DEM code is not yet available.

The Matlab package Packing2D[1] is employed in the present work to create our granular samples. It is based on a Fourier-Voronoï method and generates a set of grains with user-defined size distribution and control on key morphological descriptors (such as elongation, circularity, and roundness). This control is performed by choosing a Fourier spectrum that quantifies the frequencies and amplitudes of the grain surface asperities. The advantage of this code is to create granular media with complex particle shapes, such as angular and faceted particles impossible to generate from the DEM code itself. More information is available in (Mollon & Zhao, 2012) and (Mollon & Zhao, 2014) for 3D particles.

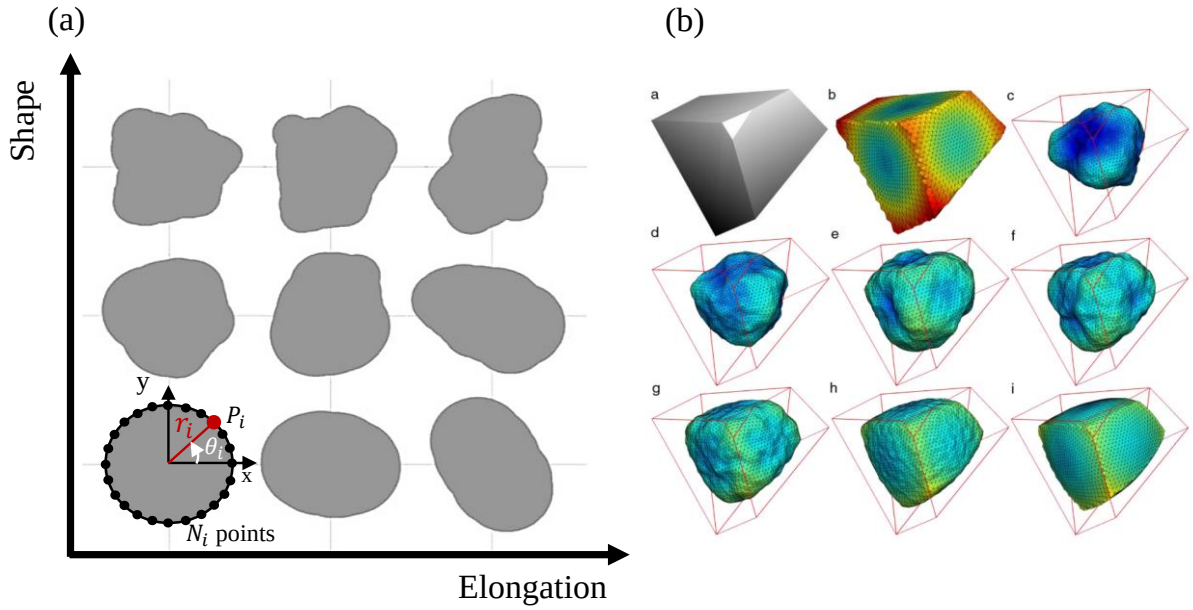

Figure 33. (a) Example of particles from a selected spectrum: first a random sampling of phase angles, then the computation of the random signals r(θ), and finally plotting of the corresponding particles contours by varying elongation or shape of particles. Image modified from (Mollon & Zhao, 2012) (b) 3D cell-filling algorithm: a. Polyhedral cell to be filled; b. Same cell expressed as a geodesic structure; c to i. Particle filled in a cell with increasing fitting parameter from 0 to 2562. Image from (Mollon & Zhao, 2014).

2.3.1. Method for granular sample creation

The code Packing2D is divided into three main steps based on coupled **Bounded Voronoï tessellation and Inverse Monte-Carlo Method**:

[1] Packing 2D is available for download at http://guilhem.mollon.free.fr

– The first step generates a constrained Voronoi Tessellation, Figure 34, with polygonal subdomains following a target size distribution and cells orientation.

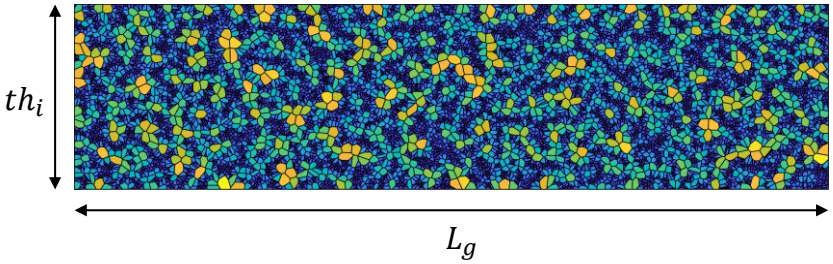

Figure 34. Example of Voronoi Tesselation generated with Packing2D. Fractal distribution of particles. th_i is the initial thickness of the numerical gouge and L_g the length of the numerical gouge, both in meters.

The user chooses the size of the granular sample created (creation of the domain th_i x L_g in Figure 34) and the number of granular particles *N*. Then the type of distribution wanted, such as fractal, Gaussian, uniform, lognormal, bimodal, can also be specified. Finally, the Voronoi Tesselation evolves over several iterations, according to the target error allowed (specified by the user), until it reaches, as much as possible, the model characteristics chosen.

– Within Step 2, the user can define the shape of particles wanted, based on a Spectrum of morphologic descriptors, called **Fourier descriptors**, (complete procedure in (Mollon & Zhao, 2012)). The code considers a contour of particle discretized by N_i points separated by an angle θ_i at a certain distance r_i from the centre of the particle, Figure 35 (a). According to Discrete Fourier Transform (DFT), the signal $r(\theta)$, Figure 35 (b), can be written as the sum of N harmonics:

$$r(\theta) = r_o + \sum_{n=1}^{N_i} [A_n \cos(n\theta_n) + B_n \sin(n\theta_n)] \tag{2.13}$$

Where r_o is the average radius. Then each harmonic n allows defining a normalized amplitude D_n, called "Fourier Descriptor":

$$D_n = \frac{\sqrt{A_n^2 + B_n^2}}{r_o} \tag{2.14}$$

These normalized amplitudes, presented in Figure 35 (c), correspond to different morphologic descriptors of particle contours known in granular mechanics as Elongation, Roundness, Circularity, and Regularity, (Mollon & Zhao, 2012).

The Fourier Descriptor D_2 essentially affects particle elongation (or the ratio between the smallest dimension of grain under a direction oriented in a particular angle), and has limited influence on the roundness of particles. Descriptors D_3 to D_8 define the shape modes or the importance of main irregularities within the grain contour. For example, a reduction of D_3 leads to rounder particles in Figure 36 (a) and (b). Finally, descriptors higher than D_8 characterize the roughness, considered as small irregularities within the contour increasing with D_8 value, Figure 36 (c). An inverse Fourier Transform on normalized amplitudes allows getting the real shape of a particle in a 2D domain as presented in Figure 35 (a).

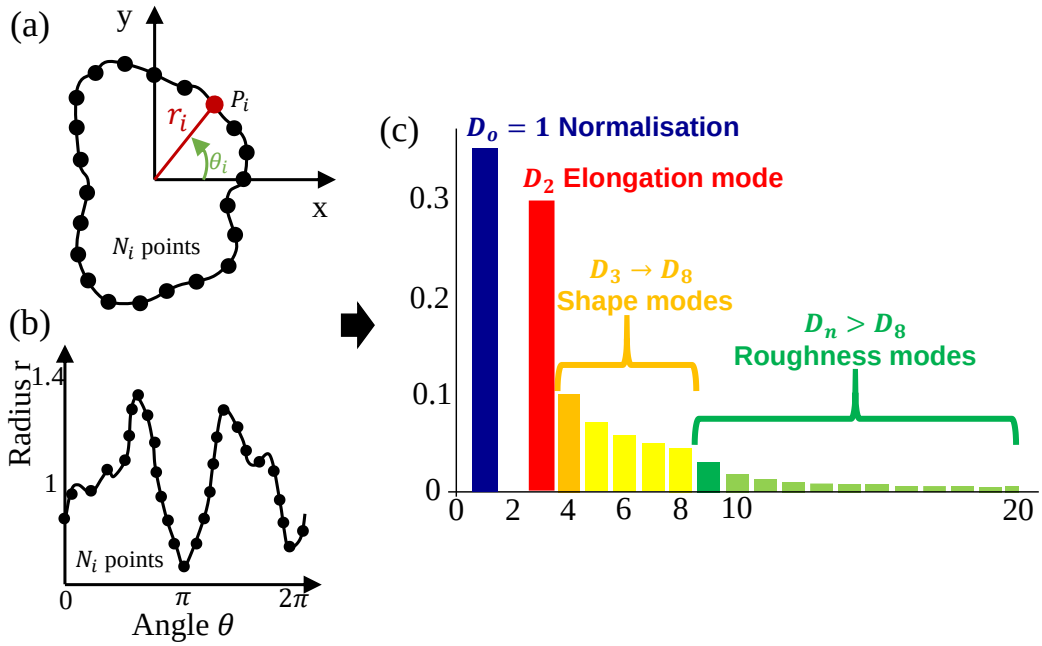

Figure 35. Process of grain shape characterization. (a) The contour of a particle discretized by N_i points, each point is associated to a radius and position angle in polar coordinates (b) Signal described by the position of the N_i points in polar coordinates (c) Fourier descriptors as a function of the mode. The two decays observed within shape modes and roughness modes are described by: $\Delta_1 = 2^{\lambda_1 \log_2\left(\frac{n}{3}\right)+\log_2(D_3)}$ $(for\ 3 < n < 8)$ and $\Delta_2 = 2^{\lambda_2 \log_2\left(\frac{n}{8}\right)+\log_2(D_8)}$ $(for\ n > 8)$. With λ_1 and λ_2 two constants equal to -2.

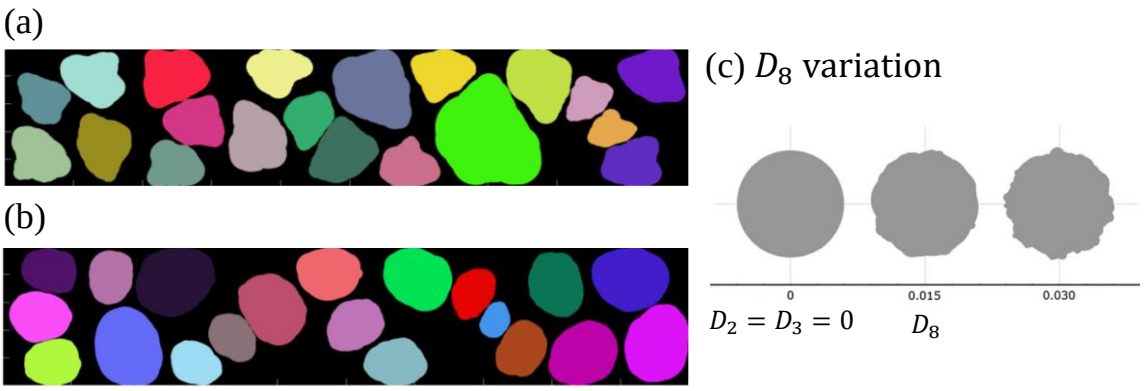

Figure 36. Example grain samples with different Descriptor variation. (a) $D3 = 0.1$ (b) $D3 = 0.03$, (c) particle with different D8 for $D2 = D3 = 0$ (i.e. circular particle), last image from (Mollon & Zhao, 2012).

– The last step of the code, Figure 37, consists of randomly filling the initial Voronoï Tesselation (Figure 34), with the spectrum of granular particles created, Figure 35 (a). It is possible to both play on the initial solid fraction (percentage of filling of the Voronoi cell) and faceting of particles (more or less tangential to cell contours). Once the entire sample has been generated, it is possible to recover data such as the areas of grains generated S_p, their position, and parameters as the inscribed and circumscribed radii, etc.

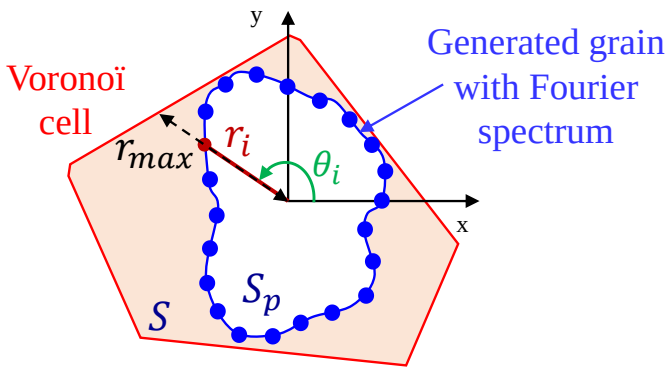

Figure 37. Voronoi cell (red) and grains generated inside the cell (blue), image modified from (Mollon & Zhao, 2012). To have grains with flat facets, the optimization parameter N_{Optim} can vary between 0 and 63, where 0 corresponds to a grain as defined in the spectrum and 63 a grain as much as possible with facets. Increasing this parameter is very helpful to have angular particle shapes, but it also increases a lot the calculation costs during sample generation. By increasing the target Solid fraction F_S (equal to S/S_p), it decreases the compaction time of the granular sample. However, the final solid fraction of the sample also depends on how the grains will conform to the shapes of the Voronoi cells formed.

2.3.2. Three types of granular samples

This section presents the three different granular samples designed for the Thesis and used within the next chapters. It displays the type of granular samples, details numerical parameters, and shows a final representation of the numerical sample.

(i) Grains with angular shape (Chapter 3)

Mineral grains morphologies can be very diverse, but as mentioned in Chapter 1, granular gouges generated by comminution are expected to exhibit rather rough and angular shapes. To be closer to these shapes, angular and faceted particles are chosen to be modeled for the main granular sample of the Thesis. Since the morphological descriptors of the grains of granular gouges may vary significantly between faults, we calibrate our spectrum by visual comparison with published pictures of real gouges, Figure 38 (a) (more granular fault sample image library in Appendix 1. A). After several trials and variations of the Fourier descriptors, a suitable typical grain shape is selected, Figure 38 (b). The chosen numerical Fourier descriptors and numerical parameters are gathered in Table 1.

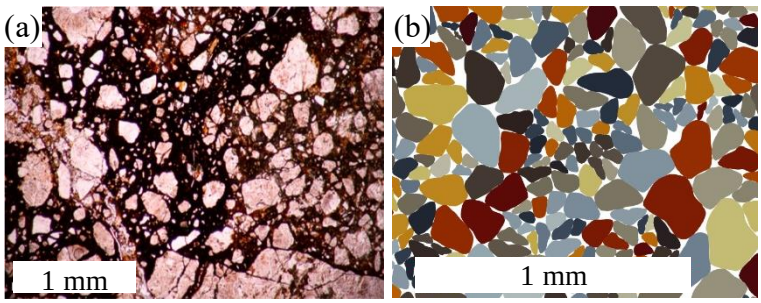

Figure 38. (a) Quartz, photomicrograph (crossed polars) of ATTL fault gouge from (Muto et al., 2015). (b) Zoom on a granular sample generated with packing2D, with angular and faceted shapes, and compacted in MELODY2D. Input parameters in table Table 1.

Table 1. Input Parameters in Packing 2D to generate the sample. D_2 to D_8 are Fourier descriptors, λ_1 and λ_2 are the two constants needed to calculate the two decays Δ_1 and Δ_2 (formulas in Figure 35). S_F and N_{Optim} comes from the cell filling step in the legend of Figure 37.

Fourier Spectrum properties					Cell filling	
D_2	D_3	D_8	λ_1	λ_2	F_S	N_{Optim}
0.2	0.1	0.01	-2	-2	1	63

(ii) Matrix particles sample (Chapter 4)

For matrix particles, we consider fine particles in a very dense packing. To generate this kind of particle, a small code called Cvoro (C++) is used. In fact, this code is a simplified version of the previous method presented with a Voronoï tessellation algorithm, allowing to create a dense packing of polygonal particles.

It is possible to choose the size of particles $\emptyset_{eq}$ (equivalent diameter of particles, calibrated on total area) and also the "perturbation parameters" $P_{0.i}$ (i.e. the homogeneity/regularity of the hexagonal cells). Figure 39 displays the three types of shape of matrix particles used in Chapter 4, with a variation in perturbation parameter. The equivalent diameter of particles $\emptyset_{eq}$ was chosen equal to $20\ \mu m$ (Appendix 2. B). The initial porosity, or void fraction $F_v = S_{voids}/(S_{particle} + S_{voids})$ within the sample is negligible, with less than 1%, which leads to a state of compaction very close to intact rocks.

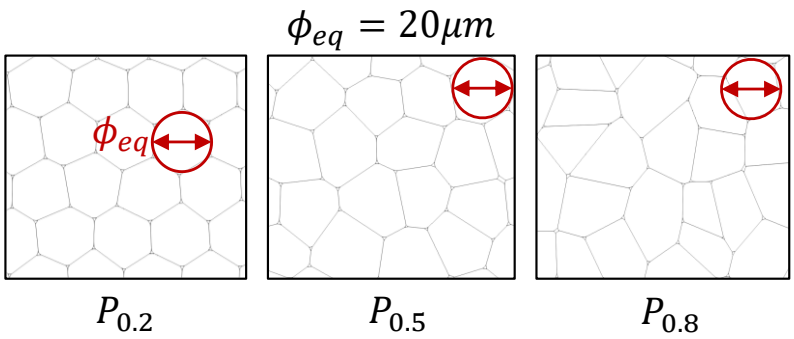

Figure 39. Change in the perturbation of particles, from $P_{0.2}$ to $P_{0.8}$ modifying the final cell shape, from hexagonal cells to angular polygonal cells.

(iii) Granular sample with matrix particles (Chapter 4)

This last type of granular sample is a combination of the two previous samples, Figure 40. The method first consists in identifying the overlapping zones between the matrix sample and angular particles. Then matrix cells that most fit the contour of angular particles are kept and matrix cells located in the geometrical domain of angular particles are removed. The final roughness of angular particles is not identical to the initially generated contour, but the choice of a small enough size of matrix cells enables to maintain the global shape of angular particles.

These three types of samples will be used all along the Thesis with some variations on physical and geometrical parameters and contact laws. More details are provided in each associated chapter.

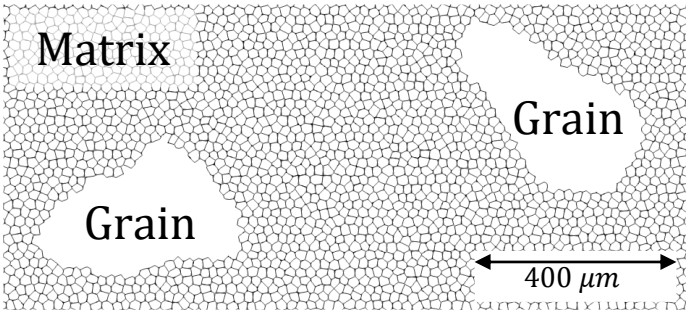

Figure 40. Zoom in on the merged sample with matrix cells and angular particles. For this last sample type, matrix cells have an equivalent diameter $\emptyset_{eq} = 20\ \mu m$ and a perturbation $P_{0.i} = 0.5$.

2.4. Numerical framework

2.4.1. Direct shear modeling

Within this Thesis, direct shear modeling was chosen to simulate faulting and to allow comparison with Laboratory experiments. This subsection presents the different steps of a simulation, the assumptions, and the configuration of final models. Details on each model type will be discussed in the corresponding chapters.

Compaction step

Once the granular sample is generated with Packing 2D, it is then inserted between two rock walls in the pre-processing step. The first simulation step consists of compacting the sample with the chosen normal stress to obtain a mechanically stable packing of grains with a controlled granular density, Figure 41 (a). We observe that the interparticle friction used during compaction controls the initial porosity within the sample (Appendix 2. C). When the granular sample is compacted and mechanically stable, the appropriate mechanical laws between particles in contact are implemented, Figure 41 (b).

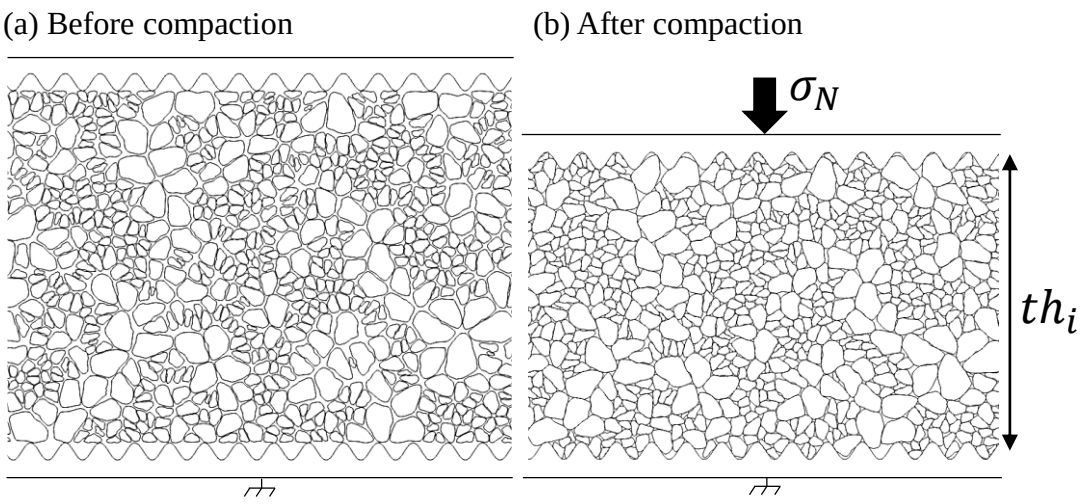

Figure 41. Compaction of the granular sample (a) Step 0, before compaction of the sample, (b) Step 1, just after compaction. σ_N is the normal stress applied on the upper rock wall and th_i is the initial gouge thickness at the end of the compaction step.

Overview of the sheared granular fault model

Once the pre-processing step has been completed (application of contact laws and physical parameters), direct shear experiments can be settled. Figure 42 presents the 2D-DEM model of the simulated granular fault gouge, with rock walls at the top and bottom sides of the granular sample. In the following chapters, different granular materials are implemented as briefly described in the previous subsection. However, all the models present the same structure and external parameters: the lower wall is fixed, while normal stress (y-direction) and a sliding velocity (x-direction) are applied on the upper rock wall (defined in next section 2.4.2). Gravity is ignored in the model, assuming that the fault can be oriented in a wide range of directions, and that gravity forces are negligible compared to those related to normal and deviatoric stresses applied on the gouge. Periodic boundary conditions are present on both right- and left-hand sides of the sample to maintain the continuity of the movement at large slips, as a difference with (Gao et al., 2018) simulations. The movement of the upper rock wall in the y-direction remains free to accommodate dilation or compaction of the sample.

A dry contact model is considered here, to investigate infill material influence, without fluid. Fault gouge and rock walls are considered rigid with a constant numerical stiffness used to limit interpenetration between grains (identical for normal and tangential directions) while mimicking the local deformation of the grains in the contact vicinity (section 2.2). The tangential and normal numerical stiffnesses are equal in this model and grain comminution is disregarded. In this study, we choose to simulate a density of 2600 kg/m^3 for particles, leading to an appropriate time step for these simulations of 10^{-9} s. An explicit solver is used (Symplectic Euler scheme) to integrate in time the motion of each body.

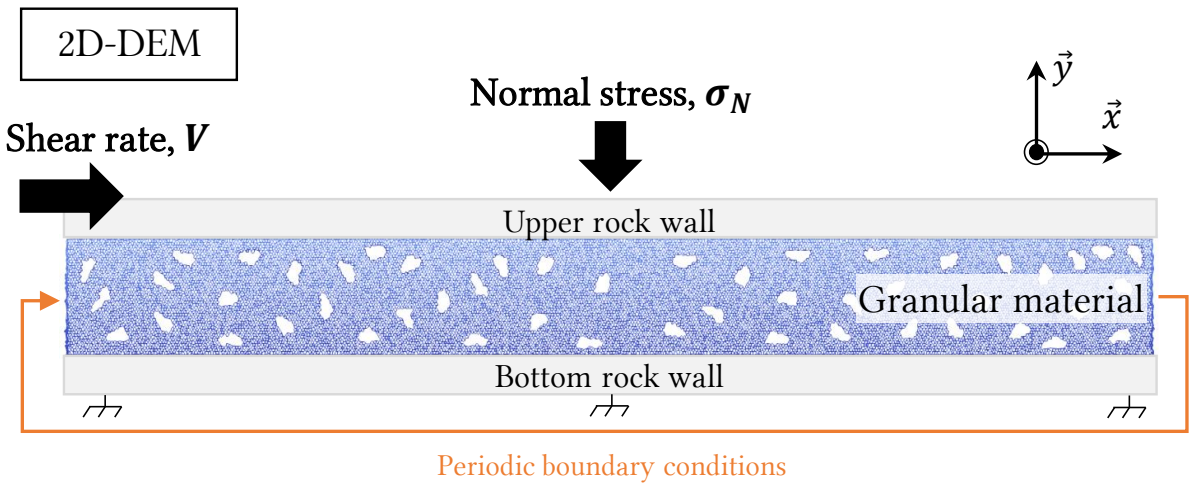

Figure 42. Schema of the DEM model of a granular fault gouge

Interparticle friction is equal to 1 at the contact interface between walls and particles to make sure that the motion is fully coupled at the wall-grains boundary. The interparticle friction μ_{num} between particles in contact is in the range of $0.3 - 0.5$ in the different Chapters. These values are often used in DEM gouge experiments and are in the range of interparticle friction found for two mineral particles in contacts [(Sandeep & Senetakis, 2019) & (S. Kasyap & Senetakis, 2020)].

Measure and control during the simulation

To characterize the slip behavior within the simulation, different quantities and parameters are extracted, calculated, and observed during simulations. These results are then stored at various time intervals ($\sim 10^{-6} - 10^{-8}$s, depending on the model):

- A typical quantity investigated all other the manuscript is the **effective friction** $\boldsymbol{\mu^* = \tau/\sigma_N}$ (Chapter 1), Figure 43 (a). This effective friction is not to be confused with the Coulomb-Mohr coefficient of friction μ_f or interparticle friction μ_{num}. Effective friction is recovered at the interface between the gouge and the upper rock wall, with $\boldsymbol{\tau}$ depending on the normal stress applied on the rock wall, Figure 43 (b). The same quantity is used in other researches [(GRD Midi, 2004), (Azéma & Radjaï, 2014), (Berger et al., 2015)]. It is also important to differentiate the effective friction peak μ_p^* (maximum effective friction) and the steady-state effective friction μ_{ss}^* which is the average value of the effective friction once the plateau zone is reached and for a constant applied shearing velocity, Figure 43 (a).
- The **dilation** of the granular sample is also measurable and corresponds to the thickness variation Δth in the vertical direction, divided by the initial granular sample thickness $\boldsymbol{\varepsilon_y = \Delta th/th_i}$, (as the upper wall is displacement free in the $y-$direction).
- The initial surface **percentage of porosity** $\boldsymbol{(P_{pore})}$ within the sample is the total surface of voids divided by the total surface (voids and particles) $\boldsymbol{P_{pore} = 100\,(S_{voids}/S_{gouge})}$. It can also be expressed by the mean of the void ratio F_{void} and Solid fraction Fs, which is $F_{void} = 1 - F_S$, (Appendix 2.C).
- For each model, particles' granular flow needs to remain in a quasi-static regime in order to avoid inertial effects within the simulation. A way of quantifying this is to calculate the Inertial number I_p, which is a dimensionless number used to measure the inertial effects for dry granular flow in-plane shearing [(Pouliquen & Forterre, 2002), (Iordanoff & Khonsari, 2004), (Da Cruz et al., 2005), (Jop et al., 2006), (Pouliquen et al., 2006)]:

$$I_p = \frac{|\dot{\gamma}|\phi_{av}}{\sqrt{\sigma_N/\rho_p}} \tag{2.15}$$

  With σ_N being the applied stress, ϕ_{av} the mean particle diameter (or it can be the local mean particle diameter defined by volume fraction of each size), ρ_p the density of particles and the shearing rate $\dot{\gamma} = \Delta v/th$. A quasi-static regime is observed for $I_p \leq 10^{-3}$, then I_p characterizes a transitional regime until reaching $0.2 \approx I_p$. For $0.2 < I_p$, the regime is considered as collisional with dynamics becoming dependent on the particle restitution coefficient. Moreover, the particle size distribution within the sample can highly modify the granular flow and its behavior (Pouliquen, 2011).

Dedicated post-processing tools are also used in order to analyze the spatial distribution of the solid fraction, force chains, or velocity fields patterns during the onset of slip, in order to bring a new understanding of the physics observed from a granular point of view.

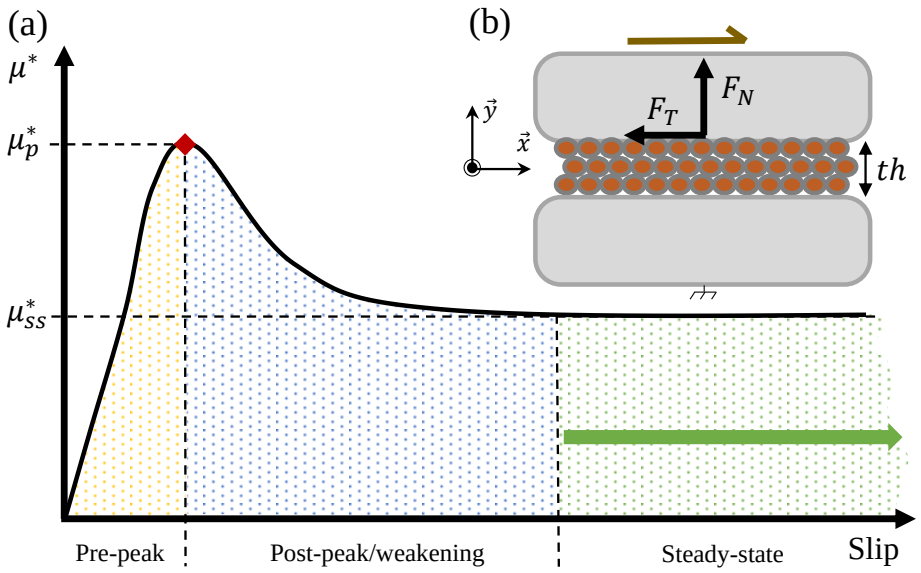

Figure 43. (a) Typical friction curve as a function of slip displacement of the upper rock wall. μ_p^* is the effective friction peak, i.e. maximum effective friction, and μ_{ss}^* is the steady-state effective friction, which is an average value of the effective friction once the plateau zone is reached (also called residual friction). (b) Schema of the sheared gouge with the total normal and tangential forces (F_N & F_T) applied on the upper rock wall.

2.4.2. Main assumptions of the model

Due to the complexity of the parameters involved in the behavior of fault gouges (Chapter 1), it was decided to fix some physical parameters. In this section, we present the assumptions and choices that will be kept in the next chapters.

Normal stress

The model aims to simulate a sheared granular fault zone, subjected to a normal stress proportional to the depth of the fault. The pressure exerted by the rocks above the fracture is represented by the application of a normal stress to the wall in the y-direction. The fault is modeled parallel to the surface, for the sake of simplicity, but it is a simplification, as it is clearly not the case everywhere (Giorgetti et al., 2019). The normal stress, as well as the shear rate, are non-negligible parameters of the gouge model (Chapter 1), that must be chosen with precision to have a meaningful model (Aharonov & Sparks, 2004). Parametric studies were carried out with different normal stresses, 1, 5, 10, 40 & 100 MPa, for a sheared granular gouge with 2500 angular particles (size of the 2D granular sample 2x10mm²). Figure 44 (a) presents the effective friction (peak and steady-state) and dilation as a function of the applied normal stress (Mpa). For the cases studied, $0.5 \leq \mu_p^* \leq 0.6$ and slightly decreasing with an increase in normal stress. The μ_{ss}^* value is similar and equal to ~ 0.45 for all cases except for the 1 MPa case, which is supposed not enough constrained relatively to the interparticle stiffness applied between particles. The variation amplitude of effective friction oscillations is decreasing towards the same behavior with increasing normal stress. The evolution of dilation is almost similar to effective friction peak evolution with a decrease at 100 Mpa, meaning that the too high pressure prevents sample dilation. In our results, a clear quasi-static regime is only observed with a normal stress above 10 Mpa and begins to stabilize with $\sigma_N = 40\ Mpa$, Figure

44 (b). A possible interpretation is that in the range $5 - 40\ Mpa$, the 3 quantities (friction & dilation inertial number) are constant and considered as the domain of validity of your model. Outside this range, different effects disturb the results. For low stresses, it is certainly due to the inertial number (much higher than for other cases), and for high stresses, it may be caused by important interpenetrations between grains and to the collapse of the assumption of rigid grains. Increasing the normal stress until $100\ MPa$ will imply adjusting numerical stiffnesses within the model to limit overlapping caused by the high-pressure increase, and will thus increase calculation costs. As normal stress is also known to control the shear modulus of the granular sample (Lyu et al., 2019), it will imply a material with a nonphysical Young modulus in our case.

Regarding the stabilization of our results after $10\ MPa$, the results from the literature, and trying to limit calculation costs, we decided to focus on a medium value of normal stress of **$40\ Mpa$** for all the Thesis experiments. This pressure corresponds to a depth of about $1.5\ km$ which is the early beginning of the natural seismogenic zone and it is also an interesting depth for all geoengineering studies, such as enhanced Geothermal Systems.

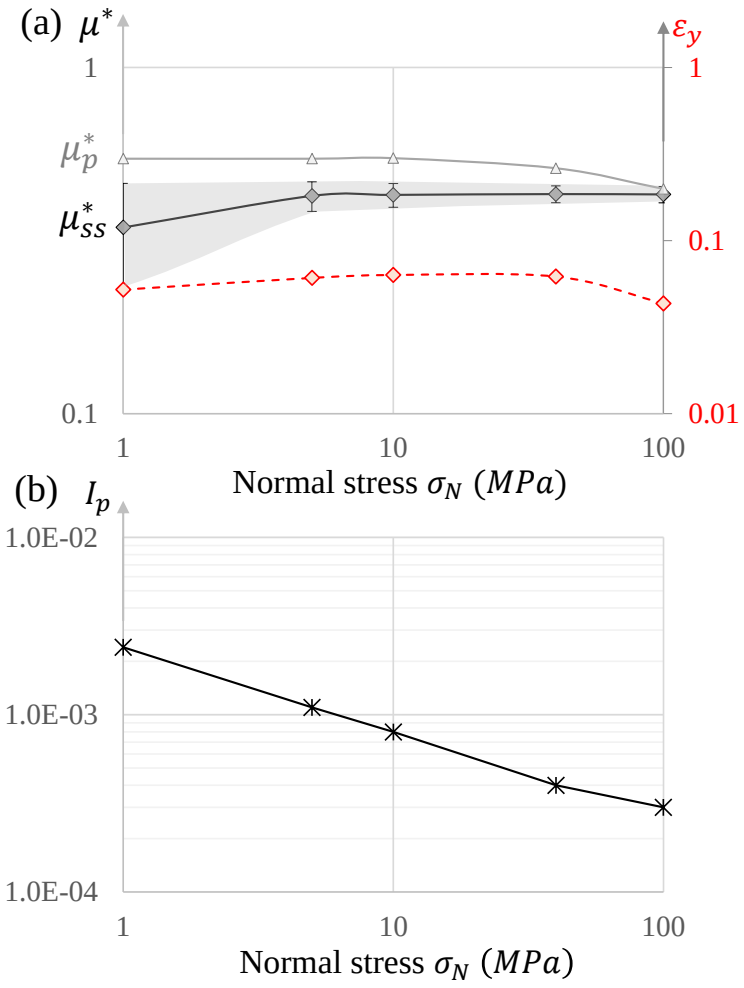

Figure 44. (a) Effective friction $\mu^*$and dilation ε_y as a function of normal stress σ_N (MPa) (b) Steady-state inertial number I_p as a function of normal stress.

Shear velocity

The shearing rate is also a difficult parameter to choose and mainly depends on the type of earthquake studied. The increase of velocity induces a modification in the contact law basically presenting a peak of effective friction and a weakening until a steady state. Small initial tests have been carried out to see the global influence of shearing velocity within the model of a sheared granular gouge with 2500 angular particles (size of the 2D granular sample 2x10 mm^2). Figure 45 presents effective friction, dilation, and inertial number as a function of different shearing velocities, 0.01, 0.1, and 1 m/s. The gouge has been sheared with the applied normal stress of 40 MPa for the first case and 10 MPa for the other ones. In all the simulations, the inertial number is observed to be bellow 10^{-3}, Figure 45 (b), indicating that the granular flows observed remain in the quasi-static dense granular flow.

The obtained results are pretty similar in terms of effective friction and dilation. That is why, to have observable results in a reasonable computation time while avoiding disturbing inertial effects since the dimensionless inertial number, **we chose a shearing velocity of 1 m/s for the rest of the Thesis**.

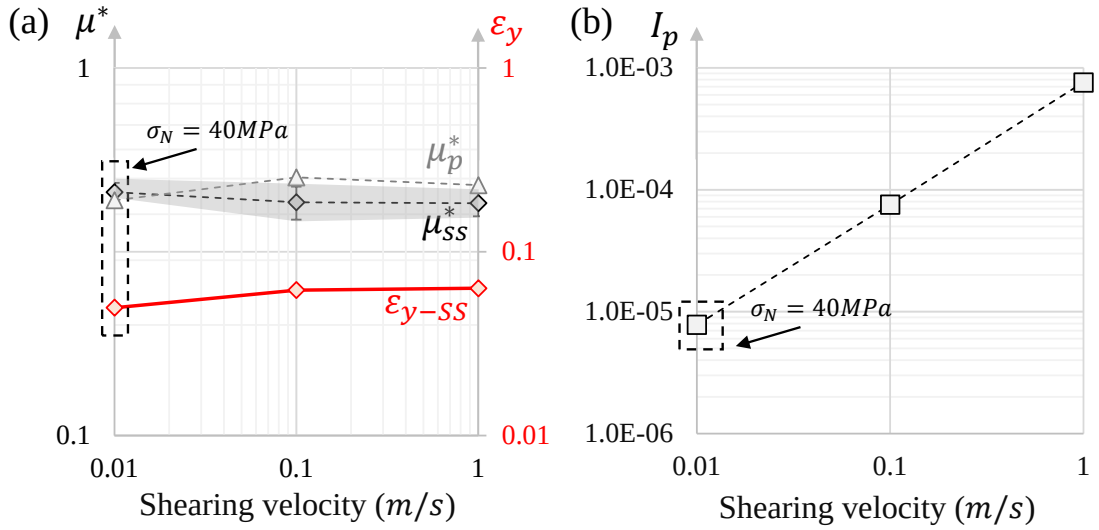

Figure 45. (a) Effective friction μ^*(at peak and steady-state) and dilation ε_y (at steady-state) as a function of the shearing velocity (m/s), (b) Steady-state inertial number as a function of shearing velocity (m/s)

Effect of grain shape (circular vs angular particles)

To be closer to fault gouges observed within fault cores, angular and faceted particles are employed in this Thesis. However, to validate the importance of modeling these shapes of grains compared to circular shapes, and compare our model with literature, two samples were implemented: one with angular and faceted particles (the one used for the study) and another one with circular grains. This second sample is then discarded in the next chapters, but the results are presented in this subsection. The numerical and physical characteristics of both samples are presented in Appendix 2.D.

The granular layer with circular shapes of grains is generated with the same parameters as the one with angular particles, Figure 46 (a) & (b). But due to the circular shape of particles, the fractal dimension is a bit lower with $D = 2.5$ (vs $D = 2.6$ for angular sample) and with a corresponding equivalent diameter in the range 20 – 181 μm (vs 28 – 226 μm for angular), Figure 46 (c). To have the same initial gouge thickness ($1.7\ mm$) and a similar total surface of particles (26 mm² for circular particles and 29 mm^2 for angular particles), the gouge with circular particles is composed of 7515 grains.

The two samples (circular and angular) are sheared with the same parameters (Appendix 2.D) and with a simple friction law to consider a typical case with only frictional contacts. As in previous studies, the effective friction is smaller for circular grains and steady-state effective friction tends to 0.45 for angular grains and 0.3 for circular grains, Figure 47. Because of their invariance by rotation, smooth spherical shapes tend to roll to accommodate deformation of the grain assembly whereas interlocking between angular grains tends to promote dilation (Anthony & Marone, 2005). The effective friction observed with our results is lower than for 3D experimental studies ((Frye & Marone, 2002) and Chapter 1). However, gouge behaviors obtained fit well with previous 2D results with angular and circular shapes [(Jensen et al., 1999), (Mair et al., 2002), (Nouguier-lehon et al., 2003), (Guo & Morgan, 2004)]. It was also shown recently that mechanical effects of grains surface roughness can only be mimicked by intergranular friction to a certain extent, and that proper modeling of the shear behavior of granular samples requires realistic shapes (Mollon et al., 2020). Here the large fractal dimension D promotes a stable sliding even for circular particles (Morgan & Boettcher, 1999).

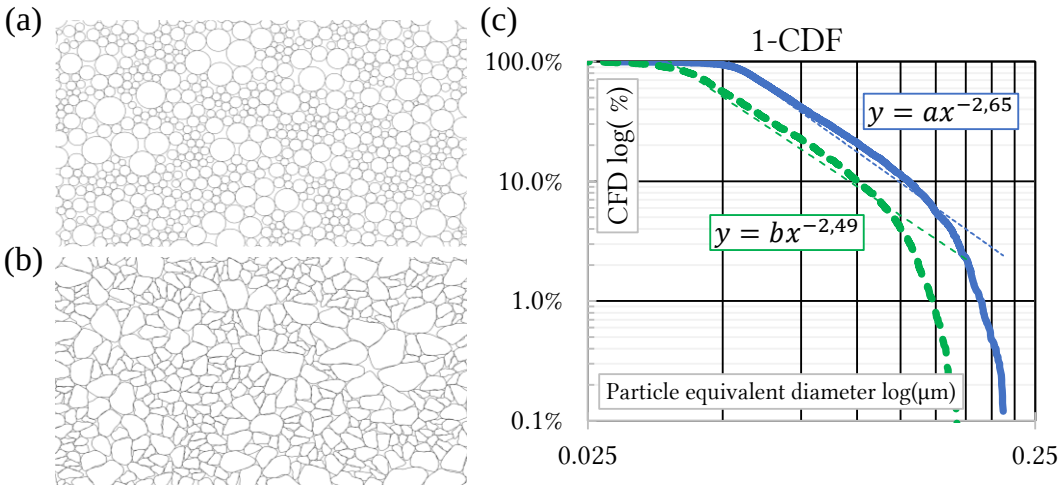

Figure 46. (a) Granular sample generated with packing2D, with circular shapes, and compacted in MELODY2D (b) Granular sample generated with packing2D, with angular and faceted shapes, and compacted in MELODY2D. (c) Log-log graphs showing the cumulated number of particles (Y-axis) plotted against particle equivalent diameters (X-axis) from the numerical gouge sample with CDF (Cumulative Distribution Function). The fractal dimension D equals 2.65 for angular grains (blue line) and fractal dimension D equals 2.5 for circular grains (green line). They have almost the same total surface of particles (26 mm² vs 29 mm²).

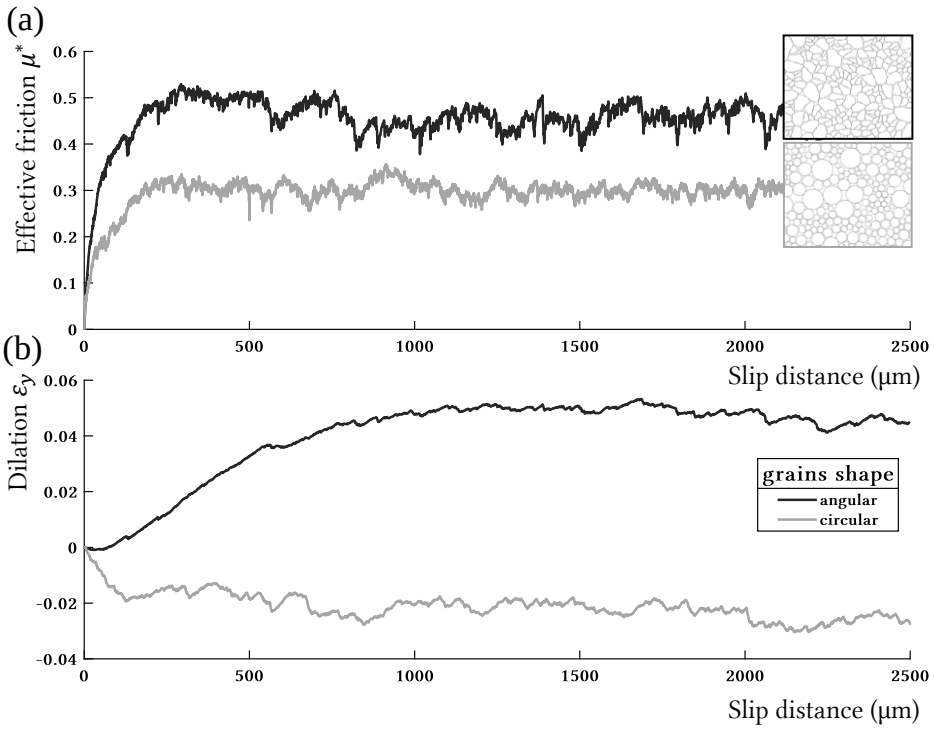

Figure 47. (a) Effective friction for samples with angular or circular shapes of grains as a function of the slip distance (µm) (b) Dilation variation (µm) as a function of the slip distance (µm), for angular or circular shapes.

Table 2. Numerical and physical characteristics.

The results confirm that the behavior of angular and circular grains, without cementation, is different, and using circular shapes is disadvantageous for the strength of gouge behavior and is not reflecting real contact interactions. The next chapters will thus deal with non-circular particles.

Representative Surface Element (RSE)

To justify that the size chosen for gouge samples is a RSE, three different lengths of models have been studied with identical numerical parameters and identical gouge thickness ($\sim 2\,mm$). The different sizes of models (6x2 mm^2, 10x2 mm^2, and 20x2 mm^2) induce a change in the total number of particles to keep the same equivalent diameter for particles (respectively 1500 grains, 2500 grains, and 5000 grains). By increasing the number of grains in the model, as well as the length of the gouge, similar behaviors of the sheared gouge layers are observed. The effective friction coefficient follows the same trend for the three model sizes. The effective friction peak μ_p^* is also of the same order of magnitude $(0.73 - 0.78)$, Figure 48. As the number of grains increases, there is, therefore, an increase in normal and tangential forces applied to the upper rock wall, but the higher number of grains makes it possible to maintain similar effective friction in the three models. Moreover, by comparing force chains in the gouge for the three models, we do not see significant changes, Figure 49 (a). They are oriented at $30 - 45$ ° relatively to the upper rock wall and normal forces seem oriented in this same direction, Figure 49 (b).

Even though the three models showed similar behaviors, we selected the model with 5000 particles, in order to have a chance to observe local mechanisms and rupture patterns (more difficult with smaller length). It is therefore not necessary to represent a larger model for this type of micromechanical study. It would have been interesting to do the same kind of experiment by modifying the thickness of the gouge layer, as it is known as a really influent factor in the contact mechanisms (Chapter 1). However, by changing this thickness, we also modify the RSE in length, the model studied is therefore a compromise between length, gouge thickness and number of grains in the thickness. We judged that our models allow being in the case of a mature enough fault gouge to observe deformation patterns with a gouge thickness fixed at around $2\ mm$ (a value consistent with the literature (Rice & Cocco, 2002)).

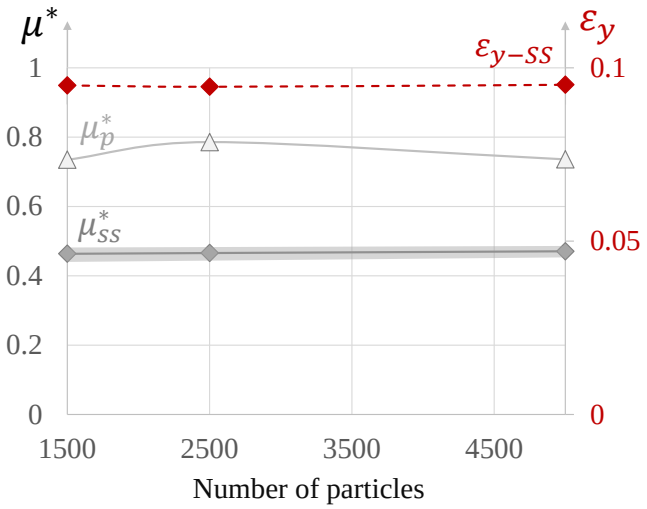

Figure 48. Effective friction μ^*(at peak and steady-state) and dilation ε_y (at steady-state) as a function of the number of grains in the model. A slightly higher μ_p^* is observed for the case with 2500 grains, probably due to a slightly different stacking of the particles during the sample compaction. The effective friction curve obtained with the 1500-grains sample is noisier because the dynamic effects are more noticeable with fewer grains.

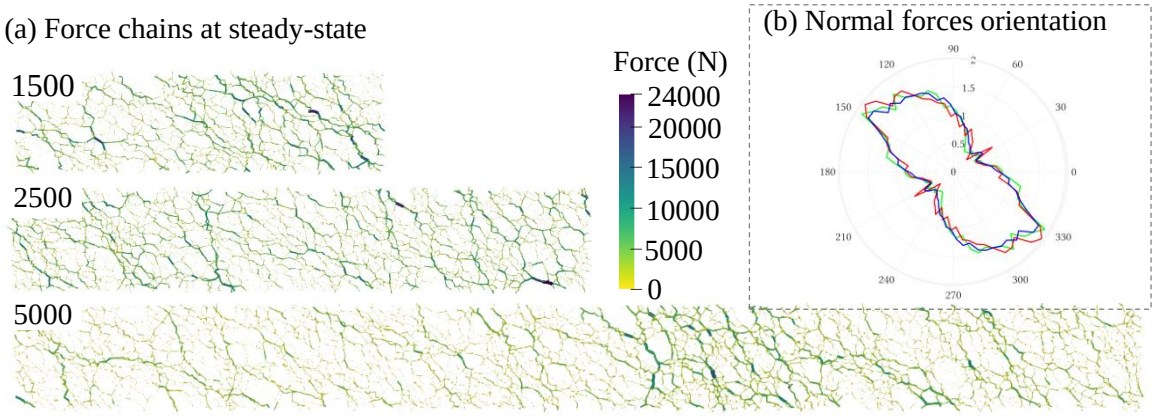

Figure 49. (a) Force chains magnitude in Newton for 1500 grains, 2500 grains, and 5000 grains – (b) Number of contacts with a normal vector oriented in a given direction (using polar diagrams where the Theta-axis is the orientation and the R-axis is the number of contacts). Normal forces orientation as a function of the model, at steady state. Small sample with 1500 particles in red, the middle sample with 2500 particles in green, and the bigger sample in blue.

Stability conditions

The granular literature related to fault mechanics often explores stick-slip instabilities, considering strain energy storage either at grain-scale [(J. Leeman et al., 2015), (Dorostkar et al., 2018)] or in the loading system (Sathwik Kasyap & Senetakis, 2021) and can thus be carried out in a stable or unstable way. Our model is not totally realistic as, the sliding is imposed by the Boundary Conditions, and the non-deformability of the rock does not allow energy storage within the fault system. Although such energy storage is not present in our simulation, it is to be kept in mind from the perspective of upscaling the frictional behaviors we report to actual fault dynamic systems.

2.5. Concluding remarks

This chapter has detailed the main principles of the Discrete Element Method (DEM) and how to apply it to a granular fault gouge containing infill materials such as mineral cementation or fine matrix particles. For that purpose, in the first part, the general algorithm has been detailed, as well as the contact laws which will be used in the following chapters. In a second part, we proposed a numerical tool to create a numerical gouge sample with angular and facetted shapes (Packing2D). This method allows creating three main types of granular samples: a fault gouge with angular particles in which cement will be added through contact laws, a fault gouge simply composed of polygonal matrix particles and a mixture between angular grains surrounded by matrices. The last section presented the 2D direct shear model simulated using DEM and the important parameters of the model. It also highlighted several preliminary analyses defining the physical and geometric parameters of numerical fault gouges (applied normal stress of 40 MPa and a shearing velocity of 1 m/s). It has been confirmed that the shape of the grains has a significant influence on the coefficient of friction and the shear behavior of the gouge, justifying the use of angular grains with facets.

However, there are some limitations to these numerical models, such as:

- The small wavelength used for rock walls, as opposed to a mature fault which may be very eroded with higher rock walls wavelength.
- The choice of constant normal stress, shearing velocity, and gouge thickness implies results corresponding to a specific case of study.
- The impossibility of a direct study of seismic or aseismic behavior, since the model cannot store energy.

The following chapters propose two different models of a sheared granular fault gouge with cemented material (Chapter 3) or matrix material (Chapter 4) with the associated contact algorithms detailed above. Both granular samples try to be as realistic as possible with angular and faceted particles for “clasts” and hexagonal cells for matrix particles.

Chapter 3. Slip behavior of a sheared cemented gouge

3.1. Foreword

Within a mature fault gouge, mineral cementation coming from rock dissolution, melting, or other processes derived from previous slips, can fill remaining pore spaces between particles and change the global state of cohesion (Philit et al., 2018). The objective of this chapter is to establish a link between the micro-mechanical and structural properties of a cemented gouge layer, and its rheological behavior under shearing, Figure 50. We also aim to understand the influence of interparticle bonds on slip mechanisms by employing the Discrete Element Method (Chapter 2). We consider a direct shear model without fluid in 2D, based on a granular sample with angular and faceted shapes. Section 3.2 presents the fault segment model in 2D involving two rough surfaces representing the rock walls separated by the cemented fault gouge. Section 3.3 describes and characterizes the cemented materials used for the numerical campaign. Focusing on the physics of contacts inside the granular medium, we explore strength evolution, gouge kinematics, and force chains within the gouge in section 3.4. We aim in this section to study the effect of cementation and initial porosity on mechanical behaviors and kinematics of shear bands. The last section 3.5 offers a discussion on new insights and relations between cementation within the gouge, shear localization, and relevance of Coulomb-Mohr theory for fault models.

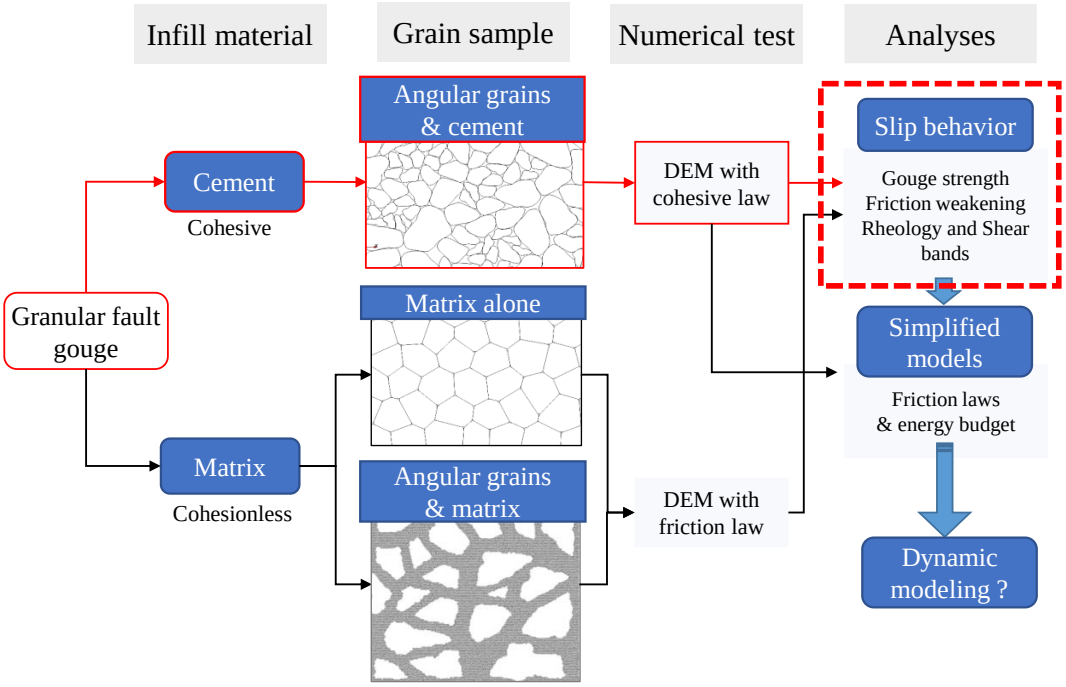

Figure 50. Main schema of Chapter 3.

This chapter is mostly based on the following paper:

Casas, N., Mollon, G., & Daouadji, A. (2022). DEM Analyses of Cemented Granular Fault Gouges at the Onset of Seismic Sliding: Peak Strength, Development of Shear Zones and Kinematics. Pure and Applied Geophysics. https://doi.org/10.1007/s00024-021-02934-5

3.2. Numerical framework and sample generation

3.2.1. Granular fault gouge sample

Numerical fault gouge

The software Packing2D (Chapter 2) is employed to create a realistic granular sample with angular and faceted shapes of particles. Since the morphological descriptors of the grains of granular gouges may vary significantly between faults, the spectrum was calibrated by visual comparison with published pictures of real gouges and results in the "Grains with angular shape" of Chapter 2, Figure 51 (a).

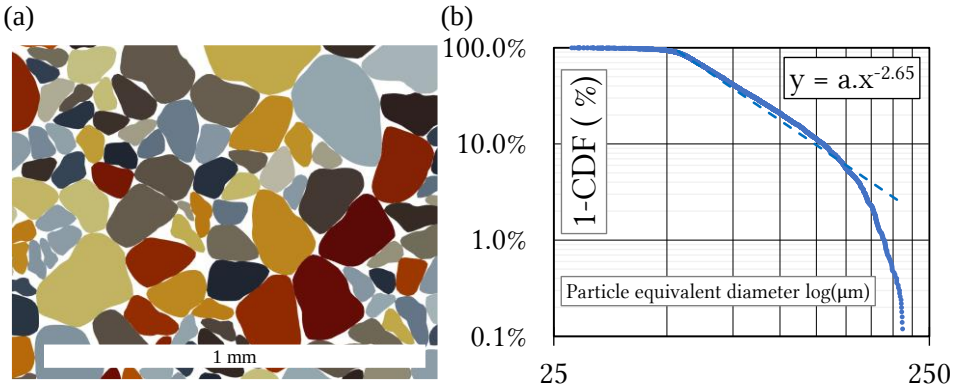

Figure 51. (a) Zoom on a granular sample generated with packing2D, with angular and faceted shapes, and compacted in MELODY2D (b) Particle size distribution of the synthetic sample, fractal dimension with $D = 2.65$.

A 2mm-thick granular fault gouge is created before compaction, resulting in 1.7 mm after compaction. A gouge of 2 x 20 mm^2 is found to be satisfactory (RSE, Chapter 2) and falls within the same order of magnitude as previous studies [(Ferdowsi, 2014) & (Dorostkar et al., 2017b)]. A fractal size distribution is chosen to fit with the literature on granular gouge composition, [(Olgaard & Brace, 1983), (Blenkinsop, 1991), (Billi & Storti, 2004), (Billi, 2005), (Muto et al., 2015)] with a fractal dimension factor D close to 2.6. The gouge with angular grains is composed of 4960 particles with a corresponding equivalent diameter in the range of 28 – 226 µm (average value of 81 µm) and a (D_{50}) equal to 70 μm, Figure 51 (b).

Two initial states

Once the granular sample is generated with Packing 2D, it is then inserted between two rock walls and the first simulation step consists in compacting the sample with $\sigma_N = 40\ MPa$ to create a stabilized packing of granular material (Chapter 2). Thanks to a preliminary study on the influence of interparticle friction during compaction and shearing steps (Appendix 2.C), we chose to keep two initial porosities for this chapter, $P_{pore} = 16\ \%$ (i.e. $F_S = 0.84$) and $P_{pore} = 11\ \%$ (i.e. $F_S = 0.89$) that are respectively called "mid-dense samples" and "dense samples". When the granular media obtained is sheared (without cementation), the initial density has a considerable influence on the initial peak of effective friction and dilation phase with slip distance: the chosen samples correspond to two granular behaviors when the gouge is sheared without cementation, as observed in Figure 52.

The mid-dense sample ($F_S = 0.89$) shows a higher friction resistance than the mid-dense sample ($F_S = 0.84$) that does not exhibit the same friction with a friction peak almost missing. The evolution of the gouge thickness Figure 52 (a) is also consistent with the initial density of both samples: the denser sample presents higher dilation.

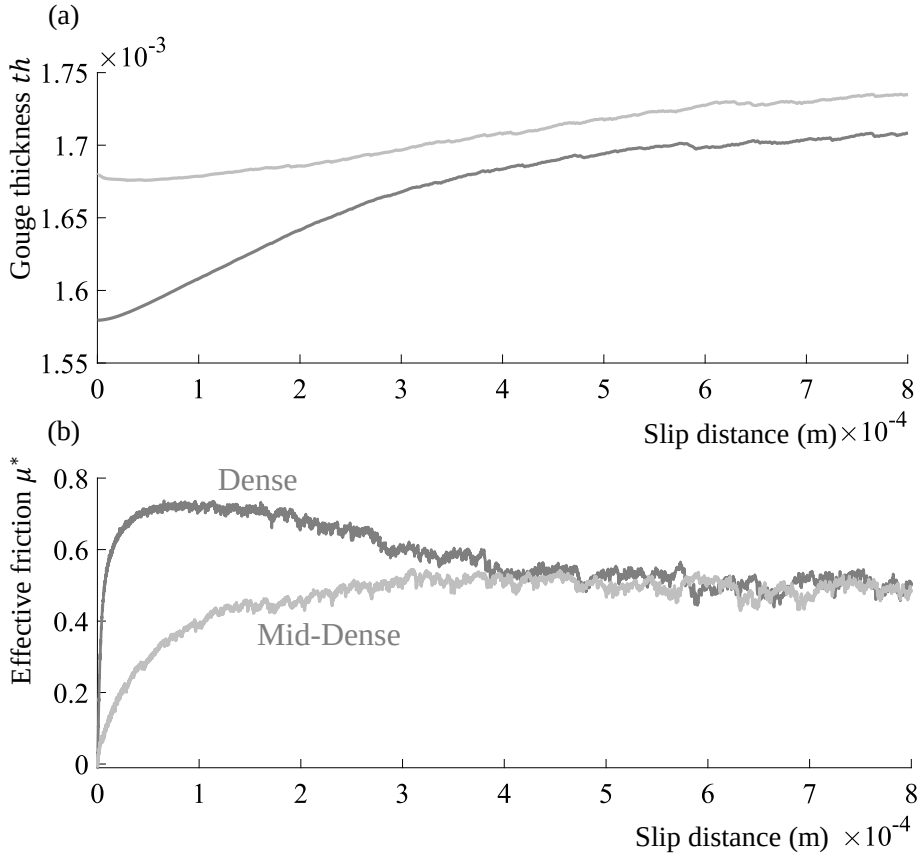

Figure 52. (a) Gouge thickness (m) as a function of the slip of the upper rock wall (m) - for dense and mid dense sample (b) Effective friction as a function of of the slip of the upper rock wall (m), results from the shearing of granular samples with the following parameters ($\sigma_n = 40\ MPa, V = 1\mathrm{m}/s$, $\rho_r = 2600\ \mathrm{Kg/m^3}$, $k = 10^{15}\ N.m^{-3}, \mu_{num} = 0.5$ (during shearing)).

If we want to study the onset of sliding, it is important to know what is the initial state of the system, and more particularly the initial porosity of the granular material. Depending on the type of rock or the previous shearing in the gouge, the sample can have different initial states that will resist differently to shearing. Within the next sections, we will consider the two identified initial porosities, ($P_{pore} = 16\ \%$) for mid-dense samples and, ($P_{pore} = 11\ \%$) for dense samples.

3.2.2. Numerical setup for direct shear simulations

Introduction of cementation between particles

As the cement present a rather "cohesive" behavior [(Riedmüller et al., 2001), (Wibberley et al., 2008)], it can be explicitly simulated in DEM by considering breakable cohesive bonds between particles. The "Bonded Mohr-Coulomb" law adapted to the complex grain shapes is, therefore, applied considering a pressure C_{num} to maintain the contact between particles (Chapter 2).

The numerical cohesion C_{num} considered in the code cannot be directly related to real cementation in rocks and does not bear much physical signification by itself. A good way to associate a quantitative description to this numerical parameter is to define an associated level of cementation. In the initial state of our model, each cohesive bond between any pair of contacting grains requires a certain amount of mechanical energy for breaking. The energy of de-cementation E_{Cem}, represents the total energy needed by the system to break all cohesive bonds initially present within the gouge. It can be described by a relation between properties of the initial contact network (i.e. at the end of the compacted state):

$$E_{Cem} = \left(\sum_{i=1}^{N}\left(\sum_{j=1}^{n} L_{p-cij}\right)\right)\left(\frac{C_{num}}{2}\right)^2 \frac{1}{2\,k_n\,L_g} \quad [J.m^{-2}] \tag{3.1}$$

With L_{p-cij} the contact length of one particle bond in one side of a particle, Figure 53 (a), N the total number of particles, n the number of contact bonds for each particle, k_n the normal numerical stiffness, C_{num} the initial numerical cohesion and L_g the length of the model.

The idea is then to be able to relate this energy to the physical characteristics of rocks. To do so, the total amount of energy that would be needed in order to break all the initial bonds between cemented particles is normalized with respect to a representative surface energy E_S. This energy is applied to the contour of each particle which is assumed to be cemented on its entire contour, (a unit length is considered in the third dimension for any necessary purpose). The maximal energy for a fault patch of 1 m^2 width (third direction) and cemented bonds covering the total external surface of all particles in the gouge, as in Figure 53 (b), could be written as:

$$E_{max} = 2\,E_S\,\frac{\sum_{j=1}^{N} P_j}{L_g} \quad [J.m^{-2}] \tag{3.2}$$

With P_j the perimeter of a particle "j" and, E_S the surface energy of 62 J/m^2 which was reported for the Chilhowee quartzite and considered as an upper limit for rock surface energy by (Friedman et al., 1972).

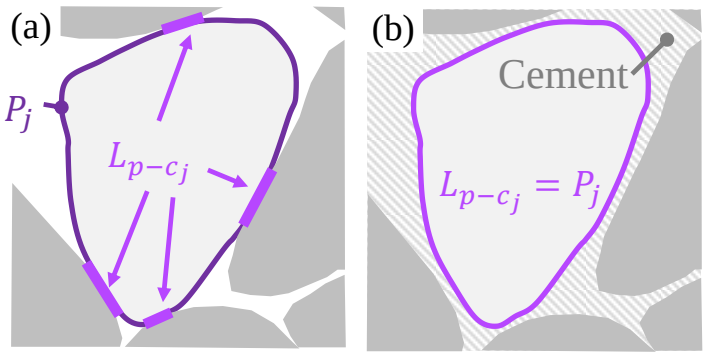

Figure 53. (a) Real contact between angular particles, the central grain is a grain 'j', with its total perimeter P_j and total contact length of one grain L_{p-cj} (different from the total contact length of the sample L_{p-c}) (b) Theoretical view of a contact fully cemented (100 % cementation) where L_{p-cj} is equal to the perimeter of the grain.

The next step is to determine which numerical cohesion corresponds to this state of total cementation Figure 53 (b), this value is called $C_{num-100\%}$. We can thus express the de-cementation energy in our initial sample as a percentage of cementation P_{cem} proportionally to the 100 % cemented material.

$$E_{Cem} = E_{max} \ [J.m^{-2}] \tag{3.3}$$

$$C_{num-100\%} = \sqrt{\frac{16\, E_S \left(\sum_{j=1}^{N} P_j\right) k}{\left(\sum_{j=1}^{N}\left(\sum_{i=1}^{n} L_{p-cij}\right)\right)}} \ [MPa] \tag{3.4}$$

$$P_{cem} = 100 \left(\frac{C_{num}}{C_{num-100\%}}\right) \ [\%] \tag{3.5}$$

Hence, any initial state of cementation effectively introduced in the numerical samples by the means of the numerical cohesion C_{num} can be defined as a certain percentage of this complete cementation. Thus, a simulation case with cementation of $P_{cem} = 20\,\%$ is to be interpreted in the sense that, in its initial state, the energy needed to break all its bonds is equal to 20 % of that of the fully cemented case. After compaction and stabilization, the contact law between grains is introduced with a percentage of cementation P_{cem} from 0 % to 95 %.

Direct shear simulations

Figure 54 presents the DEM model of the cemented granular fault gouge, with rock walls at the top and bottom sides of the granular sample.

Contact surfaces of rock walls are sinusoidal to introduce a certain roughness and avoid wall-slip effects since we want to ensure that slip accommodation takes place within the gouge. This is a pure modeling choice, and the rock surfaces should be considered as nominally flat. Interparticle friction is equal to 1 at the contact interface between walls and particles to make sure that the motion is fully coupled at the wall-grains transition. Interparticle friction μ_{num} is set to 0.5 between particles in contact. Since the parametric study realized in Chapter 2, a normal stress of 40 MPa and a sliding velocity of 1 m/s are applied on the upper rock wall.

To limit interpenetration between grains while mimicking the local deformation of the grains in the contact vicinity, a constant numerical stiffness of $10^{15}\ Pa/m$ is used (Appendix 3.A). This constant value was chosen to obtain the overall deformability of the sample of the same order of magnitude as the one for bulk granite or shearing modulus ($\approx 10 - 25\ MPa$ depending on initial porosity, see next section). All the parameters are gathered in Table 3 and are reproducible (Appendix 3.B).

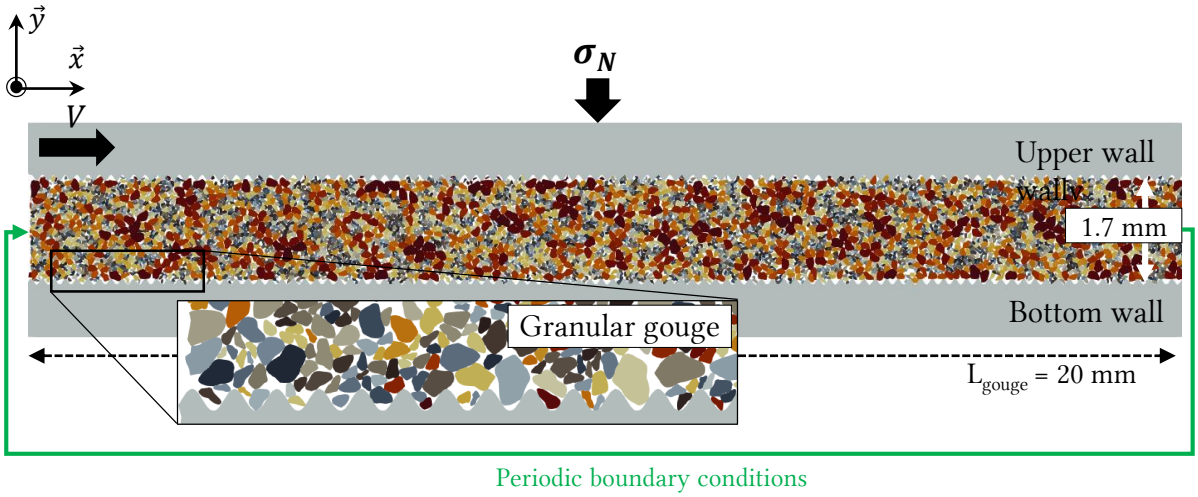

Figure 54. DEM model of a granular fault gouge, 4960 angular particles in a 1.7x20 mm domain. As explained in Chapter 2, gravity is ignored in the model, assuming that the fault can be oriented in a wide range of directions, and that gravity forces are negligible compared to those related to normal and deviatoric stresses applied on the gouge. Periodic boundary conditions are present on both right- and left-hand sides of the sample to maintain the continuity of the movement at large slips. The movement of the upper rock wall in the y-direction remains free to allow gouge dilatancy while the bottom rock wall is fixed. In this study, the chosen density of 2600 kg/m^3 for particles, leads to an appropriate time step for these simulations of 10^{-9} s.

Table 3. Numerical setup and properties for the experimental campaign.

Property	Associated variable	Value
Normal stress	σ_N	40 MPa
Shear velocity	V	1 m/s
Rock density	ρ_r	2600 kg/m^3
Contact stiffness	k_n & k_t	10^{15} Pa/m
Cohesive bond strength	C_{num}	0 → 2500 MPa
Percentage of cementation	P_{cem}	0 % → 100 %
Percentage of initial porosity	P_{pore}	11 % & 16 %
Interparticle friction	μ_{num}	0.5 (grains – grains) 1 (grains – walls)
Initial sample size	th_i x L_g	1.7 x 20 mm
Particle equivalent diameter	$\phi_{min} - \phi_{max}$	28 – 226 μm
Number of particles	N	4960
DEM time step	Δ_t	10^{-9} s
Proximity updating period	$\Delta_{t-contact}$	10^{-7} s

3.3. Cemented materials characterization

3.3.1. Characterization under biaxial simulations

The strength of granular materials (may they be cemented or not) and rocks is generally considered to follow the Coulomb-Mohr criterion (Chapter 1). In this model, the effective stresses are equal to the total stresses as the material is dry.

To characterize our synthetic cemented gouges (in the sense of Coulomb-Mohr), we ran independent biaxial simulations of samples with the same characteristics as those used for our sheared fault gouge (in terms of grain shapes, size distributions, initial solid fraction,

interparticle cementation, and interparticle friction). Rectangular granular samples (4 mm wide and 10 mm high) are placed between four rigid walls, Figure 55 (a). The lower wall is fixed in displacement, the upper wall is submitted to a constant downwards velocity V_y, and the lateral walls are submitted to a confining pressure σ_3, fixed in vertical and rotational motions, and free to move horizontally.

For each cementation level and each initial porosity, three tests are performed with confining stresses of 10 MPa, 40 MPa, and 80 MPa. The vertical stress σ_1 is monitored during vertical compression (series of pictures with relative damage, Figure 55 (a)). Biaxial simulations are only used for the cemented material characterization in this section in order to obtain the internal friction angle φ and the cohesion C. These parameters are not to be confused with the interparticle cohesion (C_{num}) and friction (μ_{num}) that are introduced in the DEM contact laws, since they represent a collective response of the granular material to shearing.

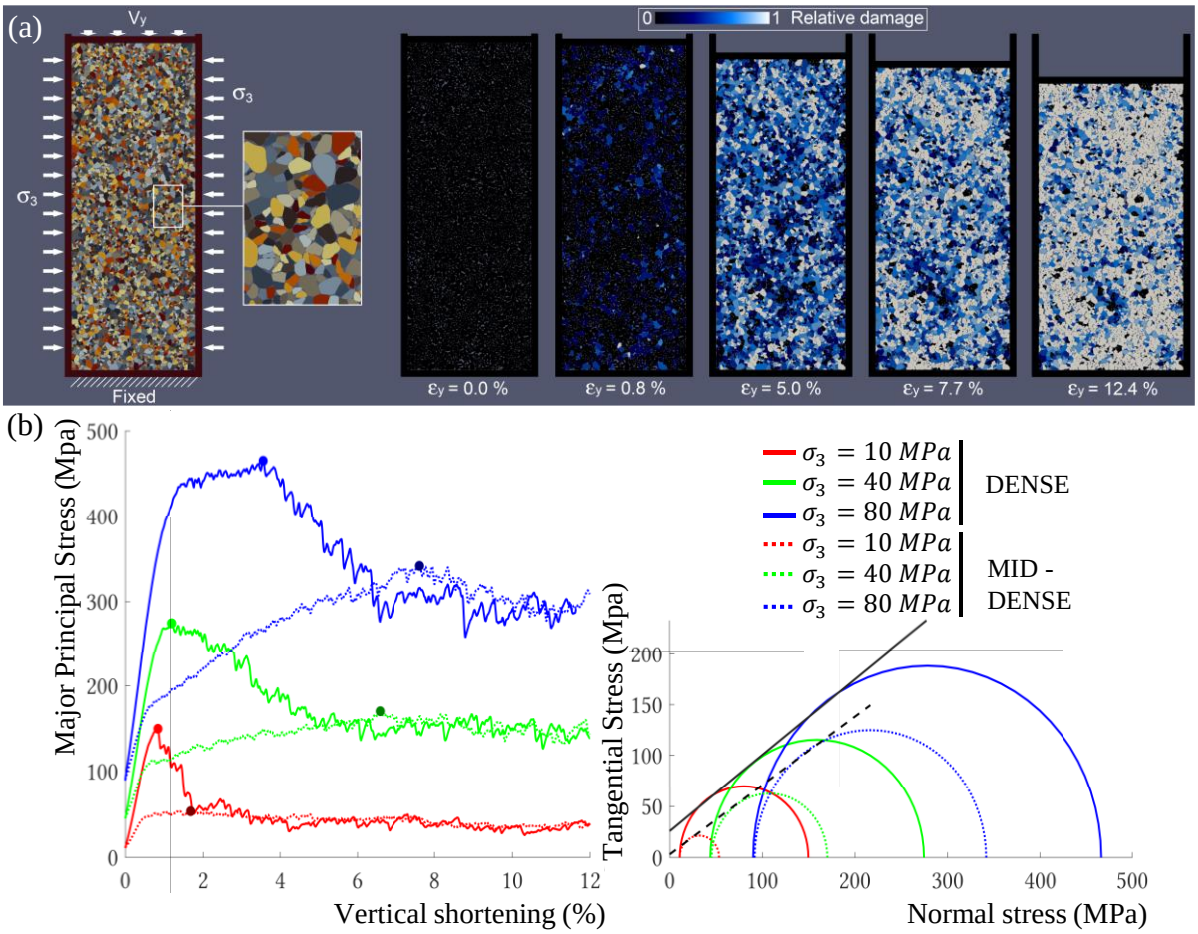

Figure 55. Illustrative results for a numerical cohesion $C_{num} = 1000\ MPa$ (a) Views of experiment and damage evolution for different percentage of vertical shortening under confining stress of 80 MPa - (b) Major principal stress as a function of vertical shortening and associated Mohr circles, for three confining stresses (10 MPa, 40 MPa, and 80 MPa) for both dense and mid-dense samples.

Figure 55 (b) and (c) provide illustrative results for a numerical cohesion $C_{num} = 1000\ MPa$ (corresponding to $P_{cem} = 38\ \%$ in the dense case and $P_{cem} = 40\ \%$ in the mid-dense case). Graphs show that dense samples quickly reach a peak strength before softening towards a plateau value, while mid-dense samples are less stiff and reach the same plateau (approximately

at the same level of vertical strain) without passing by a well-defined peak. When plotting the Mohr circles corresponding to the maximum values of σ_1, Figure 55 (b), we confirm that all samples follow the Coulomb-Mohr failure criterion, which makes it possible to characterize their cohesion C and internal friction angle φ. For each initial state, elasticity moduli E (not strictly equal to Young's moduli because of biaxial conditions) are also extracted based on the vertical stiffness of the samples at low (<<1 %) vertical strains.

Similar Coulomb-Mohr graphs were plotted for the other C_{num} values and also result in following the Coulomb-Mohr criterion. The main results are gathered in Figure 56:

(a) internal friction angle φ is only moderately influenced by the cementation level in the mid-dense samples and is a non-monotonous function of the cementation in the case of dense samples. It is also strongly linked to initial density: mid-dense samples have friction angle values of $32-35°$, while dense samples have friction angle values up to $36-44°$.

(b) Cohesion increases monotonously with cementation (as found in the literature by (Wissa, 1965) and (Lade & Overton, 1989)) and reaches much larger values for dense samples (up to 70 MPa for $P_{cem} \approx 100$ %) than for mid-dense samples (up to 20 MPa). It can also be noted that a certain percentage of cementation is needed to have a measurable cohesion within the gouge ($P_{cem} > 20$ % for mid-dense samples and $P_{cem} > 10$ % for dense samples).

(c) However, Elasticity moduli is rather unaffected by cementation and is close to $11-12$ GPa for mid-dense samples and to $25-26$ GPa for dense samples.

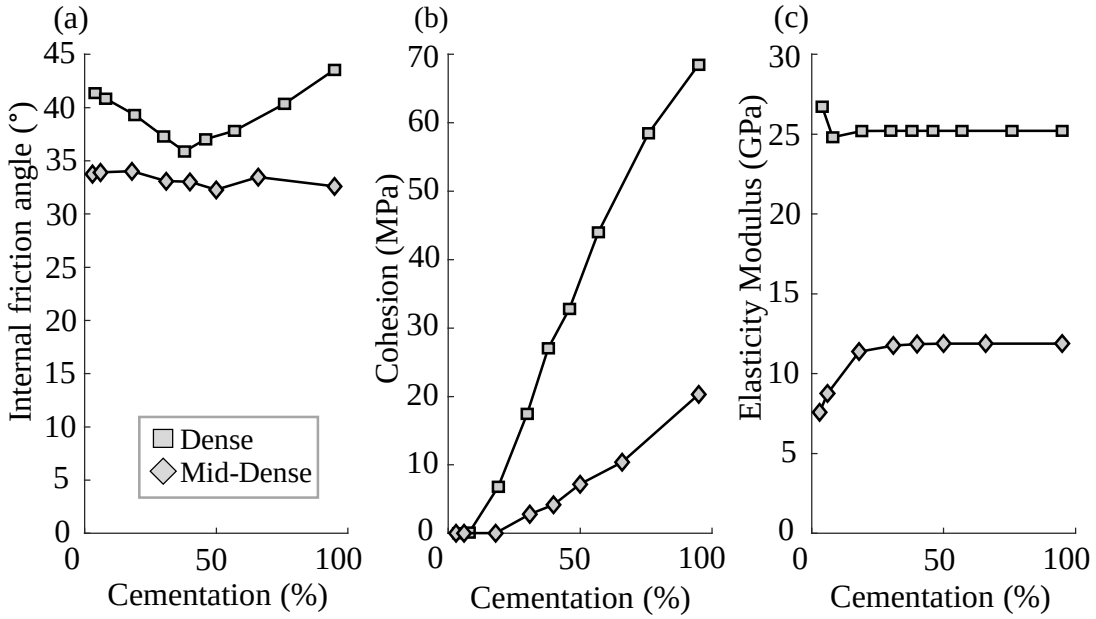

Figure 56. (a) Internal friction angle (°), (b) Cohesion (MPa), and (c) Elasticity moduli (GPa) as a function of the Cementation (%) for dense and mid-dense samples.

3.3.2. Comparison to real cemented material and rocks

The cementation considered in this chapter has a clear definition from a numerical point of view (3.2.2) but it is also interesting to characterize and compare our samples with real materials. For this reason, it is instructive to consider Coulomb-Mohr properties of cemented gouges, for

which characterization techniques are available. Figure 57 compares the different synthetic materials tested in this chapter (with different initial percentages of cementation and porosities) with typical rock properties found in the literature (Schellart, 2000), in terms of internal friction angle and cohesion.

We observe that our samples have adequate values of internal friction angle (especially in the mid-dense case) and are in the lower range of cohesions. The low cohesion is consistent with the fact that we are simulating cemented gouges instead of intact rock. Figure 57 confirms that our samples have similar Coulomb-Mohr properties to some real rocks: (a) dense poorly cemented samples present similar Coulomb-Mohr properties to Quartz sand, (b) the dense gouge with $P_{cem} = 75$ % looks like rock "8" (Tennessee sandstone), (c) highly cemented gouge (mid-dense) has similar properties to rock "1" (Granite).

Even though some friction angle and cohesion are close to some Coulomb-Mohr values, a fault gouge develops a complex Riedel band structure reflecting a heterogeneous stress field different from the one observed for intact rocks (Lockner & Beeler, 2002). Future work might be undertaken to target the Coulomb-Mohr properties of a cohesive rock for which direct shear experimental results are available, in order to propose a direct comparison with our simulations.

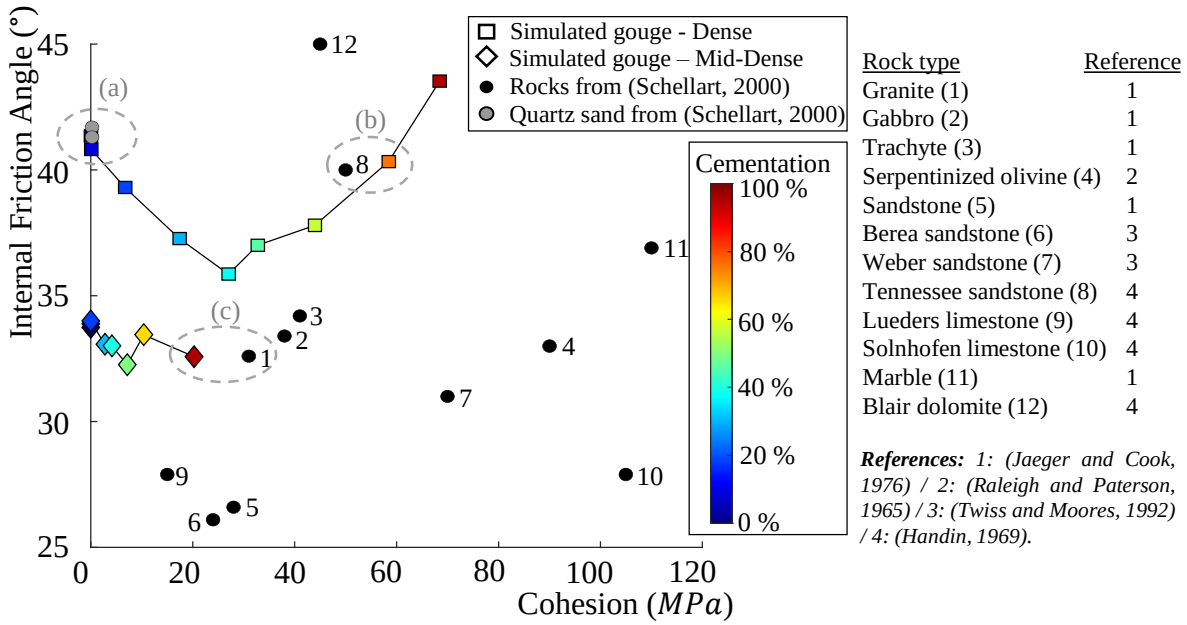

Figure 57. Internal friction angle as a function of Coulomb-Mohr cohesion for the simulated materials, as characterized by numerical biaxial tests (Figure 55). Dense samples are marked by squares and mid-dense samples by diamonds. It can be noted that the samples used are large enough to avoid any size effect or any thickness dependence. The discs correspond to experimental characterizations of different rocks referenced in (Schellart, 2000) listed in the table next to the graph.

3.4. Influence of the cementation on gouge kinematics

Simulations with various cementation levels are performed for both dense and mid-dense samples with the numerical setup for a direct-shear experiment (section 3.2.2). In the next sections, we will use the effective friction μ^* and the dilation ε_y (Chapter 2) to analyze the mechanical behavior of gouges. It is important to keep in mind that cementation makes μ^*

dependant on the normal load and thus different from a stress-independent Coulomb-like friction coefficient, hence the term "effective friction". Dataset from direct shear simulation is available in (Appendix 3.C).

3.4.1. Effective friction and dilation within dense samples

Friction and gouge strength

Figure 58 (a) & (b) provides typical curves of the measured effective friction of the fault as a function of the horizontal displacement imposed to the upper wall. In all cases, the tangential force increases linearly with cementation until a maximum effective friction μ_p^*, demonstrating the maximal effort that the loading system must provide to overcome interlocking in the gouge and accommodate imposed shearing. The linear elastic part of the curves represents the stiffness of the granular material. It should be noted that this stiffness is only related to the gouge layer itself since no other compliance (related to the surrounding medium, for example) is considered in the simulations (Chapter 2). All simulations with initial dense samples follow the same elastic slope, and adding more cementation extends the elastic part before effective friction peak, Figure 58 (a).

The peak strength evolves from a smooth, delayed, and of moderate amplitude shape (poorly cemented cases) to a sharp, short, and intense shape (highly-cemented cases). After the peak, the effective friction decreases in all cases towards a plateau and does not evolve significantly anymore until the end of the simulation. All steady-state values oscillate around the same effective friction μ_{SS}^*, (averaged from the beginning of the plateau until the end of the simulation), close to 0.5 (ranging from 0.45 to 0.51). This value is in agreement with other numerical studies (Rathbun et al., 2013), but lower than typical 3D experimental values (which are usually above 0.6). This discrepancy is related to the 2D character of the simulations (Frye & Marone, 2003). More details on that subject can be found in Chapter 1.

Brittleness

According to the literature, shear strength is enhanced with cohesion, (Wissa, 1965), and thus with the increase of cementation, Figure 56 (b). Cohesive strength in granular materials is known to correlate with an increase in the brittleness (Meng et al., 2021), of the material (Das et al., 2014), and this is confirmed by Figure 58 (c), which presents the evolution of brittleness within each sample (based on strength ratio (Bishop, 1971)).

Despite the cementation level of each simulation, all the dense samples exhibit an overconsolidation peak. A reduction of this peak may appear for higher applied normal stress as found by (Haines et al., 2013). A qualitative change in behavior is observed close to $P_{cem} = 10\,\%$. This transition corresponds to the value where cementation starts to induce cohesion within the gouge (red line). From this moment a marked evolution in terms of peak strength is observed, with the emergence of a sharp peak strength increasing with cementation.

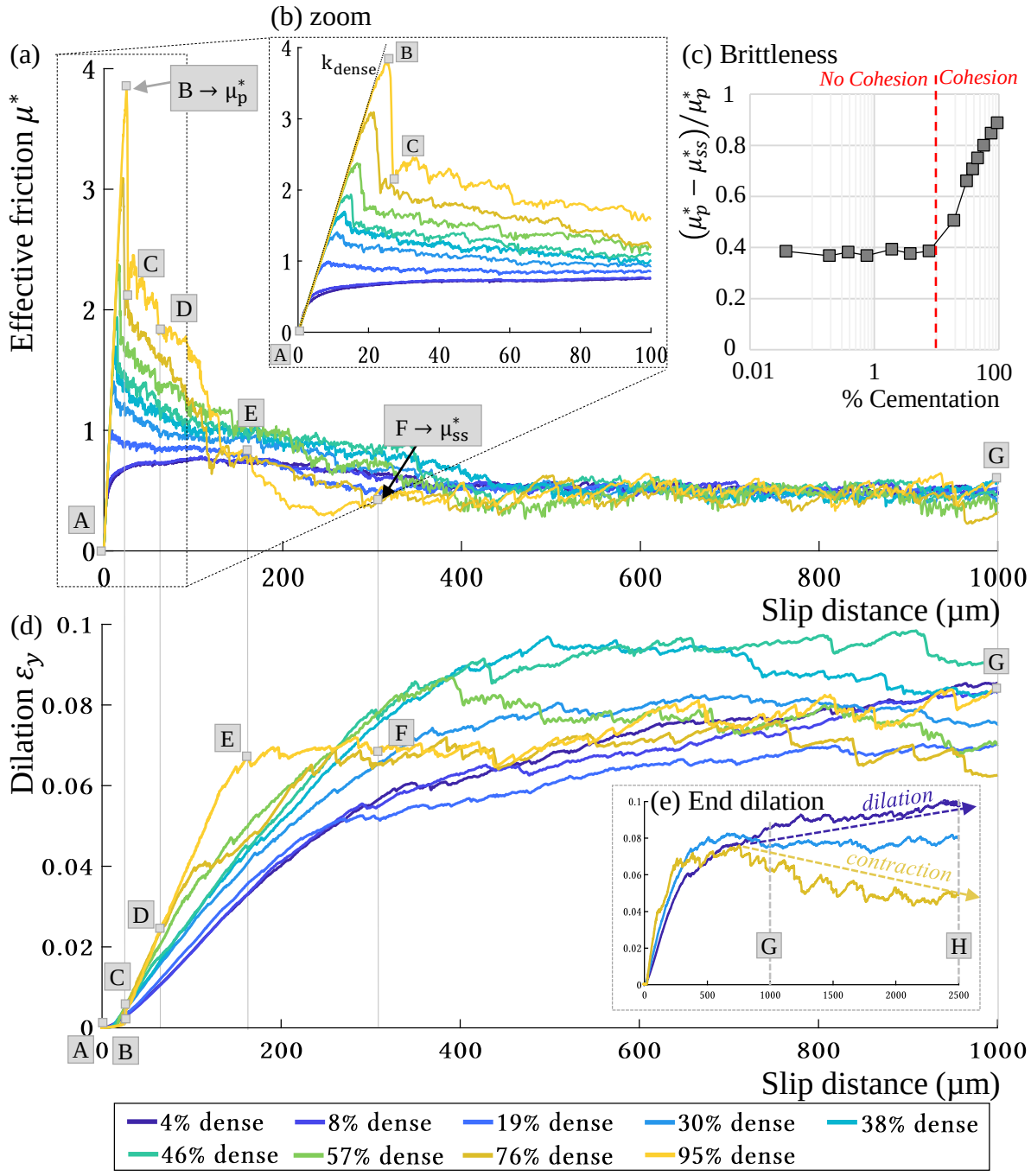

Figure 58. (a) Effective friction curve for different surface percentages of cementation for dense samples as a function of the slip distance (µm), (b) Zoom in on the peak, (c) Brittleness as a function of cementation, the brittleness is expressed as the ratio of $(\mu_p^* - \mu_{ss}^*)$ divided by μ_p^*, (d) Dilation variation ε_y as a function of the slip distance (µm) for dense samples – (e) Zoom out on the dilation curve, higher slip distance.
Letters correspond to different steps in curves presented: [A] is the initial state before shearing and is identical in all cases. [B] is the peak location, [C] is the end of the first peak (only appears for dense samples with a lot of cementation), [D] is half-peak, [E] is the end of the major dilation phase, [F] is the observed end of the effective friction peak, [G] is a common state for beginning of steady-state and [H] is the end of simulation with $Ds = 2500\ \mu m$ (results table in Supporting Information S7). The case "0 cementation" is not represented here as it is similar to the case with 4 % cementation in terms of friction and dilation variation. These results are not in the range of small deformations, as the total slip displacement ($H = 2.5\ mm$) is higher than the gouge thickness ($\approx 1.75\ mm$).

Dilation

For $P_{cem} \leq 10$ %, dilation is similar to a case without cementation as the cohesion in the sense of Coulomb-Mohr is smaller than 1 MPa (i.e. negligible compared to the normal stress). A progressive dilation until the steady-state "G" is observed. The increase of cementation (for $P_{cem} \geq 10$ %) seems to accelerate the dilation of the gouge, Figure 58 (d), which appears earlier with slip distance. This dilation enhancement is possible because some frictional contacts begin to form with the breakage of cemented bonds. Observing the second part of simulations from "G" to "H", Figure 58 (e), three main trends are highlighted: materials with medium cementation (~ 10 % $\leq P_{cem} \leq 75$ %) reach a stabilized dilated material whereas poorly cemented materials continue to dilate and highly cemented materials present a contractive behavior. The higher dilation observed for poorly cemented materials ($P_{cem} \leq 10$ %) can be explained by the fact that these simulations present more frictional contacts than cohesive contacts, and that frictional particles are known to enhance dilation (Roy & Luding, 2017). For extremely high cementation ($P_{cem} \geq 75$ %), although the steady-state friction value announces a friction stabilization at "G", a contracting behavior is later observed (from "G" to "H"). This contraction is attributed to the rupture of the asperities formed by cohesive links (i.e. agglomerates) at the beginning of the shear localization "F", see Section 3.4.4.

3.4.2. Interface failure modes within dense samples

Cohesive strength correlating with brittleness increase has a major influence on strain localization (Maurer, 1965). From observations on friction and dilation, the simulated materials can be gathered in three different cementation regimes: poorly cemented ($P_{cem} \leq 10$ %), cemented (10 % $\leq P_{cem} \leq 75$ %), and highly-cemented ($P_{cem} \geq 75$ %), corresponding to three modes of deformation zone.

The rupture of a cohesive bond is represented by the increase of damage to the concerned grains. This damage is set to 0 for each grain when cohesive bonds are first established (all the bonds are intact) and may evolve until 1 if all these bonds reach the "broken" status (Chapter 2). It is thus a relative damage with respect to the initial state. The representation of the relative damage gives a picture of the state of cementation between grains and their location within the gouge, Figure 59, Figure 60 & Figure 61. As shear band formation and evolution vary with the level of bond strength (Jiang et al., 2013), the damage allows following the formation of failure patterns (Riedel cracks, shear bands, etc.) and their orientation.

(i) For poorly-cemented materials ($P_{cem} \leq 10$ %), the interparticle cementation introduced between grains is not sufficient to maintain cohesive bonds during shearing. The simulation for $P_{cem} = 4$ %, Figure 59, reveals very few tensile forces consistent with the low percentage of cementation within the sample. As soon as the upper rock wall is set into motion, almost all cohesive bonds break and only a few of them resist until friction peak "B_4". Dilation is found to influence shear bands and strain localization (Mead, 1925), and the limited dilation in the first stages of shearing is consistent with the absence of shear band formation.

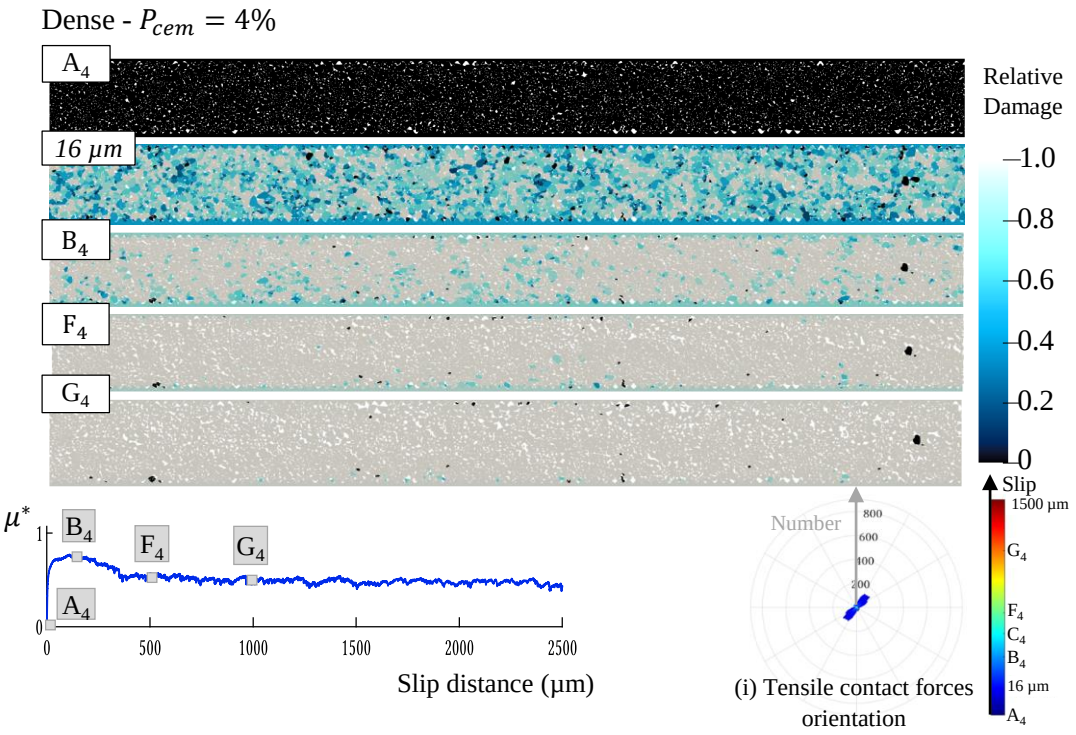

Figure 59. Relative damage snapshot for $P_{cem} = 4\,\%$ in the dense sample (entire granular gouge). Letters correspond to different steps in the curves presented in Figure 58 ("A4": no damage and no-slip distance, "G4": maximum damage and slip distance of 1mm). (i) Tensile contact force orientations allow getting a grasp on the way load is transferred through a granular sample. This information is coded in a polar diagram which provides the distribution of the orientation of tensile contacts.

(ii) The second type of material, Figure 60, corresponds to a cemented granular material (P_{cem} = 38 %). In contrast with the first case, this material presents clear augmentation of tensile forces for both initial states "A_{38}" in dark blue and final states in red in Figure 60 (i). Tensile contacts then reduce from effective friction peak "B_{38}" to the end of the peak "F_{38}" with the breakage of cohesive bonds. However many of the cohesive bonds remain intact, influencing gouge behavior. Friction peak "B_{38}" is the starting point of a movement within the gouge, highlighting a preferential localization of cohesive bonds rupture (white arrow in Figure 60 is considered as the first Riedel deformation (Tchalenko, 1970)). This rupture develops in the next stages of the simulation "B_{38} to H_{38}" with a pattern similar to a Riedel band R (oriented in the sheared direction, ~12° from the upper wall). The progression of the Riedel band towards a shear band increases until the end of the effective friction peak, where it is no longer detectable among the damage zone. The different Riedel geometries are associated with different shear deformation degrees. Conjugate Riedel bands R' are not visible in the numerical results, but tensile fractures T are observed. This is in line with findings reported in (Cho et al., 2008), who highlighted that tensile fracturing is very important in the development of a shear zone, particularly at low normal stress.

From friction peak "B_{38}", damage evolution also highlights the presence of cohesive agglomerates formed by intact bonds within the gouge (ex: Ag_1), with size decreasing with time. In contrast with poorly cemented material where contacts take place between two particles, contacts occur here between clusters of cohesive grains.

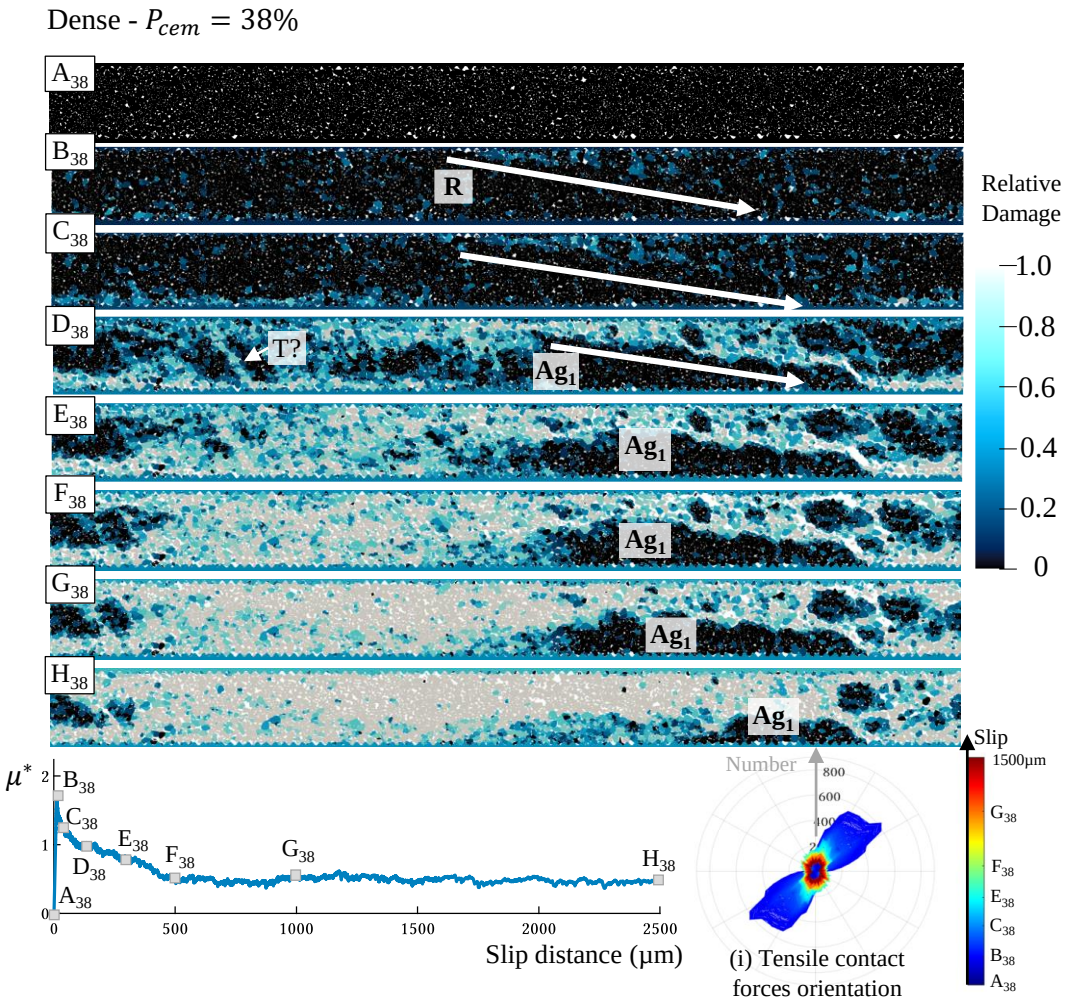

Figure 60. Relative damage snapshot for $P_{cem} = 38\ \%$ in the dense sample (entire granular gouge). Letters correspond to different steps in the curves presented in Figure 58. ("A38": no damage and no slip, "H38": slip distance of 2.5 *mm*). "Ag1" denotes a large agglomerate followed during its motion. The white arrow follows the low angle Riedel shear "R1" inside the gouge and "T" is an example of extension (or tensile) fracture. (i) Tensile contact forces orientation allows getting a grasp on the way load is transferred through a granular sample. This information is coded in a polar diagram which provides the distribution of the orientation of tensile contacts.

These clusters can lead to rather inhomogeneous behaviors inside the granular gouge, changing the whole geometry and particle size distribution. Similar observations were made by [(Cho et al., 2008) & (Rognon et al., 2008)]. Cohesive agglomerates also participate in increasing the overall dilation before steady-state, Figure 58 (b), as also found by (Lade & Overton, 1989) for large cemented particles at low confining pressures. Even though dilation is needed to observe shear bands, this cemented material (presenting the highest dilation after peak strength) inhibits the persistence of shear bands until the end of the shearing. This may be due to the important breakage of cohesive links into frictional contacts after the end of the effective friction peak.

(iii) Increasing again P_{cem} leads to a highly-cemented material ($P_{cem} = 95\ \%$) where most cohesive bonds stay intact during the entire simulation, Figure 61. The numbers of tensile forces are obviously higher than in previous materials, Figure 61 (i), and correspond to (Lade & Overton, 1989) results.

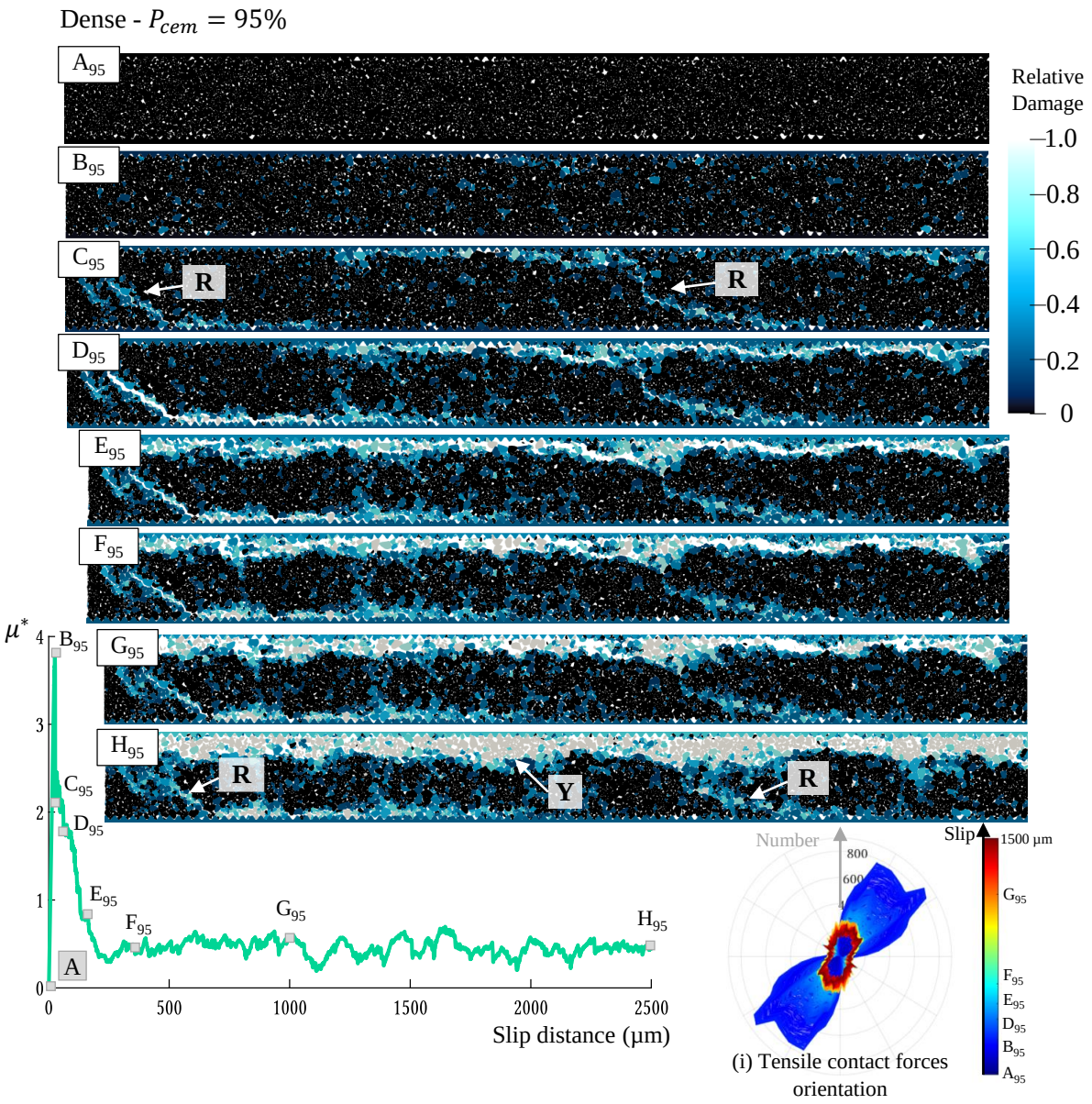

Figure 61. Relative damage snapshot for P_{cem} = 95 % in the dense sample (entire granular gouge). Letters correspond to different steps in the curves presented in Figure 58. ("A95": no damage and no slip distance, "H95": slip distance of 2.5 *mm*). *R* represents the Riedel shear bands and *Y* the horizontal shear localization. (i) Tensile contact force orientations allow getting a grasp on the way load is transferred through a granular sample. This information is coded in a polar diagram which provides the distribution of the orientation of tensile contacts.

This highly cemented rock enhances the formation of two Riedel cracks R at the second friction peak in "C_{95}". Then, "D_{95}" shows the largest Riedel thickness, as this step also corresponds to the maximum dilation peak in the simulation. In the next steps, from "E_{95}" to "H_{95}", Riedel bands thickness progressively reduces in favor of a horizontal shear localization *Y* at the top of the granular gouge in "H_{95}". This shear thickness reduction was also observed in other numerical studies with the increase of strain inside the model (Cundall, 1989). As previously supposed (Section 3.4.1), the progressive breakage of cohesive agglomerates (i.e. asperities) at the interface between gouge and rock boundary seems to explain the contractive response observed in Figure 58 (e), from "G_{95}" to "H_{95}". The shearing localizes on the bottom or top part of the gouge (depending

on the simulation) and lets the majority of particles (still cemented) behave as a single solid-like body. This shearing or "active" zone increases with slip distance.

3.4.3. Influence of initial porosity with cementation

The same percentages of cementation have been tested on a second set of samples with a higher initial porosity $P_{pore} = 16\ \%$ (termed as mid-dense in what follows, as opposed to the dense samples with $P_{pore} = 11\ \%$). The three types of cemented materials previously highlighted have been kept to compare the results between dense and mid-dense samples. The trend observed for mid-dense samples is similar to dense samples, but we note an influence of both initial porosity and cementation on the strength of cemented materials.

Friction & dilation

The increase of initial porosity is supposed to reduce the fracture strength (Taylor, 1948). Our results present the same conclusion, but different shapes of effective friction peak are observed: the peak strength may be sharp, short, and intense (dense and highly cemented cases) or smooth, delayed and of moderate amplitude (mid-dense and moderately cemented cases), Figure 62 **(**a) & (b). Denser samples show higher dilation rates than mid-dense samples Figure 62 (d), as the initial gouge is initially more compacted (Wood, 1990). When the steady-state is reached, a maximum dilatancy is also observed for denser initial samples with twice the deformation obtained with mid-dense samples, for all initial cementations ($\varepsilon_y = 8\ \%$ for dense samples vs $\varepsilon_y = 4\ \%$ for mid-dense).

Brittleness

Figure 62 (c) gathers the brittleness as a function of cementation for the whole simulation campaign and gives more precise information on the transition zone. For samples where a measurable Coulomb cohesion exists, an increase of cementation increases the brittleness for both dense and mid-dense samples, and thus enhances the strength of the gouge, Figure 62 (a). However, the increase of initial porosity leads to a weaker material in terms of cohesive strength.

Without the effect of cementation, we can observe that the brittleness is almost four times higher for dense samples (i.e. ~ 0.4) than for mid-dense samples (i.e. ~ 0.1), meaning a smaller overconsolidation peak. The mid-dense material with the lower cementation is assumed to be here, the weaker material tested. When the cementation level reaches values close to its maximum ($P_{cem} \approx 100\ \%$), the brittleness can reach almost 0.9 in the dense material and almost 0.66 in the mid-dense material. Such high values are likely related to the fact that the cementation of the sample is very high while the confining stress ($40\ MPa$) is rather low (Lade & Overton, 1989).

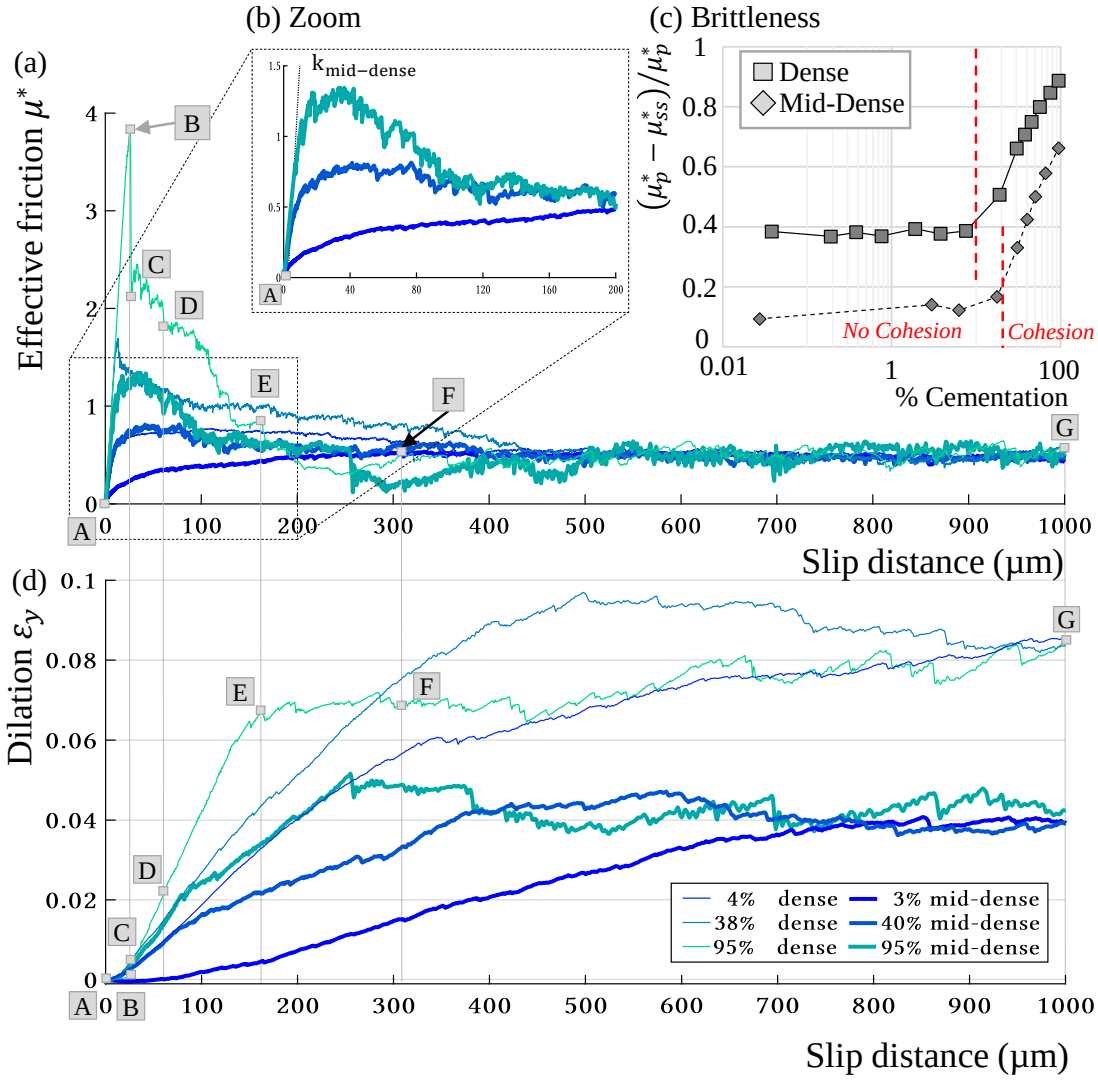

Figure 62. (a) Effective friction curve, comparison between dense and mid-dense samples as a function of the slip distance (µm) for the three different cemented materials highlighted. (b) Zoom in on the peak for mid-dense samples. (c) Brittleness as a function of cementation for both porosity states, the brittleness is expressed as the ratio of $(\mu_p^* - \mu_{ss}^*)$ divided by μ_p^* .(d) Dilation variation as a function of the slip distance (µm) for dense and mid-dense samples. Letters correspond to different steps in curves presented: [A] is the initial state before shearing and is identical in all cases. [B] is the peak location, [C] is the end of the first peak (only appears for dense samples with a lot of cementation), [D] is half-peak, [E] is the end of the major dilation phase, [F] is the observed end of the effective friction peak, [G] is a common state for beginning of steady-state and [H] is the end of the simulation.

Failure patterns

Mid-dense samples also present higher relative damage with easier grains reorganizations, Figure 63, which agrees with the relatively low Coulomb cohesion involved. One high angle Riedel shear band *R'* in the 40 % case, and two high angle Riedel bands *R'* in the 95 %, are followed by a horizontal shear localization *Y* at the bottom of the granular gouge. Conjugate Riedel bands observed do not have the same orientation as those observed with dense materials and are less persistent during shearing. The more ductile character observed for mid-dense samples could be a reason for the different Riedel angles observed (Misra et al., 2009). Moreover, the non-persistence of shear bands for mid-dense samples is in adequation with previous studies on sandstones [(Dunn et al., 1973), (Antonellini & Pollard, 1995)]. They have

shown that gouges with high porosities enhance a distributed deformation that takes the form of cataclastic flow, in contrast with low porosity sandstones which better fail by localization and strain softening (Hirth & Tullis, 1989).

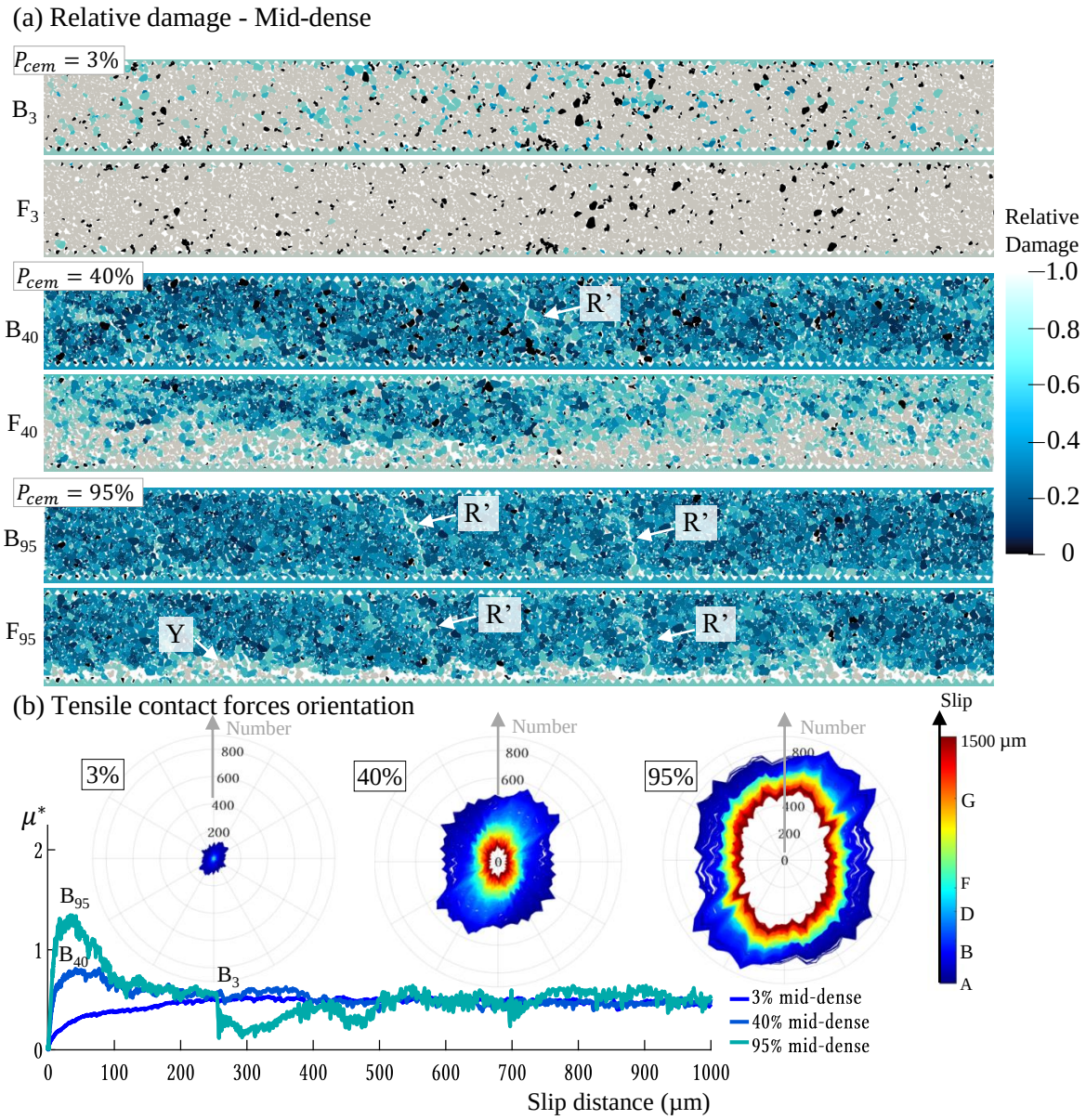

Figure 63. (a) Relative damage snapshots for mid-dense sample (entire granular gouge). For both peak [B] and end [F] of effective friction peak. Letters correspond to different steps in the curves presented in Figure 7. R2 represents high angle Riedel shear bands and Y the horizontal shear localization. Evolution of ductility with cementation and porosity. (b) Tensile contact forces orientation allows to get a grasp on the way load is transferred through a granular sample. This information is coded in a polar diagram which provides the distribution of the orientation of tensile contacts.

3.4.4. Influence of ductility with cementation and porosity

Force chains are key elements to understand the kinematics of the gouge layer and illustrate changes in ductility behavior inside the granular gouge as a function of cementation or porosity. It should be noted that, in the present context, "ductility" is to be understood in the sense of granular mechanics: it is related to the suddenness or slowness of the post-peak frictional weakening but does not involve any visco-plastic phenomenon.

Evolution of ductility with cementation

Force chains are plotted between grains centers (for each contact) in Figure 64. They are commonly used in granular physics for load transfer observation [(Radjai et al., 1996), (Radjai et al., 1999), (Majmudar & Behringer, 2005), (Zhang et al., 2017)]. Similar information is coded in polar diagrams which provide the distribution of the orientation of contact normal vectors. The poorly cemented materials ($P_{cem} < 10 - 25\ \%$) show a ductile behavior, with a progressive particle reorganization, and no localized shear observed, Figure 59. They display a preferential orientation for force chains inclined at 45° from the upper rock wall, Figure 64 (a). Similar force chains orientations have been observed by (Morgan & Boettcher, 1999) for circular particles. The change of orientation of normal forces at 45° appears before the effective friction peak, showing that the gouge started to dilate before reaching the peak. The evolution of the granular flow gives way to simple contact law with interparticle friction only. Once the gouge has dilated, grains can reorganize to allow shearing, and the gouge tends towards a steady state of sliding. The combination of a limited cementation (mostly frictional contact, no cohesion in the sense of Coulomb-Mohr), gouge dilation (Figure 58), and preferred orientation of force chains confirm a typical granular Couette flow for the poorly cemented material [(GRD Midi, 2004), (Da Cruz et al., 2005)].

With the increase of cementation ($P_{cem} = 38\ \%$), the orientation at 45° is not yet present at friction peak "B", because no significant motion has occurred yet and grains are still in their initial configuration. Instead, there are a large number of smaller ramified force chains distributed in a homogenous distribution of force networks. The strength of the material is linked to the development of force chains (Zhang et al., 2017), and our results confirm that the intensity of force chains is enhanced with cementation, as strength is also enhanced, Figure 64 (a). Combining force chains and relative damage makes it possible to identify from the force network the cemented agglomerates highlighted in section 3.4.2 (red arrows). Each cemented agglomerate is crossed by force chains, while isolated frictional particles are not, Figure 64 (a). These cemented clusters also modify the particle size distribution within the gouge, which is well-known to act on shear bands formation in addition to the initial density of the sample (Marone & Scholz, 1989).

For a dense sample with 95 % cementation, some particles are detached from the cohesive band at the end of friction peak, and operate alone (within the active or shearing zone), defining clear geometrical asperities. These asperities create contacts between the cemented layer and the rock wall, which concentrate the normal load. A steady-state is reached when enough of this tribological third body (Chapter 1) has been released to avoid any asperity contact and to produce a three-body sliding. Gouge first dilates thanks to the emergence of asperities (i.e. grains emerging from cohesive bond breakage) and clusters of grains, forming interparticle bridges, which releases gouge in the interface as the rupture is going on. Normal forces orientation follows the same trend as the dilation: a first increase at the first step (due to interparticle bridge formation) and a decrease back to the initial state, as the majority of cohesive bonds are still active, Figure 64 (i). Cementation also enhances local dilation during

the strength weakening, increasing local porosity inside the gouge as found by (Faqih et al., 2006).

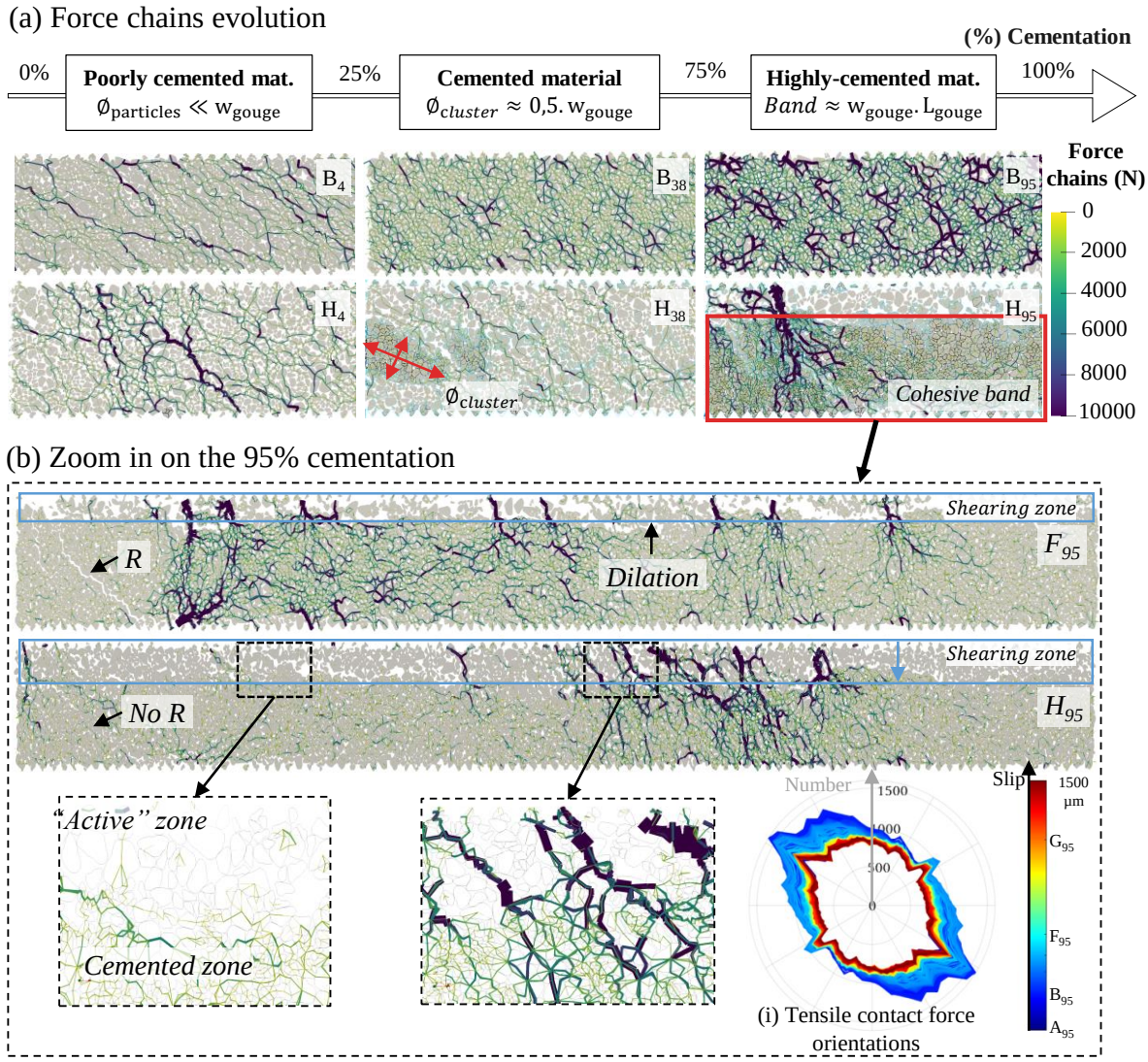

Figure 64. (a) Snapshot of the force-chains network for dense samples at friction peak [B] and at the end of simulation [H]. Force chains are defined according to the typical level of stress present in the system (here the applied normal stress) and thickness evaluates between 0 and 1 between the minimum and maximum strength (0 to 10^4 N). A cut-off is made at 10^4 N to have the same visualization for all cases (higher force chains are observed for a high percentage of cementation). The norm of the contact force is coded by the thickness and color of each chain. In the case of edge-edge contacts, handled through the nodal contacts at the extremities of the contact segment, the total resulting force is considered and coded in a unique force chain. It allows to get a grasp on the way load is transferred through a granular sample. (b) Zoom in on the material with $P_{cem} = 95$ %, snapshot of the force-chains network at the end of friction peak [F] and the end of the simulation [H]– (i) Tensile contact forces orientation allows getting a grasp on the way load is transferred through a granular sample. This information is coded in a polar diagram which provides the distribution of the orientation of tensile contacts.

Evolution of force chains with initial porosity

Figure 65 compares force chains and normal contact orientation for dense and mid-dense samples. Whatever the cementation level at zero displacements "A", dense samples lead to a homogeneous repartition of the initial preferred orientation of normal forces, and mid-dense

samples present normal forces mostly oriented perpendicularly to rock walls, Figure 65 (b). At effective friction peak, initially denser samples favor a more homogenous distribution of force chains, Figure 65 (a), passing through almost all particles. Results are consistent with the previous section showing that the strength increased with a highly cemented and dense sample. This difference is assumed to be related to the more brittle behavior observed for dense samples, for which no reorganization of the grains occurs before the peak. It preserves the initial homogeneous contact network, but makes the failure more sudden, in contrast with mid-dense materials where irreversible grains motions occur before the peak.

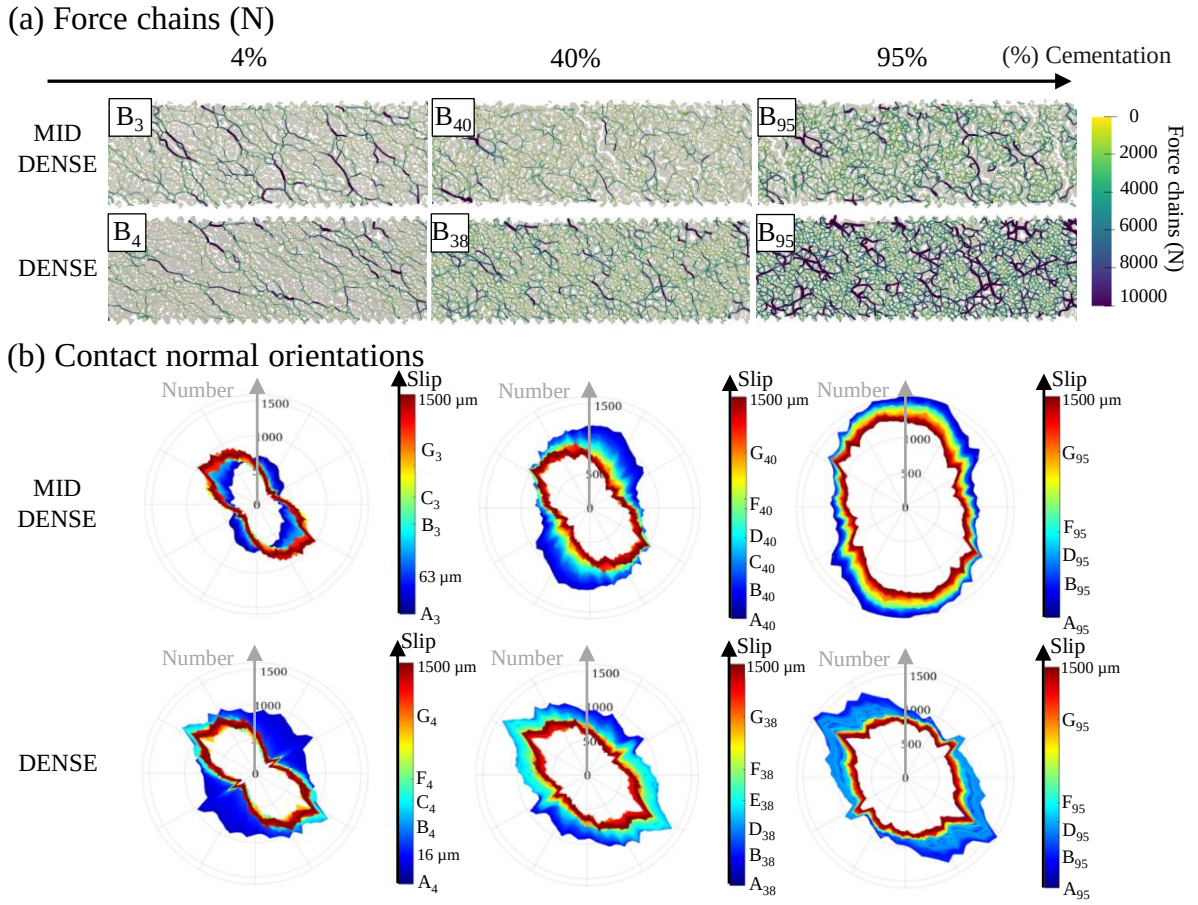

Figure 65. (a) Snapshots of the force-chains networks at the effective friction peaks [B] for six chosen cases (0 to 10^4 N). For $3-4$, $40-38$, and 95 % of cementation. In the pictures, only a quarter of the total gouge is displayed, and even if the global behavior is similar to one quarter, force chains are not homogeneously distributed within the gouge after friction peak. (b) The graph provides the numbers of contacts with a normal vector oriented in a given direction (using polar diagrams where the Theta-axis is the orientation and the R-axis is the number of contacts), and with a color evolving during the different stages of each simulation.

3.5. Rheology and weakening mechanisms

3.5.1. Critical dilation

Critical dilation can be defined as the necessary dilation for macroscopic shear failure formation [(Kranz & Scholz, 1977), (Scholz, 2019)]. In our simulations, it corresponds to the dilation ε_{yp} obtained at the effective friction peak (Figure 58 & Figure 66) which is different from the final dilation ε_{y-SS} previously introduced.

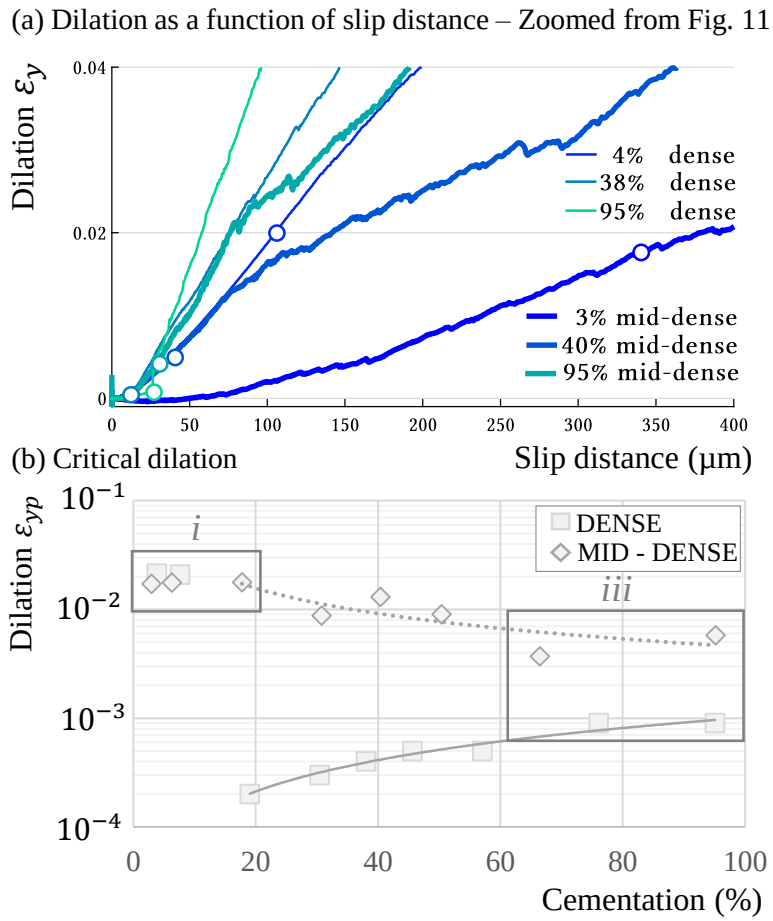

Figure 66. (a) Total dilation as un function of slip distance, the marked point locates the critical dilation for the 3 cemented materials (b) Critical dilation for macroscopic failure for both dense and mid-dense samples as a function of the percentage of cementation.

For cases with limited cementation ($P_{cem} < 10\,\%_{dense} - 25\,\%_{middense}$) – where 100 % frictional contact is quickly reached and no localized shear is observed – the critical dilation is similar for both dense and mid-dense samples and presents the highest values (~ 2 % in Figure 66). The initial porosity effect, without cementation, does not have a major influence on critical dilation. The high dilation rate presents in the pre-peak phase is consistent with the important dilation observed at friction peak.

For cases with moderate to high cementation ($P_{cem} > 10\,\%_{dense} - 25\,\%_{middense}$), two main trends are observed with the increase of cementation: 1) a decrease of the critical dilation for mid-dense samples, 2) an enhancement of the critical dilation for dense samples. It can be noted that all critical dilations observed in this zone are smaller than in zone "i", Figure 66. For cohesionless materials, dilation is supposed to be larger for a denser granular gouge, but the introduction of cementation creates the opposite effect. Similar results have been found with other types of dense cohesive materials experiments (Faqih et al., 2006). The critical dilation is here smaller for dense samples than for mid-dense samples, a result that may be due to the real cohesion values involved within the sample (i.e. higher for dense sample).

Comparing shear band formation and critical dilation, we can deduce that with more than 1 % of critical dilation (for both dense and mid-dense samples), shear band formation is inhibited.

Then, the persistence of shear bands until steady-state mostly depends on cementation, and occurs for highly-cemented materials, corresponding to a critical dilation between 0.08 % and 1 %, zone "iii" in Figure 66. (Noel et al., 2021) found that for Tavel limestone (11 % initial porosity corresponding to our dense sample), a critical dilation of about 1 % has to be reached to obtain shear failure of an initially ductile rock subjected to a pore fluid pressure increase. Their higher critical dilation could be explained by the fact that they study intact rocks, but also by the higher confining pressure used and the presence of fluid.

3.5.2. Evolution of weakening mechanisms

D_{pp} value, similar to the critical distance of slipping, is the distance needed to weaken the fault from friction peak to the steady-state of sliding, it is also relevant for rupture energy calculation (Chapter 5).

Two main trends are highlighted for the evolution of D_{pp}, with cementation Figure 67 (c). Initial porosity seems to affect the weakening length only for cases with limited cementation ($P_{cem} < 10\ \%_{dense} - 25\ \%_{middense}$), mid-dense samples need a higher displacement than dense samples to reach their steady-state regime (810 vs 300 μm). When cementation is large enough ($P_{cem} > 10\ \%_{dense} - 25\%_{middense}$), the initial state of porosity doesn't have an additional influence on D_{pp}, decreasing similarly with P_{cem} for both dense and mid-dense samples. The transition between these two trends corresponds to the mechanical limit between the cohesionless and cohesive model (i.e. formation of cohesion in the sense of Coulomb-Mohr theory) represented by the red line in Figure 67 (c). Adding more cementation within the gouge seems to diminish the porosity effect regarding the peak length. The evolution of the peak distance D_p (i.e. distance reached at effective friction peak), is similar to the evolution of critical dilation, Figure 67 (b).

Double weakening shapes are observed in some effective friction curves in Figure 67. This pattern seems to be a characteristic of dense and cemented materials, as mid-dense materials only show one weakening phase. When it exists, the first weakening period seems to follow a decreasing affine law and appears for dense samples with $P_{cem} \geq 10\%$. Similar double weakening has been observed experimentally as reported in an incoming paper from (Paglialunga et al., 2021). With the separation into two weakening phases, it appears that Riedel bands only form at the beginning of the 2nd weakening phase (letter C in previous figures). In fact, the first weakening phase just allows movement within the gouge by breaking some isolated bonds, but actual sliding needs dilation to operate and thus is mostly observed within the 2nd weakening. Isolating contributions from each mechanism (bond breakage, dilation, friction) and through energetical considerations, Chapter 5 provides a detailed analysis of these two weakening periods.

As it is observed, a micro-scale friction variation appears during the 2nd weakening phase, that could look like stick-slip instabilities which is a major subject of interest in fault system [(Byerlee & Brace, 1968), (Aharonov & Sparks, 2004), (Dorostkar, 2018), (Sathwik Kasyap & Senetakis, 2021)]. However, *earthquake sliding involves the release of strain energy stored in the surrounding rock, at the metric or kilometric scale. Such energy storage is not present in*

our simulation (no deformable rock walls or stiffness of the loading apparatus), that is why these variations should not be considered as stick-slip. The numerical model of [(Aharonov & Sparks, 2004), (Ferdowsi, 2014)] studying stick-slip motion does consider a certain stiffness connected to their rock walls allowing to study stick-slip properly.

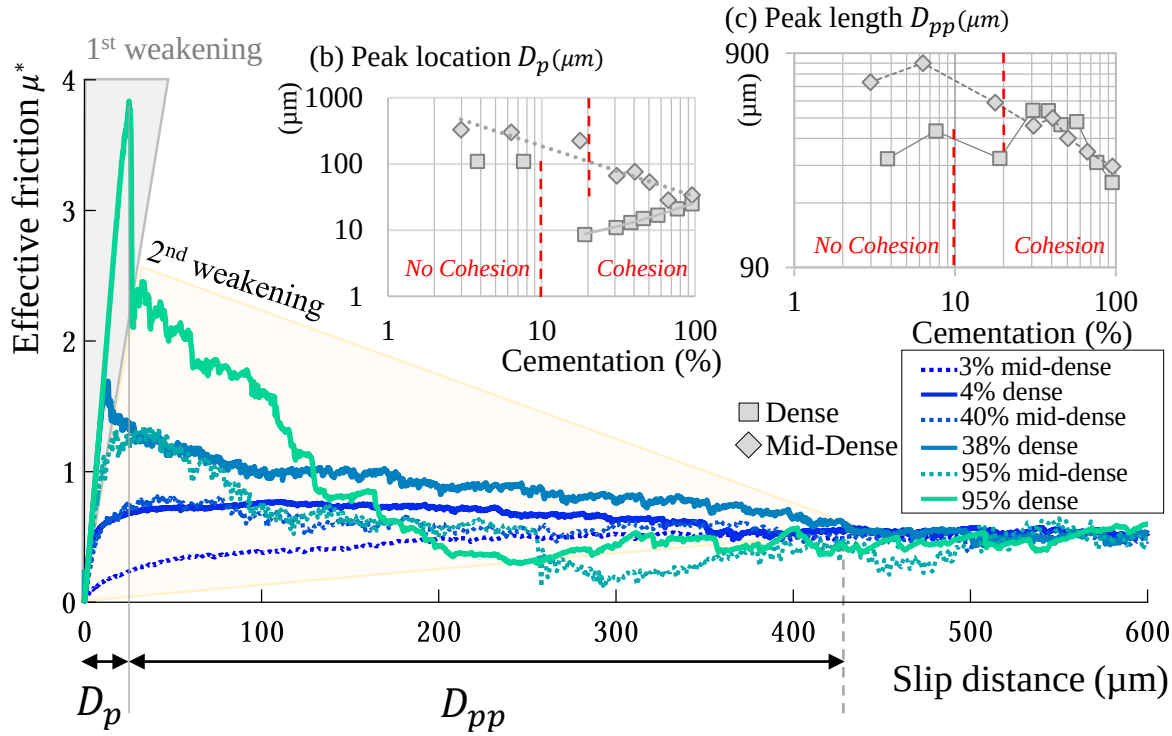

Figure 67. (a) Effective friction curves as a function of the slip distance. (b) Peak distance D_p (μm), (c) Peak length $D_{pp}(\mu m)$, for both dense and mid-dense samples, as a function of the percentage of cementation within the gouge. D_{pp} is the distance between the peak of effective friction and the beginning of the steady-state

3.5.3. Cemented materials and Coulomb-Mohr theory

Cemented gouges have interesting behavior because they are not intact rock and neither are simple frictional gouges. In this section, we compare failure criteria applied to intact rock or fault gouge layer to the cemented gouges presented in the study in order to evaluate which criterion can best fit the failure of cemented gouges.

(Byerlee & Savage, 1992) also analyzed a fault gouge layer under shearing and observed that it behaves as a Coulomb material, with an elastic deformation until failure. However, (Marone et al., 1992) proposed another adapted criterion that is more suitable to thin fault gouge layer. The two failure criteria considered to support these assumptions are:

$$\tau/\sigma_N = C/\sigma_N + \tan\varphi \tag{3.6}$$

$$\tau/\sigma_N = C * \cos\varphi/\sigma_N + \sin\varphi \tag{3.7}$$

The first criterion (3.6) is dedicated to intact rocks, the normal and tangential stresses σ_N and τ are applied on a shear crack with a clear orientation. It is called "Coulomb failure" and provides the "true" Coulomb-Mohr properties C and φ of the intact rock. The second criterion (3.7) is dedicated to a domain where shearing occurs in a distributed and continuous way and the

stresses σ_N and τ are not requested to apply on a specific crack. Rather, their orientation is related to that of the principal stresses that develop in the sheared domain. This is known as "Coulomb plasticity". As explained in (Marone, 1995), the first criterion could be applied to faults with very thin layers of gouge, while the second one might be relevant to the case of thick layers of granular gouge where such rotation of the principal stresses could occur. In that case, Coulomb plasticity could lead to a reduction of the effective friction of the fault. This assumption was validated experimentally in a cohesionless material by (Marone, 1995).

It is instructive to determine to which extent these two expressions can predict the fault strength, solely from the "true" Coulomb-Mohr properties of the rock. This comparison can be done using our numerical results on fault direct shear tests and biaxial tests. Figure 68 thus presents the effective friction in the fault as obtained numerically with direct shear simulations in section 3.4 of the present work, as a function of the effective friction predicted by both failure criteria (3.6) and (3.7) based on our independent determination of C and φ. With this graph, the strength ratio obtained with both models can be compared (direct shear and biaxial test) realized with the same conditions and characteristics (cf. section 3.3.1). Indeed, gouges behaving as granular material (i.e. with no cohesion) present lower friction than intact rocks, as predicted by literature (points under the dotted line). However, cemented gouges present the opposite behavior once the percentage of cementation account for a small cohesion (i.e. for more than 10 % $< P_{cem}$ for dense samples and 25 % $< P_{cem}$ for mid-dense samples). The increase of cementation increases the effective friction of the cemented gouge compared to intact rock, and the reduction of porosity overstate the difference. It appears that the proposed adapted law (3.7) for fault gouges (Marone et al., 1992), does not fit very well with cemented gouges either, blue line. The initial stress ratio from the Coulomb criterion, equation (3.6), is closer to values found for our mildly cemented gouges but is not suitable as cementation increases, grey line.

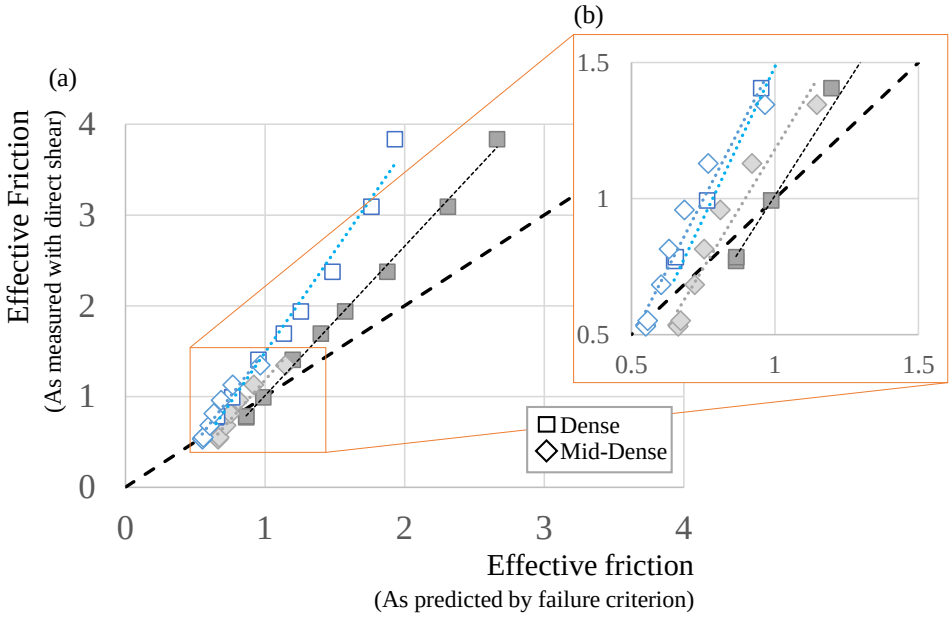

Figure 68. Effective friction as measured with direct shear experiments (simulation campaign) as a function of effective friction as predicted by failure criterion (calculated with internal friction angle and cohesion found with Biaxial tests), for dense and mid-dense samples. The blue line (empty marker points) represents the effective friction given for sheared gouge with equation 3.7 (Marone et al., 1992) compared to the grey line (filled marker points), effective friction for intact rock with equation 3.6 (Handin, 1969).

One of the reasons explaining these differences could be the different boundary conditions used for the two kinds of tests (direct shear/ biaxial experiment). In particular, the presence of the two walls of the fault might act as barriers to the natural development of Riedel shear bands and increase the fault strength. Another key of understanding could be the heterogeneity of the stress field in the fault (in relation to the kinematic constraints mentioned above), which would prevent a simplistic use of the criteria (3.6) and (3.7). As further analyses and simulations are needed to confirm these hypotheses, these propositions will be discussed in future work comparing different gouges with cement or matrix particles.

3.6. Concluding remarks

A 2D granular fault gouge model has been implemented in the framework of DEM in order to establish a link between gouge properties (cement and initial porosity) and rheological behavior. One originality of this Chapter is the use of the angular and faceted shape of particles instead of circular ones. Our results confirm that both initial porosity and cementation influence gouge behavior. They play a role in the internal structure and geometry of the gouge and thus modify the rheological behavior of the fault. In the range of our numerical experiments (normal stress 40 MPa & slip rate $1m/s$), the increase of cementation within the gouge leads to an increase of effective strength whereas an increase of initial porosity tends to a reduced strength.

(i) The strength peak is sharp, short, and intense for dense and highly cemented materials and smooth, delayed and of moderate amplitude for mid-dense and moderately cemented materials. Brittleness is enhanced with cementation, especially in the case of dense materials. It evolves similarly with the internal cohesion (Coulomb-Mohr) within the gouge and leads to different failure patterns. The highly-cemented material with low initial porosity presents clear Riedel band formation evolving as in the theory of (Tchalenko, 1970). The high cohesion and internal friction angle values make this material very close to intact rock properties. In opposition, the weakest material is obtained with the highest porosity state and for no cementation: no failure pattern is observed and a typical granular Couette flow is highlighted.

(ii) Shear failures need a critical dilation to form. For poorly-cemented material, not presenting enough cohesion (i.e. $C < 1MPa$), the same critical dilation is observed for both dense and mid-dense samples. The initial porosity does not have a major influence on critical dilation for cohesionless materials. However, when cohesion is present within the particles, the critical dilation appears to be smaller for denser samples and increases with cementation, whereas mid-dense samples present the opposite behavior.

(iii) Effective friction curves present double weakening shapes for dense samples with enough cementation, triggered by different mechanisms (Chapter 5). The peak length (analogous to the D_c from rate and state laws) mainly decreases with the percentage of cementation.

(iv) The increase of cementation increases the effective friction of the cemented gouge compared to intact rock, especially with dense cemented gouges. Effective friction, from the Coulomb failure criterion or the Coulomb plasticity criterion (Marone et al., 1992), does not predict very well our values for cemented fault gouges. The different boundary

conditions and stress fields obtained for the direct shear experiment and the biaxial test could explain the difference, but further analyses are needed to confirm these hypotheses.

In future work, we will extend this numerical campaign to cover a wider range of normal stresses and gouge thickness, in order to derive an empirical slip-weakening friction law based on the micromechanical properties of the gouge. This law could then be implemented in dynamic rupture modeling at a larger scale for a dialogue with seismological data. An interesting line of work could also be to investigate the time scale of the cementation evolution in a fault and to evaluate to what extent the associated evolution of the fault strength interacts with its seismic cycle.

Chapter 4. Rheology and weakening of a sheared fault gouge with matrix particles

Main Foreword

In Chapter 3, we simulated a cemented granular fault zone with angular and faceted grains linked by cohesive bonds to model the cementation. Based on the previous description of infill material (Chapter 1), we now consider another brecciation process for which the observed infill material is incohesive. This infill material is called "matrix" particles and refers to very thin particles produced by previous fragmentation or introduction of sediments within the fault gouge (Woodcock & Mort, 2008).

The principal objective of this chapter is thus to understand the "mechanical/geometrical" role of matrix particles as opposed to the physical cementation (bonded law as cohesion) used in the previous chapter. Is a very dense granular fault gouge being as resistant to shearing as cemented cataclasites? The DEM approach is also suitable for this kind of granular-type filling and this chapter is divided into two main parts with two types of granular samples:

- Part A concerns granular samples with only hexagonal matrix particles. This granular media represents a highly dense packing of particles and reveals Riedel bands formation. This first part gives an understanding of localization patterns and evolution in this very dense packing of particles with different gouge characteristics.

- Part B presents some results on composite mixtures between angular and faceted grains surrounded by hexagonal cells representing a matrix of fines. It highlights similarities and differences with the previous model with only matrix particles (Part A) and with cementation (Chapter 3).

As said in Chapter 2, in these models the sliding is imposed by boundary conditions (imposed slip velocity), but this is not a realistic case. In real seismic faults, the sliding is driven by the elasticity of the surrounding medium, and can therefore take place in a stable or unstable way. The models used here are local micromechanical studies of the behavior of fault gouges, which are designed to be inserted in larger-scale dynamic models.

This chapter is partly based on the following papers:

Casas, N., Mollon, G., & Daouadji, A. (2021). Shear bands in dense fault gouge. *EPJ Web of Conferences - Powders and Grains*, *249*, 1–4. https://doi.org/10.1051/epjconf/202124911006

Casas, N., Mollon, G., & Daouadji, A. (2022) The role of matrix particles within granular fault gouge through Riedel bands observations. (*in prep*)

Part A – Matrix material and kinematics of Riedel bands

4.1. Foreword

This first part studies the kinematics and strength of a sheared granular gouge with matrix particles alone. The first section 4.2 presents the numerical model and granular materials used within the study. As for the previous Chapter 3, a sample characterization is made with biaxial simulation on the same granular material used for direct shear experiments. The second section 4.3 reviews the different behaviors of a sheared matrix gouge obtained for variations in the initial parameters of the gouge. The role of the shear modulus, the interparticle friction, and the ratio between the thickness of the gouge on the size of particles will be discussed. Finally, the last section 4.5 concludes on the main elements highlighted through the entire part A. The main schema of part A, Chapter 4 is shown in Figure 69.

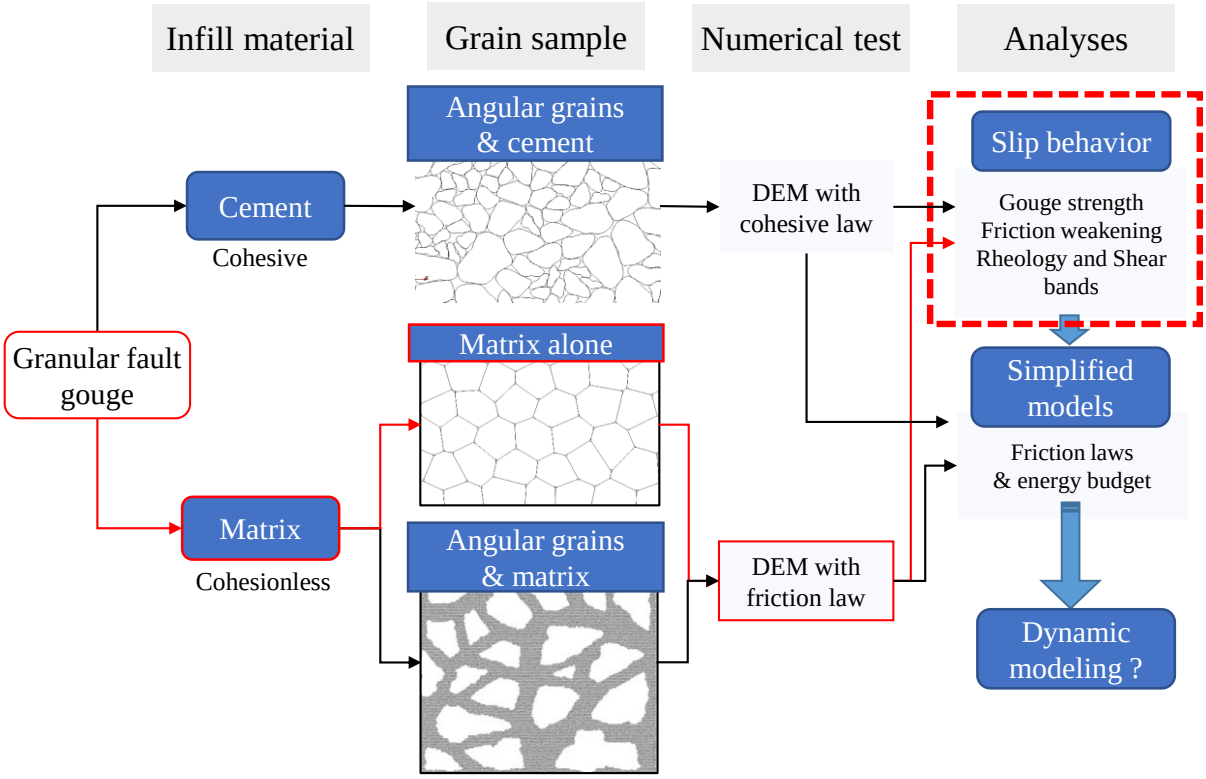

Figure 69. Main schema of Chapter 4, Part A

4.2. Numerical framework and sample generation

4.2.1. Granular matrix samples

Creation of the granular media

The granular matrix is created with hexagonal cells to represent a highly dense packing of particles. As the shape is hexagonal, a Voronoï tessellation algorithm is used, in which the size of cells and their perturbation (i.e. the inhomogeneity of the hexagonal cells) are specified

(Chapter 2). To realize parametric studies, a standard case (M-S) for "Matrix-Standard", is defined as a reference model. For this model, an almost constant size of cells is considered for all particles ($\emptyset_{eq} \approx 20\ \mu m$), with a perturbation of 0.5, meaning that cells are not perfectly regular hexagons, Figure 70.

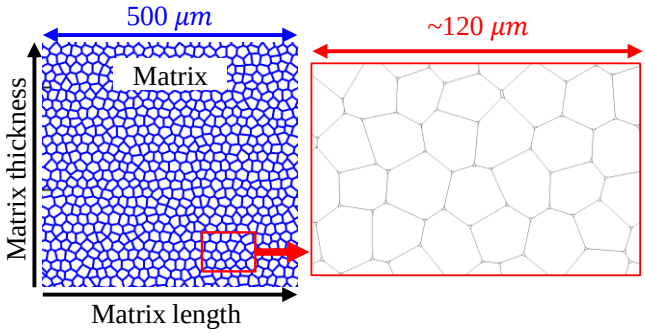

Figure 70. Matrix shape and size, equivalent diameter 20 μm. Left, zoom in on a 500 μm x 500 μm square part, right, zoom in on this sample.

The initial gouge thickness is equal to $2\ mm$ and the length is equal to $20\ mm$. As in the previous model, a Representative Elementary Surface is used here, as a result of the parametric study on the model length which is provided in Appendix A4.A.

Compaction and initial state

Once the granular sample is generated, it is then inserted between two rock walls. The first simulation step consists in compacting the sample with $\sigma_N = 40\ MPa$ to create a stabilized packing of granular material (Chapter 2). As the generated sample is already very compact, Figure 70, this compaction stage is only influenced by the numerical stiffness and interparticle friction inserted between particles in contact. At the end of the compaction the sample is almost identical, but with a little interpenetration between particles (~ 0.1 % of the size of the particle) which provides mechanical equilibrium. An interesting point is that the initial porosity within the gouge is negligible here, with $P_{pore} < 1$ %, resulting in an extremely dense compacted sample.

4.2.2. Numerical setup for direct shear simulations

The granular matrix is then submitted to direct shear experiments, Figure 71. The lower rock wall is fixed and normal stress of 40 MPa and slip velocity of $1\ m/s$ are imposed on the upper rock wall. Periodic boundary conditions are present on both right- and left-hand sides of the sample to maintain the continuity of the movement at large slips, but the upper rock wall can freely move in the y-direction to allow dilatancy. A dry contact model with rigid bodies is considered, without gravity. A Coulomb friction contact law is also settled, meaning that every contact depends on the interparticle friction μ_{num}, numerical stiffnesses k_n (constant and equal to $10^{15}\ Pa/m$ in the reference case) and a stabilizing numerical damping γ (numerically set to 0.2). To avoid wall-slip effects with smooth boundaries, a certain cohesion is introduced at the interface between matrix and rock walls ($500\ MPa$). It enables the creation of a certain roughness by cementing particles to the top and bottom layer.

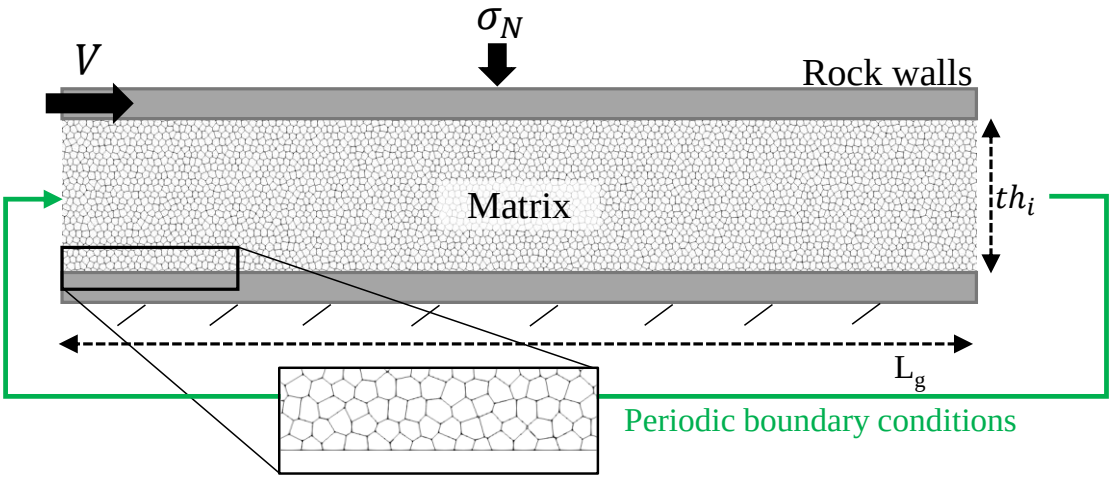

Figure 71. DEM model of a direct shear experiment with granular fault gouge composed of matrix particles. V is the applied shearing velocity (m/s), σ_N is the normal stress (MPa), th_i is the initial gouge thickness (m) and L_g is the gouge length (m).

It can be noted that interparticle friction μ_{num} is equal to 0.3 in the (M-S) reference case, which is lower than the one used in the model of Chapter 3. The objective is to test the property of matrix particles as a weaker material with limited friction. It should be noted that the boundary conditions, in particular the non-deformable walls, can induce differences in the results found with those of the literature studying stick-slip experiments (in particular, in the formation of the Riedel bands). All the parameters are gathered in Table 4 and are reproducible.

Table 4. Numerical setup and properties for the experimental campaign (set for standard cases). The top part of the table (grey color) concerns properties that do not vary within the simulation campaign.

Property	Associated variable	Value
Normal stress	σ_N	40 MPa
Shear velocity	V	1 m/s
Rock density	ρ_r	2600 kg/m^3
Interparticle cohesion	C_{num}	500 MPa at boundaries
Interparticle friction	μ_{num}	0.3
Contact stiffness	k_n & k_t	10^{15} Pa/m
Perturbation	P_i	0.5
Sample size	th_i x L_g	2 x 20 mm
Particle equivalent diameter	ϕ_{eq}	20 μm
Number of particles	N	115 825
DEM time step	Δ_t	5.10^{-10} s
Proximity updating period	$\Delta_{t-contact}$	10^{-8}s

4.2.3. Characterization of matrix material with biaxial tests

Using the same Coulomb-Mohr representation as in Chapter 3, independent biaxial simulations of samples were run with the characteristics previously presented for sheared fault gouge (in terms of grain shapes, size distributions, initial solid fraction, interparticle cementation, and interparticle friction). Rectangular granular samples (4 mm wide and 10 mm high) are placed

between four rigid walls. The lower wall is fixed in displacement and the upper wall is submitted to a constant downwards velocity V_y, and the lateral walls are submitted to a confining pressure σ_3, fixed in vertical and rotational motions, and free to move horizontally.

Three tests are performed on the standard case (M-S), with confining stresses of 10 MPa, 40 MPa, and 80 MPa and for two interparticle stiffnesses ($k_n = 10^{15}, 10^{16}\ Pa/m$), Figure 72 (a) and (b). The vertical stress σ_1 is monitored during vertical compression, providing a series of pictures of cumulated slip (vertical displacement minus the elastic part), Figure 72 (c).

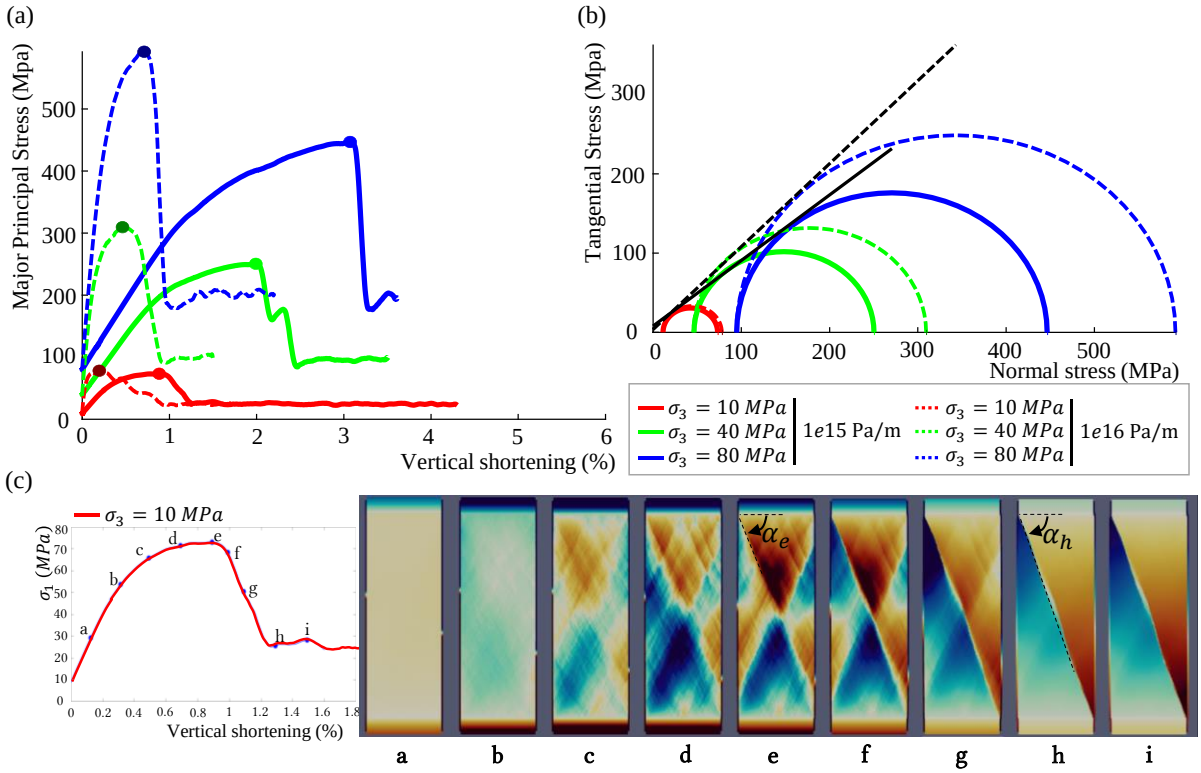

Figure 72. Illustrative results for a standard material (M-S) with different initial interparticle stiffness (a) Major principal stress as a function of vertical shortening, and (b) associated Mohr circles, for three confining stresses (10 MPa, 40 MPa, and 80 MPa) for samples with $k_n = 10^{15}\ Pa/m$ and $k_n = 10^{16}\ Pa/m$. (c) Snapshots of cumulated slip (vertical displacement minus the elastic part) for biaxial experiment with an elastic membrane, for an applied stress $\sigma_n = 10\ MPa$ for a standard case with $k_n = 10^{15}\ Pa/m$. Each point in the curve corresponds to an image above. The evolution of shear bands can be observed and the orientation angle increases with vertical shortening ($\alpha_h > \alpha_e$).

In Figure 72, the slope of shear bands changes between the peak (e) and the plateau (h), this is because the effective friction also changes, corresponding to a reorganization of the failure pattern and a rotation of the stress field. Based on the observed results:

- Almost no cohesion is observed for matrix material (in the sense of Coulomb-Mohr), Figure 73. It is in adequation with the description of matrix material which is an incohesive material (Chapter 1).
- A change of interparticle stiffness does not have much influence on the internal friction angle, but increases the effective friction peak observed, Table 5 and Figure 73. By multiplying by ten the numerical stiffness, the resulting Elasticity modulus is ten times

higher. This will probably have an impact on gouge kinematics. This point will be discussed in section 4.3.

– The orientation angle of the major shear bands formed is growing from the effective friction peak to the steady-state zone, Figure 72 (c).

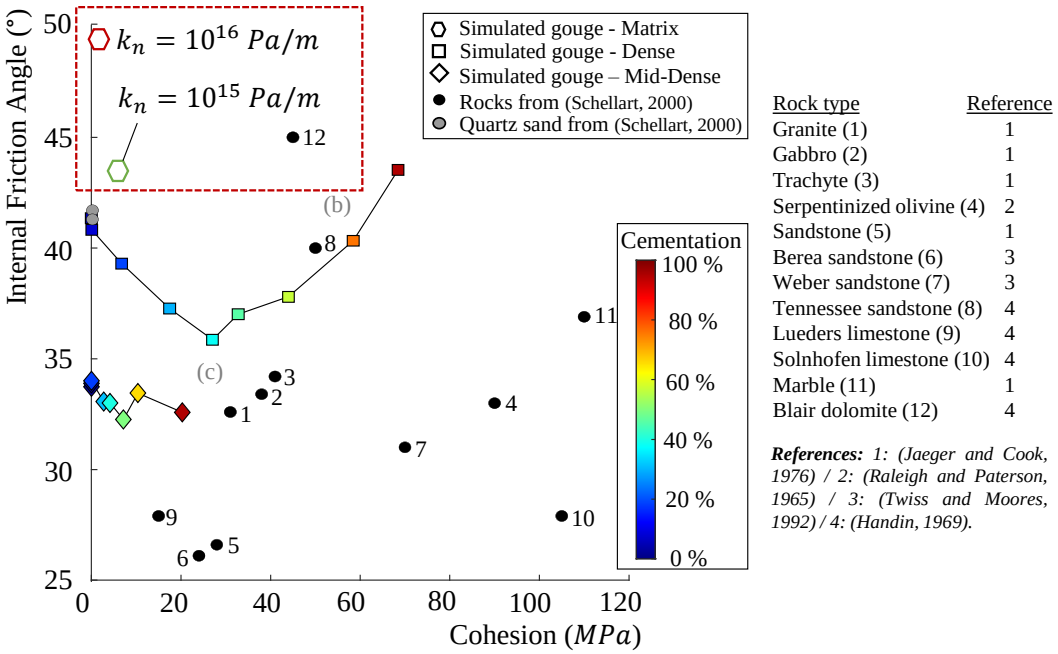

Figure 73. Internal friction angle as a function of Coulomb-Mohr cohesion for the simulated materials, as characterized by numerical biaxial tests, the same graph is used in Chapter 3. Matrix samples are marked by hexagons with two different interparticle stiffness, $k_n = 10^{15}\ Pa/m$ (green) and $k_n = 10^{16}\ Pa/m$ (red). It can be noted that the samples used are large enough to avoid any size effect or any thickness dependence. The discs correspond to experimental characterizations of different rocks referenced in (Schellart, 2000) listed in the table next to the graph.

Table 5. Numerical results of the biaxial campaign for two interparticle stiffnesses.

Property	$k_n = 10^{15}\ Pa/m$	$k_n = 10^{16}\ Pa/m$
Effective friction peak μ_p^*	0.94	1.17
Internal friction angle φ	43.3°	49.5°
Cohesion C	6.4 MPa	2.0 MPa
Elasticity Modulus E	18.96 GPa	118.39 GPa

4.3. Matrix characteristics & gouge kinematics

In order to characterize the matrix material, several parametric studies are performed and presented in this section. The purpose of these studies is not only to observe the influence of each parameter on the mechanical behavior but also to observe the rheological behavior through Riedel band formation and evolution. The wide range of variations in Riedel bands deserves to be properly presented here as they can be a marker of the stability of the system [(Byerlee, 1978), (Gu & Wong, 1994)]. If an unstable frictional sliding is observed, it will certainly show Riedel bands localization, although the reverse proposition is not necessarily true. Indeed, Riedel bands can be observed in stable sliding without any instabilities. The angle between the *R*-band and the fault core boundary could be a critical point to distinguish whether instabilities

can be present or not [(Moore et al., 1988), (Moore & Byerlee, 1992)], and this angle depends on physical and numerical properties of the model.

4.3.1. Qualitative and quantitative results for the reference case

This first subsection aims to present typical results obtained for the standard granular sample (M-S) as it will be used for comparison in the rest of the chapter. Typical effective friction μ^* and dilation ε_y are presented in Figure 74, and Figure 75 shows deformation profiles observed at different times of the simulation, (with letters from A to E from Figure 74).

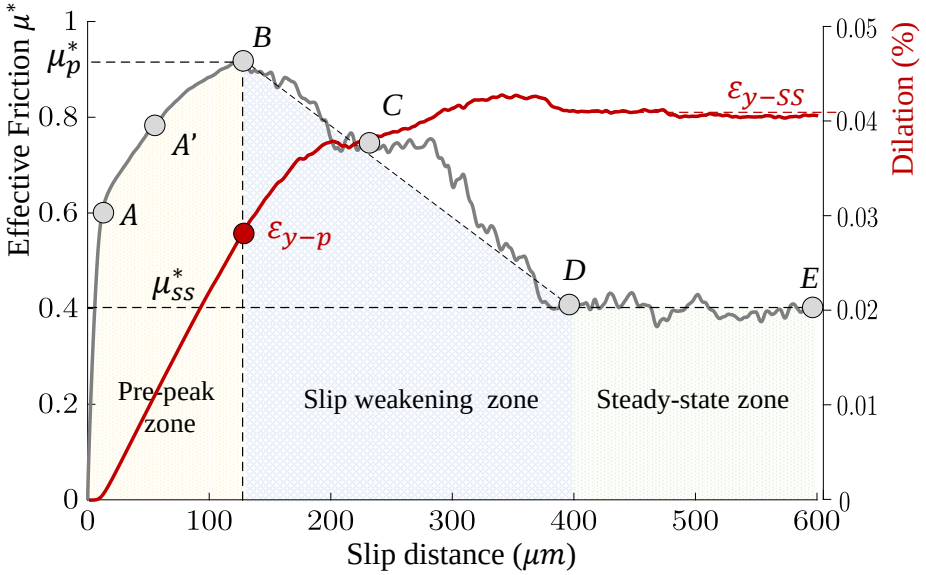

Figure 74. Effective friction μ^*(grey curve) and dilation ε_y (red curve) as a function of the slip distance for the standard case (M-S). A is the end of the elastic zone. The zone from zero to B describes the pre-peak zone, followed by the slip weakening zone (B to D) and then by the steady-state zone (D to E). ε_{y-p}^* represents the critical dilation.

We distinguish three main steps within direct shear experiments, according to the main stages of Riedel shears formation (Chapter 1):

- A pre-peak zone is first observed, which is composed of an elastic phase (0-A) involving the shear modulus of the gouge and the overall stiffness. Once the elastic zone is over, the sample starts to deform in a non-reversible way until the friction peak (A-B), for which the maximum shear strength of the gouge is reached (B). During all this part, the sample dilates (red curve), but the critical dilation ε_{y-p} is still lower than the averaged steady-state dilation ε_{y-ss}. As presented in Chapter 1, direct shear makes appear typical patterns of shear bands, called Riedel shear bands for a very dense granular sample [(Tchalenko, 1970), (Marone, 1998), (Bedford & Faulkner, 2021)]. These patterns follow closely what is commonly observed in natural faults (Y. Katz et al., 2004). Just before friction peak (B), five main Riedel bands have formed. They can be separated into two kinds of low R-bands: primary R-bands R_3, R_4, and R_5 (appearing first) and secondary R-bands R_1 and R_2 with slightly higher Riedel angle orientation α_i.
- Once the friction peak has passed, we enter the slip weakening zone, or post-peak phase (B to D), where the friction gradually decreases until it reaches a friction stabilization plateau at D. The dilation is not yet at its maximum. In this zone, primary R-bands

disappear in favor of the two main secondary *R*-bands R_1 and R_2, which localize all the gouge deformation (Figure 75). A boundary shear Y_1 also starts growing at the top of the gouge layer.

– Once the steady-state zone is reached (D to E), and without modification of numerical parameters, the gouge reaches a stationary state of evolution. The friction evolves very weakly around a mean value which is similar in most of the simulations and ranges between 0.4 and 0.5. From this moment, the dilation of the granular sample is maximum and stabilized. Even though the main *R*-bands do not evolve anymore, the Y_1-band is fully formed at the top rock wall (D), and a secondary Y_2-band is partly observed at the bottom rock wall.

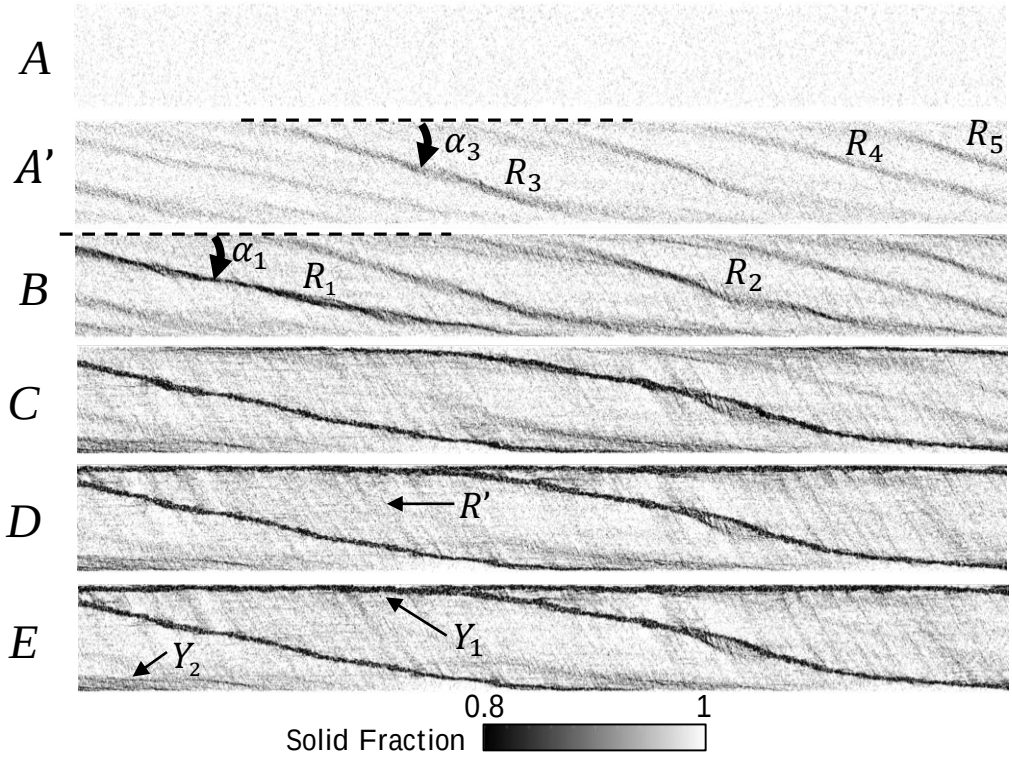

Figure 75. Solid fraction snapshots for standard sample (M-S). The solid fraction is used here to observe the rheology and deformations within the granular gouge and underline zones of slip and shear concentration. Letters correspond to different steps in the effective friction curve Figure 74. The solid fraction is plotted between 0.8 and 1. R_1 and R_2 are secondary *R*-bands, $R_3, R_4,$ and R_5 are primary *R*-bands, orientated at angle α_i from the direction of shearing. R' are conjugate Riedels orientated at angle α_i' from the direction of shearing. *Y* is the slip localisation at the boundary: Y_1 is the main localisation zone occupying all the slip surface and Y_2 is a partially boundary zone at the opposite surface. [MOVIE]

Conjugate Riedel bands R' are also observed in the simulations in the slip weakening and steady-state phases. These are oriented at about $\alpha' \approx 60°$ from the top wall, a higher angle than for simple tensile *T*-bands (oriented in the direction of the major stress at 45°), but lower than that described for R'-bands observed in the literature, which approaches 75°[(Davis et al., 2000), (Y. Katz et al., 2004)]. It is assumed that this is a rotation of the *T*-bands tending towards R'-bands, as in the scheme presented by (Y. Katz et al., 2004). Moreover, the theory of Riedel bands is based on the Coulomb-Mohr model, which is an idealized model that does not consider the latest shear variation. It is thus considered that the bands observed between 50 and 60° are indeed R'-bands according to their link with the observed Riedel structures.

Although the solid fraction is an accurate and relevant quantity to follow in order to study the formation of Riedel bands, similar results can be observed with velocity profiles as presented in Figure 76. They show that the highest velocity discontinuities are concentrated within Riedel and boundary shear bands, especially in the middle of the weakening part (C). Once the gouge is stabilized, the x-velocity discontinuity is localized in the Y-band in the upper part of the gouge and equal to the applied shear velocity of 1 m/s. Changing the length of the fault gouge sample does not inhibit the formation of shear bands but it modifies the rate of friction weakening with the slip distance (Appendix 4.A).

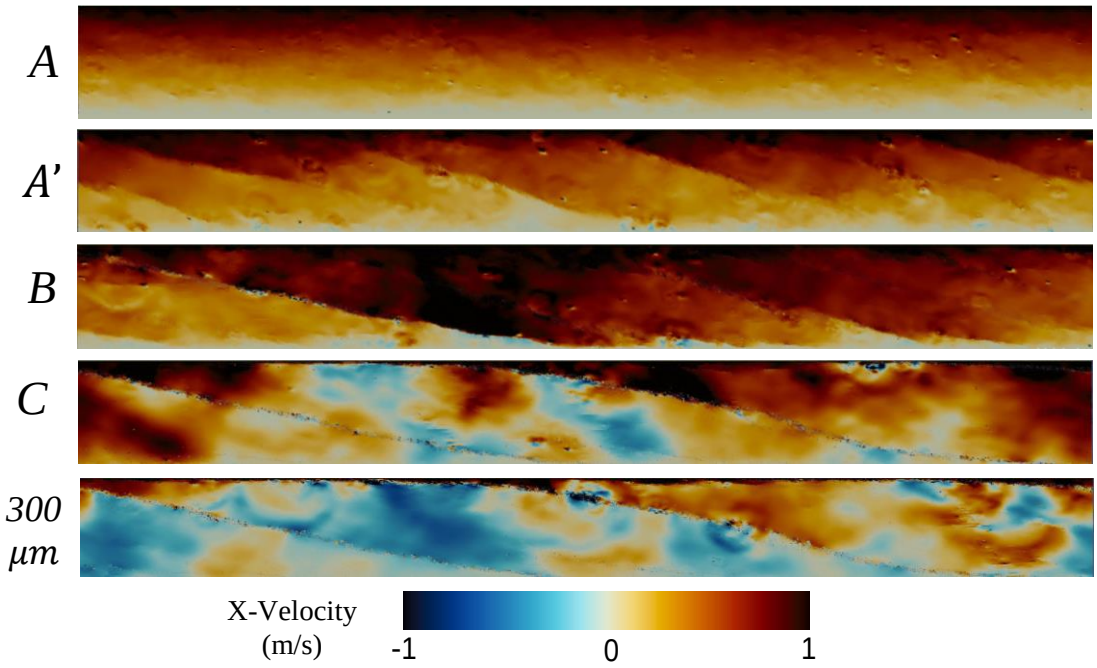

Figure 76. Velocity profiles in the x-direction for standard sample (M-S). Letters correspond to different steps in the effective friction curve Figure 74. The velocity profile is plotted between -1 and 1 m/s. [MOVIE]

4.3.2. Influence of interparticle friction and particle shape

The standard model is used here with a modification of interparticle friction (μ_{num}) or of the initial shape of particles (with a variation in perturbation P_i). Analyses of interparticle friction and particle shape are gathered in this section because they appear to have similar consequences on Riedel band formation. The different modified samples are gathered in Table 6 and the rest of the parameters are identical to those presented in section 4.2.2.

Table 6. Sample names and associated modifications with standard case (M-S) presented in section 4.3.1.

Section	Sample Name	Modified variable	Numerical value
i	M-F01	Interparticle friction μ_{num}	0.1
	M-F02		0.2
	M-F06		0.6
ii	M-P-02	Perturbation shape P_i	0.2
	M-P-08		0.8

i. Interparticle friction

Numerical experiments are difficult to calibrate, as input data injected in the model are poorly documented in real granular media (i.e. interparticle friction). A change in interparticle friction coefficient from 0.1 to 0.6 can yield significant differences in friction peak values, Figure 77 (a). But all numerical experiments tend to the same averaged friction at a steady-state ($\mu_{ss}^{*} = 0.42$).

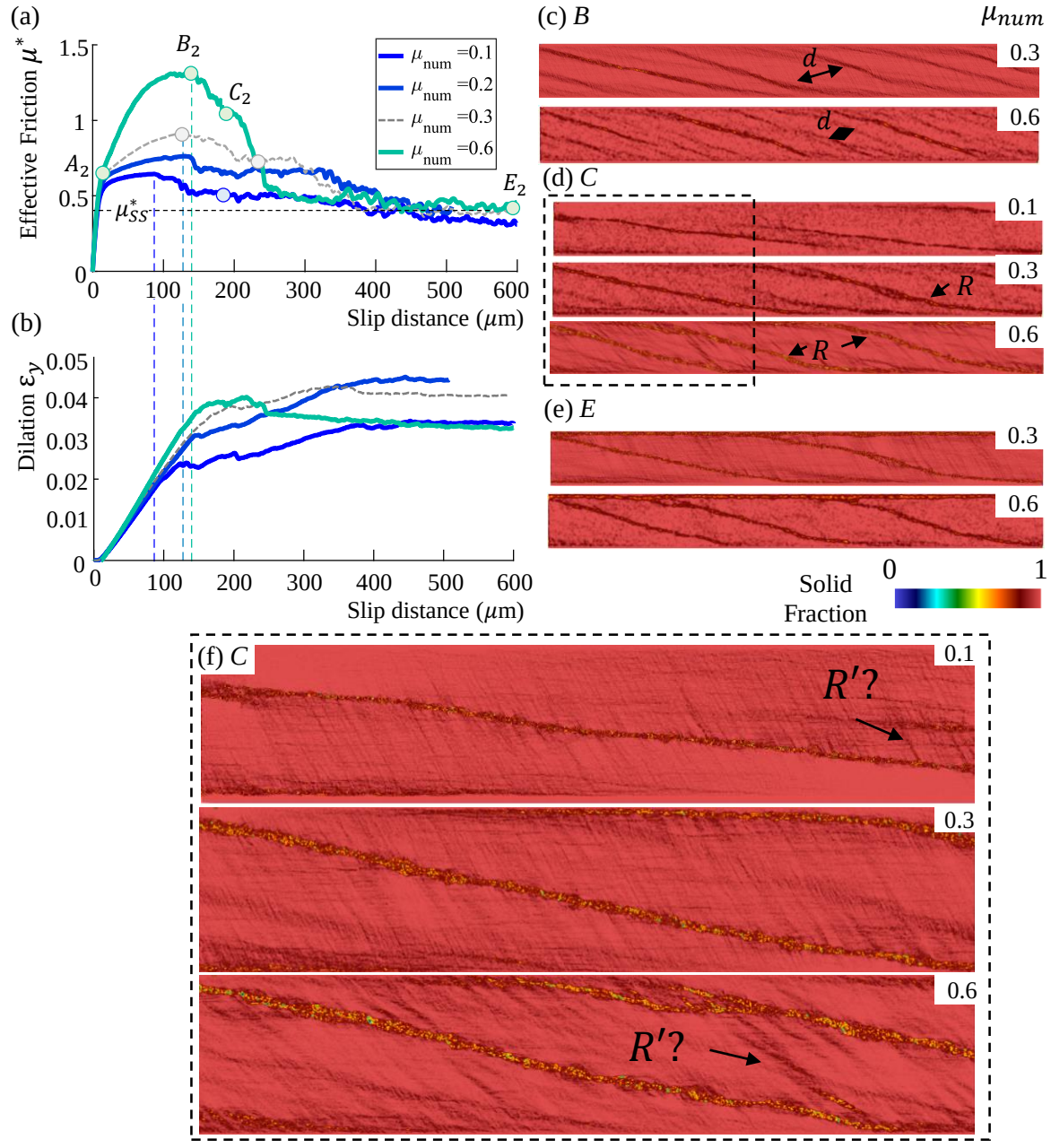

Figure 77. (a) Effective friction μ^* as a function of the slip distance (μm) for different interparticle friction (μ_{num} ranging from 0.1 to 0.6). (b) Dilation ε_y as a function of the slip distance (μm) for the same materials. The solid fraction is displayed for three different interparticle frictions ($\mu_{num} = 0.1, 0.3$ & 0.6), (c) at friction peak *B*, (d) at slip distance *C*, (e) at slip distance *D*. (f) Zoom in on the Weakening zone, point C. The grey and dashed curve presents the (M-S) case.

A modification in interparticle friction changes the main orientation of Riedel shear bands ($\approx 16°$ from the horizontal shear direction with $\mu_{num} = 0.6$ and $\approx 6°$ for $\mu_{num} = 0.1$). These values are inferior to the orientation from Coulomb-Mohr theory, requiring an angle equal to $\varphi/2$ for direct shear, which corresponds to 21.5° for the (M-S) case. Increasing interparticle friction also seems to increase the number of Riedel bands formed at the beginning of the friction peak (B_2 in Figure 77 (c)) and within the decreasing friction part (C_2 in Figure 77 (d)). This augmentation results in reducing the averaged distance d between Riedel bands. Conjugate Riedels ($> 45°$ from the horizontal shear direction) are also more pronounced with higher friction, (at C_2 in Figure 77 (c)).

The two types of Riedel bands described as low-angle (R) and high angle (R') do not have the same growth pattern. They both depend on porosity-weakening and strain-rate-weakening mechanisms (R. Katz et al., 2006). The initial state of porosity is not modified here, but interparticle friction plays a role in the rheology of the granular media, as it changes the contact between every hexagonal cell. It may explain why high-angle Riedel bands are more pronounced with higher friction. The increasing number of Riedel bands with interparticle friction can be explained with contact mechanics (Morgan, 1999). For the peak phase, when μ_{num} is low, slip may occur between hexagonal cells, and particles are mobilized within the shear zone, with minimal dilation. With a higher μ_{num}, sliding is partly inhibited and particles tend to separate leading to higher dilations, and thus in our case, higher number of Riedel bands (i.e. dilation in specific direction). However, at the end of weakening, Riedel bands reduce toward a stabilized form and thickness. The observed thickness of the R-bands within the weakening phase also seems to increase with increasing friction, Figure 77 (f). As shown in Figure 77 (a), an interparticle friction of 0.6 also leads to a more sudden post-peak weakening, which is prone to switch the fault behavior from a ductile aseismic response to a brittle seismic slip, depending on the stiffness of the surrounding medium.

ii. **Shape of particles and irregularities**

The evolution of particle shape is settled at the creation of the matrix sample by varying the "perturbation" parameter (Chapter 2). Three different perturbations (0.2, 0.5, and 0.8) are used with from almost perfect hexagonal cells ($P_{0.2}$) to more angular and random hexagonal cells ($P_{0.8}$). Figure 78 presents the evolution of effective friction and dilation as a function of the slip distance for these three different initial shapes of particles. (Mair et al., 2002) used 3D experimental data, and (Nouguier-lehon et al., 2003) used 2D numerical modeling, in order to analyze the influence of grain shape and angularity on the behavior of granular materials. Both studies result in the same conclusion: the increase of angularity increases the resistance to friction, and thus the effective friction peak. Our grains shapes are not perfectly hexagonal here, and particles present a small variation in angularity according to the perturbation applied. This difference remains quite low as the global shape is mainly hexagonal, but can explain the small difference in friction peak observed in Figure 78 (a). Due to their homogeneity and less angular shape, the $P_{0.2}$ material also presents less dilation than the two other granular media, Figure 78 (b).

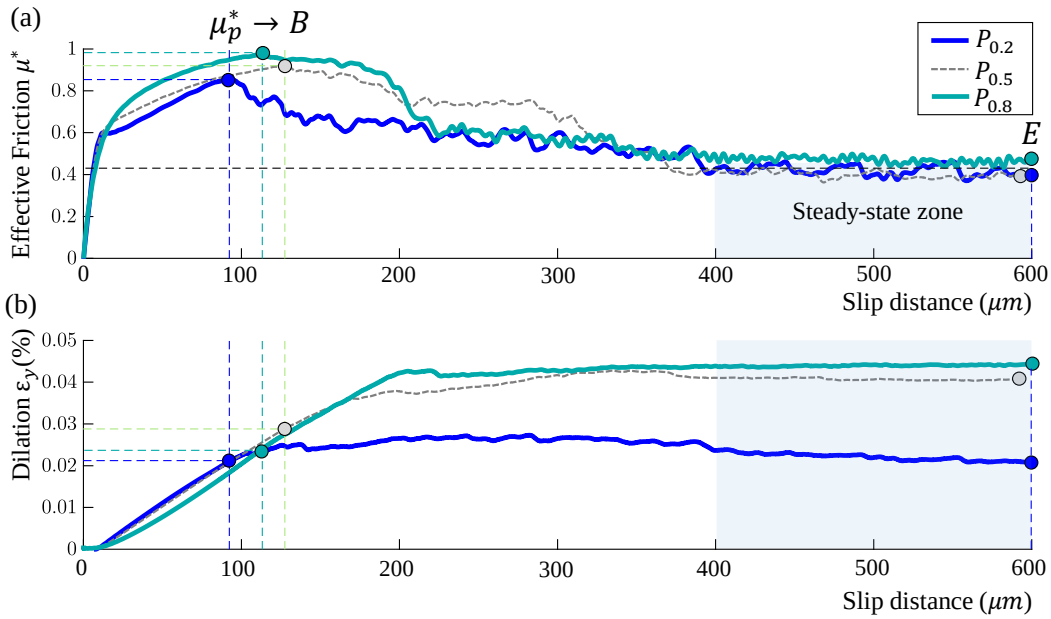

Figure 78. (a) Effective friction as a function of the slip distance (μm) for different initial shape perturbations (P_i = 0.2, 0.5 & 0.8). (b) Dilation as a function of the slip distance (μm) for the same cases. The grey and dashed curve presents the (M-S) case.

Visual analysis shows that the $P_{0.2}$ material is pathological and too regular to represent the real granular samples observed in faults. However, its representation gives interesting patterns and rheological behavior concerning Riedel bands in Figure 79.

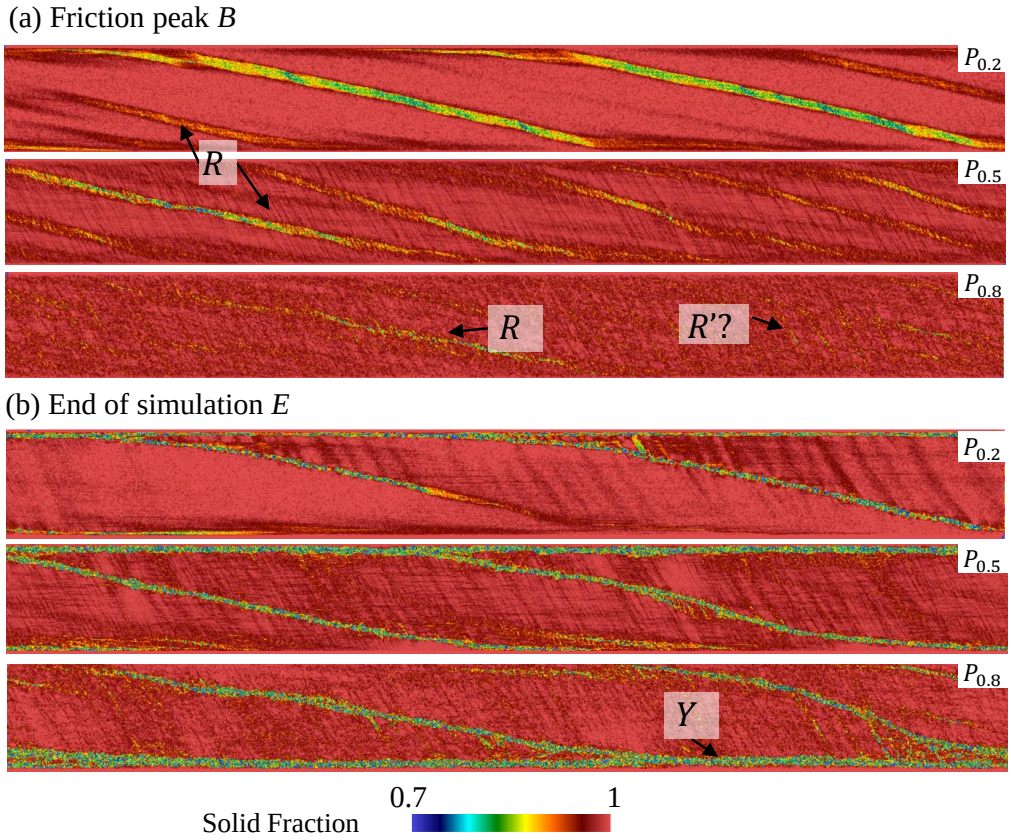

Figure 79. Solid fraction at two different times of experiments, for the three materials (P_i = 0.2, 0.5 & 0.8). (a) At friction peak B, (b) at steady state E. These two different moments are displayed in Figure 78 by points B and E.

At friction peak, the regularity of the shape of the cells seems to be quite important in the development of shear bands. In the same way as interparticle friction, an increase in angularity also implies a change in the number of Riedels. A higher angularity (similar to more disorder, $P_{0.8}$) results in a larger number of low-angle Riedels at friction peak, less marked, and of lower thickness. We also observe some possible high-angle Riedel bands *R'* (against no high-angle Riedel for $P_{0.2}$). When the steady-state is reached, all three samples have the same number of low-angle Riedels *R* (secondary Riedels). These bands have a similar orientation α_i and thickness, meaning that the change in the angularity of particles is too small to affect Riedel's angle orientation at steady-state. To better understand how these mechanisms operate, two chains of grains were followed during the deformation of the gouge, Figure 80. Comparing both chain's evolution, we first note that the place where the chain breaks is composed of several grains belonging to the Riedel band. This result is different from the patterns of granular chain theory proposed by (Anthony & Marone, 2005), where the breaking point of the chain just gives two different chains sliding parallel to each other. However, in their case, no *R*-band was present within the granular sample. We conclude that the presence of low and high *R*-bands modifies the kinematic of particles chains.

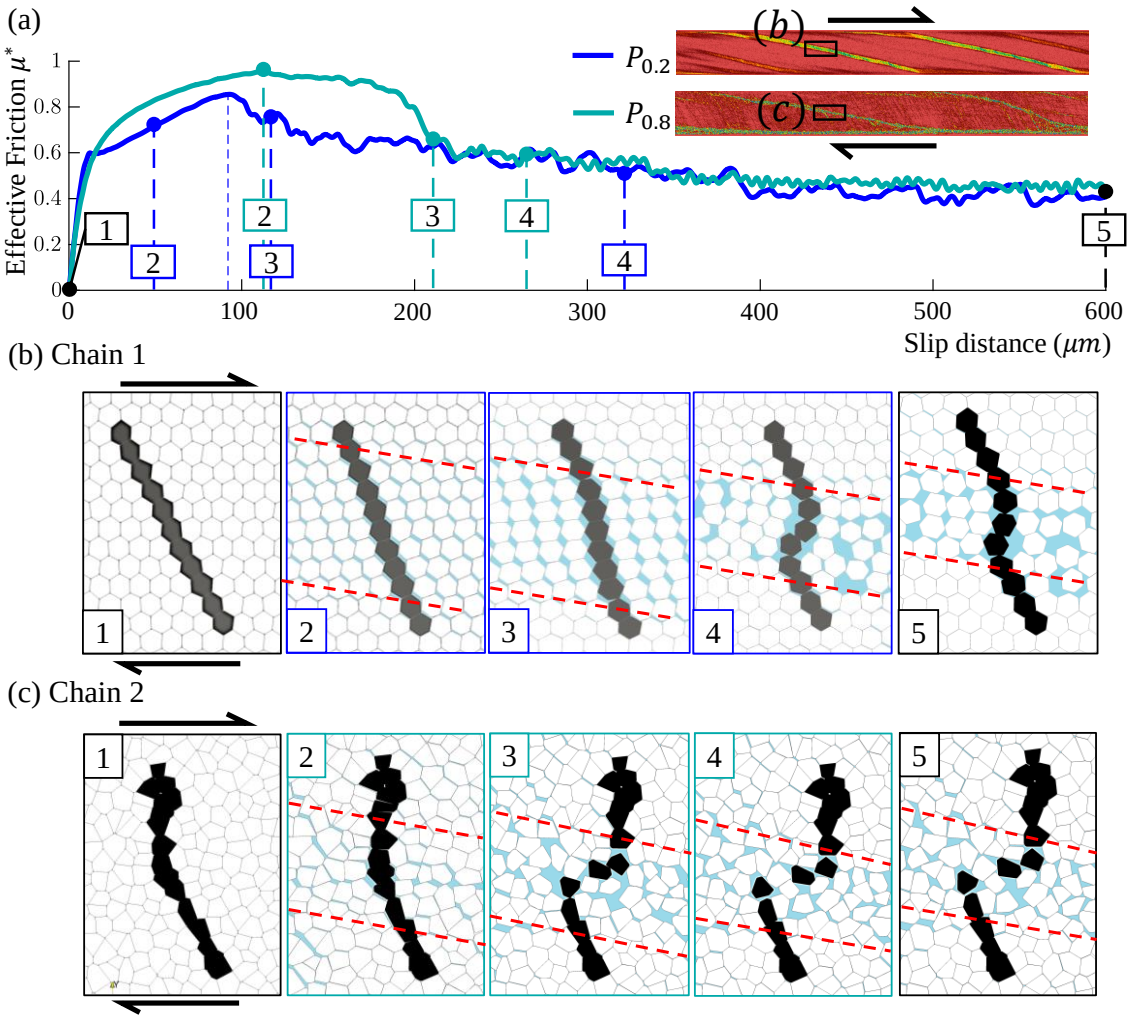

Figure 80. The figure displays the evolution of two chains of particles within the principal low-angle *R*-band at several instants of the simulation for the two extreme perturbation cases ($P_{0.2}$ and $P_{0.8}$). (a) Effective friction curves with instants taken (b) Chain 1, one chain of the $P_{0.2}$ case at five different moments. (c) Chain 2, one chain of the $P_{0.8}$ case at five different moments.

Although the total dilation in Figure 78 (b) is higher for the $P_{0.8}$ case, the Riedel of the $P_{0.2}$ case dilates more than the $P_{0.8}$ Riedel just before friction peak (larger band in Figure 80 (b) n°3 and (c) n°2). It explains the higher thickness observed in Figure 79 (a). The initialization and development of shear bands are often accompanied by an increase of the void ratio and particle rotations inside the shear band (Chapter 1). This phenomenon is specific to the shape of particles which needs to create spaces before particles movements. However, at the steady-state, both chains tend to have the same thickness, with 3-4 grains belonging to the Riedel, consistent with previous Figure 79 (b).

The results from this section are summarized in the following Figure 81 with the effective friction curve and Riedel structure formed at steady-state of sliding.

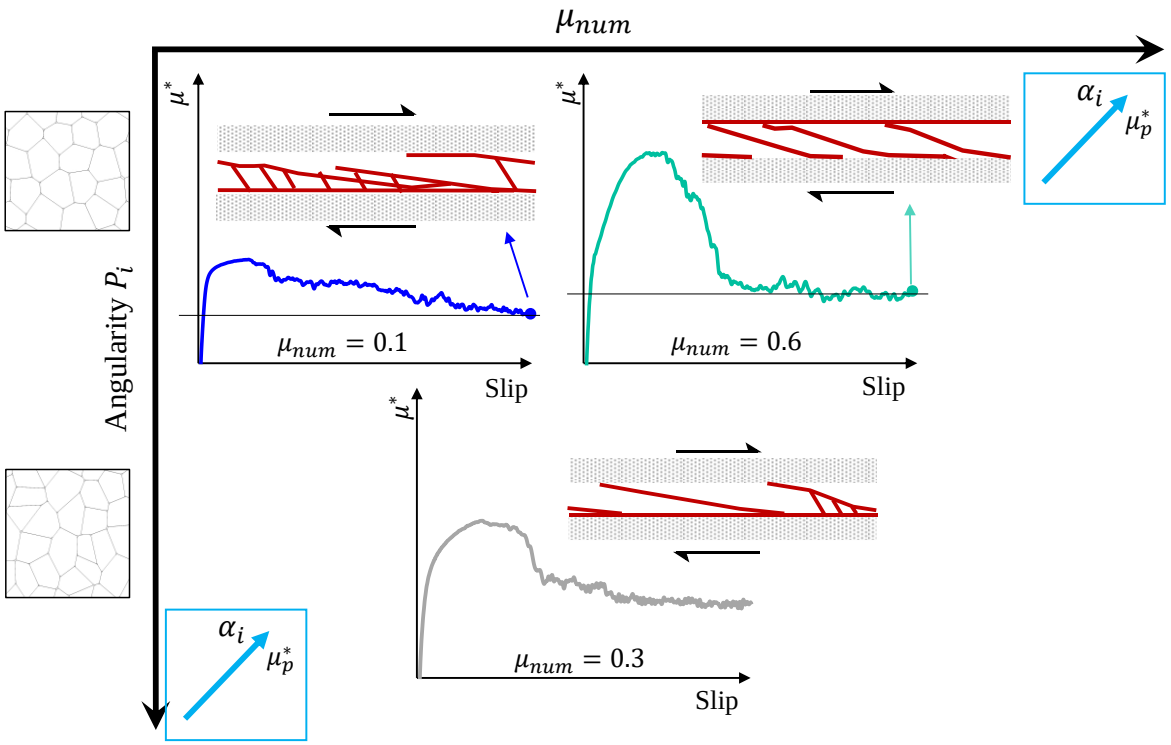

Figure 81. A simplified view of the influence of the interparticle friction μ_{num} and the angularity of the particles P_i on gouge strength and rheology. μ^* is the effective friction during the slip of the gouge. The effective friction peak μ_p^* and is the angle between the direction of shearing and the main Riedel band α_i are both increasing with an increase in μ_{num} or P_i.

4.3.3. Influence of the number of particles within the gouge thickness and Global Stiffness

In this section, two ways of modifying the global stiffness of the gouge layer are compared: an increase in the interparticle stiffness or in the size of particles. The different mechanisms influence the formation and evolution of Riedel bands in the granular gouge. The corresponding samples variation are gathered in Table 7.

Table 7. Sample names and associated modifications with standard case (M-S) presented in section 4.3.1.

Section	Sample Name	Modified variable	Numerical value
i	M-K-2	Interparticle stiffness k_n	2.10^{15} Pa/m
	M-K-5		5.10^{15} Pa/m
	M-K-10		1.10^{16} Pa/m
ii	M-PS-30	Size of particles ϕ_{eq}	30 µm
	M-PS-40		40 µm
	M-PS-50		50 µm
	M-PS-30-Keq	Size of particles and equivalent stiffness ϕ_{eq} and k_{eq}	30 µm $-$ 6.8 10^{14} Pa/m
	M-PS-40-Keq		40 µm $-$ 4.7 10^{14} Pa/m
	M-PS-50-Keq		50 µm $-$ 4 10^{14} Pa/m
iii	M-Th-1	Thickness of the gouge th_i	1 mm
	M-Th-3		3 mm
	M-Th-4		4 mm

i. Interparticle stiffness modification

How interparticle stiffness acts on Riedel band formation? To be in the same conditions as for the first model (Chapter 3), and because the magnitude of particle diameter was the same, the standard case (M-S) was implemented with an interparticle stiffness of 10^{15} Pa/m (section 4.2.2) and then by varying k_n from two to ten times the reference value (respectively samples M-K-2 and M-K-10).

The increase of stiffness both increases the effective friction peak, the shear modulus (later discussed), and the total energy released by the weakening phase, Figure 82 (a) & (b). The pattern of the friction curve was predictable for the elastic part, as numerical stiffness is only supposed to play on the overlapping of particles which modifies the elastic part of the effective friction curve: an augmentation in interparticle stiffness increases the global stiffness and thus the shear modulus. But we would have thought that the friction weakening part would follow a similar slope for each granular sample. Such a discussion can only take place when the sliding scenario is well established, which will only be the case in the next Chapter 5: it is necessary to save explanations for later.

A difference in interparticle stiffness (i.e. modification in shear modulus) also seems to affect the angle orientation of Riedel bands, Figure 82 (c). In the case with higher stiffness, the orientation angle of the main Riedel band α_i is reduced from 12 ° to 7 ° and the number of Riedel bands at friction peak is reduced to one big Riedel band.

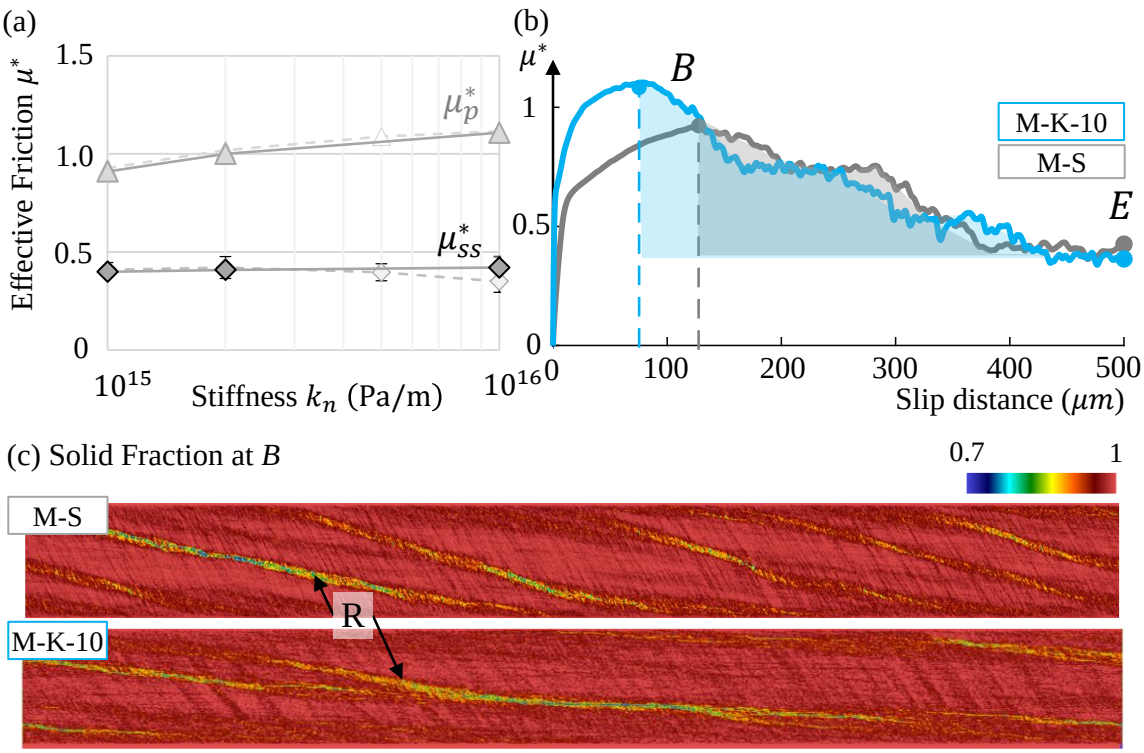

Figure 82. (a) Effective Friction as a function of the interparticle stiffness at friction peak and averaged value for the steady-state zone. The samples are M-S, M-K-2, M-K-5, and M-K-10 (respectively 10^{15} Pa/m, 2.10^{15} Pa/m, 5.10^{15} Pa/m and 10^{16} Pa/m), for two samples lengths (L=4mm and 20 mm) (b) Peak zone for the two extreme stiffness cases M-S and M-K-10 (10^{15} Pa/m and 10^{16} Pa/m) with peak location. (c) The solid fraction between 0.7 and 1 for the two cases in (b) at B.

Even after reaching the steady state, it can be observed that the increase in stiffness has completely changed the kinematics inside the gouge, Figure 83 (a). The (M-K-10) material has a single final R-band that runs the length of the gouge and appears to have two slopes with different orientations. In this simulation, the Y-localization occurred on the lower part of the gouge, as the entire upper part moves as one unit, as seen in the velocity map, Figure 83 (c3), unlike the (M-S) material which localizes at the top, due to the left Riedel band which only allows part of the gouge to move along the x-axis.

The R'-bands rotate at a higher speed than the R-bands and usually disappear as they grow to give way for R-bands. R'-bands are rarely observed because of their short duration and limited thickness [(Morrow and Byerlee, 1989), (Logan et al., 1992), (Morgan & Boettcher, 1999)]. That is why in other studies [(Schmocker et al., 2003), (R. Katz et al., 2006)], the low-angle R-bands are the only bands observed. In this study, high-angle Riedel bands R' are very pronounced in the case with higher stiffness, Figure 83 (a) & (c1). These R'-bands are present during the whole simulation and seem to be responsible for the difficulty of the material (M-K-10) to deform by shearing, inhibiting multiple R-bands formation.

The distribution of force chains in the gouge allows us to better understand the formation of R'-bands. While the R-bands seem to correspond to an area free of force chains, the R'-bands show the opposite behavior with R'-bands located where force chains are connected within the R-band, Figure 83 (c2). It explains why they are more pronounced for stiffer or stronger materials and with a higher magnitude of force chains.

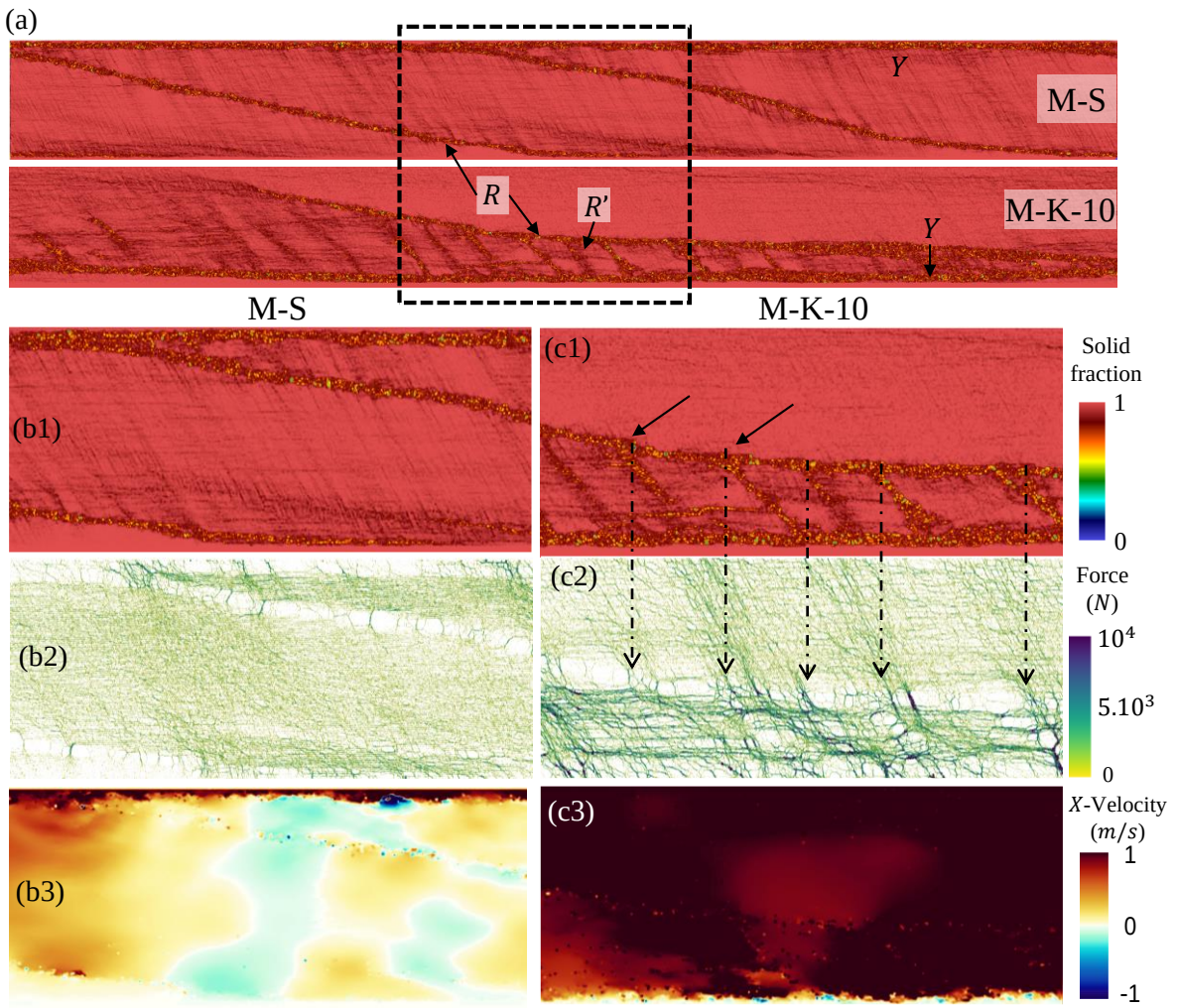

Figure 83. (a) The solid fraction between 0 and 1 for the two samples at E, Figure 82 (b). (b) Details on gouge M-S (b1) Solid fraction between 0 and 1, (b2) Snapshot of the force-chains network (from 0 to 10^4 N), (b3) Velocity profiles in the x-direction (between 1 and -1 m/s); (c) Details on gouge M-K-10 (c1) Solid fraction between 0 and 1, (c2) Snapshot of the force-chains network (from 0 to 10^4 N), (c3) Velocity profiles in the x-direction (between 1 and -1 m/s). Force chains are defined according to the typical level of stress present in the system (here the applied normal stress) and thickness and color are evaluated between the minimum and maximum contact force (0 to 10^4 N). A cut-off is made at 10^4 N to have the same visualization for all cases (higher force chains are observed for higher stiffness).

ii. Size of particles and equivalent stiffness

The constant initial gouge thickness (th_i) chosen in models implies that an increase in the size of particles also increases the global stiffness of the granular sample, Figure 84 (a), (c), (d) (full lines). Indeed, the places of elastic accommodation are much less numerous while having the same individual elastic response. The size augmentation reduces the total number of particles in the gouge thickness from 100 to 40 (respectively for (M-S) ($\phi_{eq} = 20\ \mu m$) and (M-PS-50) ($\phi_{eq} = 50\ \mu m$)), and leads to a similar behavior as the one observed for a modification of interparticle stiffness (Figure 82): an increase of effective friction peak and a longer slip weakening part. However, the steady-state effective friction is increasing from 0.4 to 0.5, Figure 84 (c), contrary to all the previous simulations observed.

Without the stiffness effect

In order to only study the influence of cell size variation, the interparticular stiffness is modified to keep the same initial shear modulus for all models, Figure 84 (b), and to remove the "stiffness effect". The secant shear modulus is selected similar to the one of the standard material (M-S) and calculated at 40 % of the maximum shear stress (36.5 MPa). Then, a new stiffness k_{eq} is calculated for each model with a diameter of cells ϕ_i, as

$$k_{eq_i} = k_n \frac{G_{M-S}}{G_{\phi i}} \tag{4.1}$$

where k_n is the interparticle stiffness of the standard case (10^{15} Pa/m), G_{M-S} is the shear modulus of the standard case, with a cell's diameter of 20 μm, and $G_{\phi i}$ the shear modulus corresponding to each size variation (Appendix A4.C). The equivalent stiffness k_{eq_i} is then inserted in the numerical model, leading to the results presented in, Figure 84 (b) and with dotted lines in Figure 84 (c) & (d), corresponding to samples (M-PS-30-Keq), (M-PS-40-Keq), and (M-PS-50-Keq).

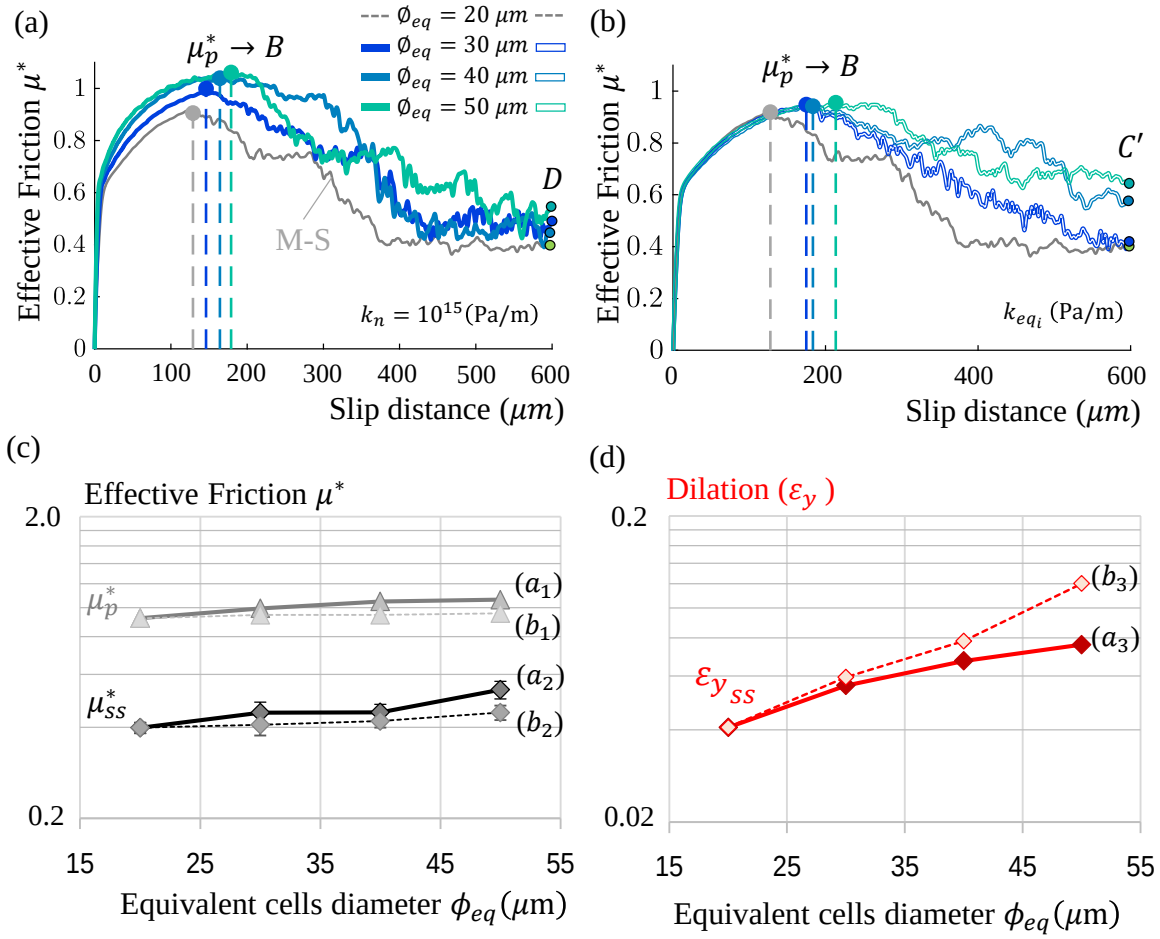

Figure 84. This figure presents results from two simulation campaigns related to global stiffness variation: (a) Effective friction curves for a variation in cells size only (from 20 to 50 μm with an interparticle stiffness of 10^{15} Pa/m) and, (b) Effective friction curves for a variation of both cells size and interparticle stiffness to have the same secant shear modulus for each simulation (interparticle stiffness of 10^{15} Pa/m, 6.8 10^{14} Pa/m, 4.7 10^{14} Pa/m, 4 10^{14} Pa/m), (c) Effective friction results as a function of the size of the cells for both simulation campaigns (d) Steady-state averaged dilation (%) as a function of the size of the cells for both simulation campaigns. The grey curve presents the (M-S) case.

The direct consequence of an increase in the size of particles (without stiffness effect) is a longer slip weakening duration, meaning that more energy is needed to deform the gouge and to reach a steady state. But it also means that this long and smoother slip weakening may reduce the probability of a big instability to occur (discussed in Chapter 5). The pre-peak section, on the other hand, is identical for all grain sizes, which validates the stiffness calibration of Eq. (4.1). The equivalent stiffness also allows keeping μ_p^* and μ_{SS}^* almost constant, dotted lines Figure 84 (c). However, the value of μ_{SS}^* obtained for (M-PS-50) is biased because it has not yet reached its stabilized steady-state of sliding in the picture.

From a purely kinematic point of view, by doubling the particle size, the steady-state dilatancy is not doubled for the same interparticle stiffness (full red line, Figure 84 (d)). But if one passes in equivalent stiffness, (i.e. only considering the change of particles size), a multiplication by two of particles size doubles the steady-state dilatancy value (from 0.04 to 0.08 %, Figure 84 (d), red dashed line).

Riedel angle

The angle of the main Riedel band at friction peak seems to depend on the shear modulus value, as we found the same angle for the standard case (a) in Figure 85 and the case (c) (which have the same shear modulus), whereas the case (b) presents a different Riedel angle (and a different shear modulus). At this step, it can be hypothesized that the size of particles does not change the rheology of the gouge but changes the temporality of Riedel bands formation and particularly the duration of slip weakening.

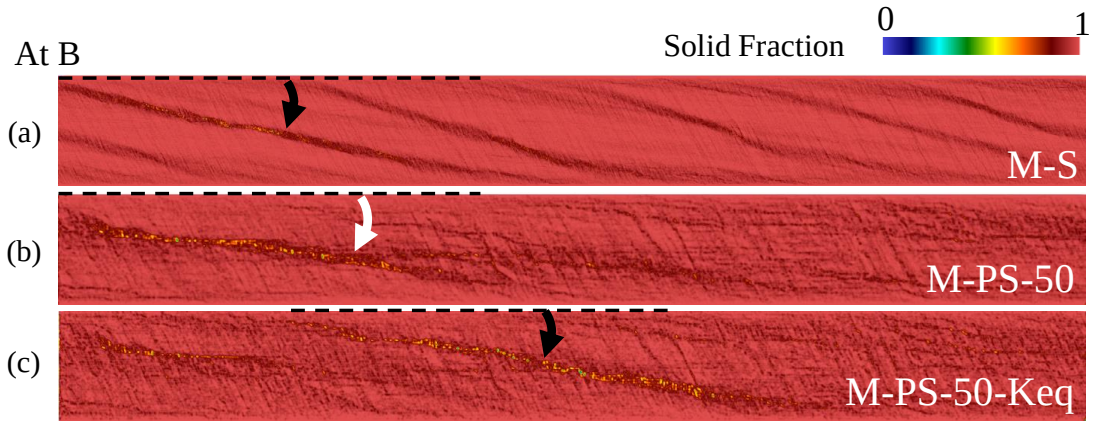

Figure 85. The solid fraction between 0 and 1 at friction peak B for three samples: (a) $\phi_{eq} = 20\ \mu m$ (b) $\phi_{eq} = 50\ \mu m$ for the standard stiffness and (c) $\phi_{eq} = 50\ \mu m$ with equivalent stiffness.

Conjugate Riedels (*R'*)

The effect on *R'*-bands is similar to the one observed for a change in interparticle stiffness. By increasing the size of particles, *R'*-bands become more persistent and may have consequences on the longer critical slip distance observed. The antithetic particle movement, due to the persistence of *R'*-band, appears to modify the entire kinematics with the creation of a Riedel structure [(Y. Katz et al., 2004), (Y. Katz & Weinberger, 2005)] during the slip weakening part observed in Figure 86. They are mainly caused by granular flow sub-parallel to the *R*-bands, which both induce grain reorganization and rotation of *R'* (Y. Katz et al., 2004). Although

Riedel structures are more visible when the size of particles is increased, in Figure 86 (d), we suppose that all gouge models evolve as a kind of Riedel structure. The reason why they are more visible with larger particles is that increasing the size of particles, increases the interparticle stiffness and thus force chains between particles.

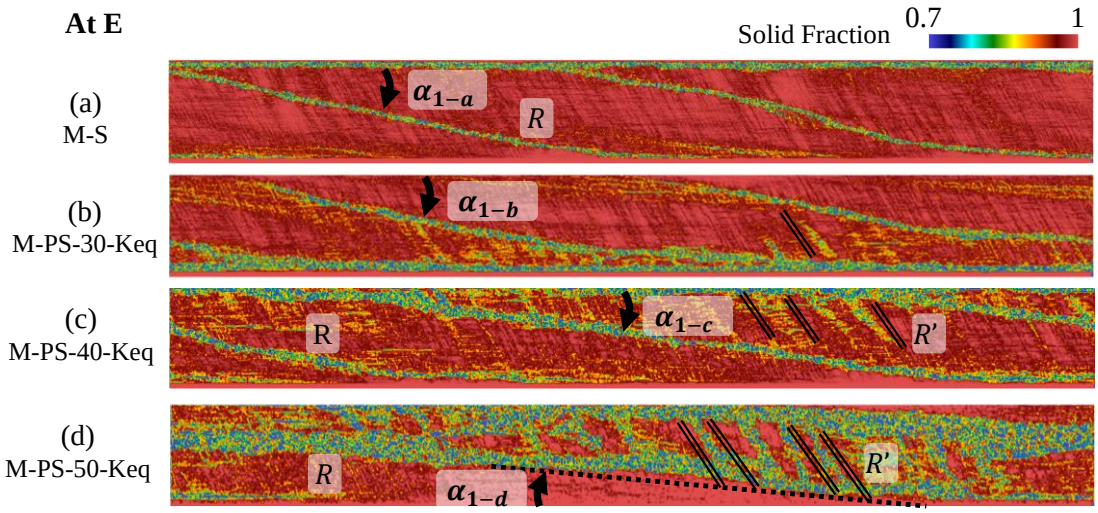

Figure 86. The solid fraction between 0.7 and 1 at point E (steady-state of sliding), for the four samples with equivalent stiffness ((a) $\phi_{eq} = 20\ \mu m\,(b)\ \ \phi_{eq} = 30\ \mu m$ (c) $\phi_{eq} = 40\ \mu m$ and (d) $\phi_{eq} = 50\ \mu m$). The angle α_i represents the orientation of the R-bands from the direction of shearing and decrease with increasing particle size: $\alpha_{1-a} > \alpha_{1-b} > \alpha_{1-c} > \alpha_{1-d}$.

iii. Gouge thickness

To a certain extent, decreasing the thickness of the granular sample has similar frictional behavior as an increase in the size of cells. Indeed, Figure 87 (a) shows that the same number of particles within the gouge thickness ($nb_1 = th_i/\Phi_{eq}$) leads to the same effective friction at peak and steady-state for two kinds of study: the one with reduction of initial thickness but with the same size of particles (grey line) or the one with an increase in the size of particles (section ii), with the same initial thickness and without stiffness effect in yellow (equivalent stiffness previously described). However, the dilation behavior is not similar, Figure 87 (b).

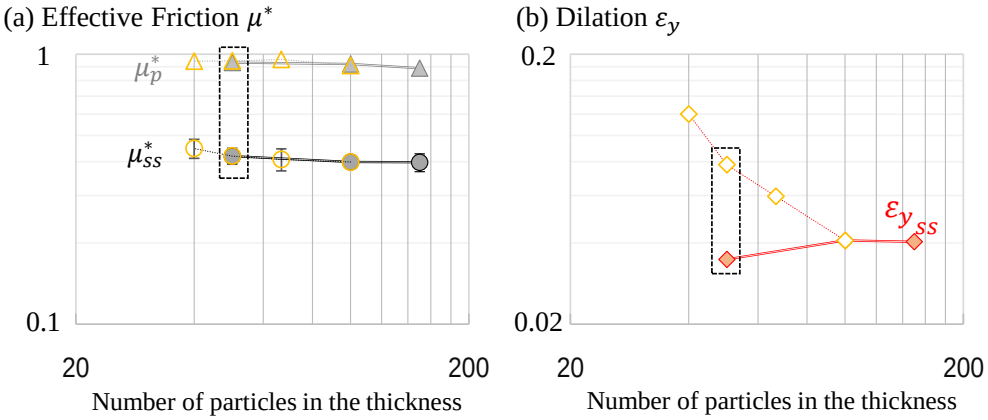

Figure 87. (a) Effective friction as a function of the number of particles within the gouge thickness nb_1, (b) averaged dilation at steady-state, obtained for variations in gouge thickness (full markers with a thick line, grey) and variations of the size of particles (yellow markers, study with equivalent stiffness). The pointed rectangles surround the two cases with the same number of particles within the gouge thickness (nb_1 =50 particles) for the sample (M-Th-1) with an initial thickness of 1 mm and equivalent cells diameter of ϕ_{20} and the sample (M-PS-40-Keq) with an initial thickness of 2 mm and equivalent cells diameter of ϕ_{40}.

The ratio of gouge thickness to grain size

Two samples with the same ratio of gouge thickness to grain size are compared: (M-PS-40-Keq) and (M-Th-1), which both have 50 particles within the gouge thickness. The box in Figure 87 shows their mechanical characteristics, but to have a more precise comparison Figure 88 is added with the evolution of effective friction and dilation as a function of the fault slip distance.

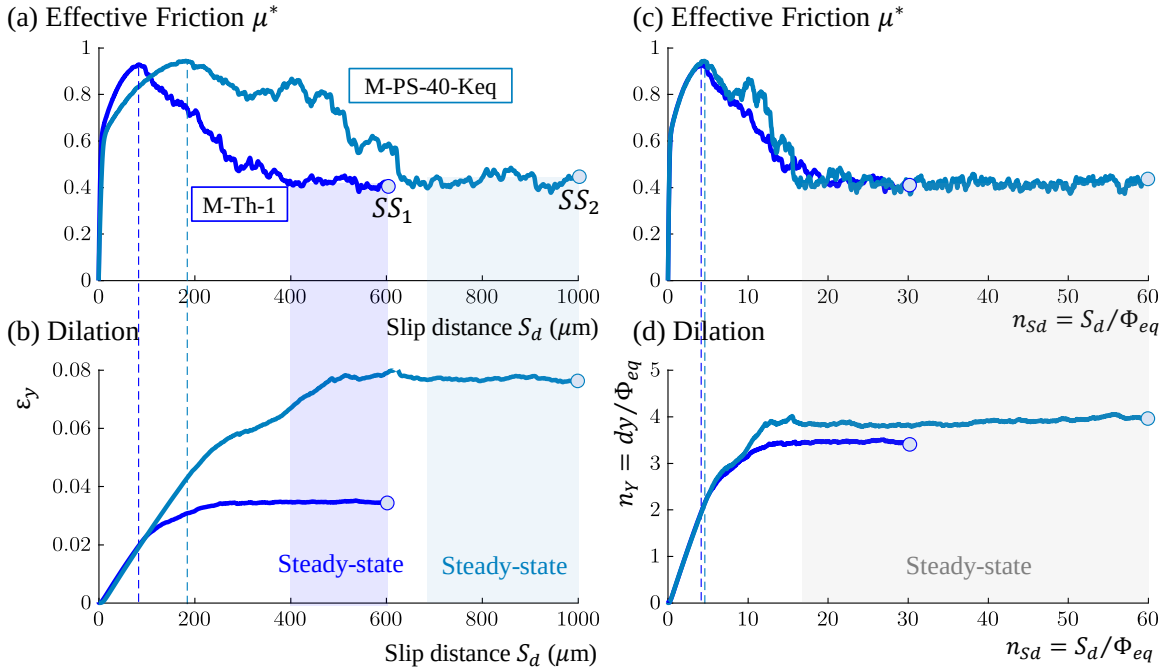

Figure 88. (a) Effective friction μ^*as a function of slip distance $S_d(\mu m)$. (b) Dilation ε_y (%) as a function of slip distance $S_d(\mu m)$. (c) Effective friction μ^* as a function of n_{Sd}, which is the ratio between the fault slip distance S_d and the equivalent diameter of particles ϕ_{eq}. (d) Dimensionless dilation n_Y(number of particles) as a function of n_{Sd}. The two cases in the hyphen box in Figure 87 are displayed: a simulation with a gouge thickness of 2 mm, an equivalent cell diameter of ϕ_{40} and an equivalent stiffness of 4.7 10^{14} Pa/m (M-PS-40-Keq), and a simulation of 1 mm thickness, with an equivalent cell diameter of ϕ_{20} and the standard stiffness of 10^{15} Pa/m, (M-Th-1).

Although the resulting peak of effective friction is similar in both cases, Figure 88 (a), the friction evolution as a function of slip is very different. Indeed, sample (M-PS-40-Keq) needs almost twice more slip along the fault gouge to reach the resistance peak ($184\ \mu m$ vs $83\ \mu m$) and then to reach the steady-state plateau zone ($700\ \mu m$ vs $400\ \mu m$). These results are consistent with the results presented for equivalent stiffness. Similarly, the averaged dilation ε_{SS} in the steady-state zone of the sample (M-PS-40-Keq) is doubled (0.078 vs 0.035), Figure 88 (b).

However, results can also be presented with dimensionless parameters (right side pictures), considering: the fault slip distance as a dimensionless number n_{Sd}, number of particles (or ratio between the fault slip distance S_d and the equivalent diameter of particles ϕ_{eq}), and dilation as n_Y which is the ratio between the y-displacement of the rock wall divided by the equivalent diameter of particles ϕ_{eq} (number of particles). With this representation, it is observed that both friction and dilation curves are similar. These two simulations also have similar tangent and secant shear moduli (respectively $G_{tan} = 12.2\ GPa$ et $G_{sec} = 6.2 - 5.77\ GPa$). Figure 89 compares Riedel bands for these two cases and displays the same type of deformation for both simulations at steady-state. The low-Riedel (R) of both models are oriented at an angle equal to

$8-9°$, and similarly, the high-Riedel angles (R') are both oriented at an angle equal to $58-63°$. From this comparison, a conclusion is that the same number of particles within the gouge thickness ($nb_1 = th_i/\Phi_{eq}$) leads to similar R'-bands and Riedel structures with the gouge.

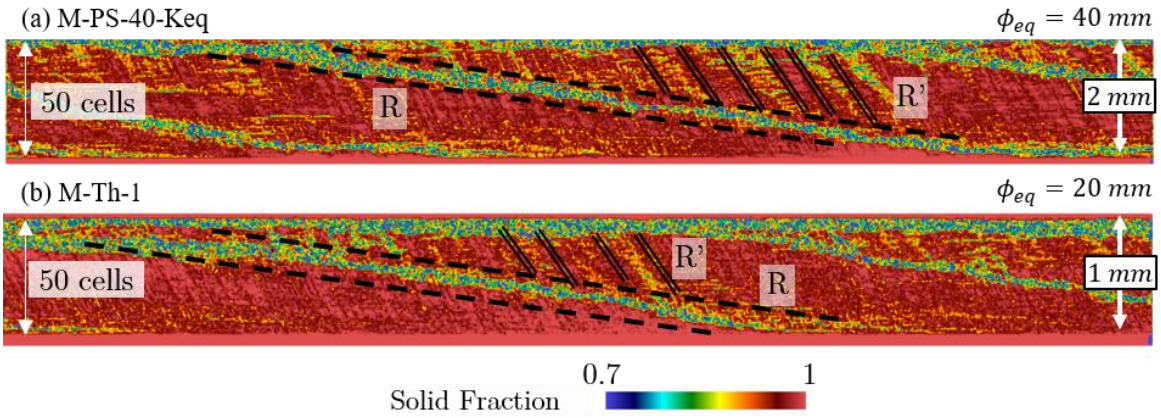

Figure 89. The solid fraction between 0.7 and 1 at steady-state for the two samples in the hyphen box in Figure 87: (M-PS-40-Keq) (a simulation with a gouge thickness of 2mm, an equivalent cell diameter of ϕ_{40} and an equivalent stiffness of 4.7 10^{14} Pa/m) and (M-Th-1) (a simulation of 1 mm thickness, with an equivalent cell diameter of ϕ_{20} and the standard stiffness of 10^{15} Pa/m). They both have 50 particles within the gouge thickness.

iv. Influence of shear modulus

Figure 90 gathers all the simulations presented in this section in a graph of the secant shear modulus as a function of nb_1(number of particles within the gouge thickness). As previously presented, an increase in the global stiffness of the gouge (interparticle stiffness or size of particles) increases both the shear modulus and the maximum shear stress (orange and purple lines). The results with an augmentation of the size of particles, but with equivalent stiffness, almost delete the effect on shear modulus (blue line). However, a modification in the gouge thickness does not influence the shear modulus nor the maximum shear stress (green line).

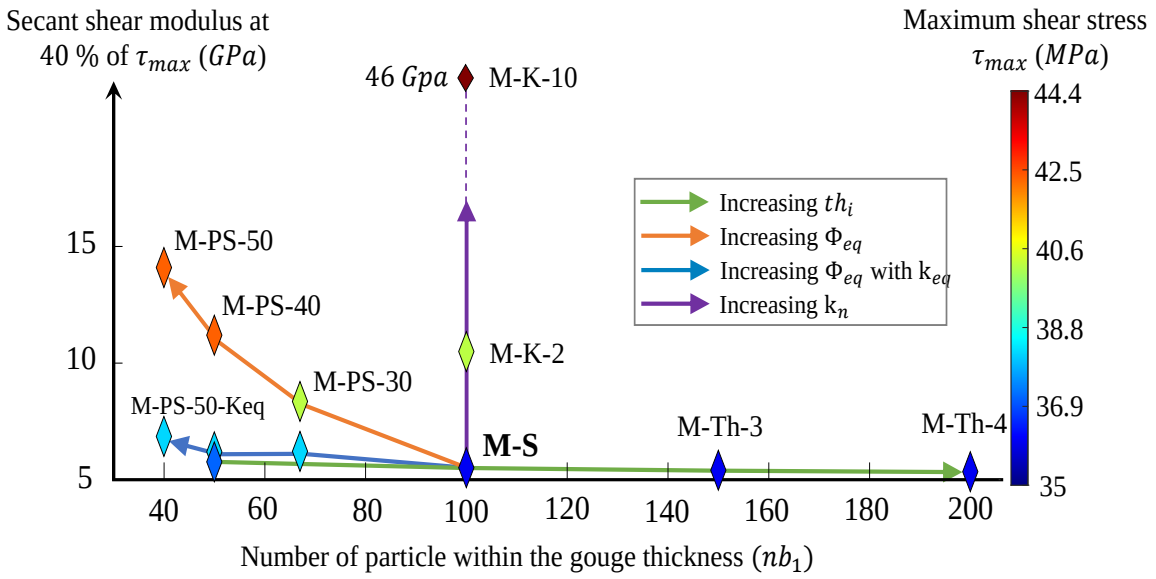

Figure 90. Secant shear modulus (GPa) as a function of the number of particles within the gouge thickness nb_1 for different values of maximum shear stress (MPa) (colored marker). The color of arrows corresponds to the different parameters increased and the color of the diamonds to the maximum shear stress (MPa).

Following these first results, nb_1, the number of particles within the gouge thickness seems to control the magnitude of frictional data observed (both at effective friction peak and steady-state), and it may influence the orientation angle of R-bands. It also controls the dilation and slip distance observed through dimensionless numbers n_Y and n_{Sd}.

Moreover, the shear modulus played on Riedel kinematics inside the sample, numbers of R-bands, Riedel structure, temporality, partially presented in Figure 90.

4.4. Discussions

4.4.1. The orientation angle of main Riedel bands

In previous sections, it was observed that the orientation angle α_i of low R-bands, or angle between the direction of shearing and the R-band, was changing with the modification of some grains' properties. This section proposes to gather all the previous results concerning the orientation angle of the R-bands at steady-state.

It is interesting to note that almost all the tested parameters have an influence on the orientation angle of Low Riedel bands except the angularity of the cells which does not allow to conclude on a significant modification. The three relevant quantities in a change of principal orientation angle of low R-bands at steady-state are: (a) interparticle friction, Figure 91 (a), (b) the geometry of the model through the number of particles within the gouge thickness nb_1 previously investigated, Figure 91 (b), and (c) the shear modulus.

a) An increment in the interparticle friction between particles drastically increases the orientation angle of the main Riedel bands (from the beginning of the simulation and until steady-state), because it is linked to the internal friction φ. This is a typical result of Coulomb-Mohr's theory [(Tchalenko, 1970), (Y. Katz et al., 2004)]. (Gu & Wong, 1994) plotted the evolution of Riedel angles α_i as a function of effective friction and also found an increase in α_i with the increase of internal friction angle (which is equal to μ^* with a cohesionless material as in this study).

b) An increment in nb_1 also increases the orientation of the main Riedel bands, both by reducing the size of particles or increasing gouge thickness. This result was only partially discussed in the literature, in the sense that particle size evolution was found to be responsible for the R-band angle as well as the gouge thickness, but the link between these two parameters is less investigated. For an increase in the initial gouge thickness, a change in orientation is observed close to the boundaries, which may come from edge effects due to the larger sample.

c) At steady-state, a change in shear modulus also has a huge influence on Riedel bands orientation, Figure 91 (a) orange and purple lines. A drastic decrease in Riedel orientation is observed with an increase in Shear modulus.

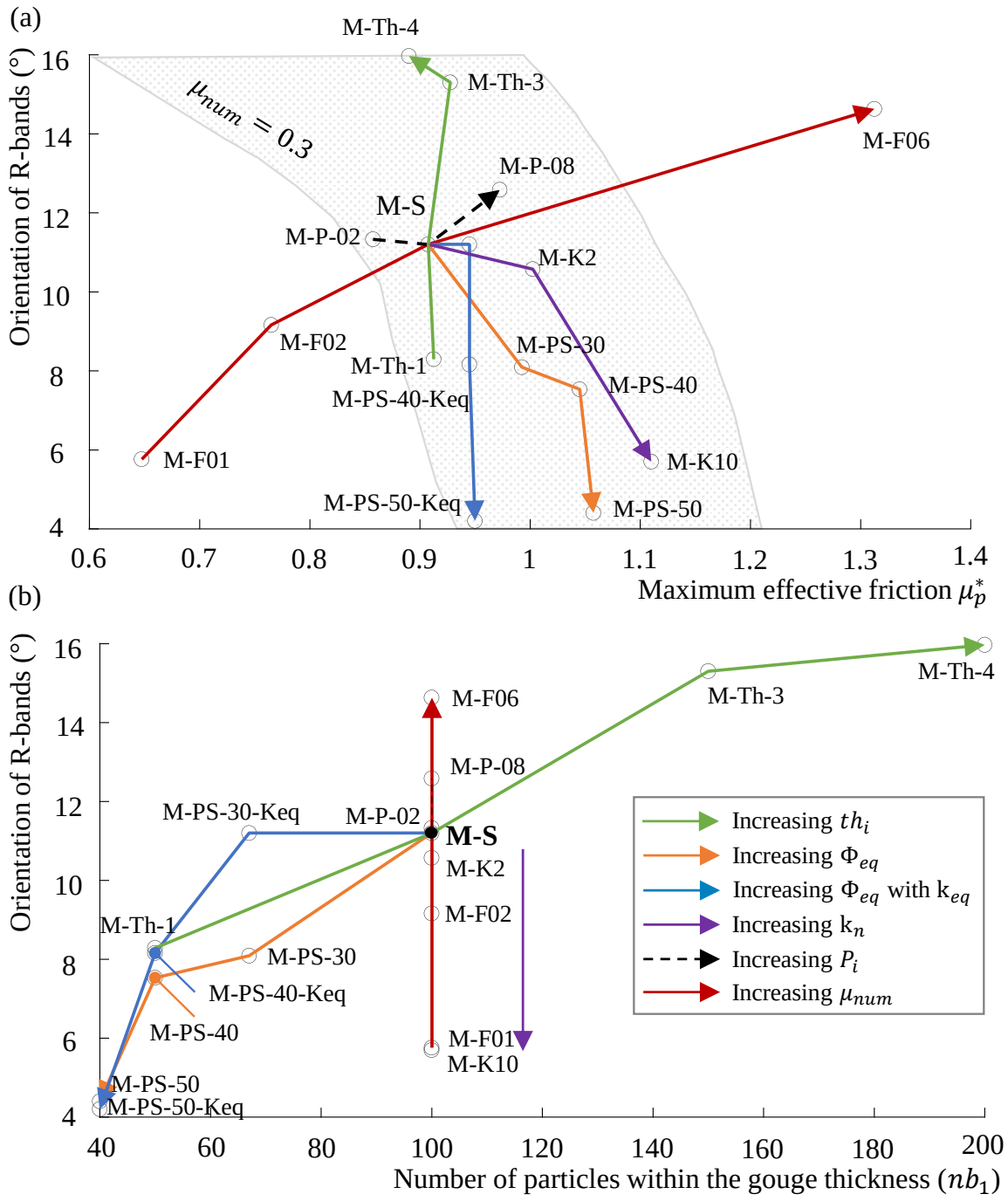

Figure 91. The orientation angle of *R*-bands at steady-state (averaged value for different *R*-bands), for all the simulations, as a function of the (a) effective friction peak μ_p^*, (b) the number of particles within the gouge thickness nb_1 (i.e. thickness of the gouge divided by the size of particles). The sense of the arrow indicates the increase of the different parameters and the names correspond to the ones presented in the previous sections. In figure (a) the interparticle friction μ_{num} evolves from left to right.

This α_i angle also evolves during the simulation before stabilizing at a steady-state. In the standard material (M-S), α_i variation with the slip distance is not very significant ($\sim 1-2\,°$) and evolves similarly for each simulated material. It was not studied in the present study and could be been done properly at a different moment of the simulation (elastic phase, effective friction peak, weakening part…) within the next research work. What remains much more interesting are the shapes of these Riedel bands, which are most of the time not really linear and

present some lower angle at the boundaries, as found by (Hirata et al., 2017). In some cases, the R'-bands present within the gouge modify the structure and slip temporality. These bands are unfortunately complex to follow during the simulation but could be the subject of further study.

(Moore et al., 1988) also worked on the kinematics of sliding and compared sliding behavior and internal geometry of laboratory fault zones. They observed that stick-slip samples with the largest stress drops also had the higher Riedel angles. On the contrary, their samples with low Riedel angles corresponded to stable sliding. In our case, we are not able to compare our results to stick-slip as defined in (Moore & Byerlee, 1992), but the Riedel angles observed can be correlated with friction strength and to the critical distance to reach a steady-state of sliding. Considering the orientation angle of the different granular materials observed, the smaller orientation angles could be linked to gouge stability.

4.4.2. The combined effect of Shear modulus, number of particles in the gouge thickness, and interparticle friction on rheology and weakening mechanisms

From previous sections, it has been shown that a reduction of Riedel angle can be both due to a decrease in interparticle friction or nb_1, or, an increase in shear modulus. In this section, the objective is to look into the combined effect of a modification of the shear modulus (G) with a different number of particles in the gouge thickness (nb_1) and/or a variation in interparticle friction (μ_{num}) between particles in contacts. Data were collected from sections 4.3.2 and 4.3.3 and gathered in Figure 92 and Figure 93 trying to connect possible interactions between parameters and comparing Riedel-bands evolution with their distinct elastic characteristics.

Zone (i): gouges with low G & low μ_{num} or low nb_1

Materials within the identified zone (i) present a reduction of interparticle friction μ_{num} (or angularity via P_i) or a reduction of nb_1, but they have a low shear modulus similar to the one of the standard material (M-S) (G_{sec}~5.7 GPa and G_{tan}~12.2 GPa). A decrease in the number of particles within the gouge thickness (nb_1) with stiffness modification (i.e. equivalent stiffness, (M-PS-Keq)) also belongs to this zone, as it is not linked to the increase in shear modulus, Figure 93 (e). At steady-state, these characteristics lower both the orientation angle α_i of secondary Riedels (cf. section 4.4) and the effective friction peak μ_p^*.

These mechanical changes enhance the life duration of R'-bands in their maximum size: explaining why more Riedel structures are observed, Figure 92 (a) and (c), and increasing the critical weakening length. Materials from this zone are prone to enhance stability within the gouge sample but can easily go into a slip. They can be related to weak gouges behavior [(Collettini et al., 2019), (Bedford et al., 2022)] which are supposed to have a very small effective friction.

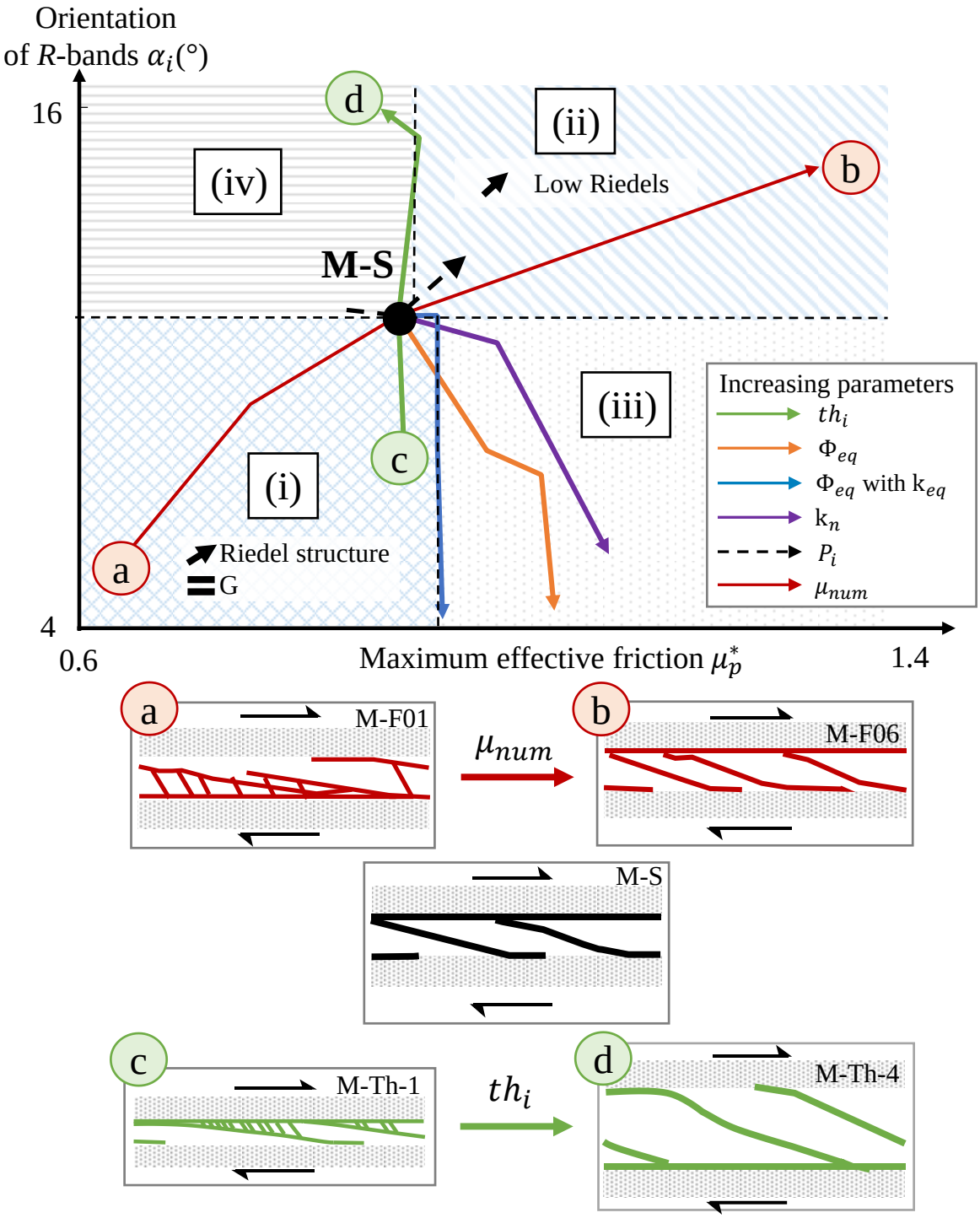

Figure 92. Schematic view of the previous Figure 91 (a) of the orientation of *R*-bands as a function of the effective friction peak, with distinction between 4 major zones of interest: (i) reduction of interparticle friction μ_p^* or nb_1 (without modification of the shear modulus), (ii) Increase in μ_p^*, (iii) Decrease of nb_1 with increase in shear modulus (iv) Increase in gouge thickness. The sense of the arrow represents an augmentation of all the parameters previously presented as detailed within the legend. Main Riedel structure at steady-state are represented below the figure and corresponds to the two extreme cases of interparticle friction study (a) and (b) and of thickness study (c) and (d). Details on Shear modulus values can be found in Appendix 4.C.

Zone (ii): gouges with low G & high μ_{num}

On the contrary, an increase in interparticle friction increases a lot the maximum shear stress, and thus μ_p^* without changing the shear modulus. These materials lead to an increase of the number of Low Riedel bands within the gouge, and a higher angle of orientation at steady-state, Figure 92 (b). If interparticle friction and shear modulus both increased, we could expect to observe more numerous R-bands at friction peak and lower Riedel angle and Riedel structure creation during the slip weakening part. A reduction of the critical slip distance is observed, leading to a more sudden post-peak weakening, which is prone to switch the fault behavior from a ductile aseismic response to a brittle seismic slip, depending on the stiffness of the surrounding medium. Materials with high interparticle friction coefficient (and low stiffness) are also known to present greater slippage and a decrease in the recurrence time between two slip events (Dorostkar & Carmeliet, 2019).

Zone (iii): gouges with high G

As seen in the previous sections, the shear modulus increases due to an increase of interparticle stiffness or a decrease in the number of particles within the thickness. Materials with high shear modulus present a small orientation α_i of R-bands. As previously found, they also present some Riedel structures caused by a longer life duration of R'-bands, Figure 93 (f), and (g). It can be noticed that a very small interparticle friction ($\mu_{num} = 0.1$) leads to almost the same R-angle. Similar values of both shear modulus G and nb_1within the gouge thickness (for two different samples) give similar kinematics of evolution of the Riedel structures (Figure 89) but they will not have the same slip temporality depending on the other characteristics of the model. The stiffness of the fault was found to depend on the ratio of the shear modulus to the size of the rupture nucleation zone. A fault with a very low shear modulus (and/or large regions) is more likely to tend towards slow slip nucleation (J. R. Leeman et al., 2016).

Zone (iv): gouges with low G & high nb_1

This area is specific to an increase in the nb_1 number with no change in either the interparticle friction or the shear modulus. These materials present a large gouge thickness (20 % of the total fault patch) without changing the size of particles, Figure 93 (d). They are not very representative of reality, since an increase of the gouge necessarily induces the wear of the particles in the center of the sliding zone and thus tends towards a reduction of the size of certain particles. For these materials μ_p^* slightly decreases and μ_{ss}^* have values similar to those of the (M-S) case, however, the orientation angle of Riedel bands increases. According to (Scholz et al., 1972), an accumulation of gouge layer tends to stabilize the system, and according to (Moore & Byerlee, 1992)'s theory, low Riedel angles also tend to stabilize the system. In our case, we have an increase in the orientation angle of the R-bands, which is a bit in disagreement with the theory, maybe due to the non-realistic material observed. These results could also be related to the stick-slip phenomenon by (Lyu et al., 2019) testing a variability of gouge thickness with different normal stress. They observe that an increase in layer thickness, (i.e. an augmentation of the number nb_1), implied a reduction of stress drop and friction and has a significant effect on stick-slip.

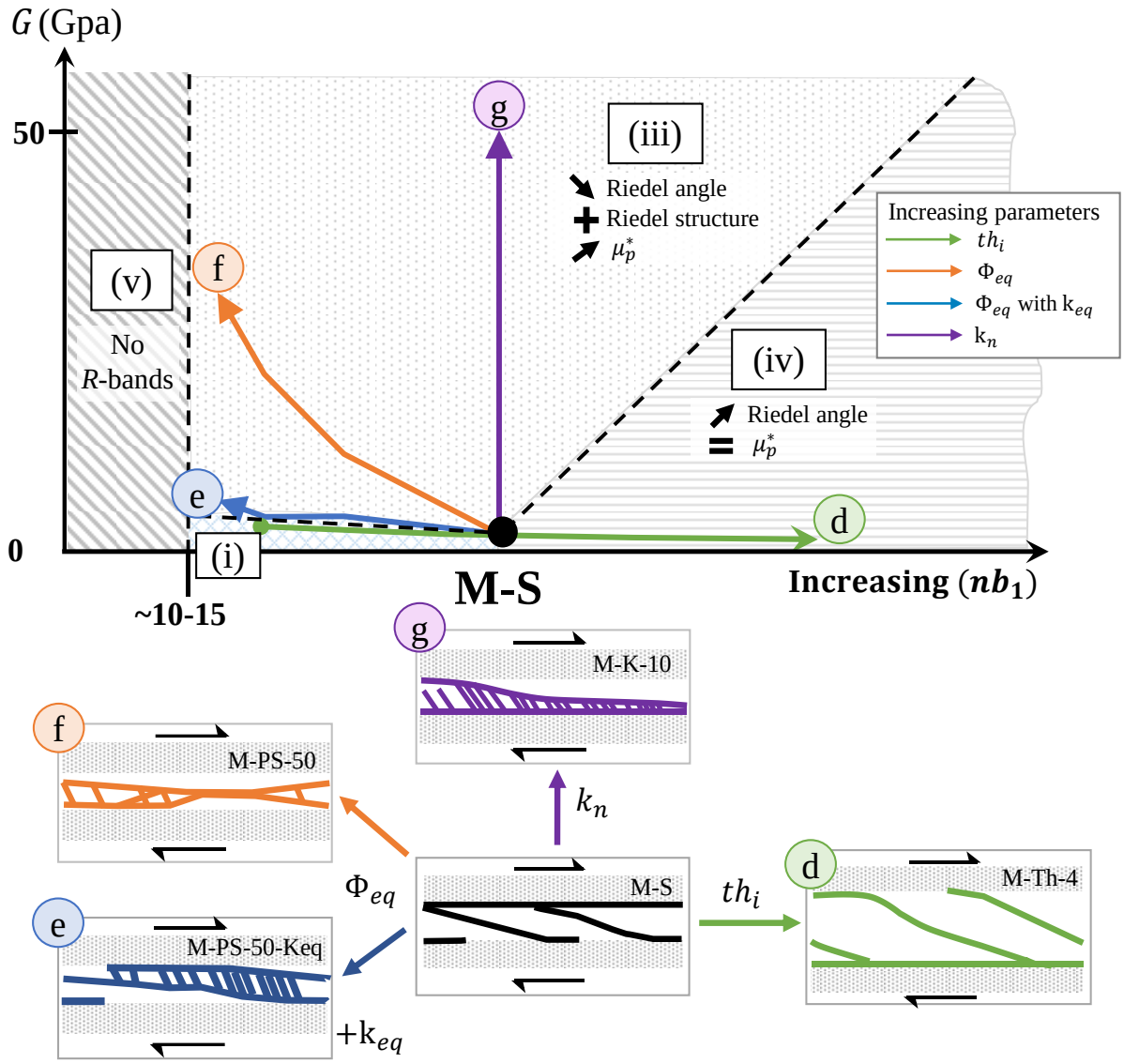

Figure 93. Schematic view of the shear modulus G (GPa) as a function of the ratio nb_1, with distinction between 4 major zones of interest: (i) reduction of interparticle friction μ_p^* or nb_1 (without modification of the shear modulus), previously presented in Figure 92; (iii) Decrease of nb_1 with increase in shear modulus (iv) Increase in gouge thickness, (v) Thin gouges with no Riedel formation. The sense of the arrow represents an augmentation of all the parameters previously presented as detailed within the legend. Main Riedel structure at steady-state are represented below the figure and corresponds to the extreme cases of thickness study (d), variation of particle size (e) and (f), and variation of interparticle stiffness (g). Details on Shear modulus values can be found in Appendix 4.C.

Zone (v): extremely low nb_1

Some very thin gouges were also modeled ($th_i = 200\ \mu m$) to avoid any Riedel formation Figure 93. By reducing the number of particles within the gouge thickness to a value lower than 10-15, and for any change in other gouge characteristics, Riedel band formation is prevented. The maximum shear stress also increases whereas the dilation is slightly reduced, as previously found by (Biegel et al., 1989) for a reduction in fault gouge thickness.

The results can also be related to the observed dilation at steady-state as a function of the ratio nb_1:

Zone (vi): gouges with similar size of particles

For granular samples with the same size of particles ($\phi_{eq} = 20\mu m$), values confirm that an increase in nb_1 also increases the total averaged dilation at steady-state (from left to right in Figure 94). Similar results were found in the study of (Lyu et al., 2019) for different normal stress. But an increase in gouge thickness (green line) seems to show a stabilization of dilation for a large ratio $nb_1 > 100$.

Zone (vii): gouges with a decrease in size of particles

A decrease in particle size remains the most important factor in reducing granular samples dilation. A higher size of particles may also rise the amount of slip needed to weaken the fault. However, if the dilation is expressed as a dimensionless number, similar dilation is found for each material (Section 4.3.3). Markers in this zone also correlate with a reduction in Riedel angle orientation.

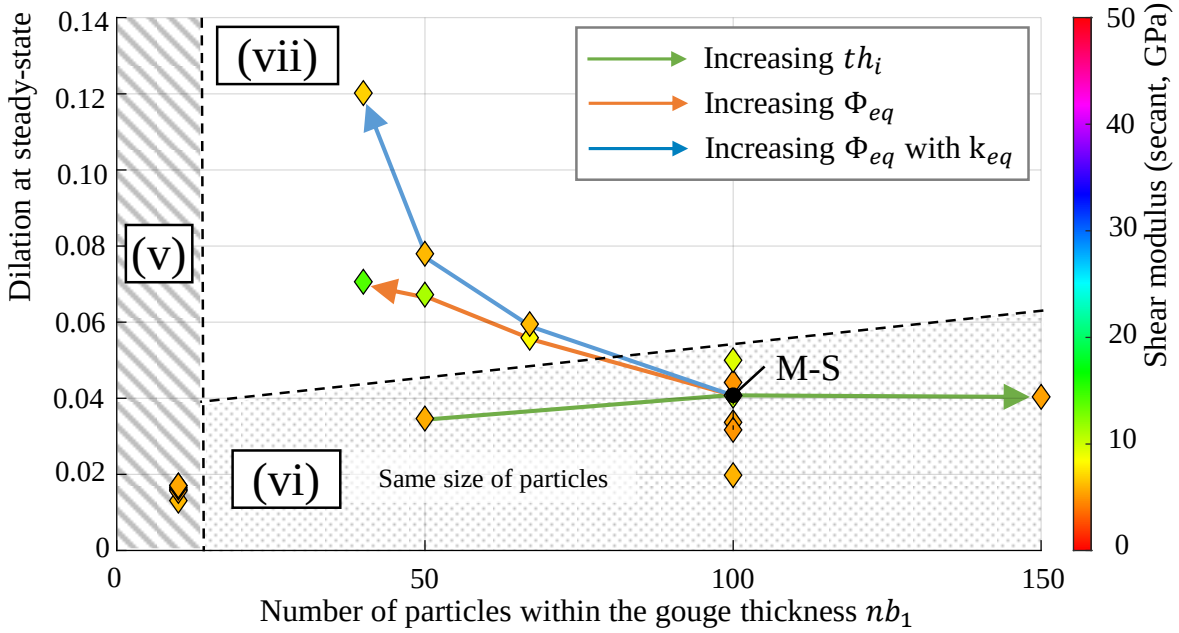

Figure 94. Averaged dilation at steady state, as a function of the number of particles within the gouge thickness for all the simulations. Zone (v), is a zone where the thickness of the gouge is too small ($th_i = 200\mu m$) to present any Riedel band formation (even with the same parameter variation than previously described), zone (vi) is a zone where all the simulation have the same size of particles ($\Phi_{eq} = 20\mu m$) (vii) is a zone where a change in the size of particles is observed. The secant shear modulus at 40% of the maximum shear stress is calculated for all cases and plotted as colors corresponding to the color bar on the right-hand side. The standard case M-S is situated on the graph.

These simulations represent different behaviors that can occur within the gouge during a fault slip for different types of materials. For example, although it is not possible in our numerical code to represent grain fragmentation, the variation in particle size and the ratio of the number of particles in the thickness of the gouge, gives us a glimpse of the changes that fragmentation could have on the sliding behavior. (Kenigsberg et al., 2020) found that "the interplay between gouge composition, fabric, and shear enhanced compaction elucidates the importance of these factors in governing the elastic and mechanical properties

of faults." With our simulations, we flipped the problem in the other direction to understand the effects of a change in the mechanical property of the gouge on its shear and sliding behavior. But the main conclusion remains the importance of a co-evolution between mechanical and elastic gouge properties from one side, and kinematics of shearing from the other side.

4.5. Conclusion of Part A

Another 2D granular fault gouge model has been implemented in the framework of DEM in order to study the influence of matrix particles characteristics on the fault rheological behavior and Riedel bands evolution. This chapter first gave an overview of a wide range of Riedel bands kinematics for different gouge parameters. For a highly dense granular matrix, small variations in physical or numerical characteristics of the model change the kinematics of the gouge:

- Gouge materials with high interparticle friction present an increase in the effective friction peak (typical results from Coulomb-Mohr theory). This high friction also influences shear bands formation with two main consequences: low-angle Riedel bands R are mostly observed (few or no conjugate Riedels) and their number increases within the gouge. Conversely, for materials with low interparticle friction, Riedel structures are formed accompanied by: a reduction of α_i and the formation of a single low-angle Riedel linked to the Y slip localization by conjugated Riedel bands. A modification in shape angularity and disorder have the same consequences, but with less amplitude of variation. As the orientation angle of Riedels can be seen as an indicator of stability for granular fault gouge (Moore & Byerlee, 1992), the reduction in interparticle friction is prone to switch fault gouge behavior from sudden and seismic slip to moderate and slow slip.

- Some parameters appear to modify the global stiffness of gouge materials by increasing the interparticle stiffness or the size of particles, leading to a rise of the shear modulus. A higher shear modulus is mainly responsible for a higher number of conjugate Riedels and Riedel structures observed: they inhibit the formation of low R-bands and slow down the arrival of the steady-state of the system. Even if the orientation angle of Riedel bands is mainly affected by a change in the ratio between the size of gouge thickness and size of particles, it is also influenced by the shear modulus.

- The direct consequence of an increase in the size of particles, without the stiffness effect, is a longer peak duration, meaning that more energy is needed to deform the gouge and to reach a steady state of sliding. The size of particles does not change the shape of the Riedel structure observed but changes the temporality of their formation and evolution, particularly the duration of the slip weakening part. But it also means that a longer and smoother slip weakening decreases the probability of instabilities to occur.

- For all the simulation campaigns, three main quantities are relevant in the formation and evolution of Riedel bands and main stability of the granular gouge: (a) the bulk shear modulus, (b) the ratio of gouge thickness to grain size (i.e. number of particles within the gouge thickness), and (c) the interparticle friction. They all participate in a modification in

the orientation angle of Riedel bands and the entire Riedel structure, having a strong impact on gouge stability. The combined effects of these three parameters lead to different gouge materials more or less likely to generate stable or unstable slips.

Studies from next part B are dedicated to a mixture between hexagonal cells with angular grains representing cataclastic clasts surrounded by matrix particles (i.e. hexagonal cells). Different results are expected in terms of Riedel patterns as the internal structure will be less homogeneous.

Part B – Granular fault zone with a composite mixture of angular grains and matrix particles

4.6. Foreword

The objective of this section is to properly study the influence of matrix particles within a granular sample by combining the matrix previously studied with angular grains used in Chapter 3, Figure 95. The first section 4.7 presents the granular material with a composite mixture between matrix particles and angular grains. In the second section 4.8, a qualitative comparison is made between the kinematics and rheology of this composite mixture under shearing and previous gouge samples.

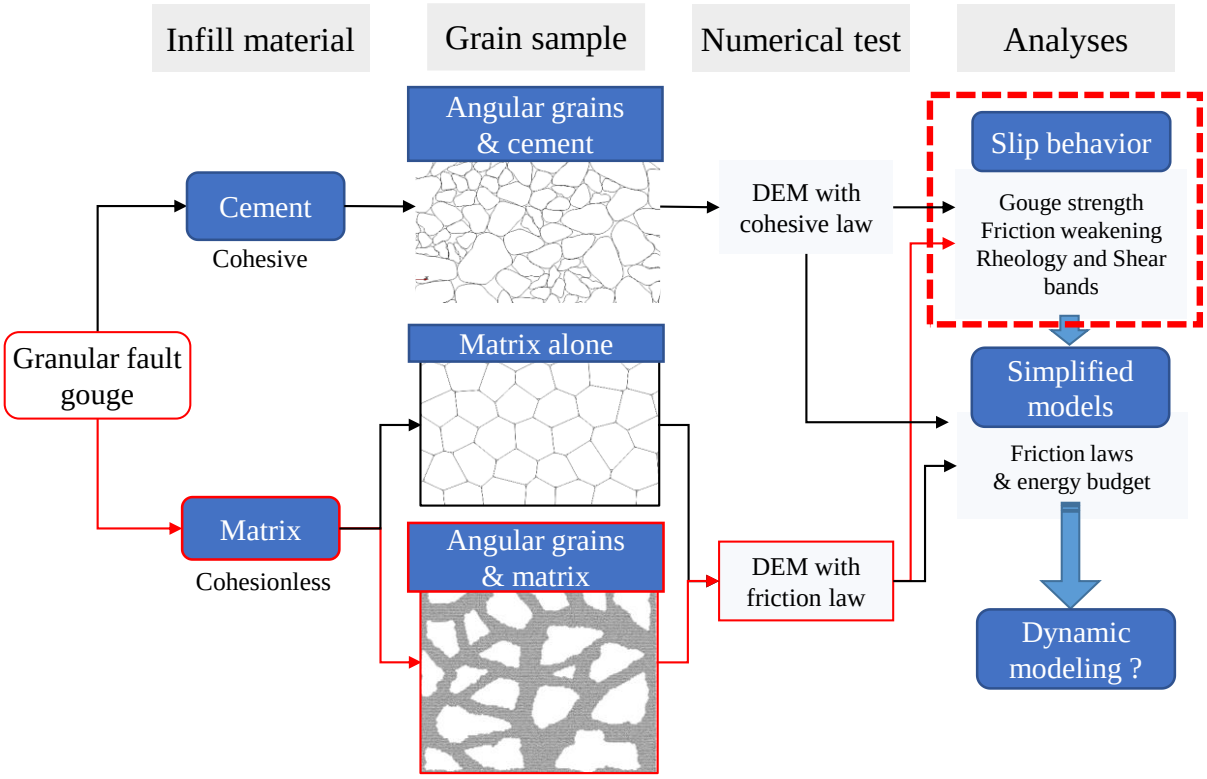

Figure 95. Main schema of Chapter 4, Part B

4.7. Model and numerical framework of a composite mixture

4.7.1. Generation of the gouge sample

A new granular sample with both angular particles and matrix particles is created. For the sake of simplicity and to easily compare results with previous parts, the model of Chapter 3 with angular grains is partly reused. This granular sample presents a gouge already sheared with a fractal distribution of particles settled to $D = 2.6$. To create the new composite mixture, the granular sample generated in Chapter 3 is kept, and a certain amount of the smallest angular grains is replaced by matrix particles. The first step consists in removing a certain percentage of the smallest particles within the selected sample, Figure 96 (a). In a second time, this material (a) is merged within matrix particles sample (M-S) to form the new composite mixture, Figure

96 (b). Due to the fractal distribution of particles within the granular sample, the composite mixture has a non-homogeneous particles distribution.

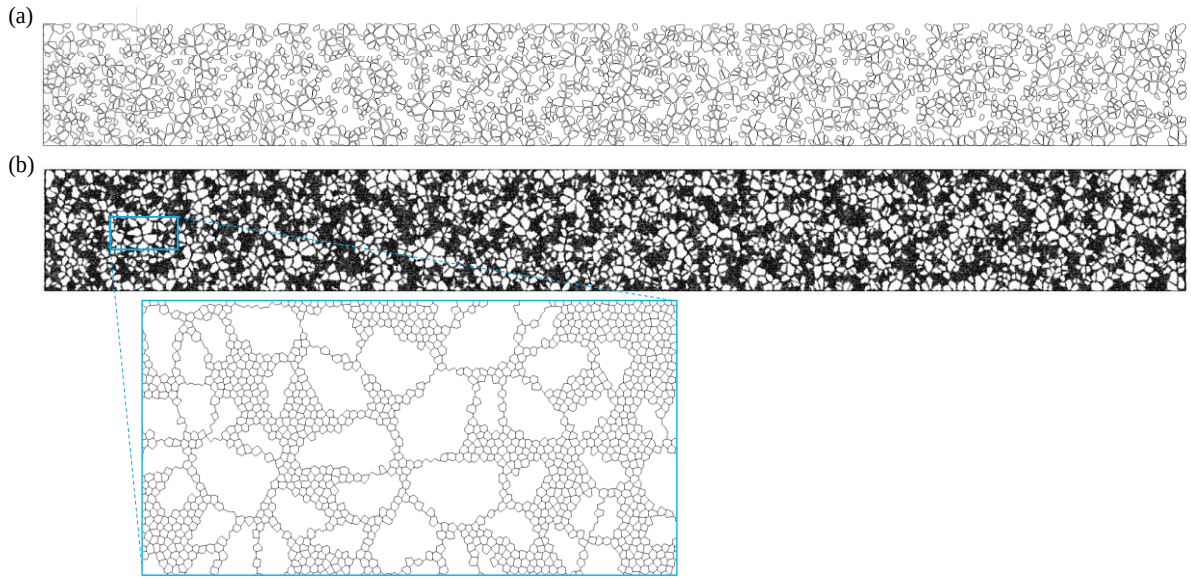

Figure 96. (a) Granular material from Chapter 3 with a certain number of small particles removed, (b) Mixture between angular particles and matrix particles.

The ratio between the area of matrix particles and the area of angular particles gives the surface percentage of matrix particles within the sample P_{matrix}:

$$P_{matrix} = \frac{S_{matrix-equiv}}{S_{matrix-equiv} + S_{grains-equiv}} = 1 - P_{grains} \quad (4.2)$$

With $S_{matrix-equiv}$ the equivalent area of the sum of all matrix particles, $S_{grains-equiv}$ the equivalent area of the sum of all angular clasts particles, P_{grains} the percentage of clasts particles. The inverse Cumulative Distribution Function (1-CDF) is plotted for 7 composite samples (MG-i), with varying matrix percentages (P_{matrix}) between 29 % and 60 % (MG for "Matrix-Grains" samples and "i" for the percentage of matrix particles), Figure 97.

From this preliminary study, only two of those samples are selected for direct shear simulations: (MG-33) 33 %, and (MG-56) 56 % of matrix particles. The behavior of the two selected samples (MG-33) and (MG-56) is then compared with a case with only granular particles (G-C-4), and with $P_{cem} = 4$ % (its behavior was similar to a case with no cementation in Chapter 3) and with a sample with only matrix particles (M-S), standard case simulation from Chapter 4 (Part A), considered with $P_{matrix} = 100$ % and no angular particles.

In the two samples with only one kind of particles, the amount of initial porosity is measured: $P_{pore} = 11$ % for (G-C-4) and less than 1 % for (M-S). Samples with a composite mixture do not present any porosity in their initial configuration, as the "merging step" between matrix and angular particles removes any porosity initially present. There is, in fact, about as much porosity as in the matrix samples. This conceptualization was chosen to fit with cementation cases observed in literature where cementation can lead to nearly zero porosity (Molenaar et al., 2007). The main characteristics of the four samples are gathered in Table 8.

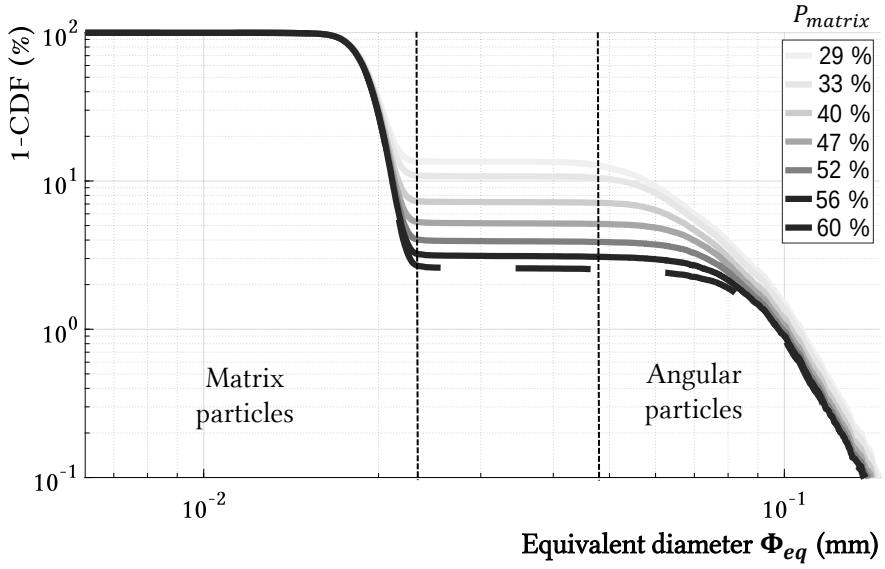

Figure 97. (1-CDF), with CDF the Cumulative Distributive Function, as a function of the equivalent diameter of particles in mm, for different surface percentages of matrix particles (29 to 60 %). Samples are named from (MG-29) to (MG-60). Note that the remaining composite mixtures not used in this study are available for an extended analysis on this topic.

Table 8. Information on the samples used for direct simulations and compared in this section. P_{matrix} is the surface percentage of matrix particles, μ_{num} is the numerical interparticle friction, P_{pore} is the surface percentage of initial porosity within gouge samples, $\phi_{eq-matrix}$ is the equivalent diameter of matrix cells, $\phi_{eq-grains}$ is the equivalent diameter of grains, N_{grains} is the total number of angular grains and N_{matrix} is the total number of matrix cells.

Samples name	P_{matrix}	μ_{num}	P_{pore}	$\phi_{eq-matrix}$	$\phi_{eq-grains}$	N_{grains}	N_{matrix}
G-C-4	0 %	0.5	11 %	-	$28 - 226\ \mu m$	4960	-
MG-33	33 %	0.3	0 %	$20\ \mu m$	$48 - 226\ \mu m$	4149	34097
MG-56	56 %	0.3	0 %	$20\ \mu m$	$79 - 226\ \mu m$	1852	56571
M-S	100 %	0.3	< 1 %	$20\ \mu m$	-	-	115825

4.7.2. Numerical setup for direct shear modeling

Apart from the shapes and sizes of the grains, the model used in this section is the same direct shear model as in Part A. Interparticle friction μ_{num} is equal to 0.3 between each particle (matrix-matrix, matrix-grains, and grains-grains).

To avoid wall-slip effects with smooth boundaries, a certain cohesion is introduced at the interface between matrix and rock walls and between angular grains and rock walls ($500\ MPa$). It enables the creation of a certain roughness by cementing particles to the top and bottom layer.

All the other physical and geometrical parameters are identical to those used for Part A, but for the sake of clarity the numerical setup and properties are gathered in Table 9 below.

Table 9. Numerical setup and properties for the composite gouge simulation.

Property	Associated variable	Value
Normal stress	σ_N	40 MPa
Shear velocity	V	1 m/s
Rock density	ρ_r	2600 kg/m^3
Contact stiffness	k_n & k_t	10^{15} Pa/m
Interparticle friction	μ_{num}	0.3
Interparticle cohesion	C_{num}	500 MPa at boundaries
Sample size	th_i x L_g	2 x 20 mm
Particle equivalent diameter	ϕ_{eq}	20 μm
Number of particles	N	varying
DEM time step	Δ_t	10^{-10} s
Proximity updating period	$\Delta_{t-contact}$	10^{-9}s

4.8. Rheology of the composite mixture

4.8.1. Mechanics and Kinematics

Effective friction

The addition of some matrix particles within the initial sample (G-C-4) densifies the sample by removing the initial porosity. The effective friction peak observed in Figure 98 (b) is much higher for the two composite mixtures compared to both 0 % (G-C-4) and 100 % (M-S) matrix samples where some porosity is observed (respectively $P_{pore} = 11$ % and ~1 %). The effect of initial porosity (or increase in initial density) on effective friction is in adequation with our previous Chapter 3 and with literature (Taylor, 1948). In their study, (McBeck et al., 2019) confirm numerically that an increase in the initial porosity tends to reduce the maximum failure stress or peak of effective friction. Although the initial porosity of the granular gouge is a key parameter it needs to be combined with gouge fabric. Indeed, an augmentation of the percentage of matrix particles reduces this effective friction peak (from MG-33 to M-S). The insertion of matrix particle corresponds to a reduction of the broader grain size distribution (that strengthens the gouge), weakening the gouge for the same reason of increasing particles of similar sizes (i.e. reducing the fractal dimension D), as observed by [(Sammis et al., 1987), (Morgan & Boettcher, 1999)].

As usual, the steady-state effective friction averaged in the "plateau" zone is almost similar with the four different samples ($\mu^*_{SS} \approx 0.5$). But minor differences can be discerned for the sample without matrix with $\mu^*_{SS-(G-C-4)} > \mu^*_{SS-(M-S)}$, because the interparticle friction used within the model from Chapter 3 is slightly higher than the one used in this chapter ($\mu_{num-(G-C-4)} = 0.5 > \mu_{num-(M-S)} = 0.3$). The augmentation of matrix particles also lowers the steady-state friction from 0.54 to 0.40 from the sample (MG-33) to (M-S). It is consistent with the change of particles shapes present within the sample (reduction of broad particles with angularities and augmentation of small hexagonal particles).

The (MG-33) sample presents a higher number of angular particles and a non-homogeneous particle size distribution within the sample enhancing again the shearing resistance.

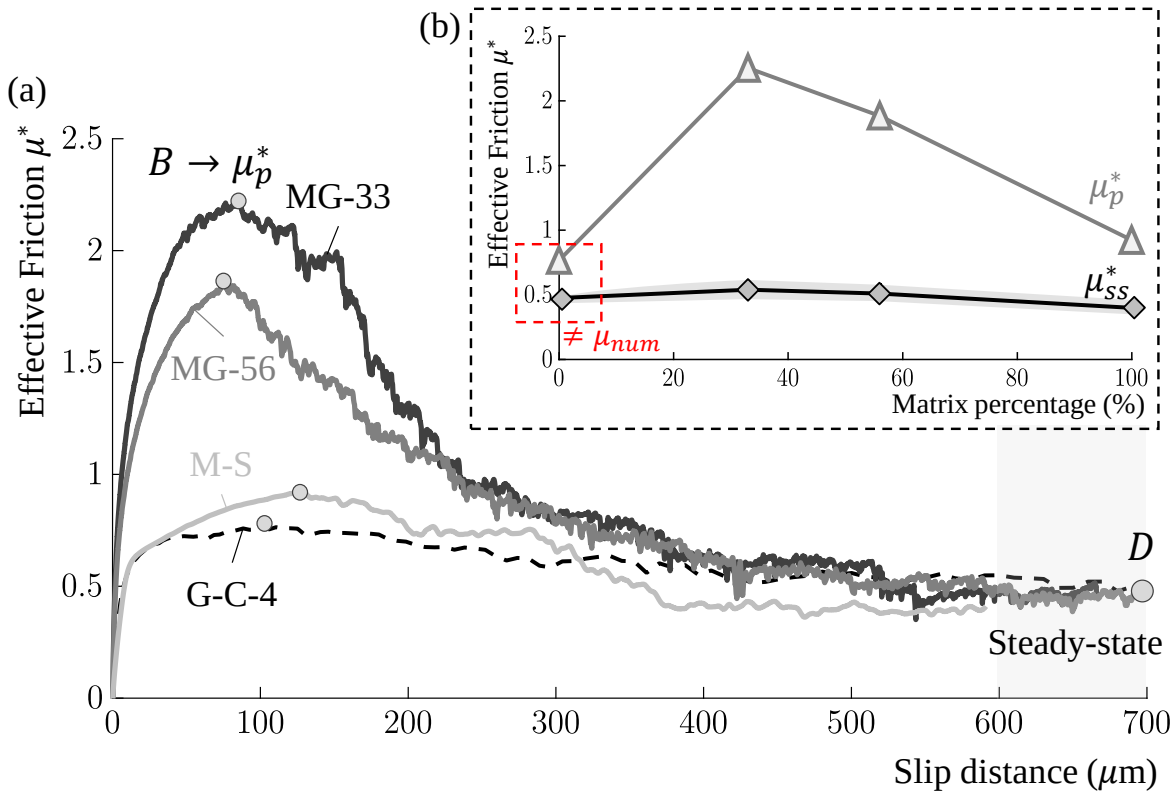

Figure 98. (a) Effective friction μ^* as a function of slip distance (μm) for the different surface percentages of matrix particles ($P_{matrix} = 0, 33, 56$ & 100 %) respectively corresponding to samples (G-C-4), (MG-33), (MG-56) and (M-S). (b) Peak of effective friction as a function of the percentage of matrix particles (triangles) and averaged value for the steady-state zone (diamonds). Sample (G-C-4) also has a different initial thickness of 1.7 mm, as opposed to 2 mm for the other cases and a different interparticle friction $\mu_{num} = 0.5$.

Homogeneity and dilation

The elastic part of the effective friction curve is similar for a percentage of matrix particles of 0 % (G-C-4) or 100 % (M-S), which are composed of only one sort of particle, whereas the two samples with composite mixture have a similar elastic part too. This evolution in the early beginning of the friction curve is mostly due to the initial presence of porosity which modifies the shear modulus and global rigidity of the gouge.

In terms of dilation, the more matrix particle is added, the less dilation is observed (Figure 99), which seems logical because the shape of the matrix particles (hexagonal) allows less expansion than angular grains. The (G-C-4) sample expands a lot because the whole gouge localizes the shear (Chapter 3), which is consistent with a high fractal dimension (Morgan & Boettcher, 1999).

On the other hand, in the material with only matrix (M-S), smaller cells imply finer displacement of particles and localization in the form of *R*-bands. The two inhomogeneous materials (MG-33) and (MG-56) are a composition of these two behaviors, with progressive decrease of dilation (at steady state).

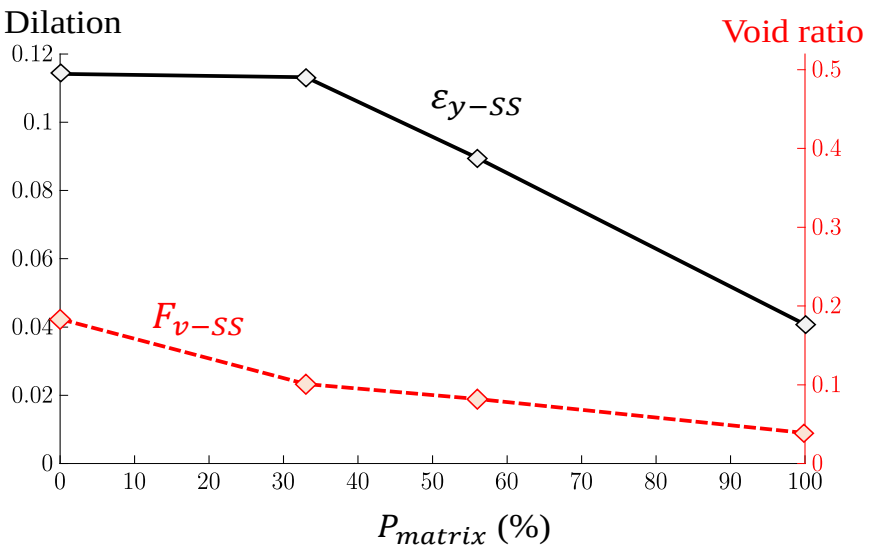

Figure 99. Dilation ε_{y-SS} and void ratio F_{v-SS} (porosity) at steady state as a function of the matrix percentage P_{matrix} within the gouge. (Dilation curves in Appendix 4.D)

Riedel bands formation and evolution

As described in the previous Part A, it is possible to study Riedel band formation and evolution thanks to the evolution of solid fraction with shearing. For material ($MG-33$), Riedel bands form before friction peak (as for (M-S) sample in previous Part A). Letters *A* to *D*, Figure 100 (a), refer to different states of the gouge with slip distance. The observed behavior is a mix between the sample used in Chapter 3 (with angular particles and cementation) and Chapter 4, part A (with matrix particles only):

(i) From the beginning of shearing and until effective friction peak (images *A* to *B*), the observed kinematic behavior is comparable to the one observed with 100 % matrix particles (M-S), where small Riedel bands progressively form. The granular sample behaves as a very dense packing.

(ii) During the weakening part (images B to D), the gouge rheology evolves and *R*-bands are less homogeneous. Two secondary *R*-bands (R_1 and R_2) tend to concentrate the total kinematic deformation but they do not reach the boundary shears.

(iii) At the end of the weakening part (images D to the end), in contrast with the behavior observed for (M-S), the *R*-bands disappear in favor of a global shear zone (*Y*) at the center of the composite mixture. This behavior is very close to the one observed for the cemented model with less than 75 % of cementation (Chapter 3), except that the shear zone is localized in the middle zone of the granular gouge. Agglomerates of particles are also observed. An explanation is that the *Y*-band cannot be formed because of the lack of *R*-bands, interrupted by the presence here and there of large unbreakable grains. The only way to shear the gouge is not by localization, but by shearing in the mass of the sample, thus necessarily by localizing on a thicker band. Normally, from an energetic point of view, the system always goes towards the solution that is the least costly. Here, there is no "easy" solution because each beginning of the previously formed *R*-band collides with some very large and rigid angular grains on their trajectory. The system is thus obliged to use the most expensive solution which consists in

expanding the whole sample. So necessarily there is more energy spent and a higher friction coefficient at the peak as observed in Figure 98. By increasing the percentage of matrix particles, we tend towards a system less expensive energetically, and the small matrix particles also result in reducing fault resistance, lowering magnitudes of coseismic slip, (Fournier & Morgan, 2012).

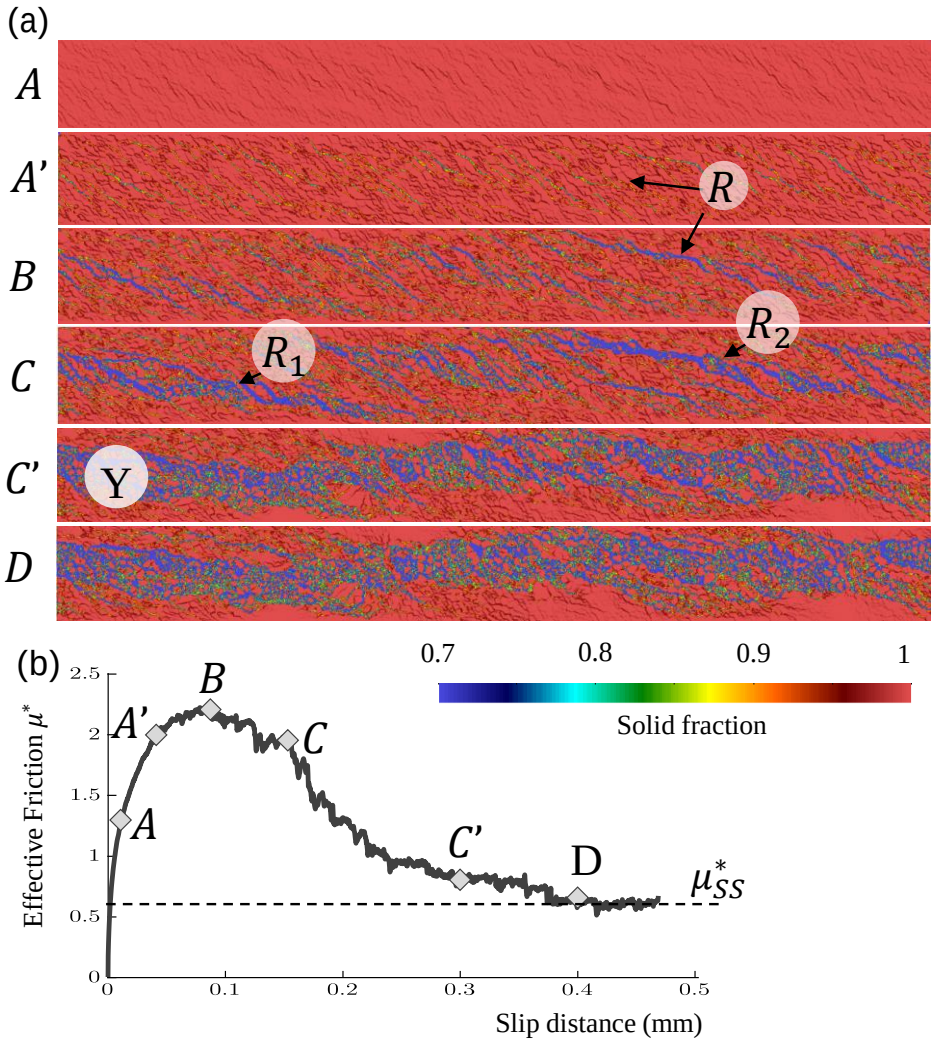

Figure 100. Solid fraction snapshots for the sample with $P_{matrix} = 33$ %, $(MG - 33)$. Letters correspond to different steps in the effective friction curve, from A to D, the beginning of the plateau zone. The solid fraction is plotted between 0.7 and 1.

4.8.2. Influence of fabric and ratio of matrix to angular grains

Qualitative comparison between the different models

Although porosity reduction is commonly recognized to have a dominant effect on the mechanical and elastic properties of sediments and other granular materials [(Schöpfer et al., 2009), (McBeck et al., 2019), (Casas et al., 2022)], the proportion of matrix, or conversely the proportion of clasts into the matrix can also have a non-negligible effect on kinematics and shear strength of granular materials. Considering previous results of section 4.8.1, and in order to compare results with a different distribution of Matrix-Grains particle, another granular sample with the same characteristics as (M-S) was modeled. This is a bi-disperse mixture with

the addition of 50 angular particles homogeneously distributed within the matrix model. The sample is called (MG-H-86), Table 10 and Figure 101.

In this section, we not only consider two particle sizes (matrix vs grains), but also different particle shapes (angular vs hexagonal) and different granular distributions (fractal distribution vs homogeneous distribution), meaning that we can only conclude on global tendency and qualitative comparisons. These are preliminary results and more experiments need to be done in order to analyze in detail the full parametric space of this sort of simulation.

Figure 101. New sample MG-H-86 with a bi-disperse mixture between matrix particles and 50 angular grains homogeneously distributed and of the same equivalent diameter ($\Phi_{eq} = 315\ \mu m$). (MG-H-86, for Matrix-Grains sample with Homogeneous distribution and 86% of matrix particles)

Table 10. Information on the sample with 50 angular particles surrounded by matrix particles. The name MG-H-86 comes from the 'MG' Matrix-Grains sample, 'H' for homogeneous distribution, and '86' for a sample with 86 % of matrix particles. P_{matrix} is the surface percentage of matrix particles, μ_{num} is the numerical interparticle friction, $\phi_{eq-matrix}$ is the equivalent diameter of matrix cells, $\phi_{eq-grains}$ is the equivalent diameter of grains, N_{grains} is the total number of angular grains and N_{matrix} is the total number of matrix cells.

Sample name	P_{matrix}	μ_{num}	$\phi_{eq-matrix}$	$\phi_{eq-grains}$	N_{grains}	N_{matrix}
MG-H-86	86 %	0.3	20 μm	315 μm	50	104 274

Shear modulus

The combined evolution of maximum shear stress and shear modulus is displayed as a function of the percentage of matrix particles, for all samples from Part B, Figure 102. Matrix percentage modifies the elastic properties of the gouge, which is both logical and an artifact of our simulation: materials with larger grains present fewer sites of elastic accommodation, and the sample is automatically stiffer with more clasts. On the other hand, the material with only angular grains (G-C-4) has a much less rigid behavior with a smaller shear modulus, because its initial porosity is much higher ($P_{pore} = 11\ \%$).

It can be observed in Figure 102 that both the maximum shear stress and the shear modulus are higher for the bi-disperse and composite mixtures, zone (ii), compared to samples with only matrix or only grains, zone (i). An augmentation of matrix content, from 33 % to 100 %, reduces the initial rigidity of the sample and thus the shear modulus. A gouge material with a high shear modulus does not present the same consequences on gouge rheology from Part A: although it increases the shearing resistance, the presence of large grains disturbs the initial mechanism and prevents the formation of a successful Riedel structure. Assuming that sample (MG-33) (with no initial porosity) and sample (M-S) (with less than 0.1 % of initial porosity) are in the same initial state of porosity, the difference between both slip behaviors is very important and mainly caused by the surface percentage of grains and matrix.

An increase in matrix content weakens the gouge until material (M-S), where a minimum shear stress and shear modulus are observed. The ratio of matrix particles content, or any different type of infill particles content, needs to be identified in each granular material and has to be

linked with the homogeneity of particle distribution within the gouge. Although it is done for most Lab experiment samples, it is not obviously considered in numerical simulations where mostly mono-disperse representations of gouge particles are simulated.

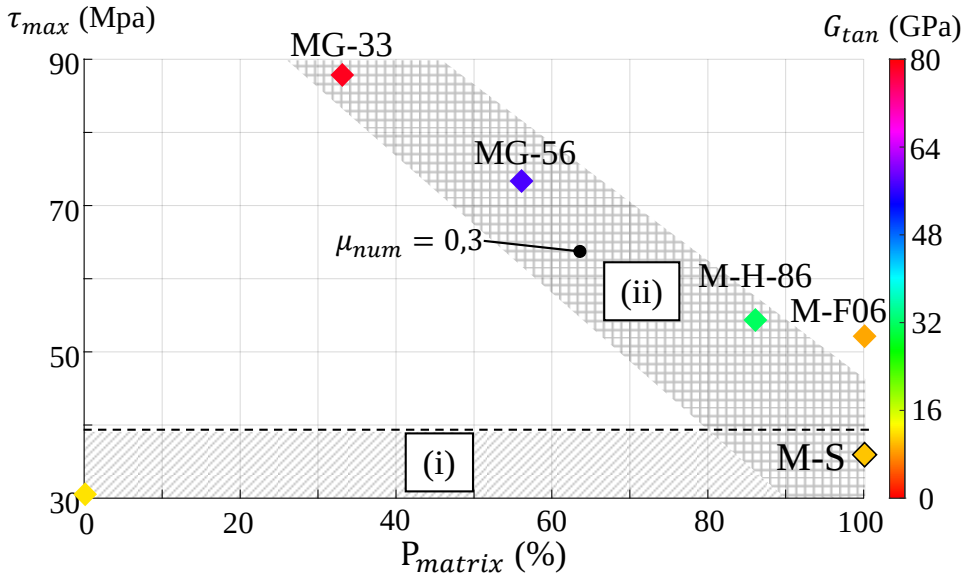

Figure 102. Maximum shear stress $\tau_{max}(MPa)$ and Initial tangent shear modulus G_{tan} (GPa) as a function of the percentage of matrix particles P_{matrix} within the sample. (i) Zone with one type of granular material (only grains or only matrix), (ii) zone with composite granular samples (grains and matrix).

Focus on clasts

In Figure 103 and Figure 104, three granular samples are compared: the standard sample (M-S) with only matrix particles, the sample (MG-H-86) with 50 big angular particles, and the sample with 56 % of matrix particles and fractal distribution of angular particles (MG-56). The three granular materials considered here have similar initial porosity (P_{pore} ~ 0 %) but different distribution and size of clasts content (angular grains). The first remark is that, whatever the angular grain distribution, an introduction of larger angular grains within the matrix model reinforces the shear strength and shear modulus. In general, the presence of large particles within shear bands limits the deformation observed (Marone & Scholz, 1989). The consequences of the addition of bigger clasts within the gouge can be separated into the three slip phases, Figure 103:

A. **Pre-peak phase.** The composition of the granular sample and the proportion of angular particles within the gouge has a huge effect on the pre-peak stage. Both shear modulus or strength peak increase with an increase of angular particles content within the model, which makes the granular media much more resistant to shearing. (Wojatschke et al., 2016) found similar results with their synthetic fault gouge mixing Clay matrix (size< $63\mu m$) and Clasts (size> $63\mu m$). Moreover, the slip distance needed to reach the peak of effective friction is smaller when the proportion of angular particles increases.

B. **Weakening phase.** When the effective friction peak is reached, three kinds of weakening are observed. In contrast with (M-S) weakening slope which is almost linear from μ_p^* to μ_{SS}^*, the slope of material (MG-H-86) is very abrupt which suggests a more

sudden post-peak weakening, reducing the slip weakening distance D_c from the one observed for (M-S). This behavior is prone to switch the fault behavior from a ductile aseismic response to a brittle seismic slip, (depending on the stiffness of the surrounding medium, which is infinite in our case). Contrarily to what we could expect, the weakening observed for material (MG-56), with more angular particles, does not follow the sudden slip-weakening of material (MG-H-86), and presents a non-linear weakening. The fractal distribution of particles in the gouge (MG-56) may be responsible for this different weakening slope. Despite the mechanical difference between sample (M-S) and (MG-H-86) in terms of strength peak, the rheological behavior at effective friction peak does not seem to be disturbed, Figure 104 (a) & (b) image 1. The same Riedel bands are observed for both samples. Gouge (MG-56) have different Riedel bands at effective friction peaks, which are more numerous and homogeneously distributed within the gouge, maybe due to the non-homogeneity of the material. It is a kind of "dense fractured network" where no principal Riedel band manages to develop sufficiently.

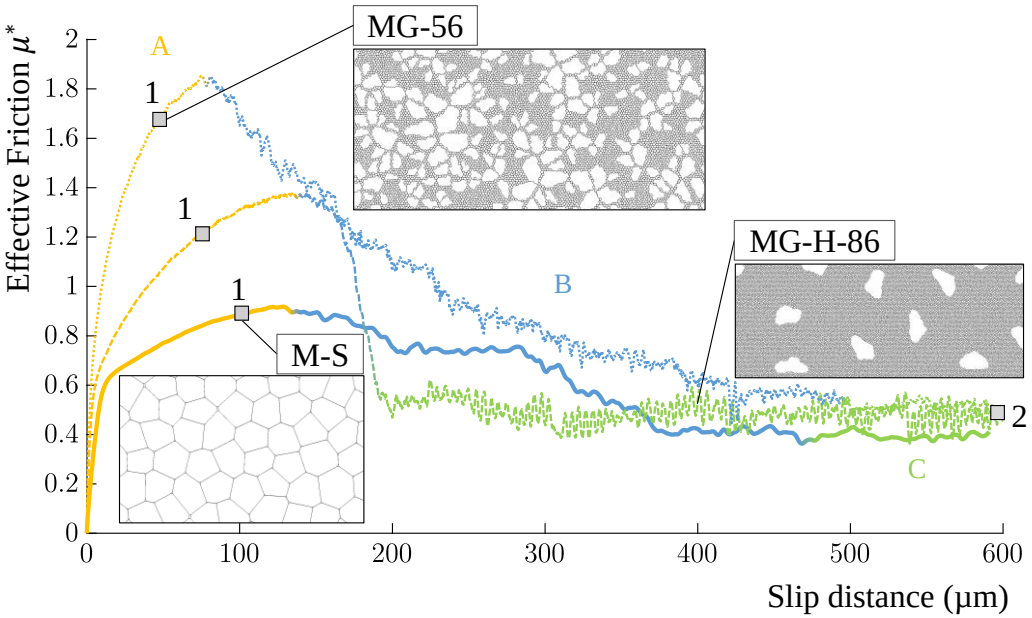

Figure 103. Effective friction μ^* as a function of slip distance (μm) for three granular samples: (a) the standard gouge sample (M-S) with only matrix particles, (b) the gouge (MG-H-86), and (c) the gouge with matrix particles and fractal distribution of angular particles (MG-56). The three granular materials are considered to have identical initial porosity (P_{pore} ~ 0 %). Zone A is the pre-peak zone, zone B is the weakening zone and zone C is the steady-state zone.

C. **Steady-state zone.** Steady-state effective friction tends to a similar value for the three gouges. Samples (M-S) and (MG-H-86) present the same two Secondary Riedels, meaning that in the sample (MG-H-86), the addition of big clasts is not sufficient to change the rheology of the gouge. However, differences are observed near clasts, leading to small and very localized conjugate Riedels, Figure 104 (i). The last gouge (MG-56) has a completely different rheology with no Riedel bands observed (as for MG-33 described in 4.8.1). This granular material presents agglomerates of particles surrounded by porosity with a clearly identified and unique shearing zone at the center

of the gouge. It is supposed that the shearing zone will be extended to the entire gouge thickness for a longer time of the experiment. These results seem consistent with those of (Y. Lu et al., 2017) increasing percentage of clasts contents, or (Wojatschke et al., 2016) increasing clay content within a fault gouge mixture of clay matrix and clasts: by increasing clast content the development of Riedel shears is less evident. (Wojatschke et al., 2016) also noticed that the percentage of clasts controlled the degree of orientation of the strain localization.

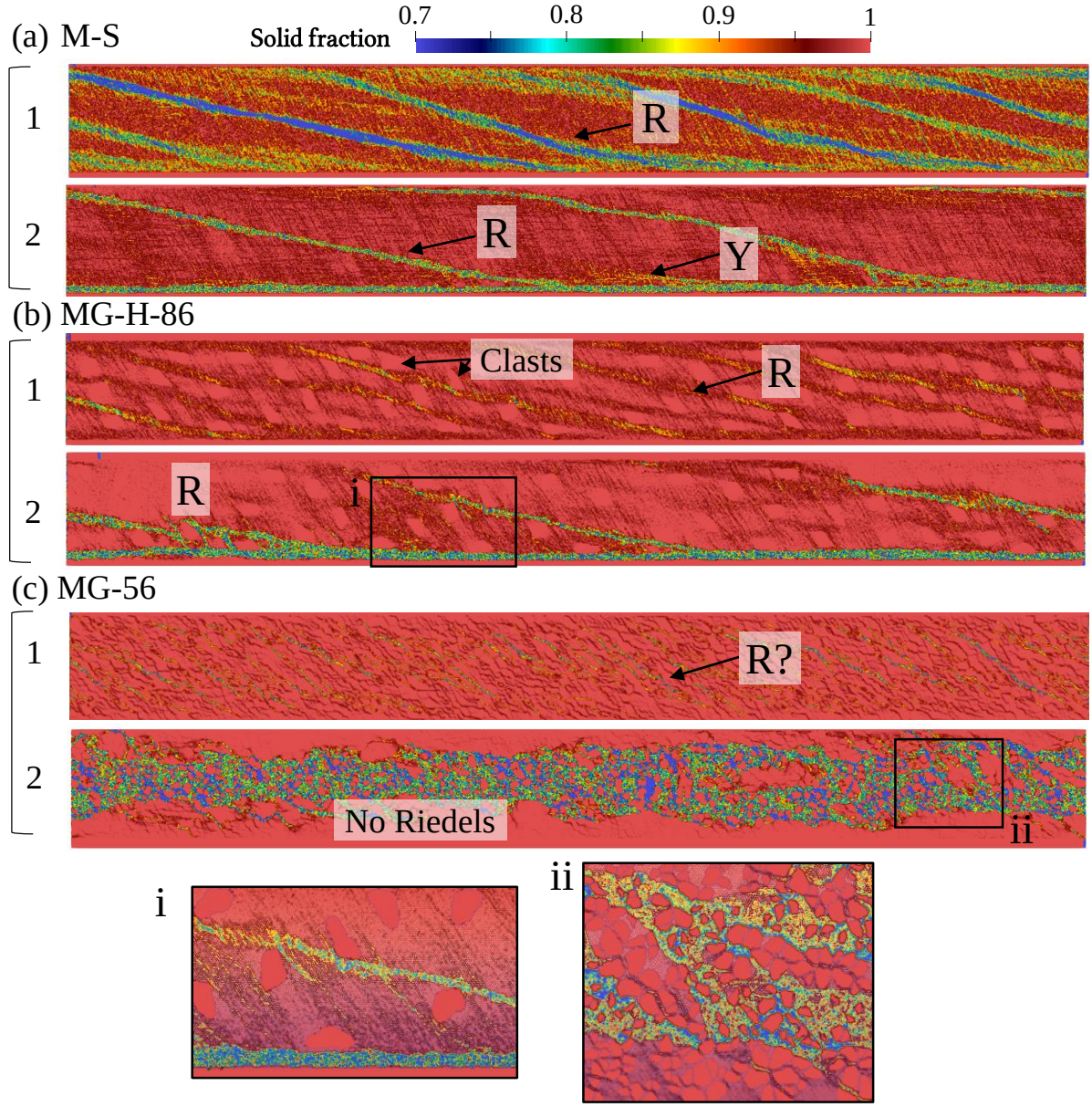

Figure 104. Riedel bands evolution through solid fraction representation (0.7 to 1) for the three different samples: (a) the standard sample (M-S) with only matrix particles, (b) the new sample (MG-H-86), and (c) the sample with matrix particles and fractal distribution of angular particles (MG-56). (i) Zoom in on the steady-state of the sample (MG-H-86) and (ii) zoom in on the steady-state zone of the sample (MG-56).

The oscillations observed in the effective friction curves for samples (MG-H-86) and (MG-56) could look similar to oscillations from stick-slip experiments, but here they are simply due to variation in friction created by changing contact interactions at the interface.

Granular materials from type (MG-i) seem to be the most optimal configuration to increase the shearing resistance, and the absence of Riedel bands at steady-state reduces the possibility of stick-slip to happen. On the other hand, very loose material or with a low diversity of material (homogeneous material) will lead to break much more easily with sudden stress drop, as material (MG-H-86). However, these results do not consider clay materials, for example, which have different elastic and frictional properties that can also lead to a loss of gouge strength and thus a change in stability. In their studies (Collettini et al., 2009) show for example that the sliding behavior of rocks is weakened by the presence of phyllosilicate (talc and smectite). They concluded that fault weakening strongly depends on rock fabric and on the distribution of weak phases within a fault zone. (Kenigsberg et al., 2020) proposed that, depending on matrix or particle content (smectite in that paper), fabric and shear plane development also play a key role in the evolution of these properties with shearing. In lab experiments or real faults, fragmentation of particles is also observed (Marone & Scholz, 1989), decreasing the porosity within the sample with shearing (Kenigsberg et al., 2019). It modifies the total contact of particles and plays a role in fabric evolution, and so on effective friction and elastic properties, a phenomenon that we don't have here as no fragmentation is considered.

4.9. Conclusion of Part B

Direct shear tests were conducted on the composite mixture, clearly showing that the surface percentages of both matrix and angular particles have a huge influence on the mechanics and rheology of fault gouge. The existence of angular particles or initial porosity also affects the shape and thickness of shear bands in the specimens. Inserting angular particles within matrix cells or matrix cells within a granular sample strengthens the gouge and gives different weakening behaviors depending on the type of particle distribution within the sample.

- For a gouge with a small matrix percentage, the friction peak shape is sharper, and slip weakening is more sudden with higher stress drop, also implying the possibility to switch the fault behavior to a more brittle seismic slip. The high number of angular particles and the non-homogeneous particle size distribution within the sample enhance again the shearing resistance. The energy needed to weaken the fault is much higher: Riedel bands cannot join the rock walls and form boundary shears, leading to a deformation of the entire gouge thickness.
- Inhomogeneous and fractal particle distribution seems to favor a smoother slip weakening than homogeneously distributed clasts.
- The temporality of Riedel bands formation depends on the percentage of the infill matrix material.

More results are needed to analyze the different behaviors observed such as a modification of the intrinsic deformability of matrix material, to represent clay content for example.

Chapter 5. From energy budget to simplified models, towards dynamic simulations

Main foreword

This last chapter is both a synthesis of previous chapters and an opening for the continuation of the thesis. Starting from the results of Chapters 3 and 4, and focusing on friction laws and energy budget, the objective is to define friction laws characteristic of each type of infill material that can be injected into a large-scale dynamic fault model. For that we will distinguish three completely independent parts:

- Part A is a comparison of numerical frictional responses to linear slip weakening models from the previous models of Chapters 3 and 4. The linear slope of slip weakening, the associated fracture energy, and the nucleation length are extracted, compared and discussed.

- Part B restarts from the results of Chapter 3 on cemented models. A new partitioning of breakdown energy is discussed, allowing to differentiate three energy contributions from Coulomb friction, dilation and cementation failure process. This representation allows the construction of a simplified macroscopic friction model which has the final objective to be injected into dynamic failure models at a higher scale. The fracture energy and slip behavior of the fault gouge appears to be controlled by the intensity and temporality of these three mechanisms.

- Part C is built on the results of Chapter 4, Part A, and presents a Spatio-temporal analysis of Riedel bands activations and their implication in the global behavior of fault gouges. We connect the mechanical behavior inside each band to the entire gouge kinematics by the means of an energetic approach.

This chapter will lead to two upcoming papers:

Casas, N., Mollon, G., & Daouadji, A. (2022) Energetic study and simplified models for cemented granular fault gouges. (*in prep*)

Casas, N., Mollon, G., & Daouadji, A. (2022) Time and space evolution of Riedel bands in a dense granular material, relation to the evolution of the entire gouge. (*in prep*)

Part A – Comparison to classical slip weakening

5.1. Foreword

In order to study more deeply the results obtained in the previous chapters (cement and matrix), it may be interesting to first interpret them according to a very simplified model such as the linear slip weakening model (Chapter 1). Thanks to this representation it is possible to extract the slope associated to slip weakening models, which gives information on the stability of the system. The rupture energy and critical nucleation length associated with each model are calculated to relate to the intensity of seismic events that may occur. In the first section 5.2, the method used to recover and compute the different parameters is explained. Section 5.3 compares and discusses the results obtained for the different models, with a focus on the critical nucleation length associated with simulations and on the influence of each of the tested materials, section 5.3.2. This section gathers the data obtained for each simulation used during the Thesis work as sketched in Figure 105.

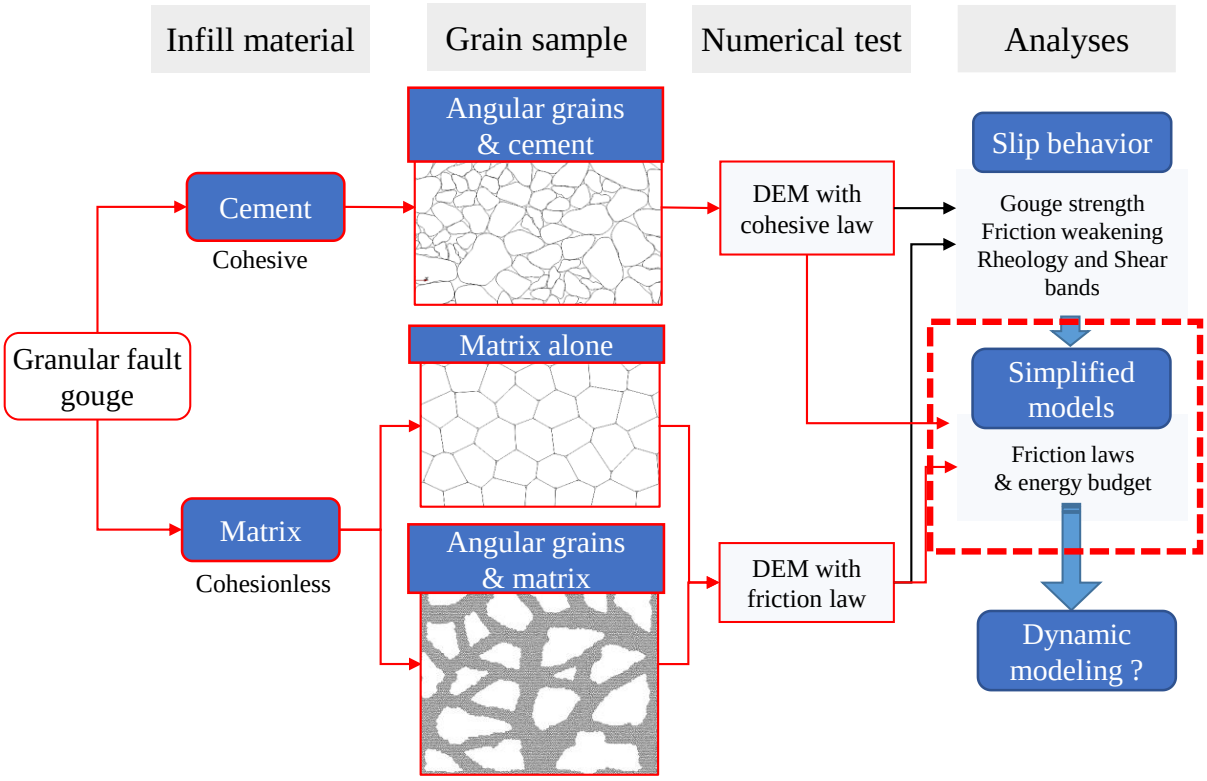

Figure 105. Main schema of Chapter 5, Part A. All the data are collected from each model.

5.2. Method and theory

Breakdown energy

Throughout an earthquake, energy is dissipated during fault sliding by the means of different mechanisms, gathered in the total energy budget ΔW, the sum of a fracture energy E_G, a radiated energy E_R and a frictional energy E_H (Chapter 1). In this section, the focus is made on post-peak rupture energy called E_G (J/m^2), or Breakdown Energy, which is the potential energy needed to weaken the fault. It can be calculated from previous numerical results of Chapters 3

and 4, as the area under the friction-slip curve, corrected by subtracting the steady-state friction (eq. (1.11) of Chapter 1).

Critical weakening slope

One possibility to determine the laboratory rock failure stability is to compare the stiffness of the fault with its weakening rate. The objective here is thus to calculate the equivalent critical slope K_c of the slip weakening models (Chapter 1, eq. (1.9)), for all simulation cases with different infill materials (cementation and matrix).

Slip instabilities may occur if the loading stiffness of the fault K (i.e. stiffness of the loading system) appears to be lower than K_c ($K_c > K$). Apart from being an essential parameter for RSF laws, K_c is thus an essential quantity in terms of stability. It is expressed here in GPa/m and can be extracted from each of the friction curves presented all over the manuscript, provided that we accept to fit a linear weakening model on the post-peak frictional response of each of our faults, Figure 106. The Breakdown energy E_G (J/m^2) is first computed as the area under the shear stress curve from the stress peak τ_p to the averaged steady-state shear stress τ_{SS}. The critical sliding distance D_c, is determined to obtain an energy $E = (\tau_p - \tau_{ss}) * D_c/2$, similar to the E_G previously calculated (yellow area, Figure 106). In Figure 106, K_c fits well with the shape of the decreasing shear stress, but it is not as satisfactory for all the models tested (Appendix 5.A).

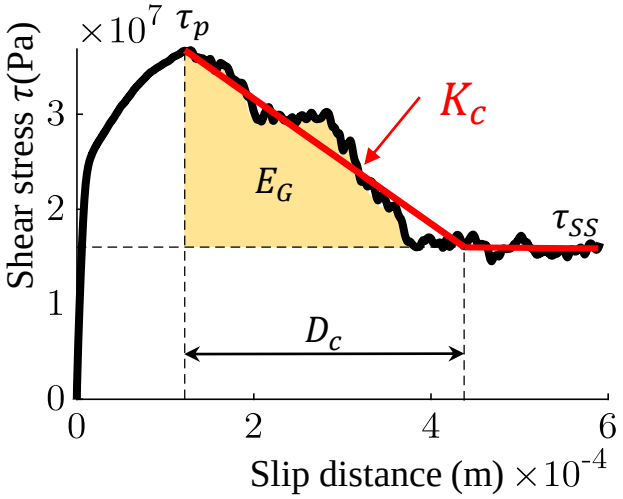

Figure 106. Illustration of the two parameters previously described for the standard case M-S (Chapter 4) where the shear stress variation (Pa) is observed as a function of the slip distance (m). The slope $K_c = \frac{|\tau_{SS} - \tau_p|}{D_c}$ is calculated to have the same energy in J/m^2 for the triangle generated by the slope line than the E_G (colored in yellow). Breakdown energy can be calculated as $E_G = \int_0^{D_c} (\tau(U) - \tau_{ss})\, d_U \approx (\tau_p - \tau_{ss}) * \frac{D_c}{2}$. With τ_p the maximum shear stress (Pa), τ_{ss} the dynamic (or steady-state) shear stress (Pa) and D_c is critical slip weakening distance (m).

Nucleation length

Even though K_c can be extracted from each model, the difficult question remains: what is the stiffness of the crust, and to what quantity should the critical stiffness be compared? In laboratory experiments, it should be the stiffness of the loading apparatus, but for numerical experiments, we don't have such value to consider. From crack theory, the global loading

stiffness K is defined by the ratio of stress to displacement $K = \tau/U$. The fault stiffness K is found to be proportional to the ratio G/L, with G the shear modulus and L the length of the slipping fault section, meaning that the loading stiffness decreases as the slipping fault section increases, Figure 107 (a).

If the slipping region is treated as an elliptical crack (Scholz, 2019), the critical nucleation length before instabilities can be calculated as

$$L_c = \frac{E}{2(1-\nu^2)K_c} \tag{5.1}$$

With E a relevant young modulus (or equivalent elasticity modulus), ν the Poisson ratio and L_c the critical length of the slipping region. The fault is supposed to be unstable when the slipping fault section exceeds the critical nucleation length L_c. Figure 107 (b) illustrates the dynamic behavior observed when L_c is reached.

The objective here is not to have the "exact" value of L_c, but to observe the global trend and to put forward a dependence on certain gouge characteristics. The choice was made to compare all the results with the same Young modulus and Poisson coefficient as if the same fault rock material was compared. Medium values for granite material are considered, E~60 GPa, and $\nu = 0.3$, with an approximative K_{mean}~900 GPa/m (considering the 20 mm- length gouge).

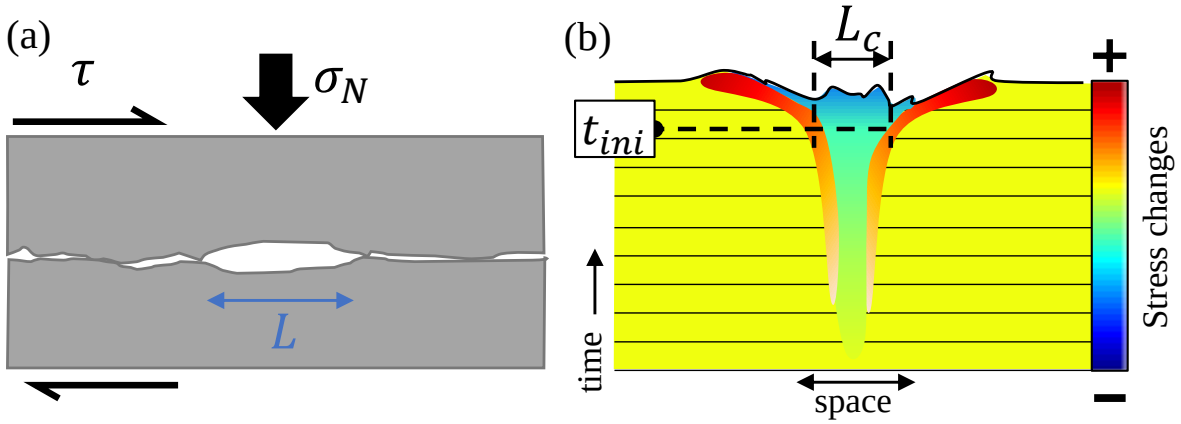

Figure 107. (a) A schematic figure showing the nucleation length L on a frictional fault plane, (figure redrawn from (Kanamori & Brodsky, 2004)). (b) Initiation of dynamic rupture from a smooth nucleation model, (figure redrawn from (McLaskey, 2019)).

5.3. Comparison between the different gouge materials

5.3.1. Evolution of the slope of slip weakening and breakdown energy

In this section, all the results from the previous chapters are gathered in terms of Breakdown energy E_G, Figure 108, and linear weakening slope K_c, Figure 109. From a first glance at the results, it can be observed that the percentage of infill material, either matrix or cement (image (b) and (c) in each figure) has much more influence on these two quantities than the inner characteristics of the gouge that show a smaller difference between the extrema obtained.

Breakdown energy

The observed breakdown energy E_G ranges between 1 kJ/m^2 and 10 kJ/m^2, values in the range to those of laboratory and seismological estimated fracture energy, ranging between 1 J/m^2 and 10 MJ$/m^2$ for minerals and rocks [(Abercrombie & Rice, 2005), (Nielsen et al., 2016), (Scholz, 2019)]. According to (Nielsen et al., 2016) and large data set from our simulations, the total associated slip observed for our fault gouge would be ranged between 1 and 10 mm.

The evolution of breakdown energy appears to mostly depend on the ratio of infill material within the granular sample, Figure 108 (b) and (c), with values close to $10^4\ J/m^2$. While increasing the percentage of cementation promotes higher fracture energy, increasing the percentage of matrix decreases the fracture energy: a matrix percentage higher than 80 % shows breakdown energy around $10^3\ J/m^2$, as well as mid-dense and low cemented models. On the other hand, for dense materials (either very cemented or with a very little percentage of matrix particles), energies are displayed around $10^4\ J/m^2$, suggesting much more intense seismic events in case of slip initiation. Changing cells perturbation, Figure 108 (a4), does not have a huge influence on the total breakdown energy. However, an increase in breakdown energy is observed when changing the interparticle friction from 0.1 to 0.6, Figure 108 (a1), the size of particles from 20 to 50 mm, Figure 108 (a2), or even the interparticle stiffness from 10^{15} to $10^{16}\ Pa/m$, Figure 108 (a3).

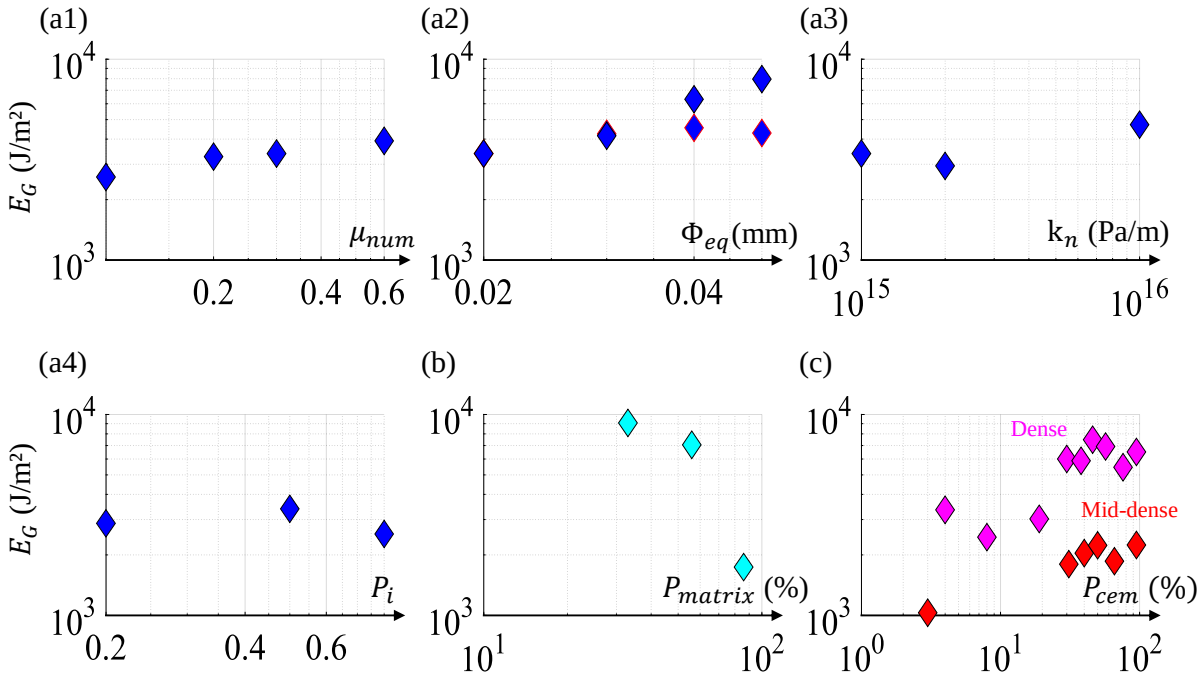

Figure 108. Evolution of the breakdown energy (J/m^2) as a function of different parameters. (a) Matrix samples (M-…) with gouge parameters variation: (a1) as a function of the interparticle friction μ_{num}, (a2) as a function of the size of particles Φ_{eq} (mm), (a3) as a function of the interparticle stiffness in k_n (Pa/m), (a4) as a function of the cell perturbation P_i. (b) Composite mixture between matrix and grains (MG-samples) with variation of matrix percentage. (c) Cemented samples (G-samples) with variation in the percentage of cement for both dense and mid-dense samples.

Linear weakening slope

Even though the inner characteristics of the gouge have more influences on the Linear weakening slope K_c, they are still negligible compared to the variation in the surface percentage of matrix or cement, Figure 109. In line with the results of Chapter 4, Part A, a significant influence of the interparticle friction coefficient and the particle size is observed on the K_c value. Increasing friction increases the inclination of the weakening slope, which enhances the probability of generating an instability while the increase in the size of the particles has the opposite effect when it is cumulated with an equivalent stiffness allowing to have a constant shear modulus.

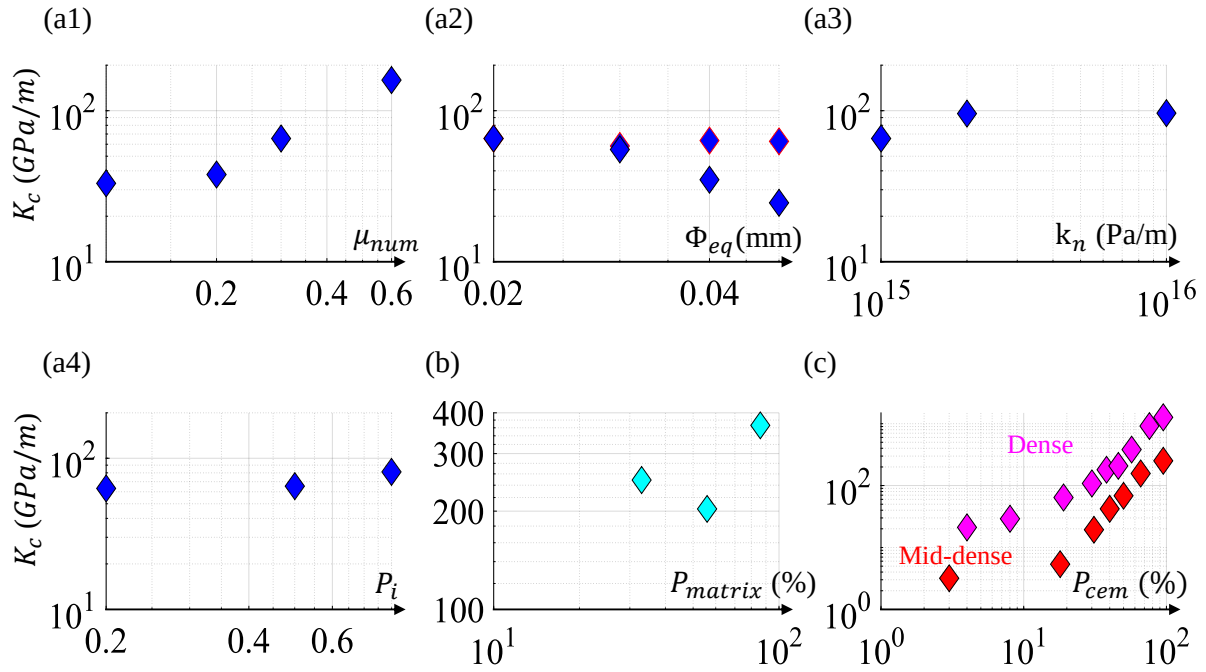

Figure 109. Evolution of the linear slope of weakening $K_c\ (GPa/m)$ as a function of different parameters. (a) Matrix samples (M-…) with gouge parameters variation: (a1) as a function of the interparticle friction μ_{num}, (a2) as a function of the size of particles Φ_{eq} (mm), (a3) as a function of the interparticle stiffness in k_n (Pa/m), (a4) as a function of the cell perturbation P_i. (b) Composite mixture between matrix and grains (MG-samples) with variation of matrix percentage. (c) Cemented samples (G-samples) with variation in the percentage of cement for both dense and mid-dense samples.

Shear modulus, friction, and number of particles within the gouge thickness, Figure 110

As interparticle friction, the shear modulus, and number of particles within the gouge thickness selected in Chapter 4, were playing on the Riedel structure observed, they also influence E_B and K_c. Going back to the matrix materials dataset, a link between the breakdown energy and the ratio nb_1 is observed: a slight increase in E_G is observed when decreasing nb_1 with the opposite effect on K_c. However, an increase of K_c, even for a low energy, can be quite penalizing, as it also implies a reduction of the sliding distance necessary to weaken the fault, which could tend to rather an unstable sliding.

These results agree with the Riedel structure observed in Chapter 4: materials with lower K_c presented lower Riedel angles and a highly visible Riedel structure, promoting slip stability. A high value of initial tangent shear modulus increases both K_c and E_G, although its influence is less important than nb_1 or μ_{num}.

In the case where there is both an increase of shear modulus and a decrease in nb_1, the two effects compensate with almost no variation in both K_c and E_G, as observed for an increase in the size of particles, Figure 109 (a2).

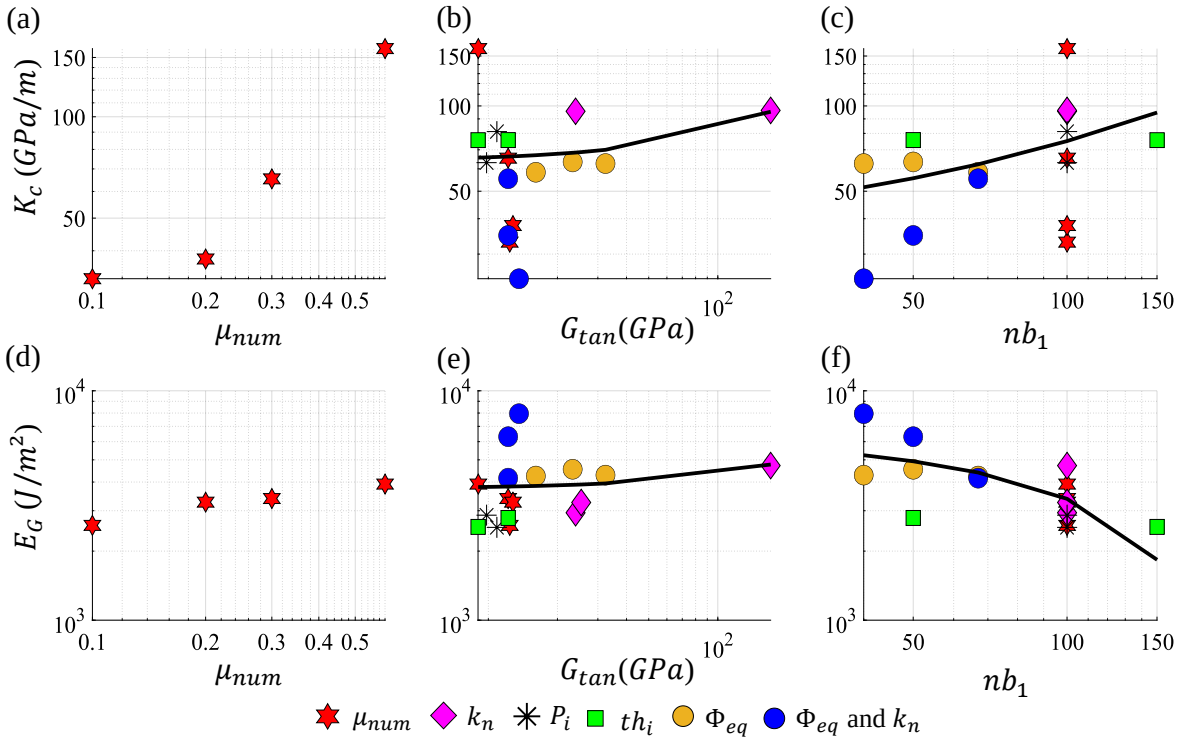

Figure 110. Evolution of the linear slope of weakening $K_c\ (GPa/m)$ as a function of (a) the interparticle friction μ_{num}, (b) the initial tangent shear modulus $G_{tan}\ (GPa)$ and (c) nb_1 the ratio of gouge thickness on particle size. Evolution of the breakdown energy $E_G\ (J/m^2)$ as a function of (a) the interparticle friction μ_{num}, (b) the initial tangent shear modulus $G_{tan}\ (GPa)$ and (c) nb_1 the ratio of gouge thickness on particle size. Matrix samples (M-…) with gouge parameters variation: particle size with equivalent stiffness (dark blue circles), particle size (orange circles), the initial thickness of the gouge (green squares), interparticle stiffness (pink diamonds), interparticle friction (red hexagrams) and perturbation shape (black asterisks). Linear regression line in black.

5.3.2. Critical nucleation length and stability consequences

A slip within fault can become problematic when a change from slow slip to fast stick-slip is observed, which is mainly due to an alteration of the elastic stiffness of the crust (for crustal faults) or the loading apparatus (for laboratory experiments) or a change within gouge material properties. According to several recent studies, it has been shown that the evolution of the gouge fabric is of major influence in the observed slip patterns with shearing.

Simulations from this Thesis work do not allow to conclude on the stability of the system, as shearing is perfectly displacement-controlled and no global stiffness is present. Although we cannot calculate the total nucleation length of the system, it is possible to calculate for each experiment a critical nucleation length from which, depending on the medium stiffness, the fault could switch to fast stick-slip and thus instabilities.

The evolution of the critical nucleation length Lc is computed according to the previous method (Section 5.2). The obtained curves, Figure 111, are directly the inverse curves of those observed for Kc, as a direct consequence from equation (5.1). These results can then be interpreted in terms of instabilities and linked to higher-scale faults.

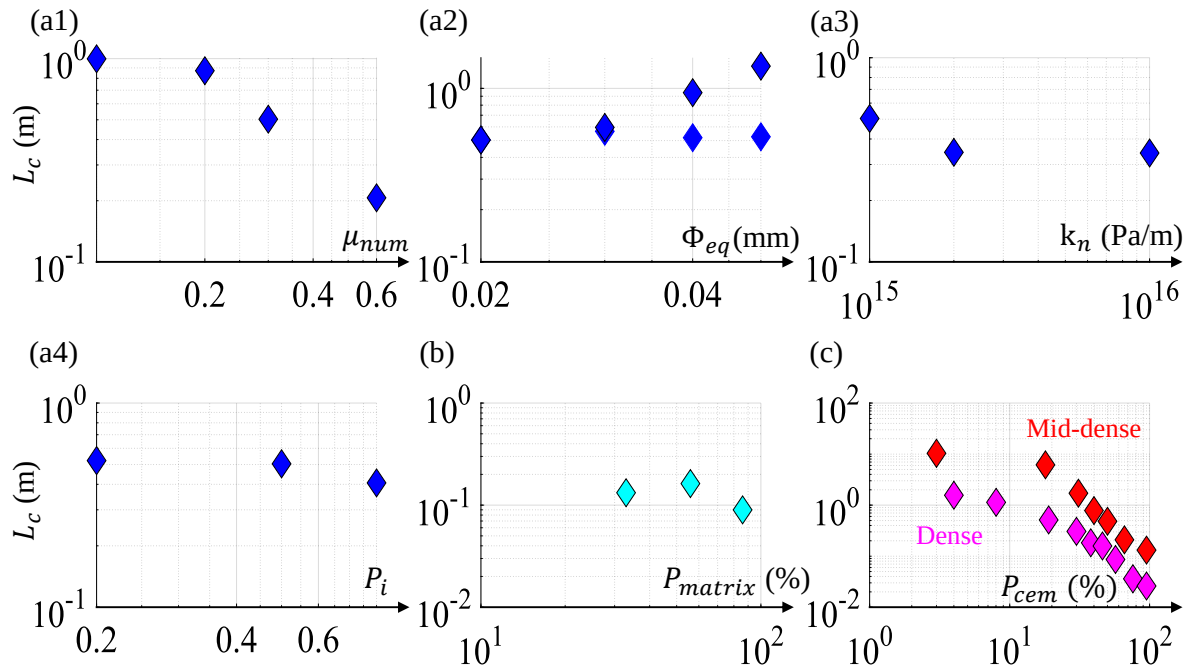

Figure 111. Evolution of the critical nucleation length L_c (m) as a function of different parameters. (a) Matrix samples (M-…) with gouge parameters variation: (a1) as a function of the interparticle friction μ_{num}, (a2) as a function of the size of particles Φ_{eq} (mm), (a3) as a function of the interparticle stiffness in k_n (Pa/m), (a4) as a function of the cell perturbation P_i. (b) Composite mixture between matrix and grains (MG-samples) with variation of matrix percentage. (c) Cemented samples (G-samples) with variation in the percentage of cement for both dense and mid-dense samples.

The last Figure 112 presents the critical nucleation length as a function of the breakdown energy for each simulation. The majority of critical nucleation lengths are observed in between 0.1 and 1 m but some off-center zones are noticed:

(i) **High L_c and low E_G** – The mid-dense samples with nearly no cementation ($P_{cem} < 25\ \%$) show a material with a large critical nucleation zone ($L_c > 3\ m$) and very low breakdown energy ($E_G \leq 10^3\ J/m^2$). By increasing the critical nucleation length, more flexibility of movement is allowed within the sliding zone before going into instabilities, Figure 107, leading to a less rigid fault. This implies that these materials are not very susceptible to become unstable. Even if instability were to occur, the energy released by slip would be small compared to other materials tested. These mid-dense materials without cementation have characteristics that are rather susceptible to generate slow sliding.

(ii) **Medium L_c and medium to large E_G** – This second zone gathers most of the samples studied. For $E_G > 10^3\ J/m^2$, a linear relation describes the link between the observed fracture energy and its associated critical nucleation length (black line). Although the range of observed L_c is similar, the gradient of fracture energy observed is more important. As previously observed in section 5.3.1, higher fracture energy mostly corresponds to higher resisting strength of material: high cementation, a small percentage of matrix particles, or high interparticle friction. Increasing the size of

particles (top right corner) both increases the L_c and the E_G resulting in delaying earthquake nucleation.

(iii) **Low L_c and high E_G** – In contrast, this last zone is characteristic of highly dense and cemented materials ($P_{cem} > 75$ %). For a very small critical nucleation zone, there is not much mobility allowed for the system and more risks that the model goes into instability with a high-stress release. It also depends on the length of the fault which will add rigidity to the global model (but here all samples have the same length). As a difference with the ductile material presented in (i), these materials are almost brittle, the consequences in terms of instabilities and energy release are mostly related to this brittle behavior.

The main behavior differences appear for the two extremes cemented materials observed in Chapter 3, which seems consistent since they represent a rather ductile behavior (mid-dense, with no cementation), which tends to give a rather stable sliding and its brittle opposite (dense and highly cemented) which tends to rapid changes of behavior, leading to a rather unstable sliding. Another lecture of the data is possible by looking at the linear regression lines corresponding to each of the four types of materials tested. The two cemented materials (dense and mid-dense) follow similar evolutions with a shift due to the initial porosity of the sample. In the same way, the two materials with matrix particles follow the same evolution with a shift in the nucleation length, this time due to the presence of large grains in the sample which decreases the critical nucleation length. Samples with matrices follow a different slope than those without: the presence of matrix particles changes the scaling. It would be interesting to compare these data with in-situ or lab experiments.

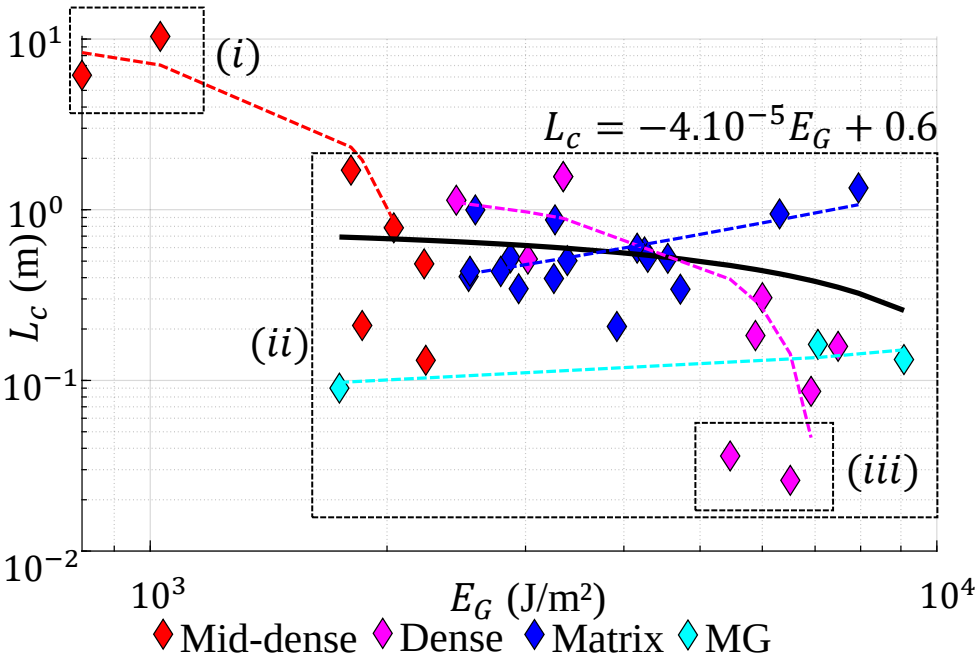

Figure 112. Evolution of the critical nucleation length L_c (m) as a function of the breakdown energy (J/m^2) for different parameters. Matrix samples (M) with matrix parameters variation are colored in dark blue, (b) Matrix-grains samples (MG) composite mixture) with a variation of surface percentage of matrix particles are colored in light blue. Cemented gouge samples (G) with a variation of the surface percentage of cement for both dense (colored in pink) and mid-dense samples (colored in red). The black line represents the linear regression of the data set for the selected zone. The three different zones are explained within the text.

Analyses could be improved by studying these same materials with the presence of water. Besides, in the proposed definition of L_c, time dependence is not considered. However, according to a recent study (McLaskey, 2019), L_c has to be carefully used for rough and heterogeneous faults which need an intrinsic time dependence law such as power density (strain energy released per unit time per unit area). It could be another comparison to make with our samples. Then, there are two very important aspects that we almost didn't address here: the influence of normal stress (because the results presented here are only valid for 40 MPa) and the gouge thickness, probably inoperative in some cases (dense and very cemented materials that fracture horizontally) and important in other cases (inclined Riedel of matrix cases that have more or less time to develop). It is obvious that a change in the applied normal stress will affect these parameters. It would be interesting to repeat this study for cases where the confining pressure is much higher, in order to judge the evolution of these parameters under such stresses.

> Even though we can compute and compare the critical nucleation lengths with literature, it is not possible, at this step, to say whether or not the system is stable or unstable. For this reason, friction laws observed need to be inserted in dynamic modeling considering the global stiffness of the fault and a dynamic rupture process. This is expected to be a natural perspective of the present thesis.

5.4. Conclusion of Part A

Infill materials, which are playing on gouge fabric, have a major role in the critical nucleation length and fracture energy released. The cementation within the gouge seems to be the most influent parameter tested and an initially dense cemented material will tend to a very short slip distance before instabilities occur (small L_c) as well as a high breakdown energy (high E_G).

Even though they take place in a specific range of experiments (constant imposed pressure, constant slip velocity, and absence of water), our results raise the question of the slip weakening shape. It appears that only mid-dense cemented samples and some matrix samples can be easily modeled with the classical linear form (Appendix 5.A). Dense cemented samples display a bilinear decreasing shape that can be compared to a model proposed by (Abercrombie & Rice, 2005). Exponential weakening models are used by (Sone & Shimamoto, 2009) in their high-velocity friction experiments. Although their results cannot be directly compared with those presented here, the friction curve described by an exponential fit is consistent with some of our mid-dense cemented samples but not for dense cemented samples. A reason that could explain this difference is that a simple exponential weakening considers that all the physics is acting at the same time, which is maybe not the case for very cemented material.

Simple slip weakening models are intended to approximate behaviors to make them more tractable to use for understanding fault weakening with displacement (Chapter 1). Real fracture is well known to be much more complex, but complex models are difficult to upscale. A balance must be found between a too simple and a too complex model. For this reason, we propose other friction and energetic laws linking local rheology and gouge mechanics in the next two sections.

Part B – Energetic study of cemented gouges: a way to friction laws

5.5. Foreword

Previous simulations from Chapter 3 show that a modification of the initial porosity (i.e. density), or of the cementation within the sample could induce an important change in slip mechanisms. In order to isolate the main mechanisms acting on fracture processes, a partitioning of the total macroscopic friction generated during the shearing of a granular gouge sample is proposed. Based on the physical content of the numerical model used, three factors are identified as playing a role in the total effective friction and energy partitioning:

- The dilation of the gouge, or deformation in the y-direction perpendicular to the sliding
- The damage coming from the breakage of cohesive bonds due to cementation
- The friction generated by sliding contact interactions

These contributions will be calculated thanks to global potential energy recovered at each time step, from the data set presented in Chapter 3 and computations details presented in the next sections, Figure 113. The objective of this part is not to "re-discover" the main mechanisms involved in fracture mechanics, but above all to be able to clearly locate and quantify these three mechanisms and their interaction with fault rheology.

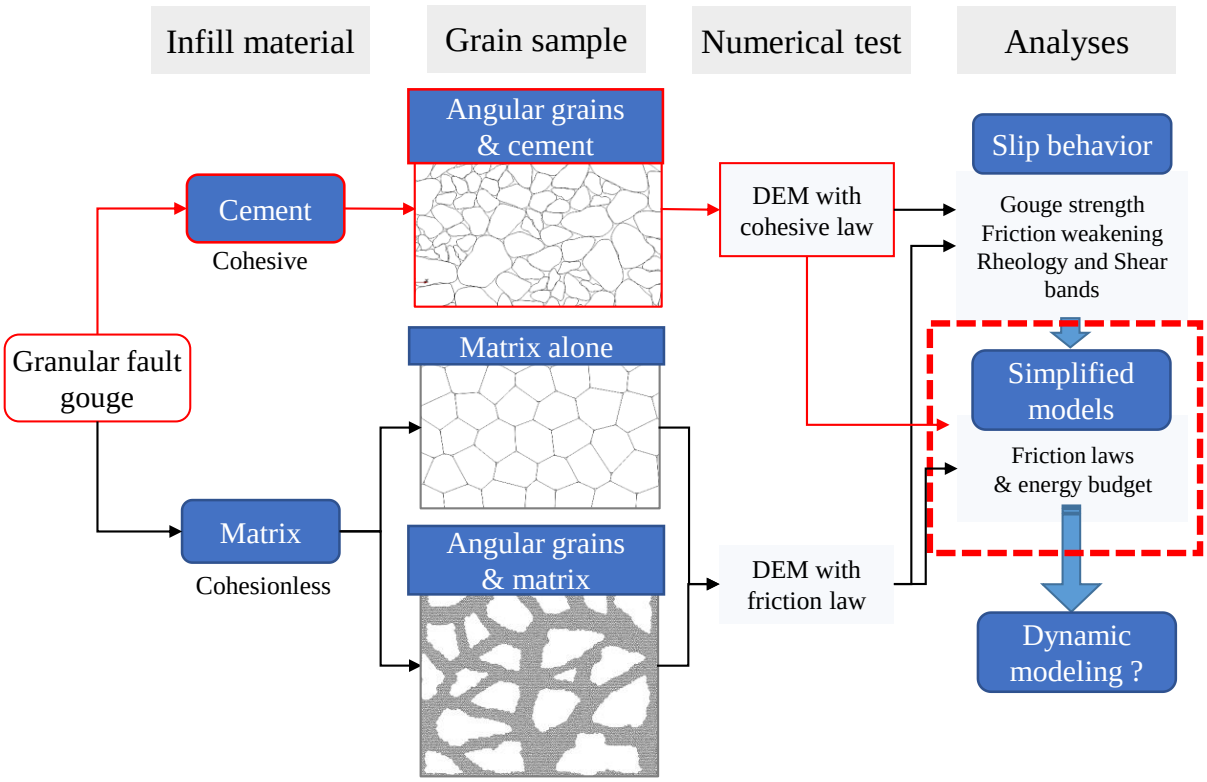

Figure 113. Main schema of Chapter 5, Part B. All the data are collected from cemented granular gouge model (Chapter 3).

5.6. Decomposition of sliding friction – Method

5.6.1. Breakdown energy partitioning

Definition of breakdown energy

In this section, the focus is also made on post-peak rupture energy called E_G (J/m^2), for Breakdown Energy, previously calculated on Part A. It is calculated from previous numerical results (Chapter 3), as the area under the friction-slip curve, corrected by subtracting the steady-state effective friction value:

$$\mathrm{E_G} = \int_{U_p}^{U_{end}} (\mu^*(U) - \mu^*_{ss})\sigma_N \, d_U \tag{5.2}$$

With $\mu^*(U)$ the current effective friction, U_p the x-displacement at effective friction peak, U_{end} the x-displacement at the end of effective friction peak, and U the current slip distance.

According to previous assumptions and the three main mechanisms highlighted in the cemented fault model, the total Breakdown energy can be divided into three energy contributions: a dilation energy E_{Dil} linked to sample dilation (mechanical energy), a Damage energy E_{Dam} coming from the breakage of cementation (rupture of cohesive links with surface creation energy) and E_{fr} a part of the total frictional energy E_f as presented in Figure 114. The remaining Coulomb energy E_{fr} collects all frictional energy that is not considered in the constant part $E_{fc} = \tau_{ss} * D_{pp}$. Considering that the E_{fc} is similar to the definition of the E_H part of the energy budget, E_{fr} could be compared to excess (or a deficit, if negative) of heat creation with respect to the steady-state rate of such heat creation.

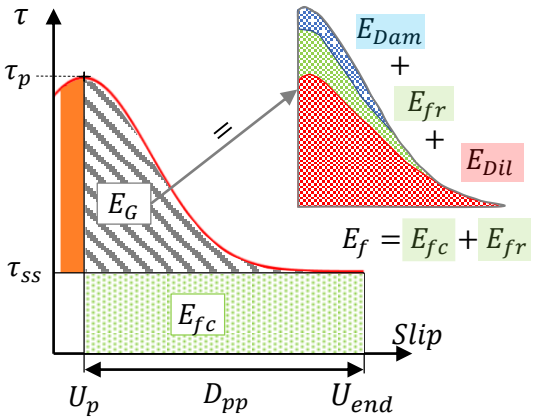

Figure 114. Proposed model (function shape strongly varies depending on cementation and initial porosity), with the decomposition of the breakdown energy E_G. E_G gathers a dilation energy E_{Dil} linked to sample dilation (mechanical energy), a Damage energy E_{Dam} coming from the breakage of cementation (surface creation energy) and E_{fr} a part of Coulomb energy E_f. τ_p is the maximum shear stress, τ_{ss} is the steady-state shear stress, or dynamic shear stress. D_{pp} is the duration of the slip weakening part (post-peak), similar to the critical weakening distance. Coulomb energy E_{fr} collects all the Coulomb energy that is not considered in the constant part $E_{fc} = \tau_{ss} D_{pp}$. Note that in the sketch, E_B and E_{fc} are in Joule and not in J/m² as in the following equations.

Calculation of the different energies

As the model does not present any radiated or heat energy consumption, it is admitted that the total energy of the model, to which the Coulomb friction part (E_{fc}) and a potential pre-peak part would have been subtracted, will be similar to the breakdown energy previously presented.

The objective here is to calculate each term of the Breakdown energy contribution previously described, meaning the energy posterior to the effective friction peak: the dilation energy E_{Dil-pp}, the frictional energy E_{f-pp} and the Damage energy E_{Dam-pp} (pp for post-peak). The total energy of the sheared gouge model E_{tot} (J/m^2) is first calculated for every slip distance $\mathrm{U}(i)$ (i.e. at every time step i of the simulation), knowing the total tangential force F_T acting on the upper rock wall (x-direction):

$$E_{tot}(i) = E_{tot}(i-1) + \frac{\big(U(i) - U(i-1)\big)\big(F_T(i) + F_T(i-1)\big)}{2S_g} \tag{5.3}$$

The surface S_g is the surface perpendicular to the applied normal stress σ_N, due to the (2D) simulation, with a width of 1 m with $S_g = L_g * 1\ \mathrm{m}^2$. Parameters are shown in Figure 115.

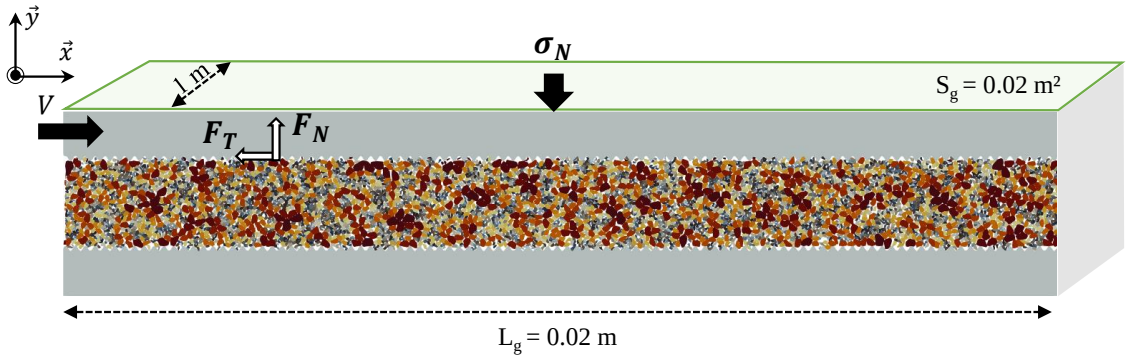

Figure 115. Schema of the model with the different parameters used. V is the shearing velocity applied on the upper rock wall (m/s), σ_N is the applied normal stress on the upper rock wall (MPa), S_g is the surface perpendicular to the applied normal stress (m^2), L_g is the gouge length (m), F_T and F_N are respectively the total tangential and normal forces acting on the upper rock wall (x −direction), (N).

The total dilation energy E_{Dil} (J/m²) is the product between the vertical distance covered by the upper rock wall Δ_{th} (the y-displacement is allowed in the model) and the total normal force F_N acting on this rock wall (y-direction):

$$E_{Dil}(i) = \frac{\Delta_{th}(i) F_N(i)}{S_g} \tag{5.4}$$

It is also possible to calculate an averaged post-peak dilation energy E_{Dil-av} equal to $\left[th_{SS} - th_p\right] * \sigma_N$. With th_{SS} the gouge thickness at steady-state, th_p the gouge thickness at friction peak and σ_N the normal stress.

Finally, the Damage energy E_{Dam} (J/m^2) is calculated considering the contact parameters of each particle as follows

$$E_{Dam}(i) = \frac{\sum L_{p-c}(i)}{2}\left(\frac{C_{num}}{2}\right)^2 \frac{1}{k_n}\frac{1}{L_g} \tag{5.5}$$

With $\sum L_{p-c}(i)$ the total contact length of contacting grains evolving during shearing, C_{num} the numerical cohesion described in Chapter 3, and k_n the interparticle stiffness. Frictional energies E_f is the remaining energy of the model:

$$E_f = E_{tot} - E_{Dil} - E_{Dam} \tag{5.6}$$

As an example, Figure 116 displays the evolution of energy released for a granular sample with $P_{cem} = 57$ % (G-C-57), as a function of the slip distance. Figure 116 (a) presents the evolution of each energy contribution through slip distance evolution. The sum of the 3 contributing energies (Dilation, Damage, and Friction) gives the black curve which is the total energy released during the sliding (pre and post-peak), increasing with slip distance. By derivation of each energy term, an associated friction can be calculated, allowing to obtain the specific frictional contribution of each mechanism presented above, Figure 116 (b). These friction contributions will be used to propose simplified models in section 5.6.2. Figure 116 (c) helps analyze the percentage of energy consumed in pre-peak or post-peak phases, where we see for this sample that pre-peak energy dissipation can be neglected (although this conclusion does not stand for all samples). The surface percentage of cementation (presence of cohesion) remaining in the sample with the increasing slip distance can be observed in Figure 116 (d), it represents the damage observed in Chapter 3. Similar data are extracted from each experiment of Chapter 3, both for dense and mi-dense samples.

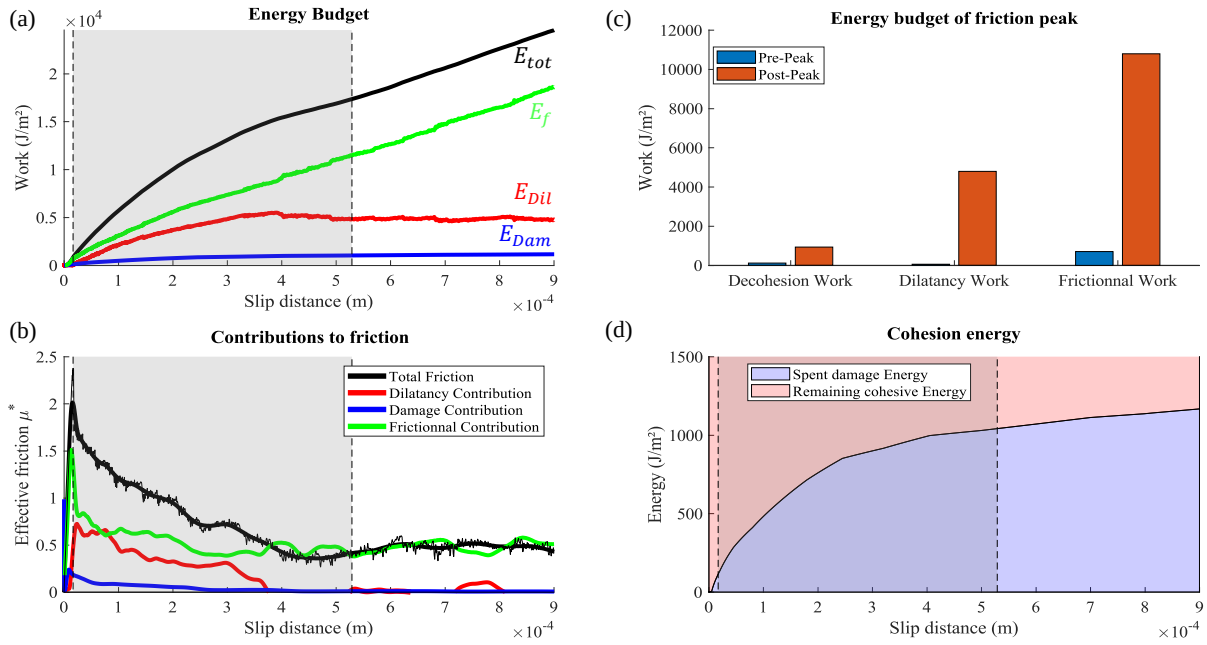

Figure 116. Dense sample with 57 % of cementation (a) Energy budget (J/m^2) as a function of slip distance (m) for the different contributions. (b) Effective friction μ^* extracted from energy consumption. (c) Energy budget (J/m^2) in pre-peak and post-peak phase; (d) Cementation spent and remaining expressed as cohesive energy (J/m^2) in the sample as a function of the slip distance (m).

5.6.2. A way to friction laws

Now that each friction contribution has been identified and calculated, the objective is to obtain a simplified friction law that accounts for the three main mechanisms (dilation, friction and damage) and that takes as input the physical parameters of the gouge. Once this friction law is determined, it will be possible to simulate the mechanical and energetic behavior of any cemented gouge (within the framework of the hypotheses of the thesis) by simply changing the percentage of cementation (P_{cem}) present in the sample.

Depending on the percentage of cementation and thus on the three different types of cemented materials previously identified in Chapter 3 (poorly cemented, cemented, and highly cemented), the simplified model can give the evolution of the effective friction as a function of the slip distance with a well-detailed slope of slip weakening. The following section explains the relationship between each parameter of the gouge and the steps leading to the final friction laws. The method aims to find a simplified model for each frictional contribution, as observed in Figure 116.

Behavior laws of shape parameters

Figure 117 (a) shows the evolution of effective friction (black curve) and its different contributions as a function of the slip distance, Figure 116 (b), for this granular sample: the green curve is the frictional or Coulomb contribution μ_f^*, the dilation contribution μ_{dil}^* appears in red and the damage contribution μ_{dam}^* in blue. The first step consists in selecting and recovering all the essential parameters from these three contributive frictions and making appear a global tendency of evolution for each of them. Figure 117 (b), (c), and (d) present an example with friction contributions and simplified models, highlighting the main parameters selected to reproduce a reliable empirical simplified model. These parameters evolve as a function of the surface percentage of cementation and initial porosity within the gouge, Figure 118:

– The dilation friction evolution μ_{dil}^* is illustrated employing three parameters, Ψ_p the maximum dilatancy angle (Rowe, 1962), U_{dp} the slip distance needed to reach the dilation peak, and ΔH_d, the gain in gouge thickness at the end of the dilation phase, Figure 117 (c). These parameters do not follow linear laws and both poorly and ultra-cemented samples present constant values for Ψ_p and ΔH_d, meaning that major evolution occurs for mildly cemented materials, Figure 118 (a) and (c). As Ψ_p is increasing with the percentage of cementation, the slip distance U_{dp} associated with maximum dilation is reducing, which is consistent with results from Chapter 3. ΔH_d gives the shape of the Gaussian model. Even though a lognormal law seemed to better fit the dilation friction contribution than a Gaussian law, it was not satisfactory for the total friction law. The U_{dp} is higher for mid-dense materials and decreases with higher cementation, Figure 118 (b).

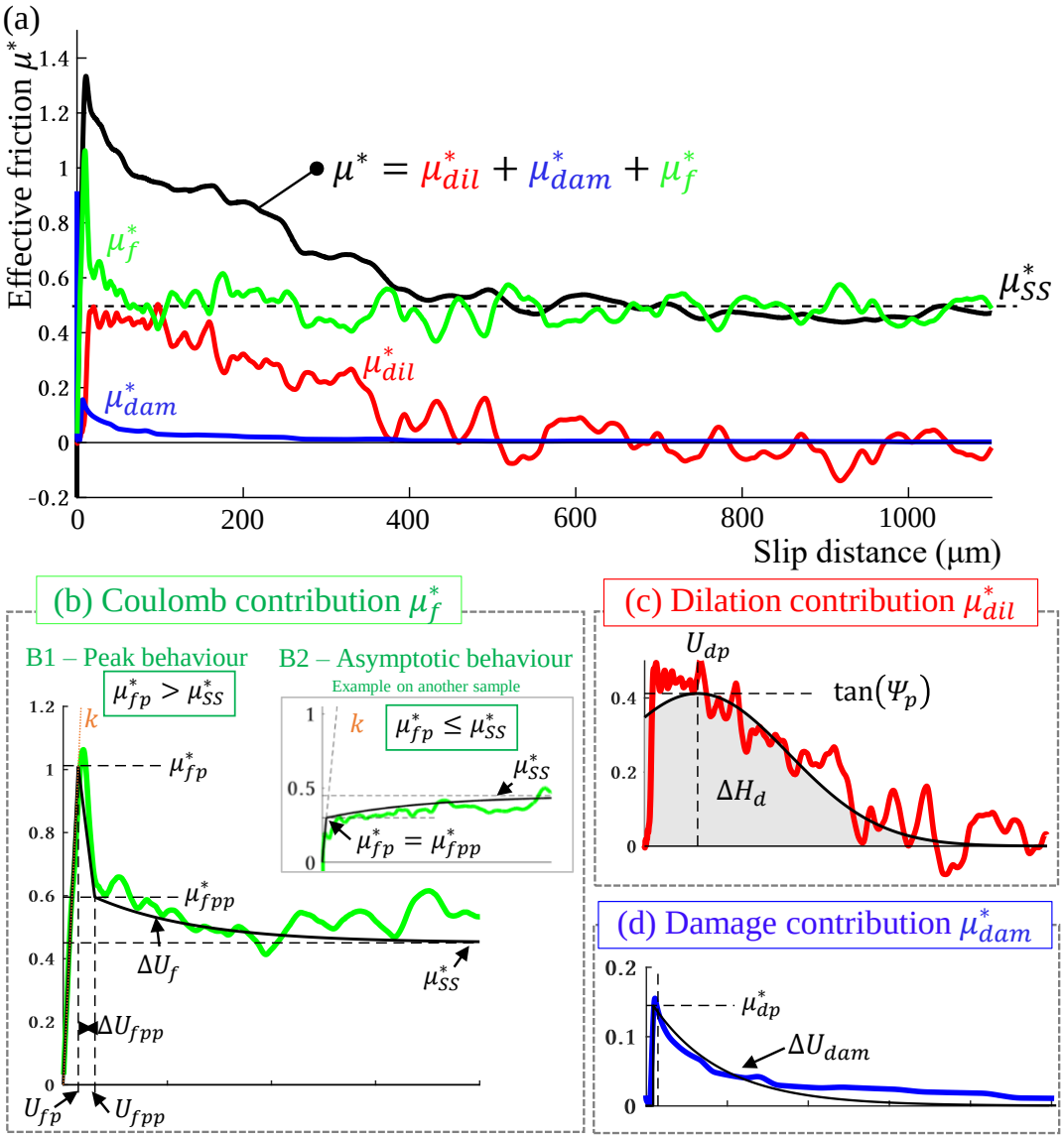

Figure 117. As an example of the method, a dense sample with 30 % of cementation (G-C-30) is used. (a) Friction-slip curve with different contributions (dilatancy in red, Coulomb in green, and damage in blue), dense sample with $P_{cem} = 30$ %. The black curve is the sum of all contributions. (b) Zoom in on the Coulomb contribution with simulation data in green and simplified model in dark, two behaviors are observed (B1 and B2). The interesting parameters are: the effective friction peak at the end of the elastic phase μ^*_{fp}, the post peak friction μ^*_{fpp} and the characteristic distance of the exponential decay ΔU_f. B1 corresponds to the granular sample studied with $\mu^*_{fp} > \mu^*_{SS}$ and B2 is an example of the second type of behavior, observed for the 30 % mid-dense case with $\mu^*_{fp} \leq \mu^*_{SS}$. (c) Zoom in on dilation contribution μ^*_{dil}, simulation data in red and simplified model in dark with: the maximum dilatancy angle Ψp, the slip distance corresponding to the maximum dilation U_{dp} and the gain in gouge thickness ΔH_d at the end of the dilation phase. (d) Zoom in on the damage contribution μ^*_{dam} with the characteristic distance of the exponential decay ΔU_{dam} and the maximum friction induced by breakage of cohesive links μ^*_{dp}. It can be noted that k, μ^*_{ss}, and ΔU_{fpp} do not depend on the cementation and are taken as constant.

– Friction contribution μ^*_f is more complex to model because two different behaviors are observed in Figure 117 (b), B1 and B2. The first one has a peak behavior where the effective friction peak μ^*_{fp} is higher than μ^*_{SS}, whereas the second one has an asymptotic behavior with $\mu^*_{fp} \leq \mu^*_{SS}$, meaning no friction peak. Pushing up the cementation increases both Coulomb friction peak μ^*_{fp} and post-peak friction μ^*_{fpp} following a linear law, Figure 118

(d), with a characteristic distance ΔU_f remaining almost constant for dense samples, and decreasing for mid-dense samples as a function of cementation, Figure 118 (e). This evolution is related to the type of frictional model observed B1 or B2: a larger distance of decay is observed for asymptotic behaviors B2, Figure 117 (b).

– Damage contribution μ^*_{dam} presents a peak μ^*_{dp} with rising linear law from 0 to 100 % cementation, Figure 118 (f), consistent with previous results since increasing cementation increased the resistance of bonded particles to shearing (Chapter 3).

These parameters are chosen and adjusted to picture the global trend of friction contributions. The separation zone between the three distinct regimes described in Chapter 3 is marked by a vertical dotted line. The objective of these graphs is not to reproduce the exact location of dilation friction peak, but to model a global and consistent shape evolution from one case to another. For the sake of simplicity, ΔU_{fpp} (distance between the slip distance at μ^*_{fp} and the slip distance at μ^*_{fpp}), k (the elasticity slope) and μ^*_{SS} are independent of cementation and taken as constant. The distance ΔU_{fpp} is equal to 8 µm for dense samples and 40 µm for mid-dense samples. The gouge layer stiffness k is proposed equal to 140 kN/m for dense samples and to 80 kN/m for mid-dense samples. Details on the equations allowing to obtain these curves are presented in Appendix 5.B.

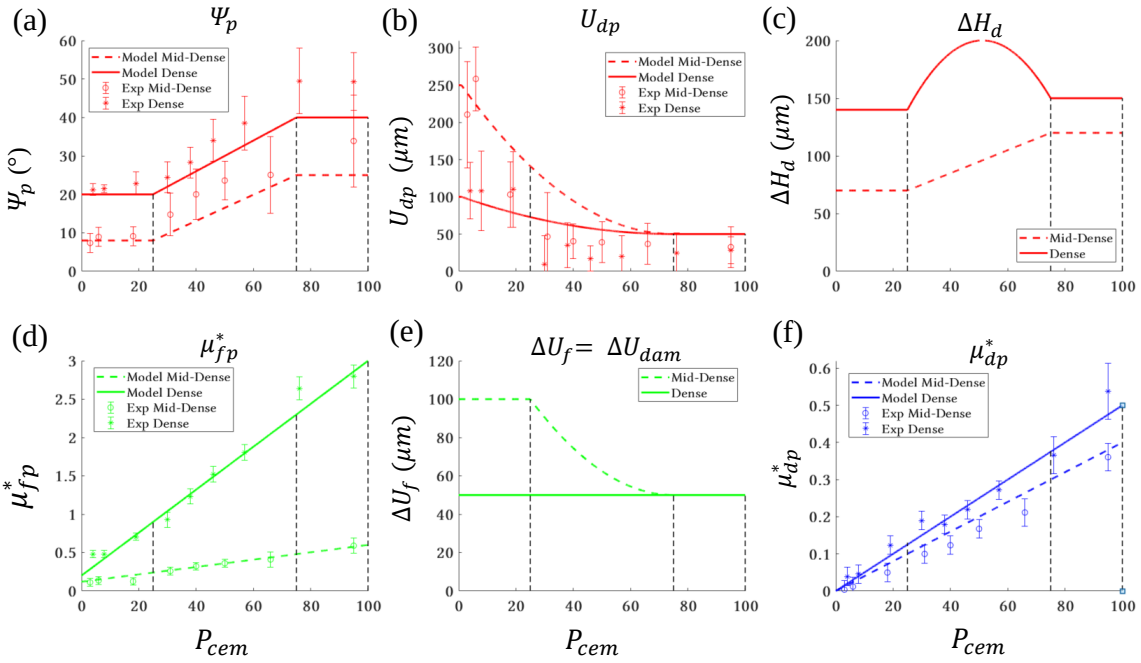

Figure 118. Behavior laws of each of the 7 parameters considered in the simplified models. It can be noted that k, μ^*_{SS}, and ΔU_{fpp} do not depend on cementation and are taken as constant. (a) Maximum dilatancy angle Ψp (°), the difference observed between prediction and real values comes from a compromise between the friction peak value and a consistent friction shape from the dilatation. We chose an "average" value of Ψp that allows us to obtain a consistent shape. (b) Slip distance corresponding to the maximum dilatancy U_{dp} (μm). (c) Gain in gouge thickness at the end of the dilatancy phase ΔH_d(μm). (d) Peak friction at the end of the elastic phase μ^*_{fp} and post peak friction μ^*_{fpp}. (e) Characteristic distance of the exponential decay ΔU_f (μm). (f) Maximum friction induced by rupture of cementation μ^*_{dp}. Dots are experimental data derived from DEM modeling with error bars. Some are not aligned with numerical modeling as some peak values are difficult to identify on raw data and the error can be important. ΔH_d and ΔU_f don't have experimental data, as they are completely created for the model.

Equations of each friction contribution

Thanks to the global parameters' laws observed in the previous Figure 118, it is now possible to propose a simplified model for each friction contribution μ_{dil}^*, μ_f^* and μ_{dam}^*.

- **Dilation contribution (μ_{dil}^*).** The three dilation parameters (Ψ_p, U_{dp} and ΔH_d) are introduced in a Gaussian-like law with maximum dilatancy friction of $\tan(\Psi_p)$ and a squared exponential decrease as a function of slip:

$$\mu_{dil}^*(U) = tan(\Psi_p) \cdot e^{-\log(2)\left(\frac{U - U_{dp}}{U_{d_{half}} - U_{d_p}}\right)^2} \tag{5.7}$$

U is the current displacement of the upper rock wall and U_{dhalf} is the distance between U_{d_p} and the slip distance for a half reduced dilatancy-related friction. This last parameter is determined by solving numerically:

$$\frac{U_{dhalf} - U_{dp}}{2} \cdot \tan(\Psi_p) \cdot \sqrt{\frac{\pi}{\log(2)}} \cdot \left(1 + erf\left(\frac{U_{dhalf}}{U_{dhalf} - U_{dp}} \cdot \sqrt{\log(2)}\right)\right) = \Delta H_d$$

- **Friction contribution (μ_f^*).** The Coulomb contribution is more complex due to the two possible behaviors B1 and B2, Figure 117. The peak behavior where the effective friction peak μ_{fp}^* is higher than μ_{SS}^* exhibits a first linear elastic part, characterized by a stiffness k (gouge layer stiffness) from 0 to μ_{fp}^*. Then friction decreases linearly until a post-peak value called μ_{fpp}^*. Friction contribution finally diminishes exponentially until μ_{SS}^* taken equal to 0.45 to simplify the model. Each part is modeled by a specific equation:

$$\mu_{f-B1}^*(U) = \begin{cases} kU, & U \leq U_{fp} \\ \frac{(\mu_{fpp}^* - \mu_{fp}^*)}{\Delta U_{fpp}}(U - U_{fp}) + \mu_{fp}^*, & U_{fp} \leq U \leq U_{fpp} \\ \mu_{SS}^* + (\mu_{fpp}^* - \mu_{SS}^*) \cdot e^{-\frac{U - U_{fpp}}{\Delta U_f}}, & U_{fpp} \leq U \end{cases} \tag{5.8}$$

With ΔU_f a characteristic distance of the exponential decay, $U_{fp} = \frac{\mu_{fp}^*}{k}$, ΔU_{fpp} the slip distance between U_{fp} and U_{fpp} and $U_{fpp} = U_{fp} + \Delta U_{fpp}$.

The second type with $\mu_{fp}^* \leq \mu_{SS}^*$ displays the succession of an elastic part from 0 to μ_{fp}^* followed by an asymptotic exponential behavior until μ_{SS}^*, Figure 117 (b) B2. This case is especially observed in mid-dense samples or for mildly cemented materials:

$$\mu_{f-B2}^*(U) = \begin{cases} kU, & U \leq U_{fp} \\ \mu_{SS}^* + (\mu_{fp}^* - \mu_{SS}^*) \cdot e^{-\frac{U - U_{fp}}{\Delta U_f}}, & U_{fp} \leq U \end{cases} \tag{5.9}$$

With $\mu_{fpp}^* = \mu_{fp}^*$ and $U_{fp} = \frac{\mu_{fp}^*}{k}$.

- **Damage contribution (μ^*_{dam})**. The last contribution is the damage, characterized by an absence of contribution during elastic loading, and a maximum friction peak μ^*_{dp} followed by an exponential decrease until 0, Figure 117 (e):

$$\mu^*_{dam}(U) = \begin{cases} 0, & U \leq U_{dam} \\ \mu^*_{dp} \cdot e^{-\frac{U - U_{dam}}{\Delta U_{dam}}}, & U_{dam} \leq U \end{cases} \quad (5.10)$$

With ΔU_{dam}, a characteristic distance of the exponential decay, and $\Delta U_{dam} = \Delta U_f$.

Validation of the model

Figure 119 presents the simplified models and the initial effective friction evolution for dense and mid-dense samples for the three types of cemented materials.

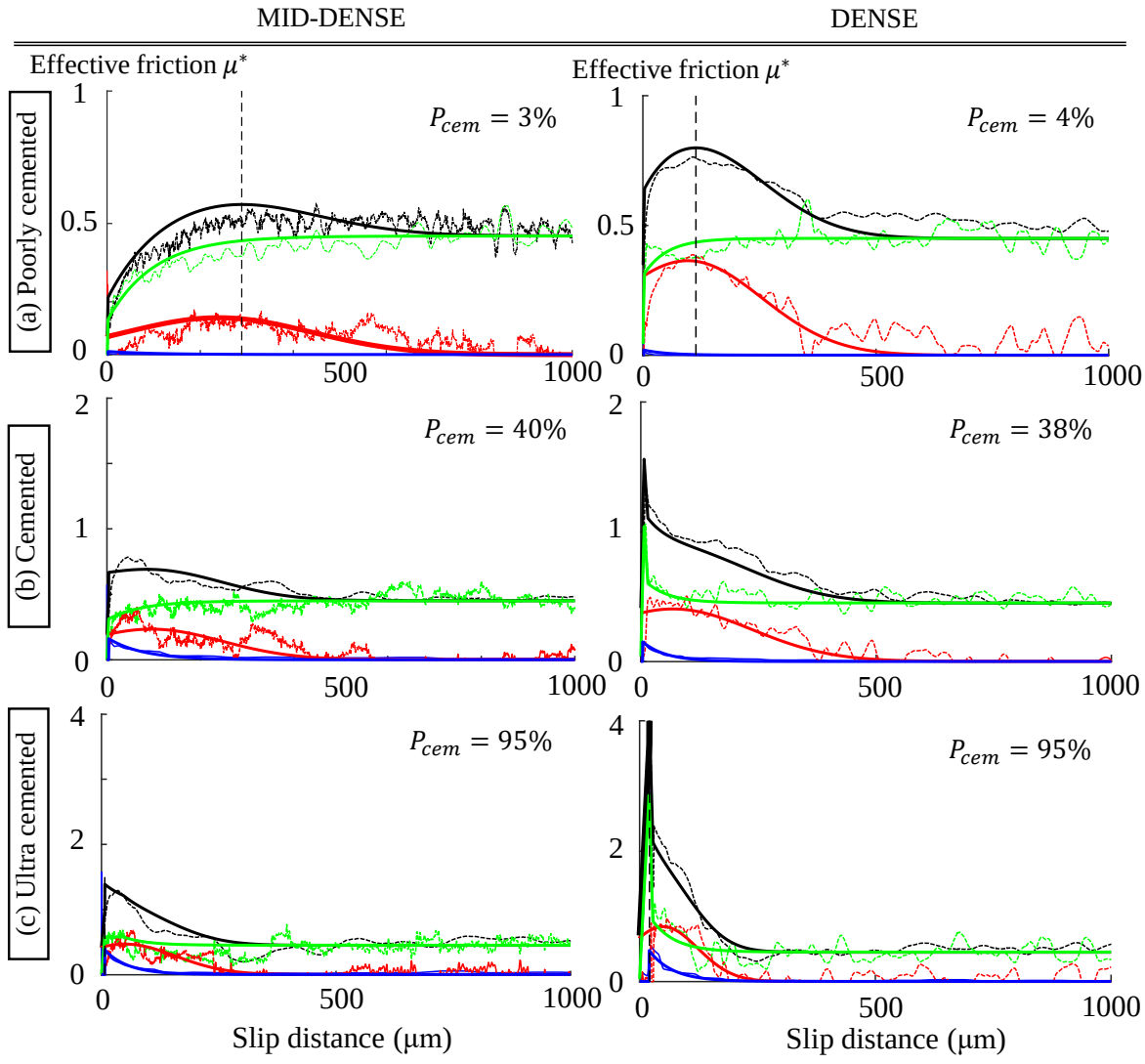

Figure 119. Mid-dense and dense granular samples – validation of simplified models. Effective friction as a function of the percentage of cementation. Effective friction contributions are colored (dilation in red, Coulomb in green, and damage in blue) and the black curve is the sum of all contributions. (a) Poorly cemented materials, where the observed pre-peak phase is important. (b) Cemented materials with a diminution of the pre-peak phase with the increase of cementation. (c) Ultra cemented materials with almost no pre-peak phase. Dashed lines represent results from simulations and the solid lines the curved calculated with simplified models' equations.

These six chosen cases are presented here to validate the experimental friction curves with the friction decomposition proposed: one case for each cemented material described in Chapter 3 (poorly cemented, cemented and ultra- cemented) and for each type of compacted sample (dense and mid-dense). Despite its simplicity, the empirical model fits all the materials quite remarkably and can be implemented with confidence in large-scale rupture models. The mid-dense and poorly cemented patterns are the least well represented by the model and may require some improvement. The rest of the models and validation are presented in Appendix 5.C. Considering every friction contribution μ_{dil}^*, μ_f^* and μ_{dam}^*, this new model gives a simplified representation of the effective friction coefficient μ^*as a function of the initial percentage of cementation. The proposed functional expressions and parameters evolutions of this model remain theoretical and might be modified or improved based on future findings, but allow to enrich slip-weakening laws by proposing a more general model that could be implemented in dynamic rupture modeling.

5.7. Results & Discussions

5.7.1. Breakdown energy evolution

Thanks to the previous method, the breakdown energy E_G as well as its three contributed parts (E_{Dil-pp}, E_{f-pp} and E_{Dam-pp}) are calculated with previous equations, Figure 120. As the energies calculated with the previous models depend on simulation data, the observed results are of the same order of magnitude as those observed in Chapter 3 and Part A of this chapter. The energetic behavior can be analyzed regarding the three distinct cemented materials previously identified:

- Poorly cemented materials ($P_{cem} \leq 25$ %) present a low and almost constant energy release (although larger for denser samples) remaining relatively small compared to the two other cemented materials: $10^3\ J/m^2$ for mid-dense materials and around $3.10^3\ J/m^2$ for dense materials, Figure 120 (a) & (b). It is characteristic of the ductile trend highlighted in Chapter 3 with progressive particle reorganization and no localized shear requiring less energy from the system.

- For cemented materials ($25 < P_{cem} < 75$ %), E_G is increasing with the percentage of cementation, characterized by the chaotic character of the gouge observed with particles agglomerates. These large agglomerates are a hindrance to the stabilization of the gouge and explain the need for more energy to reach a stabilized state.

- Ultra-cemented materials ($P_{cem} \geq 75$ %) display an almost constant energy released, but more than twice higher than for the poorly cemented materials. Due to the rather brittle nature of the highly cemented materials (Chapter 3), the frictional resistance strongly increases, which amplifies the energy required to weaken the friction to its steady-state value. As the critical weakening distance also decreases, a stabilization of the energy is reached for the highly cemented models.

A difference is observed between the total Energy, considering the pre-peak energy part (dashed lines), and the breakdown energy (full lines). For mid-dense and poorly cemented samples, the pre-peak part is very important and is probably caused by the early beginning of dilation due to the more ductile behavior of this material. On the other hand, dense and highly cemented samples also present higher E_{tot}, the pre-peak energy is increasing with the increase of friction peak. (Ohnaka, 2003) reinterpreted the shear rupture energy E_G as the sum of a fracture energy G_{c1} (i.e. pre-peak energy) and of the post- peak energy G_{c2} required for the breakdown from peak strength to residual friction. Without G_{c1}, intact rock cannot fail, so this pre-peak energy cannot always be neglected. The only case that we found consistent to neglect the pre-peak energy is for dense cemented or ultra-cemented materials, where the majority of the energy is released after friction peak. To include or not this pre-peak energy in the total energy budget is thus questioned, and also strongly depends on the initial stress applied on the fault before the arrival of the sliding front and on the heterogeneity of the stress state on the fault.

The grey diamonds represent the breakdown energy directly extracted from simulations. The dense simplified models reproduce well the energetic behavior of the cemented gouge, but further improvements need to be done for mid-dense and highly cemented materials, Figure 120 (a). The difference found can be explained in three ways: (i) the shape parameters of mid-dense simplified friction can still be improved, (ii) the original curves of mid-dense samples are very noisy, which explains why the energy calculated in Part A is not exactly the same as the one obtained with the simplified model, (iii) the steady-state value is equal for all simplified models, whereas plateau zones are not very "linear" for the real friction curves, Appendix 5.C.

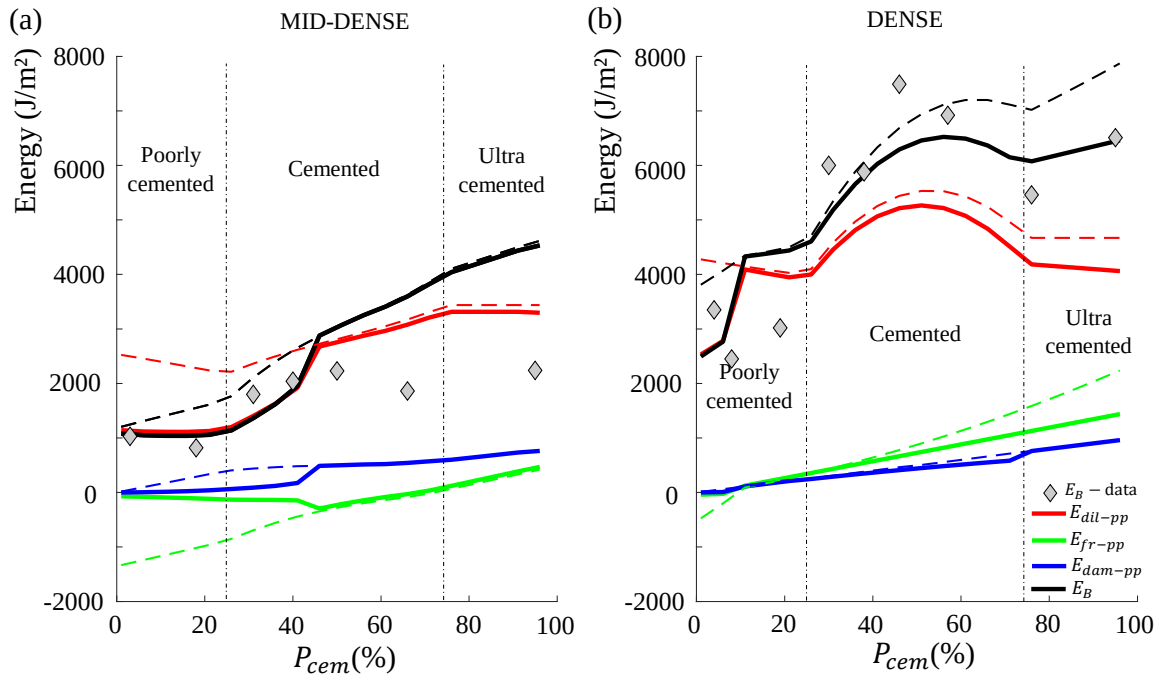

Figure 120. Breakdown energy E_B (J/m^2) coming from the different contributions as a function of the percentage of cementation within the gouge. (a) Mid-dense samples (b) Dense samples. E_B (in black) gathers a dilation energy E_{dil-pp} (in red) linked to sample dilation (mechanical energy), a Damage energy E_{dam-pp} (in blue) coming from the breakage of cohesive links (surface creation energy) and E_{fr-pp} (in green), a part of the total Coulomb energy E_f. Dashed lines represent the sum of the breakdown energy and the pre-peak energy for each contribution.

E_{Dil-pp} both increases with the percentage of cementation (cohesion forces greater dilation due to resistance to fracture) and the initial porosity of the sample. This is consistent with previous results showing higher dilation for denser samples, Chapter 3. As cementation increases, both damage (E_{Dam-pp}) and frictional energy (E_{fr-pp}) increase, but they are still negligible compared to dilation energy which represents almost 70 % to 80 % of the total energy and breakdown energy. Damage energy is almost independent of the initial state of porosity as the energy needed to break a cohesive link rather depends on the contact length and the initial percentage of cementation.

E_{fr-pp} presents a special behavior with a zero contribution for poorly cemented materials and a small increasing contribution for the other materials, Figure 120 (a) & (b). An interesting point is that this energy contribution is the only one that may lead to heat creation in the system (in addition or subtraction of the steady-state friction) since dilation energy is nothing but a mechanical work and damage energy is related to surface creation. The constant part of friction energy E_{f_c} (not considered in E_G) appears to be twenty times higher than E_G for the total slip considered here. This high difference explains why (J. Chester et al., 2005) consider that the Fracture energy is negligible in comparison to other energies presented in the theoretical energy budget, Chapter 1. However, the knowledge of E_G is crucial for the understanding of the onset of sliding.

5.7.2. The role of dilation energy

Why is dilatancy so important? Dilation is assumed to be very influential in the way a fracture grows. [(Rice & Rudnicki, 1979), (Rice, 1983), (Caniven et al., 2021), (Aben & Brantut, 2021)] studied the fault-zone models where dilatancy is assumed to occur within the fault zone during the nucleation process (with or without fluid). In gouge or breccia materials, dilation appears with shearing and constitutes the basis of the well-known slip-weakening models. According to the theory, and in the presence of fluid, dilation has two major effects, the reduction of pore pressure and an increase in frictional resistance due to dilatancy hardening mechanism. As a result, a potential stabilization of the fault can be observed thanks to the delay or even a suppression of the nucleation process.

The energy partitioning previously presented gives some additional understanding of this phenomenon from a micro-mechanical point of view (and without fluid). It helps to identify the slip stages where the dilation energy is higher and how it interacts with frictional and damage energy, Figure 121. Comparing the scale of each energy in Figure 120, dilation is indeed the most influential factor, while the other energies do not exceed 2 kJ/m². This is not a new observation as dilation is well understood as a primary factor influencing the energy balance in granular shear.

In the representation of (Caniven et al., 2021), the expansion of dilation energy implies the storage of more elastic strain energy increasing the radiated energy, which may lead to fast earthquakes and instabilities. According to them, high roughness and asperities within the fault slip plane obviously reduce the contact area between the two walls, enhancing dilation and an important fault strength reduction with instability conditions ($K_c > K$). In our results a

correlation between the inner fault plane roughness and asperities, the rapidity of stress drop (D_{pp}), and the dilation energy was observed (Chapter 3 and Part A). For mid-dense materials, increasing the cementation increases the dilation and total breakdown energies and decreases the critical distance of sliding D_{pp} (i.e. increase K_c).

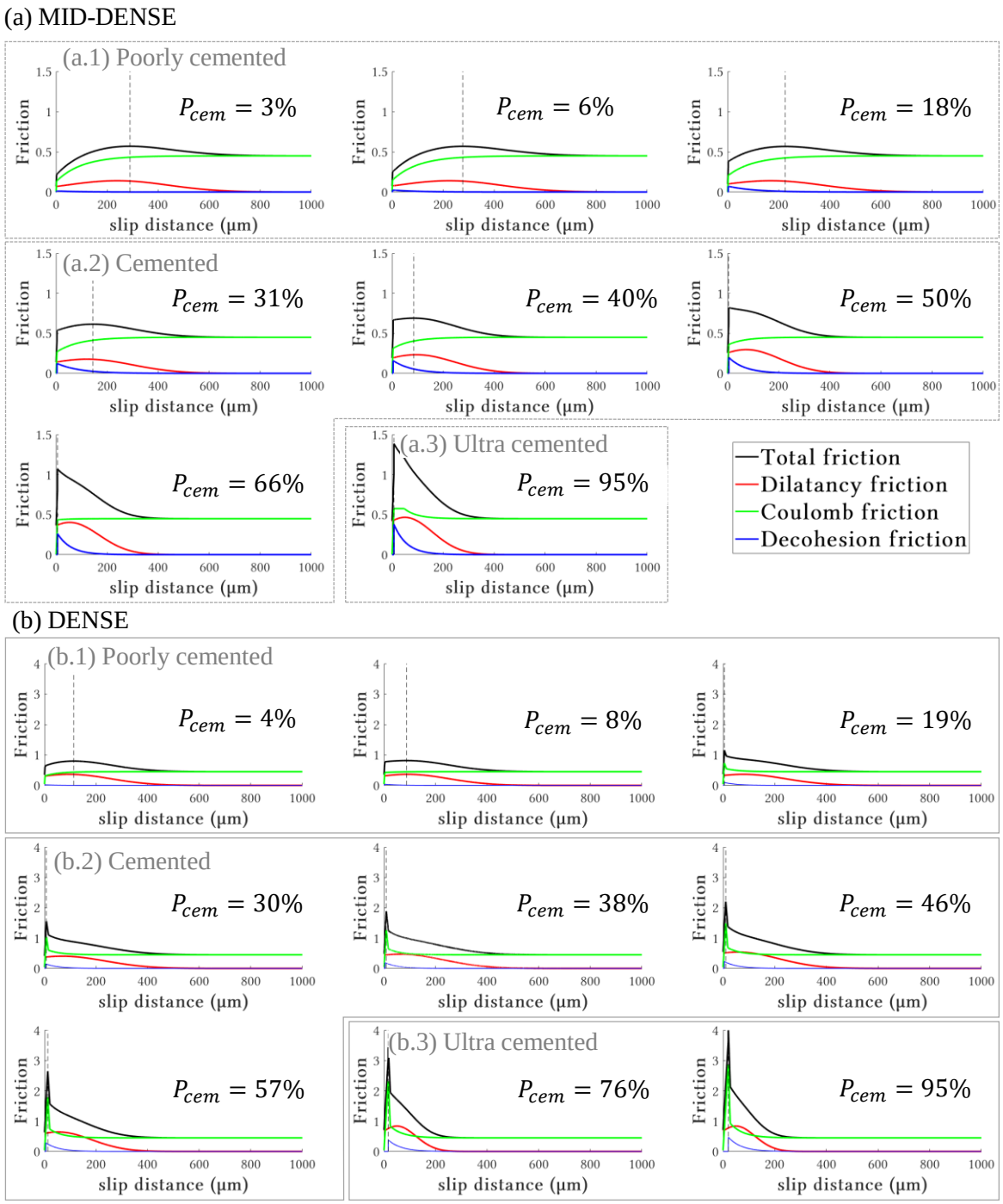

Figure 121. Simplified model for each cemented material, the dashed line represents the effective friction peak. (a) Mid-dense samples: (a.1) Poorly cemented materials, where the observed pre-peak phase is important, (a.2) Cemented materials with a diminution of the pre-peak phase with the increase of cementation, (a.3) Ultra cemented materials with no pre-peak phase. (b) Dense samples:(b.1) poorly cemented materials with a diminution of the pre-peak phase with the increase of cementation, (b.2) Cemented materials with a negligible pre-peak phase but an important influence of friction peak, (b.3) Ultra cemented materials with almost not pre-peak phase and a very high Coulomb friction peak.

Through energy observations and previous dilation results of Chapter 3, behaviors of dense materials can be summarized in Figure 122. The observed cohesive agglomerates formed within the dense cemented samples create large contact asperities within the fault plane, drastically enhancing the dilation energy and reducing the critical slip distance needed for the stress drop. These materials could enhance regular to fast earthquakes, based on the representation of (Caniven et al., 2021), due to its higher dilation energy that is likely to give a much higher slip velocity response to sliding. However, for dense and ultra-cemented samples, the contact plane was closer to a particle-plane asperity contact (a highly cohesive band with micro-roughness), the actual dilation energy is thus decreasing in comparison with cemented samples as observed in Figure 120 (b). This is also consistent with the global dilation/contraction ratio of the gouge (Caniven et al., 2021). For this cemented material, the ratio is decreasing at the end of the observed slip as a very contractive behavior was observed. Even though the effective friction peak is higher for these ultra-cemented materials, the resulting breakdown energy and, by deduction, the elastic energy storage is smaller than for cemented materials, probably due to the change of roughness created by cemented particles. In comparison, for poorly cemented materials, the dilation begins in the pre-peak phase, giving an important "pre-peak" dilation energy, Figure 121 (a.1) & (b.1). In this case, the system has already been set into motion before reaching the breaking point, leading to a drastic reduction of the breakdown energy (post-peak) dissipated by the system which does not need much dilation energy to slide. Frictional energy is also reduced (with some negative values, Appendix 5.C) as all particles slide together with no significant shearing resistance. The observed variation of effective friction, Figure 119 (a) is diffuse and oscillating as observed by (Caniven et al., 2021) for this kind of asperity contact leading to a rather slow sliding.

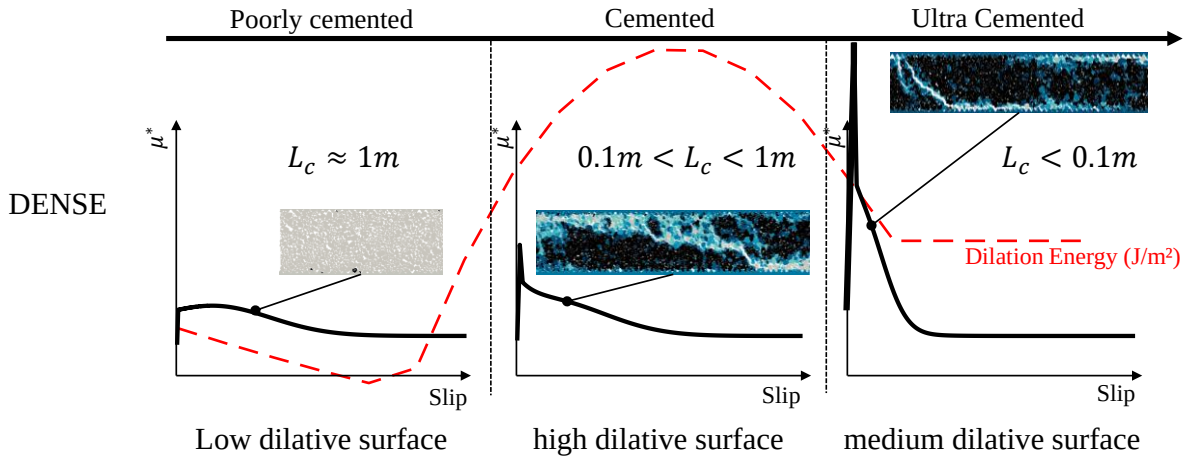

Figure 122. Schematic view of the different mechanisms operating within dense materials for different surface percentages of cementation. Poorly cemented materials (left) have low peak strength, small breakdown energy and high critical nucleation length. Ultra cemented materials (right) have very high peak strength, high breakdown energy and a very small critical nucleation length. Cemented materials (center) have high peak strength, very high breakdown energy and a medium critical nucleation length.

The recent study by (Caniven et al., 2021) is relevant to this topic, although it does not consider gouge material. Here the cementation adds a different mechanism that slightly modifies the rheological behaviors they observed. Hence, even though dilation can prevent an earthquake to happen (Aben & Brantut, 2021), it is also related to the unlocking of an asperity and can

drastically accelerate the slip when the fault is relocking. With more time, it would have been interesting to observe these phenomena in detail and to make similar simulations with compliant walls to represent locally the dilatancy changes in the model. Another perspective would be to study the different asperities, the agglomerates formed, due to the cementation and track their shape and evolution as a function of slip to be able to observe their link with the dilation energy.

5.7.3. Double weakening shape and stress excess

What are the mechanisms acting on the two weakening peaks? Chapter 3 showed cemented and ultra-cemented materials presenting a double weakening shape. In this section, another understanding of this double shape is brought thanks to energetic studies Figure 121 (b2) and (b3).

- The first weakening period depends on both interparticle friction, cement breakage, and dilation, and generates high frictional contacts between the few grains which are not cohesive anymore. The energy generated by this first peak strongly increases with the cementation which reduces the number of particles that can move in relation to each other, and mostly corresponds to frictional contact energy, Figure 121 (b). If there was temperature control within the simulations we could have observed higher temperature for this slip, which could be able to change the fabric inside the fault and modify gouge behavior. But the question remains, is the first weakening important within the behavior of the fault? The near tip breakdown work is also called "stress excess" (Kanamori & Brodsky, 2004). This first weakening is important in the nucleation of the fault since it controls the initiation of the rupture, but its energy is, most of the time, not considered because the amount of slip during this high-stress stage is small so that little energy is involved. Similar results were found for the cemented models: the value of the peak frictional resistance is significant, however, its energy value is low compared to that of the second weakening.
- The second weakening period is mainly due to dilation mechanisms and more precisely corresponds to the weakening part of the dilation friction. It ends with the end of the dilation energy part, also corresponding to the "plateau" zone. In fact, it is not so much the dilation phenomenon that produces this weakening but rather its progressive disappearance. However, the existence of this second peak needs a previous dilation. This energetic separation in two phases adds a new key of understanding for weakening mechanisms.

This double weakening has already been observed in shears with dynamic weakening, a first weakening due to mechanics and friction and a second one which can be generated by thermal effects. However, our models do not consider the temperature, this mechanism is purely due to the addition of cementation, combined with a very dense initial model.

Recent research on the fracture process tries to understand how and to which extent the frictional rupture can be viewed as an ordinary fracture process [(Barras et al., 2019), (Barras et al., 2020), (Paglialunga et al., 2021)]. According to them, the friction scaling laws previously presented in Chapter 1 need to be used with care: (i) the residual stress τ_1 (assumed to be an interfacial property) is not fixed, and has been shown to depend on the external applied stress, on the properties of the bodies surrounding the interface, and on the rate dependence of the frictional behavior, (ii) the effective fracture energy $G_{c,}$ calculated from crack-like theory, is

not representative for all the breakdown energy dissipation E_G (in excess compared to G_c). This result could explain the two-step weakening process: sharp stress drop that takes place over a relatively small slip followed by a slower and longer-term process bringing the friction to its residual value.

5.8. Conclusion of Part B

This part takes up the mechanical results obtained in Chapter 3. The objective was to study the behavior of cemented gouges through an energetic approach as it appears that cementation was the most influential parameter on breakdown energy in Part A. To do so, we decomposed the friction and energy variables into three main mechanisms: dilation, friction between the particles and breakage of the cemented links. Through this decomposition, the first objective was to propose a simplified friction model μ^*, as the sum of the three contributions: $\mu^* = \mu^*_{dil} + \mu^*_{dam} + \mu^*_f$. The advantage of this decomposition is to be able to locate the different mechanisms over time and see their implication in the evolution of the fault gouge. This same decomposition was performed from an energetic point of view, on the breakdown energy E_G.

This breakdown energy is mainly composed of the energy related to the dilation of the sample, which always has a preponderant role in the mechanisms of rupture and cracks propagation. We could observe that, according to the initial porosity of the sample or the percentage of cementation, the influence of the dilation is not similar and does not induce the same mechanical behavior. The mid-dense materials have a rather linear increase of the breakdown energy (and of the energy necessary to dilate the sample) whereas the behavior of the dense materials is more complex. Indeed, the material most likely to generate sliding instabilities appears to be dense cemented materials (between 25 % and 75 % cementation). The agglomerates of cohesive particles generated in the gouge make the fault rather heterogeneous and increase significantly the roughness in the fault, which enhances the dilation energy more significantly and implies a much higher slip velocity response.

A double weakening was observed for dense and highly cemented material, although no temperature variation is present. The first weakening is a mixture of the three mechanisms (dilation, friction and cement breakage), but with an increase in frictional energy with the increase in cementation. The reduction of the number of particles in contact, coupled with the shear rate applied to the gouge increases the friction between particles. On the other hand, the observation leads to a second weakening mainly due to the decrease of dilation, which progressively weakens the effective friction.

Simplified models proposed are pretty convincing about the final shape and could be adapted to a variable imposed stress and velocity if properly fed with additional simulations. However, the characterization of mid-dense cemented models could be improved because the total breakdown energy does not fit very well with the data observed.

Part C – Time and space evolution of R-bands in a dense granular material

5.9. Foreword

The previous Chapter 4 revealed many interesting behaviors of fault gouges, but further analyses can be done on Riedel bands and their link to deformation evolution and stability of the system, Figure 123. First of all, it is possible to observe both global and local variations of Riedel band activation. The orientation angle of these bands can be different depending on whether the observed zone is in the center of the gouge or close to rock walls (Section 5.10.1). Then we can wonder about the temporal and spatial evolution of sliding in the Riedel bands, focusing on the local variation of each band. When, where, and how does each band appear? (Section 5.10.2). Finally, we will investigate the role that these bands can have on the entire behavior of the gouge and try to connect the mechanical behavior inside each band to the entire gouge kinematic (Section 5.11). Section 5.11.3 is a proposed energetic interpretation composed by the behavior of each R and Y-band.

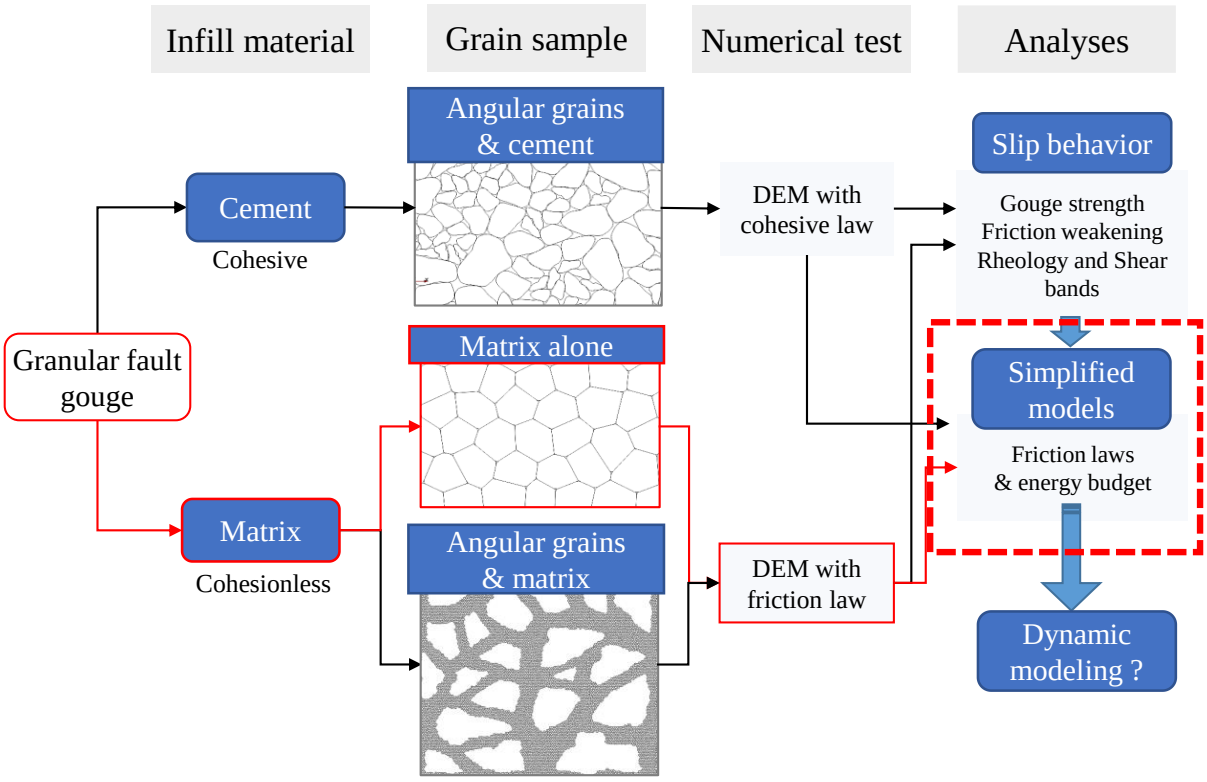

Figure 123. The main schema of chapter 5, Part C. All the data are collected from matrix gouge models, Chapter 4.

For all the results presented in this Part C, the standard sample "M-S" is used (details in Chapter 4). We will refer to the following *R* and *Y*-bands formed during the gouge shearing, Figure 124, where we can distinguish: two kinds of low Riedel bands, **the primary *R*-bands** R_3, R_4 and R_5 (which appear first and grow more rapidly), **the secondary R-bands** R_1 and R_2 (which are persistent within the entire sliding event), and **boundary shears** Y_1 and Y_2 (which grow

progressively until steady-state). R' represents the conjugate Riedel bands appearing during the slip, but are only indirectly quantified here.

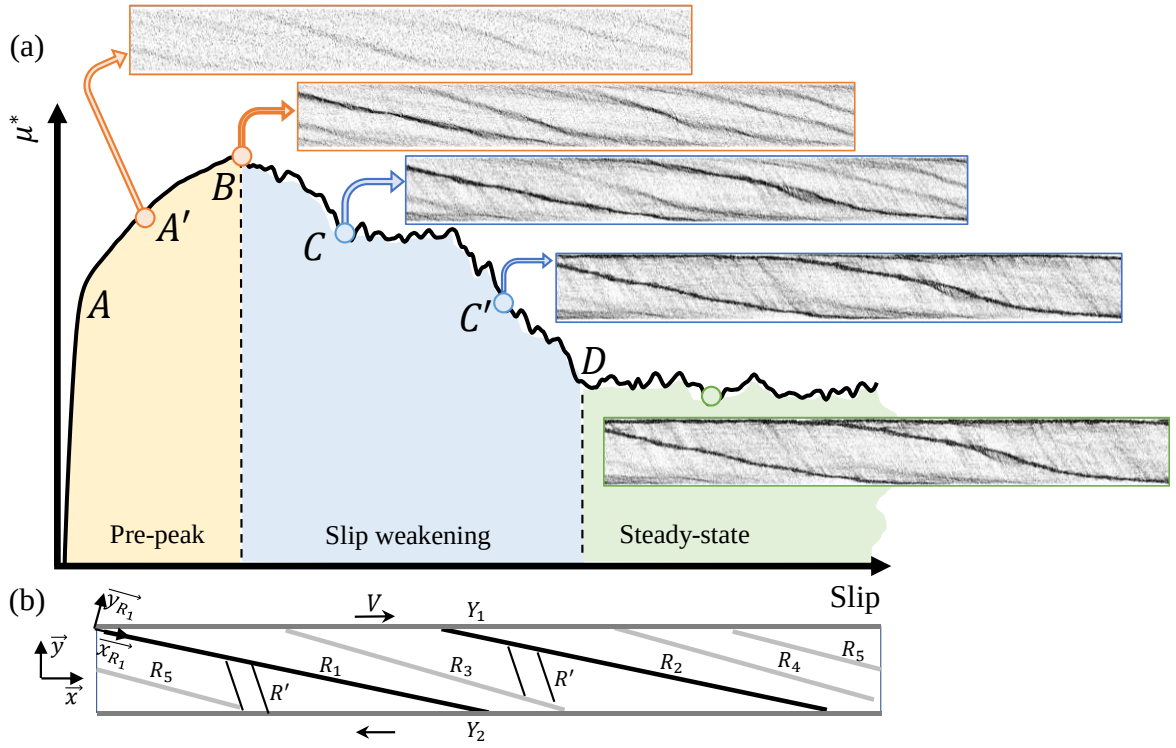

Figure 124. Schema of the Riedel and shear bands observed during the shearing of the M-S standard case used in Chapter 4. (a) Friction-Slip curve with the three different zones presented in Chapter 4 (pre-peak, weakening, steady-state), associated with pictures of the evolution of Riedel and boundary shear bands. (b) Name and position of the different types of bands, **the primary *R*-bands** R_3, R_4 and R_5, **the secondary R-bands** R_1 and R_2, and **boundary shears** Y_1 and Y_2. R' represents the conjugate Riedel bands. [video of the simulation]

5.10. Opening of *R*-bands

5.10.1. Method and first results

The objective of the proposed method is to recover precisely the time evolution of *R*-bands thanks to the opening of each shear band in real simulation time. It consists in extracting particles' positions from each side of a *R* or *Y* band, and deriving displacement jumps in the directions perpendicular and tangential to the band orientation, for different total slip values (i.e. different time steps). Particles A and B are two particles selected from each side of the band R_1, Figure 125.

The variation in the Y_R-direction, ΔY_{open}, characterizes the opening of each band and corresponds to the relative displacement between particle A and B through time and space. It remains different from the actual thickness of the *R*-band, $R_{thickness}$, observed on the pictures. However, ΔY_{open} and $R_{thickness}$ are linked together and determining ΔY_{open} is an easy way to understand the evolution of $R_{thickness}$. The method is detailed in Appendix 5.D.

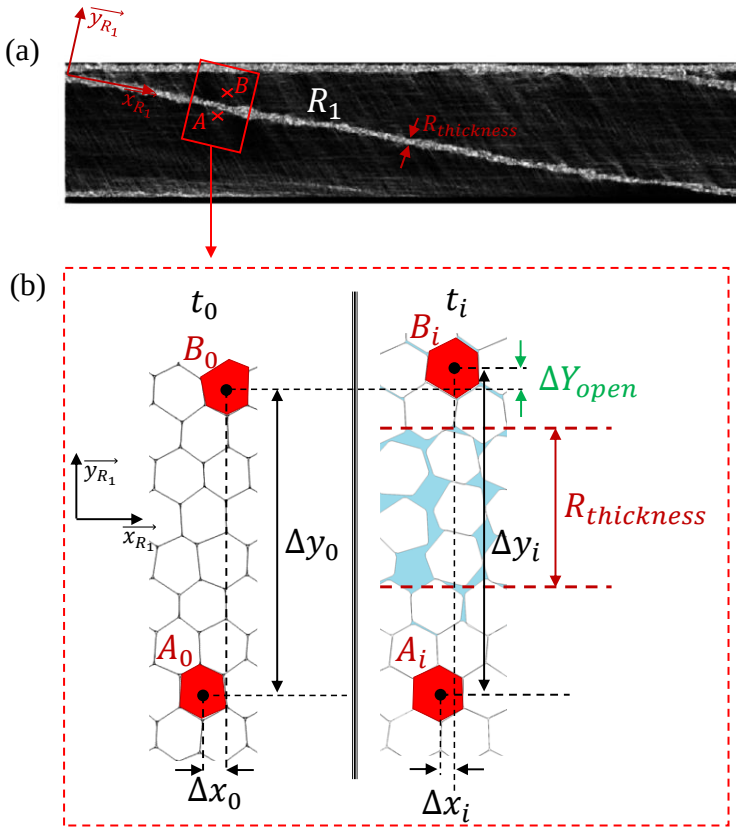

Figure 125. (a) Snapshot of the model at steady-state, where Riedel band R_1 can be observed (only half part of the model here). (b) Sketch of the method used to measure the Riedel band opening. We first select points on each side of the interested band and measure the vertical displacement perpendicular to the band direction, called $\Delta Y_{open} = \Delta y_i - \Delta y_0$ (for more details, see appendix 5.D). The same method is applied on the displacement in the band direction, $\Delta X_{slip} = \Delta x_i - \Delta x_0$.

The horizontal and vertical displacements of each band (in the local reference frame $(\overrightarrow{x_R}, \overrightarrow{y_R})$) are spatially interpolated at different times of the simulation on each side of the band (Appendix 5.D). The ΔY_{open} is then calculated for the interpolated couples of points along each *R*-band. It can be observed that each band evolves differently from the others in terms of space and time (i.e. total slip distance), but they can be gathered in three groups, Figure 126 and Figure 127:

- For **Primary *R*-bands** R_3 and R_4, the ΔX_{slip} (total slip within each band), and the ΔY_{open} (total opening of each band) mostly increase before the effective friction peak of the entire gouge (dark blue lines). Past this point, both quantities seem to reduce until a final state in red. Interestingly, a reduction of ΔX_{slip} implies a negative X_{slip} which means that grains are moving backward in the weakening part within these bands. The R_5 bands, not represented here, evolves similarly.
- **Secondary *R*-bands** R_1 and R_2 evolve differently from the primary bands. Both the ΔX_{slip} and the ΔY_{open} increase until steady-state where they stabilize. The total slip ΔX_{slip} observed within the secondary R-band is almost five times higher than the one observed for primary bands and corresponds to the size of five particles ($\sim 100\ \mu m$). It means that particle sliding within these bands is more important than inside the Primary *R*-bands, which may explain their longer duration and higher importance within the entire slip. The total

opening ΔY_{open} at the end of the shearing is twice the one of primary bands and corresponds to the size of two particles ($\sim 40\ \mu m$).

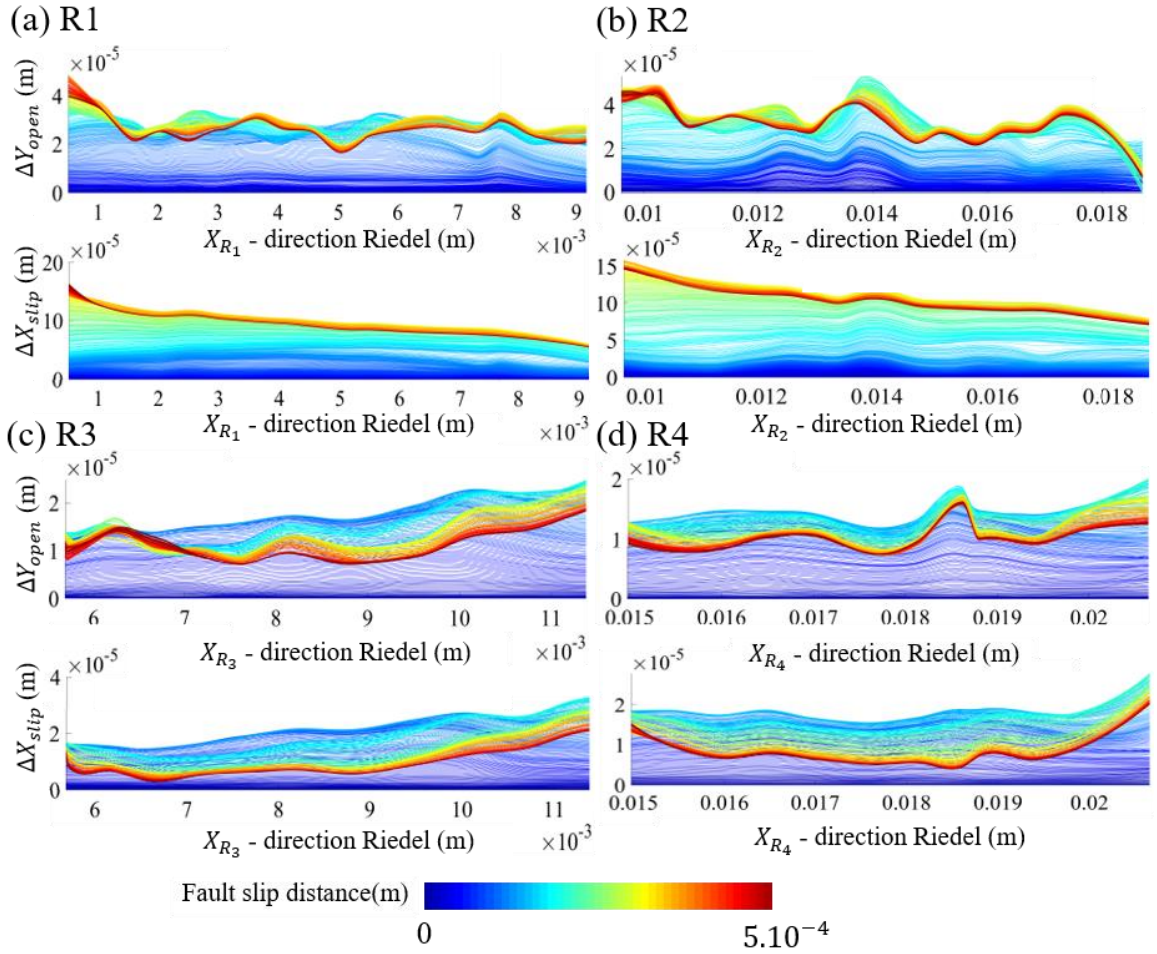

Figure 126. Opening $\Delta Y_{open}\ (m)$ and total slip $\Delta X_{slip}\ (m)$ of the R-bands as a function of the X_R- direction of the Riedel band for different total slips during the simulation (m), (a) for the R_1 band, (b) for the R_2 band, (c) for the R_3 band, (d) for the R_4 band. The four different bands are presented in Figure 124.

– **Y-boundary shear**s present interesting patterns with a slightly higher ΔX_{slip} for Y_1 than for the other bands. This is because this is the principal shear plane and we consider the upper rock wall as a reference, which is moving with a constant slip velocity of $1\ m/s$. Local behaviors also appear on each ΔY_{open} variation as a really nonlinear opening. Besides, there is clearly a progressive activation of Y-bands starting from the point of connection of R-bands: the very regular slopes appearing in figure Figure 127 (a) & (b) for ΔX_{slip} correspond to a characteristic deformation, which can be related to stress through Young's modulus, or simply mentioned as a maximum compression deformation. Y_1 presents two major slopes between the top connection points of R_1 and R_2 (slope of about 1.5 %) whereas in the ΔX_{slip} of Y_2 we can clearly identify four connection points of primary and secondary R-bands (slope of about -0.5 %). In biaxial experiments, the maximum principal stress was observed for a vertical shortening equal to 2% for a confining stress of 40MPa, meaning that for both Y-bands the rupture of the material is not reached. Results are close to the Coulomb-Mohr rupture criterion in the vicinity of the R-band (and to the rupture within it).

For the R- bands evolution, we also suppose that the peaks or troughs observed – when the final value is smaller than the previous value during the simulation – correspond to a change of orientation of Riedel bands. Indeed, in Chapter 4, for the two secondary R – bands $R_1$and R_2, we remark that the orientation angle was changing at the boundaries, meaning that the R_1 band has at least three different orientations. The proximity to rock boundaries seems to diminish the Riedel band angle that becomes part of the next Y-bands formed. This assumption seems interesting, but a validation of this theory, also mentioned in (Hirata et al., 2017), would need further research.

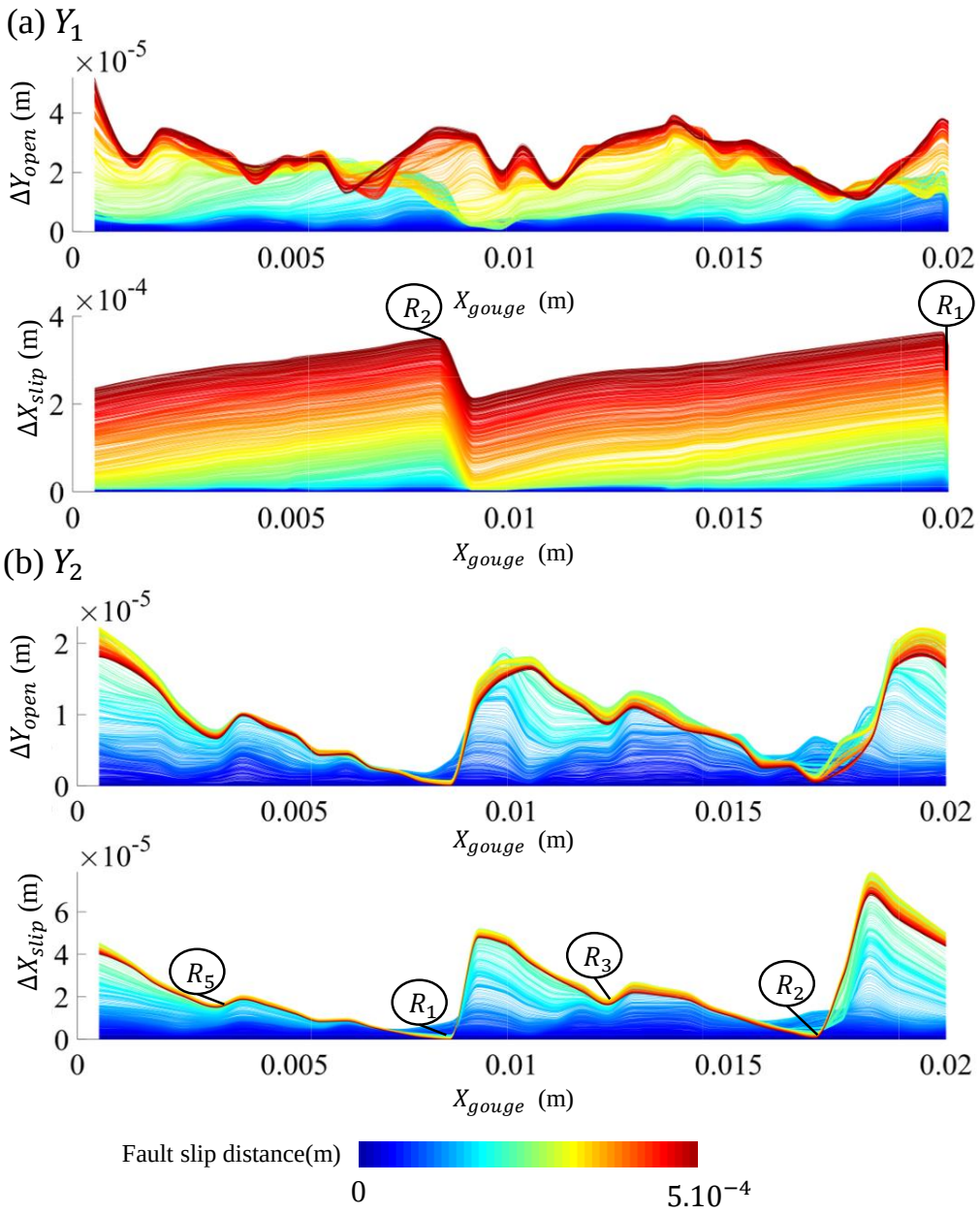

Figure 127. Opening $\Delta Y_{open}\,(m)$ and total slip $\Delta X_{slip}\,(m)$ of the Y-bands as a function of the X –direction of the gouge for different total slips during the simulation (m), (a) for the Y_1 band, and (b) for the Y_2 band. The two different bands are presented in Figure 124.

5.10.2. Time evolution of *R*-bands

Opening of R-bands through time

Thanks to the two variables ΔY_{open} and ΔX_{slip}, it is now possible to know the variation of each band in space (local evolution on the total band thickness) and time (evolution as a function of the total slip of the entire gouge). In order to see the evolution through time of the opening of each band, an average value $\Delta Y_{open-av}$ (of ΔY_{open}) is computed on the total length of each band. A component of $\Delta Y_{open-av}$ represents the average opening for a specific slip distance of the total fault. The evolution of $\Delta Y_{open-av}$ (in meter), Figure 128 (b), for the relevant *R* and *Y* - bands presented in Figure 124, gives the same trends of evolution that have been presented in chapter 4. The observed effective friction peak is not very sudden, and *R*-bands have time to grow between the end of the elastic part (A) and the friction peak (B) (letters are from effective friction curve Figure 128 (a). The three different behaviors (primary and secondary Riedels and Y bands) presented in the previous section are now evident. $\Delta Y_{open-av}$ allows to localize the important events in the life of the different bands and their interactions with each other:

- Primary bands (R_3, R_4 and R_5) grow faster than secondary *R*-bands from *A* to *A'*. They are in their maximum opening just before the effective friction peak (*A'* to *B*) and then start to disappear giving way to the secondary *R*-bands which are still opening. Their orientation angle is also higher ($\sim 15°$ for primary bands and $\sim 11°$ for secondary bands). Primary bands R_3 & R_4 clearly present the smaller $\Delta Y_{open-av}$, confirming their less important role in the gouge history. In Chapter 4, we postulated that only secondary *R*-bands and *Y*-bands were present in the steady-state, however, this representation lets us think that although they are almost not visible on our previous images, primary bands are still present in the model at steady-state, Figure 128.
- The effective friction peak seems to be reached when the opening of each secondary band (R_1 and R_2) exceeds the maximum opening of the primary bands. However, the maximum opening of secondary *R*-bands appears during the slip weakening phase, where the dilation of the gouge has reached its maximum value (grey curve). Then they slightly diminish until the steady-state where they stabilize.
- Finally, the evolution of the *Y*-bands (or should we say "Y planes in a B-shear zone", as described in (Bedford & Faulkner, 2021), is quite different as they slowly grow from the end of the elastic part – where the still inconspicuous *R*-bands connect to the rock walls – to the steady-state, where all bands opening stabilize. While Y_1 tends to a $\Delta Y_{open-av}$ similar to secondary bands, Y_2 approaches the behavior of primary *R*-bands. This different behavior is probably due to the one side shearing.

Three remarkable points indicate a change between active (i.e. visible or with high opening) and inactive bands (i.e. non-visible or with low opening): point B, where primary bands become active (friction peak), point C, where Y_1 become active opening more than primary Riedels (small friction plateau), and points E where the opening of Y_1 as reached the opening of R_1 (steady-state). As previously presented, high angle Riedel bands *R'* exist, but they are too thin and too numerous to be measured and quantified with this method (Chapter 4).

We notice that at steady-state, the sum of each $\Delta Y_{open-av}$ is not equal to the total ΔY_{open} (i.e. dilation of the gouge), this is not surprising as the orientation of the opening of each band is different, which makes this addition not directly possible. Moreover, there are certain areas of contracting behavior that counteract these values, and these are "averaged" values that do not reflect the heterogeneity of each band.

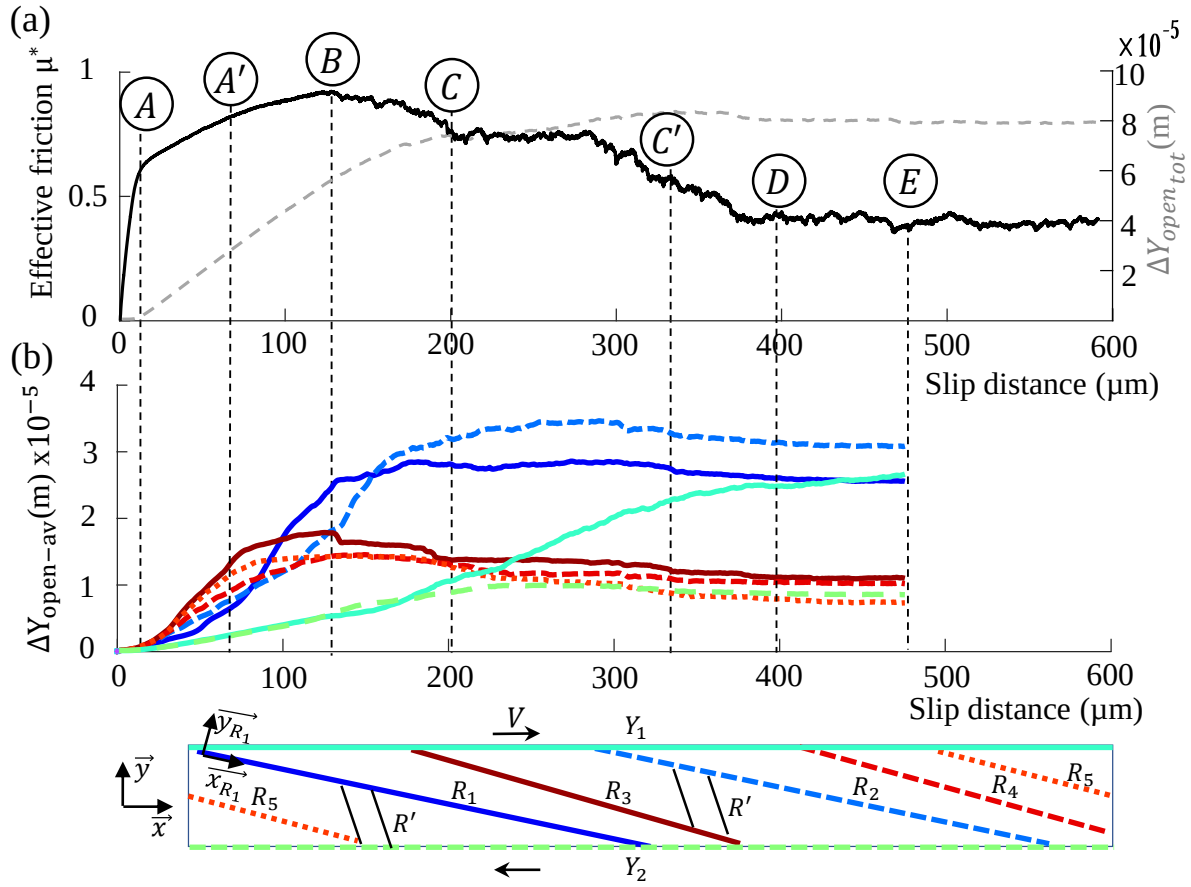

Figure 128. (a) Effective friction for the standard case (M-S), letters A to E are remarkable points and changes in Riedel band evolution. (b) Opening of the three presented bands, $\Delta Y_{open-av}$ (m) (average value over the entire length of the band). The primary bands (R_3, R_4 and R_5) appear in red, the secondary bands (R_1 and R_2) appear in bleu, and the boundary shears (Y_1 and Y_2) appear in green. Both variables μ^* and $\Delta Y_{open-av}$ are presented as a function of the total slip distance (m) of the gouge.

This representation of Riedel band opening is pretty new in the literature, as it is complicated to measure, quantify and follow *R*-bands through lab experiments. Moreover, the distinction into two kinds of R-bands (primary, secondary) is not very common but makes sense after analyzing the ΔY_{open} evolution and images of each *R*-band. The *R*-bands evolution in the pre-peak zone is scarcely investigated in the literature [(Marone & Scholz, 1989), (Kenigsberg et al., 2019), (Bedford & Faulkner, 2021)], but thanks to this representation, it is possible to see that these two types of bands (*R* and *Y)* start to appear just after the end of the elastic part and before the effective friction peak. The absence from the literature of Riedel bands within the pre-peak zone can firstly be explained by the fact that the effective friction peak is not very sudden (contrary to other studies) and allows a gradual growth of the band opening. Moreover, at μ_p^* the $R_{thickness}$ is not as its maximum, and it is possible that *R*-bands existence before the peak was not detected in other studies because of this low thickness, and simply neglected in

the rest of the study. (Kenigsberg et al., 2019) studied a Clay-rich fault gouge with different material characteristics which also may lead to a different evolution of *R*-band within the gouge that the one observed here.

Opening and Riedel thickness

As the ΔY_{open} does not provide the real thickness $R_{thickness}$ of *R*-bands, it has been measured manually with the ImageJ software (Appendix 5.D), giving an overall trend similar for both variables. The $R_{thickness}$ values are not very precise due to artifacts between the filter chosen for the solid fraction observed, image saturation, and the difficulty to measure manually such a small distance. The values found for $R_{thickness}$ $(100-300\mu m)$ are consistent with values found in previous studies for a similar thickness of initial gouge (Marone & Scholz, 1989). A factor of ten was also observed between the values of ΔY_{open} and $R_{thickness}$ measured on the images, but additional measurements on other gouges would be necessary to confirm if this order of magnitude is always true. We did not explore these values, but as the global trend is consistent with $\Delta Y_{open-av}$, it confirms that ΔY_{open} gives a consistent evolution of the opening of *R*-bands.

Analyses of simulation with cells with an equivalent diameter of 40 µm (M-PS-40) were also carried out. The maximum opening for one band corresponds approximately to the size of one particle, and we do know that there is a link between the number of particles within the thickness and global shearing and dilatancy behavior (Chapter 4). The size of particles does not have a huge relative impact on the ΔY_{open} at steady state both on total gouge opening or secondary R-bands opening, Figure 129 (a). For both sizes of particles, the opening of one R-band represents between 30-40% of the total opening of the gouge at steady-state, except for the primary bands that are only 15% of the total opening at steady-state, Figure 129 (b).

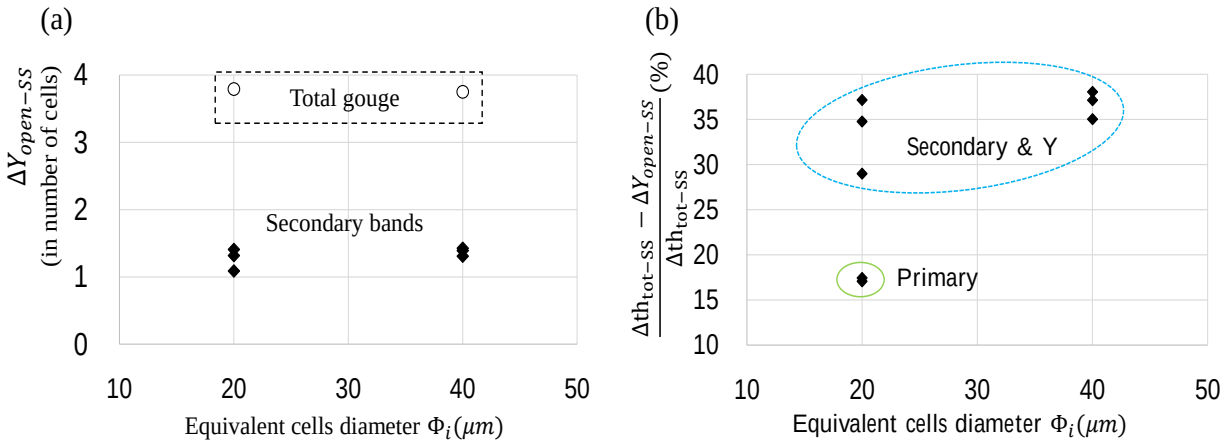

Figure 129. (a) Opening of the total gouge Δth_{tot-SS} at steady state (empty circles) and opening of the secondary and *Y*-bands $\Delta Y_{open-SS}$ at steady state for the two sizes of particles Φ_{20} and Φ_{40}. (b) Opening ratio of the bands to the total gouge Δth_{tot-SS}, for each band and for the two simulations with equivalent cells diameter of Φ_{20} and Φ_{40}, at the steady-state (letters E from Figure 124). The blue dotted circle selects the secondary and *Y* -bands, while the green circle surrounds the Primary bands (R_2 and R_3).

5.11. The inner mechanical behavior of R-bands: towards energetic models

5.11.1. Friction into *R*-bands

To link the mechanical behavior of each band and that of the entire gouge, we decided to go further in the understanding of both local and global mechanisms. This section briefly presents the first analyses and observations leading to the objective of this chapter on simplified models: to isolate specific laws for each *R* and *Y*-band (friction/dilatancy) and to try to relate it to the global behavior of the entire gouge.

To isolate the local behavior of each band, the idea was first to model "**Thin Bands**" (TB) of gouge material, with a thickness similar to the one observed in *R* and *Y*-bands. The objective of these TB is to simulate the mechanical behavior (friction/deformation) of a R-band within the gouge. The chosen thickness must be low enough to avoid any development of other inclined Riedel bands, but not too small to avoid an excessive increase in friction (because if it is narrower than a natural shear band, friction is overestimated). Previously observing that the thickness of a *Y*-band (or *R*-band) was composed of around 10 particles, we simulated thin gouges of a 10-particles thickness (similar to an initial band thickness $R_{thickness} = 200\ \mu m$) with the same physical and numerical characteristics as the entire gouge, to have the local mechanical and kinematic behavior of one single band, Figure 130. However, the TB model is displacement-driven, meaning that the whole length of this gouge model slides simultaneously. This is not the case of the individual shear bands previously described (either *R* or *Y*) in the full gouge model, which develops spontaneously following complex histories, with a sliding distance varying along with their spatial extension at a given time. Hence, the TB model should be considered as an average approximation of the local behavior (i.e. at a given point) of any *R* or *Y* band. The friction curve and dilation of all thin bands generated can be observed in Appendix 5.E.

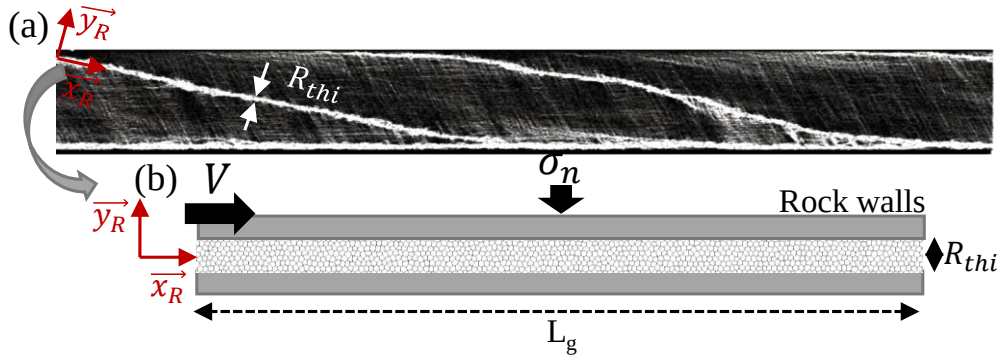

Figure 130. (a) Entire gouge with Riedel bands. The Riedel thickness R_{th_i} of about 10 particles with $\phi_{eq} = 20\ \mu m$. (b) Simulated thin band with the same thickness as the observed $R_{thickness}$, $R_{th_i} = 200\mu m$, and sheared within the same conditions as the previous models.

For the standard case (M-S), the total opening of the entire gouge, as well as the one of the thin bands associated with the model, is presented in Figure 131. Effective friction is obviously higher for the thin band presenting a thickness ten times smaller. The order of magnitude of the

resulting thin band opening is consistent with the ΔY_{open} variation of the Riedel bands found in the previous part ($\sim 2.10^{-5}\ to\ 3.10^{-5}\ m$). This result confirms that the thickness chosen for the thin gouge is appropriate and gives good hope to find some convolution between all the *R*-bands and the overall behavior of the gouge. It raises two interesting questions: if the whole fault is concerned with the sliding of a certain number of *R* and *Y* bands, why is the maximum fault friction lower than that of each shear band? And why is its breakdown energy larger?

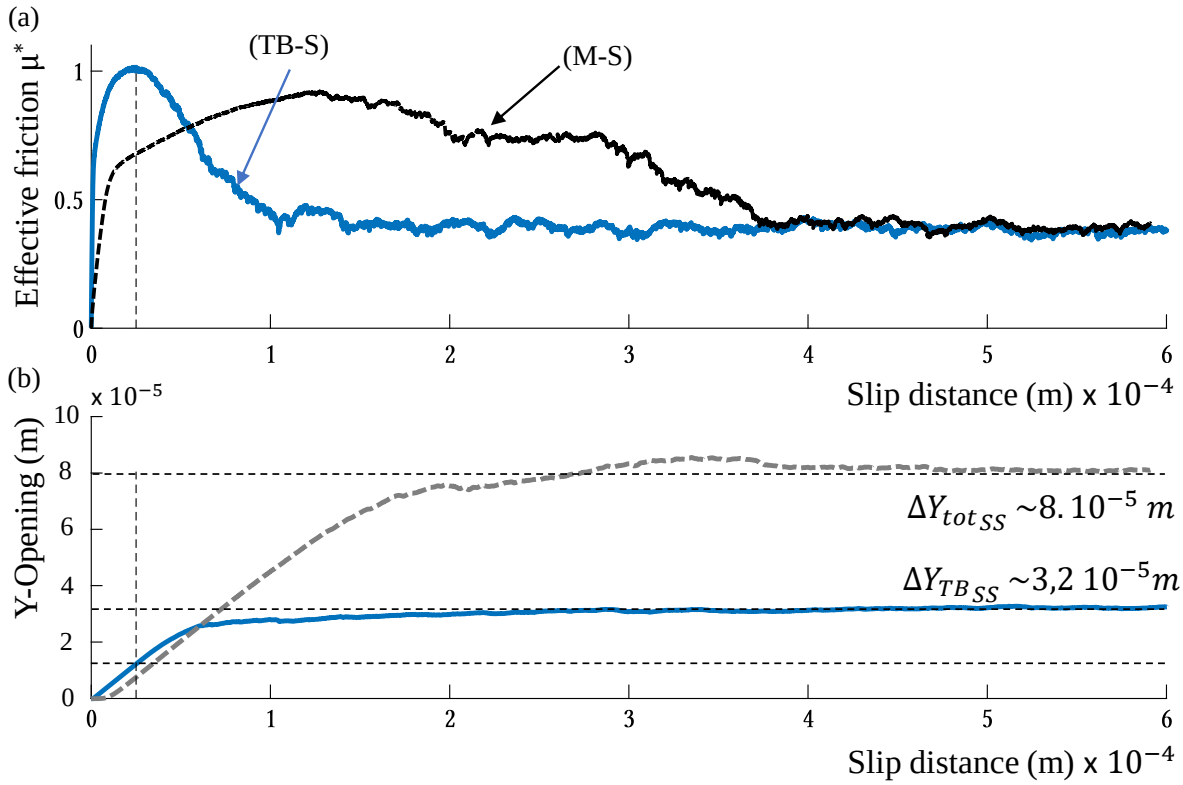

Figure 131. (a) Effective friction μ^* as a function of the slip distance for the standard case (black pointed curve) and the associated thin gouge (blue line). (b) Opening of the gouge in the y-direction (ΔY_{open} for the entire gouge) as a function of the slip distance (m) for the standard case (grey pointed curve) and the associated thin gouge (blue line).

5.11.2. Trajectories and opening of *R*-bands

We superimpose the *Y*-opening observed in Figure 131 (b) with the different dilation-sliding trajectories corresponding to the main *R*-bands and *Y*-bands present within the gouge (i.e. $\Delta Y_{open-av} = f(\Delta X_{slip})$), Figure 132. It can be seen that each *R*-band seems to follow the initial slope of the thin band opening (until $X_{slip} = 1\ 10^{-4}\ m$), implying a similarity in behavior and giving us information on when and to which point the bands participate in the global behavior. The *Y*-band has a major role in global behavior with an opening almost similar to the one of the thin gouges. We can add to this the evolution of the bulk deformation (grey cross) which is the deformation of the sheared granular flow, following the slope of the "total" opening of the gouge (which is the displacement of the upper rock wall in the y-direction, direction perpendicular to the fault gouge). (Y. Katz & Weinberger, 2005) suggested that the granular flow is the dominant deformation mechanism at the early stage of the movement, and progressively gives way to Riedel structure as the dominant mechanism of deformation. Our

results seem to confirm this theory but will require separating the dilation and friction from each mechanism to understand their role.

To each value of slip distance from the total behavior of the gouge, we can zoom in on each *Y* and *R*-bands and see how it is opening ("thin band" opening with slip distance) and what is the associated friction law ("thin band" effective friction with slip distance). The next section presents the results and assumptions used to link local and global behavior in order to get a simplified frictional model of a gouge with matrix particles from these results.

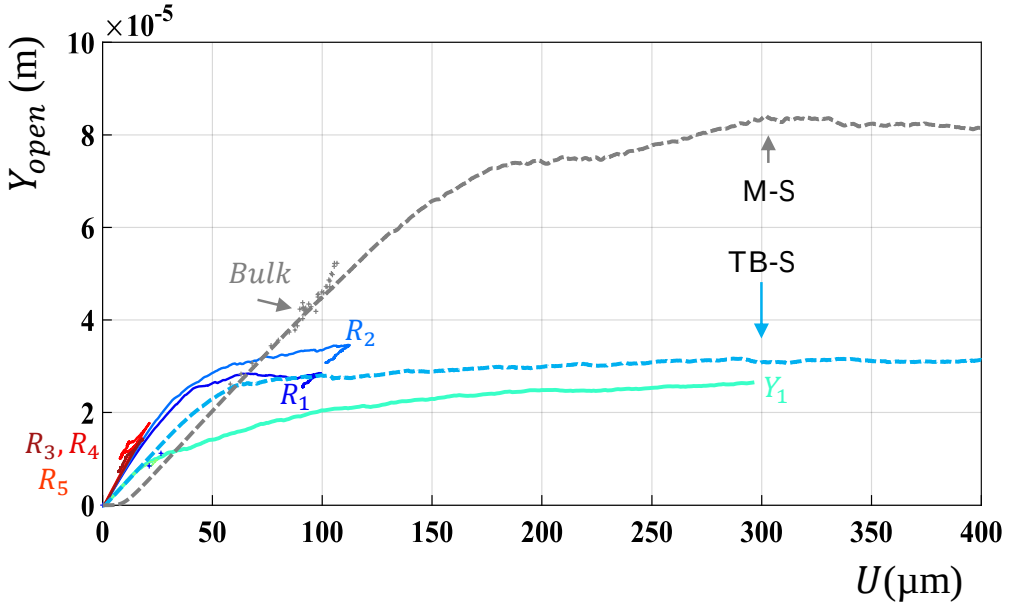

Figure 132. Opening of the entire gouge [$Y_{open} = f(U)$] for the standard case ($20 \times 2\ mm^2$, dashed grey line) and the associated thin band ($20 \times 0.2\ mm^2$, dashed blue line), and dilation-sliding trajectories of each band [$\Delta Y_{open-av} = f(\Delta X_{slip})$]. For (M-S) and (TB-S), U is the actual slip distance, and for the *R*-bands, U is the respective displacement within each band (called ΔX_{slip}) and total slip distance for the dashed grey line.

5.11.3. Energetic interpretations

Now that the mechanical behavior of each band observed in the model is known, we propose to gather all their contributions into a single energetic interpretation. This small exploratory part is also based on energetic distributions.

Proposed method

Based on the previously defined rupture energy, the total energy E_{tot} spent by the fault at a given sliding distance U can be linked to the observed friction and the normal stress applied to the fault:

$$E_{tot}\ (U) = \int_0^U \sigma_N\, \mu^*(u)\, \mathrm{d}u \qquad (5.11)$$

It can also be written as a small increment of energy $\mathrm{d}E_{tot}$ spent for a sliding increment $\mathrm{d}u$, such that: $\mathrm{d}E_{tot} = \sigma_N \mu^*(u)\, \mathrm{d}u$, with $\mu^*(u)$ the current effective friction of the fault gouge for a current slip U (in the x-direction of the fault), and σ_N the normal stress applied to the fault.

All these data have been exploited or calculated in Chapter 4 and Part A of this chapter so that they are all known.

The objective here is to reconstruct the effective friction μ^* observed on the entire fault with the μ^*_{TB} extracted from thin bands simulations. This reconstruction is done at each instant of the simulation, i.e. for each slip increment of the fault.

If we start from the small energy increment of the complete fault, we can write that the small increment of energy spent $\mathrm{d}E_{tot}$ is also the sum of all the incremental energies $\mathrm{d}E_{TB}$ spent in the *Y* and *R* bands present within the fault integrated on the total band length, plus some possible energy spent in the bulk of the gouge outside of the localization sites:

$$\mathrm{d}E_{tot}\,(U) = \sum_{N_{bands}} \int_{L_{TB}} \mathrm{d}E_{TB}(U_{TB})\mathrm{d}l \qquad (5.12)$$

With N_{bands} the total number of *R* and *Y* bands selected for the model (here R_1, R_2, R_3, R_4, R_5, Y_1 and Y_2), L_{TB} the length of each band and U_{TB} the current slip inside each band.

$$\mathrm{d}E_{tot}\,(U) = \mathrm{d}E_{R1}\,(U) + \mathrm{d}E_{R2}\,(U) + \cdots + \mathrm{d}E_{Y2}\,(U) + \mathrm{d}E_{Bulk}\,(U) \qquad (5.13)$$

For example, the spent incremental energy on R_1 is

$$\mathrm{d}E_{R1}\,(U) = \int_{L_{R_1}} \left(\sigma_N \mu^*_{R_1}\left(U_{R_1}(x)\right)\mathrm{d}U_{R_1}(x)\right)\mathrm{d}x$$

with $\mu^*_{R_1}\left(U_{R_1}(x)\right)$ the current effective friction on R_1 at the abscissa U_{R_1} and $\mathrm{d}U_{R_1}$ which is the incremental slip on R_1 (corresponding to the previous ΔX_{slip} calculated at each time step and for the different spatial locations). The $\mathrm{d}U_{R_1}$ values come from previous calculations on each *R*-band and the $\mu^*_{R_1}\left(U_{R_1}\right)$ comes from the effective friction extracted from Thin Bands simulations presented in 5.11.1.

First results

Figure 133 presents the effective friction of the entire gouge as a function of the slip distance and the energetic contribution of each band during the shearing, represented by a colored area under the friction curve. When the energetic contribution of each band is summed, it is observed that energy is missing in the pre-peak part. This energy is considered as a bulk energy from internal gouge deformation. This bulk energy is mainly active before effective friction peak and progressively disappears as deformation localizes within the different shear bands (mainly *R*- and *Y*-bands).

The energetic behavior obtained seems to be consistent with the previous results observed and reveals the importance of each band within the model, (numeration on Figure 133):

i. The energetic contribution of primary bands is observed at the beginning of the friction curve in the pre-peak part and is small compared to other contributions.

ii. Then comes the energy contribution of secondary bands R_1 and R_2 with maximum energy spent just after friction peak

iii. At the middle of the weakening part, the energetic contribution of *Y*-bands becomes dominant (both for Y_1 and Y_2) and progressively reduces and stabilizes until the steady-state zone.

iv. The green energetic peaks may come from contractive bulk response which is not considered here. Further improvement could be done on that.

v. When the steady-state plateau is reached, the two boundary shears total all the spent energy of the system, suggesting that the rest of the gouge is stabilized. The secondary bands' activity (R_1 and R_2) has died out, although they are still physically present and visible in the gouge (chapter 4). The only "active" band at steady state is the Y_1boundary shear.

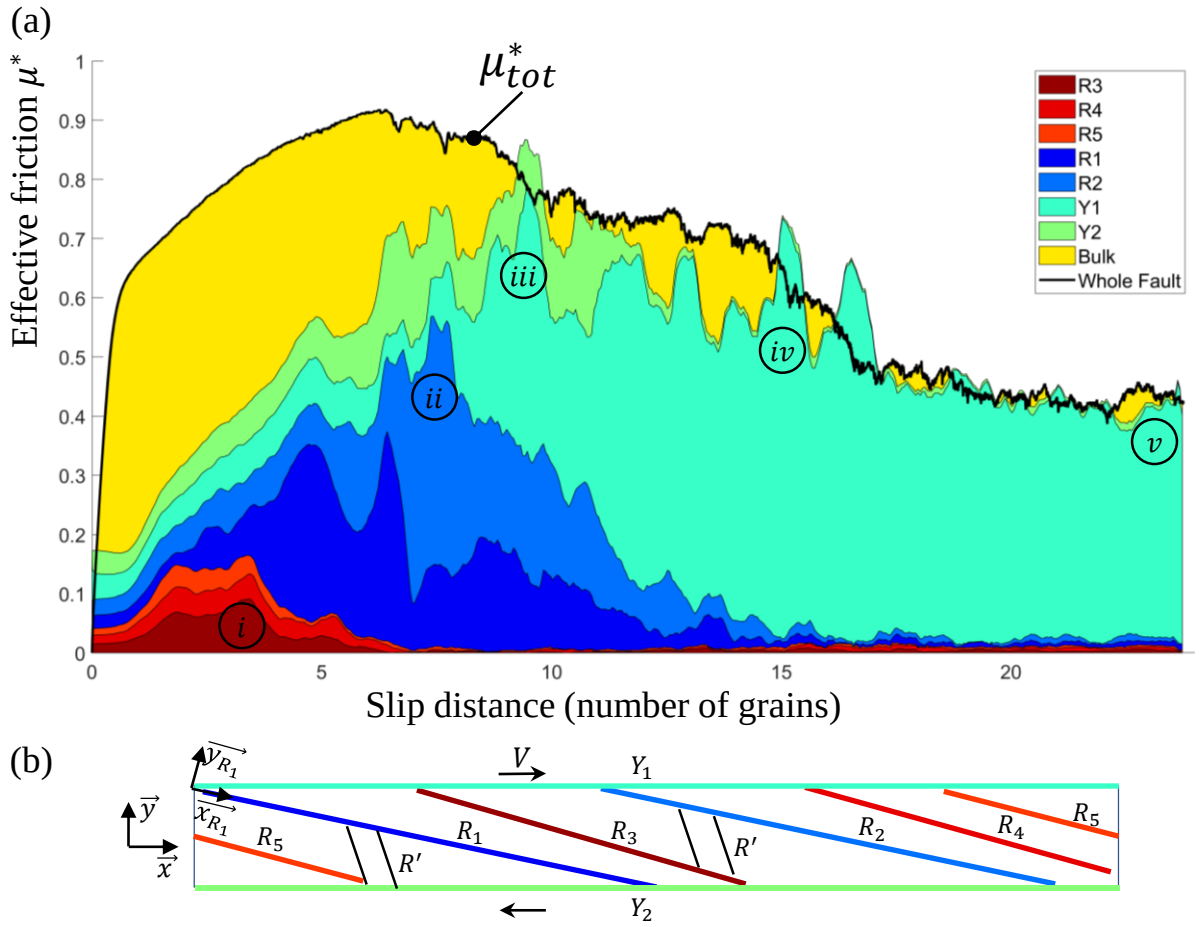

Figure 133. (a) Effective friction on the entire gouge (black curve) as a function of the slip distance. Note that the slip distance is expressed as a dimensionless quantity which is the ratio between the slip distance (m) under the size of particles (m), giving an equivalent number of particles. The energetic contribution of each band during the shearing is colored under the friction curve such as the legend. Zone from (i) to (v) are points of interest explained within the text. (b) Schema of the standard gouge (M-S) with the principal Riedels and boundary shears observed.

Internal mechanisms

As for Part B, it is possible to calculate the part of released energy related to the dilation of the gouge (dilation energy E_{Dil}), for the whole gouge, as well as for the different bands, Figure 134 (a). As there is no cementation in these models, the total remaining energy is considered as

frictional energy $E_f = E_{tot} - E_{Dil}$, Figure 134 (b). Contrary to the behavior observed for cemented materials there is first a dilation contribution and then a frictional contact contribution. This seems logical as the very dense matrix gouge first dilates and as dilation decreases, frictional contacts are enhanced. As mentioned above, it is possible that areas of contraction, not considered here, can compensate for the excess energy caused by the expansion of the Y_1 and Y_2 bands observed, Figure 134 (a) zone i.

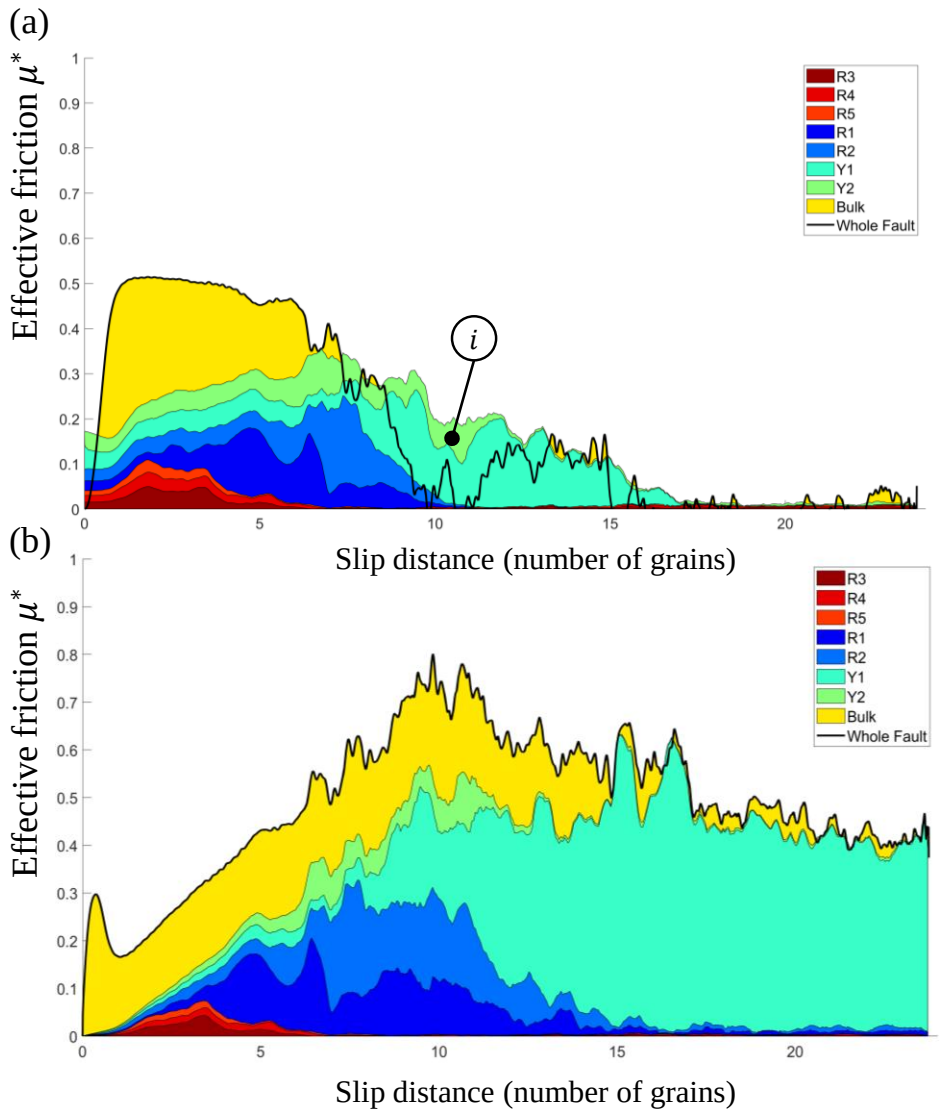

Figure 134. (a) Dilation contribution to the effective friction of the entire gouge (black curve) as a function of the slip distance. The energetic contribution of each band to dilation energy is colored under the friction curve such as the legend. Zone (i) is a point of interest explained within the text. (b) Frictional contribution to the effective friction of the entire gouge (black curve) as a function of the slip distance. The energetic contribution of each band to frictional energy is colored under the friction curve such as the legend. Note that the slip distance is expressed as a dimensionless quantity which is the ratio between the slip distance (m) under the size of particles (m), giving an equivalent number of particles.

These energetic models seem to confirm the importance of *Y*-bands in the development of fault zones. The sum of the energetic contributions of all bands is higher than the bulk energy participation. We also note the non-equal and non-simultaneous contributions of the primary and secondary bands:

- The primary bands participate in the pre-peak phase for both dilation and frictional contributions. If the *R'*-bands were considered, it is assumed that they would play in this same zone. These bands are a precursory event in the life of a fault and could characterize the type of gouge material studied. Interestingly these primary bands did not appear for cemented material. It could be explained by the longer pre-peak zone observed here, and we suppose that they are characteristic of dense and non-cohesive material. Cemented materials with their brittle character directly switch to secondary *R*-bands.
- The secondary bands and *Y*-bands seem to always form for dense materials (cemented or not) starting from the pre-peak zone and growing until the beginning of the weakening zone.

Comments on unanswered questions

- Why is the effective friction peak of the complete fault lower than that of the individual thin bands? It is a question of lack of synchronicity. Each *R*- or *Y*-band reaches its friction peak at different times, from one band to another, but also within each band individually (by the spatial variability of slip on each of them). As they do not synchronize to reach their own peak together, the peak of the entire gouge is thus lower than the individual peaks.
- Why is the energy of the complete fault much higher than that of the thin bands? It is here a question of chronology. If there was only the Y_1 −band, there would be a perfect equality between the two energies. However, within the real simulated gouge, before activating this Y_1 −band and sliding on it alone, the fault takes lots of energetic dead ends: primary bands, then the secondary bands, the second Y_2 −band, and the bulk deformation. All these detours consume energy unnecessarily and contribute to increase the breakdown energy of the fault. In the end, these patterns (i.e. Riedel bands) lead to (i) reduce the intensity of the friction peak and (ii) increase the breakdown energy: consequently, it reduces considerably the weakening rate (i.e. the downward slope of the friction curve): it has, therefore, a powerful stabilizing effect on the fault.

In future studies, we plan to perform these same studies on several models presented in Chapter 4. The idea is to be able to observe different energetic behaviors depending on the parameters of the gouge and insert these models in dynamic modeling. Interparticle friction or stiffness may have a non-negligible influence on the link between local and global behavior. Another good reason to expand this study is to understand why the fault takes these different kinematic paths and be able to model them in order to write a friction law of the whole fault based on the energetic decomposition proposed.

5.12. Conclusion of Part C

This last section goes further in the analysis of Riedel bands and their link to deformation evolution and energy release of the system. First of all, it is possible to observe both global and local variations of Riedel band opening and sliding. The orientation angle of these bands can be different depending on whether the observed zone is in the center of the gouge or close to rock walls. Then, we observed the temporal evolution of Riedel bands with slip distance, focusing on the global opening variation of each band. Primary bands and secondary bands appear together, but primary bands grow faster, giving spaces to secondary bands at friction

peak. When the secondary bands become “active”, they des-activate the primary bands. The *Y* bands evolve progressively until steady-state where they become the only “active” bands. This representation of Riedel bands is really promising to realize microanalyses of the inside of each *R*- and *Y*-bands.

Finally, we wondered about the role that these bands might have on the global behavior of the gouge and tried to connect the mechanical behavior inside each band to the entire gouge kinematic. An overview of the method is proposed with energetic description and proper relations between each band and the gouge. The energetic contribution of each band agrees with their time and space location but gives another way to observe Riedel mechanisms and to conclude on their role and activity.

Although some simplifications and research are still missing to have a better energetic model, this little simplified model is very promising to study the Energy budget and the role of each Riedel band within the weakening mechanism as a function of the characteristics of each infill material.

Chapter 6. Conclusions & Perspectives

6.1. Conclusions

The fault gouge, coming from the wear of previous slips, acts on friction stability and plays a key role in the sudden energy release. A large part of slip mechanisms is influenced, if not controlled, by fault gouge characteristics and environment. During this thesis work, 2D Discrete Element Modelling was performed for a better understanding of (i) how infill materials (matrix or cement) participate in the strengthening or weakening of the fault, (ii) the rheological behavior observed highlighting shear band formation, and its link with gouge characteristics, (iii) the contribution of each of these mechanisms in the observed breakdown energy and friction laws. Three main types of gouge samples were generated to simulate a mature fault gouge with infill material and then inserted between two rock walls to realize direct shear experiments using the software MELODY2D (Chapter 2). A dry contact model was considered to investigate mechanisms without fluid (displacement-driven and under constant confining pressure). Numerical simulations were performed and the associated analyses provided answers to the questions raised in the General Introduction.

- **What role plays cementation in the weakening of mature fault gouges?**

Do cemented materials promote slips in faults? A first fault gouge model was implemented with a cohesive law to mimic the cementation within the gouge (Chapter 3). Both initial porosity and surface percentage of cementation influence gouge weakening and slip behaviors, playing a role in the gouge strength (brittleness, cohesion) and granular flow (particles agglomerates, Riedel bands). High cementation within materials increases the shearing resistance, limiting in some way the number of slips that could take place in the fault, given that high stress is needed to observe a nucleation. However, for these materials, the observed stress drop is much larger and also steeper (sharp, short, and intense peak), which means that if the shear stress peak is reached, the observed slip is more likely to occur in an unstable manner and with high energy release. Both the critical distance of slipping and the nucleation length decrease with an increase in cementation (Chapter 5), confirming that not much mobility is allowed within the system, and increasing the risks of instabilities to happen. Riedel bands, which are key elements in the understanding of stability in faults, are significantly affected by a change in contact laws between particles (cohesion or friction) occurring with cement breakage. They only appear for dense materials when a threshold of cementation is reached and are directly linked to the importance of the dilation phase since the majority of the gouge remains cemented even after the weakening phase. Low cemented materials follow a rather ductile behavior without observation of apparent Riedel bands inhibited by a critical dilation higher than 1%, whatever the tested samples are dense and mid-dense. The whole gouge area is sheared with low fracture energy and a low dilatancy.

Although Riedel bands are not sufficient to detect unstable behavior, they are nevertheless necessary conditions, leading to the conclusion that dense and highly cemented materials are

more likely to generate unstable behaviors, while mid-dense or dense materials with very low cementation will rather tend towards a ductile, and stable behavior.

How can the energy balance of a cemented gouge be decomposed and what mechanisms remain most influential? The effective friction was decomposed into three main mechanisms: gouge dilation, friction between particles, and breakage of the cemented bonds (Chapter 5, Part B). Using this decomposition, a simplified friction model is proposed as the sum of these three contributing frictions. The advantages of the proposed model are its ability to locate the different mechanisms over the fault displacement and quantify their relative contribution to fault gouge weakening. The same decomposition was performed from an energetic point of view, on the breakdown energy. Results obtained during simulations agree with previous research and highlight that the dilation phenomenon is the main mechanism involved in the breakdown energy, even for cemented gouge. Although mid-dense materials have a rather linear increase in both the breakdown energy and the necessary energy to dilate the sample, the behavior of dense materials is more complex. As previously stated, the increase in cementation has a general tendency to promote unstable behaviors, but materials most likely to generate sliding instabilities are not the most cemented material but the mildly-cemented ones (between 25% and 75% cementation). Indeed, the agglomerates of cohesive particles generated within the gouge make the fault rather heterogeneous and increase the roughness within the slip surface, which has the effect of significantly increasing the dilation energy. This could generate a much higher slip velocity response during sliding.

The energetic decomposition performed also allowed us to understand the reasons for a double weakening observed for dense and cemented materials. Effective friction curves present double weakening shapes for dense samples with a sufficiently high percentage of cementation (to create an internal cohesion higher than 1 MPa or 2.5 % of the applied normal stress). The first weakening is a combination of the three mechanisms (dilation, friction, and cement breakage), and the first corresponding stress peak increases with the increase in cementation (proportionally to the peak of frictional energy). The reduction of the number of particles in contact, coupled with the shear rate applied to the gouge increases contact friction for these particles. According to our observations, a second weakening is observed, mainly due to the decrease of dilation energy, which progressively weakens the effective friction.

- **What role plays matrix particles in the weakening behavior of mature fault gouges?**

How important are the different physical and geometric characteristics of matrix particles in the slip behavior and in Riedel bands formation and evolution? To answer this question, another gouge model was implemented in DEM, with a very dense sample composed of hexagonal-shaped particles representing matrix grains. The variation of the different geometrical (shape, size, and distribution of the grains) or physical (stiffness and interparticle friction) properties of the matrix represents different rock lithologies, allowing to observe a large variety of rheological behavior (Chapters 4 and 5). It appeared that all these lithologic variations could be summarized into only three parameters: (a) the bulk shear modulus, (b) the

ratio of gouge thickness to grain size (i.e. number of particles within the gouge thickness), and (c) the interparticle friction.

A fault gouge with a small interparticle friction coefficient, a low number of grains in the gouge thickness, or a high shear modulus will, in all three cases, tend to decrease the orientation angle of Riedel bands. This small angle is partly due to the presence of a Riedel structure with a large number of *R'* -bands (conjugate Riedels) inhibiting the formation of the *R*-band and delaying the arrival of a steady-state. However, their consequences on gouge strength, nucleation length, and breakdown energy are not similar and lead to different types of sliding behavior. Materials with both a **low shear modulus** and **low interparticle friction**, also show a reduction in the maximum frictional resistance. These materials are close to those defined as weak gouge materials [(Collettini et al., 2019), (Bedford et al., 2022)], with a rather ductile behavior that tends to increase both the critical slip distance and the critical nucleation length. Greater mobility is thus allowed within the fault, and the associated breakdown energy remains low, as for weak cemented materials previously studied. The very low shear modulus combined with large regions of nucleation is more likely to tend towards slow slip nucleation (Leeman et al., 2016). On the contrary, for low shear modulus with **increasing interparticle friction** (ex. mineral transformation, chemistry, surface and grain shape roughness…), both the orientation angle of Riedel bands and the number of Riedels observed are increasing. The critical slip distance is reduced (as the critical nucleation zone), leading to a more sudden weakening, which is prone to switch the fault behavior from a ductile aseismic response to a brittle seismic slip, depending on the stiffness of the surrounding medium. No more Riedel structure is observed. Materials with **high shear modulus** (ex. increase in interparticle stiffness) produce a higher resistance to slipping, giving a shorter nucleation length and slightly higher fracture energy. A rather strong, but unstable behavior is observed. For a **reduction in the number of particles in the gouge thickness** (ex. increase in the size of particles, reduction of the gouge thickness), the observed breakdown energy increases as well as the critical nucleation length. The mechanical behavior tends to the one of weak materials, but with a material that struggles to stabilize over time, explaining the higher fracture energy observed. But it also means that this long and smooth slip weakening decreases the probability of instabilities to occur.

To which extent is there an influence on the proportion of matrix/grain and their distribution in the fault gouge samples? Direct shear tests conducted on a composite mixture between matrix and angular particles showed that the percentages of both matrix and angular particles, and initial porosity participate in the mechanics and rheology of fault gouge (Chapters 4, and 5 Part A). Mixing angular grains with matrix grains strengthens the gouge regardless of the granular distribution in the sample. Indeed, gouges composed of a single type of material have a lower frictional resistance, partly due to a higher initial porosity, but also to a change in the distribution of contacts at the granular scale.

The most slip-resistant material appears to be the one with the lowest percentage of the matrix but in which the porosity is close to zero. It is therefore a material with a very high shear modulus, implying a reduction of the orientation angle of the Riedel bands and the formation of a more important Riedel structure. An increase in fracture energy is observed with decreasing matrix percentage as angular particles inhibit Riedels to join the Boundaries of the gouge and

to form Y-bands, leading to a deformation of the entire gouge. However, inhomogeneous and fractal grains distribution (angular particles) seems to favor a smoother and stable slip weakening than homogeneously distributed clasts which promote a very sudden friction drop, very likely to generate seismic instabilities.

How the behavior of each Riedel shear band observed in the fault gouge can be related to the overall behavior of the gouge? To answer this question, the evolution of each Riedel band's thickness was followed over time and space (Chapter 5, Part C). For this purpose, the variation of the band opening was measured during the shearing process at different points of the Riedel band, giving a glimpse of both global and local variations of the band opening. Two types of low Riedels were observed: "Primary Riedels" grow faster with slip distance. When the friction peak is reached they give way to another family of Low Riedels called, "Secondary Riedels" (with slightly higher angle orientation). When secondary bands reach their maximum thickness, they de-activate the primary bands, which are no longer visible. These secondary bands persist during the whole shearing process. The Y bands, on the other hand, evolve progressively from the end of the elastic phase and until the steady-state is reached, where they become the only "active" bands (localizing particle displacements).

Finally, the mechanical behavior inside each band has been connected to the entire gouge kinematic. To do so, the mechanical behavior of a single Riedel band was needed (friction and deformation). By shearing a gouge with tens of particles, inhibiting other Riedel formations in the Riedel, we model a one Riedel band behavior enabling to recover the associated friction and dilation. Each friction recovered from a single Riedel can be transformed into an energetical contribution to the whole gouge. By adding each energetic contribution as a function of the fault slip distance, an energy distribution map is drawn as a function of the total slip distance. The energetical contribution of each band is in adequation with their time and space location but gives another way to observe Riedel mechanisms and to conclude on their role and activity. This energetic model is still to be improved but allows a new form of decomposition of the breakdown energy according to the different rheological mechanisms that take place during the slip.

- **What friction laws can be used to model fault gouges with infill materials in dynamic models?**

Classical slip weakening models were first applied to the friction curves obtained, intending to approximate behaviors by making them more tractable to use for understanding fault weakening (Chapter 5, Part A). The linear slip weakening model is not valid for all the granular samples tested, since it is not accurate enough for some granular materials, such as dense and highly cemented fault gouges that exhibit double frictional weakening. However, similar difficulties would have been encountered for a non-linear slip weakening model. A balance must be found between a too simple and a too complex model. For this reason, Chapter 5 proposes other friction and energetic laws linking local rheology and gouge mechanics. Simplified models proposed for cemented gouges (Part B) are pretty convincing about the final friction shape and evolution and the different mechanisms involved in gouge shearing. These friction laws could be adapted to a large range of imposed stress and velocity if properly fed with additional simulations. The energetic model used in Part C also intends to be easily integrated into a larger scale dynamic model in which one could specify the number of Riedel bands present and their

category and thus be able to test a multitude of deformation cases at larger scales and especially with a thorough study of the seismic or aseismic behavior generated by these slip localizations.

These friction laws are primarily intended to be integrated into dynamic models at larger scales and are proposing a different view of friction laws that can be completed by rate-and-state laws widely used in fault mechanics.

6.2. Perspectives

Following the work done, several perspectives are proposed to this thesis either to improve our numerical models, to propose the next research steps, or to answer questions emerging from the Thesis work.

Improvement in the present research

- For several reasons explained in Chapters 1 and 2, the research carried out focused on a certain set of numerical experiments under a normal stress of 40 MPa, a sliding velocity of 1 m/s, and an initial gouge thickness of 2 mm. It might be interesting to extend the numerical campaign to cover a wider range of normal stresses, velocities, and gouge thicknesses, in order to derive an empirical friction law based on the micromechanical properties of the gouge.
- The friction law obtained for cemented gouge (Chapter 5, Part B) can also be improved by changing the parameters law for mid-dense and poorly cemented materials. Further simulations might be undertaken to fulfill this objective. Cement evolution mostly depends on reaction-diffusion equations mimicking the transport and precipitation of minerals (Magnus Wangen, 1998). An interesting line of work could be the investigation of the characteristic time of cementation in a fault and to evaluate to what extent the associated evolution of the fault strength interacts with its seismic cycle.
- The detailed analysis of the evolution of Riedel bands during sliding (Chapter 5, Part C) has only been performed for one gouge sample. It would be interesting to perform the same post-treatment study on the other simulations with different kinematics (variation of friction or interparticle stiffness, grain size, gouge thickness...). The results will allow us to observe how each characteristic of the gouge will influence the opening and activity of the different Riedel bands. It will also enrich the proposed energetic model according to the characteristics of the gouge.

Study of the seismic and aseismic character of the tested granular fault gouge with dynamic modeling and earthquakes recurrence models

Now that we have proposed energetical models for the different fault gouge studied, it would be interesting to insert them into larger-scale dynamic models to study the seismic or aseismic behavior of these different gouge materials. These models would be very instructive to complete the information learned about infill materials (cement and matrix) at the millimeter scale and especially to test our friction laws on larger dynamic scales. This part will be the subject of an upcoming study.

The well-known Burridge-Knopoff model [(Burridge & Knopoff, 1967), (Stefanou, 2020)], is a good starting point to quantify the seismic character of a fault. This model consists of an N-degrees of freedom spring-slider system with specific friction laws at the sliding interface between blocks and sliding walls, Figure 135 (a). This model is very simple and allows a quick overview of the stability of the studied system as well as the prediction in time of slip events that can occur at the scale of the whole fault, Figure 135 (b). As a better perspective, we would like to turn to physics-based dynamic models of earthquake rupture that couple friction laws and the elastodynamics of coseismic off-fault damage and their effect on rupture dynamics, radiation and the global energy balance (Okubo et al., 2019a). The idea is to implement our different friction and energetic laws (Chapter 5) into such models and see if these laws have an impact on the entire behavior of the fault.

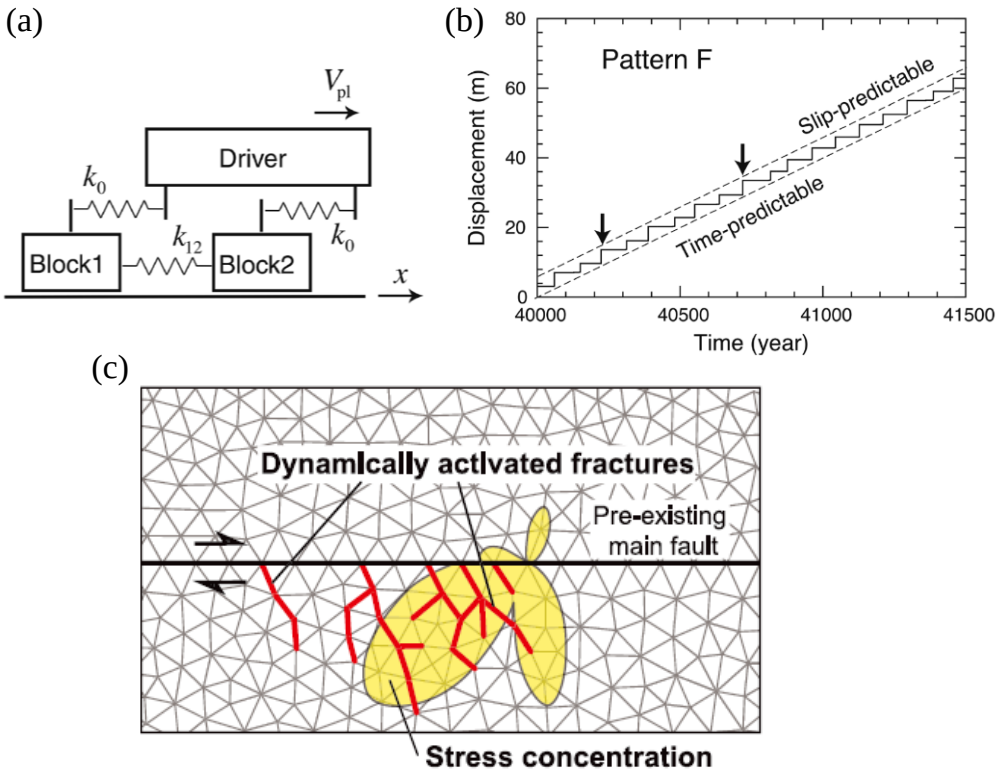

Figure 135. 2-blocks model with RS friction. (a) Schema of the model, (b) Displacement versus time for block 1. Arrows indicate cycles when both blocks slipped simultaneously. (From Abe and Kato, 2013 and (Scholz, 2019)), (c) Image of dynamic rupture models with mesh discretization and the off-fault fractures. Every interface between elements is regarded as a potential failure plane. Typical friction laws can be implemented within the code, and image from (Okubo et al., 2019a).

Heterogeneous cemented faults

Heterogeneous faults are known for their important role in friction weakening (Collettini et al., 2019). A recent study by (Bedford et al., 2022) confirmed this result showing that heterogeneous faults (composed of quartz and clay) have a higher frictional weakening behavior and are less stable than their equivalent homogeneous fault gouges (composed of the same percentage of materials). In line with their work and our previous work on matrices and cement, it would be interesting to model a gouge composed of cemented and non-cemented materials

non-homogeneously distributed, Figure 136. This could induce locking points within the fault, changes in dilatancy, and slip localization zones.

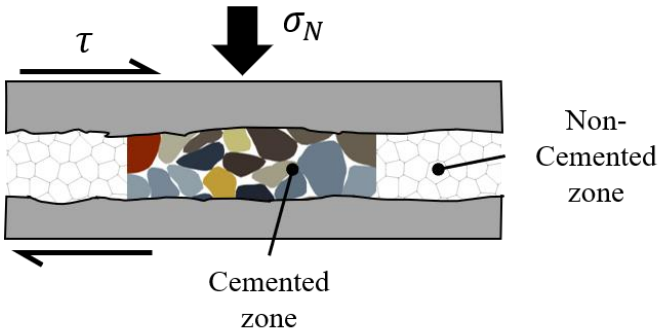

Figure 136. Schema of a granular fault gouge with two different materials non-homogeneously distributed. τ is the applied shearing stress and σ_N the normal stress.

Weak gouge representation as a mixture of hard and soft particles

In our work, completely rigid grains are assumed for both matrix and angular particles. However, it is obvious that weak materials with deformability properties, such as clays or talc, have a significant influence on the weakening behavior of faults [(Haines et al., 2009), (Orellana et al., 2018), (Kenigsberg et al., 2019)]. It would therefore be interesting to start again from the composite mixture of grains and matrix simulation and to replace the matrix grains with deformable particles.

The software MELODY used for DEM modeling allows to deal with mixtures of both deformable and rigid grains and has already shown very interesting results for studies in the field of granular materials [(Mollon, 2018b), (Bouillanne et al., 2021)]. These studies could be compared with results already observed in Laboratory earthquakes. They would also provide insight into the behavior of weak or deformable mineral inclusions in gouge rheology and their implication in slow slip events: the proportion of weak minerals going into Riedel band localization, their deformability rate, and also the stresses observed within each compliant particle.

Wear evolution during gouge shearing

Another interesting approach is to observe the influence of a change in wall roughness due to the wear of the rock during sliding. For this, it is possible to model a fault gouge in three parts: a continuous and rigid part representing the host rock, a gouge material already presents in the fault and a degradable part (pre-cut) which may separate into wear particles (i.e. rock grains), Figure 137. This model can be realized with a (CZM)-contact law, often used in tribology applications to consider the effect of the wear of a material. Thus, it will be possible to observe several interesting phenomena such as a variability in the wavelength of the walls and an increase in the gouge during the sliding which will be likely to modify the slip weakening behavior. The addition of deformable rock walls also allows to observe the associated stress field, but this will be very costly in computing time.

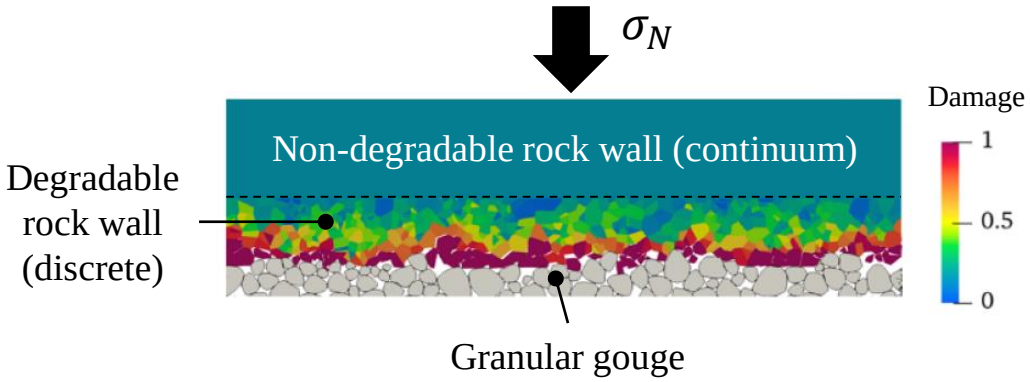

Figure 137. Image modified from (Quacquarelli, 2021) with CZM -contact law, which is a "fatigue" law.

Temperature control and dynamic weakening

Temperature control in fault gouges simulations is a major asset since it allows to highlight melting zones that are responsible for both a change in material behavior and rheology as well as a weakening of the gouge [(Otsuki et al., 2003), (Niemeijer et al., 2011)]. Recently temperature control has been instrumented in the DEM software MELODY, allowing to follow temperature evolution during sliding by temperature increment in grains (Mollon et al., 2021b). It could be considered to add a module allowing to transform the initially rigid grains into deformable grains when the temperature becomes sufficiently high. The idea is to be able to observe the dynamic weakening effect, or secondary weakening observed with thermal activation.

Appendices

Appendices to chapter 1

A. Collection of Gouges

For the creation of the numerical granular samples, we relied on numerous images of fault gouge from natural faults [(Olgaard & Brace, 1983), (Rutter et al., 1986), (Sammis et al., 1987), (Blenkinsop, 1991), (F. Chester et al., 1993), (Antonellini et al., 1994), (An & Sammis, 1994),(Antonellini & Mollema, 2002), (Billi et al., 2003), (Billi & Storti, 2004), (Billi, 2005), (Wibberley et al., 2008), (Muto et al., 2015)] and experimental results [(Sammis et al., 1986), (Biegel et al., 1989), (Marone & Scholz, 1989), (Marone et al., 1990), (Beeler et al., 1996), (Mair & Marone, 1999), (Mair et al., 2002), etc] as well as on the work done by Heiarii Pons during its internship, who gathered the following images and descriptions of granular fault gouges in Figure 138. This graph gave us an idea of the wide variability of matrix percentages found in the literature. The numbers on the graph correspond to the images below N° [X].

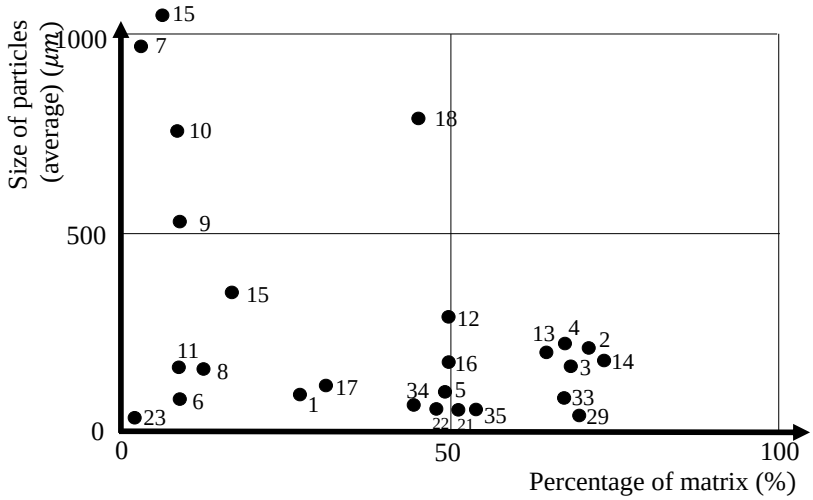

Figure 138. Size of gouge particles (average) in (μm) as a function of the percentage of the matrix with the granular sample. Graph from Heiarii Pons and created thanks to the images below and description in the associated papers.

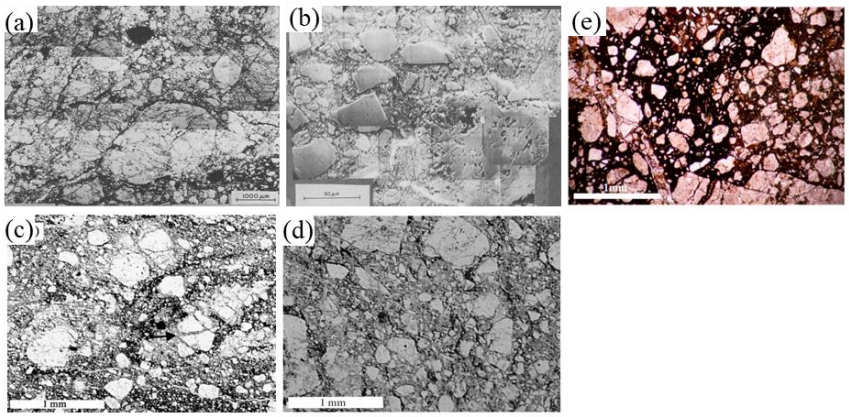

Figure 139. (a) & (b) Gneiss (15% chlorite), from San Gabriel Mountains, California, (Sammis et al., 1987); Optical photomicrograph showing the microtexture of (c) granitic cataclasite from the Itoigawa–Shizuoka tectonic line at Shimotsutaki Village, (d) the cataclastically deformed granitic conglomerate, Tanakura, Japan. Images from (Monzawa & Otsuki, 2003). (quartz et feldspar) (e) **[N°21]** Photomicrograph (crossed polars) of ATTL fault gouge. The particles are angular in shape, with fractal distribution ranging between $1.86 \leq D \leq 2.92$ and sizes between $17.5 \leq \Phi \leq 480$ μm. Friable rocks and lack of cohesion. Images from (Muto et al., 2015).

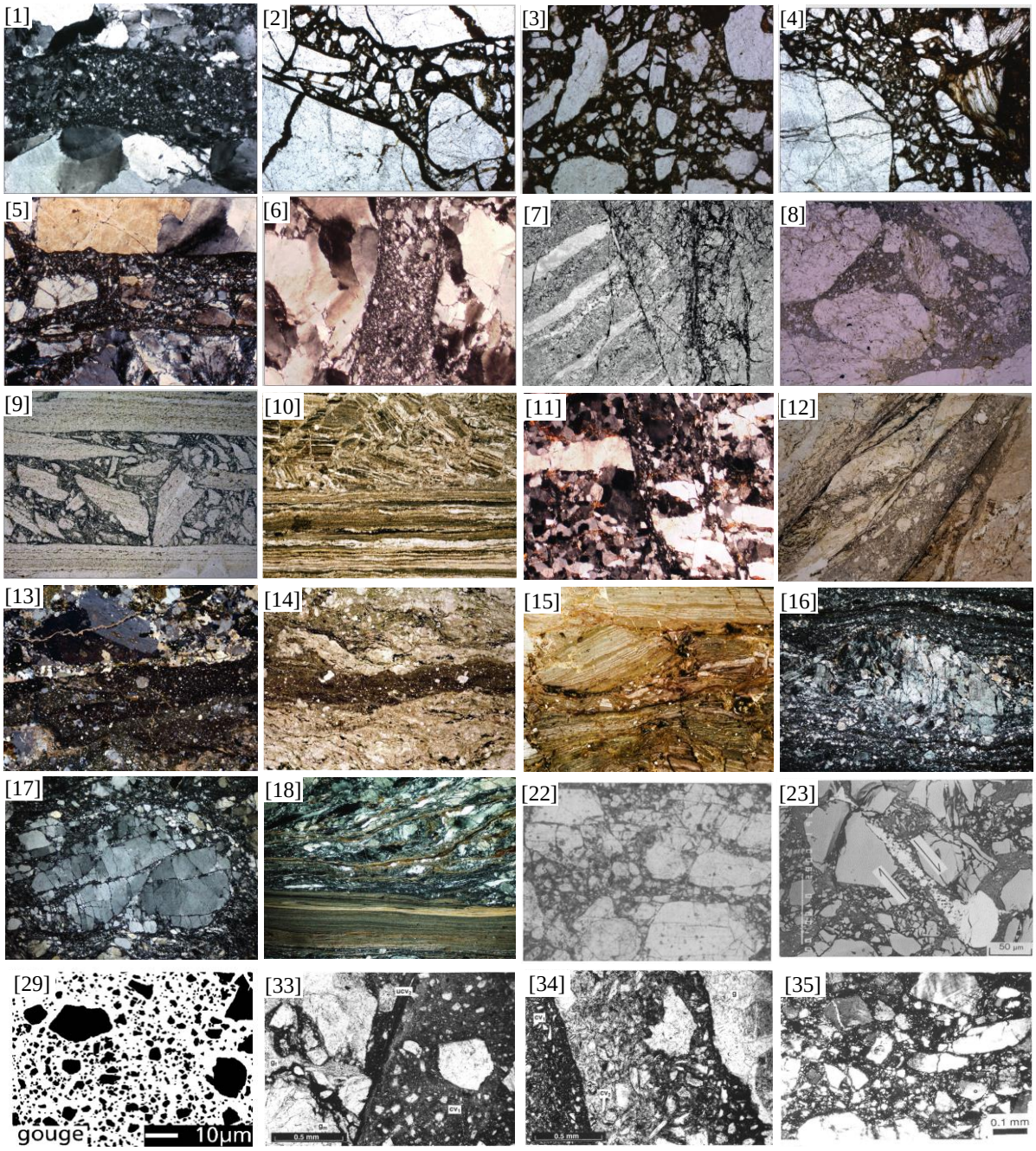

Figure 140. **[N°1]** Deformed quartzite with a cataclastic shear zone. Guapé, southern Minas Gerais State, SE Brazil. Width of view 4 mm. CPL, **[N°2]** Narrow zone of fault breccia and cataclasite in a quartzitic parent rock. Buzios, Rio de Janeiro States SE Brazil. Width of view 4 mm. PPL (left). CPL (right), **[N°3]** Cataclasite showing angular rock fragments, mainly of quartz, embedded in a matrix of iron oxide. Buzios, Rio de Janeiro State, SE Brazil. Width of view 4 mm. Plain Polarized Light (PPL), **[N°4]** Transition between a fractured rock at lower left to a fault breccia in the center and to a mica bearing cataclasite in the upper right-hand part of the photograph. Buzios, Rio de Janeiro-State, SE Brazil. Width of view 3 mm. PPL, **[N°5]** Quartzite shows evidence of weak ductile deformation transected by a cataclastic shear zone. Guapé, southern Minas Gerais State, SE Brazil. Width of view 4 mm. CPL, **[N°6]** Deformed low-grade quartzite with a cataclastic shear zone in vertical position. Guapé, southern Minas Gerais State, SE Brazil. Width of view 4 mm. CPL, **[N°7]** Fault breccia, formed in a lowgrade mylonite derived from a quartz-feldspathic rock. Guapé, southern Minas Gerais State, SE Brazil. Width of view 22 mm. PPL, **[N°8]** Cataclasite is derived from a protomylonitic granite. Pyrenees, Spain. Width of view 20 mm. PPL, **[N°9]** Cataclasite developed in a mylonitic granite. Uruguay. Width of view 16 mm. PPL, **[N°10]** Low-grade ultramylonite, transformed into a fault breccia in the upper part. Uruguay. Width of view 20 mm. PPL, **[N°11]** Fault breccia developing in a quartz-rich gneiss. San Juan, Argentina. Width of view 12 mm. CPL, **[N°12]** Cataclastic zone in deformed granite. Kaokoveld, Namibia. Width of view 16 mm. PPL, **[N°13]** Amphibole-

bearing granodiorite (upper part) cut by a cataclastic fault zone (lower part). San Juan, Argentina. Width of view 23 mm. CPL, **[N°14]** Cataclastic to protomylonitic granite cut by a zone of cataclasite (subhorizontal through the center). Leiden collection. Width of view 15 mm. PPL, **[N°15]** Cataclasite developed in an ultramylonite. Virginia, southern Minas Gerais State, SE Brazil. Width of view 20 mm. PPL, **[N°16]** A very low-grade mylonite, transitional to cataclasite, derived from hornblende syenite. Twijfelfontein, Kaokoveld, NW Namibia. Width of view 14 mm. CPL, **[N°17]** Example of a mosaic-fragmented feldspar porphyroclast in a low-grade mylonite derived from granite. St. Barthélemy Massif, French Pyrenees. Width of view 4 mm. CPL, **[N°18]** Low-grade mylonite derived from granite. St. Barthélemy Massif, French Pyrenees. Width of view 12 mm. CPL (Images from (Trouw et al., 2009).), **[N°22]** Cenozoic cataclasis of granite, from the Cajon Pass dritlhole, southern California, with (b) Particle Size Distributions with values of D equal to 2.32, depth 701 m. Images from (Blenkinsop, 1991). **[N°23]** Backscattered electron micrograph with trail development in experimentally deformed clay-silt gouge, through the intersection of an R1 shear, included ruffle particle in white, Betic Zone of southeastern Spain. Image from (Rutter et al., 1986). **[N°29]** Granular fault gouge. Enlarged view of microstructures: black = particles; white = matrix. Scale (10 μm) applies to crack and gouge microstructures. The granite was collected in the Val Verzasca, Switzerland, and consists of 35% quartz, 29% plagioclase, 27% K- feldspar, and 7% mica (mainly biotite). Image from (Heilbronner & Keulen, 2006), **[N°33]** Hematitic cataclasite fracture-filling separated by shear surface from microbrecciated and locally cataclastically foliated granite. Image from (Snoke et al., 1998). **[N°34]** Cataclasite fracture-fillings in granite. (b) **[N°35]** Cataclasites from a wide fault. Grains of quartz lied in a matrix of sericite and feldspar. Images from (Snoke et al., 1998).

Appendices to Chapter 2

A. Time step (adaptative vs constant)

The evolution of the peak and steady-state effective friction (average friction value within the plateau zone) is quite different depending on whether an adaptive time step or a constant time step is used for calculation. In order to quantify this difference between adaptive time step and constant time step, several studies have been carried out by varying the density of bodies. With a very small constant time step ($\Delta_t = 10^{-9}\ s$), a progressive increase of the friction peak (orange) is observed, whereas the evolution of the friction peak with an adaptive time step is varying a lot, Figure 141.

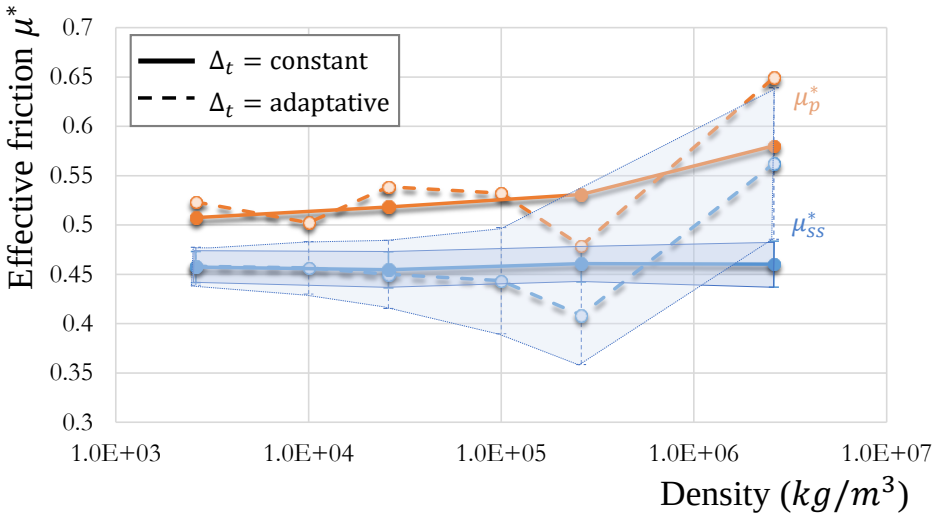

Figure 141. Effective friction μ^* (peak in orange and stady-state in blue) as a function of particle density (kg/m^3), for constant time step and adaptative time step.

At constant time step, the steady-state friction keeps the same average value of 0.46. However, for an adaptive time step the density is much more taken into account in the physics of the model. Indeed, the value of the steady-state friction increases as a function of the density of the bodies, until reaching a value of 0.56. The inertial effects are also much more marked in the case of an adaptive time step (blue area around friction curve), characteristics of the consideration of the increase in particle density. It appears that the adaptive time step of the software MELODY has been coded for deformable grains, having no or very little digital stiffness. The fact that a great numerical stiffness is used ($k_n = 10^{14} \rightarrow 10^{16}$ Pa/m) disturbs the adaptive computation of the time step. It is, therefore, preferable to use a constant time step in these simulations with non-deformable rigid bodies.

B. Generation of matrix particles

The code Cvoro (C++) is a simplified version of the method presented with a Voronoï tessellation algorithm (Packing2D), allowing the creation of a dense packing of polygonal particles. It is possible to play on the size of particles $\emptyset_{eq}$ (equivalent diameter of particles, calibrated on total area) and also on the "perturbation parameters" $P_{0.i}$ (i.e. the

homogeneity/regularity of the hexagonal cells). Figure 142 presents different equivalent diameters of particles merged with angular grains created with Packing2D. As expected, the smaller matrix better fits the grain-matrix contour, keeping more information on the roughness of particles. If the grains are too close, we lose some information when a too high size matrix is used ($\emptyset_{eq} = 25\ \mu m$). In order to limit calculation costs due to the higher number of particles, we chose a $\emptyset_{eq} = 20\ \mu m$ for the rest of the Thesis work, small enough to observe a matrix layer between all big particles. However, in the case of a mixture between angular particles and matrix, some roughness information will be lost or modified.

For more information on how works « Cvoro » and how to use it, you can either contact Guilhem Mollon or Nathalie Casas.

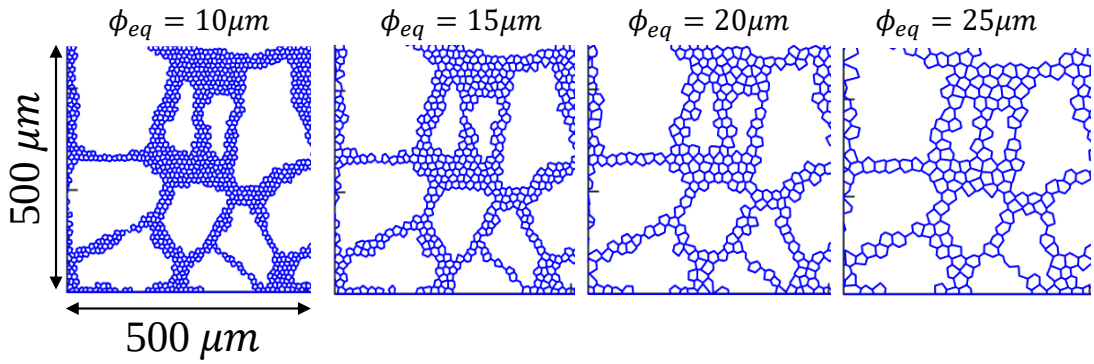

Figure 142. Variation of the equivalent size of matrix particles with angular grains. From $\emptyset_{eq} = 10\ \mu m$ to $\emptyset_{eq} = 25\ \mu m$

C. Initial porosity and state of density

The solid fraction F_s is the ratio of the surface occupied by the grains ($S_{particles}$) to the apparent surface of the sample (S_{gouge}). Since we are here in 2D, we will take an area rather than a volume, considering that the 3rd dimension is the same in the numerator and denominator. In the associated manuscript, we mostly talk about the percentage of porosity (i.e. the ratio of the surface occupied by voids (S_{voids}) to the apparent surface of the sample). The solid fraction and porosity in a sample can therefore be calculated as follows, with S a surface area:

$$F_s = \frac{S_{particles}}{S_{gouge}} \qquad (A.2.1)$$

$$F_v = \frac{S_{voids}}{S_{gouge}} = 1 - F_s \rightarrow P_{pore} = F_v * 100 \qquad (A.2.2)$$

$$S_{gouge} = S_{voids} + S_{particles} \qquad (A.2.3)$$

Compaction step – The initial interparticle friction coefficient (i.e. numerical friction μ_{num}) is used during the compaction phase of the gouge, to control the initial porosity of the sample (noted P_{pore} and defined as the ratio of the area occupied by voids to the apparent area of the sample). Eleven samples were compacted with different initial interparticle friction μ_{num} and the solid fraction was measured at the end of the compaction step. With $\mu_{num} = 0$ between each particle in contact, the only contact parameter between grains is the numerical stiffness

k_n giving a quite dense packing of particles ($F_S = 0.89$). On the opposite, with $\mu_{num} = 1$, friction reduces possible movements and the resulting solid fraction is smaller, meaning much more porosity within the compacted state ($F_S = 0.83$). Similar results have been found on the influence of interparticle friction for the initial packing of particles (Shi et al., 2020). The idea is, therefore, to see the influence of this initial state on gouge shearing. The compaction of samples was carried out on a sample of 4960 grains generated according to a fractal distribution law (dimension factor $D = 2.6$), i.e. with the same initial sample before the compaction step. Parameters used for sample compaction and shearing are written in Table 11. Figure 143 displays the solid fraction and gouge thickness (mm) for each sample generated with a different interparticle friction coefficient. We observe that gouge thickness decreases with the increase of solid fraction.

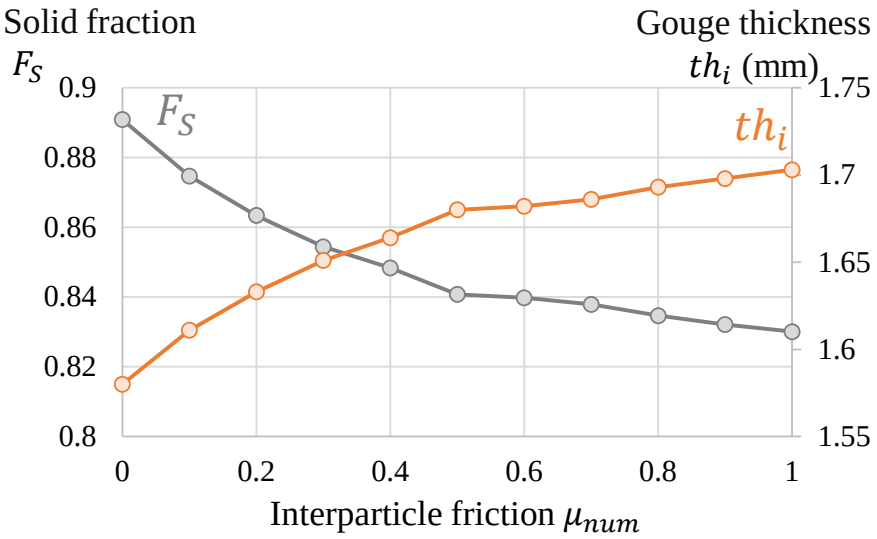

Figure 143. Evolution of solid fraction F_S (in grey) and gouge thickness th_i (in orange) as a function of the interparticle friction μ_{num} used to compact samples.

The highest solid faction (0.89) corresponds to a very dense sample in which there is very little porosity between grains. In contrast, the lowest solid fraction (0.83) corresponds to a slightly less dense sample, with a gouge thickness of $0.12\ mm$ greater, (5 % of the total thickness).

> Samples used in chapter 3 are sample 10 ($F_S = 0.89$ or $P_{pore} = 11$ %) and 15 ($F_S = 0.84$ or P_{pore}=16 %).

Shearing step (for Chapter 3) – All the different initial compacted states have been sheared with an imposed velocity of 1m/s (with frictional contact law only) in order to quantify the influence of this initial state in the slip behavior of the gouge. Figure 144 shows that, to a certain extent, the initial state of compaction of the sample does influence the first steps of the gouge behavior. Comparing the evolution of effective friction as a function of the initial solid fraction, we observe that the denser initial sample ($F_S = 0.89$ or $P_{pore} = 11$ %) presents the higher friction strength with a friction peak $\mu_p^* = 0.75$. The same behavior is observed between $0.86 \leq F_S \leq 0.89$, with an increasing peak strength with the increase of solid fraction. Particles organized themselves to upgrade packing and reduce voids between them. The increase of initial density of the granular sample (i.e. higher solid fraction) significates that packings of

grains become more difficult to unpack, and moving the entire sample asks for more energy to the system to reach a steady state. For lower solid fraction ($0.86 \geq F_S$), the compaction state does not seem to be an obstacle to shearing and the effective friction progressively increases until a plate where we suppose the system is in steady-state (cf. inertial number). The mid-dense sample ($F_S = 0.84$ or P_{pore}=16 %), has a friction peak almost missing. Even though the effective peak depends on the initial solid fraction, if the shearing proceeds for a certain time of the experiment, all the samples exhibit the same mechanical behavior with the same steady-state friction μ_{ss}^*.

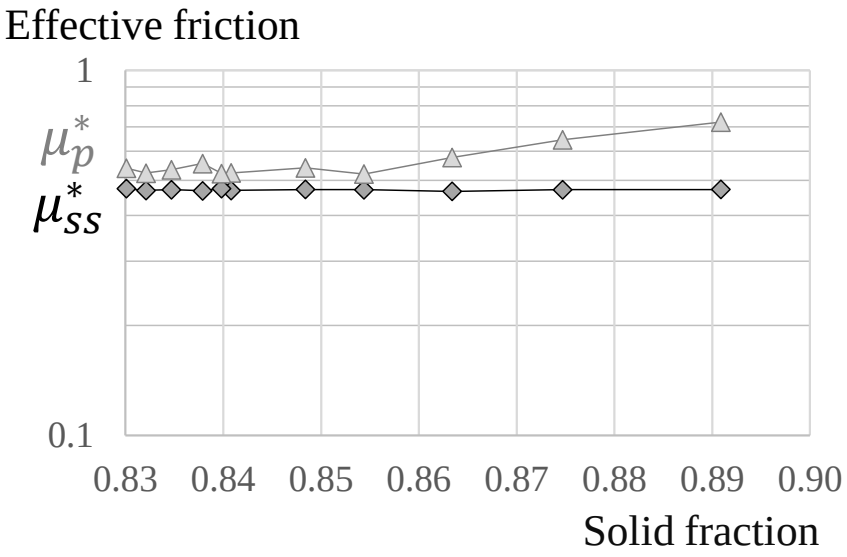

Figure 144. Effective friction μ^* as a function of the initial solid fraction F_S (at the end of the compacted state), results from the shearing of granular samples with the following parameters ($\sigma_N = 40\ MPa, V = 1m/s$, $\rho_r = 2600\ kg/m^3, k = 10^{15}\ Pa/m, \mu_{num} = 0.5$).

Table 11. Numerical setup and properties for the experimental campaign

Property	Associated variable	Value
Normal stress	σ_N	40 MPa
Shear velocity	V *(for shearing only)*	1 m/s
Rock density	ρ_r	2600 grains kg/m^3
Contact stiffness	k_n & k_t	$10^{15}\ Pa/m$
Interparticle friction (compaction)	μ_{num}	From 0 to 1
Interparticle friction (shearing)	μ_{num}	0.5 (grains – grains) / 1 (grains –walls)
Initial Sample size	$th_i \times L_g$	2 x 20 mm
Particle equivalent diameter	$\phi_{min} \rightarrow \phi_{max}$	$28 \rightarrow 226\ \mu m$
Number of particles	N	4960
DEM time step	Δ_t	10^{-9} s (Δt = cst)
Proximity updating period	$\Delta_{t-contact}$	10^{-7} s

D. Circular vs angular particles

The numerical and physical characteristics of both samples (circular and angular particles) used in Chapter 2 are presented in Table 12.

Table 12. Data of both models with circular or angular particles. The granular layer with circular shapes of grains is generated with the same parameters as the one with angular particles.

Property	Angular particles	Circular particles
Normal stress, σ_N	40 MPa	
Shear velocity, V	1 m/s	
Rock density, ρ_r	2600 grains $kg/m3$	
Contact stiffness, k_n & k_t	10^{15} Pa/m	
Interparticle friction, μ_{num}	0.5 (grains – grains) / 1 (grains –walls)	
Sample size, $th\ x\ L_g$	1.7 x 20 mm	
Particle equivalent diameter, $\phi_{min} - \phi_{max}$	28 – 226 µm	20 – 181 µm
Number of particles, N	4960	7515
DEM time step, Δ_t	10^{-9} s	
Proximity updating period, $\Delta_{t-contact}$	10^{-7} s	

Appendices to Chapter 3

A. Numerical stiffness influence

As explained in Chapter 2, numerical stiffnesses are not completely physical nor numerical but make it possible to quantify the rate of interpenetration between the bodies in contact. A stiffness that tends towards infinity will give grains that will be tangent, while a weak stiffness will make that the bodies in contact can be allowed to overlap. Tests were carried out with different stiffnesses from $10^{14}\ Pa/m$ to $10^{17}\ Pa/m$, in order to quantify the interpenetrations between the particles in contact. Figure 145 presents the evolution of effective friction as a function of the numerical stiffness between particles.

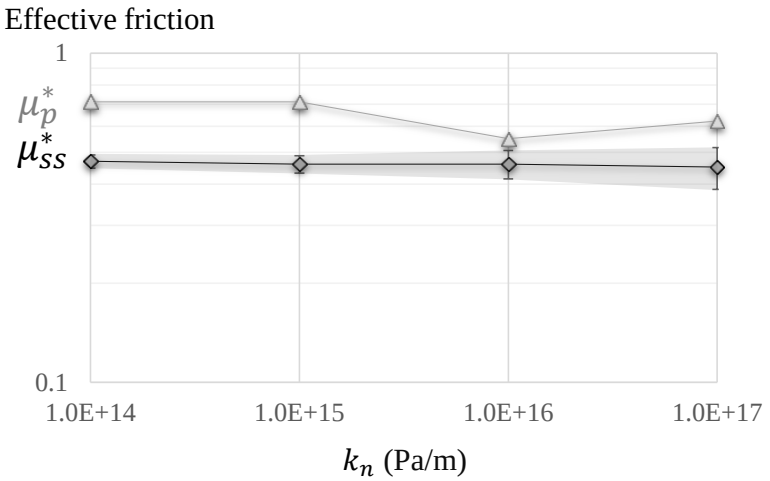

Figure 145. Effective friction μ^* as a function of numerical stiffness $k_n\,(Pa/m)$.

Changing the numerical stiffness does not have a major influence on the effective steady-state friction coefficient which has the same averaged value $\mu_{ss}^* \approx 0.45$. On the other hand, we note that an increase in numerical stiffness augments the standard deviation from the average friction value. In other words, the dynamic effects are greater with higher stiffness, since the interpenetrations which could also serve as damping are reduced. It is interesting to be able to choose both a fairly high stiffness, allowing to have realistic modeling concerning the contacts between the bodies, but also about the dynamics of the system. A stiffness of $10^{14}\ Pa/m$ reveals too high interpenetrations, whereas a stiffness of 10^{16} or $10^{17}\ Pa/m$ gives too many spaces for dynamic effects in the numerical shearing. The stiffness $10^{15}\ Pa/m$ allows us to obtain more precise results than $10^{14}\ Pa/m$, while remaining in models with a standard deviation from the average steady-state friction lower than 10 %.

Besides, it is also possible to compute the equivalent Young modulus E for a typical rock as granite for our cemented materials, thanks to the parameter of a cemented contact between particles:

$$E = \frac{\sigma}{\varepsilon} = \frac{C_{num}}{\frac{C_{num}}{k_n} * \frac{1}{\phi_g}} = \phi_g . k_n \ [Pa] \qquad (A.3.1)$$

With σ the normal stress applied on a contact (Pa), ε the deformation of the contact, C_{num} the numerical cohesion implemented in the cemented materials (Pa), k_n the numerical stiffness (Pa/m), ϕ_g the equivalent particle diameter (m).

Figure 146 displays the equivalent Young modulus E as a function of the interparticle stiffness for different equivalent grain diameter ϕ_g and comparing values to those observe in real rocks (blue band). Using an interparticle stiffness of $10^{15}\ Pa/m$ gather more values of young modulus from common rocks than the other values.

It was thus chosen to continue the simulation campaign with a numerical stiffness of $10^{15}\ Pa/m$ which is numerically and physically consistent.

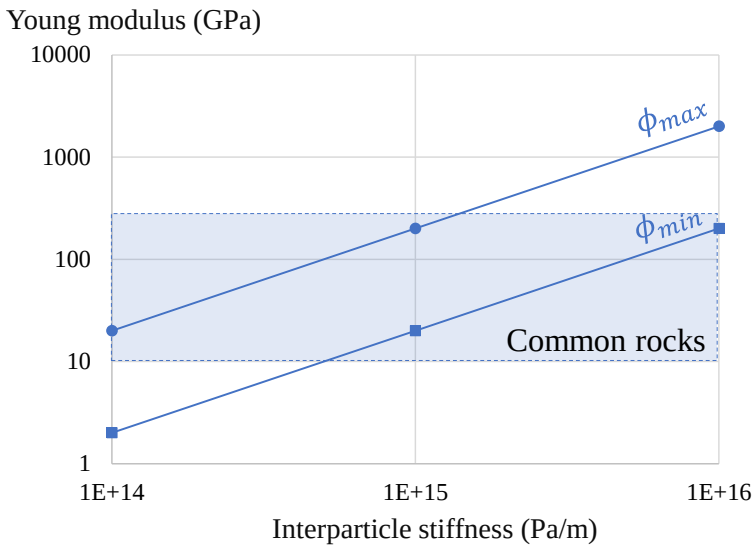

Figure 146. Equivalent Young modulus (GPa) as a function of the interparticle stiffness μ_{num} for the maximum equivalent grain diameter ϕ_{max} and the minimum grain diameter ϕ_{min}. The blue band represents the range of Young modulus values for common rocks.

B. Reproducibility

In order to validate the model and results obtained within packing 2D and the DEM code MELODY, reproducibility tests have been carried out with the same parameters as the material of Chapter 2. Four granular samples were generated randomly with the same initial characteristics (with Packing2D) meaning that the granular samples are globally identical, but locally different (each sample is unique in terms of grain position and shapes). They are all composed of 5000 grains distributed randomly according to a fractal granular distribution in the defined area of 2x20 mm² and their initial solid fraction is equal to 0.89. The four samples are named from 1 to 4, Figure 147. By comparing the results from the different samples, it can be seen that the effective friction peak, the averaged values at steady-state of friction and dilation remain constant over the four samples: steady-state friction is around 0.47 with a relative margin of 2 % from this value, and dilation is also similar with an averaged value at steady-state ≈ 0.092. Although steady-state values remain very close, each sample represents a different stack of grains distinct local evolutions of the gouge with upper wall slip distance.

This small study validates that a granular sample generated and sheared with the same initial conditions (i.e. same global geometry, numerical and physical boundary conditions), produces the same mechanical results. The resulting kinematic is also similar.

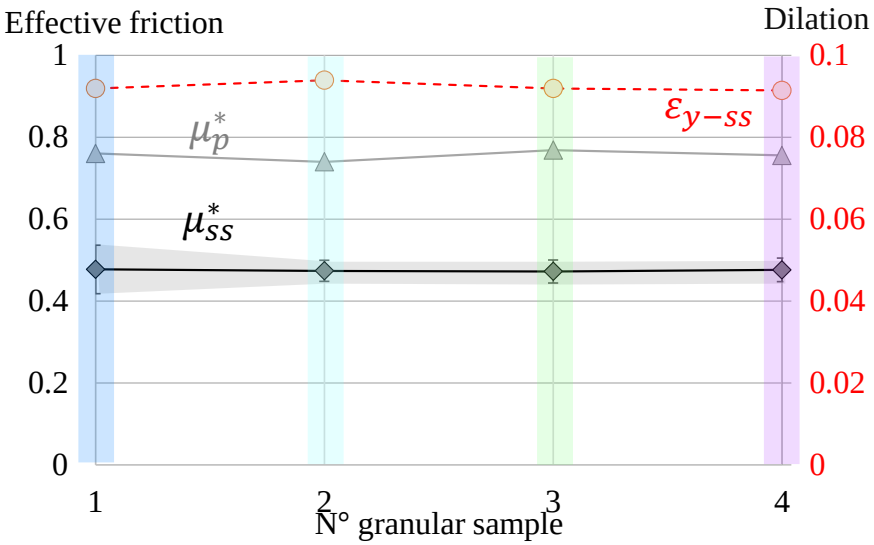

Figure 147. (a) Effective friction peak μ_p^* and steady-state effective friction μ_{ss}^* (respectively in grey and black) and dilation at steady-state ε_{y-ss} (in red) for the four samples randomly generated with the same initial conditions.

C. Results tables for cemented materials

Table 13. Results for **dense samples** ($P_{pore} = 11\%$ or solid fraction SF=0.89). With $\Delta\tau$ (Pa) the stress drop from the effective friction peak to the plateau, μ_{SS}^* the steady-state effective friction, μ_p^* the effective friction peak, F_{S-SS} the steady-state solid fraction, $P_{pore-SS}$ the steady-state porosity, th_{SS} the steady-state gouge thickness.

C_{num}	100	200	500	800	1000	1200	1500	2000	2500
P_{cem} (%)	4	8	19	30	38	46	57	76	95
$\Delta\tau$ (Pa)	1.1+07	1.1E+07	1.8E+07	3.0E+07	3.6E+07	4.2E+07	5.3E+07	6.8E+07	8.8E+07
μ_{SS}^*	0.481	0.482	0.490	0.477	0.496	0.484	0.475	0.473	0.431
μ_p^*	0.771	0.786	0.994	1.406	1.695	1.938	2.376	3.094	3.838
F_{S-SS}	0.869	0.867	0.876	0.877	0.869	0.87	0.884	0.895	0.889
$P_{pore-SS}$	0.131	0.133	0.124	0.123	0.131	0.13	0.116	0.105	0.111
th_{SS} (mm)	1.72	1.726	1.707	1.705	1.72	1.719	1.691	1.671	1.681

Table 14. Results for **mid-dense samples** ($P_{pore} = 16\%$ or initial solid fraction SF=0.84) With Δτ (Pa) the stress drop from the effective friction peak to the plateau, μ^*_{SS} the steady-state effective friction, μ^*_p the effective friction peak, F_{S-SS} the steady-state solid fraction, $P_{pore-SS}$ the steady-state porosity, th_{SS} the steady-state gouge thickness.

C_{num}	100	200	500	800	1000	1200	1500	2000
$P_{cem}(\%)$	3	6	18	31	40	50	66	95
$\Delta\tau$ (Pa)	3.0E+06	2.6E+06	3.7E+06	9.1E+06	1.4E+07	1.9E+07	2.6E+07	3.6E+07
μ^*_{SS}	0.461	0.466	0.460	0.458	0.469	0.479	0.476	0.455
μ^*_p	0.536	0.531	0.552	0.684	0.815	0.959	1.130	1.346
F_{S-SS}	0.855	0.854	0.852	0.85	0.851	0.857	0.864	0.858
$P_{pore-SS}$	0.145	0.146	0.148	0.15	0.149	0.143	0.136	0.142
th_{SS} (mm)	1.749	1.752	1.756	1.766	1.757	1.745	1.73	1.742

More data and results files are available at: "Casas, Nathalie; Mollon, Guilhem (2022), "Cohesion and Initial Porosity of Granular Fault Gouges", Mendeley Data, V3, doi: 10.17632/7c3dcj7spw.3"

The representation of the relative damage gives a picture of the state of cementation between grains and their location within the gouge. This damage is set to 0 when cohesive bonds are first established (all the bonds are intact) and may evolve until 1 if all these bonds reach the "broken" status (cf. Chapter 3). It is thus a relative damage with respect to an initial state. The following movies illustrate the evolution of the gouge state as a function of the slip distance:

Movie S1. Comparison of the evolution of relative damage with slip distance for dense samples (entire granular gouge), between 8% cementation (mildly cemented material) and 38% cementation (cemented material). From zero imposed slip [A] to the beginning of steady-state [G].

Movie S2. Comparison of the evolution of relative damage with slip distance for dense samples (entire granular gouge), between 38% cementation (cemented material) and 95% cementation (ultra-cemented material). From zero imposed slip [A] to the beginning of steady-state [G].

The following movies present the evolution of solid fraction as a function of the slip distance for the three regimes highlighted in the paper. Another way to observe Riedel bands and cracks within the gouge.

Movie S3. The solid fraction in the dense sample (entire granular gouge) as a function of the slip distance for 8% cementation (mildly cemented material). From zero imposed slip [A] to the beginning of steady-state [G].

Movie S4. The solid fraction in the dense sample (entire granular gouge) is a function of the slip distance for 38% cementation (cemented material). From zero imposed slip [A] to the beginning of steady-state [G].

Movie S5. The solid fraction in the dense sample (entire granular gouge) as a function of the slip distance for 95% cementation (ultra-cemented material). From zero imposed slip [A] to the beginning of steady-state [G].

Appendices to Chapter 4

A. Representative Surface Element (RSE)

Different lengths of matrices are created to evaluate the influence of this parameter on shear localization and granular behavior. In order to observe the influence of the length of the granular third body, five samples are generated: L_2 ($2 \times 2\ mm^2$), L_4 ($4 \times 2\ mm^2$), L_{10} ($10 \times 2\ mm^2$), L_{20} ($20 \times 2\ mm^2$), & L_{40} ($40 \times 2\ mm^2$) with an interparticle friction μ_{num} equal to 0.3 between cells. In Figure 148, from 0 to point A_1, a first elastic linear part is observed with the same behavior for all samples. At point B_1 (friction peak), almost all samples behave in the same way except for the L_2 sample, which has a specific behavior due to its particularly small size. Point C_1 is very interesting, this is the decreasing friction point located at the middle distance between friction peak and steady-state friction. An evolution of suddenness of friction weakening is observed (i.e. slip distance needed for friction to drop from μ_p^* to μ_{ss}^*) and this area is also the place of maximum dilatancy. Increasing the length of the matrix softens the transition between μ_p^* to μ_{ss}^* until a certain limit. It also expands the dilation of the sample, Figure 148 (b). Friction transition evolution stops evolving from after L_{20} (i.e. Representative Surface Element obtained for this gouge thickness, see the path of L_{40} in Figure 148 (a). The same behavior is obtained for dilation, increasing until L_{20}. However, changing the gouge thickness or size of particles modifies the global stiffness of the granular media and thus could influence the RSE.

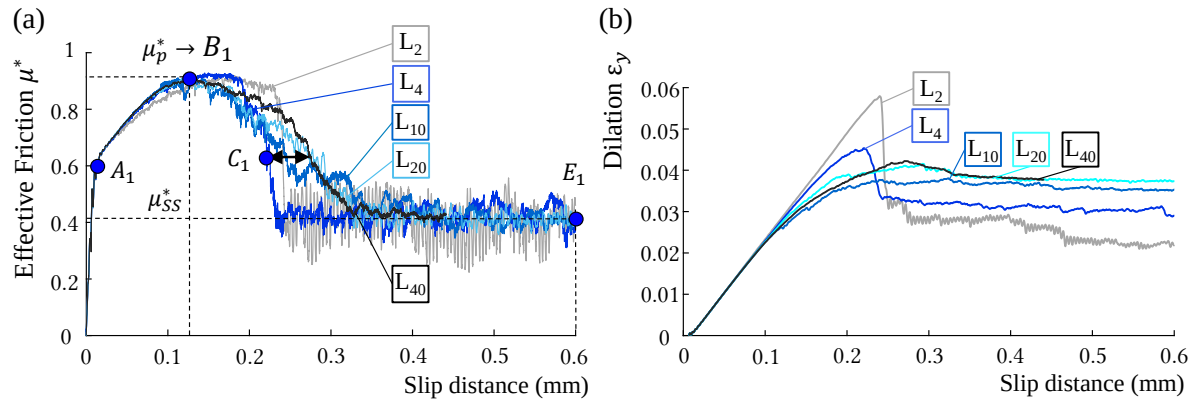

Figure 148. (a) Effective friction μ^* as a function of the slip distance (mm) for different sizes of models, L_2 (2x2 mm²), L_4 (4x2 mm²), L_{10} (10x2 mm²), L_{20} (20x2 mm²), L_{40} (40x2 mm²). μ_p^* is the peak friction and μ_{ss}^* the steady state friction; (b) Dilation as a function of the slip distance (mm) for the same sizes of models.

Between μ_p^* and μ_{ss}^*, crack opening takes place in a preferred Riedel band R at C_1, where a maximum dilatancy is observed (i.e. minimum solid fraction inside the Riedel shear). The augmentation of the length of the matrix does not seem to change the formation of observed Riedel shear bands. However, this increase creates a larger observation window displaying more Riedel bands within the sample. These bands are always inclined with the same orientation of $\approx 10\,°$ from the main shear direction. They grow from the top surface to the bottom rock wall in the opposite direction of shearing. Steady-state is reached with the formation of a localized horizontal shear band S at the top or bottom part of the granular media.

B. Gouge thickness

Figure 149 presents the effective friction and dilation as a function of the effective friction for two different gouge thicknesses, 1 and 3 mm. All the other parameters are similar. The effective friction peak is almost similar for both cases, as the steady-state friction. But the dilation is higher with a more important gouge layer, which is consistent with the theory.

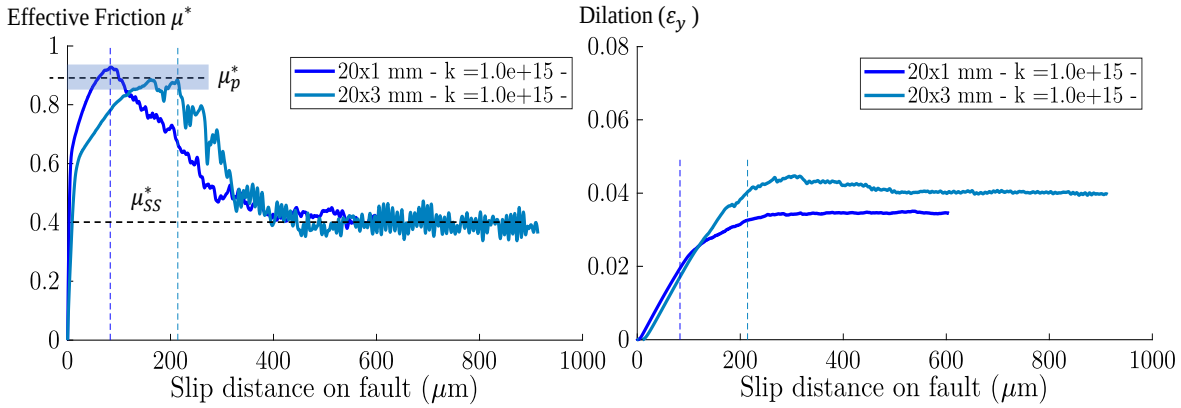

Figure 149. Effective friction μ^* and dilation ε_y as a function of the effective friction for two different gouge thicknesses, 1 and 3 mm.

C. Shear modulus calculi and graphs

The shear modulus, Figure 150, can be calculated as

$$G = \frac{\tau}{\gamma_{xy}} = \frac{\tau . th_i}{\Delta_x} \qquad (A.4.1)$$

where τ is the shearing stress, th_i the initial gouge width and Δ_x the slip distance at the secant point. We compute both the secant shear modulus (at 40% of the maximum shear stress) and the initial tangent shear modulus. The results for all the models are presented in Table 15.

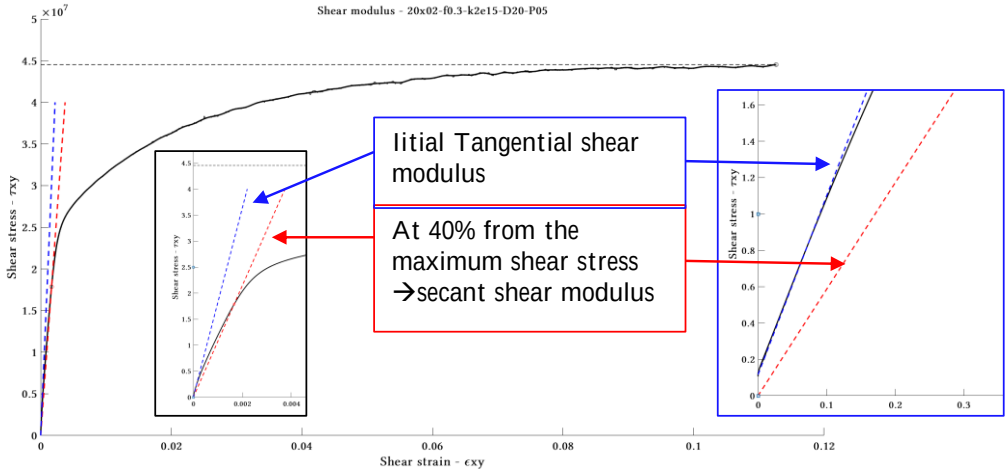

Figure 150. Automatic calculation with Matlab 2020a. Sketch of the shear stress as a function of the shear strain with the secant shear modulus at 40 % of the maximum shear stress (red) and the initial tangential shear modulus (blue). Example realized for the thin gouge of the standard case (size 20 x 0.2 mm^2, $\mu_{num} = 0.3$, $k_n = 10^{15}\ Pa/m$, P0.5, $\Phi = 20\mu m$).

Table 15: Secant shear modulus and tangential shear modulus for the different cases of study.

name	Size $L_g \times th_i$ (mm)	Friction μ_i	Stiffness k_n (Pa/m)	Diameter Φ_i (mm)	Gsec G_s (GPa)	Gtan G_t (GPa)	P P_i
M-S	20x2	0.3	10^{15}	0.02	5.52	10.4	0.5
M-S-bis	20x2	0.3	10^{15}	0.02	5.73	12.2	0.5
M-RES-3	10x2	0.3	10^{15}	0.02	5.54	10.4	0.5
M-RES-2	4x2	0.3	10^{15}	0.02	5.5	10.3	0.5
M-RES-1	2x2	0.3	10^{15}	0.02	5.53	10.9	0.5
M-RES-4	40x2	0.3	10^{15}	0.02	5.49	10.4	0.5
M-RES-3-F	2x2	0.6	10^{15}	0.02	4.76	9.17	0.5
M-RES-2-F	4x2	0.6	10^{15}	0.02	4.71	8.89	0.5
M-RES-1-F	10x2	0.6	10^{15}	0.02	5.11	9.07	0.5
M-F01	20x2	0.1	10^{15}	0.02	5.38	12.4	0.5
M-F02	20x2	0.2	10^{15}	0.02	5.71	12.8	0.5
M-F06	20x2	0.6	10^{15}	0.02	5.05	9.04	0.5
M-RES-4-F	40x2	0.6	10^{15}	0.02	4.98	9.02	0.5
M-PS-30	20x2	0.3	10^{15}	0.03	8.36	16.1	0.5
M-PS-30-K_{eq}	20x2	0.3	$6.8.10^{14}$	0.03	6.22	12.2	0.5
M-PS-40	20x2	0.3	10^{15}	0.04	11.2	23.3	0.5
M-PS-40- K_{eq}	20x2	0.3	$4.7.10^{14}$	0.04	6.2	12.2	0.5
M-PS-50	20x2	0.3	10^{15}	0.05	14.1	32.4	0.5
M-PS-50- K_{eq}	20x2	0.3	4.10^{14}	0.05	6.86	13.6	0.5
M-Kx2	20x2	0.3	2.10^{15}	0.02	10.5	24	0.5
M-Kx10	20x2	0.3	10^{16}	0.02	41.9	170	0.5
M-P-02	20x2	0.3	10^{15}	0.02	5.87	9.83	0.2
M-P-08	20x2	0.3	10^{15}	0.02	5.02	10.9	0.8
M-P-08-Kx2	20x2	0.3	2.10^{15}	0.02	9.39	25.4	0.8
M-Th-1	20x1	0.3	10^{15}	0.02	5.77	12.2	0.5
M-Th-3	20x3	0.3	10^{15}	0.02	5.41	9.015	0.5
M-Th-4	20x4	0.3	10^{15}	0.02	5.35	9.15	0.5
M-SG-P02	20x0.2	0.3	10^{15}	0.02	6.07	9.12	0.2
M-SG-S	20x0.2	0.3	10^{15}	0.02	5.85	9.83	0.5
M-SG-k10	20x0.2	0.3	10^{16}	0.02	46.6	85.7	0.5
M-SG-P08	20x0.2	0.3	10^{15}	0.02	5.17	10.6	0.8
M-SG-k2	20x0.2	0.3	2.10^{15}	0.02	10.7	18.7	0.5
M-SG-k5	20x0.2	0.3	5.10^{15}	0.02	24.5	44.8	0.5
M-SG-F06	20x0.2	0.6	10^{15}	0.02	5.6	9.7	0.5

D. Mechanical behavior of a bi-disperse mixture

Figure 151 presents friction and dilation curves as a function of the slip distance for the four samples detailed in chapter 4, part B: (G-C-4), with $P_{matrix} = 0$ %, (MG-33) with $P_{matrix} = 33$ %, (MG-56) with $P_{matrix} = 56$ % and (M-S) with $P_{matrix} = 100$ %.

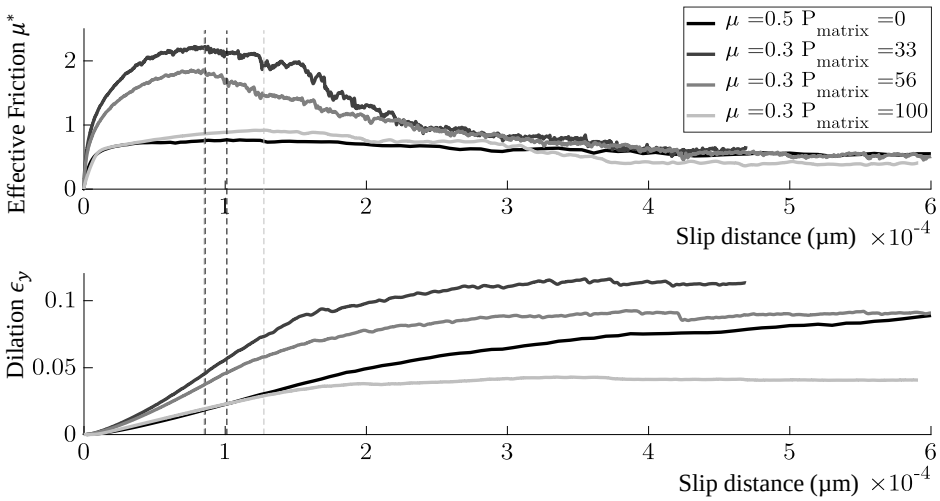

Figure 151. (a) Effective friction as a function of the slip distance (mm) for different percentages of matrix particles ($P_{matrix} = 0, 33, 56$ & 100%). (b) Dilation (%) as a function of the slip distance (mm) for the same cases. The first points for simulation with 0% of matrix particles or only angular particles have been made with interparticle friction of 0.5 which is higher than the one used in the other studies.

Appendices to Chapter 5

A. Weakening slope (Part A)

In the following graphs, the slope of slip weakening is extracted from each model previously presented thanks to the method described in Chapter 5, (Figure 152, Figure 153, Figure 154, Figure 155, Figure 156, Figure 157).

❖ Cemented materials

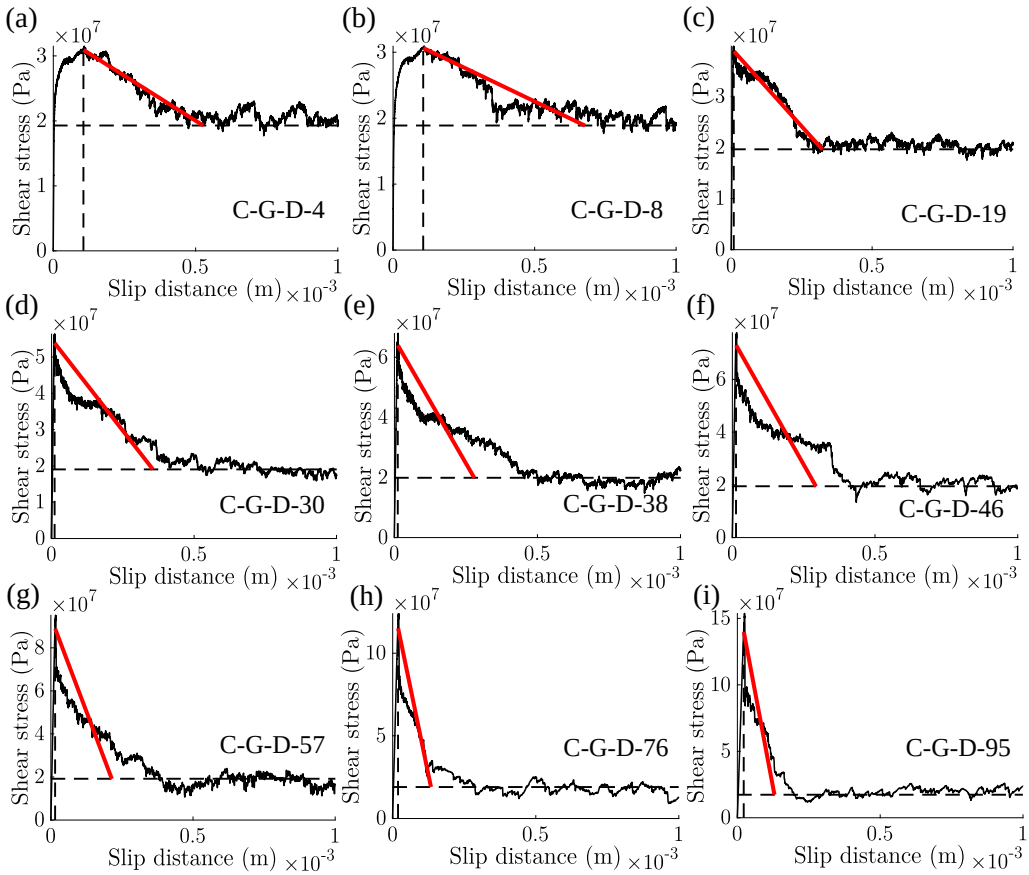

Figure 152. Shear stress (Pa) as a function of the slip distance (m) for **dense cemented models** (Chapter 3). Percentage of cementation from $P_{cem} = 4 \rightarrow 95\%$. The red slope is the linear slip weakening slope needed to equal the breakdown energy E_G.

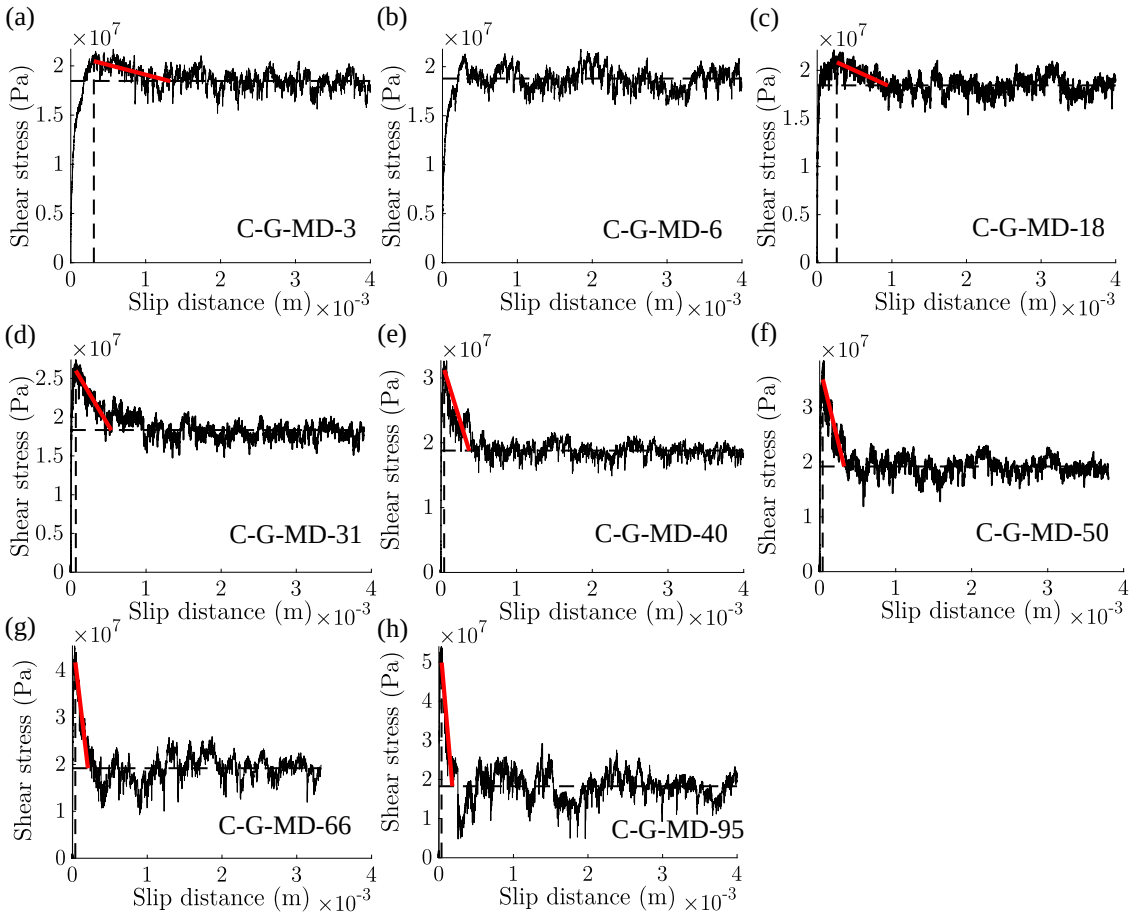

Figure 153. Shear stress (Pa) as a function of the slip distance (m) for **mid-dense cemented models** (Chapter 3). Percentage of cementation from $P_{cem} = 3 \rightarrow 95\%$. The red slope is the linear slip weakening slope needed to equal the breakdown energy E_G.

❖ Matrix models

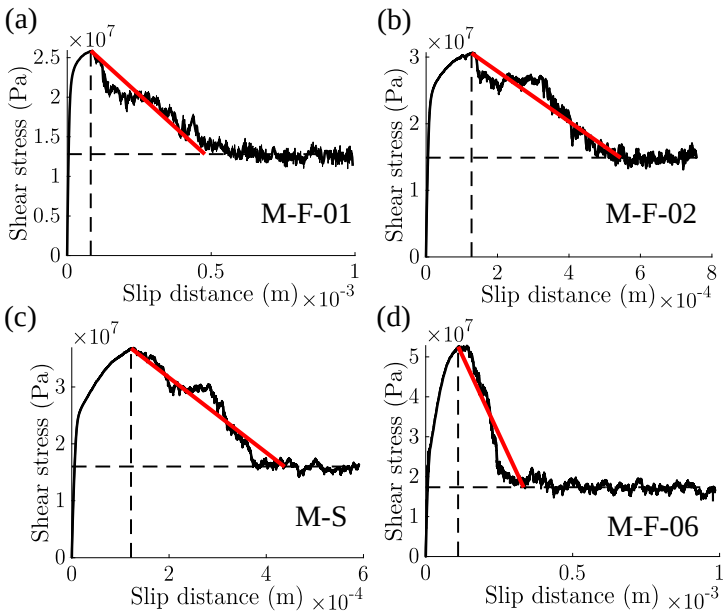

Figure 154. Shear stress (Pa) as a function of the slip distance (m) for matrix models (chap. 4, part A). **Variation of the interparticle friction** $\mu_{num} = 0.1 \rightarrow 0.6$. The red slope is the linear slip weakening slope needed to equal the breakdown energy E_G.

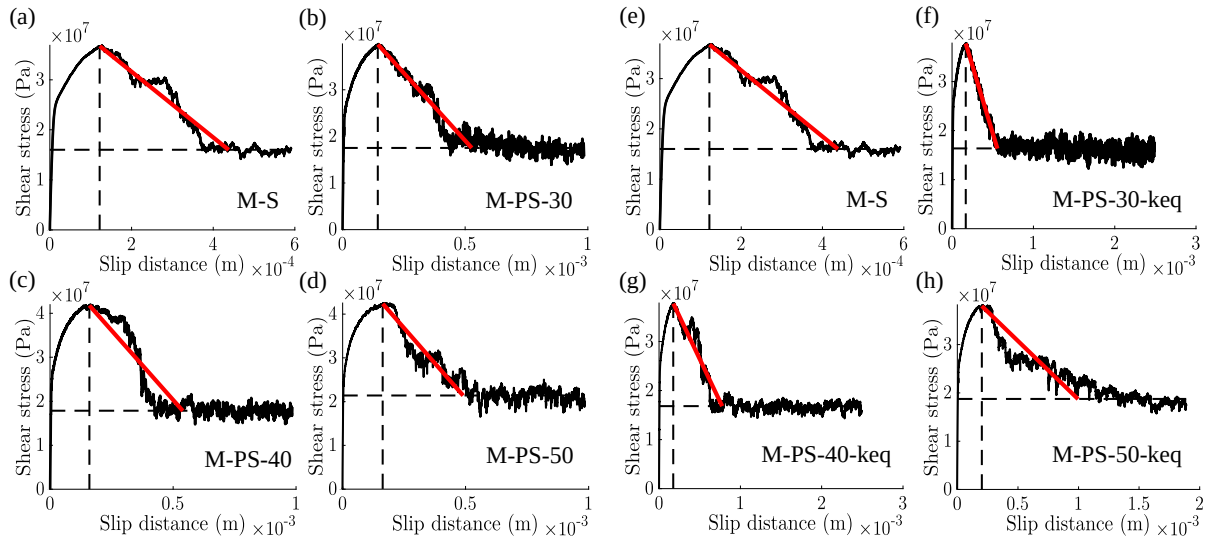

Figure 155. Shear stress (Pa) as a function of the slip distance (m) for matrix models (chap. 4, part A). **(a) to (d): Variation of the size of particle** from $\Phi_{eq} = 20 \rightarrow 50\ \mu m$. **(e) to (h):** Variation of the size of particle from $\Phi_{eq} = 20 \rightarrow 50\ \mu m$ with equivalent stiffness. The red slope is the linear slip weakening slope needed to equal the breakdown energy E_G.

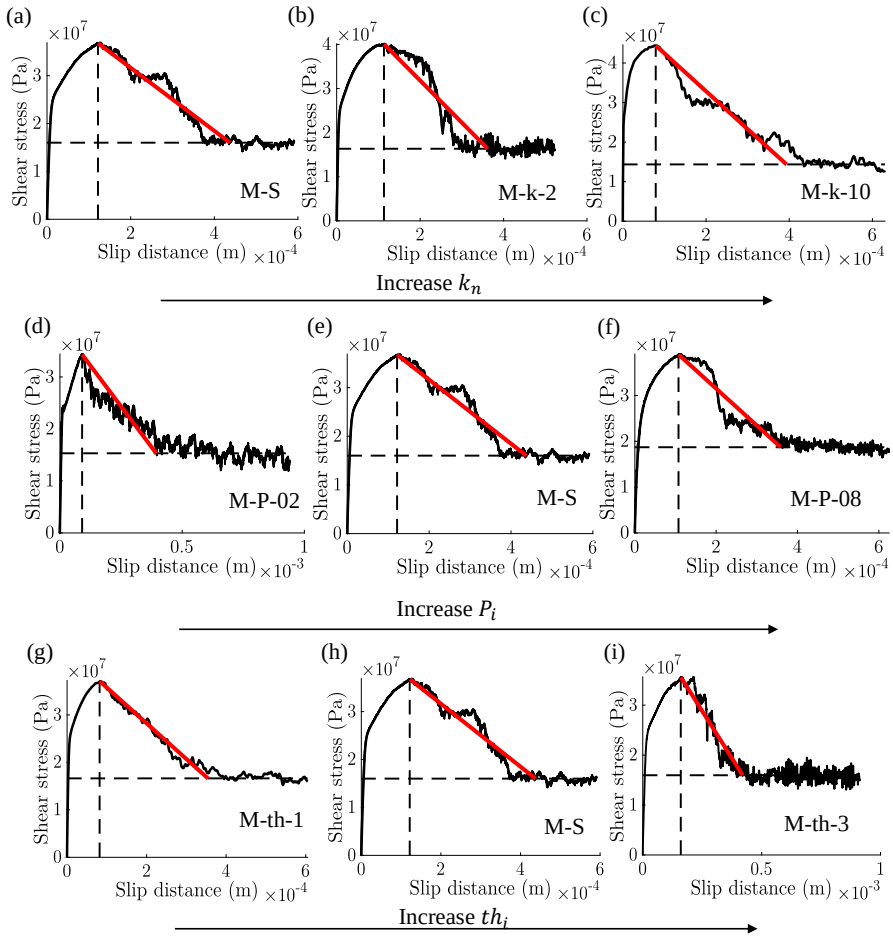

Figure 156. Shear stress (Pa) as a function of the slip distance (m) for matrix models (chap. 4, part A). **(a) to (c): Variation of the interparticle stiffness** from $k_n = 10^{15} \rightarrow 10^{16}\ Pa/m$. **(d) to (f): Variation of the perturbation** from $P_i = 0.2 \rightarrow 0.8$. (g) to (i): **Variation of the initial thickness** $th_i = 1 \rightarrow 3\ mm$. The red slope is the linear slip weakening slope needed to equal the breakdown energy E_G.

❖ Matrix & grains models

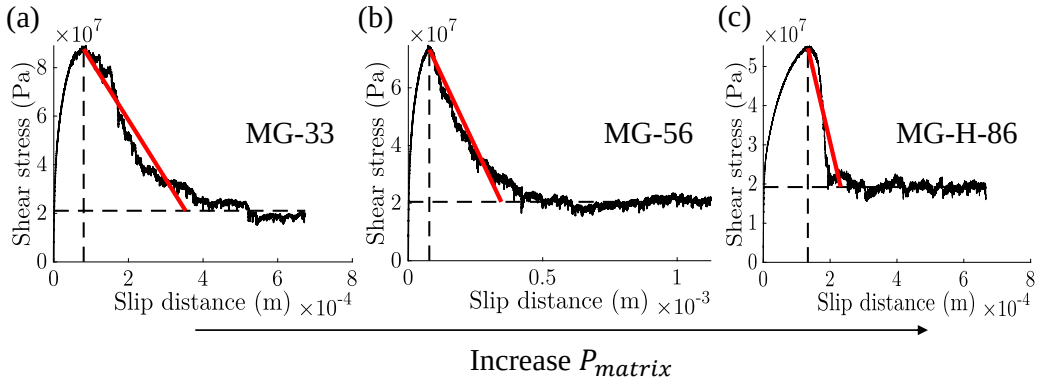

Figure 157. Shear stress (Pa) as a function of the slip distance (m) for matrix models (chap. 4, part A). Variation of the interparticle stiffness from $P_{matrix} = 33 \rightarrow 86\%$. The red slope is the linear slip weakening slope needed to equal the breakdown energy E_G.

B. Empirical parametric laws (Part B)

The laws used to represent the evolution of the shape parameters are presented below. These are the behavior laws of each of the 7 parameters considered in the simplified models. Constant and numerical variables are displayed in Table 16.

- **Parameters used for dilation law:**

Maximum dilatancy angle Ψp (°):

$$\Psi_p(P_{cem}) = \begin{cases} \Psi_{p-min}, & P_{cem} \leq C_{\min} \\ \Psi_{p-min} + (P_{cem} - C_{\min}) * \dfrac{(\Psi_{p-max} - \Psi_{p-min})}{(C_{\max} - C_{\min})}, & C_{\min} < P_{cem} < C_{\max} \\ \Psi_{p-max}, & P_{cem} \geq C_{\max} \end{cases} \quad (A.5.1)$$

Slip distance corresponding to the maximum dilatancy $U_{dp}(\mu m)$:

$$U_{dp}(P_{cem}) = \begin{cases} U_{dp_{val}}(1) \leftarrow & P_{cem} = C_{\min-2} \\ c_1 * P_{cem}^2 + c_2 * P_{cem} + c_3 \leftarrow & C_{\min-2} < P_{cem} < C_{\max} \\ U_{dp_{val}}(3), & P_{cem} \geq C_{\max} \end{cases} \quad (A.5.2)$$

$$\text{With } coef_s1 = \begin{pmatrix} C_{\min-2}^2 & C_{\min-2} & 1 \\ C_{\max-2}^2 & C_{\max-2} & 1 \\ 2C_{\max-2} & 1 & 0 \end{pmatrix} \Big/ \begin{pmatrix} U_{dp_{val}}(1) \\ U_{dp_{val}}(2) \\ U_{dp_{val}}(3) \end{pmatrix} = [c_1, c_2, c_3]$$

Gain in gouge thickness at the end of the dilatancy phase $\Delta H_d(\mu m)$:

$$\Delta H_d(P_{cem}) = \begin{cases} H_d(1) \leftarrow & P_{cem} \leq C_{\min} \\ c_{11} * P_{cem}^2 + c_{22} * P_{cem} + c_{33} \leftarrow & C_{\min} < P_{cem} < C_{\max} \\ H_d(3), & P_{cem} \geq C_{\max} \end{cases} \quad (A.5.3)$$

$$\text{With } coef_s2 = \begin{pmatrix} C_{\min}^2 & C_{\min} & 1 \\ \left(\dfrac{C_{\max} + C_{min}}{2}\right)^2 & \left(\dfrac{C_{\max} + C_{min}}{2}\right) & 1 \\ C_{\max}^2 & C_{\max} & 1 \end{pmatrix} \Big/ \begin{pmatrix} H_d(1) \\ H_d(2) \\ H_d(3) \end{pmatrix} = [c_{11}, c_{22}, c_{33}]$$

- **Parameters used for Coulomb friction law:**

Peak friction at the end of the elastic phase μ_{fp}^* and post-peak friction μ_{fpp}^*:

$$\mu_{fp}^*(P_{cem}) = \left\{\mu_{fp\_val}^*(1) + \frac{P_{cem}}{100} * \left(\mu_{fp_{val}}^*(3) - \mu_{fp_{val}}^*(1)\right)\right. \quad (A.5.4)$$

$$\mu^*_{fpp}(P_{cem}) = \{\mu^*_{fpp\_val}(1) + \frac{P_{cem}}{100} * (\mu^*_{fpp\_val}(3) - \mu^*_{fpp\_val}(1)) \quad (A.5.5)$$

$$With\ \ \mathrm{U_{fp}}(P_{cem}) = \mu^*_{fp}/k$$

Characteristic distance of the exponential decay $\Delta U_f(\mu m)$:

$$\Delta U_f(P_{cem}) = \begin{cases} \Delta U(1) \leftarrow \ P_{cem} \leq C_{\min} \\ c_{111} * P_{cem}^2 + \ c_{222} * P_{cem} + c_{333} \leftarrow \ C_{\min} < P_{cem} \ < C_{\max} \\ \Delta U(3), \qquad P_{cem} \ \geq C_{\max} \end{cases} \quad (A.5.6)$$

$$\text{With } coef_s 3 = \begin{pmatrix} C_{\min}^2 & C_{\min} & 1 \\ C_{\max}^2 & C_{\max} & 1 \\ 2C_{\max-2} & 1 & 0 \end{pmatrix} \Big/ \begin{pmatrix} \Delta U(1) \\ \Delta U(2) \\ 0 \end{pmatrix} = [c_{111}, c_{222}, c_{333}]$$

- **Parameters used for damage law:**

Maximum friction induced by rupture of cementation μ^*_{dp}:

$$\mu^*_{dp}(P_{cem}) = \frac{P_{cem}}{100} * \mu^*_{dp\_max} \quad (A.5.7)$$

Characteristic distance of the exponential decay $\Delta U_{dam}(\mu m)$:

$$\Delta U_{dam}(P_{cem}) = \Delta U_f(P_{cem}) \quad (A.5.8)$$

Table 16. Numerical variables are used to calculate the different parameters. H_d is the change in height dilatancy at the end of the Gaussian. $H_{d-final}$ is the total change in height dilation. k, μ^*_{SS}, and ΔU_{fpp} do not depend on cementation and are taken as constant.

Variable	Value	
	DENSE	MID-DENSE
$[C_{\min}, C_{\max}]$	[25 %, 75 %]	
$[C_{\min-2}, C_{\max-2}]$	[1 %, 75 %]	
μ^*_{ss}	0.45	
$\Psi_{\mathrm{p-min}}$	20°	8°
$\Psi_{\mathrm{p-max}}$	40°	25°
$U_{dp_{val}}$	[100, 50, 50] (μm)	[250, 50, 50] (μm)
H_d	[140, 200, 150] (μm)	[70, 95, 120] (μm)
$H_{d-final}$	[140, 0, 80] (μm)	[70, 0, 60] (μm)
k	140 000 kN/m	80 000 kN/m
$\mu^*_{fp\_val}$	[0.2,3]	[0.12, 0.6]
$\mu^*_{fpp\_val}$	[0.45,0.95]	[0.2, 0.25]
$\Delta \mathrm{U_{fpp}}$	8 μm	40 μm
$\Delta \mathrm{U} = \Delta \mathrm{U_f} = \Delta U_{dam}$	[100, 50] μm	[50,50] μm
$\mu^*_{dp\_max}$	0.5	0.4

C. Simplified model validation (part B)

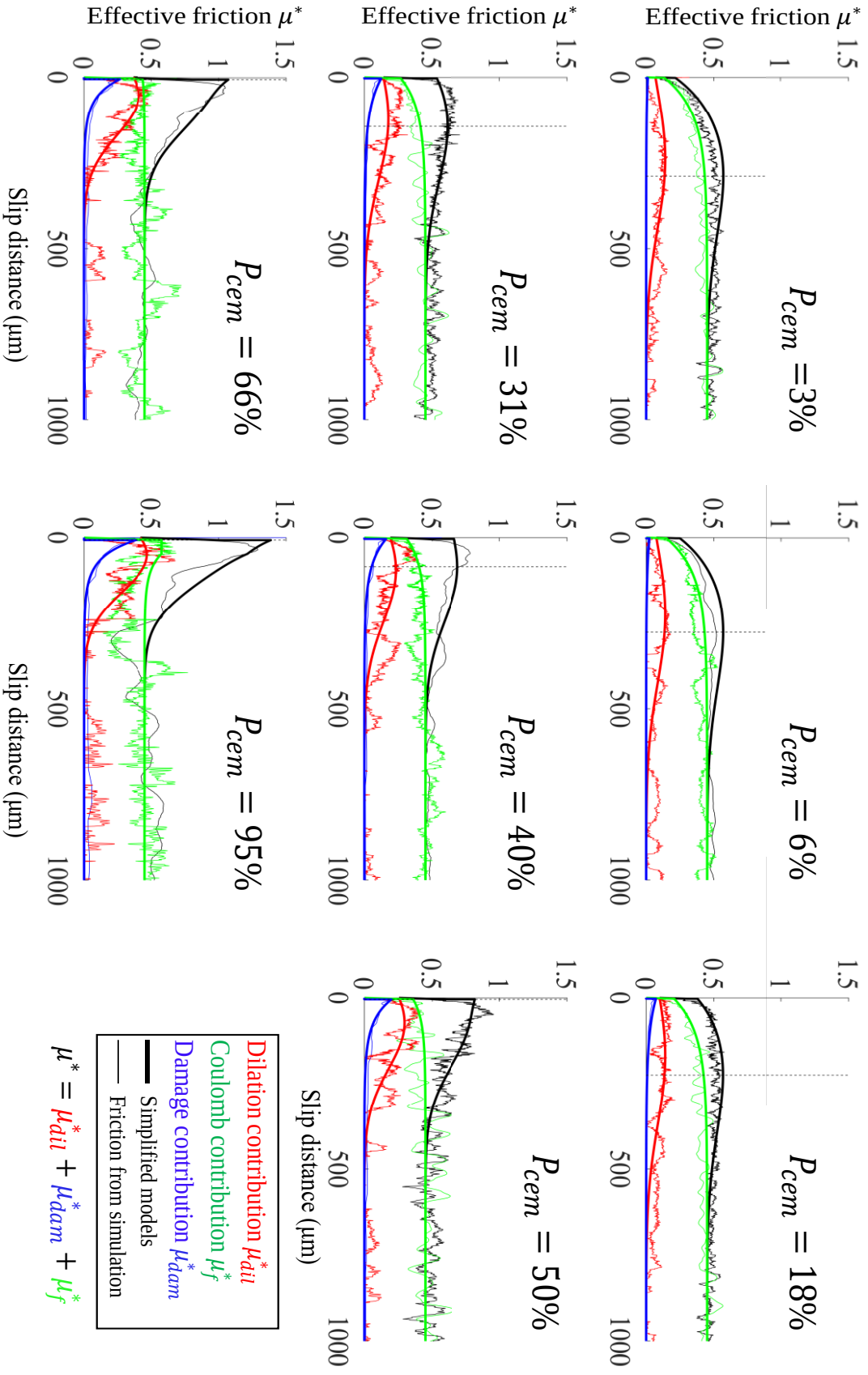

Figure 158. Proposed simplified models - Evolution of friction contributions as a function of the initial percentage of cementation for mid-dense materials.

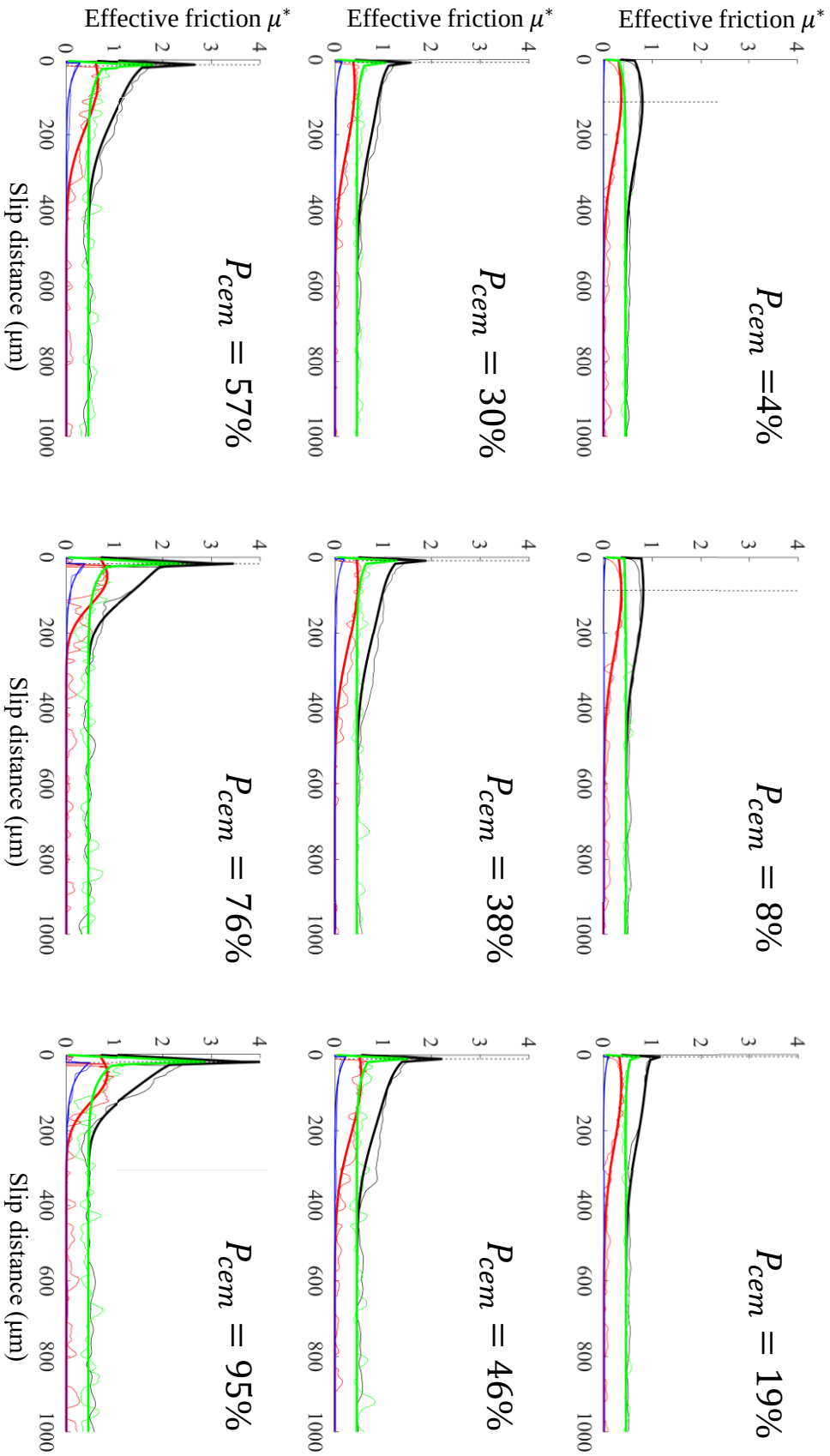

Figure 159. Proposed simplified models - Evolution of friction contributions as a function of the initial percentage of cementation for dense materials.

D. Method to measure shear bands aperture (part C)

- **Measure of the ΔY_{open} opening of each *R* or *Y* -band**

- Collection of particles around the *R*-band (~ 10 to 20 on each side) with the software Paraview and calculation of the orientation angle (α) between the horizontal axes (X) and the direction of the *R*-band (angle compared to the measured data), Figure 160 (a).
- Projection of the position of selected cells in the reference mark of the *R*-band ($R_B = (0, \overrightarrow{x_R}, \overrightarrow{y_R})$), with an offset in the *y*-direction to take the displacement of the center of the reference mark th_i into account, Figure 160 (b).
- Addition of linear interpolation to have an *x*-alignment of the points on each side of the fault (with 'pship' option in Matlab), Figure 161.
- Calculation of the needed values from the collected data. $\Delta\Delta yi$ is the relative displacement in the y_R −direction for each time step. It is calculated as

$$\Delta Y_{open} = \Delta\Delta yi = (y_{B_i} - y_{A_i}) - (y_{B_0} - y_{A_0}) \qquad (A.5.9)$$

to consider the displacement of both particles within the gouge. With the same method, we calculate the relative displacement in the x_R −direction,

$$\Delta X_{slip} = (x_{B_i} - x_{A_i}) - (x_{B_0} - x_{A_0}) \qquad (A.5.10)$$

Both variables are observed in Figure 162. The graph of the ΔY_{open} as a function of ΔX_{slip} will give the trajectory of each band.

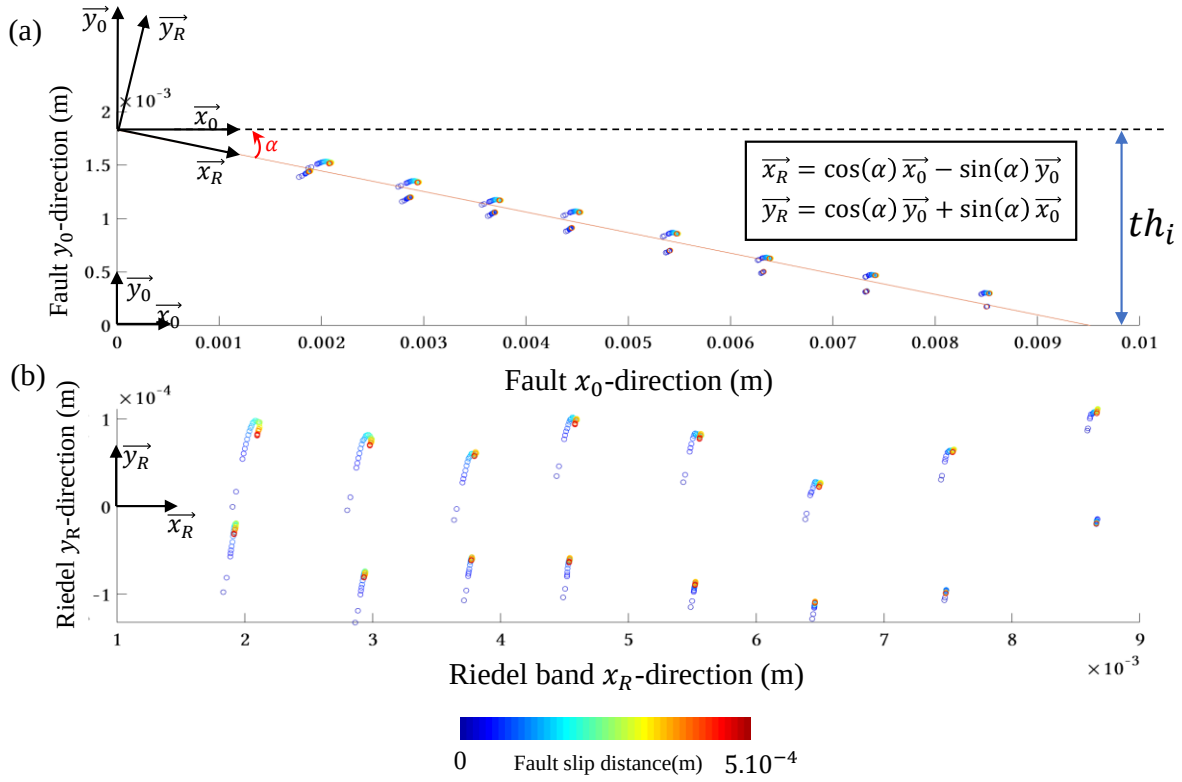

Figure 160. (a) Selected points in the reference mark $R_0 = (0, \overrightarrow{x_0}, \overrightarrow{y_0})$. (b) Selected points projected in the *R*-band mark $R_B = (0, \overrightarrow{x_R}, \overrightarrow{y_R})$. Points color coded with their position with the fault slip distance from 0 to 0.5 mm.

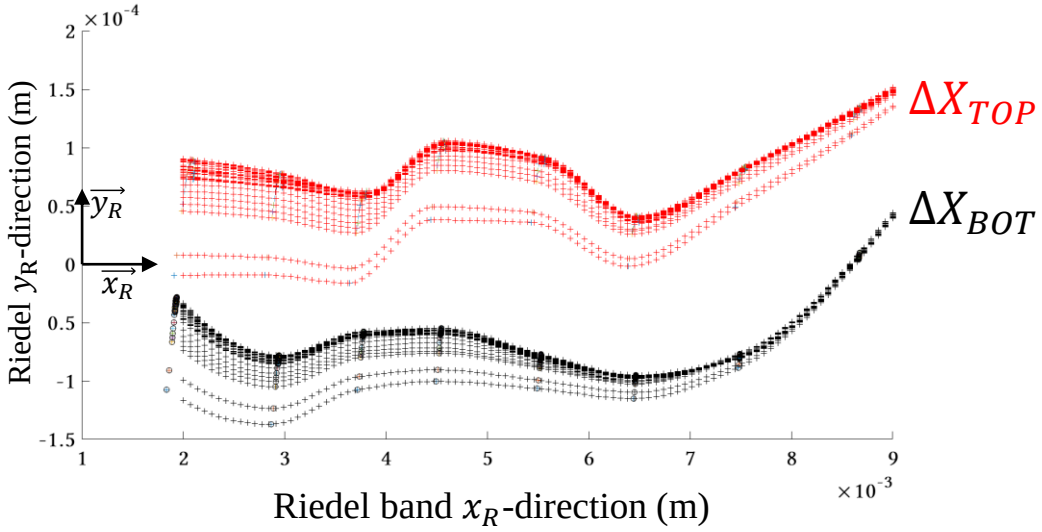

Figure 161. Linear interpolation of the position of cells in the *R*-band mark R_B, for each time step.

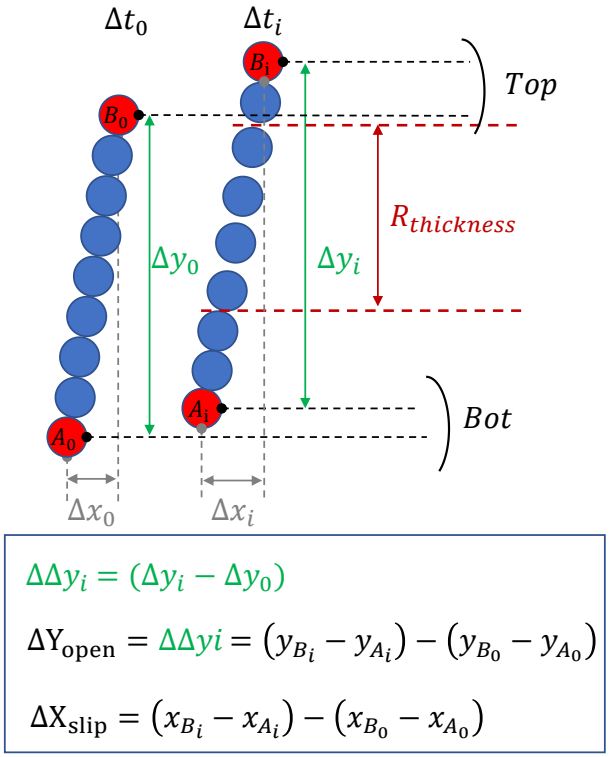

Figure 162. Schema of the method used to measure the Riedel band opening. We first select points on each part of the interested band and measure the vertical displacement perpendicular to the band direction, called $\Delta\Delta y_i$. The same method is applied on the displacement in the band direction, $\Delta\Delta x_i$.

- **Measure of the $R_{thickness}$ with ImageJ**

With the software ImageJ, the thickness of each Riedel band was measured manually. The main steps are the following:

- Recover Field images from MELODY, showing Solid fraction evolution at each time step.
- Application of a filter to threshold only a certain solid fraction value in the software Paraview. For example, we only extracted zones of high solid fraction (from 0.95 to 1). (Figure 163)

- Transformation of the images in .png or .jpg that it is possible to open with ImageJ.
- Manual measurement of the $R_{thickness}$ of each selected band, Figure 164.

This is a long way method, but it enables us to have the first idea on *R*-band temporality for three different simulations and to have an average value of the width $R_{thickness}$ of *R* and *Y*-bands.

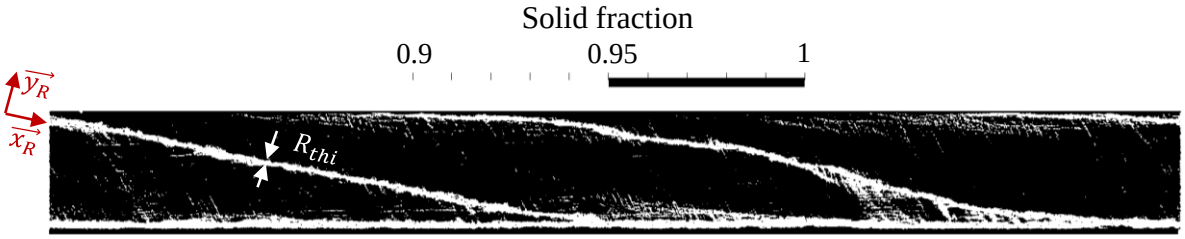

Figure 163. Image of the M-S sample with a filter on the solid fraction to threshold the solid fraction from 0.95 to 1.

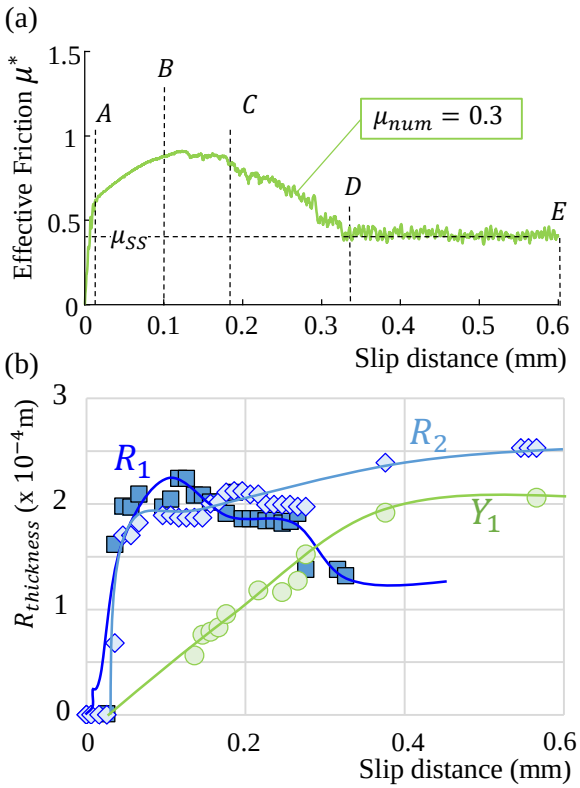

Figure 164. (a) Effective friction μ^* as a function of the slip distance (mm) M-S materials. (b) $R_{thickness}$ measured with ImageJ as a function of the slip distance (mm).

E. Thin bands results (Part C)

This appendix presents the friction and dilation results for the small gouges generated for Chapter 5. Data are also used with the graph of Chapter 4 to represent a gouge layer without shear localization. Figure 165 gathers all the results in a graph of the effective friction as a function of the interparticle friction. Figure 166, Figure 167, Figure 168 present the total effective friction curve with the associated dilation for all the thin gouges tested, listed in table Figure 165.

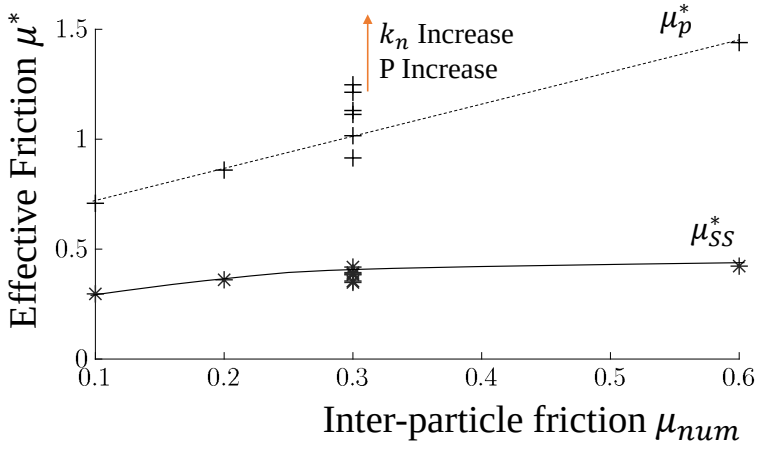

Sample Name	Modified variable	Numerical value
M-SG-P02	Perturbation shape P_i	0.2
M-SG-S		0.5
M-SG-P08		0.8
M-SG-F0.1	Interparticle friction μ_{num}	0.1
M-SG-F0.2		0.2
M-SG-F0.6		0.6
M-SG-k2	Interparticle stiffness k_n	2e15 Pa/m
M-SG-k5		5e15 Pa/m
M-SG-k10		1e16 Pa/m

Figure 165. Effective friction μ^* as a function of the interparticle friction for all the thin bands. Cross for the peak of effective friction and stars for steady-state effective friction. In the table, sample names and associated modification with standard case (M-SG-S). Size of the samples $20 \times 0.2\ mm^2$.

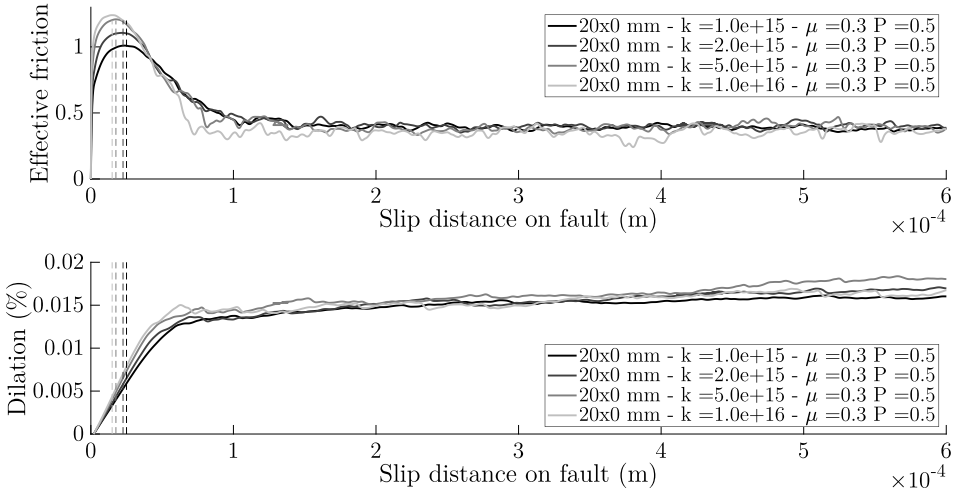

Figure 166. Effective friction μ^* and dilation ε_y (%) as a function of the slip distance (m) for different values of the interparticle stiffness k_n, for thin band models ($20 \times 0.2\ mm^2$).

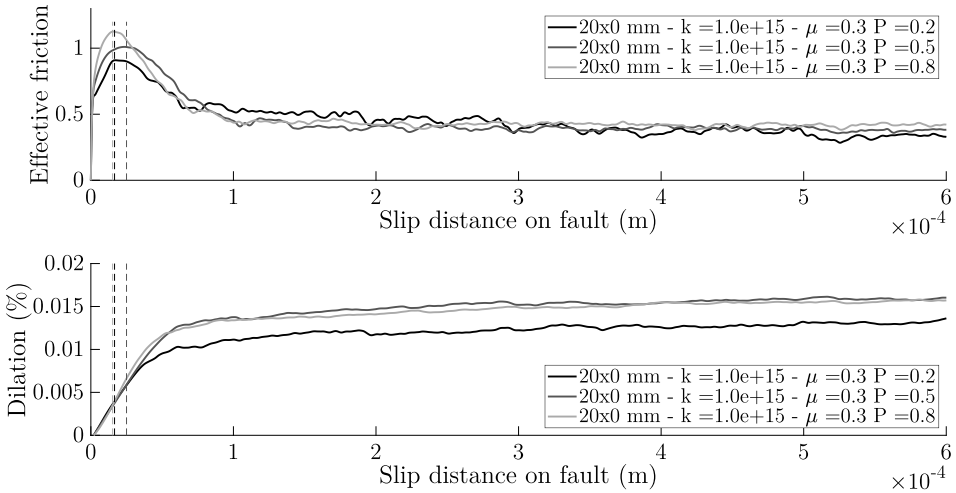

Figure 167. Effective friction μ^* and dilation ε_y (%) as a function of the slip distance (m) for different values of perturbation P_i, for thin band models ($20 \times 0.2\ mm^2$).

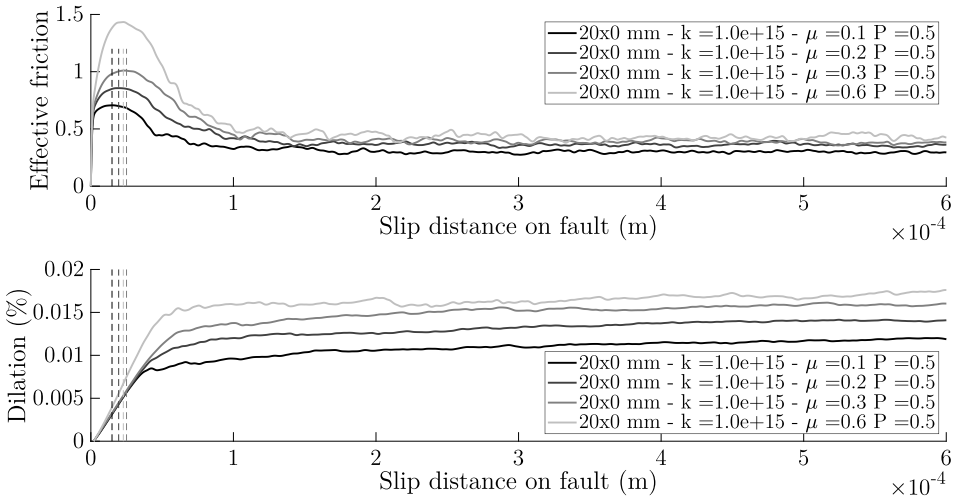

Figure 168. Effective friction μ^* and dilation ε_y (%) as a function of the slip distance (m) for different value of interparticle friction $\mu_{num} = (0.1, 0.2, 0.3, 0.6)$, for thin band models ($20 \times 0.2\ mm^2$).

Nomenclature

The indicated chapter concerns the first chapter where the parameter was defined, but it can be used in other chapters.

A_n	Pair Fourier coefficient, morphologic descriptors, (Chap. 2)
B_n	Odd Fourier coefficient, morphologic descriptors, (Chap. 2)
C	Cohesion in the sense of Mohr-Coulomb, (Chap. 1)
C_{num}	Numerical interparticle cohesion (Pa), (Chap. 2)
$C_{num-100\%}$	Numerical interparticle cohesion (Pa) for complete cementation, (Chap. 3)
D	Fractal Dimension factor, (Chap. 1)
D_c	Critical slip distance (m), (Chap. 1)
D_n	Normalized amplitude for Fourier descriptors, (Chap. 2)
D_p	Total displacement before friction peak (m), from zero displacement, (Chap 3.)
D_{pp}	Slip weakening part (m), similar to Dc, (Chap 3.)
D_s	End of slip displacement (m), (Chap 5.)
dy	y-displacement of the upper rock wall (m), (Chap. 4)
E	Elasticity moduli E (Pa), (Chap. 3)
E_{Cem}	The energy of de-cementation (J/m²), (Chap. 3)
E_{Dam}	Damage energy (J/m²), suffix -pp for post-peak, (Chap. 5)
E_{Dil}	Dilation energy (J/m²), suffix -pp for post-peak, (Chap. 5)
E_{Dil-av}	Average post-peak dilation energy (J/m²), (Chap. 5)
E_f	Frictional energy (J/m²), suffix -pp for post-peak, (Chap. 5)
E_{fc}	Constant part of the frictional energy (J/m²), Coulomb energy, (Chap. 5)
E_{fr}	Remaining frictional energy (J/m²), (Chap. 5)
E_G	Breakdown energy, energy needed to weaken the fault (J/m²), (Chap. 1)
E_H	Heat or frictional energy (J/m²), (Chap. 1)
E_R	Radiated energy (J/m²) , (Chap. 1)
E_S	Representative surface energy (J/m²), (Chap. 3)
E_{tot}	Total energy generated by gouge sliding (J/m²), (Chap. 5)
e	Chosen parameter around 1/50 for time step calculation, (Chap. 2)
$\overrightarrow{F_A}$	Resultant of forces acting on a particle A, (Chap. 2)
F_N	Total normal force (N) on the upper rock wall (y-direction), (Chap. 2)
F_s	Solid fraction, $S_{particle}/(S_{particle}+S_{voids})$
F_T	Total tangential force (N) on the upper rock wall (x-direction), (Chap. 2)
F_v	Voids fraction, $S_{voids}/(S_{particle}+S_{voids})$
G	Shear modulus (GPa), (Chap. 4)
I_p	Inertial number, (Chap. 2)
K	Stiffness of the loading system (GPa/m), (Chap. 5)
K_c	Critical slip weakening slope (GPa/m), (Chap. 1)
k	Gouge layer stiffness, (Chap. 3)

k_{eq}	Equivalent interparticle stiffness (Pa/m), (Chap. 4)
k_n	Normal interparticle stiffness (Pa/m), (Chap. 2)
k_t	Tangential interparticle stiffness (Pa/m), (Chap. 2)
L_c	Critical nucleation length (m), (Chap. 5)
L_g	Length of the numerical gouge sample (m), (Chap. 2)
L_{p-c}	Contact length between two particles (m), (Chap. 2)
m_A	Mass of a particle from a grain A (kg), (Chap. 2)
m_{min}	Mass of the smallest particle (kg), (Chap. 2)
N	Number of particles within the numerical gouge sample, (Chap. 2)
N_i	Number of points within the contour of a particle, (Chap. 2)
N_{Optim}	Optimization parameter between 0 and 63, (Chap. 2)
n	Number of contact bonds for each particle, (Chap. 3)
nb_1	Ratio between th_i (m) and equivalent diameter Φ_{eq} (m) of particles, (Chap. 4)
n_{Sd}	Ratio between S_d (m) and Φ_{eq} (m), (Chap. 4)
n_Y	Ratio between dy (m) and Φ_{eq} (m) of particles. (Chap. 4)
P	Primary shear, (Chap. 1)
P_i	Perturbation parameter (regularity of shape of particles), (Chap. 2)
P_{cem}	Surface percentage of cementation within the gouge sample (%), (Chap. 3)
P_{grains}	Surface percentage of angular grains within the gouge sample, (Chap. 4)
P_j	Perimeter of a particle "j" (m), (Chap 3)
P_{matrix}	Surface percentage of matrix particle within the gouge sample, (Chap. 4)
P_{pore}	Surface percentage of porosity within the sample $= 100 * F_v$, (Chap. 2)
R	Riedel shear bands in the R-orientation, (Chap. 1)
R'	Antithetic (or conjugate) Riedel shears in the R' orientation, (Chap. 1)
$R_{thickness}$	Thickness of a Riedel band (m), (Chap. 5)
r_0	Averaged grain radius used (m), (Chap. 2)
r	Signal of the grain radius, (Chap. 2)
S	Total Voronoï cell area (m^2), (Chap. 2)
S_d	Slip distance (m), (Chap. 4)
S_g	Gouge area perpendicular to the applied normal stress (m^2), ($S_g = L_g \times 1$ (2D))
$S_{grains-equiv}$	Total equivalent angular grains area within the gouge (m^2), (Chap. 4)
$S_{matrix-equiv}$	Total matrix particles area within the gouge (m^2), (Chap. 4)
S_p	Total area of one particle (m^2), (Chap. 2)
$S_{particles}$	Total particles area within the gouge (m^2), (Chap. 2)
S_{voids}	Total voids area within the gouge (m^2), (Chap. 2)
th	Thickness of the numerical granular gouge model (m), (Chap. 2)
th_i	Initial thickness of the numerical gouge sample (m), (Chap. 2)
U_{dp}	Slip distance corresponding to the maximum dilatancy (m), (Chap. 5)
U_{end}	Slip distance at the end of the simulation (m), (Chap. 5)
U_p	Slip distance at the effective friction peak (m), (Chap. 5)
V	Initial shearing velocity applied on the upper rock wall (m/s), (Chap. 2)

V_y	Downwards velocity used for biaxial numerical experiments (m/s), (Chap. 3)
$\overrightarrow{x_A}$	Position vector of a particle A, (Chap. 2)
Y	Boundary shear bands, (Chap. 1)
γ_n	Normal interparticle damping, (Chap. 2)
γ_t	Tangential interparticle damping, (Chap. 2)
γ_{xy}	Shear strain $\gamma_{xy} = \Delta_x / th_i$, (Chap. 5)
$\dot{\gamma}$	Shearing rate
Δ_t	DEM current and constant time step (s), (Chap. 2)
$\Delta_{t-contact}$	Proximity updating period (s), (Chap. 2)
Δth	y displacement of the upper rock wall (m), (Chap. 2)
Δ_x	x displacement of the upper rock wall or slip distance (m), (Chap. 5)
ΔH_d	Gain in gouge thickness (m), (Chap. 5)
ΔU_f	Characteristic distance of the exponential decay, (Chap. 5)
ΔW	Total energy budget (J/m²), (Chap. 5)
ΔX_{slip}	The variation in the X_R-direction, Slip within each band (m), (Chap. 5)
ΔY_{open}	The variation in the Y_R-direction, opening of each band (m), (Chap. 5)
$\Delta Y_{open-av}$	Average opening for a specific slip distance of the total fault (m), (Chap. 5)
δ_n	Normal interparticle gap (m), (Chap. 2)
δ_t	Tangential interparticle gap (m), (Chap. 2)
δ_{detec}	Limit of the interparticle gap (m), (Chap. 2)
ε_y	Vertical dilation of the granular model ($\varepsilon_y = \Delta th / th_i$) in %, (Chap. 2)
α_i	Angle orientation of *R*-bands (°), (Chap. 1)
μ	Coefficient of friction (from Amonton's laws), (Chap. 1)
μ^*	Effective friction (ratio of the shear stress under normal stress), (Chap. 2)
μ_a	Apparent friction (From Riedel shears (Lockner & Byerlee, 1993)), (Chap. 3)
μ^*_{dam}	Damage contribution of effective friction, (Chap. 5)
μ^*_{dil}	Dilation contribution of effective friction, (Chap. 5)
μ^*_{dp}	Maximum friction induced by rupture of cementation, (Chap. 5)
μ^*_f	Frictional contribution of effective friction, (Chap. 5)
μ^*_{fp}	Peak friction at the end of the elastic phase, (Chap. 5)
μ_f	Coefficient of friction (From Mohr-Coulomb definition), (Chap. 1)
μ_{num}	Interparticle friction, (Chap. 2)
μ^*_p	Effective friction peak, (Chap. 2)
μ^*_{ss}	Effective friction at steady-state, (Chap. 2)
ν	Poisson coefficient, (Chap. 5)
ρ_p	Particle density (kg/m^3), (Chap. 2)
ρ_r	Rock density (kg/m^3), (Chap. 2)
σ_1	Maximum principal stress (Pa), (Chap. 1)
σ_3	Minimum principal stress (Pa), (Chap. 1)
σ_{eff}	Effective stress, $\sigma_{eff} = \sigma_n - P_f$

σ_N	Normal stress applied on the upper rock wall (MPa), (Chap. 2)
σ_n	Contact normal stress between two particles (MPa), (Chap. 2)
σ_t	Contact tangential stress between two particles (MPa), (Chap. 2)
τ	Shear stress between the gouge and the upper rock (MPa), (Chap. 2)
τ_p	Maximum shear stress (MPa), (Chap. 5)
τ_{ss}	Steady-state shear stress (MPa), (Chap. 5)
φ	Internal friction angle in the sense of Mohr-Coulomb, (Chap. 1)
ϕ_{av}	Average particle diameter (m), (Chap. 2)
ϕ_{eq}	Particle equivalent diameter (m), (Chap. 2)
ϕ_{max}	Particle maximum diameter (m), (Chap. 2)
ϕ_{min}	Particle minimum diameter (m), (Chap. 2)
Ψ_p	Maximum dilatancy angle (°), (Chap. 5)

References

Abdelmalak, M. M., Bulois, C., Mourgues, R., Galland, O., Legland, J., & Gruber, C. (2016). Tectonophysics Description of new dry granular materials of variable cohesion and friction coef fi cient : Implications for laboratory modeling of the brittle crust. *Tectonophysics*, *684*, 39–51. https://doi.org/10.1016/j.tecto.2016.03.003

Aben, F. M., & Brantut, N. (2021). Dilatancy stabilises shear failure in rock. *Earth and Planetary Science Letters*, *574*, 117174. https://doi.org/10.1016/j.epsl.2021.117174

Abercrombie, R. E., & Rice, J. R. (2005). Can observations of earthquake scaling constrain slip weakening ? *Geophysical Journal International*, *162*(2), 406–424. https://doi.org/10.1111/j.1365-246X.2005.02579.x

Acosta, M., Passelègue, F. X., Schubnel, A., & Violay, M. (2018). Dynamic weakening during earthquakes controlled by fluid thermodynamics. *Nature Communications*, *9*(1). https://doi.org/10.1038/s41467-018-05603-9

Agnew, D. C. (2014). Variable star symbols for seismicity plots. *Seismological Research Letters*, *85*(4), 775–780. https://doi.org/10.1785/0220130214

Aharonov, E., & Scholz, C. H. (2018). A Physics-Based Rock Friction Constitutive Law: Steady State Friction. *Journal of Geophysical Research: Solid Earth*, *123*(2), 1591–1614. https://doi.org/10.1002/2016JB013829

Aharonov, E., & Sparks, D. (1999). Rigidity phase transition in granular packings. *Physical Review E - Statistical Physics, Plasmas, Fluids, and Related Interdisciplinary Topics*, *60*(6), 6890–6896. https://doi.org/10.1103/PhysRevE.60.6890

Aharonov, E., & Sparks, D. (2004). Stick-slip motion in simulated granular layers. *Journal of Geophysical Research: Solid Earth*, *109*(9), 1–12. https://doi.org/10.1029/2003JB002597

Al-Hinai, S., Fisher, Q. J., Al-Busafi, B., Guise, P., & Grattoni, C. A. (2008). Laboratory measurements of the relative permeability of cataclastic fault rocks: An important consideration for production simulation modelling. *Marine and Petroleum Geology*, *25*(6), 473–485. https://doi.org/10.1016/j.marpetgeo.2007.07.005

An, L.-J., & Sammis, C. G. (1994). Particle Size Distribution of Cataclastic Fault Materials from Southern California : a 3D study. *Pure and Applied Geophysics*, *143*(1), 203–227. https://doi.org/10.1007/BF00874329

Anthony, J. L., & Marone, C. (2005). Influence of particle characteristics on granular friction. *Journal of Geophysical Research: Solid Earth*, *110*(8), 1–14. https://doi.org/10.1029/2004JB003399

Antonellini, M. A., & Mollema, P. (2002). Cataclastic Faults in the Loiano Sandstones ; Northern Apennines , Italy, *121*(September), 163–178.

Antonellini, M. A., & Pollard, D. D. (1995). Distinct element modeling of deformation bands in sandstone. *Journal of Structural Geology*, *17*(8), 1165–1182. https://doi.org/10.1016/0191-8141(95)00001-T

Antonellini, M. A., Aydin, A., & Pollard, D. D. (1994). Microstructure of deformation bands in porous sandstones at Arches National Park, Utah. *Journal of Structural Geology*, *16*(7), 941–959. https://doi.org/10.1016/0191-8141(94)90077-9

Archard, J. (1953). Contact and rubbing of flat surfaces. *Journal of Applied Physics*, *24*(8), 981–988.

Aubry, J., Passelègue, F. X., Deldicque, D., Girault, F., Marty, S., Lahfid, A., et al. (2018). Frictional Heating Processes and Energy Budget During Laboratory Earthquakes. *Geophysical Research Letters*, *45*(22), 12,274-12,282. https://doi.org/10.1029/2018GL079263

Aubry, Jérôme. (2019). *Séismes au laboratoire : friction , plasticité et bilan énergétique*.

Azéma, E., & Radjaï, F. (2014). Internal structure of inertial granular flows. *Physical Review Letters*, *112*(7), 1–5. https://doi.org/10.1103/PhysRevLett.112.078001

Badt, N. Z., Tullis, T. E., Hirth, G., & Goldsby, D. L. (2020). Thermal Pressurization Weakening in Laboratory

Experiments. *Journal of Geophysical Research: Solid Earth*, *125*(5), 1–21. https://doi.org/10.1029/2019JB018872

Barras, F., Aldam, M., Roch, T., Brener, E. A., Bouchbinder, E., & Molinari, J. F. (2019). Emergence of Cracklike Behavior of Frictional Rupture: The Origin of Stress Drops. *Physical Review X*, *9*(4), 41043. https://doi.org/10.1103/PhysRevX.9.041043

Barras, F., Aldam, M., Roch, T., Brener, E. A., Bouchbinder, E., & Molinari, J. F. (2020). The emergence of crack-like behavior of frictional rupture: Edge singularity and energy balance. *Earth and Planetary Science Letters*, *531*, 115978. https://doi.org/10.1016/j.epsl.2019.115978

Bayart, E., Svetlizky, I., & Fineberg, J. (2016). Slippery but Tough: The Rapid Fracture of Lubricated Frictional Interfaces. *Physical Review Letters*, *116*(19), 1–5. https://doi.org/10.1103/PhysRevLett.116.194301

Bedford, J. D., & Faulkner, D. R. (2021). The Role of Grain Size and Effective Normal Stress on Localization and the Frictional Stability of Simulated Quartz Gouge. *Geophysical Research Letters*, *48*. https://doi.org/10.1029/2020GL092023

Bedford, J. D., Faulkner, D. R., & Lapusta, N. (2022). Fault rock heterogeneity can produce fault weakness and reduce fault stability. *Nature Communications*, *13*(1), 1–7. https://doi.org/10.1038/s41467-022-27998-2

Beeler, N. M., Tullis, T. E., Blanpied, M. L., & Weeks, J. D. (1996). Frictional behavior of large displacement experimental faults. *Journal of Geophysical Research B: Solid Earth*, *101*(4), 8697–8715. https://doi.org/10.1029/96jb00411

Berger, N., Azéma, E., Douce, J. F., & Radjai, F. (2015). Scaling behaviour of cohesive granular flows. *Epl*, *112*(6). https://doi.org/10.1209/0295-5075/112/64004

Biegel, R. L., Sammis, C. G., & Dieterich, J. H. (1989). The frictional properties of a simulated gouge having a fractal particle distribution. *Journal of Structural Geology*, *11*(7), 827–846. https://doi.org/10.1016/0191-8141(89)90101-6

Billi, A. (2005). Grain size distribution and thickness of breccia and gouge zones from thin (<1 m) strike-slip fault cores in limestone. *Journal of Structural Geology*, *27*(10), 1823–1837. https://doi.org/10.1016/j.jsg.2005.05.013

Billi, A., & Storti, F. (2004). Fractal distribution of particle size in carbonate cataclastic rocks from the core of a regional strike-slip fault zone. *Tectonophysics*, *384*(1–4), 115–128. https://doi.org/10.1016/j.tecto.2004.03.015

Billi, A., Salvini, F., & Storti, F. (2003). The damage zone-fault core transition in carbonate rocks: Implications for fault growth, structure and permeability. *Journal of Structural Geology*, *25*(11), 1779–1794. https://doi.org/10.1016/S0191-8141(03)00037-3

Bishop, A. W. (1971). The Influence of Progressive Failure on the Choice of the Method of Stability Analysis. *Géotechnique*, *21*(2), 168–172. https://doi.org/10.1680/geot.1971.21.2.168

Blanpied, M. L., Lockner, D. A., & Byerlee, J. D. (1995). Frictional slip of granite at hydrothermal conditions. *Journal of Geophysical Research: Solid Earth*, *100*(B7), 13045–13064. https://doi.org/10.1029/95JB00862

Blenkinsop, T. G. (1991). Cataclasis and Processes of Particle Size Reduction. *Pure and Applied Geophysics*, *136*(1), 59–86. https://doi.org/10.1007/BF00878888

Borja, R. I., Song, X., Rechenmacher, A. L., Abedi, S., & Wu, W. (2013). Shear band in sand with spatially varying density. *Journal of the Mechanics and Physics of Solids*, *61*(1), 219–234. https://doi.org/10.1016/j.jmps.2012.07.008

Bouillanne, O., Mollon, G., Saulot, A., Descartes, S., Serres, N., Demmou, K., & Chassaing, G. (2021). Detecting vorticity in cohesive deformable granular material. *EPJ Web of Conferences*, *249*, 08005. https://doi.org/10.1051/epjconf/202124908005

Bourouis, S., & Bernard, P. (2007). Evidence for coupled seismic and aseismic fault slip during water injection in the geothermal site of Soultz (France), and implications for seismogenic transients. *Geophysical Journal International*, *169*(2), 723–732. https://doi.org/10.1111/j.1365-246X.2006.03325.x

Brace, W. F., & Kohlstedt, D. L. (1980). Limits on lithospheric stress imposed by laboratory experiments.

Journal of Geophysical Research: Solid Earth, *85*(B11), 6248–6252.

Brodsky, E. E., & Kanamori, H. (2001). Elastohydrodynamic lubrication of faults. *Journal of Geophysical Research: Solid Earth*, *106*(B8), 16357–16374. https://doi.org/10.1029/2001jb000430

Bürgmann, R. (2018). The geophysics, geology and mechanics of slow fault slip. *Earth and Planetary Science Letters*, *495*, 112–134. https://doi.org/10.1016/j.epsl.2018.04.062

Burridge, R., & Knopoff, L. (1967). Model and theoretical seismicity. *Bulletin of the Seismological Society of America*, *57*(3), 341–371.

Byerlee, J. D. (1978). Friction of rocks. *Pure and Applied Geophysics PAGEOPH*, *116*(4–5), 615–626. https://doi.org/10.1007/BF00876528

Byerlee, J. D., & Brace, W. F. (1968). Stick slip, stable sliding, and earthquakes-Effect of rock type, pressure, strain rate, and stiffness. *Journal of Geophysical Research*, *73*(18), 6031–6037. https://doi.org/10.1029/JB073i018p06031

Byerlee, J. D., & Savage, J. C. (1992). Coulomb plasticity within the fault zone. *Geopgysical Reschearch Letters*, *19*(23), 2341–2344. https://doi.org/10.1029/92GL02370

Byerlee, J. D., Mjachkin, V., Summers, R., & Voevoda, O. (1978). Structures developed sliding and stick-slip in fault gouge during stable. *Tectonophysics*, *44*, 161–171.

Caine, J. S., Bruhn, R. L., & Forster, C. B. (2010). Internal structure, fault rocks, and inferences regarding deformation, fluid flow, and mineralization in the seismogenic Stillwater normal fault, Dixie Valley, Nevada. *Journal of Structural Geology*, *32*(11), 1576–1589. https://doi.org/10.1016/j.jsg.2010.03.004

Caniven, Y., Morgan, J. K., & Blank, D. G. (2021). The Role of Along-Fault Dilatancy in Fault Slip Behavior. *Journal of Geophysical Research : Solid Earth*, 1–21. https://doi.org/10.1029/2021JB022310

Casas, N., Mollon, G., & Daouadji, A. (2022). DEM Analyses of Cemented Granular Fault Gouges at the Onset of Seismic Sliding: Peak Strength, Development of Shear Zones and Kinematics. *Pure and Applied Geophysics*. https://doi.org/10.1007/s00024-021-02934-5

Chen, T., & Lapusta, N. (2009). Scaling of small repeating earthquakes explained by interaction of seismic and aseismic slip in a rate and state fault model. *Journal of Geophysical Research: Solid Earth*, *114*(1), 1–12. https://doi.org/10.1029/2008JB005749

Chen, T., & Lapusta, N. (2019). On behaviour and scaling of small repeating earthquakes in rate and state fault models. *Geophysical Journal International*, *218*(3), 2001–2018. https://doi.org/10.1093/gji/ggz270

Chester, F., Evans, J., & Biegel, R. (1993). Internal Structure and Weakening Mechanisms of the San Andreas Fault, *98*, 771–786.

Chester, J., Chester, F., & Kronenberg, A. (2005). Fracture surface energy of the Punchbowl fault, San Andreas system. *Nature*, *437*(7055), 133–136. https://doi.org/10.1038/nature03942

Cho, N., Martin, C. D., & Sego, D. C. (2007). A clumped particle model for rock. *International Journal of Rock Mechanics and Mining Sciences*, *44*(7), 997–1010. https://doi.org/10.1016/j.ijrmms.2007.02.002

Cho, N., Martin, C. D., & Sego, D. C. (2008). Development of a shear zone in brittle rock subjected to direct shear. *International Journal of Rock Mechanics and Mining Sciences*, *45*(8), 1335–1346. https://doi.org/10.1016/j.ijrmms.2008.01.019

Cohen, J. D., Lin, M. C., Manocha, D., & Ponamgi, M. (1995). I-COLLIDE: An interactive and exact collision detection system for large-scale environments. *Proceedings of the Symposium on Interactive 3D Graphics*, 189–196.

Collettini, C., Niemeijer, A., Viti, C., & Marone, C. (2009). Fault zone fabric and fault weakness. *Nature*, *462*(7275), 907–910. https://doi.org/10.1038/nature08585

Collettini, C., Tesei, T., Scuderi, M. M., Carpenter, B. M., & Viti, C. (2019). Beyond Byerlee friction, weak faults and implications for slip behavior. *Earth and Planetary Science Letters*, *519*, 245–263. https://doi.org/10.1016/j.epsl.2019.05.011

Cornelio, C., & Violay, M. (2020). Parametric analysis of the elastohydrodynamic lubrication efficiency on induced seismicity. *Geophysical Journal International*, *222*(1), 517–525. https://doi.org/10.1093/GJI/GGAA180

Cornelio, C., Passelègue, F. X., Spagnuolo, E., Di Toro, G., & Violay, M. (2019). Effect of Fluid Viscosity on Fault Reactivation and Coseismic Weakening. *Journal of Geophysical Research: Solid Earth*, *125*(1), 1–18. https://doi.org/10.1029/2019JB018883

Cornelio, C., Spagnuolo, E., Di Toro, G., Nielsen, S., & Violay, M. (2019). Mechanical behaviour of fluid-lubricated faults. *Nature Communications*, *10*(1), 1–7. https://doi.org/10.1038/s41467-019-09293-9

Cornet, F. H. (2016). Seismic and aseismic motions generated by fluid injections. *Geomechanics for Energy and the Environment*, *5*, 42–54. https://doi.org/10.1016/j.gete.2015.12.003

Da Cruz, F., Emam, S., Prochnow, M., Roux, J. N., & Chevoir, F. (2005). Rheophysics of dense granular materials: Discrete simulation of plane shear flows. *Physical Review E*, *72*(2), 1–17. https://doi.org/10.1103/PhysRevE.72.021309

Cundall, P. A. ., & Strack, O. D. L. (1979). A discrete numerical model for granular assemblies. *Géotechnique*, *29*(1), 47–65. https://doi.org/10.1680/geot.1979.29.1.47

Daouadji, A., & Hicher, P. (2010). An enhanced constitutive model for crushable granular materials. *International Journal for Numerical and Analytical Methods in Geomechanics*, *34*, 555–580. https://doi.org/10.1002/nag

Daouadji, A., Hicher, P., Rahma, A., Daouadji, A., Hicher, P., & Rahma, A. (2001). An elastoplastic model for granular materials taking into account grain breakage. *European Journal of Mechanics - A/Solids*, *20*(1), 113–137. https://doi.org/10.1016/S0997-7538(00)01130-X

Das, A., Tengattini, A., Nguyen, G. D., Viggiani, G., Hall, S. A., & Einav, I. (2014). A thermomechanical constitutive model for cemented granular materials with quantifiable internal variables. Part II - Validation and localization analysis. *Journal of the Mechanics and Physics of Solids*, *70*(1), 382–405. https://doi.org/10.1016/j.jmps.2014.05.021

Davis, G. H., Bump, A. P., García, P. E., & Ahlgren, S. G. (2000). Conjugate Riedel deformation band shear zones. *Journal of Structural Geology*, *22*(2), 169–190. https://doi.org/10.1016/S0191-8141(99)00140-6

Dieterich, J. H. (1972). Time-dependent friction in rocks. *Journal of Geophysical Research*, *77*(20), 3690–3697. https://doi.org/10.1029/jb077i020p03690

Dieterich, J. H. (1979). Modeling of Rock Friction Experimental Results and Constitutive Equations. *Journal of Geophysical Research*, *84*(9), 2161–2168.

Dorostkar, O. (2018). Stick-slip dynamics in dry and fluid saturated granular fault gouge investigated by numerical simulations. *PhD Thesis*. https://doi.org/10.3929/ethz-a-010782581

Dorostkar, O., Guyer, R. A., Johnson, P. A., Marone, C., & Carmeliet, J. (2017a). On the micromechanics of slip events in sheared, fluid-saturated fault gouge. *Geophysical Research Letters*, *44*(12), 6101–6108. https://doi.org/10.1002/2017GL073768

Dorostkar, O., Guyer, R. A., Johnson, P. A., Marone, C., & Carmeliet, J. (2017b). On the role of fluids in stick-slip dynamics of saturated granular fault gouge using a coupled computational fluid dynamics-discrete element approach. *Journal of Geophysical Research: Solid Earth*, *122*(5), 3689–3700. https://doi.org/10.1002/2017JB014099

Dorostkar, O., Guyer, R. A., Johnson, P. A., Marone, C., & Carmeliet, J. (2018). Cohesion-Induced Stabilization in Stick-Slip Dynamics of Weakly Wet, Sheared Granular Fault Gouge. *Journal of Geophysical Research: Solid Earth*, *123*(3), 2115–2126. https://doi.org/10.1002/2017JB015171

Dratt, M., & Katterfeld, A. (2017). Coupling of FEM and DEM simulations to consider dynamic deformations under particle load. *Granular Matter*, *19*(3), 1–15. https://doi.org/10.1007/s10035-017-0728-3

Dunn, D. E., LaFountain, L. J., & Jackson, R. E. (1973). Porosity Dependence and Mechanism of Brittle Fracture in Sandstones. *Journal of Geophysical Research*, *78*(14). https://doi.org/10.1029/JB078i014p02403

Estrada, N., Taboada, A., & Radjaï, F. (2008). Shear strength and force transmission in granular media with rolling resistance. *Physical Review E - Statistical, Nonlinear, and Soft Matter Physics*, *78*(2), 1–11. https://doi.org/10.1103/PhysRevE.78.021301

Estrada, N., Lizcano, A., & Taboada, A. (2010). Simulation of cemented granular materials. I. Macroscopic stress-strain response and strain localization. *Physical Review E*, *82*, 1–11. https://doi.org/10.1103/PhysRevE.82.011303

Faqih, A., Chaudhuri, B., Muzzio, F. J., Tomassone, M. S., & Hammond, S. (2006). Flow - Induced Dilation of Cohesive Granular Materials, *52*(12). https://doi.org/10.1002/aic

Faulkner, D. R., Lewis, A. C., & Rutter, E. H. (2003). On the internal structure and mechanics of large strike-slip fault zones: Field observations of the Carboneras fault in southeastern Spain. *Tectonophysics*, *367*(3–4), 235–251. https://doi.org/10.1016/S0040-1951(03)00134-3

Faulkner, D. R., Jackson, C. A. L., Lunn, R. J., Schlische, R. W., Shipton, Z. K., Wibberley, C. A. J., & Withjack, M. O. (2010). A review of recent developments concerning the structure, mechanics and fluid flow properties of fault zones. *Journal of Structural Geology*, *32*(11), 1557–1575. https://doi.org/10.1016/j.jsg.2010.06.009

Ferdowsi, B. (2014). *Discrete element modeling of triggered slip in faults with granular gouge Application to dynamic earthquake triggering*. ETH Zurich. https://doi.org/10.3929/ethz-a-010232908

Ferdowsi, B., & Rubin, A. M. (2020). A Granular Physics-Based View of Fault Friction Experiments, (May), 1–32. https://doi.org/10.1029/2019JB019016

Ferdowsi, B., Griffa, M., Guyer, R. A., Johnson, P. A., Marone, C., & Carmeliet, J. (2014). Three-dimensional discrete element modeling of triggered slip in sheared granular media. *Physical Review E*, *89*(4), 1–12. https://doi.org/10.1103/PhysRevE.89.042204

Ferellec, J. F., & McDowell, G. R. (2008). A simple method to create complex particle shapes for DEM. *Geomechanics and Geoengineering*, *3*(3), 211–216. https://doi.org/10.1080/17486020802253992

Fialko, Y. (2007). Fracture and Frictional Mechanics - Theory. *Treatise on Geophysics*, *4*, 83–106. https://doi.org/10.1016/B978-044452748-6.00062-6

Fillot, N., Iordanoff, I., & Berthier, Y. (2007). Wear modeling and the third body concept, *262*, 949–957. https://doi.org/10.1016/j.wear.2006.10.011

Fisher, Q. J., & Knipe, R. J. (2001). The permeability of faults within siliciclastic petroleum reservoirs of the North Sea and Norwegian Continental Shelf. *Marine and Petroleum Geology*, *18*(10), 1063–1081. https://doi.org/10.1016/S0264-8172(01)00042-3

Fondriest, M., Mecklenburgh, J., Passelegue, F. X., Artioli, G., Nestola, F., Spagnuolo, E., et al. (2020). Pseudotachylyte Alteration and the Rapid Fade of Earthquake Scars From the Geological Record. *Geophysical Research Letters*, *47*(22), 1–9. https://doi.org/10.1029/2020GL090020

Fournier, T., & Morgan, J. (2012). Insights to slip behavior on rough faults using discrete element modeling, *39*(May), 1–6. https://doi.org/10.1029/2012GL051899

Friedman, M., Handin, J., & Alani, G. (1972). Fracure-surface energy of rocks. *International Journal of Rock Mechanics and Mining Sciences & Geomechanics*, *9*(6), 757–764. https://doi.org/10.1016/0148-9062(72)90034-4

Frye, K. M., & Marone, C. (2002). Effect of humidity on granular friction at room temperature. *Journal of Geophysical Research: Solid Earth*, *107*(B11), ETG 11-1-ETG 11-13. https://doi.org/10.1029/2001jb000654

Frye, K. M., & Marone, C. (2003). The effect of particle dimensionality on Granular friction in laboratory shear zones. *Geophysical Research Letters*, *29*(19), 22-1-22–4. https://doi.org/10.1029/2002gl015709

Fulton, P. M., & Rathbun, A. P. (2011). Experimental constraints on energy partitioning during stick-slip and stable sliding within analog fault gouge. *Earth and Planetary Science Letters*, *308*(1–2), 185–192. https://doi.org/10.1016/j.epsl.2011.05.051

Gao, K., Euser, B. J., Rougier, E., Guyer, R. A., Lei, Z., Knight, E. E., et al. (2018). Modeling of Stick-Slip

Behavior in Sheared Granular Fault Gouge Using the Combined Finite-Discrete Element Method. *Journal of Geophysical Research: Solid Earth*, *123*(7), 5774–5792. https://doi.org/10.1029/2018JB015668

Geng, Z., Bonnelye, A., Chen, M., Jin, Y., Dick, P., David, C., et al. (2018). Time and Temperature Dependent Creep in Tournemire Shale. *Journal of Geophysical Research: Solid Earth*, *123*(11), 9658–9675. https://doi.org/10.1029/2018JB016169

Gentier, S. (2013). Les EGS : une méthode d'exploitation gétohermique généralisée pour les températures de 130 à 180 °C. *Geosciences*, 54–63. https://doi.org/10.1051/lhb/2010051

Di Giacomo, D., Robert Engdahl, E., & Storchak, D. A. (2018). The ISC-GEM Earthquake Catalogue (1904-2014): Status after the Extension Project. *Earth System Science Data*, *10*(4), 1877–1899. https://doi.org/10.5194/essd-10-1877-2018

Giorgetti, C., Tesei, T., Scuderi, M. M., & Collettini, C. (2019). Experimental Insights Into Fault Reactivation in Gouge-Filled Fault Zones. *Journal of Geophysical Research: Solid Earth*, *124*(4), 4189–4204. https://doi.org/10.1029/2018JB016813

Godet, M. (1984). The third-body approach: a mechanical view of wear. *Wear*, *100*, 437–452.

Goren, L., Aharonov, E., Sparks, D., & Toussaint, R. (2011). The Mechanical Coupling of Fluid-Filled Granular Material Under Shear. *Pure and Applied Geophysics*, *168*(12), 2289–2323. https://doi.org/10.1007/s00024-011-0320-4

GRD Midi. (2004). On dense granular flows. *European Physical Journal E*, *14*(4), 341–365. https://doi.org/10.1140/epje/i2003-10153-0

Griffith, A. (1924). The theory of rupture. In *First Int. Cong. Appl. Mech* (pp. 55–63).

Grigoli, F., Cesca, S., Priolo, E., Rinaldi, A. P., Clinton, J. F., Stabile, T. A., et al. (2017). Current challenges in monitoring, discrimination, and management of induced seismicity related to underground industrial activities: A European perspective. *Reviews of Geophysics*, *55*(2), 310–340. https://doi.org/10.1002/2016RG000542

Gu, Y., & Wong, T. F. (1994). Development of shear localization in simulated quartz gouge: Effect of cumulative slip and gouge particle size. *Pure and Applied Geophysics PAGEOPH*, *143*(1–3), 387–423. https://doi.org/10.1007/BF00874336

Guo, Y., & Morgan, J. K. (2004). Influence of normal stress and grain shape on granular friction: Results of discrete element simulations. *Journal of Geophysical Research: Solid Earth*, *109*(B12). https://doi.org/10.1029/2004JB003044

Hadizadeh, J., Tullis, T. E., White, J. C., & Konkachbaev, A. I. (2015). Shear localization, velocity weakening behavior, and development of cataclastic foliation in experimental granite gouge. *Journal of Structural Geology*, *71*, 86–99. https://doi.org/10.1016/j.jsg.2014.10.013

Haines, S. H., Van Der Pluijm, B. A., Ikari, M. J., Saffer, D. M., & Marone, C. (2009). Clay fabric intensity in natural and artificial fault gouges: Implications for brittle fault zone processes and sedimentary basin clay fabric evolution. *Journal of Geophysical Research: Solid Earth*, *114*(5). https://doi.org/10.1029/2008JB005866

Haines, S. H., Kaproth, B., Marone, C., Saffer, D., & Van der Pluijm, B. (2013). Shear zones in clay-rich fault gouge: A laboratory study of fabric development and evolution. *Journal of Structural Geology*, *51*, 206–225. https://doi.org/10.1016/j.jsg.2013.01.002

Handin, J. (1969). On the Coulomb-Mohr Failure Criterion. *Journal of Geophysical Research*, *74*(22), 5343–5348. https://doi.org/10.1029/JB074i022p05343

Hardy, W. B. (1920). Some Problems of Lubrication. *Nature*, *106*, 569–572. https://doi.org/10.1038/106569a0

Harmon, J. M., Karapiperis, K., Li, L., Moreland, S., & Andrade, J. E. (2021). Modeling connected granular media : Particle bonding within the level set discrete element method. *Computer Methods in Applied Mechanics and Engineering*, *373*, 113486. https://doi.org/10.1016/j.cma.2020.113486

Härtl, J., & Ooi, J. Y. (2011). Numerical investigation of particle shape and particle friction on limiting bulk friction in direct shear tests and comparison with experiments Top ring Normal load Bracket Loading stem

Shear force. *Powder Technology*, *212*(1), 231–239. https://doi.org/10.1016/j.powtec.2011.05.022

Heilbronner, R., & Keulen, N. (2006). Grain size and grain shape analysis of fault rocks. *Tectonophysics*, *427*(1–4), 199–216. https://doi.org/10.1016/j.tecto.2006.05.020

Hirata, M., Muto, J., & Nagahama, H. (2017). Shear zone development and frictional instabilities. *International Journal of GEOMATE*, *12*(34), 32–37. https://doi.org/10.21660/2017.34.2660

Hirth, G., & Tullis, J. (1989). The effects of pressure and porosity on the micromechanics of the brittle-ductile transition in quartzite. *Journal of Geophysical Research*, *94*(B12). https://doi.org/10.1029/jb094ib12p17825

Im, K., Marone, C., & Elsworth, D. (2019). The transition from steady frictional sliding to inertia-dominated instability with rate and state friction. *Journal of the Mechanics and Physics of Solids*, *122*, 116–125. https://doi.org/10.1016/j.jmps.2018.08.026

Imber, J., Holdsworth, R. E., Smith, S. A. F., Jefferies, S. P., & Collettini, C. (2008). Frictional-viscous flow, seismicity and the geology of weak faults: a review and future directions. *Geological Society, London, Special Publications*, *299*(1), 151–173. https://doi.org/10.1144/sp299.10

Insua-Arevalo, J. M., Tsige, M., Sanchez-Roldan, J. L., Rodríguez-Escudero, E., & Martínez- Díaz, J. J. (2021). Influence of the microstructure and roughness of weakness planes on the strength anisotropy of a foliated clay-rich fault gouge. *Engineering Geology*, *289*(August 2020).

Iordanoff, I., & Khonsari, M. M. (2004). Granular Lubrication: Toward an Understanding of the Transition Between Kinetic and Quasi-Fluid Regime. *Journal of Tribology*, *126*(1), 137. https://doi.org/10.1115/1.1633575

Iordanoff, I., Fillot, N., & Berthier, Y. (2005). Numerical study of a thin layer of cohesive particles under plane shearing. *Powder Technology*, *159*(1), 46–54. https://doi.org/10.1016/j.powtec.2005.05.053

Irwin, G. R. (1957). Analysis of stresses and strains near the end of a crack transversing a plate. *Trans. ASME, Ser. E, J. Appl. Mech.*, *24*, 361–364.

Jaeger, J. C. (1971). Friction of rocks and stability of slopes. *Geotechniques*, *116*(4–5), 615–626. https://doi.org/10.1007/BF00876528

Jaeger, J. C., Cook, N. G. W., & Zimmerman, R. W. (2007). *Fundamentals of Rock Mechanics, Fourth Edition*.

Jean, M. (1999). The non-smooth contact dynamics method. *Computer Methods in Applied Mechanics and Engineering*, *177*(3–4), 235–257. https://doi.org/10.1016/S0045-7825(98)00383-1

Jensen, R. P., Bosscher, P. J., Plesha, M. E., & Edil, T. B. (1999). DEM simulation of granular media - Structure interface: effects of surface roughness and particle shape. *International Journal for Numerical and Analytical Methods in Geomechanics*, *547*(June 1997).

Jiang, M., Zhang, W., Sun, Y., & Utili, S. (2013). An investigation on loose cemented granular materials via DEM analyses. *Granular Matter*, *15*(1), 65–84. https://doi.org/10.1007/s10035-012-0382-8

Johansen, T. E. S., Fossen, H., & Kluge, R. (2005). The impact of syn-faulting porosity reduction on damage zone architecture in porous sandstone: An outcrop example from the Moab Fault, Utah. *Journal of Structural Geology*, *27*(8), 1469–1485. https://doi.org/10.1016/j.jsg.2005.01.014

Jop, P., Forterre, Y., & Pouliquen, O. (2006). A constitutive law for dense granular flows. *Nature*, *441*(7094), 727–730. https://doi.org/10.1038/nature04801

Kaminskaite, I., Fisher, Q. J., & Michie, E. A. H. (2019). Microstructure and petrophysical properties of deformation bands in high porosity carbonates. *Journal of Structural Geology*, *119*(December 2018), 61–80. https://doi.org/10.1016/j.jsg.2018.12.001

Kanamori, H., & Brodsky, E. E. (2001). The physics of earthquakes. *Physics Today*, *54*(6), 34. https://doi.org/10.1063/1.1387590

Kanamori, H., & Brodsky, E. E. (2004). The physics of earthquakes. *Institute of Physic Publishing*, *67*, 1429–1496. https://doi.org/10.1088/0034-4885/67/8/R03

Kanamori, H., & Heaton, T. H. (2000). Microscopic and Macroscopic Physics of Earthquakes. In J. B. Rundle, D. L. Turcotte, & W. Klein (Eds.), *Geocomplexity and the Physics of Earthquakes* (pp. 147–163). https://doi.org/10.1029/GM120p0147

Kasyap, S., & Senetakis, K. (2020). An Experimental Investigation on the Tribological Behaviour of Nominally Flat Quartz Grains with Gouge Material in Dry, Partial Saturated and Submersed Conditions. *Pure and Applied Geophysics*. https://doi.org/10.1007/s00024-020-02431-1

Kasyap, Sathwik, & Senetakis, K. (2021). Micromechanical-based experimental and analytical studies on rate effects and stick-slip instability of smooth quartz surfaces in the presence of plastic and non-plastic gouges. *International Journal for Numerical and Analytical Methods in Geomechanics*, *45*(6), 776–793. https://doi.org/10.1002/nag.3178

Katz, R., Spiegelman, M., & Holtzman, B. (2006). The dynamics of melt and shear localization in partially molten aggregates. *Nature Letters*, *442*(August), 2–5. https://doi.org/10.1038/nature05039

Katz, Y., & Weinberger, R. (2005). Strain localization in sandstone during embryonic stages of shear-zone evolution. *Terra Nova*, *17*(4), 311–316. https://doi.org/10.1111/j.1365-3121.2005.00615.x

Katz, Y., Weinberger, R., & Aydin, A. (2004). Geometry and kinematic evolution of Riedel shear structures, Capitol Reef National Park, Utah. *Journal of Structural Geology*, *26*(3), 491–501. https://doi.org/10.1016/j.jsg.2003.08.003

Kawamoto, R., Andò, E., Viggiani, G., & Andrade, J. E. (2018). All you need is shape: Predicting shear banding in sand with LS-DEM. *Journal of the Mechanics and Physics of Solids*, *111*, 375–392. https://doi.org/10.1016/j.jmps.2017.10.003

Kazerani, T., & Zhao, J. (2010). Micromechanical parameters in bonded particle method for modelling of brittle material failure. *International Journal for Numerical and Analytical Methods in Geomechanics*, *34*, 1877–1895. https://doi.org/10.1002/nag.884

Kenigsberg, A. R., Rivière, J., Marone, C., & Saffer, D. M. (2019). The Effects of Shear Strain, Fabric, and Porosity Evolution on Elastic and Mechanical Properties of Clay-Rich Fault Gouge. *Journal of Geophysical Research: Solid Earth*, *124*(11), 10968–10982. https://doi.org/10.1029/2019JB017944

Kenigsberg, A. R., Rivière, J., Marone, C., & Saffer, D. M. (2020). Evolution of Elastic and Mechanical Properties During Fault Shear : The Roles of Clay Content , Fabric Development , and Porosity Journal of Geophysical Research : Solid Earth, 1–16. https://doi.org/10.1029/2019JB018612

Kettermann, M., & Urai, J. L. (2015). Changes in structural style of normal faults due to failure mode transition: First results from excavated scale models. *Journal of Structural Geology*, *74*, 105–116. https://doi.org/10.1016/j.jsg.2015.02.013

Kilgore, B. D., Blanpied, M. L., & Dieterich, H. (1993). Velocity dependent friction of granite over a wide range of conditions. *Geophysical Research Letters*, *20*(10), 903–906.

Kloss, C., Goniva, C., Hager, A., Amberger, S., & Pirker, S. (2012). Models, algorithms and validation for opensource DEM and CFD-DEM. *Progress in Computational Fluid Dynamics*, *12*(2–3), 140–152. https://doi.org/10.1504/PCFD.2012.047457

Kranz, R. L., & Scholz, C. H. (1977). Critical Dilatant Volume of Rocks at the Onset of Tertiary Creep crack observation using the scanni0g electron microscope each quartzite, *82*(30). https://doi.org/10.1029/JB082i030p04893

Lade, P. V, & Overton, D. D. (1989). Cementation Effects in Frictional Materials. *Journal of Geotechnic Engineering*, *115*(10), 1373–1387. https://doi.org/10.1061/(ASCE)0733-9410(1989)115:10(1373)

Lambert, V., & Lapusta, N. (2020). Rupture-dependent breakdown energy in fault models with thermo-hydro-mechanical processes. *Solid Earth Discuss*, (in review). https://doi.org/10.5194/se-2020-115

Lawn, B. (1993). *Fracture of brittle solids*. Cambridge university press.

Lee, H. K., & Kim, H. S. (2005). Comparison of structural features of the fault zone developed at different protoliths: Crystalline rocks and mudrocks. *Journal of Structural Geology*, *27*(11), 2099–2112. https://doi.org/10.1016/j.jsg.2005.06.012

Leeman, J., Scuderi, M. M., Marone, C., & Saffer, D. (2015). Stiffness evolution of granular layers and the origin of repetitive, slow, stick-slip frictional sliding. *Granular Matter*, *17*(4), 447–457. https://doi.org/10.1007/s10035-015-0565-1

Leeman, J. R., Saffer, D. M., Scuderi, M. M., & Marone, C. (2016). Laboratory observations of slow earthquakes and the spectrum of tectonic fault slip modes. *Nature Communications*, *7*, 1–6. https://doi.org/10.1038/ncomms11104

Lin, A. (1999). S-C cataclasite in granitic rock. *Tectonophysics*, *304*(3), 257–273. https://doi.org/10.1016/S0040-1951(99)00026-8

Lin, A., & Yamashita, K. (2013). Spatial variations in damage zone width along strike-slip faults: An example from active faults in southwest Japan. *Journal of Structural Geology*, *57*, 1–15. https://doi.org/10.1016/j.jsg.2013.10.006

Lisjak, A., & Grasselli, G. (2014). A review of discrete modeling techniques for fracturing processes in discontinuous rock masses. *Journal of Rock Mechanics and Geotechnical Engineering*, *6*(4), 301–314. https://doi.org/10.1016/j.jrmge.2013.12.007

Lockner, D. A., & Beeler, N. M. (2002). Rock failure and Earthquakes. *International Geophysics Series*, *81*(A), 505–538.

Lockner, D. A., & Byerlee, J. D. (1993). How geometrical constraints contribute to the weakness of mature faults. *U.S Geological Survey*.

Lu, S.-M. M. (2018). A global review of enhanced geothermal system (EGS). *Renewable and Sustainable Energy Reviews*, *81*(April 2017), 2902–2921. https://doi.org/10.1016/j.rser.2017.06.097

Lu, Y., Asce, A. M., Tan, Y., Asce, M., Li, X., & Liu, C. (2017). Methodology for Simulation of Irregularly Shaped Gravel Grains and Its Application to DEM Modeling. *Journal of Computing in Civil Engineering*, *31*(5), 04017023. https://doi.org/10.1061/(asce)cp.1943-5487.0000676

Lyu, Z., Rivière, J., Yang, Q., & Marone, C. (2019). On the mechanics of granular shear: The effect of normal stress and layer thickness on stick-slip properties. *Tectonophysics*, *763*(April), 86–99. https://doi.org/10.1016/j.tecto.2019.04.010

Maeda, K. (2006). Influence of grain properties on macro mechanical behaviors of granular media by DEM. *Journal of Applied Mechanics, JSCE*, *9*(August), 623–630. Retrieved from http://sciencelinks.jp/j-east/display.php?id=000020070106A1035120

Maeda, Kenichi, Sakai, H., Kondo, A., Yamaguchi, T., Fukuma, M., & Nukudani, E. (2010). Stress-chain based micromechanics of sand with grain shape effect. *Granular Matter*, *12*(5), 499–505. https://doi.org/10.1007/s10035-010-0208-5

Mair, K., & Marone, C. (1999). Friction of simulated fault gouge for a wide range of velocities and normal stresses. *Journal of Geophysical Research: Solid Earth*, *104*(B12), 28899–28914. https://doi.org/10.1029/1999JB900279

Mair, K., Frye, K. M., & Marone, C. (2002). Influence of grain characteristics on the friction of granular shear zones. *Journal of Geophysical Research: Solid Earth*, *107*(B10), ECV 4-1-ECV 4-9. https://doi.org/10.1029/2001JB000516

Majer, E. L., Baria, R., Stark, M., Oates, S., Bommer, J., Smith, B., & Asanuma, H. (2007). Induced seismicity associated with Enhanced Geothermal Systems. *Geothermics*, *36*(3), 185–222. https://doi.org/10.1016/j.geothermics.2007.03.003

Majmudar, T. S., & Behringer, R. P. (2005). Contact force measurements and stress-induced anisotropy in granular materials, *435*(June), 1079–1082. https://doi.org/10.1038/nature03805

Marone, C. (1995). Fault zone strength and failure criteria. *Geophysical Research Letters*, *22*(6), 723–726. https://doi.org/10.1029/95GL00268

Marone, C. (1998). Laboratory-derived friction laws and their application to seismic faulting. *Annual Review of Earth Planetary Sciences*, *26*, 643–696.

Marone, C., & Kilgore, B. (1993). Scaling of the critical slip distance for seismic faulting with shear strain in

fault zones. *Letters to Nature*, *362*, 210–211. https://doi.org/10.1038/362618a0

Marone, C., & Scholz, C. H. (1988). The depth of seismic faulting and the upper transition from stable to unstable slip regimes. *Geopgysical Reschearch Letters*, *15*(8), 621–624. https://doi.org/10.1029/GL015i006p00621

Marone, C., & Scholz, C. H. (1989). Particle-size distribution and microstructures within simulated fault gouge. *Journal of Structural Geology*, *11*(7), 799–814. https://doi.org/10.1016/0191-8141(89)90099-0

Marone, C., Raleigh, C. B., & Scholz, C. H. (1990). Frictional behavior and constitutive modeling of simulated fault gouge. *Journal of Geophysical Research*, *95*(B5), 7007–7025. https://doi.org/10.1029/JB095iB05p07007

Marone, C., Hobbs, B. E., & Ord, A. (1992). Coulomb Constitutive Laws for Friction : Contrasts in Frictional Behavior for Distributed and Localized Shear. *Pageoph*, *139*(2). https://doi.org/10.1007/BF00876327

Maurer, W. C. (1965). Shear Failure of Rock Under Compression. *SPE J.*, *5*, 167–176. https://doi.org/10.2118/1054-PA

McBeck, J., Mair, K., & Renard, F. (2019). How Porosity Controls Macroscopic Failure via Propagating Fractures and Percolating Force Chains in Porous Granular Rocks. *Journal of Geophysical Research: Solid Earth*, *124*(9), 9920–9939. https://doi.org/10.1029/2019JB017825

McGarr, A., & Barbour, A. J. (2018). Injection-Induced Moment Release Can Also Be Aseismic. *Geophysical Research Letters*, *45*(11), 5344–5351. https://doi.org/10.1029/2018GL078422

McLaskey, G. C. (2019). Earthquake Initiation From Laboratory Observations and Implications for Foreshocks. *Journal of Geophysical Research: Solid Earth*, *124*(12), 12882–12904. https://doi.org/10.1029/2019JB018363

Mead, W. J. (1925). The Geologic Rôle of Dilatancy. *The Journal of Geology*, *33*(7), 685–698. https://doi.org/10.1086/623241

Menendez, B., Zhu, W., & Wong, T. (1996). Pergamon Micromechanics of brittle faulting and cataclastic flow in Berea sandstone. *Journal of Structural Geology*, *18*(l), 1–16.

Meng, F., Wong, L. N. Y., & Zhou, H. (2021). Rock brittleness indices and their applications to different fields of rock engineering: A review. *Journal of Rock Mechanics and Geotechnical Engineering*, *13*(1), 221–247. https://doi.org/10.1016/j.jrmge.2020.06.008

Michel, S., Gualandi, A., & Avouac, J. (2019). Similar scaling laws for earthquakes and Cascadia slow-slip events. *Nature*, *574*(August 2018). https://doi.org/10.1038/s41586-019-1673-6

Misra, S., Mandal, N., & Chakraborty, C. (2009). Formation of Riedel shear fractures in granular materials : Findings from analogue shear experiments and theoretical analyses. *Tectonophysics*, *471*(3–4), 253–259. https://doi.org/10.1016/j.tecto.2009.02.017

Mizoguchi, K., Hirose, T., Shimamoto, T., & Fukuyama, E. (2007). Reconstruction of seismic faulting by high-velocity friction experiments: An example of the 1995 Kobe earthquake. *Geophysical Research Letters*, *34*(1). https://doi.org/10.1029/2006GL027931

Molenaar, N., Cyziene, J., & Sliaupa, S. (2007). Quartz cementation mechanisms and porosity variation in Baltic Cambrian sandstones. *Sedimentary Geology*, *195*(3–4), 135–159. https://doi.org/10.1016/j.sedgeo.2006.07.009

Mollon, G. (2016). A multibody meshfree strategy for the simulation of highly deformable granular materials. *International Journal for Numerical Methods in Engineering*, *108*(12), 1477–1497. https://doi.org/10.1002/nme.5258

Mollon, G. (2018a). A unified numerical framework for rigid and compliant granular materials. *Computational Particle Mechanics*, *5*, 517–527. https://doi.org/10.1007/s40571-018-0187-6

Mollon, G. (2018b). Mixtures of hard and soft grains: micromechanical behavior at large strains. *Granular Matter*, *20*(39). https://doi.org/10.1007/s10035-018-0812-3

Mollon, G., & Zhao, J. (2012). Fourier-Voronoi-based generation of realistic samples for discrete modelling of

granular materials. *Granular Matter*, (5), 621–638. https://doi.org/10.1007/s10035-012-0356-x

Mollon, G., & Zhao, J. (2014). 3D generation of realistic granular samples based on random fields theory and Fourier shape descriptors. *Computer Methods in Applied Mechanics and Engineering*, *279*, 46–65. https://doi.org/10.1016/j.cma.2014.06.022

Mollon, G., Richefeu, V., Villard, P., & Daudon, D. (2012). Numerical simulation of rock avalanches: Influence of a local dissipative contact model on the collective behavior of granular flows. *Journal of Geophysical Research: Earth Surface*, *117*(2), 1–19. https://doi.org/10.1029/2011JF002202

Mollon, G., Quacquarelli, A., Andò, E., & Viggiani, G. (2020). Can friction replace roughness in the numerical simulation of granular materials? *Granular Matter*, *22*(42). https://doi.org/10.1007/s10035-020-1004-5

Mollon, G., Aubry, J., & Schubnel, A. (2021a). Reproducing laboratory earthquakes with a discrete-continuum model. *EPJ Web of Conferences - Powders and Grains 2021*, *249*, 1–4.

Mollon, G., Aubry, J., & Schubnel, A. (2021b). Simulating Melting in 2D Seismic Fault Gouge. *Journal of Geophysical Research: Solid Earth*, *126*(6), 1–19. https://doi.org/10.1029/2020JB021485

Moore, D. E., & Byerlee, J. D. (1992). Relationships between sliding behavior and internal geometry of laboratory fault zones and some creeping and locked strike-slip faults of California. *Tectonophysics*, *211*(1–4), 305–316. https://doi.org/10.1016/0040-1951(92)90067-G

Moore, D. E., Summers, R., & Byerlee, J. D. (1988). Sliding behavior and deformation textures of heated illite gouge, *I*(3).

Morgan, J. K. (1999). Numerical simulations of granular shear zones using the distinct element method: 2. Effects of particle size distribution and interparticle friction on mechanical behavior. *Journal of Geophysical Research: Solid Earth*, *104*(B2), 2721–2732. https://doi.org/10.1029/1998jb900055

Morgan, J. K., & Boettcher, M. S. (1999). Numerical simulations of granular shear zones using the distinct element method: 1. Shear zone kinematics and the micromechanics of localization. *Journal of Geophysical Research: Solid Earth*, *104*(B2), 2703–2719. https://doi.org/10.1029/1998jb900056

Munjiza, A., Bangash, T., & John, N. W. M. (2004). The combined finite-discrete element method for structural failure and collapse. *Engineering Fracture Mechanics*, *71*(4–6), 469–483. https://doi.org/10.1016/S0013-7944(03)00044-4

Muto, J., Nakatani, T., Nishikawa, O., & Nagahama, H. (2015). Fractal particle size distribution of pulverized fault rocks as a function of distance from the fault core. *Geophysical Research Letters*, *42*(10), 3811–3819. https://doi.org/10.1002/2015GL064026

Nielsen, S., Spagnuolo, E., Smith, S. A. F., Violay, M., Toro, G. Di, & Bistacchi, A. (2016). Scaling in natural and laboratory earthquakes. *Geophysical Research Letters*, *43*(2), 1504–1510. https://doi.org/10.1002/2015GL067490.1.

Niemeijer, A., & Spiers, C. (2005). Influence of phyllosilicates on fault strength in the brittle-ductile transition: Insights from rock analogue experiments. *Geological Society Special Publication*, *245*, 303–327. https://doi.org/10.1144/GSL.SP.2005.245.01.15

Niemeijer, A., Toro, G. Di, Nielsen, S., & Felice, F. Di. (2011). Frictional melting of gabbro under extreme experimental conditions of normal stress , acceleration , and sliding velocity. *Journal of Geophysical Research*, *116*(B07404). https://doi.org/10.1029/2010JB008181

Noel, C., Passelègue, F. X., & Violay, M. (2021). Brittle faulting of ductile rock induced by pore fluid pressure build-up. *Journal of Geophysical Research*. https://doi.org/10.1029/2020JB021331

Noël, C., Pimienta, L., & Violay, M. (2019). Time-Dependent Deformations of Sandstone During Pore Fluid Pressure Oscillations: Implications for Natural and Induced Seismicity. *Journal of Geophysical Research: Solid Earth*, *124*(1), 801–821. https://doi.org/10.1029/2018JB016546

Nouguier-lehon, C., Cambou, B., & Vincens, E. (2003). Influence of particle shape and angularity on the behaviour of granular materials : a numerical analysis. *International Journal for Numerical and Analytical Methods in Geomechanics*, *27*(14), 1207–1226. https://doi.org/10.1002/nag.314

Ogilvie, S. R., & Glover, P. W. J. (2001). The petrophysical properties of deformation bands in relation to their

microstructure. *Earth and Planetary Science Letters*, *193*(1–2), 129–142. https://doi.org/10.1016/S0012-821X(01)00492-7

Ohnaka, M. (2003). A constitutive scaling law and a unified comprehension for frictional slip failure , shear fracture of intact rock , and earthquake rupture, *108*, 1–21. https://doi.org/10.1029/2000JB000123

Ohnaka, M. (2013). *The physics of rock failure and earthquakes*. Cambridge University Press.

Okubo, K., Bhat, H. S., Rougier, E., Marty, S., Schubnel, A., Lei, Z., et al. (2019a). Dynamics, Radiation, and Overall Energy Budget of Earthquake Rupture With Coseismic Off-Fault Damage. *Journal of Geophysical Research: Solid Earth*, *124*(11), 11771–11801. https://doi.org/10.1029/2019JB017304

Okubo, K., Bhat, H. S., Rougier, E., Marty, S., Schubnel, A., Lei, Z., et al. (2019b). Dynamics, radiation and overall energy budget of earthquake rupture with coseismic off-fault damage, 1–41. Retrieved from http://arxiv.org/abs/1901.01771

Olgaard, D. L., & Brace, W. F. (1983). The microstructure of gouge from a mining-induced seismic shear zone. *International Journal of Rock Mechanics and Mining Sciences & Geomechanics*, *20*(1), 11–19. https://doi.org/10.1016/0148-9062(83)91610-8

Orellana, L. F., Scuderi, M. M., Collettini, C., & Violay, M. (2018). Do scaly clays control seismicity on faulted shale rocks? *Earth and Planetary Science Letters*, *488*, 59–67. https://doi.org/10.1016/j.epsl.2018.01.027

Otsuki, K., Monzawa, N., & Nagase, T. (2003). Fluidization and melting of fault gouge during seismic slip: Identification in the Nojima fault zone and implications for focal earthquake mechanisms. *Journal of Geophysical Research: Solid Earth*, *108*(B4). https://doi.org/10.1029/2001JB001711

Paglialunga, F., Passelègue, F., Brantut, N., Barras, F., Lebihain, M., & Violay, M. (2021). On the scale dependence in the dynamics of frictional rupture : constant fracture energy versus size-dependent breakdown work. *Preprint in Earth and Planetary Science Letters*, 1–33.

Passelègue, F. X., Schubnel, A., Nielsen, S., Bhat, H. S., & Madariaga, R. (2013). From sub-Rayleigh to supershear ruptures during stick-slip experiments on crustal rocks. *Science*, *340*(6137), 1208–1211. https://doi.org/10.1126/science.1235637

Passelègue, F. X., Aubry, J., Nicolas, A., Fondriest, M., Deldicque, D., Schubnel, A., & Di Toro, G. (2019). From fault creep to slow and fast earthquakes in carbonates. *Geology*, *47*(8), 744–748. https://doi.org/10.1130/G45868.1

Perrin, G., Rice, J. R., & Zheng, G. (1995). Self-Healing Slip Pulse. *Journal of the Mechanics and Physics of Solids*, *43*(9), 1461–1495. https://doi.org/0022.-5096/95 $9.50+0.000

Philit, S. (2017). *Elaboration d'un modèle structural, pétrophysique et mécanique des failles en milieu gréseux poreux; implication pour la migration et le piégeage des fluides*.

Philit, S., Soliva, R., Castilla, R., Ballas, G., & Taillefer, A. (2018). Clusters of cataclastic deformation bands in porous sandstones. *Journal of Structural Geology*, *114*, 235–250. https://doi.org/10.1016/j.jsg.2018.04.013

Potyondy, D. O. (2012). A flat-jointed bonded-particle material for hard rock. In *46th US rock mechanics/geomechanics symposium*. American Rock Mechanics Association.

Potyondy, D. O., & Cundall, P. A. (2004). A bonded-particle model for rock. *International Journal of Rock Mechanics and Mining Sciences*, *41*(8), 1329–1364. https://doi.org/10.1016/j.ijrmms.2004.09.011

Pouliquen, O. (2011). Granular Flow. In B. Duplantier, T. Halsey, & V. Rivasseau (Eds.), *Glassses and Grains. Progress in Mathematical Physics, vol 61* (pp. 77–109). Springer. https://doi.org/10.1007/978-3-0348-0084-6_4

Pouliquen, O., & Forterre, Y. (2002). Friction law for dense granular flows: application to the motion of a mass down a rough inclined plane. *Journal of Fluid Mechanics*, *453*, 133–151. https://doi.org/10.1017/S0022112001006796

Pouliquen, O., Cassar, C., Jop, P., Forterre, Y., & Nicolas, M. (2006). Flow of dense granular material: Towards simple constitutive laws. *Journal of Statistical Mechanics: Theory and Experiment*, (7). https://doi.org/10.1088/1742-5468/2006/07/P07020

Rabinowicz, E. (1951). The nature of the static and kinetic coefficients of friction. *Journal of Applied Physics*, *22*(11), 1373–1379. https://doi.org/10.1063/1.1699869

Rad, N. S., & Clough, G. W. (1982). Influence of Cementation on the Static and Dynamic Behavior of Sands. *Report - Stanford University, John A. Blume Earthquake Engineering Center*, (59).

Radjai, F., Jean, M., Moreau, J., & Roux, S. (1996). Force Distributions in Dense Two-Dimensional Granular Systems. *Physical Review Letters, American Physical Society*, *77*, 274–277. https://doi.org/10.1103/PhysRevLett.77.274

Radjai, F., Radjai, F., & Moreau, J. J. (1999). Contact forces in a granular packing. *Chaos: An Interdisciplinary Journal of Nonlinear Science, American Institute of Physics*, *9*(544), 0–7.

Rathbun, A. P., Renard, F., & Abe, S. (2013). Numerical investigation of the interplay between wall geometry and friction in granular fault gouge. *Journal of Geophysical Research: Solid Earth*, *118*(3), 878–896. https://doi.org/10.1002/jgrb.50106

Reches, Z., & Lockner, D. A. (2010). Fault weakening and earthquake instability by powder lubrication. *Nature*, *467*(7314), 452–455. https://doi.org/10.1038/nature09348

Rice, J. R. (1983). Constitutive Relations for fault slip and earthquake instabilities. *Pageoph*, *121*(3), 443–475.

Rice, J. R. (2006). Heating and weakening of faults during earthquake slip. *Journal of Geophysical Research: Solid Earth*, *111*(5), 1–29. https://doi.org/10.1029/2005JB004006

Rice, J. R., & Cocco, M. (2002). Seismic Fault Rheology and Earthquake Dynamics. *Journal of Geophysical Research*, *107*, 1000–1029.

Rice, J. R., & Rudnicki, J. W. (1979). Earthquake Precursory Effects Due to Pore Fluid Stabilization of a Weakening Fault Zone. *Journal of Geophysical Research*, *84*(B5), 2177–2193.

Rice, J. R., & Ruina, A. L. (1983). Stability of Steady Frictional Slipping. *Journal of Applied Mechanics*, *50*(2), 343. https://doi.org/10.1115/1.3167042

Riedmüller, B. G., Brosch, F. J., Klima, K., & Medley, E. W. (2001). Engineering Geological Characterization of Brittle Faults and classification of fault rocks. *Engineering Geology*, *19*(April), 13–19.

Rivera, L., & Kanamori, H. (2005). Representations of the radiated energy in earthquakes. *Geophysical Journal International*, *162*(1), 148–155. https://doi.org/10.1111/j.1365-246X.2005.02648.x

Rognon, P. G., Roux, J. N., Naaïm, M., & Chevoir, F. (2008). Dense flows of cohesive granular materials. *Journal of Fluid Mechanics*, *596*, 21–47. https://doi.org/10.1017/S0022112007009329

Rowe, P. W. (1962). The stress-dilatancy relation for static equilibrium of an assembly of particles in contact. *F.R.S*, *269*(1339). https://doi.org/https://doi.org/10.1098/rspa.1962.0193

Roy, S., & Luding, S. (2017). Effect of cohesion on local compaction and granulation of sheared soft granular materials. *Powders&Grains*, *03065*, 2–5. https://doi.org/10.1051/epjconf/201714003065

Ruina, A. (1983). 1983_slip_instability_RUINA.pdf. *Journal of Geophysical Research*, *88*(B12), 10,359-10,370.

Rutter, E. H., Maddock, R. H., Hall, S. H., & White, S. H. (1986). Comparative microstructures of natural and experimentally produced clay-bearing fault gouges. *Pure and Applied Geophysics PAGEOPH*, *124*(1–2), 3–30. https://doi.org/10.1007/BF00875717

Sammis, C. G., & Biegel, R. (1989). Fractals, Fault-Gouge, and Friction. *Pure and Applied Geophysics*, *131*, 255–271. https://doi.org/10.1007/BF00874490

Sammis, C. G., Osborne, R. H., Anderson, J. L., Banerdt, M., & White, P. (1986). Self-similar cataclasis in the formation of fault gouge. *Pure and Applied Geophysics PAGEOPH*, *124*(1–2), 53–78. https://doi.org/10.1007/BF00875719

Sammis, C. G., King, G., & Biegel, R. (1987). The kinematics of gouge deformation. *Pure and Applied Geophysics*, *125*, 777–812. https://doi.org/10.1007/BF00878033

Sandeep, C. S., & Senetakis, K. (2019). An experimental investigation of the microslip displacement of geological materials. *Computers and Geotechnics*, *107*(June 2018), 55–67.

https://doi.org/10.1016/j.compgeo.2018.11.013

Schellart, W. P. (2000). Shear test results for cohesion and friction coe ffi cients for di ff erent granular materials : scaling implications for their usage in analogue modelling. *Tectonophysics*, *324*(l–2), 1–16. https://doi.org/10.1016/S0040-1951(00)00111-6

Schmocker, M., Bystricky, M., Kunze, K., Burlini, L., Stünitz, H., & Burg, J.-P. (2003). Granular flow and Riedel band formation in water-rich quartz aggregates experimentally deformed in torsion. *Journal of Geophysical Research: Solid Earth*, *108*(B5), 1–16. https://doi.org/10.1029/2002jb001958

Scholz, C. H. (1987). Wear and gouge formation in brittle faulting. *Geology*, *15*(6), 493–495. https://doi.org/10.1130/0091-7613(1987)15<493:WAGFIB>2.0.CO;2

Scholz, C. H. (2002). *The Mechanics of Earthquakes and Faulting*, *second edition* (Cambridge). https://doi.org/10.2113/gseegeosci.13.1.81

Scholz, C. H. (2019). *The Mechanics of Earthquakes and Faulting 3rd Edition*. Cambridge University Press. https://doi.org/10.1017/9781316681473

Scholz, C. H., & Engelder, J. T. (1976). The role of asperity indentation and ploughing in rock friction. Part 1: asperity creep and stick-slip. *International Journal of Rock Mechanics and Mining Sciences & Geomechanics*, *13*, 149–154. https://doi.org/10.1016/0148-9062(76)91557-6

Scholz, C. H., Molnar, P., & Johnson, T. (1972). Detailed studies of frictional sliding of granite and implications for the earthquake mechanism. *Journal of Geophysical Research*, *77*(32), 6392–6406. https://doi.org/10.1029/jb077i032p06392

Schöpfer, M. P. J., Abe, S., Childs, C., & Walsh, J. J. (2009). The impact of porosity and crack density on the elasticity, strength and friction of cohesive granular materials: Insights from DEM modelling. *International Journal of Rock Mechanics and Mining Sciences*, *46*(2), 250–261. https://doi.org/10.1016/j.ijrmms.2008.03.009

Scuderi, M. M., & Collettini, C. (2016). The role of fluid pressure in induced vs. triggered seismicity: Insights from rock deformation experiments on carbonates. *Scientific Reports*, *6*(April), 1–9. https://doi.org/10.1038/srep24852

Scuderi, M. M., Carpenter, B. M., & Marone, C. (2014). Physicochemical processes of frictional healing: Effects of water on stick-slip stress drop and friction of granular fault gouge. *Journal of Geophysical Research: Solid Earth*, *119*, 4090–4105. https://doi.org/10.1002/ 2013JB010641

Shi, H., Roy, S., Weinhart, T., Magnanimo, V., & Luding, S. (2020). Steady state rheology of homogeneous and inhomogeneous cohesive granular materials. *Granular Matter*, *22*(1), 1–20. https://doi.org/10.1007/s10035-019-0968-5

Sibson, R. H. (1977). Fault rocks and fault mechanisms. *Journal of the Geological Society*, *133*(3), 191–213. https://doi.org/10.1144/gsjgs.133.3.0191

Sibson, R. H. (1986). Brecciation processes in fault zones: Inferences from earthquake rupturing. *Pure and Applied Geophysics PAGEOPH*, *124*(1–2), 159–175. https://doi.org/10.1007/BF00875724

Sibson, R. H. (2003). Thickness of the Seismic Slip Zone, *93*(3), 1169–1178.

Snoke, A. W., Tullis, J., & Todd, V. R. (1998). *Fault-related rocks: a photographic atlas* (Vol. 410). Princeton University Press.

Sone, H., & Shimamoto, T. (2009). Frictional resistance of faults during accelerating and decelerating earthquake slip. *Nature Geoscience*, *2*(10), 705–708. https://doi.org/10.1038/ngeo637

Spikes, H. A. (1997). Mixed lubrication - An overview. *Lubrication Science*, *9*(3), 221–253. https://doi.org/10.1002/ls.3010090302

Stefanou, I. (2020). Control instabilities and incite slow-slip in generalized Burridge-Knopoff models, 1–31. Retrieved from http://arxiv.org/abs/2008.03755

Stesky, R. M., Brace, W. F., Riley, D. K., & Robin, P. Y. F. (1974). Friction in faulted rock at high temperature and pressure. *Tectonophysics*, *23*(1–2), 177–203. https://doi.org/10.1016/0040-1951(74)90119-X

Talebi, S., & Cornet, F. H. (1987). Analysis of the microseismicity induced by a fluid injection in a granitic rock mass. *Geophysical Research Letters*, *14*(3), 227–230.

Taylor, D. W. (1948). *Fundamentals of Soil Mechanics*. (J. W. & Sons, Ed.). London - CHAPMAN & HALL, Limited.

Tchalenko, J. S. (1970). Similarities between shear zones of different magnitudes. *Geological Society Of America Bulletin*, *81*(6), 1625–1640. https://doi.org/10.1130/0016-7606(1970)81[1625:SBSZOD]2.0.CO;2

Tomac, I., & Gutierrez, M. (2020). Micromechanics of hydraulic fracturing and damage in rock based on DEM modeling. *Granular Matter*, *22*(3), 1–17. https://doi.org/10.1007/s10035-020-01023-z

Topin, V. (2009). *Matériaux granulaires cimentés : modélisation et application à l ' albumen de blé*.

Topin, V., Delenne, J. Y., Radjai, F., Brendel, L., & Mabille, F. (2007). Strength and failure of cemented granular matter. *European Physical Journal E*, *23*(4), 413–429. https://doi.org/10.1140/epje/i2007-10201-9

Di Toro, G., Pennacchioni, G., & Nielsen, S. (2009). *Pseudotachylytes and earthquake source mechanics*. *International Geophysics* (Vol. 94). https://doi.org/10.1016/S0074-6142(08)00005-3

Di Toro, G., Han, R., Hirose, T., Paola, N. De, Nielsen, S., Mizoguchi, K., et al. (2011). Fault lubrication during earthquakes. *Nature*, *471*, 494–498. https://doi.org/10.1038/nature09838

Trouw, R. A. J., Passchier, C. W., & Wiersma, D. J. (2009). *Atlas of Mylonites-and related microstructures*. Springer Science & Business Media.

Uyeda, S. (1978). *The new view of the Earth*. Sa Francisco: WH Freeman.

Vardoulakis, I., & Graf, B. (1985). Calibration of constitutive models for granular materials using data from biaxial experiments. *Géotechnique*, *35*(3), 299–317.

Violay, M., Gibert, B., Mainprice, D., Evans, B., Dautria, J. M., Azais, P., & Pezard, P. (2012). An experimental study of the brittle-ductile transition of basalt at oceanic crust pressure and temperature conditions. *Journal of Geophysical Research: Solid Earth*, *117*(3), 1–23. https://doi.org/10.1029/2011JB008884

Violay, M., Nielsen, S., Spagnuolo, E., Cinti, D., Di Toro, G., & Di Stefano, G. (2013). Pore fluid in experimental calcite-bearing faults: Abrupt weakening and geochemical signature of co-seismic processes. *Earth and Planetary Science Letters*, *361*, 74–84. https://doi.org/10.1016/j.epsl.2012.11.021

Violay, M., Nielsen, S., Gibert, B., Spagnuolo, E., Cavallo, A., Azais, P., et al. (2014). Effect of water on the frictional behavior of cohesive rocks during earthquakes. *Geology*, *42*(1), 27–30. https://doi.org/10.1130/G34916.1

Voisin, Y. (2020). *Savoirs et politiques de la sismicité induite en France (Master Thesis)*. Université de Lyon - INSA Lyon.

Walderhaug, O. (1994). Precipitation rates for quartz cement in sandstones determined by fluid-inclusion microthermometry and temperature-history modeling. *Journal of Sedimentary Research A: Sedimentary Petrology & Processes*, *64 A*(2), 324–333. https://doi.org/10.2110/jsr.64.324

Wang, C., Elsworth, D., & Fang, Y. (2019). Ensemble Shear Strength , Stability , and Permeability of Mixed Mineralogy Fault Gouge Recovered From 3D Granular Models Journal of Geophysical Research : Solid Earth, 425–441. https://doi.org/10.1029/2018JB016066

Wang, D., Carmeliet, J., Zhou, W., & Dorostkar, O. (2021). On the effect of grain fragmentation on frictional instabilities in faults with granular gouge. *Journal of Geophysical Research: Solid Earth*, *126*. https://doi.org/10.1029/2020jb020510

Wangen, M. (1999). Modelling quartz cementation of quartzose sandstones. *Basin Research*, *11*(2), 113–126. https://doi.org/10.1046/j.1365-2117.1999.00091.x

Wangen, Magnus. (1998). Modeling porosity evolution and cementation of sandstones. *Marine and Petroleum Geology*, *15*(5), 453–465. https://doi.org/10.1016/S0264-8172(98)00026-9

Wibberley, C. A. J., & Shimamoto, T. (2003). Internal structure and permeability of major strike-slip fault zones:

the Median Tectonic Line in Mie Prefecture, Southwest Japan, *25*. https://doi.org/10.1016/S0191-8141(02)00014-7

Wibberley, C. A. J., Yielding, G., & Di Toro, G. (2008). Recent advances in the understanding of fault zone internal structure: a review. *Geological Society, London, Special Publications*, *299*(1), 5–33. https://doi.org/10.1144/SP299.2

Wilson, M. P., Foulger, G. R., Gluyas, J. G., Davies, R. J., & Julian, B. R. (2017). HiQuake: The human-induced earthquake database. *Seismological Research Letters*, *88*(6), 1560–1565. https://doi.org/10.1785/0220170112

Wise, D. U., Dunn, D. E., Engelder, T., Geiser, P. A., Hatcher, R. D., Kish, S. A., et al. (1985). Fault-related rocks: Suggestions for terminology. *Geology*, *13*(3), 218. https://doi.org/10.1130/0091-7613(1985)13<218b:CAROFB>2.0.CO;2

Wissa, A. E. Z. (1965). *Effective stress-strength behavior of cemented soils (Thesis (Sc D.))*. Massachusetts institute of technology.

Wojatschke, J., Scuderi, M. M., Warr, L. N., Carpenter, B. M., Saffer, D., & Marone, C. (2016). Geochemistry, Geophysics, Geosystems. *AGU Publications - Geochemistry Geophysics Geosystems*, *17*, 4641–4668. https://doi.org/10.1002/2016GC006500.Received

Wood, D. M. (1990). *Soil behaviour and critical state soil Mechanics*. (Cambridge university Press, Ed.). https://doi.org/10.1201/9781351255400-1

Woodcock, N. H., & Mort, K. (2008). Classification of fault breccias and related fault rocks. *Geological Magazine*, *145*(3), 435–440. https://doi.org/10.1017/S0016756808004883

Wyss, M. (1970). Apparent Stresses of Earthquakes on Ridges compared to Apparent Stresses of Earthquakes in Trenches. *Geophysical Journal of the Royal Astronomical Society*, *19*(5), 479–484. https://doi.org/10.1111/j.1365-246X.1970.tb00153.x

Zhang, L., Nguyen, N. G. H., Lambert, S., Nicot, F., Prunier, F., & Djeran-Maigre, I. (2017). The role of force chains in granular materials: from statics to dynamics. *European Journal of Environmental and Civil Engineering*, *21*(7–8), 874–895. https://doi.org/10.1080/19648189.2016.1194332

Zhao, Z. (2013). Gouge particle evolution in a rock fracture undergoing shear: A microscopic DEM study. *Rock Mechanics and Rock Engineering*, *46*(6), 1461–1479. https://doi.org/10.1007/s00603-013-0373-z

Zhao, Z., Jing, L., & Neretnieks, I. (2012). Particle mechanics model for the effects of shear on solute retardation coefficient in rock fractures. *International Journal of Rock Mechanics and Mining Sciences*, *52*, 92–102. https://doi.org/10.1016/j.ijrmms.2012.03.001

Zhou, W., Yang, L., Ma, G., Xu, K., Lai, Z., & Chang, X. (2017). DEM modeling of shear bands in crushable and irregularly shaped granular materials. *Granular Matter*, *19*(2), 1–12. https://doi.org/10.1007/s10035-017-0712-y

FOLIO ADMINISTRATIF

THESE DE L'UNIVERSITE DE LYON OPEREE AU SEIN DE L'INSA LYON

NOM : **CASAS** DATE de SOUTENANCE : 10/05/2022

Prénoms : **Nathalie**

TITRE :

Insights on the behavior of fault gouges during seismic sliding: a numerical investigation from granular rheology to friction laws

NATURE : Doctorat Numéro d'ordre : 2022LYSEI040

Ecole doctorale : **MEGA**

Spécialité : **Mécanique**

RESUME : La gouge de faille, créée par l'usure des précédents glissements, joue un rôle prépondérant dans la stabilité des glissements et les mécanismes d'affaiblissement d'une faille. A cela peuvent s'ajouter des transformations physico-chimiques telles que la dissolution ou encore la fusion à haute température. Ces dernières peuvent donner naissance à des matériaux de remplissage se logeant dans les pores de la gouge et impactant le comportement mécanique et rhéologique de la faille. Au cours de ce travail de thèse, des modèles 2D (Méthode des Eléments Discrets) de gouges cisaillées ont été proposés pour mieux comprendre : (i) comment les matériaux de remplissage (matrice, ciment) participent à l'affaiblissement de la faille lors d'une réactivation de glissement, (ii) le comportement rhéologique observé à travers la formation de bandes de cisaillement et son lien avec les caractéristiques physiques et mécaniques des gouges, (iii) la contribution de chacune de ces propriétés dans l'énergie de rupture et les lois de frottement observées. Un premier modèle met en avant trois types de matériaux cimentés montrant des comportements rhéologiques et de résistance aux glissements différents en fonction du pourcentage surfacique de cimentation. Cette étude donne lieu à un nouveau découpage de l'énergie de fracture considérant trois mécanismes : la dilatance de la faille, les frottements de Coulomb et la rupture des liaisons cimentées. Ensuite, un matériau uniquement constitué de l'élément « matrice » est modélisé pour mettre en évidence la relation entre les propriétés intrinsèques de la matrice et son comportement rhéologique. L'importance du pourcentage de matrice présent dans la gouge est évaluée dans un 3ème modèle. Nous détaillons finalement une méthode énergétique permettant de relier l'évolution de chaque bande de déformation avec le comportement de la gouge entière. Les lois de frottement issues de ces modèles pourront être utilisées dans des modèles dynamiques à plus grande échelle.

MOTS-CLÉS : **Fault mechanics, Granular materials, Tribology, Modelling & Simulations**

Laboratoire (s) de recherche : Laboratoire de mécanique des Contacts et des Structures (**LaMCoS)** et Laboratoire de Géomécanique, Matériaux, Structures (**GEOMAS**), **INSA Lyon**

Directeur de thèse : **Pr. Ali Daouadji (directeur)** et **Dr. Guilhem Mollon (co-directeur)**

Président de jury : **François NICOT**

Composition du jury :

Chris MARONE,	Professor, La Sapienza – Italy	Rapporteur
Farhang RADJAÏ,	Directeur de Recherche CNRS – Montpellier	Rapporteur
Marie VIOLAY,	Assistant Professor, EPFL – Switzerland	Examinatrice
Julia K. MORGAN,	Professor, Rice university – US	Examinatrice
Elsa BAYART,	Chargée de Recherche CNRS- Lyon	Examinatrice
François NICOT,	Professor, Université Savoie Mont Blanc	Examinateur
Ali DAOUADJI,	Professor, INSA Lyon	Directeur de thèse
Guilhem MOLLON,	Maitre de Conférence, INSA Lyon	Co-directeur de thèse
Arnold BLAISONNEAU,	Docteur, BRGM-Paris	Invité